IGCAR

Excellence with Relevance

High Impact Breakthroughs

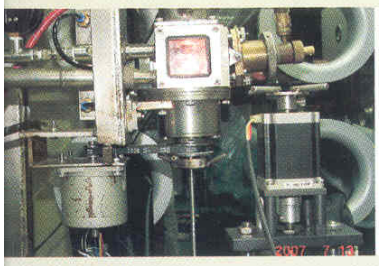




Significant Achievements

2004-2007

A Mission Centre with Science based Technology

IGCAR

Excellence with Relevance

High Impact Breakthroughs 2004-2007



Government of India
Department of Atomic Energy
Indira Gandhi Centre for Atomic Research
Kalpakkam-603 102.

Foreword



IGCAR - A Mission Centre with Science based Technology

High Impact Breakthroughs 2004-2007

IGCAR has been actively engaged in mastering Fast Reactor and associated Fuel Cycle technologies. Fast Breeder Test Reactor (FBTR), which is the flagship of IGCAR, is performing excellently with very high availability factors. The unique high plutonium content uranium-plutonium mixed carbide fuel has crossed a burn-up of 155 GWd/t without any fuel pin failure which is an international benchmark. The construction of Prototype Fast Breeder Reactor (PFBR) is progressing as per the schedule and IGCAR continues to provide robust design and technology support for construction and regulatory clearances for PFBR. Mixed carbide fuel of FBTR irradiated up to 155 GWd/t has been successfully reprocessed at the CORAL facility at IGCAR. Work on Demonstration Fuel Reprocessing Plant (DFRP) designed for reprocessing irradiated FBTR fuel on regular basis and demonstrating the reprocessing of irradiated mixed oxide of PFBR is progressing well. The work on Integrated Fast Reactor Fuel Cycle Facility (FRFCF) co-located with the PFBR plant is progressing well and is a significant step towards attaining leadership in the closing of the nuclear fuel cycle. The Centre has embarked on design of four more fast breeder reactors with emphasis on enhanced safety features, reduced cost per unit power production and high breeding with innovative metallic fuels.

In this journey of excellence, the Centre has achieved several scientific and technological milestones with international benchmarks and high impact on our mission programme. These milestones have high relevance to science based technology, being pursued at our Centre. A compendium of such benchmarks for the last three years (April 2004 to March 2007) has been prepared.

This compendium is a step in the direction of introspection by the Centre. This exercise gives assurance that the journey towards the excellence is progressing well. To quote Robert Frost "*The woods are lovely, dark and deep, But I have promises to keep, and miles to go before I sleep*" and we take this opportunity to rededicate ourselves to set new benchmarks and work towards realizing the goal of "Energy security through fast reactors with closed fuel cycle". Enhancing quality and commitment of Human Resources is the key to our strategy of achieving and sustaining excellence. We believe in innovations in management of Science and Technology for enhancing our focus, creativity and productivity.

I would like to compliment, Dr. M. Sai Baba and Dr. Vidya Sundararajan, who have worked with dedication and imagination to bring out this unique compendium.

(Baldev Raj)
Director
IGCAR

Editorial

IGCAR- A Mission Centre with Science based Technology

High Impact Breakthroughs
2004- 2007

The mission of our Centre is: "To conduct a broad based multidisciplinary programme of scientific research and advanced engineering development, directed towards the establishment of the technology of Sodium Cooled Fast Breeder Reactors (FBR) and associated fuel cycle facilities in the country". Our vision is "To be a Global Leader in Sodium cooled Fast Breeder Reactors and associated Fuel Cycle Technologies by 2020". We believe that great heights in technology can be attained only by scientific breakthroughs and innovations. This also needs a seamless interface between science and technology in a multidisciplinary Centre like ours. Inspired by the suggestion of Dr. Baldev Raj, we embarked on preparing a compendium of milestones of high relevance to the mission of the Centre. We sought contributions from various groups, which fall into either of the following categories: (i) breakthroughs in technology and basic science (ii) technological milestones of high relevance to the Centre (iii) milestones of high relevance to the Centre in basic science & (iv) research in basic science of high impact. We have received a large number of contributions from various groups of the Centre and put them through a rigorous reviewing process for identifying the contributions for this compendium. The significant achievements of the centre for the last three years (April 2004 to March 2007) is prepared and being presented in this compendium. The contributions have been classified into those belonging to science, engineering and technology. Amongst the contributions; 54 articles are categorized as benchmarks in Science, 28 in Engineering and 27 in Technology. The articles for the compendium have been written highlighting the salient features of the contribution. Groupwise contributions are also indicated in the charts. The contributions have resulted in about 150 publications in peer-reviewed journals and seven patents. Several of them also formed basis of design and project decisions.

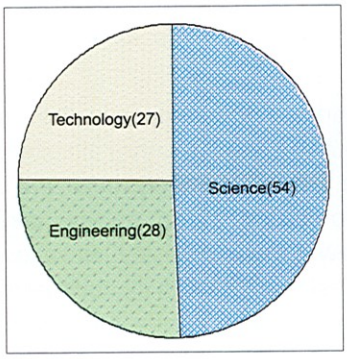

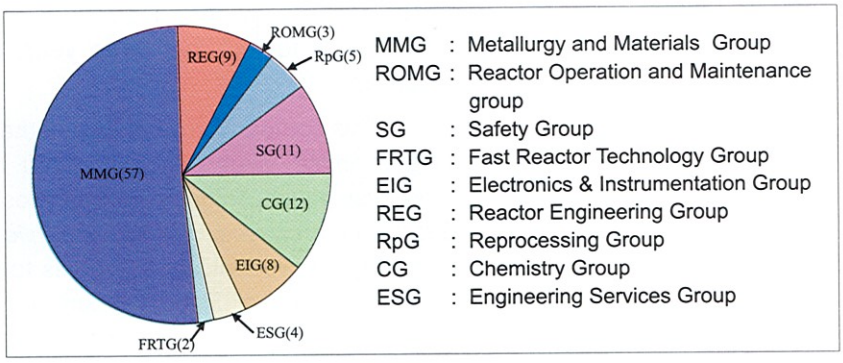

We are grateful to Dr. Baldev Raj, Director, IGCAR, who has been a constant source of encouragement and inspiration for us in bringing out this compendium. We thank him for going through the compendium and giving valuable suggestions for improving the quality of the compilation. We take this opportunity to thank all the Group Directors and colleagues of the Centre for their efforts and contributions in bringing out this compendium. It is a pleasure to acknowledge some of our friends who have helped us in editorial work in bringing out this compendium.

M. Sai Baba

Vidya Sundararajan

Contributions

IGCAR - A Mission Centre with Science based Technology

Science

MMG : Metallurgy and Materials Group
MSD : Materials Science Division (MMG)
REG : Reactor Engineering Group
ROMG: Reactor Operation and Maintenance group
RpG : Reprocessing Group
SG : Safety Group
CG : Chemistry Group

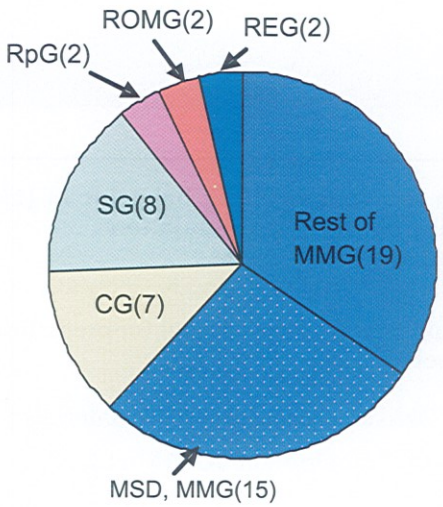

Engineering

MMG : Metallurgy and Materials Group
REG : Reactor Engineering Group
ROMG: Reactor Operation and Maintenance group
RpG : Reprocessing Group
SG : Safety Group
CG : Chemistry Group
FRTG : Fast Reactor Technology Group
ESG : Engineering Services Group
EIG : Electronics & Instrumenation Group

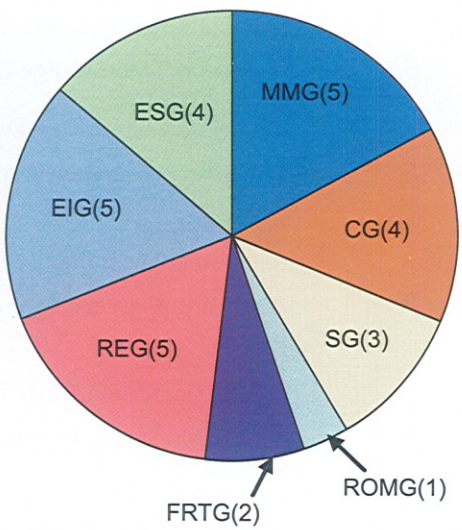

Technology

MMG : Metallurgy and Materials Group
REG : Reactor Engineering Group
RpG : Reprocessing Group
CG : Chemistry Group
EIG : Electronics & Instrumenation Group

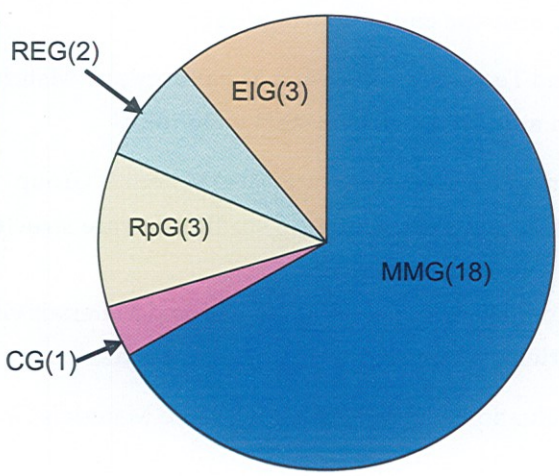

IGCAR – A Mission Centre with Science based Technology

High Impact Breakthroughs 2004-2007

Contents

SCIENCE

S.No.	Title	Page No.
1.	**Effect of titanium on the void swelling behavior in (15 Ni-14Cr)-Ti modified austenitic steels studied by ion beam simulation** Dr. B. K. Panigrahi and Dr. K.G.M.Nair, Materials Science Division, Metallurgy and Materials Group	2
2.	**A finite element method based process model for prediction of Spring back during forming of PFBR vessels** Shri Utpal Borah, Materials Technology Division, Metallurgy and Materials Group	4
3.	**Study of Ductile –Brittle Transition of 9Cr-1Mo Steels** Dr. Aniruddha Moitra, Materials Technology Division, Metallurgy and Materials Group	6
4.	**Prediction of ferrite number in stainless steel welds** Dr. M. Vasudevan, Materials Technology Division, Metallurgy and Materials Group	8
5.	**A new critical damage criterion for creep** Dr. C. Phaniraj, Materials Technology Division, Metallurgy and Materials Group	10
6.	**The effect of dynamic sodium on the cycle fatigue properties of 316L(N) Stainless steel** Dr. R. Sandhya, Mechanical Metallurgy Division, Metallurgy and Materials Group	12
7.	**High temperature low cycle fatigue of 316L(N) Stainless steel, welds and weld joints** Dr. M. Valsan, Mechanical Metallurgy Division, Metallurgy and Materials Group	14
8.	**Low cycle fatigue and creep-fatigue interaction of modified 9Cr-1Mo Steel weldments** Dr. M. Valsan, Mechanical Metallurgy Division, Metallurgy and Materials Group	16
9.	**Surface modification of Titanium to control microbial fouling** Dr.P.Muralidharan, Corrosion Science and Technology Division, Metallurgy and Materials Group	18
10.	**Evaluation of stress corrosion cracking phenomenon in an AISI type 316LN stainless steel using acoustic emission technique** Shri Hasan Sheikh, Corrosion Science and Technology Division, Metallurgy and Materials Group	20
11.	**Type IV cracking in modified 9Cr-1Mo steel weld joint** Dr. K. Laha, Mechanical Metallurgy Division, Metallurgy and Materials Group	22
12.	**Mechanical properties and microstructure studies on core structural material of Fast Breeder Test Reactor** Shri N.G.Muralidharan, Post Irradiation Examination Division, Metallurgy and Materials Group	24
13.	**Magnetic Nano particles with tunable physical properties** Dr. John Philip, Non Destructive Evaluation Division, Metallurgy and Materials Group	26

S.No.	Title	Page No.
14.	**Phase stability characterization and thermodynamic data generation on 9Cr-1Mo steel with varied microstructure-based on experimental measurements and modeling** Shri S. Raju and Shri E. Mohandas, Physical Metallurgy Division, Metallurgy and Materials Group	28
15.	**Micro chemical and micro structural variations across dissimilar joints** Dr. M. Vijayalakshmi, Physical Metallurgy Division, Metallurgy and Materials Group	30
16.	**Quasi Isoperibol actinide calorimeter** Dr. T. G. Srinivasan, Fuel Chemistry Division, Chemistry Group	32
17.	**Matrix isolation infrared spectroscopy: A window to understanding the chemistry of solvent extraction** Dr. K. S. Viswanathan, Materials Chemistry Division, Chemistry Group	34
18.	**Thermochemical behaviour of oxygen in lead, bismuth and lead-bismuth eutectic (LBE) alloy** Dr. T. Gnanasekaran, Liquid Metals and Structural Chemistry Division, Chemistry Group	36
19.	**Proton exchange membrane based compact hydrogen sensor** Dr. V. Ganesan, Material Chemistry Division, Chemistry Group	38
20.	**Prediction of long term diffusion behavior of chloride in concrete** Dr. Saroja Saibaba, Physical Metallurgy Division, Metallurgy and Materials Group	40
21.	**Method to identify the damage of concrete due to sodium fire** Shri K. Sivasubramanian and Shri N. Kasinathan, Safety Engineering Division, Safety Group	42
22.	**Atmospheric dispersion of sodium aerosol** Smt.G.Punitha and Shri N.Kasinathan, Safety Engineering Division, Safety Group	44
23.	**Biomarkers of radiation quality, dose-rate and (cancer) risk** Dr. R. K. Jeevanram and Dr.Mary N. Mohankumar, Radiological Safety Division, Safety Group	46
24.	**Characterization of aerosols for the fast Reactor safety studies** Dr. R. Baskaran and Shri V. Subramanian, Radiological Safety Division, Safety Group	48
25.	**Studies on physics parameters of metal (U-Pu-Zr) fuelled FBR cores** Shri A. Riyas and Dr. P.Mohanakrishnan, Reactor Physics Division, Reactor Engineering Group	50
26.	**Kalpakkam MINI(KAMINI)reactor :beryllium-oxide-reflected ^{233}U-fueled reactor** Dr. C. P. Reddy, Technical Service Division, Reactor Operation and Maintenance Group	52
27.	**Rapid in-situ monitoring of radio nuclides in a postulated post-accident scenario** Dr. V. Meenakshisundaram, Radiological Safety Division, Safety Group	54
28.	**Studies on radon exhalation** Dr. V. Meenakshisundaram, Radiological Safety Division, Safety Group	56
29.	**Advances in thermo luminescence and imaging phosphors** Dr.M.T.Jose and Dr.U. Madhusoodanan, Radiological Safety Division, Safety Group	58
30.	**Development of a Fast Reactor core burn up code FARCOB** Dr P. Mohanakrishnan, Reactor Physics Division, Reactor Engineering Group	60

S.No.	Title	Page No.
31.	**Development of a reflectron time-of-flight mass spectrometer for non-destructive analysis of isotope ratios in irradiated B_4C pellets** Dr. T. G. Srinivasan, Fuel Chemistry Division, Chemistry Group	62
32.	**Contact resonance imaging using Atomic Force Microscopy** Dr. S. Banerjee and Dr. A. K. Tyagi, Materials Science Division, Metallurgy and Materials Group	64
33.	**Hydro-dynamical phenomena during laser welding** Dr. N. Kumar, Dr. A.K. Tyagi and Dr. S. Dash, Materials Science Division, Metallurgy and Materials Group	66
34.	**Effect of C/N ratio on the microstructure and hardness of surface engineered over-layers** Shri P. K. Ajikumar, Dr. P.Shankar, Shri M. Kamruddin and Dr.A.K.Tyagi, Materials Science Division, Metallurgy and Materials Group	68
35.	**Novel Techniques for synthesis of Nano-structured coatings and thin films** Dr. Tom Mathews, Materials Science Division, Metallurgy and Materials Group	70
36.	**Influence of oxygen on the reactive phase formation of titanium disilicide thin films** Shri S. Ilango, Materials Science Division, Metallurgy and Materials Group	72
37.	**Mapping conductivity of graphene sheets using conducting tip AFM** Dr. S. Banerjee and Dr. A.K. Tyagi, Materials Science Division, Metallurgy and Materials Group	74
38.	**A spectroscopic resolution of the structure of $Zn(CN)_2$** Dr. T. R. Ravindran, Materials Science Division, Metallurgy and Materials Group	76
39.	**Observation of ferromagnetism in diamagnetic β-Ga_2O_3** Dr. V. Sridharan, Materials Science Division, Metallurgy and Materials Group	78
40.	**Long-range attraction between like-charged colloids** Dr . B.V.R. Tata, Materials Science Division, Metallurgy and Materials Group	80
41.	**Atomic scale study of negative thermal expansion in zirconium tungstate** Dr. R. Govindaraj, Materials Science Division, Metallurgy and Materials Group	82
42.	**Laser surface modification of thermal sprayed aluminum oxide coatings** Shri R. Krishnan and Dr. S. Dash, Materials Science Division, Metallurgy and Materials Group	84
43.	**Self assembly of CdSe nano rods by electrophoretic deposition** Dr. A. K. Tyagi, Dr. P. Shankar and Dr. S. Dash Materials Science Division, Metallurgy and Materials Group	86
44.	**Substitution of C and Li in MgB_2 :it's effect on T_c and H_{c2}** Dr. A. Bharati, Materials Science Division, Metallurgy and Materials Group	88
45.	**Surface plasmon enhanced Raman spectroscopy in metal nano particles** Shri P. Gangopadhyay, Materials Science Division, Metallurgy and Materials Group	90
46.	**Thin films of gadolinia doped ceria prepared by pulsed laser deposition** Dr. P. Kuppusami and Shri E. Mohandas, Physical Metallurgy Division, Metallurgy and Materials Group	92
47.	**A plasma assisted Metal Oxide Chemical Vapour Deposition process for synthesis of CrN/Ni composite coatings** Dr. Arup Dasgupta and Dr. P. Kuppusami, Physical Metallurgy Division, Metallurgy and Materials Group	94

S.No.	Title	Page No.
48.	**Nano structured thin films of TiAlN and TiN prepared by magnetron sputtering** Dr. P. Kuppusami and Shri E. Mohandas, Physical Metallurgy Division, Metallurgy and Materials Group	96
49.	**Modeling of nuclear solvent extraction :issues and indigenous development** Shri Shekhar Kumar, Reprocessing Research and Development Division, Reprocessing Group	98
50.	**Thermodynamic modeling of molten salt electro-refining process** Dr. K. Nagarajan, Fuel Chemistry Division, Chemistry Group	100
51.	**Determination of lanthanides in uranium matrix of pyro processing samples using reversed phase HPLC** Dr. T. G. Srinivasan, Fuel Chemistry Division, Chemistry Group	102
52.	**Synthesis of red-oil and related studies** Shri Shekhar Kumar, Reprocessing Research and Development Division, Reprocessing Group	104
53.	**Long afterglow phosphors** Dr. B. S. Panigrahi, Technical Services Division, Reactor Operation and Maintenance Group and Shri N. Suriyamurthy, Radiological Safety Division, Safety Group	106
54.	**Nitric acid loop for long term corrosion evaluation** Dr. U. Kamachi Mudali, Corrosion Science & Technology Division, Metallurgy and Materials Group	108

ENGINEERING

1.	**Post irradiation of FBTR fuel subassembly after 100 GWd/t burn-up** Shri K. V. Kasiviswanathan, Group for Remote Handling, Robotics, Irradiation experiments and Post irradiation examination, Metallurgy and Materials Group	112
2.	**Development of Ti-5Ta-1.8Nb alloy for fast reactor fuel reprocessing applications** Dr. Saroja Saibaba, Physical Metallurgy Division, Metallurgy and Materials Group	114
3.	**A remotely operable welding facility for fabrication of fuel pins for test irradiation** Shri G. Ravisankar, Chemical Facilities Division, Chemistry Group	116
4.	**Development of sensor material for application in temperature sensitive magnetic switch** Dr. P. V. Sivaprasad, Materials Technology Division, Metallurgy and Materials Group	118
5.	**An active laboratory scale facility for molten salt electro refining studies** Dr. K. Nagarajan, Fuel Chemistry Division, Chemistry Group	120
6.	**Design of special mechanical equipments for boron production facility** Shri V. Suresh Kumar, Chemical Facilities Division, Chemistry Group	122
7.	**Modifications to improve plant availability in Fast Breeder Test Reactor** Shri K. V. Suresh Kumar, Shri G. Srinivasan and Shri P. V. Ramalingam Reactor Operation Division, Reactor Operation and Maintenance Group	124

S.No.	Title	Page No.
8.	**Qualification of Control & Safety Rod Drive Mechanism and Control & Safety Rod for Prototype Fast Breeder Reactor** Shri V. Rajan Babu, Reactor Components Division, Reactor Engineering Group and Shri R. Veerasamy, Components & Instrumentation Development Division, Fast Reactor Technology Group	126
9.	**Mitigation of gas entrainment for Prototype Fast Breeder Reactor** Shri Indranil Banerjee and Shri G. Padmakumar Separation Technology & Hydraulics Division, Fast Reactor Technology Group	128
10.	**Understanding the mechanisms of gas entrainment in Prototype Fast Breeder Reactor hot pool and design solutions** Shri P. Selvaraj, Nuclear Engineering Group, Reactor Engineering Group	130
11.	**Design and development of thermal insulation for Prototype Fast Breeder Reactor safety vessel** Shri V. Balasubramaniyan, Nuclear Engineering Group, Reactor Engineering Group	132
12.	**Investigation of lifting off core subassemblies under seismic excitations** Shri P. Puthiyavinayagam, Nuclear Engineering Group, Reactor Engineering Group	134
13.	**Investigation on buckling of Prototype Fast Breeder Reactor vessels under seismic loadings with fluid structure interactions** Dr. P. Chellapandi, Nuclear Engineering Group, Reactor Engineering Group	136
14.	**Laser heated diamond anvil cell facility for synthesis of novel materials** Dr. N. Subramanian, Materials Science Division, Metallurgy and Materials Group	138
15.	**Pulse power systems** Shri.V.Venkatesam, Radiological Safety Division, Safety Group	140
16.	**Fire suppression performance evaluation of sodium leak collection tray** Shri P. Mangarjuna Rao and Shri N. Kasinathan, Safety Engineering Division, Safety Group	142
17.	**Real-time decision support system for radiological emergency** Dr. R. Venkatesan and Shri K. M.Somayaji, Radiological Safety Division, Safety Group	144
18.	**Digital design verification** Shri S. Ilango Sambasivan, Electronics & Instrumentation Division, Electronics and Instrumentation Group	146
19.	**Pulse coded safety logic system for PFBR** Shri S. Ilango Sambasivan, Electronics & Instrumentation Division, Electronics and Instrumentation Group	148
20.	**Reliability analysis of safety critical I&C systems of PFBR** Shri S. Ilango Sambasivan, Electronics & Instrumentation Division, Electronics and Instrumentation Group	150
21.	**Real time computers for instrumentation and control of PFBR** Shri S. Ilango Sambasivan, Electronics & Instrumentation Division, Electronics and Instrumentation Group	152
22.	**Safety logic with fine impulse test (SLFIT) system for PFBR** Shri S. Ilango Sambasivan, Electronics & Instrumentation Division, Electronics and Instrumentation Group	154
23.	**Particle arrival time recording technique for comprehensive plutonium assay** Shri R. Parthasarathy, Chemical Facilities Division, Chemistry Group	156

S.No.	Title	Page No.
24.	**Fabrication of dummy fuel sub assemblies(DFSA) for core mechanics experiments** Shri A. S. L. Kameswara Rao, Central Workshop Division, Engineering Services Group	158
25.	**Image processing for quality assurance of sheathed thermocouples** Dr. B. Venkatraman, Quality Assurance Division, Engineering Services Group	160
26.	**Development of morphological and wavelet based methods for feature extraction from thermal images** Dr. Baldev Raj, Director, IGCAR	162 164
27.	**Development of novel combination of immersion technique and time of flight diffraction for examination of weldments with thicknesses less than 6mm and its applications to evaluation of Hexcan welds of thickness 3mm.** Dr. B. Venkatraman and Shri R. Subbaratnam, Quality Assurance Division, Engineering Services Group	166
28.	**Double oxide coating on titanium for reconditioning (DOCTOR)** Dr. U. Kamachi Mudali, Corrosion Science & Technology Division, Metallurgy and Materials Group	

TECHNOLOGY

1.	**Technology development for hard facing of large components using Ni base hard facing alloys** Dr. A. K. Bhaduri, Materials Technology Division, Metallurgy and Materials Group	170
2	**Comprehensive in-service inspection system for PFBR Vessels** Shri K. V. Kasiviswanathan, Group for Remote Handling, Robotics, Irradiation experiments and Post irradiation Examination, Metallurgy and Materials Group	172
3	**Remote visual inspection of a dissolver vessel in fast reactor fuel reprocessing plant** Shri K. V. Kasiviswanathan, Group for Remote Handling, Robotics, Irradiation experiments and Post irradiation Examination, Metallurgy and Materials Group	174
4	**Ultrasonic procedure for in-service inspection of shell weld of core support structure in the main vessel of PFBR** Dr. T. Jayakumar, Non Destructive Evaluation Division, Metallurgy and Materials Group	176
5	**Centrifugal extractors in the back end of fuel cycle and other applications** Dr. S. B. Koganti, Reprocessing Research and Development Division,Reprocessing Group	178
6	**Development of SQUID based system for non-destructive evaluation** Shri R. Nagendran, Materials Science Division, Metallurgy and Materials Group	180
7	**Penetration enhancing Activated flux for TIG welding of stainless steels** Dr . M. Vasudevan, Materials Technology Division, Metallurgy and Materials Group	182
8	**Demonstration of reprocessing high burn-up carbide fuels** Shri R. Natarajan, Reprocessing Group	184
9	**Diffusion alloyed platinum electroplated Titanium electrodes for electrochemical processes** Dr. U. Kamachi Mudali, Corrosion Science & Technology Division, Metallurgy and Materials Group	186
10	**Corrosion Resistant Dissimilar Joints Between AISI Type 304L SS and Titanium** Dr. U. Kamachi Mudali, Corrosion Science & Technology Division, Metallurgy and Materials Group	188

S.No.	Title	Page No.
11	**Development of a computer controlled machine for remote profilometry and laser based dismantling of irradiated FBTR fuel sub assemblies** Shri Jojo Joseph, Post Irradiation Examination Division, Metallurgy and Materials Group	190
12	**Development and fabrication of D9 pressurized capsule & material irradiation capsule** Dr. S. Murugan, Remote Handling, Irradiation Experiments and Robotics Division, Metallurgy and Materials Group	192
13	**Development of miniature specimen test techniques** Shri V. Karthik, Post Irradiation Examination Division, Metallurgy and Materials Group	194
14	**Single pin chopper** Shri A. Ravisankar, Reprocessing Plant Design Division, Reprocessing Group	196
15	**Duel frequency saturation eddy current examination of ferromagnetic tubes** Dr. B.P.C. Rao, Non Destructive Evaluation Division, Metallurgy and Materials Group	198
16	**Establishing acceptance criteria for minor defects in FBR fuel pin end plug welds** Dr. P. Chellapandi, Nuclear Engineering Group, Reactor Engineering Group	200
17	**Establishing design basis loads for reactor vault of Prototype Fast Breeder Reactor** Dr. P. Chellapandi, Nuclear Engineering Group, Reactor Engineering Group	202
18	**Eddy current position sensor for Diverse Safety Rod Drive Mechanism of Prototype Fast Breeder Reactor** Dr. C. Babu Rao, Non Destructive Evaluation Division, Metallurgy and Materials Group	204
19	**Optical fiber based distributed sensor for temperature measurement** Dr. T. Jayakumar, Non Destructive Evaluation Division, Metallurgy and Materials Group	206
20	**Remote field eddy current technique for in-service inspection of ferromagnetic tubes** Dr. B. P. C. Rao, Non Destructive Evaluation Division, Metallurgy and Materials Group	208
21	**Impact echo and ultrasonic examination methods for evaluation of sodium fire exposed concrete** Dr. T. Jayakumar, Non Destructive Evaluation Division, Metallurgy and Materials Group	210
22	**Continues type oil level sensors for the dashpots of CSRDMs in PFBR** Shri B. Saha, Innovative Instrumentation Section, Electronics and Instrumentation Group	212
23	**Transformer oil monitoring** Shri B. Saha, Innovative Instrumentation Section, Electronics and Instrumentation Group	214
24	**An indigenous device for water film thickness monitoring** Shri B. Saha, Innovative Instrumentation Section, Electronics and Instrumentation Group	216
25	**Embedded design simplifies experimental automation** Shri J. Jayapandian, Materials Science Division, Metallurgy and Materials Group	218
26	**Eigen vector based Approach for enhancement of non-destructive evaluation images of defects** Dr. B. P. C. Rao, Non Destructive Evaluation Division, Metallurgy and Materials Group	220
27	**Fabrication of electrochemical oxygen sensor for use in sodium** Dr. T. Gnanasekaran, Liquid Metals and Structural Chemistry Division, Chemistry Group	222

BREAKTHROUGHS

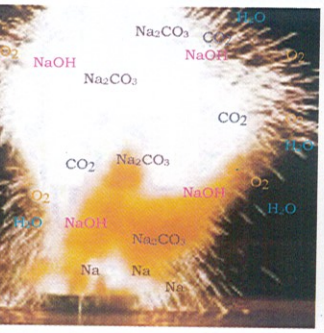



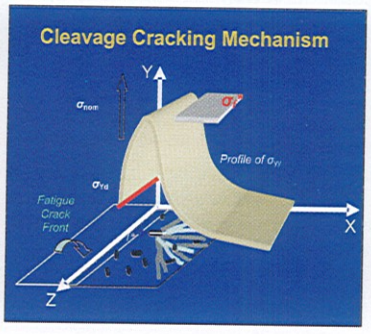

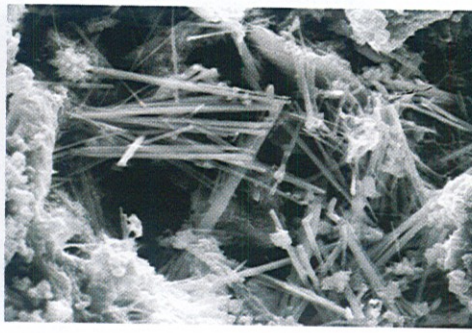

SCIENCE

Effect of Titanium on the Void Swelling Behavior in (15Ni-14Cr)-Ti modified Austenitic Steels Studied by Ion Beam Simulation

EXECUTIVE SUMMARY

One of the important property changes caused by irradiation in the reactor structural materials is void swelling, which introduces dimensional changes and thereby limits the lifetime of structural components used in a reactor. Ion simulation of void swelling in D9 alloy (Ti-modified austenitic steel) has been carried out using the heavy ion beam from the 1.7 MV Tandetron Accelerator. D9 alloy is the candidate material for clad and wrapper in the prototype fast breeder reactor (PFBR). Using heavy ion irradiation, displacement damage ~ 100 dpa can be obtained over a short period of few hours and rapid screening of alloys with regard to their irradiation behavior, specifically effect of minor alloying elements in void swelling can be carried out. The study clearly demonstrated the role of Ti concentration in the void swelling behavior of the alloy.

OUTLINE

The dimensional changes introduced by void swelling limits the lifetime of structural components used in a reactor. Therefore, resistance to void swelling is a major consideration in the choice of materials for the core components. The titanium modified steels exhibit greatly improved swelling resistance under breeder reactor conditions and consequently, have become prime candidates for structural applications. Titanium modified (15Ni, 14Cr) steel and its improved versions with phosphorous additions (designated as D9 and D9I) are envisaged for use as fuel cladding and wrapper materials in Indian Fast Breeder Reactor (FBR) programme. At IGCAR Kalpakkam there is a strong programme for the simulation of radiation effects in reactor structural materials using ion beams and modeling of radiation damage. The minor alloying elements like Ti strongly influence the void swelling resistance of austenitic steels. In the cold worked Ti modified austenitic stainless steels, the formation of fine stable precipitates of TiC termed as secondary precipitates has been reported to enhance the void swelling resistance. Fine precipitates of TiC are strong neutral sinks for vacancies and interstitials and hence act as seats for increased recombination of vacancies and interstitials. This increase in recombination reduces the swelling in these alloys. The void swelling behavior of (15Ni-14Cr)-0.25Ti and (15Ni-14Cr)-0.15Ti steels are studied using heavy ion irradiation for understanding the influence of titanium in the void swelling resistance of the alloys(Fig.1). The cold worked samples have been pre-implanted with a uniform helium concentration of 30 ppm spanning a width of about 640 nm. This was followed by a 5 MeV nickel ion irradiation to create a peak damage of ~ 100 dpa at damage rate of 7×10^{-3} dpa/s at various irradiation temperatures between 700 and 970 K. The gross swelling in the implanted range is measured by step height measurements. It is found that the peak swelling temperatures and the magnitude of swelling for the alloys are different. The swelling at the peak swelling temperature of the alloys with 0.25% of titanium and 0.15% of titanium are found to be ~4% and ~15% respectively.

In order to understand the drastically different behaviour of the two alloys with regard to void swelling, the TiC precipitate formation in these two alloys was studied by positron lifetime measurements. The un-irradiated alloys were subjected to isochronal annealing and the positron life time was measured after each annealing. These alloys show different TiC precipitate formation behavior (Fig.2). The observed variation of lifetime τ displays distinct stages viz., a monotonic decrease in τ from the initial cold worked state upto ~900 K in sample B and ~ 800 K in sample A. This is followed by a stage where there is an increase in lifetime to saturation, followed by a decrease in lifetime. The first stage corresponds to point defect recovery. This is explained by the migration of vacancies to sinks such as cold worked dislocations resulting in the annihilation of dislocations. The subsequent stage where there is an increase in lifetime τ is the result of positron trapping by the TiC precipitate-which forms during the heat treatment. The increase in average lifetime of positrons trapped in the sample A in comparison to sample B is due to the higher number density of TiC precipitates formed in the former. The difference in void swelling behavior in these two alloys with titanium variation is discussed on the basis of the role of titanium on the vacancy migration and TiC precipitate formation.

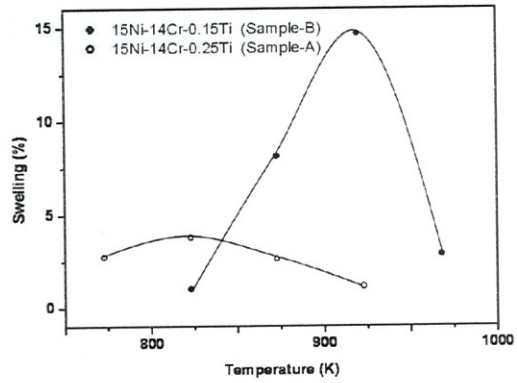

Fig. 1 : Temperature dependence of void swelling measured by surface profilometry for the D9 alloys

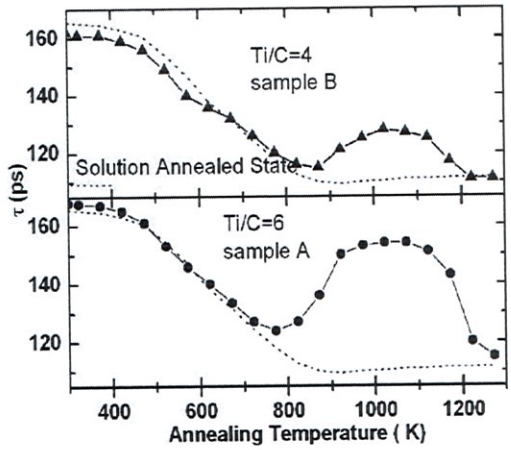

Fig. 2 : Variation of positron life time with annealing temperature for the cold - worked D9 alloys with different titanium concentration, sample A (Ti / C = 6) and sample B (Ti /C = 4)

■ ADDITIONAL INFORMATION ABOUT VOID SWELLING

The term void swelling is used to refer to the increase in volume of metals and alloys exposed to fast neutron bombardment at elevated temperature. The fast neutron irradiation gives rise to the displacement of atoms from their regular lattice positions, giving rise to the formation of point defects. The vacant lattice positions created by the displacement of atoms are called vacancies. The vacancies are mobile at elevated temperatures and cluster to form three dimensional clusters called voids. The nucleation of voids is aided by the presence of helium atoms formed by nuclear transmutation (n,α) reactions.

■ HEAVY ION SIMULATION OF VOID SWELLING

The impact of energetic ion beams gives rise to the displacements of lattice atoms from their equilibrium positions and consequently defects are generated. Due to high differential cross section for transfer of energy to the lattice, energetic charged particles (e.g., heavy ions) displace atoms in materials with much faster rate than the fast neutrons. Figure 3 gives a comparison of the rate of displacement damage production by different projectiles. Using heavy ion irradiation, displacement damage ~ 100 dpa can be obtained over a short period of few hours. The effect of helium produced by (n,α) reactions can be simulated in accelerator experiments by pre implanting appropriate concentration of helium in the sample. Ion simulation allows rapid screening of alloys with regard to their irradiation behavior. For the development of better swelling resistant D9 alloy, one needs to optimize composition of minor alloying elements like P, Si, Ti, etc., which have a major influence on the swelling. Therefore the alloy development program is in need of a test bed where one can study the effect of minor elements on swelling of the model alloys, which are exposed to high displacement damage levels. Accelerated heavy ions, which possess an inherent advantage of producing high displacement rates, have been used for evaluating the effect of minor element on swelling and for basic studies in radiation damage Through ion simulation it is possible to optimize the composition of minor alloying elements with respect to void swelling.

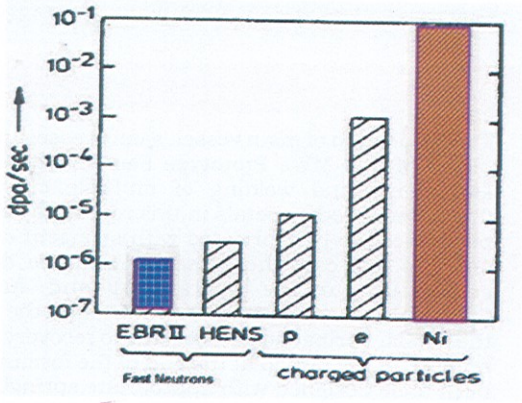

Fig. 3 : The defect production rate by different projectiles (Ion beams produce displacement damage at a much faster rate than neutrons

■ ROLE OF MINOR ALLOYING ELEMENTS IN VOID SWELLING

Minor Alloying elements like Si, Ti, P, are often added to of austenitic stainless steels to improve their swelling resistance. Some of the minor alloying additions influence the void swelling behavior through the formation of fine precipitates (TiC) which act as recombination centre for defects. The minor alloying elements also substantially modify the defect mobility.

■ ACHIEVEMENT

Accelerator irradiation has been used to probe the effect of titanium concentration in the void swelling behavior of D9 alloy. The temperature dependent void swelling in two alloys with differing Ti content has been understood in terms of TiC precipitation and the role of titanium in altering the vacancy mobility.

■ PUBLICATIONS ARISING OUT OF THIS STUDY AND RELATED WORK

Christopher David, B.K. Panigrahi, R. Rajaraman, S. Balaji, A.K. Balamurugan, K.G.M. Nair, G. Amarendra, C.S. Sundar and Baldev Raj, *J. Nucl. Mater.* (In Press)

Further inquiries:
Dr. B. K. Panigrahi and Dr. K. G. M. Nair, Materials Science Division
Metallurgy and Materials Group, IGCAR, e-mail: bkp@igcar.gov.in; kgmn@igcar.gov.in

A Finite Element Method based Process Model for Prediction of Springback during forming of PFBR Vessels

EXECUTIVE SUMMARY

A finite element method (FEM) based process model had been developed for estimation of springback during forming of multiple curvature plates. The results obtained from the simulation were validated with plate forming experiments and the correlation between the simulated results and experiments is excellent. The accuracy level of the validated process model was up to 94% in predicting the profiles of the formed plates. The process model was prepared with reduced integration shell elements incorporating dynamic explicit FEM for the loading phase and static implicit FEM for the unloading phase during plate forming. The FEM based process model would be very helpful to predict the final shape of the product for a given die, punch and plate configuration and subsequently use this information to correct the die and punch shapes for springback to manufacture the sectors of large vessels to the desired accuracy.

OUTLINE

The fabrication of main vessel, safety vessel, inner vessel and transition pieces of 500 MWe Prototype Fast Breeder Reactor (PFBR) involves assembling and welding of multiple curvature preformed plates (hereafter called as petals in this report) to form the final shape. These petals need to be fabricated with stringent dimensional tolerances in order to fabricate the vessels within the desired level of tolerance conforming to the operational and functional requirements. Springback is a major factor controlling the dimensional accuracy of the petals. Springback occurs due to recovery of the elastic strains after removal of the punch at the end of the forming operation and the tools need to be designed with appropriate springback allowances for near-net shape forming of petals. Springback is an intrinsic characteristic of the deformation process and it can only be minimized by proper process design, but cannot be completely avoided. FEM based process models for plate forming operation would help in predicting the springback as well as facilitate in designing dies for near-net-shape forming. Such a model using FEM was developed for simulating multiple curvature plate forming operations and the results were experimentally validated.

The optimum FEM formulation for plate forming was identified as sequential dynamic explicit formulation with contact modeling for the pressing phase and static implicit formulation for the unloading phase for springback calculation in the Lagrangian framework. The results from the explicit analysis were imported into an implicit FEM code and a static analysis was performed to determine the springback and the residual stress state in the plate after springback. The displacement obtained at the end of the step is the springback and the stresses and strains give the residual stress-strain state in the material after springback.

To validate the FEM process model, double curvature forming experiments were carried out on 300 mm square and 15 mm thick 316L(N) stainless steel plates. The profiles of the formed plates were measured using a CNC ZEISS Universal Measuring Machine. Figures 1 and 2 show the centre-line and diagonal sectional profiles from both experimental and FEM results superimposed on the desired (punch) surface profile. From the figures 1 and 2 it is evident that the FEM simulations of the plate forming trials compare well with the experiments, the differences between the simulated and the experimental profiles of the plates being within 6-10%. The deviation of the simulated profiles from experimental ones is more towards the edge of the plate than that at the centre-line. The radius of curvature (ROC) values at various sections were obtained for both experimental and FEM data. The variation of percentage springback, which was defined as the percentage deviation of final ROC at a section from the corresponding punch ROC, is shown in figure 3. Figure 3 clearly depicts that springback increases towards the central sections of the plate. From the FEM results it was found that the equivalent plastic strain is maximum at the centre due to maximum deformation occurring at the centre during forming. The differential distribution of strains that occurs during plate forming leads to differential springback in the plate and this in turn leads to a product shape different from the die and punch shapes. So the springback corrections on the dies and punches have to be imparted to obtain the desired product shape. It was also found from the experiments that springback is inversely proportional to the tool stiffness.

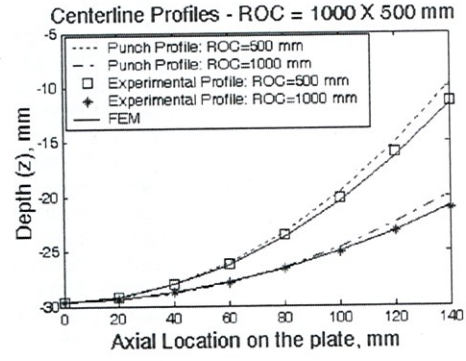

Fig. 1 : Plate profiles along transverse centrelines of the plate

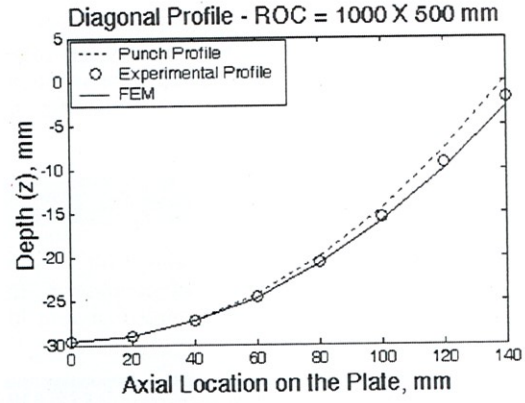

Fig. 2 : Plate profile along diagonal of the plate

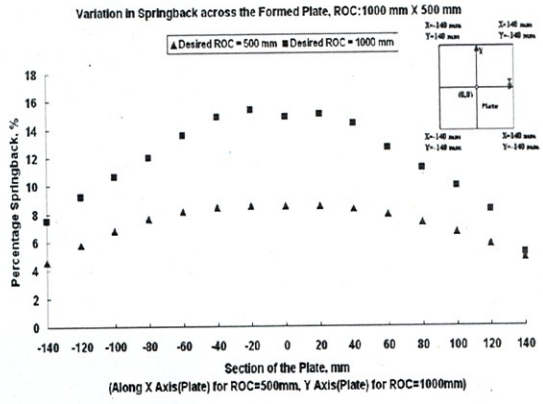

Fig. 3 : Variation of springback across formed plate

■ ADDITIONAL INFORMATION ON VESSEL TOLERANCES

The petals need to be fabricated within tight radial dimensional tolerances in order to fabricate the vessel within the desired overall tolerance limits. The amount of residual cold work is also a crucial issue in the nuclear vessels and it is specified to be within a predetermined level to ensure that the fabricated vessels see the intended life. For large vessels like the main, safety and inner vessels the cold work limit has to be adhered to strictly during the forming stage because heat treatment after forming as well as fabrication would be very difficult due to large size of the petals. While on assembly during welding, the areas of localized deformation will relax and will cause variation in dimensions of the assembled pieces. Since it is very difficult to quantify the level of cold work in the zones of localized deformation, the control of the dimensions in the assembled pieces is very difficult.

■ GENERAL EXPLANATION RELATED TO THE DESCRIPTION

The main vessel (MV) of PFBR is the most critical component in the reactor assembly and forms a part of the core supporting path. It carries ~1150 tons of liquid sodium along with the core and reactor internals (~920 tons). The vessel, made up of type AISI 316L(N) stainless steel, has cylindrical top and paraboloidal bottom with multiple radii of curvature. The vessel will be fabricated by sequentially joining together a number of preformed plates (called as petals in this report) such that the final desired shape of the vessel is obtained. Figure 4 gives the schematic of the main vessel for PFBR and a typical petal. The paraboloidal portion of the vessel consists of 40 such petals of different dimensions welded along three layers above a circular crown plate. The radius of curvature (ROC) of the petals varies from 1500 mm to 19350 mm and thickness of the petals varies from 30 mm to 40 mm. The ratio of radius of curvature to plate thickness (R/t) varies from 50 to 645 with R/t in the range of 100 to 200 for most of the petals and the ratio of deflection to the projected length in a plane (y/L) varies from 0.0123 to 0.099 with most of the petals having the ratio as 0.053. The petals will be formed into the individual shapes and dimensions by cold forming in a hydraulic press. Near-net shape forming of petals would help in keeping the cold work levels within the acceptable tolerance range. Estimation of springback in the petals is an essential step in design of the plate forming setup for near-net shape forming of petals. Since the individual petal shape is complex, finite element method (FEM) would be an ideal tool for proper design of the plate forming process and the setup by predicting the springback and the cold work level in the formed plate.

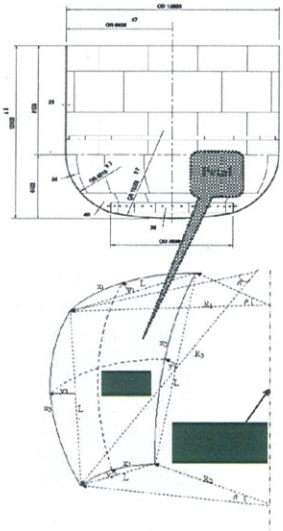

Fig. 4 : PFBR Main Vessel & a Typical Petal

■ BRIEF DESCRIPTION OF THEORETICAL BACKGROUND

Complete 3-D finite element analysis (FEA) is necessary for the petal forming process because the geometries do not conform to any idealizations like plane strain or axisymmetric analyses. The plate forming process includes both membrane and bending effects in the workpiece and so a 3D shell formulation was used to account for both these effects. The dynamic explicit FEM is a conditionally stable scheme with stable time increments of the order of 10^{-7}s for 316L(N) stainless steel and so use of reduced integration elements would be economical without losing accuracy of solution. The inevitably high surface to volume ratio in plate forming would result in large number of contact conditions in the FEM model necessitating increased execution time and convergence difficulties for a fully implicit FEM model. Geometric nonlinearity needs to be incorporated to tackle the springback, which may occasionally be quite large.

■ ACHIEVEMENT

An FEM based process model for multiple curvature plate forming was developed and the model was experimentally validated. This process model would be very useful for predicting the final shape of the product for given die, punch and plate configurations. Subsequently this information can be used to correct the die and punch shapes for springback to manufacture the sectors of large vessels to the desired dimensional accuracy and cold work level.

■ PUBLICATIONS ARISING OUT OF THIS STUDY AND RELATED WORK

1. Utpal Borah, Shreedhar Venugopal, R. Nagarajan, P. V. Sivaprasad and S. Venugopal. *Trans. IIM,* **60** (2007) 511.
2. Utpal Borah, Shreedhar Venugopal, R. Nagarajan, P. V. Sivaprasad, S. Venugopal and Baldev Raj, *Intl. Journal of Mechanical Sciences* (Accepted for publication)
3. Utpal Borah, Shreedhar Venugopal, R. Nagarajan, P. V. Sivaprasad, V. Maduraimuthu, S. Venugopal and S.L. Mannan. Proc. "Inter. Conf. on Pressure Vessels and Piping, OPE–Chennai" Feb 2006, Chennai.

Further inquiries:
Shri Utpal Borah, Materials Technology Division
Metallurgy and Materials Division, IGCAR, e-mail: borah@igcar.gov.in

Study of Ductile-Brittle Transition Temperature of 9Cr-1Mo Steels

EXECUTIVE SUMMARY

Defining the ductile to brittle transition temperature (DBTT) below which catastrophic failures occurring in structures made of ferritic steels is a major technological challenge for designers. Generally practiced empirical approaches (ASME K_{IR} Curve) to predict the fracture toughness over the DBTT regime fail to appreciate the scatter, originating from the random distribution of cleavage crack initiation sites, and often lead to ultra-conservative predictions. Recently a 'weakest link' based statistical approach to evaluate DBTT via a reference temperature (T_o) prediction (ASTM E 1921) and an associated Master Curve description claims to be more appropriate, however its applicability at high loading rates (dynamic) is yet to be resolved. This aspect has been studied with 9Cr-1Mo and Modified 9Cr-1Mo steels, the candidate FBR wrapper materials, using dynamic fracture toughness results obtained from instrumented impact tests.

OUTLINE

The 9Cr-1Mo and the modified 9Cr-1Mo steels are candidate wrapper materials for the Fast Reactors in next generation. However, the irradiation induced rise in the Ductile-Brittle Transition Temperature (DBTT) is a major technological challenge. Towards the DBTT evaluation, the recently developed Weibull statistics based ASTM E-1921 reference temperature (T_o) approach has been applied but under dynamic loading condition, as it is understood that the DBTT is sensitive to loading rate for this type of materials. The dynamic loading rate would provide a more conservative prediction of the DBTT as compared to the quasi-static loading rate, important for the material's selection for this critical component.

Dynamic fracture toughness of these materials has been determined from instrumented impact testing with pre-crackled Charpy specimens. The dynamic loading gives rise to inertial oscillations in the specimen originating from interactions of forward and reflected stress waves. Towards getting a load signal with minimum oscillation effects, testing has been conducted at reduced hammer (~1.12 m/s). Even this loading rate provides a stress intensity factor rate ~106 MPa.m$^{0.5}$/s, which is well within the dynamic regime. It has been observed that a full velocity of Charpy machine (5.12 m/s) affects the stress intensity factor rate only marginally.

The applicability of the quasi-static shape of Master Curve, as provided in ASTM E-1921, under this high strain rate has been a matter of speculation. This aspect has been experimentally verified with a large number of PCVN testing for 9Cr-1Mo steel at a temperature range well within the ductile-brittle transition regime. At temperatures of –60,-55, -52.5, -50, -47.5, -45 and –40 °C, reference temperature determined from dynamic fracture toughness datasets (termed as T_0^{dy}) have been -47.15, -45.75, -62.09, -64.13 and –63.47 °C respectively. Taking into account the experimental uncertainties involved in a dynamic fracture toughness evaluation procedure, it is reasonable to say that the T_0^{dy} remains practically unchanged (±10 °C) within the DBTT regime. Thus, it is proposed that the same shape of the Master Curve describing the fracture toughness variation under quasi-static condition also can be applied in the high strain rate loading. The T_0^{dy} of the 9Cr-1Mo steel is conservatively predicted as –45 °C and the same has been chosen to index the Master Curve, as shown in Fig. 1. Except a few, the individual dynamic fracture toughness data has been seen to lie well within the 98% and 2% confidence limit. The ASME-K_{IR} curve for this steel shows much lower fracture toughness as compared to the 2% confidence limit.

Compared to the 9Cr-1Mo steel, the modified 9Cr-1Mo steel yields a higher T_0^{dy} (15 °C). It is attributed to the change in crack initiation mechanism from carbide-matrix decohesion (for the 9Cr-1Mo steel) to cracking of prior austenitic grain boundary (for the modified 9Cr-1Mo steel). The corresponding fractographs are shown in Figure 2. The change in mechanism is attributed to grain boundary embrittlement phenomenon in the latter, originated from Phosphorus segregation at the prior austenitic grain boundaries. The Phosphorus segregation at the prior austenitic grain boundaries has been confirmed by the Secondary Ion Mass Spectrometer (SIMS) study.

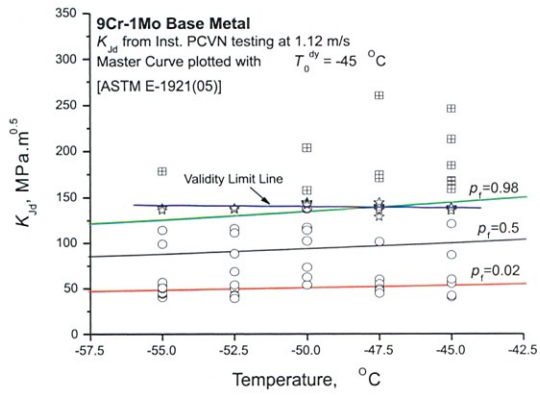

Fig. 1 : Dynamic fracture toughness results of 9Cr-1Mo steel with respect to the ASTM E 1921 Master Curve

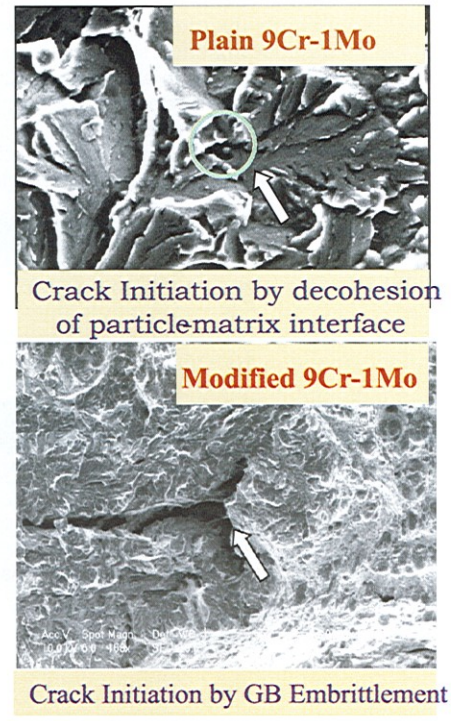

Fig. 2 : Crack initiation mechanism of 9Cr-1Mo and Mod.9Cr-1Mo steels in DBTT regime

■ ADDITIONAL INFORMATION ABOUT T_0 AND THE MASTER CURVE

The ASTM E-1921 requires the T_0 to be determined from fatigue pre-cracked specimens. Under dynamic loading condition this demands a precise temperature control and strict testing protocol to generate valid fracture toughness from generally small size (10x10x55 for PCVN) specimens. Thus a parallel testing and analysis methodology is under development which would enable determination of a conservative T_0 by conducting instrumented Charpy-V notch tests only. This involves predicting dynamic fracture toughness from Charpy energy via semi-empirical correlations over a temperature range within the DBTT regime and then using multi-temperature approach to determine the T_0 as given in ASTM E 1921. For 9Cr-1Mo steel, this aspect has been successfully verified.

■ GENERAL EXPLANATION RELATED TO THE DESCRIPTION

The fracture of ferritic steels in the DBTT regime is generally predominated by initiation controlled cleavage cracking. As the cleavage initiation is often dictated by availability of a weakest link (brittle precipitates, inclusions, weak lath boundaries etc.) in the region of highest stress buildup, the 'local approach' is proved to be more meaningful and thus the micro-cleavage fracture stress (σ_f^*) is the controlling material parameter in this regime.

In pursuit of a model to explain relationship between the microscopic cleavage fracture and the macroscopic fracture toughness, Ritche, Knott and Rice have suggested (known as RKR Model) that the applied tensile stress has to exceed the critical cleavage fracture stress, σ_f, over a critical microstructural distance, l^*. l^* can be estimated from the separation between the crack tip and appropriately configured micro-crack nucleation sites under SEM. A schematic representation of the cleavage cracking is shown in Fig.3.

Based on the finite element based assessment of stress distribution ahead of a crack, the following equation may be used to estimate σ_f:

$$\sigma_f = \sigma_0[\,Ai\ (B_i l^* \sigma_0)/(K_{IC})^2]$$

where, K_{IC} is the static fracture toughness and σ_0 is the static yield stress. A_i is a unit less constant and B_i is a constant having unit of stress (MPa) depending on the strain hardening exponent, *n*.

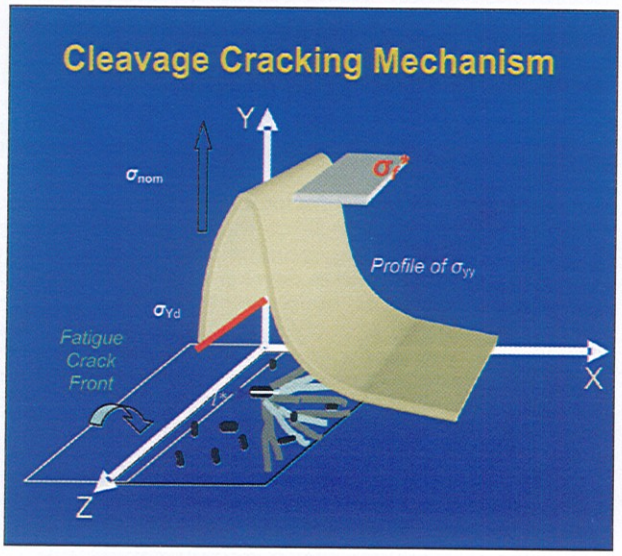

Fig. 3 : Schematic representation of the mechanism of cleavage cracking in DBTT regime

■ BRIEF DESCRIPTION OF THEORETICAL BACKGROUND

The brittle fracture originates at the weakest link ahead of a sharp crack. A 3-parameter Weibull distribution: $p_f = 1\text{-}\exp\{-[(K_{Jc}-K_{min})/(K_0-K_{min})]^b\}$, is used to model scatter in fracture toughness in DBTT regime and the temperature at which the median fracture toughness (where cumulative probability of failure is 0.5) for 1 inch thick specimen is 100 $MPa.m^{0.5}$, is defined as the reference temperature (T_0). T_0 is a material specific parameter and used to index the Master Curve, claiming to describe the fracture toughness variation of all the ferritic steels in the DBTT regime. The Master Curve equation is $K_{JC}(median) = 30 + 70\exp(0.019(T\text{-}T_0))$.

■ ACHIEVEMENT

This study extends the scope of ASTM E-1921 Master Curve description to high strain rate regime, thus enabling a conservative prediction of the DBTT of ferritic steels by taking into account the strain rate effect. The effects of trace elements like Phosphorus on the crack initiation mechanism *vis a vis* on DBTT has been understood.

■ PUBLICATIONS ARISING OUT OF THIS STUDY AND RELATED WORK

1. P. R. Sreenivasan, A. Moitra, S. K. Ray and S. L. Mannan, *Intl. J. Frac.*, **124** (2004) 387.
2. A.Moitra, P. R. Sreenivasan, S. L. Mannan and Vakil Singh., *Mater Metall. Trans.-A*, **36** (2005) 2957.
3. A. Moitra, P. R. Sreenivasan, S. Venugopal and S. L. Mannan, *Mater. Sci. Tech.*, **21** (2005) 1166.
4. A.Moitra, S. Sathyanarayanan, S.K. Albert, V.Ramasubbu, K.G. Samuel and S.K.Ray ; *International J. Pressure Vessels and Piping* (Accepted for Publication)
5. S. Sathyanarayanan, A. Moitra, K.G.Samuel, G Sasikala, S.K. Ray and V.Singh, *Mater. Sci. Engg. A* (In Press).

Further inquiries:
Dr. Aniruddha Moitra, Materials Technology Division
Metallurgy and Materials Group, IGCAR, e-mail: moitra@igcar.gov.in

Prediction of Ferrite Number in Stainless Steel Welds

■ EXECUTIVE SUMMARY

The ability to predict the delta-ferrite content expressed in terms of Ferrite Number (FN) accurately has proven very useful in assessing the performance and predicting various properties of austenitic stainless steel welds. The generalized Bayesian Neural Network model for predicting Ferrite Number in stainless steel welds has been developed using the database used for generating the WRC-1992 diagram and our laboratory data. The accuracy of the model is superior to the other existing Ferrite Number prediction methods. The optimized neural network model reveals the influence of compositional variations on ferrite content and examines the significance of individual elements on ferrite content in stainless steel welds.

■ OUTLINE

Constitution diagrams are routinely used for predicting ferrite number in stainless steel welds. The latest one is the WRC – 1992 diagram. Recently, a back propagation neural network model has been proposed as a more accurate means of predicting ferrite content. The prediction and measurement of ferrite content in stainless steel welds is of scientific and technological interest due to limitations in all the well-known methods, including some of the newer methods. In the present work, Bayesian neural network analysis has been used to develop an accurate model for predicting the ferrite content in stainless steel welds. This neural network model for ferrite prediction in stainless steel welds has been developed using database of 1020 datasets, collated from literature and our laboratory, comprising chemical composition and ferrite number for shielded metal arc (SMA) welds, representing the common 300-series austenitic stainless steel weld compositions (viz., 308, 308L, 309, 309L, 316, 316L, etc.) and the duplex stainless steel welds. Of the 1020 datasets, 948 data are those that had been used to generate WRC-1992 diagram, and the remainder datasets are from our laboratory experiments. The network employed consists of 13 input nodes x_i representing the 13 composition variables, a number of hidden nodes h_i and one output node y representing the FN value. As many as 80 different neural network models were created using the datasets, with the number of hidden units varying from 1 to 16 in which, 5 different sets of random number seeds were used to initiate each network, for a given number of hidden units. All these models were trained on the same training dataset that consisted of a random selection of one-half, i.e. 510, of the total 1020 datasets, while the remaining half were used as the test dataset to examine how the model generalises with unseen data.

Excellent agreement over the entire database is obtained between the predicted and measured FN values for the committee of models (Fig. 1), with a correlation coefficient of 0.98. Fig. 2 indicates the perceived significance σ_w of each of the input variables by all the nine neural network models in the committee. The σ_w value represents the extent to which a particular input explains the variation in the output, as for a partial correlation coefficient in linear regression analysis. It is observed from Fig. 2 that the elements Mn and Nb are not significant in influencing the FN. The optimised committee model predicts the FN in stainless steel welds with better accuracy than the constitution diagrams and other FN prediction methods (Table 1). Excellent agreement between the predicted and measured FN has also been observed for test dataset [Fig.3). Using this generalised Bayesian Neural Network (BNN) model, the influence of variations of the individual elements on the FN in austenitic and duplex stainless steel welds has been determined. It is found that the change in FN is a non-linear function of the variation in the concentration of the elements. Elements such as chromium, nickel, nitrogen, molybdenum, silicon, titanium and vanadium are found to influence the FN more significantly than the rest of the elements in stainless steel welds. Manganese is found to have less influence on the FN. While titanium influences the FN more significantly than niobium, the WRC-1992 diagram considers only niobium for calculating the chromium equivalent. The role of silicon and titanium in influencing the FN in stainless steel welds has been brought out clearly, while these elements are not given due considerations in the WRC-1992 diagram.

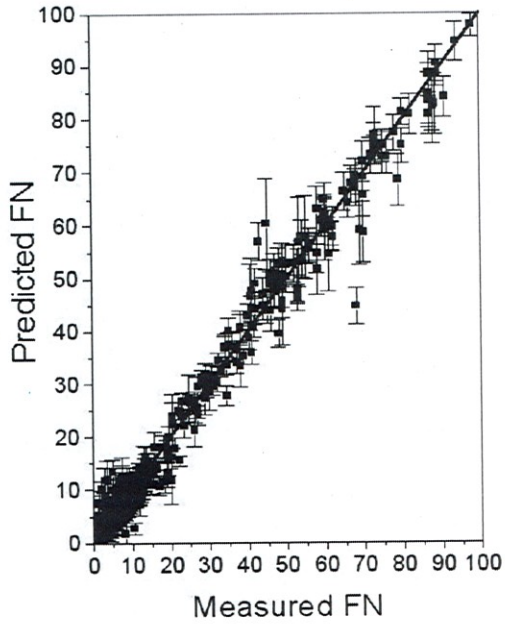

Fig. 1 : Comparison of predicted ferrite number using optimum committee of models and measured ferrite number for entire dataset (1020 datasets)

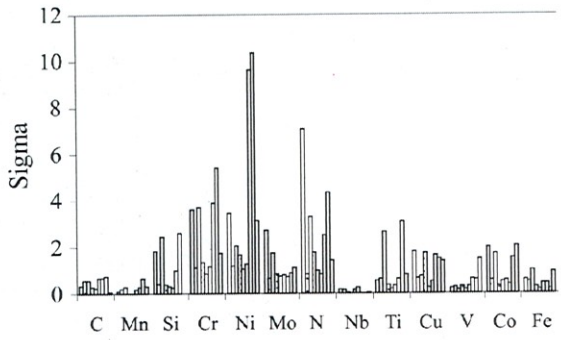

Fig. 2 : Perceived significance σ_w values of all first nine ferrite number models in the committee for each input

■ SIGNIFICANCE OF FERRITE CONTENT

A minimum ferrite content is necessary to avoid hot cracking in stainless steel welds. The amount of ferrite in the weld metal also controls the micro structural evolution during high temperature service. Moreover the amount of ferrite controls the corrosion and stress corrosion resistance. The low temperature toughness of the weld metal is also related to the weld metal ferrite content. Research is focused on quantifying the effect of various alloying elements on the ferrite content so that it is possible to control the amount of ferrite by modifying the weld metal composition. To achieve this objective, accurate predictive tool for the estimation of ferrite content as a function of weld metal composition is necessary.

Table 1
Comparison of root mean square (RMS) errors for different Ferrite Number prediction methods

FN Prediction method	RMS error *for complete training database*	RMS error *for independent dataset not used in training*
Bayesian Neural Network (BNN) model	2.1	2.03
FNN-1999 (Back Propagation Neural Network) model	3.5	2.3
WRC-1992 Diagram	5.8	2.6
Function Fit model	5.6	5.1

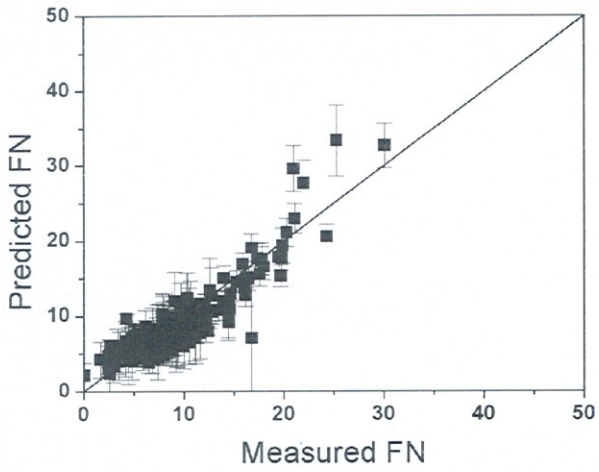

Fig. 3 : Comparison between predicted and measured FN for an independent dataset not used in the training (265 datasets)

■ BRIEF DESCRIPTION OF THEORETICAL BACKGROUND

The neural network is a simple combination of transfer functions and weights. The influence of the inputs on the output variable is together with the transfer functions implicit in the values of the weights. Neural network in a Bayesian framework allows the calculation of error bars representing the uncertainty in the fitting parameters. The method recognises that there are many functions that can be fitted into uncertain regions of the input space, without unduly compromising the fit in adjacent regions, which are rich in accurate data. Instead of calculating a unique set of weights, a probability distribution of a set of weights is used to define the fitting uncertainty. The error bars, therefore, become large when data are sparse or locally noisy.

■ ACHIEVEMENT

The model is the most accurate composition only dependent FN prediction method currently reported in literature. The RMS error for the predicted Ferrite Number using this model is less than 2. This model is 65% more accurate than the WRC – 1992 diagram and 40% more accurate than the other neural network model reported in the literature. The model published as a manuscript has been approved and published as a document by International Institute of Welding.

■ PUBLICATIONS ARISING OUT OF THIS STUDY AND RELATED WORK

1. M. Vasudevan, M. Murugananth, A.K. Bhaduri, Baldev Raj and K. Prasad Rao, *Sci. and Tech. Welding and Joining*, **9** (2004) 109.
2. M. Vasudevan, and A.K. Bhaduri, *Mater. Sci. and Tech.*, **21** (2005) 387.

Further inquiries:
Dr. M. Vasudevan, Materials Technology Division
Metallurgy and Materials Group, IGCAR, e-mail: dev@igcar.gov.in

A New Critical Damage Criterion for Creep

EXECUTIVE SUMMARY

Components used at elevated temperatures in nuclear, thermal power plants are designed for creep, and progressive deformation of a material either at constant load or stress is termed as creep. Creeping materials fail as a result of initiation and growth of damage. The design criterion for creep does not invoke creep ductility in arriving at the allowable stress. Therefore a 'critical damage criterion' is developed in terms of a new concept called 'time to reach Monkman–Grant ductility' (t_{MGD}) and is shown that damage attains a critical level at t_{MGD}. A critical damage criterion that depends only on the damage tolerance factor is deduced based on continuum creep damage mechanics (CDM) and MPC–Omega (materials property council) approaches and the validity of the criterion is demonstrated for a wide range of materials. It is also shown that it has useful implications to engineering creep design of high temperature components.

OUTLINE

Components used at elevated temperatures are designed for creep and the allowable stress for nuclear applications is based on the concept of lowest of the three; i.e., 100% of the average stress to produce 1% strain in a given time (say 105 h), 67% of the minimum stress to produce rupture in 105 h and 80% of the minimum stress to cause initiation of tertiary creep in 105 h. It may be noted that in design, creep ductility is not considered while arriving at the allowable stress. It is also important to understand when does creep damage becomes alarming so that a safe and un-safe regime concept can be defined for a creep curve. It is this intention that gave genesis for the original approach of critical damage criterion in terms of a new concept called time to reach Monkman–Grant ductility (MGD). MGD is the product of minimum creep rate and rupture life and is generally found to be a constant.

The new concept is developed in terms of time at which MGD is reached along a creep curve and is designated as t_{MGD}. Next it is addressed whether there is a relationship between t_{MGD} and tr and if so is it universal in nature. It is put forward that creep damage that grows along the creep curve attains a critical level at t_{MGD} and it is shown for a typical case of cavitation damage micro-mechanism in -iron that cavities attain a critical size at t_{MGD}. Based on CDM and MPC–Omega approaches, a critical damage criterion is deduced as universal relationship between t_{MGD} and t_r that depends only on the tolerance to resist creep damage (i.e., creep damage tolerance factor) .

Along the lines of CDM, the critical damage criterion is deduced as

$$t_{MGD}/t_r = 1\ [(\lambda-1)/\lambda]^{\lambda} = \text{constant} = f_{CDM}. \qquad \text{(Eq. 1)}$$

Similarly, based on MPC–Omega method, it is deduced as

$$t_{MGD}/t_r = 1-\exp(-1) + \exp(-\lambda) = \text{constant} = f_{MPC}. \qquad \text{(Eq. 2)}$$

The key in the above Eq. (1) is that though t_{MGD} and t_r vary, f_{CDM} is a constant independent of stress and temperature, since is material constant in a given stress–temperature domain for a specific damage mechanism. The above physically based Eq. 1 (or Eq 2) is termed as critical damage criterion because damage attains critical level at t_{MGD}, when the criterion $t_{MGD} = f_{CDM}\ t_r$ is met. The validity of damage criterion is demonstrated in Figure 1 for various materials. The symbols correspond to experimentally obtained f_{EXP} values from t_{MGD} vs. t_r plots for the respective material. Figure 2 shows the plot of t_{MGD} vs. t_r with f_{CDM} calculated according to Eq. (1) knowing the constant value of λ for the respective material.

The important implication is that t_{MGD} can be viewed as the onset of true tertiary creep damage and stress to cause t_{MGD} in 10^5 h with proper safety factor can be suggested as a new creep design criterion. For creep curves at different stresses and temperatures (i.e., with constant λ), a contour that satisfies $t_{MGD} = f_{CDM}\ t_r$ can be drawn such that the region till t_{MGD} can be considered as a safe regime. Further, when Robinson life fraction damage rule is not applicable and it predicts non–conservative values of remnant life, a modified damage rule in terms of t_{MGD} has been proposed that is conservative.

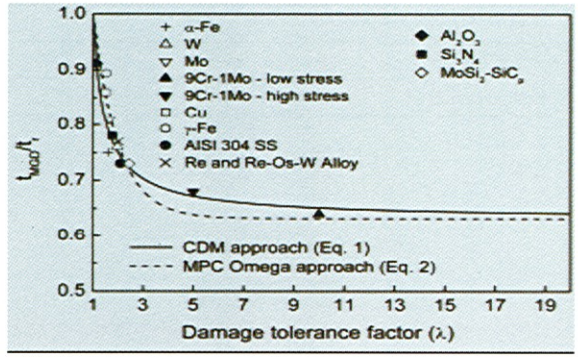

Fig. 1 : Validity of critical damage criterion for a wide range of materials. Solid symbols correspond to f_{EXP} values obtained from double logarithmic plots of t_{MGD} vs. t_r for different materials

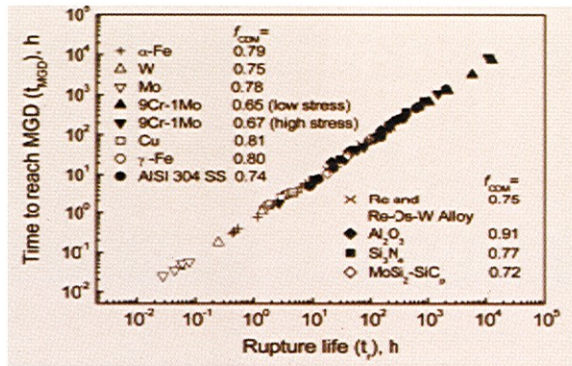

Fig. 2 : Plot of t_{MGD} vs. t_r demonstrating the validity of damage criterion with f_{CDM} values for various materials

■ ADDITIONAL INFORMATION ABOUT TIME TO REACH MONKMAN–GRANT DUCTILITY (TMGD)

Monkman–Grant in 1956 proposed that for different test conditions, the product of minimum creep rate $\dot{\varepsilon}_m$ and rupture life t_r generally is constant and this product is designated as MGD and is the minimum useful secondary ductility that is available in a creeping material. Therefore t_{MGD} is defined as the time at which this MGD is reached for a given creep curve when primary creep strain is negligible. Also t_{MGD} is the time at which the true tertiary creep damage sets in, since MGD is exhausted at t_{MGD}. Beyond t_{MGD} till failure corresponds to the accelerated growth of damage leading to linkage of cavities resulting in micro–cracks thus causing creep fracture.

■ CREEP DAMAGE CRITERION AND RELATIONSHIP BETWEEN t_{MGD} AND t_r

The concept of t_{MGD} is shown schematically along with time to onset of tertiary creep t_{ot}, limiting tertiary creep strain ε_t and damage tolerance factor for negligible primary creep strain ε_p. A large is desirable as the material can tolerate strain concentrations without local cracking and thus λ is a material performance characteristic.

CDM and MPC–Omega Approach

Monkman–Grant relation does not describe the evolution of creep damage and its coupling to the deformation rate. The two approaches that describe this coupling are CDM and MPC–Omega approaches. According to CDM, damage is treated as an internal state variable and is expressed by the two coupled differential equations where first gives the deformation rate as a function of stress, temperature and scalar damage variable. The second equation describes the evolution of damage and the damage rate is expressed as a function of stress, temperature and damage variable. Defining these two coupled equations and after integrating them at constant stress, a relationship between strain fraction and time fraction can be obtained in terms of λ. Substituting the condition at $t = t_{MGD}$, $\varepsilon - \varepsilon_p$ = MGD, the damage criterion can be easily deduced. MPC–Omega approach gives the evolution of deformation rate as a function of strain with omega parameter which is reciprocal of MGD for negligible ε_p. On similar lines to CDM, damage criterion can be deduced following MPC method.

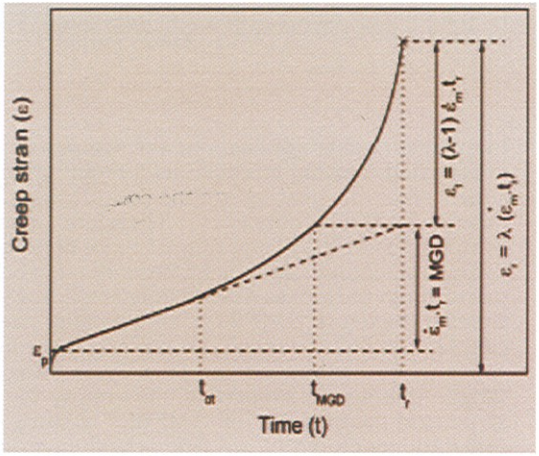

Fig. 3: Schematic creep curve with negligible primary strain ε_p illustrating t_{MGD}, t_{ot}, ε_t and damage tolerance factor λ

■ BRIEF DESCRIPTION OF THEORETICAL BACKGROUND

The essential message of Monkman–Grant relation is that creep deformation and damage are inter-related and creep fracture is strain controlled. This provided the genesis that at what time MGD is reached along a creep curve and is there any relation between t_{MGD} and t_r. If so, is it universal in nature and is it applicable to all creeping solids? Also, what is the physical meaning of t_{MGD} in terms of creep damage? Thus t_{MGD} is shown as the time at which damage attains a critical level and the critical damage criterion in terms of relationship between t_{MGD} and t_r has been deduced based on CDM and MPC approaches as these are apt to describe the coupling between the evolution of creep damage and deformation rate. The highlight of the study is that the proposed criterion depends only on that is related to damage mechanism and is constant in a given stress–temperature domain.

■ ACHIEVEMENT

The proposed new damage criterion has importance to basic understanding of creep damage and has useful implications to creep design. It is applicable even when Monkman–Grant ductility varies, since it depends only on damage tolerance factor. Further, this study has high relevance to our centre, since creep is of consideration in PFBR and also to elevated temperature applications in general.

■ PUBLICATIONS ARISING OUT OF THIS STUDY AND RELATED WORK

1. C. Phaniraj, B. K. Choudhary, Baldev Raj and K. Bhanu Sankara Rao, *J. Mater. Sci.* **40** (2005) 2561.
2. C. Phaniraj, B. K. Choudhary, Baldev Raj and T. Jayakumar, *Mater. Sci. Eng. A* **398** (2005) 373.
3. C. Phaniraj, B. K. Choudhary and Baldev Raj, Proc. "Inter. Conf. on Pressure Vessels and Piping, OPE–Chennai", Feb 2006, Chennai.

Further inquiries:
Dr. C. Phaniraj, Materials Technology Division
Metallurgy and Materials Group, IGCAR, e-mail: phani@igcar.gov.in

The Effect of Dynamic Sodium on the Low Cycle Fatigue Properties of 316L(N) Stainless Steel

EXECUTIVE SUMMARY

The use of liquid sodium as a heat transfer medium for Liquid Metal Fast Breeder Reactors (LMFBRs) necessitates the assessment of the compatibility of structural materials, and the influence of long–term exposure to sodium on the Low Cycle Fatigue (LCF) and creep-fatigue interaction properties of reactor structural materials. LCF tests conducted in flowing sodium environment at 823 and 873 K on 316L(N) stainless steel, exhibited a similar trend in cyclic stress response in air and sodium. The fatigue lives are significantly improved in sodium environment when compared to the data obtained under identical testing conditions in air environment. The lack of oxidation in sodium environment is considered to be responsible for the delayed crack initiation and consequent increase in fatigue life. Comparison with RCCMR design codes shows that the design curve based on air tests is conservative.

OUTLINE

In nuclear reactor applications the components are often subjected to repeated thermal stresses, as a result of temperature gradients which occur on heating and cooling during start-ups and shut-downs and/or transients. Therefore there is a need for comprehensive understanding of cyclic deformation behaviour and the micromechanisms which influence such behaviour. Further the use of liquid sodium as a heat transfer medium for Liquid Metal Fast Breeder Reactors (LMFBRs) necessitates the assessment of the compatibility of structural materials, and the influence of long–term exposure to sodium on the Low Cycle Fatigue (LCF) and creep-fatigue interaction properties. Currently the design of core and structural components of LMFBRs is being carried out utilizing test data generated in air. The actual environment seen by these components during service involves sodium. Moreover, the current trend being life extension of power plants, it is important to accurately determine the life of components in the actual environment, so as to determine any leverage for extension of life beyond the design life. With this view an elaborate programme has been initiated at Mechanical Metallurgy Division to evaluate the effects of dynamic sodium on the Low Cycle Fatigue (LCF), creep and creep-fatigue interaction behaviour of indigenously manufactured reactor materials such as 316L(N) stainless steel and modified 9Cr-1Mo ferritic steel and their weldments. The present report gives an update on the experiments conducted till date on the LCF properties of indigenously developed 316L(N) stainless steel in dynamic sodium environment.

The Low Cycle Fatigue (LCF) tests on 316L(N) austenitic stainless steel and modified 9Cr-1Mo ferritic steel were performed as per ASTM E 606 standards under fully reversed total axial strain control mode employing a triangular waveform. Tests were conducted at 823 K and 873 K at a constant strain rate of $3x10^{-3}s^{-1}$ with strain ranges varying from ±0.4% to ±1.0%. Sodium temperature was maintained within ±2K of the test temperature and sodium velocity was maintained at 2.5 m/s in the test chamber. The oxygen level in the sodium loop was maintained at less than 2 ppm.

The results of the LCF tests conducted at 823 K is given in Fig. 1. It is observed that the LCF lives of the fatigue tested specimens in sodium environment are significantly higher than the identical tests in air. The increase in life varies from a factor of about 5.5 at lower strain ranges to about a factor of 3 at the higher strain ranges used for the tests. The generally accepted reason for increase in life in sodium environment when compared to air environment is the lack of oxidation effects in high purity sodium. Metallographic investigations of the fracture surfaces show that environmental effects are virtually absent in a low oxygen sodium environment. Specimens are absolutely free from oxides or any other corrosion products. On the other hand fatigue tests conducted in air at high temperatures show substantial oxidation. It has been suggested that crack growth occurs from two sources, one being mechanical and the other being oxygen penetration at the crack tip; obviously in high purity, low oxygen sodium there will be virtually no contribution from the second source and hence the crack growth rate will be lower.

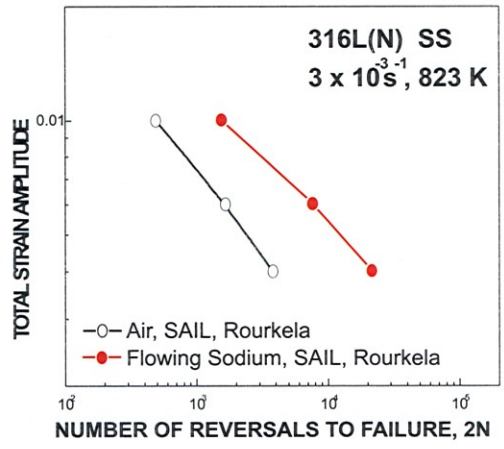

Fig. 1 : Strain – Life plots at 823 K

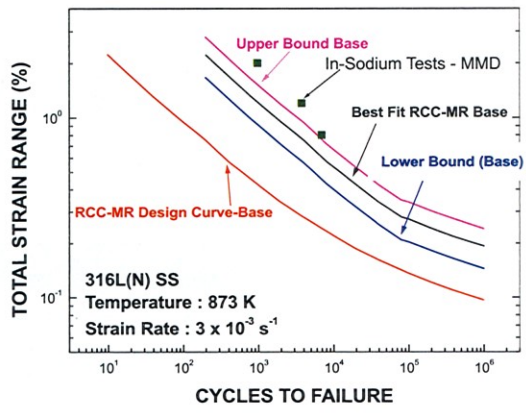

Fig. 2 : Comparison with RCC-MR Code

■ GENERAL EXPLANATION RELATED TO THE DESCRIPTION

Comparison with Codes:

The data generated in Mechanical Metallurgy Division in sodium environment is compared with the data provided in the RCCMR code for 316L(N) material at 873 K in Figure 2. The data pertaining to sodium tests lie above the upper bound curve of the air data. These results clearly indicate that design against LCF with air data is conservative.

Loop details

The cold leg region comprises of the cold trap, plugging indicator, oxygen meter and a sampler device. The hot leg region comprises of the test sections for fatigue and creep-fatigue interaction studies. Sodium is being circulated through test section by an electromagnetic pump of 5 cum./hr capacity through a heat exchanger and heater vessel of 38.5 kW capacity. The return line from the test section goes to the degassing chamber and connects just before the EM pump through a heat exchanger and air cooler. The sodium flow velocity being maintained at the test section is 2.5 m/sec.

Fatigue test chamber

A special chamber has been designed to carry out these tests. Cylindrical specimen with a gauge diameter of 9 mm and a gauge length of 21 mm were used in this programme. The details of the fatigue test chamber used for conducting LCF tests in flowing sodium environment are given in figure 3. The specimen is enclosed within a miniature primary bellow surrounding which, a secondary bellow was provided for safety. Two flanges are provided from the upper and lower portions of the specimen gauge length from which an arrangement was made to house the LVDT for strain measurement.

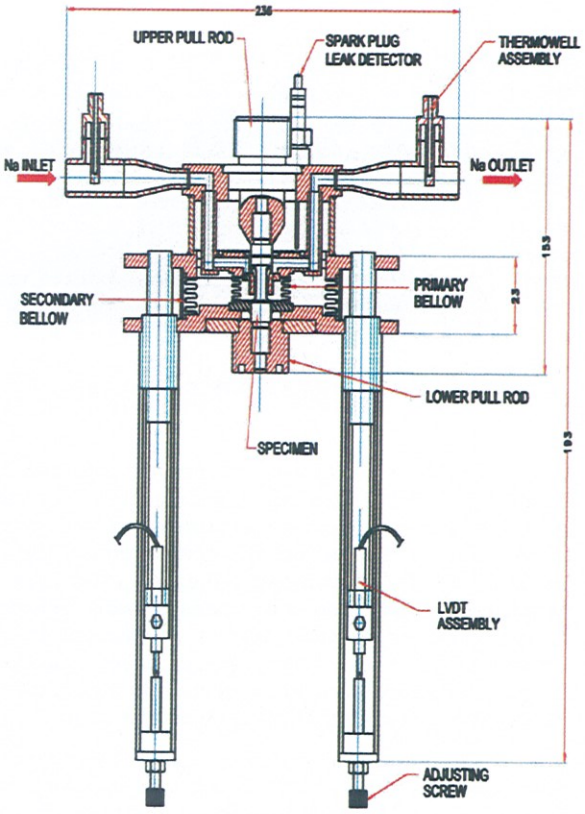

Fig. 3 : Fatigue test chamber assembly

■ ACHIEVEMENT

This work validates indigenous 316L(N) stainless Steel and indigenous sodium to be used in PFBR as far as LCF properties are concerned, and clearly brings out the fact that design of components based on air data is conservative.

■ PUBLICATIONS ARISING OUT OF THIS STUDY AND RELATED WORK

R.Sandhya, R.Kannan, V.Ganesan, M.Valsan, K.Bhanu Sankara Rao and S.L.Mannan, Proceedings of the international conference on Operating Pressure Equipment – OPE 2006, Feb. 7-9, 2006, Chennai, India.

Further inquiries:
Dr. R.Sandhya, Mechanical Metallurgy Division
Metallurgy and Materials Group, IGCAR, e-mail: san@igcar.gov.in

High Temperature Low Cycle Fatigue of 316L(N) Stainless Steel base, Welds and Weld Joints

■ EXECUTIVE SUMMARY

Cyclic stress evolution and fracture behavior of 316(N) weld metal and 316L(N)/316(N) weld joints are studied in strain controlled Low Cycle Fatigue. The fatigue life of the weld metal is found to be better than the weld joints. Microstructural heterogeneity across the weld joint has resulted in poor fatigue life with most of the failures being initiated in heat affected zone. Some failures have been observed in weld metal zone of weld joint at high strain amplitudes. Differences in flow stress of weld metal and base metal created strain incompatibility between the respective zones in the weld joint. As a first approximation to this strain incompatibility, plastic strain contribution from the weld metal and base metal zones of the weld joint are calculated by the rule of mixtures under equi-stress conditions and it is observed that base metal zone contributes to most of the plastic strain in weld joint.

■ OUTLINE

In start-up and shutdown operations, structural components operating at elevated temperatures are often subjected to reversed plasticity due to cyclic thermal stresses. Cyclic thermal stresses arise when free expansion and contraction of the component is totally/partially constrained either by external or by internal constraints. In addition to this, steady state operation at elevated temperature introduces creep resulting in creep-fatigue interaction. In view of this, design against fatigue and creep-fatigue interaction is a major consideration for Liquid Metal cooled Fast Breeder Reactor (LMFBRs) structural components.

The weldments are micro-structurally and mechanically heterogeneous, which could form one of the potential sites for the fatigue failure. In addition, this heterogeneity introduces the differences in fatigue damage evolution mechanisms, fatigue crack initiation life and crack propagation rates in three zones of the weldment, i.e., base metal, Heat Affected Zone (HAZ) and Weld metal. Therefore, weldments are the critical sections to be considered carefully in the design of LMBFR components. Most of the failures have been found to originate from HAZ in the weld joint. Occasionally, fracture was also observed in weld zone. 316L(N) austenitic stainless steel is the material chosen for the primary components in LMFBRs due to its excellent high temperature mechanical properties and compatibility with the heat transfer medium i.e., liquid sodium. LCF behavior of 316L(N) \ 316(N) weld joints and 316(N) weld metal are presented in the range 773 K - 873 K. 316L(N) SS plate and 316(N) electrode, used for weld joints, in the present study are indigenously developed materials.

Cyclic stress response represents the variation of stress response of the material during cycling and it can include regimes of hardening, softening and saturation. The relative proportion of each of these regimes depends on the initial microstructure and also the microstructural changes that take place during cycling. Weld metals displayed a gradual softening regime for the major portion of the life after a brief period of hardening. Weld joints exhibited initial hardening followed by a continuous and gradual softening regime. Initial hardening is similar to that observed in 316L(N) base metal though the degree of hardening is less. This seems to be justifiable since major part of the gauge length is made up of base metal.

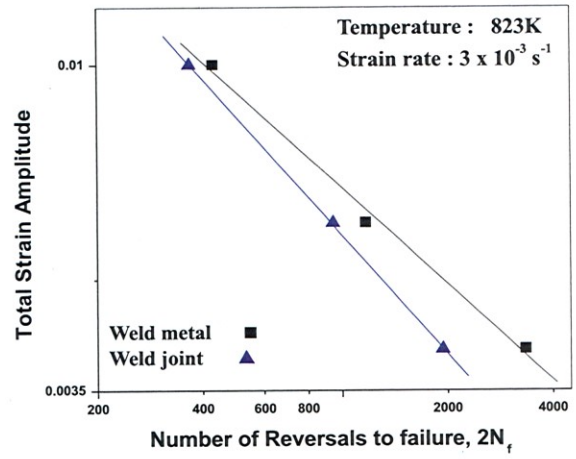

Fig 1: (a) Strain – Life plot at 823 K

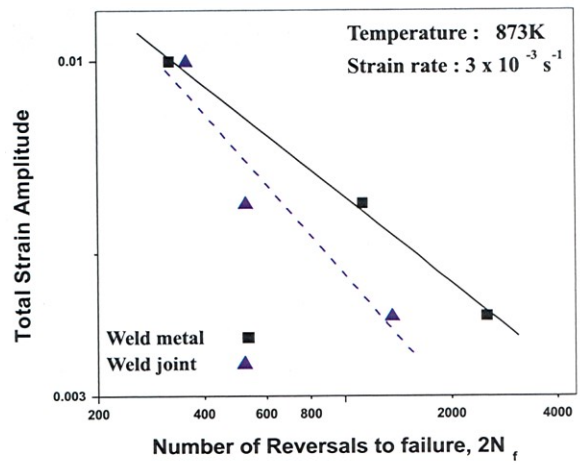

Fig 1: (b) Strain – Life plot at 873 K

■ ADDITIONAL INFORMATION ABOUT VOID SWELLING

Dislocation cell structures in weld joint and vein structures in weld metal have been observed at high strain amplitudes, while both materials evidenced dislocation tangled network at low strain amplitudes.

■ FATIGUE LIFE AND FRACTURE BEHAVIOR

At all the testing conditions, weld joints showed lower fatigue lives compared with weld metal. This can be ascribed to the microstructural influence on the fatigue crack initiation and crack propagation. Crack initiation and propagation was found to be transgranular at all testing conditions, in both weld metal and weld joints.

Crack initiation in weld joint occurred in coarse-grained HAZ as shown in Fig.2. In this figure cleavage faceted fracture corresponds to that of large grain size in HAZ. Though the observed crack initiation in both weld metal and weld joint was transgranular, there exists significant differences in crack propagation that display profound influence on their fatigue life. In austenitic stainless steel welds, the delta ferrite intentionally introduced to reduce their tendency to hot cracking and micro-fissuring gets transformed to a hard and brittle sigma phase when these materials are exposed to elevated temperatures, 773 to 1173 K, for extended periods of time. The fine duplex austenite-ferrite microstructure of weld metal, with its many transformed phase boundaries during testing, offers greater resistance to the extension of fatigue cracks by causing deflection of the crack path. This has been also observed in 316 weld metal. Crack deflection leads to reduced stress intensity at the crack tip and an associated reduction in the crack propagation rate. While in the weld joints, the resistance to transgranular crack propagation in HAZ is less due to its coarse-grain size, i.e. the smaller the grain boundary area the less is the number of crack-arrest events that causes the crack front to be held back and necessitates the crack initiation phase to occur in the adjacent grain.

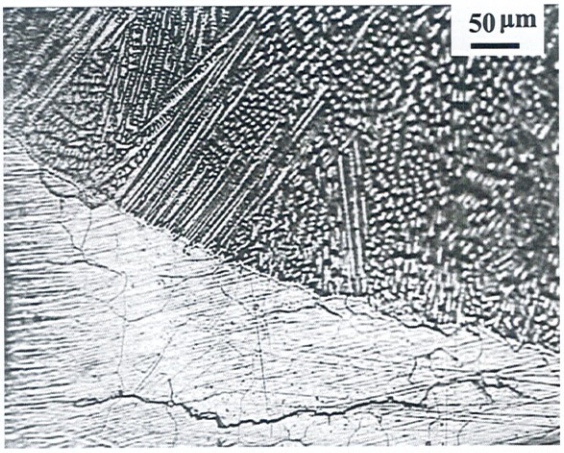

Fig. 2 : Transgranular initiation and propagation in the coarse grained HAZ of weld joint

■ CALCULATION OF PLASTIC STRAIN CONTRIBUTION FROM WELD METAL AND BASE METAL ZONES OF WELD JOINT

To determine the strain incompatibility between weld metal zone and base metal zone in weld joint, an attempt has been made (as a first approximation) to calculate strain contributions from weld metal and base metal zones, by the rule of mixtures. It states that under equi-stress conditions, stress borne by each of the phases in a composite laminate is the same, but the strains they experience are different. Base metal zone takes up most of the imposed plastic strain in the weld joint. Thus accumulated plastic strain in weld metal is small in magnitude which can cause spring-back effect on adjacent base metal. With increasing stress amplitude on weld joint, strain incompatibility and associated spring back effect on adjacent base metal increases and could cause cracking in HAZ.

■ ACHIEVEMENT

This work characterizes the deformation and damage mechanisms of indigenously developed 316L(N) SS base, weld and weld joints during Low Cycle Fatigue deformation. The mechanisms of crack initiation and propagation in weld joints and welds have been identified.

■ PUBLICATIONS ARISING OUT OF THIS STUDY AND RELATED WORK

G.V. Prasad Reddy, R. Sandhya, M. Valsan, and K. Bhanu Sankara Rao, *International Journal of Fatigue* (In Press)

Further inquiries:
Dr. M.Valsan, Mechanical Metallurgy Division
Metallurgy and Materials Group, IGCAR, e-mail: valsan@igcar.gov.in

Low cycle Fatigue and Creep-Fatigue Interaction of Modified 9Cr-1Mo Steel Weldments

EXECUTIVE SUMMARY

The influence of hold time on the high temperature low cycle fatigue (LCF) behavior of modified 9Cr-1Mo ferritic steel in the normalized and tempered condition is addressed. Total axial strain controlled LCF tests at 873 K with hold times at peak strain up to 10 min in tension and compression were carried out employing total strain amplitude of ±0.6%. The alloy in general, showed a gradual and continuous softening regime. Fatigue life was found to decrease with increase in the duration of hold time in both tension and compression. Compression hold was found to be more damaging than the tension hold. The fatigue failure in compression hold tests were marked by extensive crack branching and formation of secondary cracks. Oxidation assisted crack initiation and propagation contributed to life reduction at high temperatures in hold time tests. Additionally, the sub-structural changes of the starting microstructure were also found to be responsible for the reduction of the fatigue life.

OUTLINE

Modified 9 Cr-1 Mo steel, a modified version of plain 9 Cr-1Mo ferritic steel by the alloy addition of niobium and vanadium is used extensively as structural material for steam generator components of liquid metal cooled fast breeder reactor and fossil fired power plants. It is observed that even though the base material has superior creep rupture property compared to other low alloy steels, many in-service problems are associated with weld joints due to the mismatch in the creep behavior of the parent material, the weld metal and the heat affected zone (HAZ). The HAZ is made up of a number of relatively narrow sub-regions, which have different creep strengths. This leads to complex stress redistribution and complex states of stress is set up locally which have a great influence on the accumulation of creep damage and on the subsequent failure of the weldment. This mode of failure is known as type IV cracking and is associated with relatively large strains taking place within a very localised region of the HAZ known as the intercritical region. Apart from the strain localization in the fine grained HAZ, microstructural degradation such as coarsening of the carbide precipitates and substructural changes such as formation of cells/subgrains from the martensitic laths also occur.

Study on the evaluation of low cycle fatigue and creep-fatigue interaction behavior of modified 9 Cr-1 Mo ferritic steel weldments are relatively scanty compared to the vast data available on the creep behavior of this alloy. In view of this, an attempt has been made to further the current understanding on the low cycle fatigue and creep fatigue interaction behavior of weld joints and base material of modified 9 Cr-1 Mo ferritic steel. Low cycle fatigue tests were carried out on both base material and welded joints of the P91 material at 773, 823 and 873 K at strain rate 3×10^{-3} s^{-1}, employing various strain amplitudes. Post weld heat treatment was done on the weld joint at 1033 K for 3h followed by air cooling. Creep-fatigue interaction tests were conducted by introducing hold at peak tension and in peak compression for periods in the range 1 min to 10 min at 873K.

Fig. 1 shows continuous cyclic softening from first cycle onwards during all the tests in both weld joints and the base material. The overall stress response decreased with increase in temperature at all strain amplitudes employed during the test for both base and joint.

Fig. 2 shows the comparison of base and joint data on a strain-life plot. Both base metal and weld joint exhibited similar fatigue lives at 823 K.

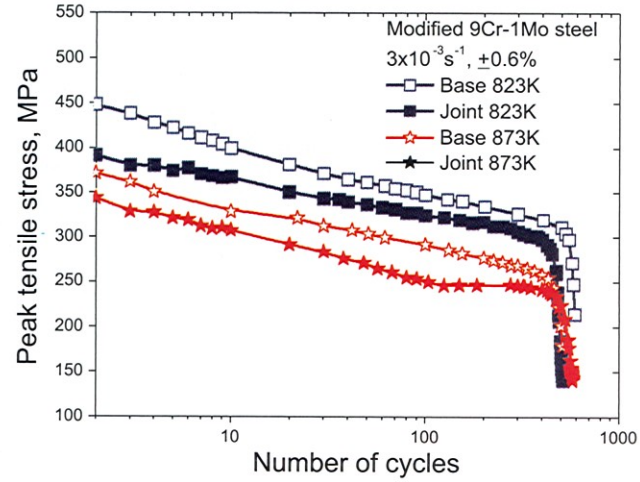

Fig. 1 : Comparison of cyclic stress response of base and weld joints

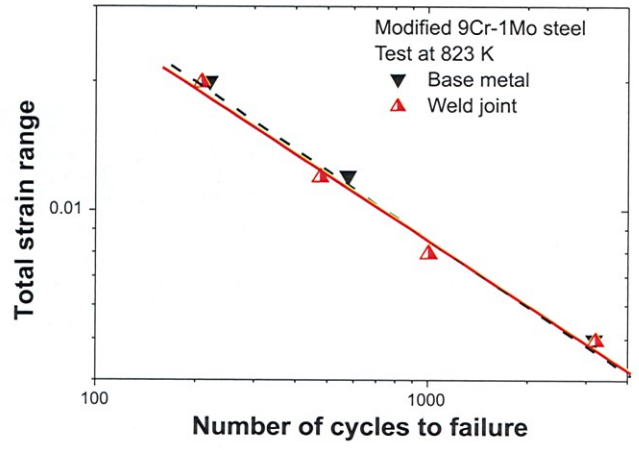

Fig. 2 : Comparison of fatigue lives of base and weld joints at 823 K

DEFORMATION SUBSTRUCTURE

The overall cyclic stress response is lower in hold time tests compared to continuous cycling. Detailed transmission electron microscopy of the samples tested to various fractions of fatigue life indicated that at room temperature the cyclic softening is attributed to annihilation of dislocations while at 873 K it is ascribed to the formation of cells and coarsening of the carbide precipitates. The substructure formed during continuous cycling without the introduction of hold is highly heterogeneous. The introduction of one minute tension hold during cycling resulted in a more well-defined cells. On increasing the tension hold time, dislocation substructure assumed configuration of well-defined equiaxed sub-grains.

GENERAL EXPLANATION RELATED TO DESCRIPTION

The fatigue life decreased with the introduction of hold and application of one minute compression hold period displayed a far more deleterious effect on the fatigue life than application of 1 minute hold under tension. Optical microscopy conducted on the longitudinal section of the tested samples, (1 minute tension and 1 minute compression) showed multiple crack initiation sites and oxidation assisted crack initiation and propagation (Fig. 3). It has been found that oxide layer spalls off during tension hold due to compressive stresses on them whereas the oxide layer cracks during compression hold due to tensile stresses. The data generated in IGCAR is compared with the best fit curve derived from the RCC-MR code for this steel at 823 K in Fig.4. All the data lie above the lower bound curve and thus it indicates RCC-MR curve can be safely used for design purposes.

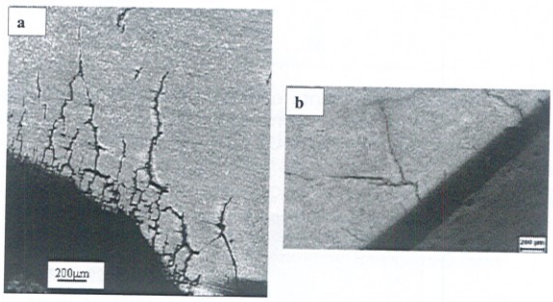

Fig. 3 : Optical Metallograph of fatigue tested sample, (a) 1 min. Compression hold and (b) 1 min. tension hold

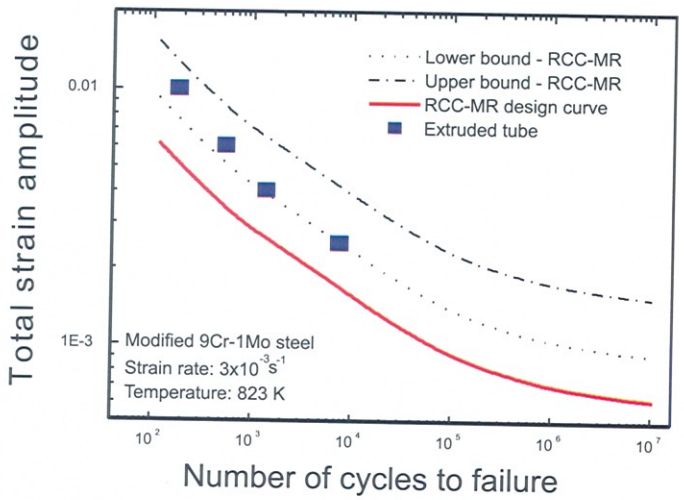

Fig. 4 : Comparison of data with RCC-MR

ACHIEVEMENT

This work has contributed to the data available on weldments of modified 9Cr-1Mo ferritic steel. The characterization of the deformation modes under fatigue, has added to the understanding of substructure evolution in this material.

PUBLICATIONS ARISING OUT OF THIS STUDY AND RELATED WORK

Vani Shankar, M. Valsan, K. Bhanu Sankara Rao, R. Kannan, S.L. Mannan and S.D. Pathak; *Mater. Sci. Eng. A*, **437** (2006) 413.

Further inquiries:
Dr. M. Valsan, Mechanical Metallurgy Division
Metallurgy and Materials Group, IGCAR, e-mail: valsan@igcar.gov.in

Evaluation of Stress Corrosion Cracking Phenomenon in an AISI type 316 LN Stainless Steel using Acoustic Emission Technique

EXECUTIVE SUMMARY

This work deals with the analysis of the acoustic emission (AE) signals to determine the micro-process during stress corrosion cracking (SCC) of AISI type 316LN stainless steel that cause the AE, and thus the mechanism of the SCC process. AE with amplitudes ranging from 27.6 to 46.5 dB with different counts, energy and rise times occurred during SCC of type 316LN stainless steel in 45% $MgCl_2$ at 413 K. The analysis of the AE signals in conjunction with fractography indicated that a surge in the AE counts and energy indicated initiation of SCC. AE was found to be continuous prior to the initiation. The time gap between AE events increased during initiation. AE events occurred in bursts during crack growth. Plastic deformation ahead of the crack tip was determined to be the major source of AE during propagation of SCC in type 316LN stainless steel. The cracking was determined to be dissolution controlled.

OUTLINE

The present study aims to understand the mechanism of SCC based on the signatures of the AE. Compact tension (CT) specimens of annealed AISI type 316LN stainless steels were subjected to SCC testing in 45% magnesium chloride solution at 413 K in the range of stress intensity factor of 13-26 $MPa.m^{0.5}$ using the constant load testing method. The AE generated during the test were monitored with respect to time using a a broad band frequency sensor. Monitoring of AE during the SCC tests indicated that both the AE counts and AE energy increased with time (Fig. 1). A sudden increment in AE counts and energy was observed at the same time. This burst in AE counts and energy was attributed to crack initiation. During the SCC test, significant amount of hydrogen evolution was observed on the surface of the CT specimen for some time much earlier to the crack initiation time. During crack initiation and propagation, hydrogen evolution ceased. Fig. 2 (a) shows that the AE signals were continuous during the start of the test (Region I in Fig. 1). As crack initiation approached (region II of Fig. 1), a larger time gap between two events in the higher time region was observed (Fig. 2 (b)). As the initiation stage was approached, the number of counts per event and the energies of the low amplitude signals just prior to initiation were much higher than the large amplitude signals. This indicated that the production of low amplitude AE events with higher counts and energies has caused the initiation of the SCC process. Fig. 2 (c) shows that during early stages of crack growth (Region III in Fig. 1), the time period between two AE events increased significantly *vis-à-vis* Regions I and II, while the AE counts and AE energy dropped significantly. Higher amplitude AE signals (> 39.8 dB) with high rise time (>120µs) did not occur. During the later stages of crack growth (Region IV of Fig. 1), the time period between two AE events increased further *vis-à-vis* region III and low amplitude AE signals dominated. From Fig. 2, it was clear that right through the tests AE with amplitudes 27.6 to 39.8 dB occurred, with maximum AE signals occurring at 31.2 dB. In another set of experiments, AE monitoring under load in absence of corrosive medium showed that the whole range of AE amplitudes, which occurred only due to plastic deformation of the precrack tip, had rise times of less than 120µs, with maximum emissions occurring in the range 31 to 34 dB. This indicated that maximum AE during SCC occurred by plastic deformation of the crack tip. The disappearance of AE of amplitudes in the range of 40.9 to 46.5 dB with higher rise times (>120µs) that were observed in Region I of Fig. 1, corresponded to ceasing of hydrogen evolution, thus implying that the AE signals of these amplitudes and rise times were due to hydrogen evolution. Though the cumulative AE parameters, such as events, counts and energy, increased with increasing crack length, the rate of AE parameters decreased with increasing crack growth rate. This could be explained as follows: There exists a triaxial state of stress ahead of the crack-tip. The material ahead of the crack tip, where the yield stress is exceeded, yields to produce a plastic zone, which blunts the crack. Larger the length of the crack, higher is the value of K_I (at the value of load applied on specimen) resulting in greater stress concentration due to which larger plastic zone forms ahead of the crack tip. This results in greater blunting of the crack tip. Larger plastic zone would imply that longer times would be required for crack to resharpen by dissolution for further crack propagation to occur. This explains the larger time gaps between two AE events during later stages of crack growth and the reduced AE rate with increasing crack growth rate. Each AE event could be attributed to the process of formation of plastic zone. The time period between two AE events corresponded to the period of material dissolution that caused crack growth. Hence, from this work, it was concluded that burst type signals could occur during SCC by dissolution controlled mechanism.

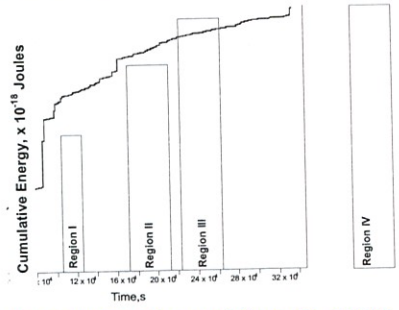

Fig. 1 : Dependence of cumulative AE energy with time during SCC of type 316LN stainless steel in 45% $MgCl_2$ solution at 413 K

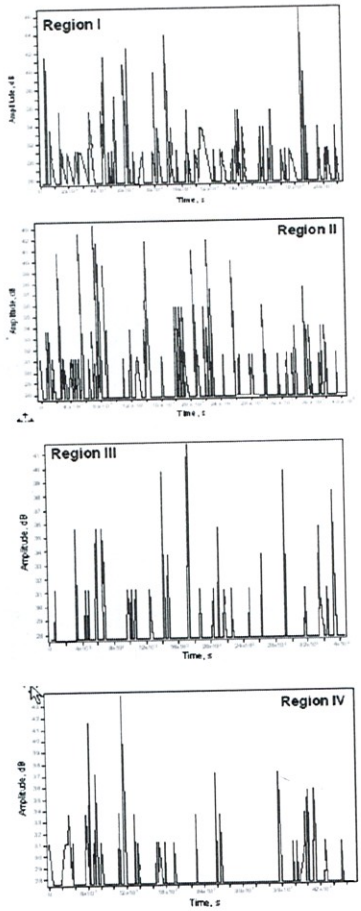

Fig 2 : Increasing time between AE events with increasing time of test (Region I to region IV of Fig. 1)

■ WHAT IS ACOUSTIC EMISSION?

The AE phenomenon is the result of transient elastic wave propagation generated by a rapid release of energy within a material due to changes in local stress and strain fields. These elastic waves propagate over a wide range of frequencies ranging from audible frequencies to frequencies in MHz range. The acoustic emission technique (AET) is a passive and non-intrusive technique and remote monitoring is possible. AET is widely used for structural integrity monitoring applications because of its ability to detect and locate dynamic defects. The success of AET depends on how well the sources of AE detected during material damage can be interpreted. AE can occur due to atomistic processes like dislocation motion or due to macroscopic processes like deformation, corrosion and crack growth.

■ CORROSION

Corrosion processes present an attractive proposition for detection and characterization by AE technique. During SCC and corrosion fatigue, processes such as hydrogen gas evolution, breakdown of thick oxide film, fracture or decohesion of precipitate and inclusions, plastic deformation by slip or twin, martensitic transformation, and micro/macro cracking produce AE. Each of these has definite range of amplitudes and can be distinguished by the amplitudes and frequencies of occurrence. In low strength steels, AE monitoring has been disappointing because the crack growth process is more chemical than mechanical and the emissions are sporadic and low in amplitude. Stainless steels and titanium alloys are borderline cases. During SCC of titanium alloys heat treated to low strength levels, major crack movements without detectable emissions were observed while the same material heat treated to higher strength levels gave substantial emissions that could be correlated to crack velocity, load drop and stress intensity factor.

AE technique has been used to differentiate between active path corrosion (APC) and hydrogen embrittlement (HE) mechanisms. During APC mechanism of SCC and in the incubation period of HE, continuous AE signals of small amplitude are emitted; while during macroscopic crack propagation during HE, AE signals of large amplitudes appeared in bursts. AE is more intense during intergranular SCC (IGSCC) than during transgranular SCC (TGSCC), suggesting that larger areas of crack growth occur per event during IGSCC.

Fig. 3 shows the AE amplitude distribution produced by microprocesses that may operate in connection with SCC or corrosion fatigue. AE generated by several of these microprocesses can occur at amplitude levels comparable with those produced by hydrogen gas evolution. Hence, detailed AE signal analysis is needed before positive mechanistic identification is made concerning CF or SCC operative in stainless steels.

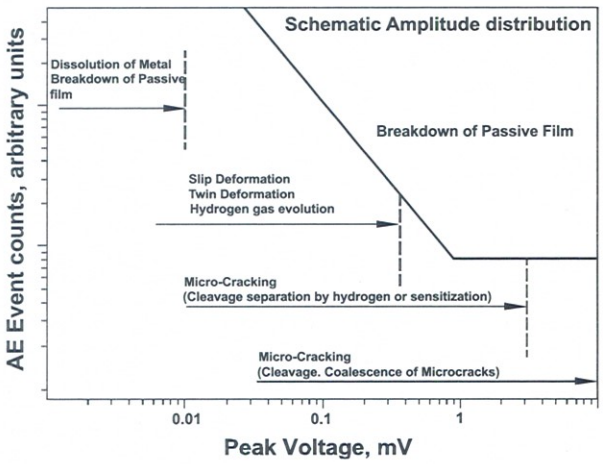

Fig. 3 : Various AE sources during SCC or corrosion fatigue processes and their energy

■ ACHIEVEMENT

This study has proved that SCC by active path corrosion or dissolution based mechanism occurs in bursts. This is contrary to what has been so far believed that SCC by dissolution controlled mechanism was a continuous cracking process and only hydrogen embrittlement occurred in burst. In words of the reviewer of this paper which was submitted to the journal 'Corrosion Science', this work has provided new insight into the mechanism of stress corrosion cracking.

■ PUBLICATIONS ARISING OUT OF THIS STUDY AND RELATED WORK

H. Shaikh, R. Amirthalingam, T. Anita, N. Sivaibharasi, T. Jayakumar, P. Manohar, H.S. Khatak, *Corr. Sci.*, **49** (2007) 740.

Further inquiries:
Shri Hasan Shaikh, Corrosion Science and Technology Division
Metallurgy and Materials Group, IGCAR, e-mail: hasan@igcar.gov.in

Type IV Cracking in Modified 9Cr-1Mo Steel Weld Joint

EXECUTIVE SUMMARY

The steam generator of the Prototype Fast Breeder (PFBR) is being fabricated out of modified 9Cr-1Mo steel. Type IV cracking in the heat affected zone (HAZ) of weld joint limits the life of the component. Detailed investigations have been carried out to understand the cracking so as to mitigate or minimize the problem. Creep tests performed on the steel and its joint revealed that the type IV cracking occurs in the inter-critical region of HAZ, which is sandwiched between relatively higher creep resistant constituents of the joint. The constrained localized deformation leads to the pronounced creep cavitation in the soft intercritical region of HAZ of the weld joint to yield type IV failure. The creep rupture life reduction due to type IV cracking in the weld joint of the steel was found to depend on the applied stress and test temperature. Based on the study the reductions in 10^5 hours creep rupture strength of the steel weld joint are estimated as 18 %, 30 % and 45 % of base metal strength at 823 K, 873 K and 923 K respectively.

OUTLINE

Modified 9Cr-1Mo ferritic steel has been selected to fabricate the steam generator of Prototype Fast Breeder Reactor (PFBR), under construction at Kalpakkam. Many concerns have been reported on the poor performance of the fusion welds especially in the thick components of the steel in the conventional fossil-fuel fired power plants due to cracking in and around the weld joint. So detailed investigations have been carried out to understand the creep properties of the modified 9Cr-1Mo steel weld joint.

Fusion weld joint of the tempered martensitic modified 9Cr-1Mo steel has a very complex heterogeneous microstructure across it, consisting of base metal, deposited weld metal and the HAZ in base metal adjacent to weld metal. Heat input during weld thermal cycle produces a complex microstructure across the HAZ. Both the base metal and weld metal has tempered martensitic structures, with weld metal having columnar grain. The HAZ is comprised of coarse prior-austenitic grain martensite, fine prior-austenitic grain martensite and intercritical structure in an order away from the weld fusion interface towards the unaffected base metal. The intercritical HAZ has a lowest hardness in the weld joint of the steel (Fig.1).

Creep rupture tests were carried out on the modified 9Cr-1Mo steel base metal and cross weld joint specimens. The specimens were fabricated out of a weld pad subjected to post weld heat treatment (PWHT) at 1033 K for 1 hour. At relatively lower stresses the cross weld joint of the steel possesses lower creep rupture life than the base steel (Fig.2). The failure occurred in the intercritical region of HAZ (Fig.3a). Progressive localization of creep deformation in the soft intercritical region of HAZ occurred during creep test. The deformation was accompanied with intense creep cavitation in the intercritical region of HAZ. The creep deformation constraint resulted from the creep deformation resistance surrounding induces creep cavitation in the soft intercritical region of HAZ (Fig.3b). Creep cavities were found to nucleate at the coarser precipitate particles. The cavitation started deep inside the specimen due to higher deformation constraint. The nucleated cavities coalesced to form micro-cracks (Fig.3c). The microcracks propagated outward to the surface of the specimen to produce type IV failure.

The creep rupture strength reduction due to type IV cracking in the weld joint of the steel was more on longer creep exposure at higher test temperature. The estimated creep rupture strength reductions of the steel weld joint are 18 %, 30 % and 45 % of base metal strength for the creep test temperatures of 823K, 873 K and 923 K respectively.

TEM investigation revealed that the recovery of the martensitic lath structure with high dislocation into subgrain with low dislocation and the coarsening of precipitates of the steel on intercritical heating during weld thermal cycle reduced the creep strength of the steel weld joint.

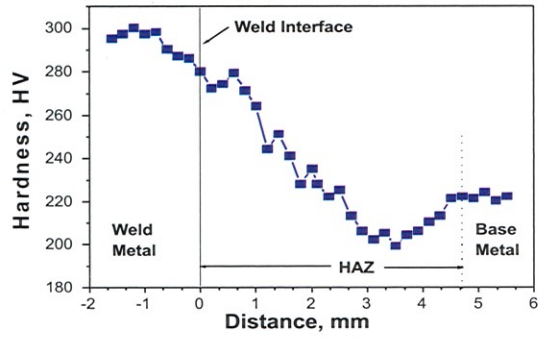

Fig. 1 : Hardness variation across the weld joint of modified 9Cr-1Mo steel

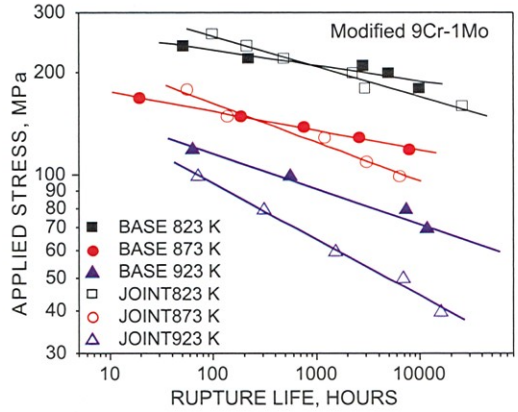

Fig. 2 : Variation of creep rupture life with applied stress of modified 9Cr-1 Mo base metal and weld joint

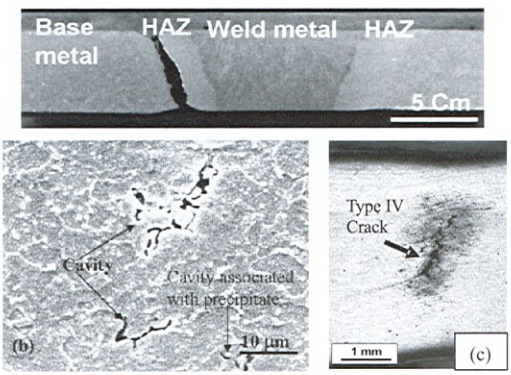

Fig. 3 : (a) Type IV failure in weld joint; (b)type IV cavity in the inter-critical region of HAZ and (c)type IV cracking in modified 9Cr-1Mo steel weld joint.

■ ADDITIONAL INFORMATION ABOUT WELD CRACKING IN Cr-Mo STEELS

Different types of cracking develop in Cr-Mo steels weld joint during laboratory creep tests and also during plant operation (Fig.4). Four types of cracking have been identified in Cr-Mo steel weld joint. They have been categorized as Type I, Type II, Type III and Type IV. The Type I and Type II cracking originate in weld metal, propagate either through the weld metal itself (Type I) or cross over in the HAZ (Type II). The Type III cracking occurs in the coarse grain region of HAZ and by refining the grain size it can be avoided. (Type IV cracking nucleates and propagates in the intercritical) fine grain region of HAZ. It is not possible to avoid Type IV cracking but it can be minimized.

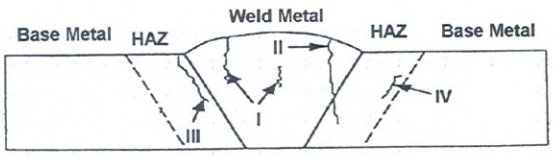

Fig. 4 : Types of cracking in weld joint of steels on service exposure

■ SOFT ZONE FORMATION IN MODIFIED 9Cr-1Mo STEEL WELD JOINT

A soft zone develops in the intercritical region of HAZ of the weld joint of modified 9Cr-1Mo steel (Fig.1). The development of the soft zone in the steel weld joint can be rationalized on the basis of microstructure of the steel and its modification on intercritical heating during weld thermal cycle. The steel derives its creep strength from solid solution strengthening, dislocation substructure strengthening and precipitation strengthening. Molybdenum mostly confers solute solution strengthening to the steel. The modified 9Cr-1Mo steel has tempered martensitic structure (Fig.4(a)). The precipitation of $M_{23}C_6$ particles stabilizes the martensitic lath structure. The additions of V, Nb and N in the steel ensure the intragranular precipitation of highly stable V,Nb-carbonitrides (MX) particles on tempering and during creep exposure to confer high creep strength. Laves phase (Fe_2M), an intermetallic compound, is found to precipitate on grain and subgrain boundaries on thermal and creep exposures in the steel. The precipitation of laves phase is expected to decrease the solute solution strengthening but it can also increase the precipitation strengthening of the steels at least when the precipitates are fine in size. On long-term high temperature thermal and creep exposures, modified Z-phase, complex Cr(V,Nb)N particle, is reported to precipitate intergranularly in the 9Cr-1MoVNb steel. They are fine in size just after precipitation, but grow quickly by dissolving the beneficial MX precipitates.

Intercritical heating by weld thermal cycle produces (i) the recovery of martensitic lath structure with high dislocation into subgrain with low dislocation (Figs.5a and 5b), (ii) coarsening of the $M_{23}C_6$ precipitate and (iii) probably the enhanced precipitation of Z-phase in the intercritical HAZ subsequently during creep exposure. The Z-phase was observed in the inter-critical region of HAZ in 9Cr-1MoVNb steel weld joint on creep exposure (Fig.5c), whereas very little was observed in base steel. The enhanced coarsening of the $M_{23}C_6$ particles and the precipitation of the Z-phase in the inter-critical region of HAZ than in the base metal at higher creep test temperatures could be the reasons for the higher reduction in creep rupture strength of joint in 9Cr-1MoVNb steel (Fig.2).

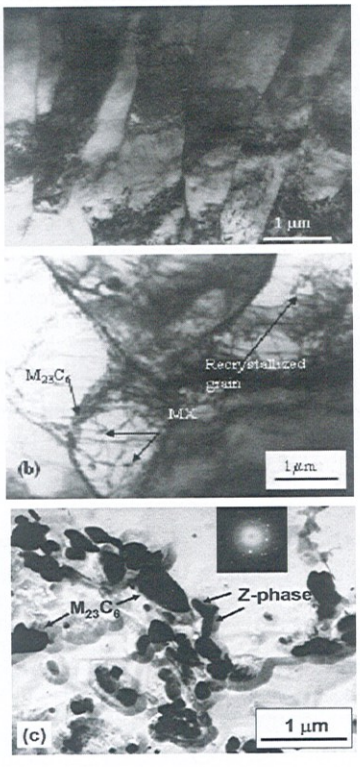

Fig. 5 : (a) Lath martensitic structure in modified 9Cr-1Mo base metal, (b) recovered subgrain structure in intercritical HAZ and © Z-phase in the intercritical HAZ

■ ACHIEVEMENT

Weld joint is the weak link in the components fabricated out of modified 9Cr-1Mo due to the type IV cracking in the intercritical region of HAZ. A 10 % reduction in creep rupture strength at 798 K (525 °C) as recommended by RCC-MR code has been adopted for the design of welded modified 9Cr-1Mo steel steam generator. The study supports the basis of such reduction in creep rupture strength of modified 9Cr-1Mo steel weld joint and also reveals a higher reduction at higher temperatures.

■ PUBLICATIONS ARISING OUT OF THIS STUDY AND RELATED WORK

K. Laha, K.S. Chandravathi, P. Parameswaran, K. Bhanu Sankara Rao and S.L. Mannan, *Met. Mater. Trans.A*, **38** (2007)58.

Further inquiries:
Dr. K. Laha, Mechanical Metallurgy Division
Metallurgy and Materials Group, IGCAR, e-mail: laha@igcar.gov.in

Mechanical Properties and Microstructural Studies on Core Structural Material of FBTR

EXECUTIVE SUMMARY

The irradiation experience worldwide has proved that the main factor affecting high fuel burn-up in fast reactors is related to the irradiation damage of the structural materials. Stainless Steel SS316 (20% cold worked) is the structural material for the fuel cladding and hexagonal wrapper of the Fast Breeder Test Reactor (FBTR) at IGCAR. To understand the irradiation performance of the SS316 in FBTR at various levels of displacement damage (dpa- displacement per atom), mechanical testing and TEM (Transmission Electron Microscopy) studies have been carried out on the core structural material of FBTR. The trends in the evolution of mechanical properties and microstructure of irradiated wrapper with dpa and void swelling have been established.

OUTLINE

The core materials of fast reactors are subjected to a high neutron flux (10^{15} n/cm^{2}s^{-1}) coupled with high temperatures (400-650°C). Under such irradiation conditions and high temperatures, austenitic stainless steels undergo significant microstructural alterations which induce dimensional changes and affect mechanical properties. The irradiation induced microstructural changes are a strong function of irradiation temperature and the displacement per atom (dpa)

Tensile Testing of Cladding

To qualify the irradiated SS 316 cladding, elevated temperature tensile testing is employed for strength and residual ductility evaluation. The remote tensile tests are executed as per the ASTM E-8 and ASTM E-21 standards using a 2 ton capacity UTM fitted with a resistance heating furnace in the hot cells. Special collet type gripping fixtures have been designed and developed in-house for holding the cladding at elevated temperatures during the test. The results of the tensile tests indicated that uniform elongation has reduced from 6.8 % for unirradiated tube to 3 % for irradiated tube of 56 dpa at test and irradiation temperature of 430°C as seen in Fig 1. The presence of sufficient strength and residual ductility in the irradiated cladding enabled extending its life to the present damage level of 83 dpa without any failure.

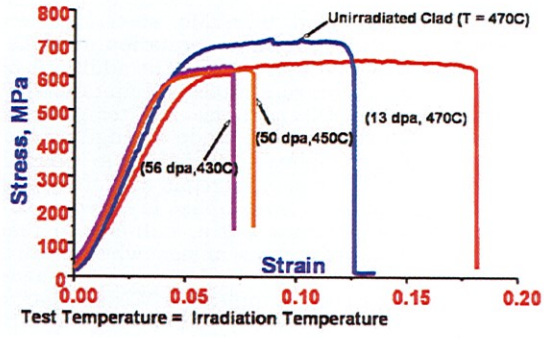

Fig. 1 : Stress strain curves of Irradiated SS316

Shear punch testing and TEM examination of Irradiated Wrapper

Small specimen test techniques are used for evaluating the changes in the mechanical properties of the irradiated wrapper. The Shear punch (ShP) testing is a small specimen testing technique, in which a cylindrical punch with a flat end is forced to punch a hole in a clamped small disk specimen of 1 mm thick and 8 mm diameter. The load-displacement curve obtained during the ShP test is similar to the load-displacement plot of a conventional tensile test and can be analyzed to extract the uniaxial tensile properties like yield strength (YS), Ultimate Tensile Strength (UTS) and % elongation. The shear punch tests have been standardized and a tensile-shear correlation established using various microstructures generated from unirradiated SS316.

Small specimens of 8 mm diameter are extracted from different axial locations of the hexagonal wrapper which has undergone different displacement damage (dpa) for microstructural studies and estimation of mechanical properties by shear punch technique. Using the shear punch test results on irradiated specimens and the correlation equations, the tensile properties of the irradiated specimens have been estimated.

Disc specimens of 3mm diameter obtained after shear punch testing are used for preparing TEM specimens for structure property correlation studies. TEM specimens are prepared using special fixtures developed for handling irradiated specimens. Irradiated specimens which had undergone displacement damage from 2 dpa to 56 dpa have been examined using 200 keV Analytical TEM. Volumetric swelling estimates as a function of dpa have also been performed on these irradiated specimens.

A considerable increase in the strength and decrease in the ductility of the wrapper with increasing displacement per atom (dpa) have been observed from the small specimen mechanical tests. The transmission electron microscopic studies revealed the presence of voids and precipitates in the matrix (Fig. 2). Precipitates were identified to be of $M_{23}C_6$ type and precipitation of second phases corroborates the hardening observed on the wrapper.

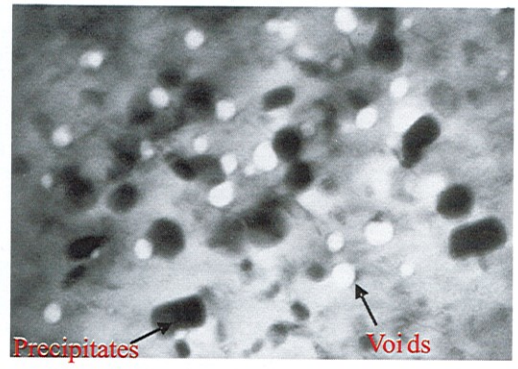

Fig. 2 : TEM image of the Irradiated SS316 at a displacement damage of 40 dpa

■ ADDITIONAL INFORMATION

Fast breeder reactor (FBR) core consists of hexagonal wrapper tubes that contain thin walled fuel pins, which forms the first barrier against possible dispersion of fissile material and fission products. Because of the use of fast neutrons which have lower fission cross sections, the neutron flux levels in FBRs are about two orders of magnitude higher ($\sim 10^{15}$ n/cm^{2}s^{-1}) than that in thermal reactors to achieve comparable power density. The core materials are, therefore, subjected to a very demanding environment of high fast neutron flux coupled with high temperatures. One major consequence of this high flux of fast neutrons is the occurrence of very high level of atomic displacements in the core structural materials. This damage is characterized in terms of the average number of times that an individual atom is displaced from its lattice site (dpa - displacements per atom) and for some core components, such exposure can be greater than 100 dpa. Under such irradiation conditions and high temperatures (400-650°C), austenitic stainless steels undergo significant microstructural alterations which induce dimensional changes and affect mechanical properties.

■ GENERAL EXPLANATION

Irradiation induced changes in properties is dependent on temperature of irradiation, prior microstructural condition and neutron fluence (dpa). One area of major concern is the loss of ductility in these structural materials. Mechanical tests provide valuable data on the residual strength and ductility and are correlated with the swelling and microstructural studies. Fig 3 shows the view of the tensile test system installed inside the hot cells for remote mechanical testing of the irradiated cladding.

Among the different radiation damage mechanisms, void swelling is the predominant factor which limits the residence time of the fuel subassembly and the achievable burnup. The immersion density measurements are used to estimate the swelling while TEM studies provided more insights into the void evolution and other microstructural related phenomena.

Limit on minimum residual ductility for the safe operation of the cladding and wrapper is not available in the literature. But international experience shows drastic ductility reduction above 12 % void swelling indicating a strong link between the void swelling and the degradation of mechanical properties.

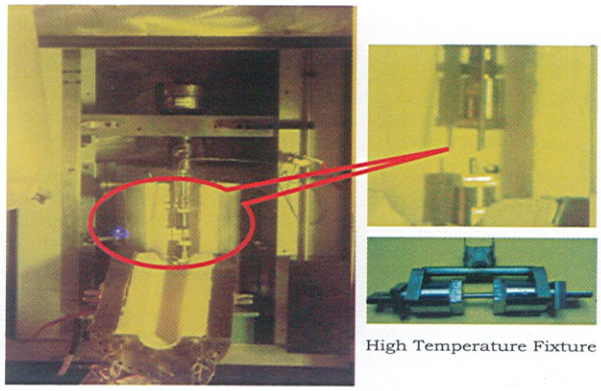

Fig. 3 : View of the remote tensile test machine inside the hot cells and fixtures

■ BRIEF DESCRIPTION OF THEORETICAL BACKGROUND

In core structural materials, significant microstructural alterations occur due to high level of atomic displacements induced by neutron irradiation. Defect structures like dislocation loops, vacancy clusters, vacancy loops, voids, helium bubbles etc form as a function of temperature of operation and neutron fluence (quantified by displacement per atom-dpa). Major phenomena affecting structural materials are void swelling, irradiation creep, phase stability and changes in mechanical properties. Voids form in austenitic stainless steels in the temperature range 400-550°C under neutron irradiation resulting from the agglomeration of vacancies. The formation and growth of voids are sensitive to all metallurgical variables like chemical composition and thermo-mechanical history and irradiation parameters like fluence, dose rate and irradiation temperature. Irradiation creep is caused due to the combined effects of external non-hydrostatic stresses and presence of both interstitial atoms and vacancies at very large super saturation levels.

■ ACHIEVEMENT

The estimation of strength and residual ductility in the irradiated cladding enabled extending the use of the SS 316 cladding in FBTR to the present level of 83 dpa without any cladding failure. The structure property correlation studies on the irradiated SS 316 provided useful insights into the irradiation performance of irradiated SS 316.

■ PUBLICATIONS ARISING OUT OF THIS STUDY AND RELATED WORK

1. N.G.Muralidharan, V.Karthik, V.Venugopal, Jojo Joseph, Shaji Kurien, V.Anandaraj, A.Vijayaraghavan and K.V.Kasiviswanathan, *J. Nucl. Mater.* (In Press)
2. N.G.Muralidharan, C.N.Venkiteswaran, V.Anandraj, V.Karthik, V.Venugopal, P.Parameswaran, Saroja Saibaba, M.Vijayalakshmi, K.V.Kasiviswanathan and Baldev Raj, International Symposium on Advances in stainless steel, (ISAS), April 9-11, 2007, Chennai.
3. N.G.Muralidharan, V.Karthik, A.Vijayaraghavan, Shaji Kurien, V.Venugopal, Jojo Joseph, K.V.Kasiviswanathan and Baldev Raj, Proceedings of "Modern Developments and Practices in Mechanical testing (MDPMT-2007), BARC, Mumbai.

Further inquiries:
Shri N G Muralidharan, Post-Irradiation Examination Division
Metallurgy and Materials Group, IGCAR, e-mail:ngm@igcar.gov.in

Magnetic Nanoparticles with Tunable Physical Properties

EXECUTIVE SUMMARY

Ferrite nanoparticles with tunable physical properties have been successfully synthesized by a simple co-precipitation technique by controlling the digestion time, alkali addition rate, solvent polarity and by using divalent cations of Mn, Co, Fe and Zn. Ferrite nanoparticles of average particle size 9 to 29 nm were synthesized by using different divalent cations of Mn, Co, Fe and Zn. The Mn, Co and Fe ferrites were magnetic in nature with saturation magnetization of 44.6, 47.38, 56.19 emu/g respectively. The increase in particle size with increasing solubility product of divalent metal hydroxide was in good agreement with the nucleation theory. Nanoparticles with higher transition temperatures have been achieved by using NaOH as an alkali.

OUTLINE

The reproducible and convenient synthesis routes for the production of nonmagnetic nanocrystals with desired properties have been a topic of intense research during the last few decades. It has been demonstrated that, at nanoscale, it is possible to tune precisely the electrical, optical, mechanical and chemical properties by modifying the crystal size and shape.

Among various reproducible synthesis routes for the preparation of nanoparticles, co-precipitation technique is one of the most convenient and versatile methods. In precipitation, nucleated particle size mostly depends on the parameters related to solubility and interfacial energy. In nano-regime, physical and chemical properties are size dependant. In order to tune these properties, various groups have been working on optimizing particle size by varying parameters such as temperature, pH and ionic strength imposed by non-complexing salts. We have developed methods to tune the nanoparticles diameter by controlling the properties of the solvent media, digestion time, alkali addition rate, and divalent cations.

The XRD patterns of samples obtained with different ethanol-water ratio are shown in Fig. 1. The broadening of the peaks with increasing ethanol concentration clearly indicates the decrease in crystalline size.

Among the mixed ferrites, $MnFe_2O_4$, Fe_3O_4 and $CoFe_2O_4$ show inverse spinel structure, where $ZnFe_2O_4$ shows normal spinel structure. Size, covalent bonding effect and crystal field stabilization energies of M^{2+} seems to influence the preferential site of ions. In inverse spinel structure, divalent metal ions occupy octahedral sites. The lattice parameter depends on ionic radii of the divalent metal ion. Since the ionic radii of Mn^{2+}, Fe^{2+} and Co^{2+} are in decreasing order (0.91, 0.83 and 0.82 Å respectively), the lattice parameter is also expected to follow the same order. Though, the ionic radii Zn^{2+} (0.83 Å) is almost the same as Co^{2+} and Fe^{2+} ions, the Zn^{2+} ions prefers to be in the tetrahedral sites leading to normal spinel structure. The observed larger lattice parameter (0.844 nm) in $ZnFe_2O_4$ seems to be due to the strong inter-atomic interactions compared to cobalt or iron ferrite. The calculated average sizes of the $MnFe_2O_4$, Fe_3O_4, $CoFe_2O_4$ and $ZnFe_2O_4$ particles are 29.1, 9.9, 14.5 and 8.9 nm respectively. Though all these samples are synthesized under identical conditions (reaction temperature, pH, solvent, etc.), the large variation at the average size of the particles shows that the divalent metal ions have a strong influence on the crystallization process.

Fig. 2 shows the magnetization curves of the different ferrite particles obtained by co-precipitation. Mn and Co ferrites show ferromagnetic nature with a hysterisis loop, whereas the magnetite sample exhibits superparamagnetic nature with negligible remenance and coercivity. The Zn ferrite shows paramagnetic nature. However, the bulk $MnFe_2O_4$, Fe_3O_4 and $CoFe_2O_4$ materials shows ferrimagnetic nature where as $ZnFe_2O_4$ paramagnetic at room temperatures.

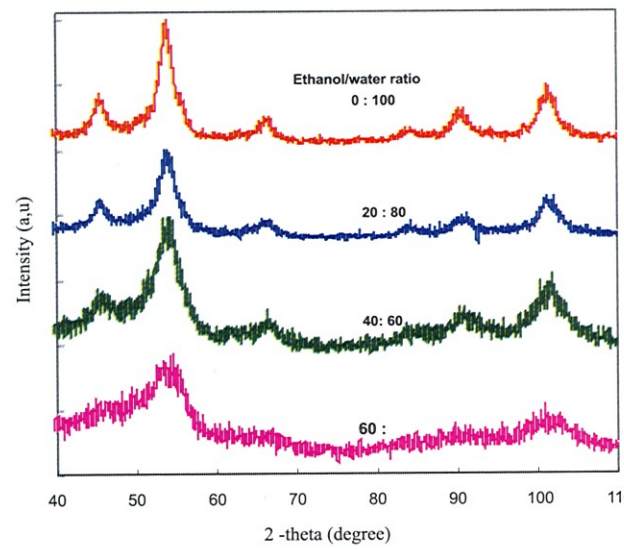

Fig. 1 : The XRD patterns of samples obtained with different ethanol-water ratio

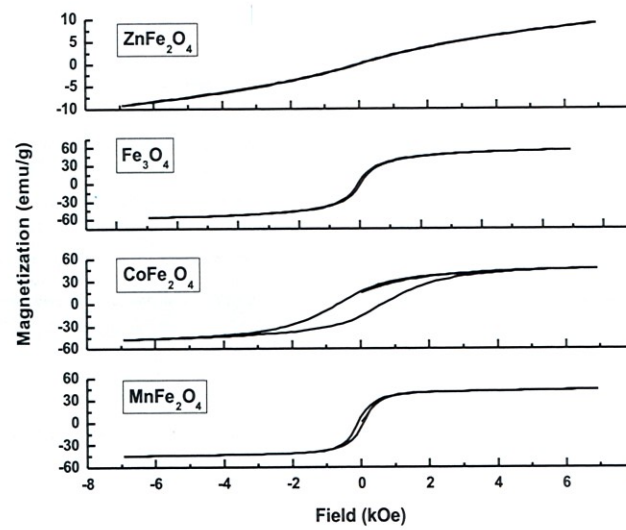

Fig. 2 : Magnetization curves of different ferrite particles

■ IMPORTANCE OF MAGNETIC NANOPARTICLES

Among various nano materials, magnetic nanocrystals have been widely used in many applications such as Ferro fluids, in recording media, in electronic, in optical and in biomedical disciplines. In addition, magnetic colloids have been found to be a wonderful model system to study fundamental aspects such as magnetic domain structures, superpara-magnetism, magnetic dipolar interactions and size dependant physical properties. The ferrofluid emulsions have also been used to probe the nature of forces acting between nanodrops and the associative behavior of polymer-surfactant interactions at droplet interfaces.

■ MAGNETIC NANOCRYSTALS

The average particle sizes obtained at digestion times of 22, 40, 120, 300, 900, 1800 and 3600 sec are 6.7, 7.2, 8.2, 8, 8.5, 8.73 and 8.7nm respectively. The TEM image of a sample prepared at 22 seconds of digestion time (average size of 6.7nm) and the size distribution is shown in Fig 3. Our experiments show that the time required to complete the growth process for magnetite nanocrystals is very short (~300sec), compared to the large digestion times (20-190 minutes) required for MnO and CdSe nanocrystals. The rapid growth of magnetite particles suggests that Oswald ripening is insignificant during the precipitation stage, probably due to the low solubility of the oxides and the domination of a solid state reaction where high electron mobility between Fe^{2+} and Fe^{3+} ions drives a local cubic close-packed ordering. A plot of the cube of radius of magnetite particles verses digestion time shows a linear dependence up to 300 sec but deviates beyond 300 sec. Therefore, the nonlinear dependence of digestion time with the cube of particle radius beyond 300 sec, shows that the solid-state reaction is dominant over dissolution - crystallization.

The average particle size decreases from 11 to 6.8 nm, when the alkali addition rate is increased from 1 to 80 ml/sec. It is also observed that the lattice constant decreases with particle size. When the average size decreased from 11 to 6.8 nm, the lattice parameter also decreased from 0.838 to 0.835 nm.

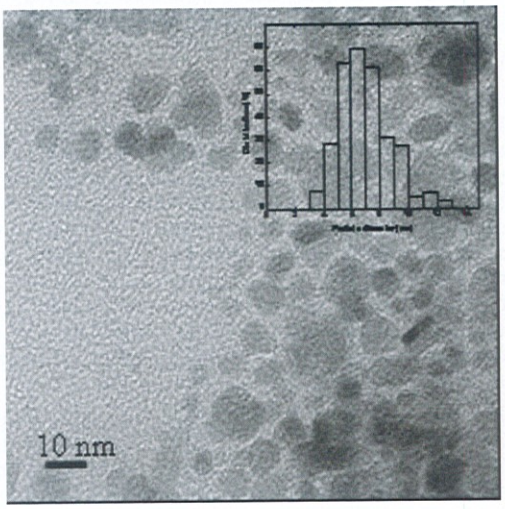

Fig. 3 : The TEM image of a sample prepared at 22 seconds of digestion time (average size of 6.7nm) and the size distribution (inset). The alkali addition rate in these experiment was 20 ml/sec

■ NANO PARTICLES

The nano particles with different sizes are prepared by controlling the solubility and reaction rates. The equilibrium critical radius (r*) of particles during nucleation in supersaturated solution is defined as:

$$r^* = \frac{2V\sigma}{k_B T \ln(S)}$$

where, V is the molecular volume of the precipitated species, σ is the surface free energy per unit surface area, k_B is the Boltzmann constant, T is the absolute temperature and S is the saturation ratio, which is defined as ratio between solute concentrations at saturation (X) and equilibrium (X_S), i.e. $S = X/X_S$. The saturation ratio is inversely proportional to the solvent dielectric constant and the equilibrium critical radius is directly proportional to the solvent dielectric constant.

■ ACHIEVEMENT

We have developed some new approaches to produce magnetic nanoparticles with tunable physical properties by controlling the digestion time, alkali addition rate, solvent polarity and by using divalent cations of Mn, Co, Fe and Zn. Particle sizes varying from 2 to 30 nm and saturation magnetization of 30 to 70 emu/g have been obtained.

■ PUBLICATIONS ARISING OUT OF THIS STUDY AND RELATED WORK

1. G.Gnanaprakash, S.Ayyappan, T.Jayakumar, John Philip and Baldev Raj, *Nanotechnology*, **17** (2006) 5851.
2. G.Gnanaprakash, John Philip, T.Jayakumar, Baldev Raj, *J. Phy. Chem. B* **111** (2007) 7978.
3. G.Gnanaprakash, S.Mahadevan, T.Jayakumar, P.K.Sundaram, John Philip and Baldev Raj, *Mater. Chem. and Phys.* **103** (2007) 168.
4. G.Gnanaprakash, John Philip and Baldev Raj, *Mater. Lett.* **61** (2007) 4545.
5. John Philip, G.Gnanaprakash, G.Paneerselvam, M.P.Antony, T.Jayakumar and Baldev Raj, *J. App. Phys.* **102** (2007) 1.

Further inquiries:
Dr. John Philip, Non Destructive Evaluation Division
Metallurgy and Materials Group, IGCAR, e-mail: philip@igcar.gov.in

Phase Stability Characterization and Thermodynamic Data Generation on 9Cr-1Mo Steel with varied Microstructure-Based on Experimental Measurements and Modeling

EXECUTIVE SUMMARY

The kinetics of austenitisation of aged 9Cr-1Mo steel is studied using differential scanning calorimetry. It is observed that the transformation temperatures and the estimated kinetic quantities exhibit a pronounced non linear dependence on the heating rate. The apparent activation energy for the overall transformation decreased with increasing heating rate. For higher heating rates, the activation energy is reflective of the carbon diffusion controlled ferrite to austenite transformation. However, for lower heating rates, it is influenced by the carbide dissolution kinetics.

OUTLINE

Despite the fact that the kinetics of austenite formation has been studied rather extensively in the case of low alloy steels there is however a relative paucity of such information on high chromium ferritic or ferritic-martensitic steels. Since carbides in high chromium alloys are comparatively more stable, their presence is expected to influence the kinetics of reaustenitisation in a significant manner. It is in this spirit, that we investigate in the present study the kinetics of austenite formation during continuous heating in a tempered and aged 9Cr-1Mo steel using differential scanning calorimetry (DSC) technique.

The composition of the steel in wt.% is as follows: 8.44 Cr, 0.94 Mo, 0.49 Si, 0.46 Mn, 0.17 Ni, 0.11Cu, 0.1C, 0.008 P, 0.011 Al, 0.002 S, 0.001V; 0.008 N; balance being Fe. The alloy was supplied in normalized and tempered state. The DSC experiments were performed with Setaram Setsys 16® heat-flux type high-temperature differential scanning calorimeter, employing clean samples of mass varying from 60 to 100 mg. The experiments were performed under a constant flow (50 ml per minute) of high pure argon. Heating rates (β) in the range, 1 to 100 °C per minute were employed.

In Figure 1, the DSC traces obtained at various heating rates for a typical aged sample are displayed. The endothermic peak arising due to the formation of austenite from α - ferrite + carbide is readily apparent in this figure. The austenite start and finish temperatures corresponding to each heating rate are marked as Ac_1 and Ac_3 respectively. The peak temperature (T_p) corresponds to the maximum in the rate of formation of austenite. It is found that for very low heating rates (1°C min^{-1}), the peak profile is comparatively broad and less well resolved as well. Since austenite formation is a typical nucleation and growth phenomenon, the transformation temperatures are expected to be sensitive to the heating rate (Fig. 2). It is clear that both Ac_1 and Ac_3 exhibit a pronounced nonlinear increase with the heating rate. In particular, the increase in Ac_3 is slightly more marked than that of Ac_1, resulting in the net effect of widening the existence domain of α-ferrite + carbide + γ-austenite phase field for higher heating rates.

The fraction of austenite (γ) formed as a function of temperature (T) in the range $Ac_1 \leq T \leq Ac_3$ is displayed in Figure 2. As may be seen, the transformation curves are reasonably sigmoidal in character. Besides, it is also noteworthy that within a certain range of values ($0.25 \leq \gamma \leq 0.75$), the slope of transformation curves, namely $(d\gamma/dT)_\beta$ for different heating rates (1-60 K min^{-1}) is nearly the same. In other words, $(d\gamma/dT)_\beta$ is almost independent of β for a range of β and γ values. This aspect yields certain interesting insight into the kinetics of austenite formation, namely that that k/β is a conserved kinetic quantity in the austenite formation reaction. Thus with increasing β, the rate constant k should also increase, implying thereby that Q must exhibit a corresponding decrease.

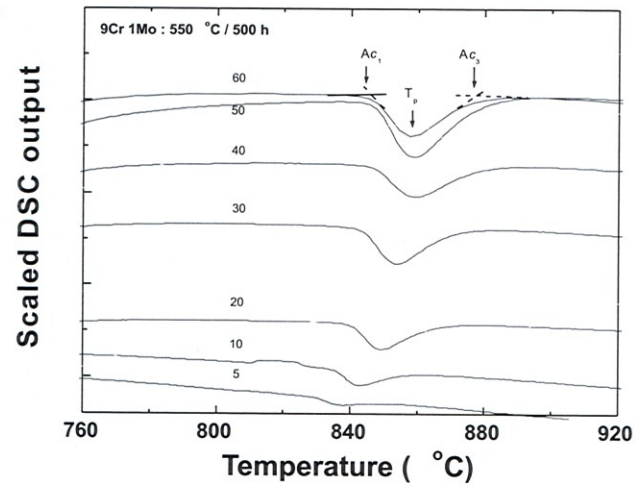

Fig. 1 : DSC profile taken at various heating rates. Ac_1, Ac_3 and T_p mark respectively the austenite start, finish and peak temperatures

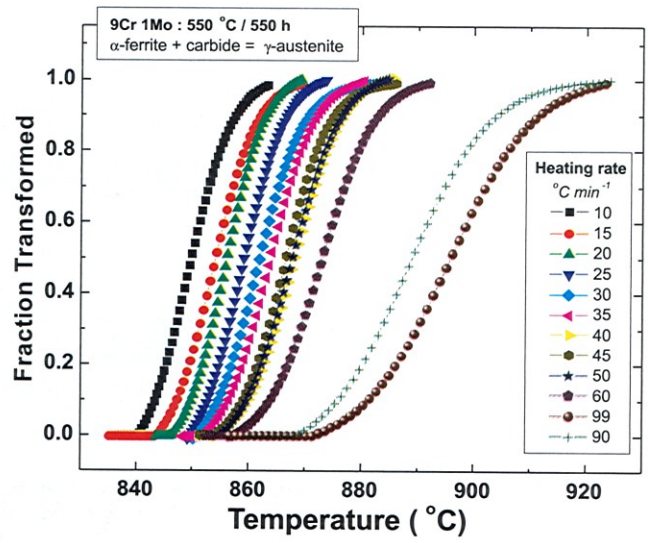

Fig 2 : Transformation plots for different heating rates

ESTIMATION OF APPARENT ACTIVATION ENERGY, Q

The deduction that k/β is a constant can also be made use of in obtaining an estimate of Q. Thus, Thus, for any fixed γ that is realised at two arbitrary heating rates, β_1 and β_2, and at respective temperatures T_1 and T_2, we may write

$$R \ln [\beta_1/\beta_2] + Q_1/T_1 \approx Q_2/T_2$$

This value can then be refined in an iterative fashion by using it in a suitable transformation model $f(\gamma)$, and effecting an optimal fit of the experimental data.

MECHANISTIC CONSIDERATIONS OF THE AUSTENITE FORMATION

Admittedly, the formation of austenite from mixed α-ferrite + carbide microstructure is not a simple metallurgical phenomenon. It is clear that upon reaching Ac_1, the lower critical temperature, both the dissolution of carbide and the structural transformation of α-ferrite austenite can in principle occur concurrently with different velocities. This is so, because in high chromium steels the carbide dissolution is rather sluggish as compared to low alloy steels [x]. Further the structural transformation of (carbon lean) ferrite to austenite is basically an interface diffusion-controlled process while carbide dissolution is a bulk or volume diffusion controlled phenomenon decided by the diffusivity of substitutional elements. The heterogeneous nucleation of austenite is catalysed by the presence of abundant ferrite/ carbide interfaces to begin with, although at later stages, some other nucleation sites like ferrite grain boundaries, grain edges and corners etc., need to get activated. This is due to the gradual dissolution of carbide particles in austenite. Thus, the nucleation rate of austenite is one of continuously decreasing with time, especially for slow heating rates. Assuming that nucleation of austenite is adequately facilitated; the issue then is one of sustaining its growth by enabling the transfer of carbon atoms across the growing austenite/ferrite interface. From a mechanistic point of view, the austenite growth is possible even at higher heating rates, if it is mediated by the transfer of highly mobile carbon atoms across the growing / interface.

Table 1
The kinetic quantities obtained by fitting the experimental data to a nonisothermal KJMA model.

β ($^0C\ min^{-1}$)	Q ($kJ\ mol^{-1}$)	k_0 (sec^{-1})	n
5	120	1.07×10^6	1.69
10	115	1.25×10^6	1.71
20	110	5.92×10^5	2.78
30	109	7.69×10^5	2.23
40	108	6.30×10^5	2.34
50	107	8.41×10^5	2.26
60	99	3.13×10^5	2.18
90	86	6.69×10^4	1.70
99	85	5.89×10^4	1.69

If on the contrary, the austenitisation is sought under very fast heating conditions, the time scales provided are simply inadequate for the successful realisation of carbide dissolution, although the ferrite to austenite structural change can still be realised at these high rates. In any case, it is highly unlikely that transformation to austenite proceeds to completion at faster heating rates upon reaching Ac_3. A slight superheating and or isothermal hold are often required to enable carbide dissolution and realise the formation of homogeneous austenite. For intermediate heating rates, the carbide dissolution and phase change proceed to different extents.

BRIEF DESCRIPTION OF THEORETICAL BACKGROUND

In summary, it may be said that austenitisation in aged 9Cr-1Mo steel is a composite reaction, governed principally by carbon diffusion in austenite. While at slower heating rates, this is accompanied by considerable carbide dissolution in the emerging austenite phase; only the $\alpha\rightarrow\gamma$ structural transformation is enabled for very high heating rates. It emerges therefore in the final analysis, that at lower heating rates the overall activation energy is influenced by the disintegration of the carbide phase, while for fast heating conditions, Q is predominantly reflective of the simple interface diffusion controlled $\alpha\rightarrow\gamma$ structural change. Further, during fast heating conditions there is not much scope for change in austenite composition, as this would call for a substantial diffusion of substitutional Cr atoms and would therefore entail higher activation energy (260 kJ mol^{-1}) as compared to interfacial carbon migration.

ACHIEVEMENT

A clear cut enunciation of the role of kinetic parameters in effecting homogenisation of the alloy in the austenite state achieved. The experiments paved way for a theoretical design of cyclic homogenisation process that results in energy and time savings for achieving effective alloy homogenisation.

PUBLICATIONS ARISING OUT OF THIS STUDY AND RELATED WORK

S. Raju, B. Jeya Ganesh, Aritra Banerjee and E. Mohandas, *Mater. Sci. Engg., A* **465** (2007) 29.

Further inquiries:
Shri S. Raju and Shri E. Mohandas, Physical Metallurgy Division
Metallurgy and Materials Group, IGCAR, e-mail : sraju@igcar.gov.in

Microchemical and Microstructural Variations across Dissimilar Joints

EXECUTIVE SUMMARY

Ferritic steels are important structural materials in the steam generator circuits of LMFBRs. The weld joints between dissimilar ferritic steels of large components are the potential zones for failure during service exposure. The microstructural instability and elemental redistribution in dissimilar weldments between 9Cr-1Mo and 2.25Cr-1Mo ferritic steels during post weld heat treatment, which can lead to severe impairment of the mechanical properties has been studied using optical and electron microscopy techniques. Based on the investigations the micromechanism responsible for the microstructural degradation has been identified and methods to improve the service life of the weldments have been suggested.

OUTLINE

In the fabrication of steam generators for nuclear power plants, both high and low Cr steels are employed depending on the service temperature experienced by the components. This results in dissimilar welding in selected locations. It is known that when these dissimilar joints are exposed to elevated temperature a hard brittle layer forms at the interface which is the weak link in the structure. To investigate the cause for such a zone formation a dissimilar joint between two ferritic steels, 9Cr-1Mo and 2.25Cr-1Mo exposed to elevated temperature of 1023 K for various time durations was studied.

It was found that after heat treatment a hard brittle zone called as the 'hard zone' characterized by (1) high hardness of ~270 VHN (compared to the rest of the weldment) and (2) carbon enrichment forms on the high alloy side of the weldment. In addition a 'soft zone' characterized by (1) low hardness of ~120 VHN (2) ferritic structure almost free of carbides forms on the low alloy side of the weldment (Fig. 1). The width of these zones was found to increase with the time and temperature of exposure. Microchemical characterization gave evidence for the redistribution of carbon across the weld interface. Using numerical methods the carbon diffusion profile across the weld interface for various heat treatment conditions was simulated. Simultaneous enrichment for Cr and C was obtained on the hard zone suggesting that the precipitates present in the hard zone are chromium carbides. Detailed transmission electron microscopy on carbon extraction replicas was carried out to identify the carbides. The precipitation sequence in the hard zone is summarized as

$$\alpha' \rightarrow \alpha + M_{23}C_6$$

The soft zone was found to be almost devoid of carbides, containing only very few M_2C or M_6C type precipitates. Carbon content in the hard zone was estimated using an indirect method which depends on the type and volume fraction of the carbides. Diffusion of carbon against the activity gradient from low Cr to high Cr steel was identified as the mechanism responsible for the formation of the zones.

Based on the understanding of the atomic processes gained from the above studies further attempt was made to evolve a methodology to prevent the formation of hard and soft zones. The following three methods were suggested in this regard: (1) use of interlayers that act as diffusion barriers to carbon (2) welding ferritic steels with graded Cr concentration and (3) adjusting the chemistry of the base metal to reduce activity gradient. One of the three methods i.e. effectiveness of diffusion barriers in preventing carbon diffusion was demonstrated using Ni based interlayers. Ni was chosen mainly because of its repulsive interaction with carbon and also because of its compatibility with ferritic steels with respect to thermal properties and weldability.

Transition joints were fabricated between 9Cr-1Mo and 2.25Cr-1Mo ferritic steels using Inconel-182 interlayer. These joints were subjected to the same heat treatment conditions as that of direct dissimilar welds. No microstructural modification was noticed at the interface of dissimilar materials as shown in Fig. 2. Ni based interlayers were found to be effective in preventing the formation of hard and soft zones in ferritic steels.

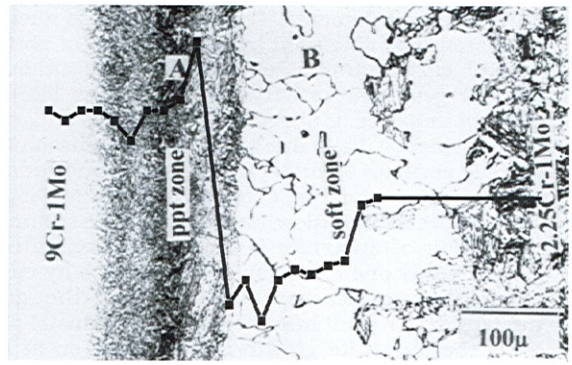

Fig. 1 : Optical micrograph and superimposed hardness profile showing the presence of hard zone 'A' and soft zone 'B'

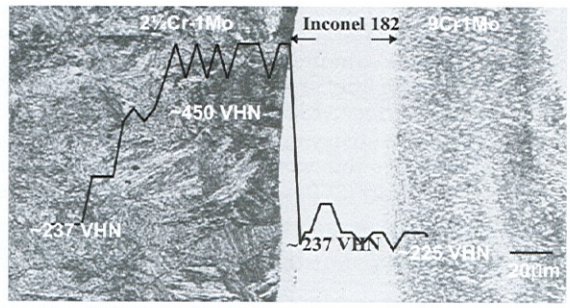

Fig. 2 : Optical micrograph showing the absence of hard and soft zones in a transition joint of ferritic steels with a Ni based interlayer

■ ORIGIN OF THE HARD AND SOFT ZONES

When dissimilar Cr-Mo steels are welded together and subjected to high temperature exposure carbon diffuses from low Cr to high Cr side. The following equation relates the activity of carbon a_c to concentration of C_r, C_{cr} and interaction parameter between Cr and C, ε_C^{Cr} :

$$a_C = C_C\left(\exp\left(C_C\varepsilon_C^{C} + C_{Cr}\varepsilon_C^{Cr}\right)\right)$$

According to this equation since chromium has a negative interaction parameter with carbon ($\varepsilon_C^{Cr} = -72$), an increase in Cr content means a decrease in carbon activity. This activity gradient between the high and low Cr sides acts as the driving force for the diffusion of carbon.

■ MECHANISTIC CONSIDERATIONS OF THE AUSTENITE FORMATION

An activity gradient in carbon from the low Cr to high Cr steel results in diffusion of carbon across the interface. The transport of carbon into 9Cr-1Mo steel far exceeding the solubility leads to formation of chromium rich carbides, which manifest as a hard and brittle zone. To maintain the equilibrium, carbides in the 2.25Cr -1Mo steel dissolve leading to the transformation of bainite to ferrite. This results in the formation of a soft zone near the low Cr side of the dissimilar weldment. As the temperature or time of heat treatment is increased diffusion of carbon, dissolution/precipitation of carbides proceeds leading to an increase in the width of the zones. Due to the various constraints on the diffusion of carbon like (1) decrease in the activity difference between the two sides (2) depletion of Cr in the weld metal and (3) low C level in transformed ferrite the width of the zones do not show an increase beyond a specific time duration and temperature.

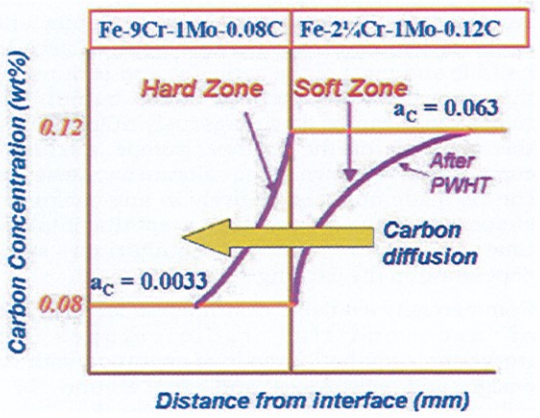

Fig. 3 : Schematic illustrating the formation of hard and soft zones

■ BRIEF DESCRIPTION OF THEORETICAL BACKGROUND

Using Finite difference method the carbon diffusion profiles and width of the zones have been predicted for various post weld heat treatment conditions.

■ ACHIEVEMENT

This work demonstrates that using a Ni based interlayer in transition joints of dissimilar ferritic steel improves their service life. The paper titled "Microstructure and microchemistry of hard zone in dissimilar weldments of Cr-Mo steels" has been awarded the Mc Kay Helm Award from the American Welding Society for the best research paper in 2006.

■ PUBLICATIONS ARISING OUT OF THIS STUDY AND RELATED WORK

1. C.Sudha, V.Thomas Paul, A.L.E.Terrance, S. Saroja and M.Vijayalakshmi, *Welding Journal*, **85** (2006) 71.
2. R. Anand, C. Sudha , T. Karthikeyan , S. Saroja , A. L. E. Terrance and M. Vijayalakshmi, Proc. Welding in South-East Asia – A challenge for the future – IIW Congress, 21st – 22nd November 2006, Bangkok, Thailand.
3. R. Anand, C. Sudha, T Karthikeyan, A.L.E Terrance, S.Saroja and M. Vijayalakshmi, Proc. Int. Symposium for research scholars on Metallurgy, Materials Science and Engineering, December 18th – 20th, 2006, IIT, Chennai, India.

Further inquiries:
Dr. M. Vijayalakshmi, Physical Metallurgy Division
Metallurgy and Materials Group, IGCAR, e-mail: mvl@igcar.gov.in

Quasi Isoperibol Actinide Calorimeter

EXECUTIVE SUMMARY

A novel, compact, economical and simple quasi isoperibol actinide calorimeter has been fabricated and performance tested for non-destructively estimating heat producing radioactive elements such as plutonium, tritium etc. The unique features of the instrument are, simplicity, single pot design, single point calibration, adjustable volume and sensitivity. Plutonium and tritium can be determined with accuracies better than 1% and 0.5% respectively. For the estimation of plutonium prior knowledge of isotopic composition and americium content of the sample is essential.

OUTLINE

Radioactive isotopes emit heat since the radiation emitted by them gets absorbed in the immediate surrounding. Radioisotopes emitting alpha and beta particles generate considerable heat subject to their half-life and most of the actinides and tritium belong to this category. The thermal power output from the radioisotope can be advantageously utilized to estimate the quantity of the isotope/isotope mixture if the composition is known using calorimetry. Measurements can be made non-destructively in any packing, in any shape, any form and any size, except that it takes a long time to achieve thermal equilibrium sometimes depending on the packing.

Commercially available calorimeters for the estimation of heat emitting radioisotopes employ isothermal/adiabatic mode of operation with complex design and electronics and cost around Rs. 20-30 million. A novel isoperibol calorimeter (Fig. 1) has been constructed to demonstrate the estimation of actinides and tritium. The unique features of the instrument are, simplicity, single pot design, single point calibration, adjustable volume and sensitivity. Plutonium and tritium can be determined with accuracies better than 1% and 0.5% respectively. For the estimation of plutonium prior knowledge of isotopic composition and americium content of the sample is essential while for tritium no other input is needed.

The experimental set-up comprises a brightly silvered glass dewar kept in a refrigerated water bath maintained at 25±0.1°C, a precision resistor for electrical calibration as well as to simulate the heat emitting radioisotope, a digital thermometer with thermistor probe and a constant current source.

The digital thermometer signals were acquired through an in house developed software written in BASIC, through the RS-232 port into a PC. the software has the features of displaying the real time temperature-time information on the monitor of the PC with auto scaling facility and saving the data as a text file at the end of acquisition, facilitating further processing the data using any generic graphic software.

The resistor was fed with different constant currents to get various heat outputs and the equilibrium temperature was noted (heating mode). Also initially a higher current was fed and later reverted to the desired value to get the equilibrium temperature (cooling mode) and the equilibrium temperature was plotted against the power output to get the calibration line and dynamic range.

The behaviour of the temperature profile of the system as a function of time is depicted in Fig. 2. The equilibrium temperature as a function of heat output is depicted in Fig. 3. It can be seen that the linearity and the dynamic range are excellent which in turn means that a single calibration is sufficient to get accurate results.

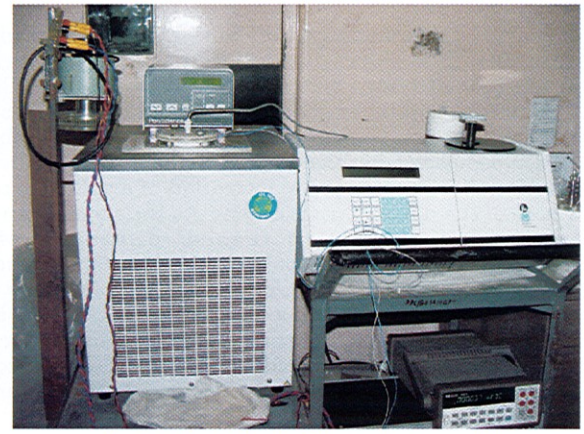

Fig. 1 : The Actinide Calorimeter Assembly

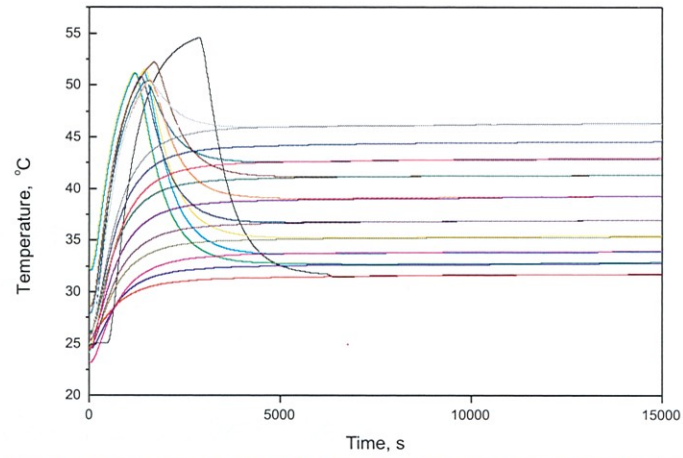

Fig. 2 : Temperature profile of the calorimeter for various power outputs

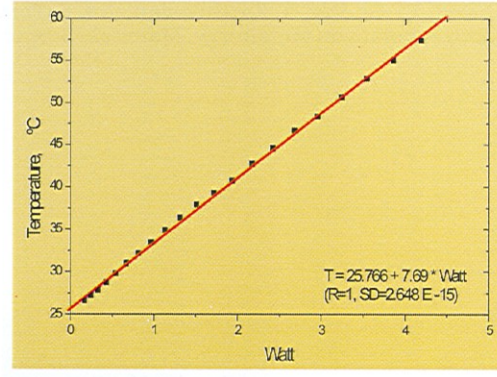

Fig. 3 : The equilibrium temperature *vs* heat output

■ ADDITIONAL INFORMATION

The concept of quasi isoperibol design for actinide and heat producing isotope measurement does not exist at present. The linearity in the calibration line and its dynamic range suggests that single point *insitu* calibration along with the unknown sample is enough for its estimation.

■ GENERAL EXPLANATION RELATED TO THE DESCRIPTION

Radioactive isotopes which decay by alpha and beta particle emission generate heat due to self absorption of the particles in the compounds containing the isotopes. The heat emission rate depends on the specific activity of the isotopic mixture. The heat emission does not depend on the size, shape or the form of the material and also the packing (provided if it is not insulating to a great extent). Thus in forms such as metals self absorption poses problem by gamma based methods and in compounds such as PuF_3/PuF_4 the neutrons produced by (α,n) reaction interfere in neutron based assay. While if the material is in the shape of a pin elaborate arrangements have to be ensured in counting techniques. Calorimetry obviates all these and is capable of estimating isotopes such as plutonium and tritium. In this mode of special nuclear material assay, the material inside a dewar flask kept in a constant temperature surroundings heats up and stabilizes to a constant temperature. The power required to achieve this equilibrium temperature can be found from the calibration line derived *insitu* by inputting known currents into the calibration heater and getting respective equilibrium temperatures. The Special Nuclear Material (SNM) content in turn can be determined from specific power derived from the isotopic composition.

■ BRIEF DESCRIPTION OF THEORETICAL BACKGROUND

Substances which emit heat when kept in insulated containers reach a particular temperature and stabilise at a constant value, when external temperature is constant. This principle is used to measure heat emitting actinides and other isotopes. Calorimeters are usually employed for measuring the heats evolved/absorbed during any process. Depending on the construction and operating principle they can be classified as, isothermal, adiabatic and isoperibol types. The isothermal and adiabatic calorimeters have complexities in the construction to maintain the temperature of the calorimeter constant and also to prevent heat exchange with the surroundings respectively as the name suggests. Isoperibol calorimeters on the contrast are very simple to construct and operate.

■ ACHIEVEMENT

The development of the calorimeter makes imports redundant and saves huge foreign exchange. A calorimeter to accommodate large volume PuO_2 containers, fuel pins and subassemblies is under fabrication.

Further inquiries:
Dr.T.G.Srinivasan, Fuel Chemistry Division
Chemistry Group, IGCAR, e-mail: tgs@igcar.gov.in

Matrix Isolation Infrared Spectroscopy: A Window to Understanding the Chemistry of Solvent Extraction

■ EXECUTIVE SUMMARY

Matrix isolation infrared spectroscopy has been used, to study molecular conformations and weak intermolecular interactions. Using this technique, which was essentially a home-built set up, we have studied the conformations of organic phosphates, such as trimethyl phosphate, triethyl phosphate and tri-n-butyl phosphate. We also showed, for the first time, that the use of a supersonic jet source together with matrix isolation is a powerful tool in studies on molecular conformations. Together with experiments, we also perform ab initio computations to corroborate our experiments. As a result of our work, we have been to able to unravel the conformational picture in these molecules unambiguously. Results of this work have provided new insights in understanding some of the chemical phenomena observed in fuel reprocessing.

■ OUTLINE

We have used the technique of matrix isolation infrared spectroscopy to study the conformations of organic phosphates. The first member in this series is trimethyl phosphate (TMP), whose conformations were uncertain when we undertook the study. Our matrix isolation studies clearly showed that this molecule existed in two conformational states. This result was corroborated by *ab initio* computations, which indicated the two structures to have a C_3 and C_1 symmetry, which are shown in the Figure 1 as conformers 'U' and 'K' respectively. While the two conformers were identified, experimental evidence was still lacking to determine the ground state conformer. This evidence was unambiguously provided in our experiments using a supersonic jet source coupled to the matrix isolation spectrometer, which showed the ground state conformer to have the 'U' structure. Our work was the first to show the utility of the supersonic jet source to determine the energy ordering of conformational states in molecules.

While our work led to an understanding of the conformations of TMP, we quickly realized that experiments and computations on larger phosphates such as triethylphosphate (TEP) and tri-n-butylphosphate (TBP) would not be easy, given the large number of conformational states that these molecules can possibly have. It was realized that it was not sufficient to determine molecular conformations, but also to understand basic factors that determine the conformational stability of molecules. Such an understanding would help us narrow our search for conformations in molecules with a large number of possible structures. Towards this end, we studied model compounds such methoxymethanes and silanes, which have a similar backbone structure as the phosphates. These studies clearly highlighted the role of anomeric interactions in deciding the conformational stability of these molecules. The anomeric interactions basically arise from the delocalization of the non-bonding electrons on the electronegative atoms into the adjacent antibonding orbitals. These interactions direct the molecule to adopt certain structures, which would facilitate the anomeric delocalizations.

With the lessons learnt from these studies, it became possible to determine the conformations of TEP. These studies also highlighted the role of the π-electrons of the phosphoryl group in the organic phosphates in determining the conformations of these molecules. This has far reaching implications in reprocessing, as metal complexation is likely to alter the π-electron density in the P=O group, which in turn can alter the conformational stabilities in the phosphates. This work is expected to lead to an understanding if this alteration of conformational stabilities in the phosphates has a bearing on the solvent extraction process.

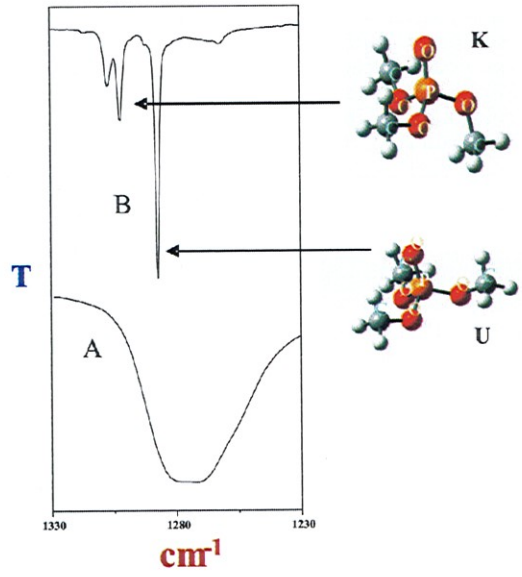

Fig. 1 : A comparison of the infrared spectra of liquid TMP (Trace A) with that obtained for TMP isolated in a N_2 matrix (Trace B). Features of the two conformers, whose structures are shown, are clearly evident in the matrix isolation spectra

■ ADDITIONAL INFORMATION

We have also devised alternate sampling methods for matrix isolation, such as laser ablation, which allows for the study of high temperature chemistry. The matrix isolation technique can also be used in conjunction with other detection schemes such as fluorescence spectroscopy and electron spin resonance. However, since our interests are in studying molecular structure and bonding, we have used Fourier transform infrared spectroscopy to probe the trapped molecules. We have also used matrix isolation spectroscopy to study hydrogen bonded systems and van der Waals interactions, again supported by *ab initio* computations.

■ WHAT IS MATRIX ISOLATION SPECTROSCOPY?

Infrared spectroscopy is an extremely powerful tool to unravel molecular structure and bonding information. However, the linewidths of infrared spectral features of solid and liquid samples are far too large to provide unambiguous information. Matrix isolation provides a means to narrow down the spectral profiles. In this technique, the molecules of interest are trapped in a solid inert gas matrix, such as Ar or N_2, at temperatures of ~12 K. Furthermore, the concentration of the sample is kept sufficiently low (inert gas: sample=1000:1) to ensure that the molecules of interest are surrounded only by the inert gas atoms/molecules, resulting in molecular isolation. At the low temperatures and in the confines of a rigid solid cage, the isolated molecules are devoid of collisions, rotations and spectral congestion, which results in linewidths that are almost an order of magnitude smaller than that observed in the usual condensed phase sampling methods, as can be seen in Fig. 1.

It is this spectral sharpening that allows one to study molecular conformations, as features due to the different conformations can now be resolved. The small linewidths also lets one to study observe small perturbations in the infrared lines, which usually result from weak intermolecular interactions; thereby opening up the possibility of studying hydrogen bonded and van der Waals interactions.

Fig. 2 shows the matrix isolation set up, consisting of the cryostat, FTIR and the nozzle for deposition. The mixing chamber is used to prepare the sample mixture in the inert gas, of the desired ratio. This equipment is essentially a home-built set up.

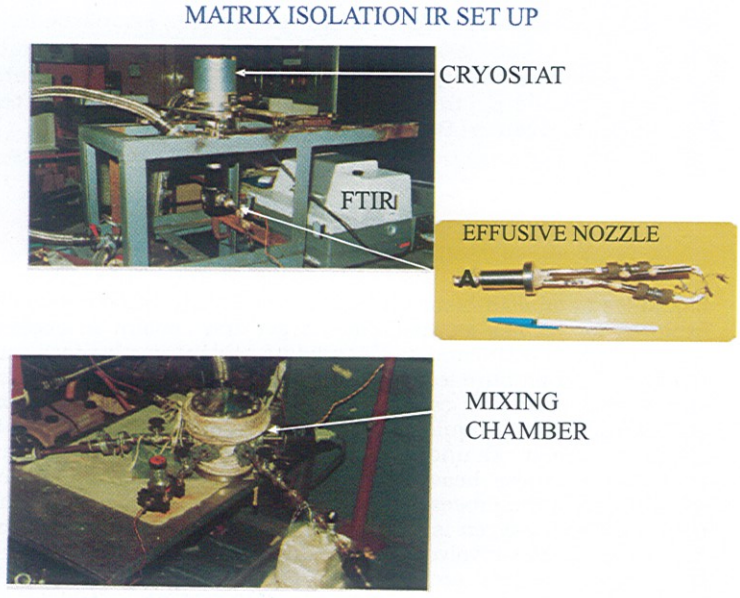

Fig. 2 : Matrix isolation spectrometer, where the cryostat, FTIR, deposition nozzle and the mixing chamber are shown

■ BRIEF DESCRIPTION OF THEORETICAL BACKGROUND

Conformations of molecules and weak intermolecular interactions have been known to influence chemical processes, such as physico-chemical properties and reactivities of molecules. A number of interesting phenomena in fuel reprocessing such as the influence of seemingly inert diluents on the extraction process and third phase formation are likely to be influenced by the molecular conformations of the extractants and the weak interactions between the diluent and the extractants. However, such studies call for specifically designed experiments, which is achieved using the technique of matrix isolation infrared spectroscopy. These studies have also important implications in the study of biological molecules, where conformations are known to play an important role in many biological phenomena.

■ ACHIEVEMENT

The conformations of organic phosphates, have been studied, both experimentally and computationally, leading to a better understanding of the structure of these molecules. Factors deciding conformational stability have also been examined. As a result of these studies, important insights into the role of conformations in solvent extraction have been obtained. Studies of weak intermolecular interactions such as hydrogen bonded and van der Waals interactions have also been done.

■ PUBLICATIONS ARISING OUT OF THIS STUDY AND RELATED WORK

1. K. Sankaran, V. Venkatesan, K. Sundararajan and K. S. Viswanathan, *J. Ind. Inst. Sci.*, **85** (2005) 403.
2. V. Kavitha, K. Sankaran and K. S. Viswanathan, *J. Mol. Struct.* **791** (2006) 165.

Further inquiries:
Dr. K. S. Viswanathan, Materials Chemistry Division
Chemistry Group, IGCAR, e-mail: vish@igcar.gov.in

Thermochemical Behaviour of Oxygen in Lead, Bismuth and Lead-Bismuth Eutectic (LBE) Alloy

EXECUTIVE SUMMARY

Partial phase diagram of Pb-Bi-O system has been established in the temperature range of 740-860 K. Thermochemical properties of $PbBi_{12}O_{19}$(s) and ϕ-$Pb_5Bi_8O_{17}$(s) were determined. Solubility of oxygen in liquid lead, bismuth and lead bismuth eutectic (LBE) were derived. Diffusivities of oxygen in Pb, Bi and LBE were measured using a potentiostatic method employing a solid electrolyte based electrochemical cell. The ternary phase diagram, data on activity, solubility and diffusivity of oxygen in LBE were reported for the first time.

OUTLINE

Liquid lead and lead-bismuth eutectic (LBE) alloy are currently being explored for service as spallation target and coolant in accelerator driven systems (ADS) and as a candidate coolant in advanced nuclear reactors. Though pure lead and LBE are corrosive towards structural steels, this corrosion can be mitigated by controlling the oxygen concentration in the liquid metal such that a protective oxide coating is formed over them. An understanding of the thermochemical behaviour of oxygen in these heavy metal coolants is needed for successful exploitation of the process. Further, the oxide that coexists with LBE saturated with oxygen is not unequivocally known. Thermochemical data of the oxides involved and solubility and diffusivity of oxygen in these liquid metals are essential parameters to understand the processes that occur in the heavy metal coolant – steel interface. Towards this direction, detailed investigations have been carried out in our centre on Pb-O, Bi-O and LBE-O systems.

Partial phase diagram of Pb-Bi-O system has been established by phase equilibration studies in the temperature range of 740-860 K (Fig.1). Thermochemical properties such as Gibbs free energies of formation, heat capacity and enthalpy increments of two ternary oxides of Pb-Bi-O system, viz., $PbBi_{12}O_{19}$ and $Pb_5Bi_8O_{17}$ were determined for the first time. The Gibbs free energies of formations of $PbBi_{12}O_{19}$ and $Pb_5Bi_8O_{17}$ were determined by measuring equilibrium oxygen pressures using solid-oxide electrolyte based EMF cells and manometry in suitable phase fields and are given by

$$\Delta_f G^\circ_m<\phi\text{-}Pb_5Bi_8O_{17}> \pm 1.5\ kJ = -3463.4 + 1.7051\ T\ (K)\ (T: 668 - 837\ K)$$

$$\Delta_f G^\circ_m<PbBi_{12}O_{19}> \pm 2.4\ kJ = -3742.8 + 1.8777\ T\ (K)\ (T: 784 - 849\ K)$$

Activity of oxygen in lead, bismuth and LBE were determined by coulometric titration experiments using solid electrolyte based EMF method. From the variation of the cell emf with temperature for different oxygen concentrations in liquid metal, the standard Gibbs free energy of dissolution of oxygen were derived for the following reactions:

$$\tfrac{1}{2}\ O_2\ (g) = [O]_M \qquad (M: Pb, Bi \text{ or } LBE)$$

and are given by

$$\Delta G^\circ_{O(Pb)}\ (\pm 560) = -121349 + 16.906\ T\ J.(g\text{-}atom\ O)^{-1} \quad (T: 815 - 1090\ K)$$
$$\Delta G^\circ_{O(Bi)}\ (\pm 720) = -108784 + 20.356\ T\ J.(g\text{-}atom\ O)^{-1} \quad (T: 753 - 1020\ K)$$
$$\Delta G^\circ_{O(LBE)}\ (\pm 717) = -127398 + 27.938\ T\ J.(g\text{-}atom\ O)^{-1} \quad (T: 812 - 1012\ K)$$

Using the above data, Gibbs free energy of formations of PbO(s) and Bi_2O_3(s) and equilibrium oxygen pressures measured over oxygen saturated LBE alloy, solubility of oxygen in liquid lead, bismuth and LBE were derived (Fig.2) and are given by

log(at.% O in Pb) (±0.04) = -5100/T + 4.32 (T: 815 – 1090 K)
log(at.% O in Bi) (±0.05) = -4476/T + 4.05 (T: 753 – 988 K)
log(at.% O in Bi) (±0.04) = -3786/T + 3.36 (T: 988 – 1020 K)
log(at.% O in LBE) (±0.06) = -4287/T + 3.53 (T: 812 – 1012 K)

As seen in Fig.2, the solubility of oxygen in LBE falls in between its solubilities in pure Pb and Bi, but more closer to that of pure Pb.

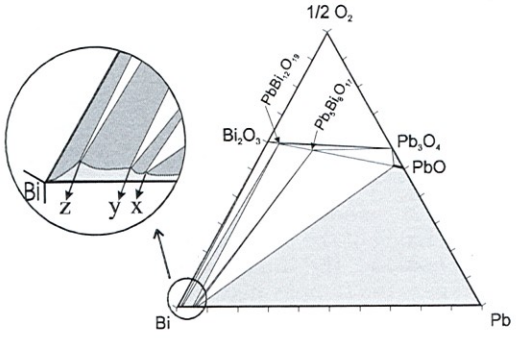

Fig. 1 : Isothermal section of the partial phase diagram of the Pb-Bi-O system at 823 K (where x, y, z are terminal compositions)

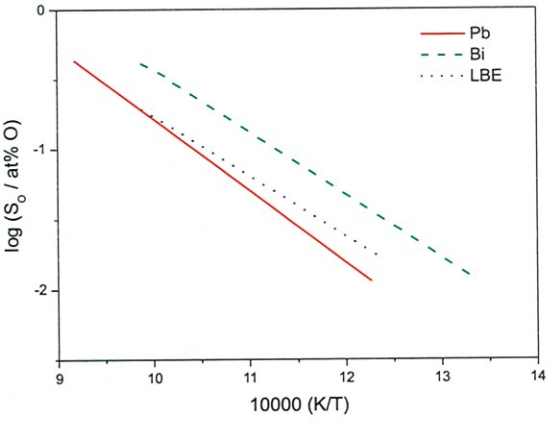

Fig. 2 : Variation solubility of oxygen in lead, bismuth and LBE alloy as a function of temperature

■ ADDITIONAL INFORMATION

What is ADS ? A reactor coupled to a particle accelerator to produce neutrons by spallation is called an Accelerator-Driven System. Most current ADS designs propose a high-intensity proton accelerator with an energy of about 1 GeV, directed towards a spallation target made of liquid lead or LBE (which would also act as a coolant) in the core of the reactor. In that way, for each proton interacting in the target, an average 20 neutrons are created to irradiate the surrounding fuel/nuclear waste containg long-lived transuranic elements. Tranuranic elements present in the nuclear waste can in principle be fissioned, releasing energy in the process and leaving behind the fission products which are short-lived.

■ MEASUREMENT OF DIFFUSIVITY OF OXYGEN

Diffusivities of oxygen in Pb, Bi and LBE were measured using a potentiostatic method employing zirconia solid electrolyte based electrochemical cell. The measured diffusion coefficients of oxygen in liquid lead, bismuth and LBE are shown as a function of temperature in Fig.3 and the linear least-squares fitted expressions to the measured data are given below:

$\log (D_o^{Pb}/cm^2.s^{-1})$ (0.070) = -2.554 - 2384/T (T: 818–1061K)

$\log (D_o^{Bi}/cm^2.s^{-1})$ (0.042) = -3.706 - 1377/T (T: 804–1090 K)

$\log (D_o^{LBE}/cm^2.s^{-1})$ (0.091) = -0.813 - 3612/T (T: 811–980 K)

Fig.3 shows that the diffusivity of oxygen in LBE is higher than that of pure Pb and Bi.

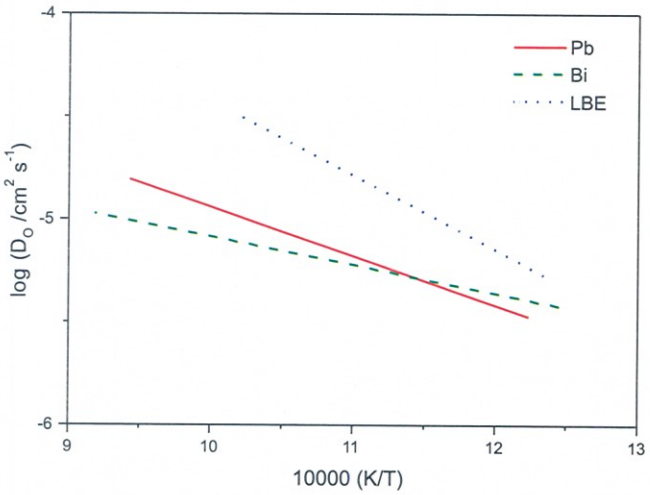

Fig. 3 : Diffusion coefficients of oxygen in liquid lead, bismuth and LBE as a function of temperature

■ BRIEF DESCRIPTION OF THEORETICAL BACKGROUND

Phase diagram gives the information about the coexistence of phases under different conditions. In this study, it is found that in pure Pb and LBE, the oxide phase that can coexist is lead oxide rich solid solution, viz., $[\beta\text{-PbO}]_{ss}$. Measurement of Gibbs energy of formation of $PbBi_{12}O_{19}$(s) and $\phi\text{-}Pb_5Bi_8O_{17}$(s) was useful for determining the alloy compositions at Bi rich location and revealed that these ternary oxides would not precipitate under relatively high oxygen concentrations. Data on diffusivity of oxygen in liquid metals is useful in the study of kinetics of formation of protective oxide layer. Data on activity and solubility of oxygen in liquid metals would be useful in controlling the oxygen concentration in the coolant circuits, in order to stabilize the protective oxide layer.

■ ACHIEVEMENT

Ternary phase diagram of Pb-Bi-O system has been established and reported for the first time in the literature. Data on activity, solubility and diffusivity of oxygen in LBE are also reported for the first time.

■ PUBLICATIONS ARISING OUT OF THIS STUDY AND RELATED WORK

1. Rajesh Ganesan, R. Venkatakrishnan, R. Asuwathraman, K. Nagarajan, T. Gnanasekaran and Raman S. Srinivasa, *Thermochimica Acta,* **439** (2005) 27.
2. Rajesh Ganesan, T. Gnanasekaran and Raman S. Srinivasa, *J. Nucl. Mater.*, **349** (2006) 133.
3. Rajesh Ganesan, T. Gnanasekaran and Raman S. Srinivasa, *J. Chem. Thermodynamics*, **38** (2006) 739.
4. Rajesh Ganesan, T. Gnanasekaran and Raman S. Srinivasa, *J. Nucl. Mater.*, (In Press).

Further inquiries:
Dr. T. Gnanasekaran, Liquid Metals and Structural Chemistry Division
Chemistry Group, IGCAR, e-mail: gnani@igcar.gov.in

Proton Exchange Membrane Based Compact Hydrogen Sensor

EXECUTIVE SUMMARY

A Proton Exchange Membrane Hydrogen Sensor (PEMHS) operable at room temperature has been developed in the Chemistry Group. The amperometric sensor is a fuel cell type device with a mechanical barrier limiting the supply of hydrogen to the sensing electrode side. The sensor is compact in design, portable and cost effective. This device is capable of detecting hydrogen in gases in ppm as well as in percentage levels. The sensor has successfully been used for measurement of diffusible hydrogen in weld samples, steam generator material, corrosion studies related to decontamination of thermal reactor components and sodium exposed fast reactor components.

OUTLINE

Hydrogen is expected to replace conventional energy sources as a pollution-free alternative. It is known that hydrogen forms an explosive mixture with air once its concentration exceeds beyond the explosion limit of four percent. When hydrogen is used as fuel in futuristic automobiles, there is need for hydrogen sensor to monitor the fuel leak. Detection of steam generator leaks in fast nuclear reactors is carried out by monitoring hydrogen in argon cover-gas. Hydrogen released during sodium cleaning of fast reactor components is required to be monitored. Hydrogen sensors with good sensitivity, stability and response time are required for all the above applications.

The PEMHS (Fig.1) developed employs NAFION as proton exchange membrane and operates in fuel cell mode. Unlike pellister type sensors, PEMHS can monitor hydrogen in both inert as well as in ambient atmospheres. The sensor has been used to monitor hydrogen in argon, carbon dioxide and air. Its operating range can be optimized to either ppm or percentage level of hydrogen. The sensor displays the concentration of hydrogen using direct read-out device (DRD) and has provision for interfacing to personal computer. The concentration of hydrogen is computed on-line in the DRD using the stored calibration parameters. The sensor is compact, cost-effective and adaptable for wide dynamic range.

Fig.2 shows the schematic of the sensor. The sample gas is passed over the sensing electrode and the counter electrode is exposed to ambient air. NAFION is used as electrolyte in the sensor. The electrolyte is sandwiched between thick films of platinum that serve as electrodes. The electrode catalysts are deposited on either sides of the NAFION membrane by transfer printing technology (decal method). A mechanical barrier limits the supply of hydrogen to the sensing electrode. The sensor operates in amperometric mode and the limiting current is linearly dependant on hydrogen concentration in sample gas. Fig. 3 shows the response curve of the sensor for hydrogen in argon in ppm range. The response time for hydrogen is ~40 s.

The sensor has been effectively employed in various applications relevant to reactor technology where hydrogen is released as by-product. Various techniques were developed based on on-line measurement of hydrogen concentration. A method employing the sensor has been developed and patented for measurement of diffusible hydrogen in weldment. The new technique is more sensitive and compact compared to conventional methods based on mercury or glycerol.



Fig. 1 : Hydrogen sensor with preamplifier and read out device

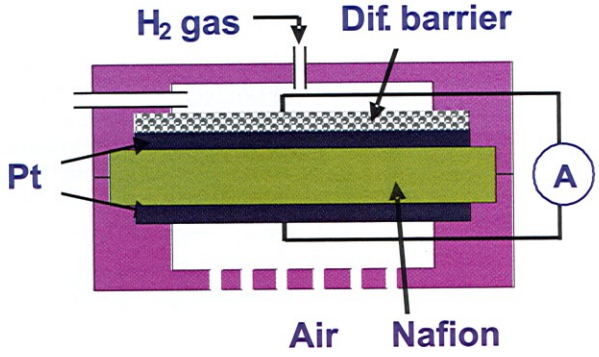

Fig. 2 : Schematic of the sensor

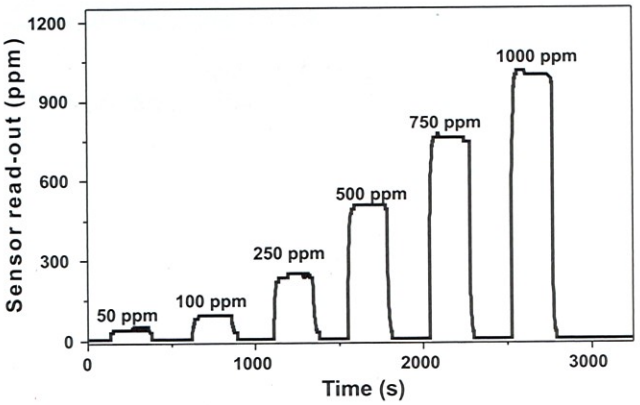

Fig. 3 : Response curve of the sensor

■ ADDITIONAL INFORMATION OF THS SENSOR

Fuel cell sensor

Fuel cell sensors are amperometric devices in which reducible gases like hydrogen get oxidised at the sensing electrode (anode) and oxygen in the ambient air gets reduced at the counter electrode (cathode) to form water. The short circuit current is linearly dependant on the concentration of the sensing gas.

Electrochemical processes at the electrodes in PEMHS

Cell configuration	:	H_2, /Pt//Nafion //Pt, air
Anode	:	$H_2 \rightarrow H^+ + 2e^-$
Cathode	:	$H^+ + 2e^- + ½O_2 \rightarrow H_2O$
Overall	:	$H_2 + ½O_2 \rightarrow H_2O$

What is nafion?

Nafion is the trade name for proton exchange membrane developed by DuPont. It is a perfluoro sulphonic acid resin exhibiting good proton conductivity at room temperature.

■ APPLICATIONS

The sensor was applied in the process simulating cleaning of sodium wetted fast reactor components for monitoring hydrogen. Fig. 4 shows application of the sensor for hydrogen monitoring during sodium cleaning by water vapour-carbon dioxide process. The sensor has also been used in simulated experiments to monitor the progress of dissolution of the degraded layer of sodium exposed fast reactor components during decontamination by sulpho-phosphoric acid technique. This sensor was successfully used to study the decontamination of primary heat transport system components of PHWR and yielded valuable information on the mechanism and kinetics of decontamination. A comparison of the H_2 evolution behaviour of Fe_3O_4 coated carbon steel (CS) as well as polished CS in decontamination formulation is shown in Fig. 5. Region (1) shows the base metal aided Fe_3O_4 dissolution, region (2) shows the base metal aided Fe_3O_4 dissolution as well as base metal corrosion while region (3) shows only the base metal corrosion represented by the reaction $Fe + 2H^+ \rightarrow Fe^{2+} + H_2$. A patent has been granted for the sensor based method for monitoring dissolution rate of metals in acid medium.

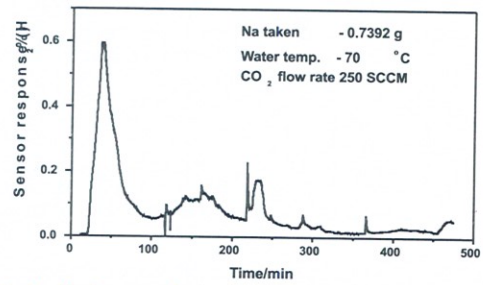

Fig. 4 : Hydrogen released during sodium cleaning process

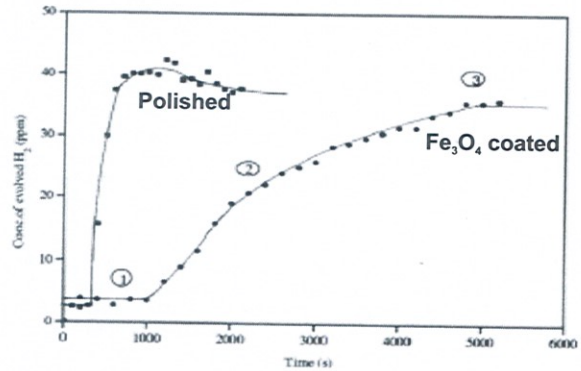

Fig. 5 : Decontamination of carbon steel and oxide coated carbon steel

■ ACHIEVEMENT

The sensor has successfully been employed in the following applications:

- Measurement of diffusible hydrogen in steel weldment -Patent granted.
- Estimation of corrosion rate of carbon steel in decontamination solution formulation-Patent granted.
- Hydrogen monitoring during sodium cleaning of FBTR mock sub-assembly by steam nitrogen process

■ PUBLICATIONS ARISING OUT OF THIS STUDY AND RELATED WORK

1. C. Remash, G. Periaswami, N. Murugesan, C.K. Mathews, S.K. Albert, P. Shankar and T.P.S. Gill, A hydrogen sensor for measurement of diffusible hydrogen in weldment, Indian Patent No. 186660.
2. C. Remash, N. Murugesan, S. Velmurugan, A.A.M. Prince, V. Ganesan and S.V. Narasimhan, A measuring system for on-line measurement of corrosion rate of metals in an aqueous medium, Indian Patent No. 20409.
3. C. Ramesh, G. Velayutham, N. Murugesan, V. Ganesan, K.S. Dhathathreyan and G. Periaswami, *J. Solid State Electrochemistry*, **7** (2003) 511.

Further inquiries:
Dr. V. Ganesan, Materials Chemistry Division
Chemistry Group, IGCAR, e-mail: ganesh@igcar.gov.in

Prediction of Long Term Diffusion Behaviour of Chloride in Concrete

EXECUTIVE SUMMARY

The long term diffusion behavior of chloride in concrete structures that got exposed to sea water during the Asian Tsunami disaster was studied, as chlorides corrode the steel reinforcement and weaken the structure. A barrier of flyash containing concrete PCC was laid over the exposed surface before building the subsequent structure. It was necessary to ensure the long term safety of the structure. Using a combination of numerical and experimental methods, the chloride distribution profile as a function of depth and time was obtained. Studies showed the chloride content to be well below the allowable limit even for 150 years.

OUTLINE

The entry of seawater into PFBR construction site demanded a study on the extent of chloride ingression in the concrete pours and its consequences on the structure built subsequently. Fig. 1 schematically shows the concretes pours 1 and 2 (P1and P2) inundated with seawater. Chloride concentrations at different depths in P1 and P2 were evaluated by BHAVINI. Chloride in the newly built layers consisting of 100 mm of PCC(concrete with 30% fly ash) as a diffusion barrier, followed by normal structural concrete (Stage V), was 0.05 kg/m^3, which is well within the permissible limit of 0.6 Kg/m^3 (as per IS: 456-2000). However, it was essential to ascertain that an increase, if any, in chloride concentration in the concrete structure due to diffusion from beneath is also within the permissible limit during prolonged service of 150 years.

The chloride ingression from the seawater exposed concrete to the PCC and structural concrete, was modeled based on one-dimensional diffusion mechanism. One-dimensional diffusion equations with appropriate initial concentrations and boundary conditions were solved using Numerical methods. The predicted chloride distributions as a function of distance for 60, 100 and 150 years and as a function of time at a position (PCC barrier) were evaluated. Inputs like initial concentrations and diffusion coefficients of chloride in concrete (D_c) and PCC (D_{PCC}) were obtained from experimental data and reports on similar type concrete. The predicted chloride concentrations were always well below the allowable limit on the surface of the PCC (Fig. 2(a)) and in the entire structure even after 150 years (Fig. 2(b)).

The selection of 'D' and its sensitivity on the concentration profiles were validated since 'D' values were taken from literature. Concentration profiles as a function of time (up to 150 years) at a distance of 100 mm above P2 were evaluated by an analytical method using D values ranging from 10^{-14} to 10^{-11} m^2/sec, reported for different types, exposure and testing conditions of concrete. It was seen that the concentration always remained below the permissible level of 0.6 Kg/m^3, even for a 'D' value as high as 10^{-9} m^2/sec. This is far higher than the highest value reported in literature and represents an extreme situation explained below.

Concrete showed an inhomogeneous microstructure consisting of a dispersion of aggregates of different shapes and sizes, binding medium of hydrated cement paste and an interface between cement and aggregates. Chloride was preferentially present in the cement phase. During curing, water reacts with tricalcium silicate mineral to form the porous hardened cement paste, where chloride species predominantly exist within the pores. Chloride profiles in a concrete cured in sea water evaluated using Proton Induced X-ray Emission gave a 'D' value of ~1.8 x 10^{-9}m^2/s. Such a value higher than that reported ~ 10^{-13}-10^{-11} m^2/s is due to the undeveloped pore system in the wet concrete in the initial stages of hydration of cement. This diffusion process, although could have proceeded indefinitely is arrested by the simultaneous hydration process of cement, which hardens the concrete introducing an impermeable, tighter pore system. Hence, such high rates of diffusion are not expected in cured concrete, which was also seen from the calculated chloride profile. The concentration is below the allowable limit up to 150 years for value of D as high as 10^{-9} m^2/sec which is an extreme situation not encountered during service. This study showed that the accidental exposure of the concrete pours to sea water has no adverse effect on the concrete structure above after long years of service.

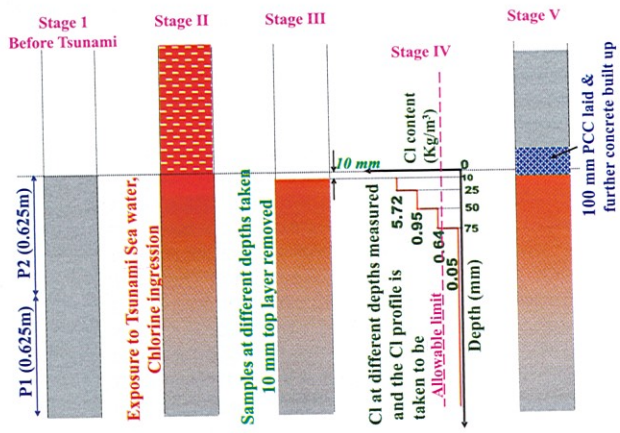

Fig. 1 : Schematic Elevation view of a section of a concrete built-up

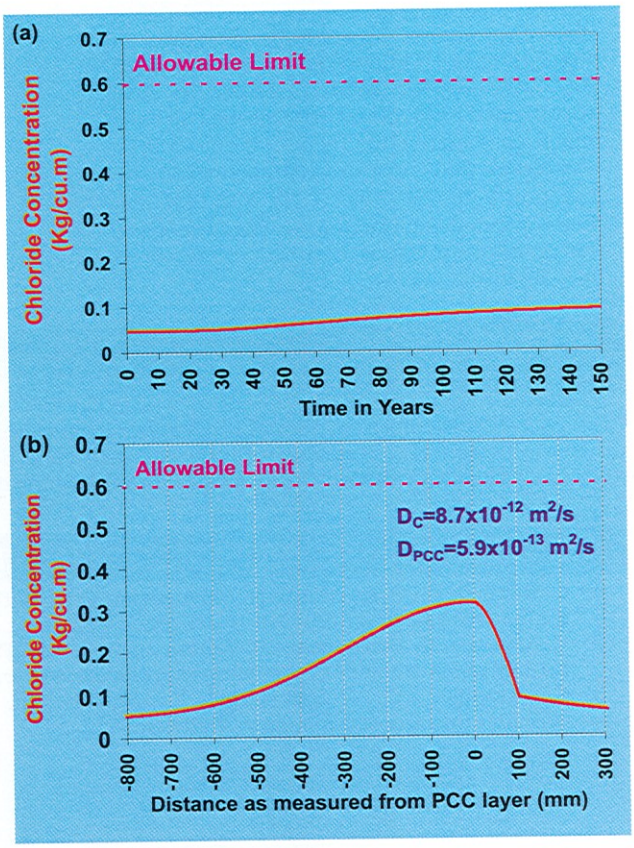

Fig. 2: Chloride concentration profile in concrete as a function of (a) time at the surface of PCC (b) depth after service life of 150 years.

■ HARMFUL EFFECT OF CHLORISE ON CONCRETE

Two physico-chemical processes, carbonation and chlorination limit the useful life of reinforced concrete. Normally, the steel bars in reinforced concrete are protected by high alkalinity (pH ~ 13) of the concrete. However, some reactions between species like $Ca(OH)_2$ and CO_2 reduce the pH. This is called carbonation and is harmful to the formation of passive ferric oxide film around the embedded steel bars. A complete breakdown of the passive film occurs when the ratio of concentration of chloride to hydroxide exceeds 0.6, or when the concentration of chloride ions in the concrete exceeds 0.05 wt%. Chlorides in water trapped at pores in concrete, introduce the same effect. Chlorination of the concrete is also deleterious to its mechanical behavior. Hence, the acceptable level of chloride in concrete is specified to be as low as 0.05 wt %.

■ MICROSTRUCTURE OF SEAWATER CURED CONCRETE

Concrete exhibits a complex non-homogeneous microstructure, consisting of stone/sand aggregates of various sizes/shapes, hydrated cement paste, interfacial transition zone-corresponding to the interface between the aggregates & hydrated cement paste, and system of voids/microcracks. Cement is primarily a mixture of oxides of various elements like calcium, aluminum, silicon and calcium sulphate. Upon mixing with water, the oxides combine with water, by a hydration reaction forming various hydrated products such as C-S-H (calcium silicate hydrate) gel, ettringite (calcium aluminum trisulphate, aluminum), AFm (calcium aluminum monosulphate) and calcium hydroxide. Figure 3 shows the SE image of the hydrated cement phase in a sea water cured concrete. The various micro-constituents of cement paste have been identified based on the elemental contrast and their morphology: Ettringite exist as long slender needles, $Ca(OH)_2$ are precipitated as hexagonal plates, while the C-S-H exhibit a fine layered network. Concretes also exhibit an interconnected pore system of various sizes: macropores, capillary pores between hydration products and fine pores within C-S-H gel. These pores can contain trapped water and the dissolved chloride ions can disperse through the concrete through these void structures. Chlorides reduce the alkaline pH environment provided by the $Ca(OH)_2$ and increases the susceptibility of corrosion of steel reinforcement.

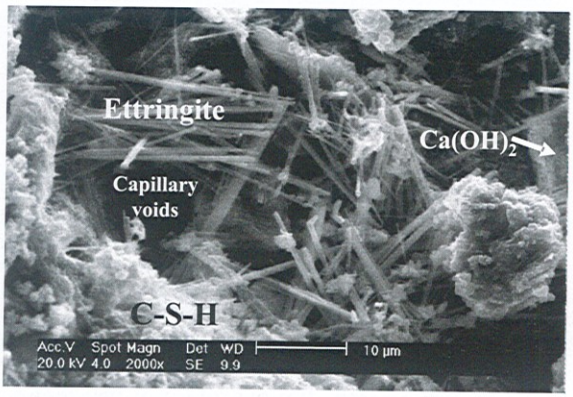

Fig. 3 : Micro constituents of hydrated cement phase of sea water cured concrete.

■ MODELING OF CHLORIDE DIFFUSION IN CONCRETE

The process of chloride ingression from the surface of the concrete into its bulk has been modeled. One-dimensional diffusion equations were set up with appropriate initial concentrations and boundary conditions and solved using Numerical methods. The predicted Chloride distributions as a function of position at 60/100/150 years and as a function of time at a position corresponding to the top of a fly-ash containing concrete layer laid as barrier, were evaluated. The inputs included initial chloride concentrations, diffusion coefficients of chloride in concrete (D_c) and fly ash containing concrete (D_{PCC}).

■ ACHIEVEMENT

The entry of seawater into the PFBR construction site on December 26, 2004, during Tsunami, demanded an assessment of extent of chloride ingression into already laid concrete and its consequences on the structure to be built. This study revealed that chloride content in the newly built concrete would be below the allowable limit of 0.6 kg/m^3 (as per IS: 456-2000), even after 150 years.

■ PUBLICATIONS ARISING OUT OF THIS STUDY AND RELATED WORK ALONG WITH THE IMPACT FACTOR

1. T.Karthikeyan, Arup Dasgupta, P.Magudapathy, S.Saroja, M.Vijayalakshmi, K.G.M.Nair, K.P.N. Murthy and Baldev Raj, *J. Mat. Engg. Performance,* **15** (2006) 581.
2. T.Karthikeyan, Arup Dasgupta, S.Saroja, M.Vijayalakshmi, P.Magudapathy, K.G.M.Nair and K.P.N.Murthy, Report No. PFBR/01120/DN/1014.
3. T.Karthikeyan, Arup Dasgupta, S. Saroja, M. Vijayalakshmi and K.P.N. Murthy, Report No. PFBR/01120/DN/1015.

Further inquiries:
Dr. Saroja Saibaba, Physical Metallurgy Division
Metallurgy and Materials Group, IGCAR, e-mail:saroja@igcar.gov.in

Method to Identify the Damage of Concrete due to Sodium Fire

EXECUTIVE SUMMARY

Hot sodium coming in contact with structural concrete in case of sodium leak in Fast Breeder Reactor system cause damage as a result of thermo-chemical attack by burning sodium. A method has been developed to identify and quantify the damage caused by the sodium fire on concrete. The method involves determination of the $Ca(OH)_2$ content in concrete samples using Differential Thermal Analysis technique. It is known that $Ca(OH)_2$ decomposes in the temperature range of 480 °C to 500 °C. The peak area at this temperature corresponds to the quantity of $Ca(OH)_2$. This compound is formed during the setting of the cement and it is present in the microscopic pores formed. Decomposition of this compound leads to increased porosity, which in turn leads to damage and loss of strength.

OUTLINE

Accidental spillages or leakages of hot liquid sodium (~ 550°C) used as the coolant in Liquid Metal Cooled Fast Breeder Reactors result in sodium fire and interaction with the structural concrete as well. The sodium-concrete interaction is initiated by the highly exothermic reaction between sodium and water reaction with the production of hydrogen. The major source of water for such interaction comes from the dehydration of concrete at high temperature. Water is present in concrete as free and bound. While the free water is the quantity present in the pores, the bound water is predominantly in the form of $Ca(OH)_2$ which results from the hydration of two major components, i.e. tri-calcium silicate and di-calcium silicate present in cement. The reactions take place as follows.

$$2(3CaO.SiO_2)+7H_2O \Rightarrow 3CaO.2SiO_2.4H_2O+3Ca(OH)_2$$
$$2(2CaO.SiO_2)+5H_2O \Rightarrow 3CaO.2SiO_2.4H_2O+Ca(OH)_2$$

$Ca(OH)_2$ formed decomposes endothermically in the temperature range 480 °C to 500 °C. according to the reaction

$$Ca(OH)_2(s) \rightarrow CaO(s)+H_2O(g)$$

DTA is a convenient method to estimate the $Ca(OH)_2$ content through its characteristic decomposition.

A state of the art Differential Thermal Analysis (DTA) system with all the necessary peripherals has been indigenously developed at SED, IGCAR, with the help of an Indian manufacturer, M/s BYSAKH, Kolkata. The system has been calibrated with suitable reference materials from 100 °C to 1000 °C.

Fig.1 and Fig. 2 show the typical results of DTA on concrete samples with and without sodium interaction for the $Ca(OH)_2$ content respectively. Measurement of the compressive strength of concrete samples with different degree of interaction with sodium is being carried out. Correlation of $Ca(OH)_2$ content and compressive strength can thus quantify the damage caused by sodium interaction. This approach to quantify the damage caused by sodium interaction can be regarded as a scientific or technological breakthrough.

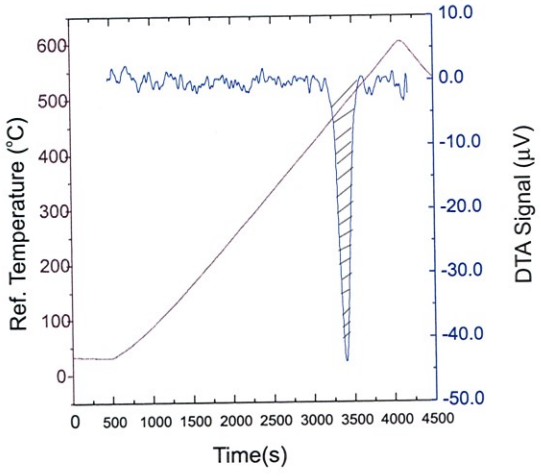

Fig 1: Thermogram of unreacted sample

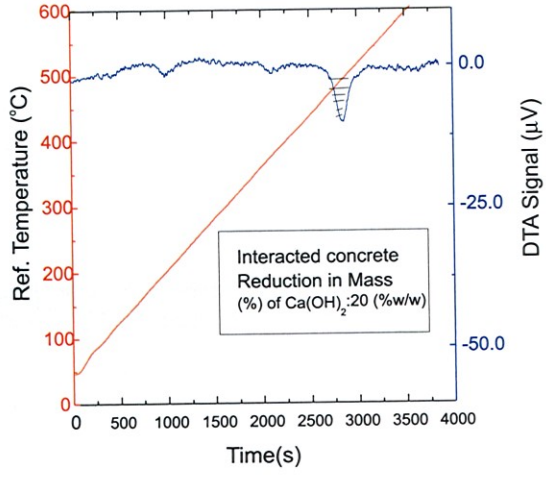

Fig. 2: Thermogram of reacted sample

■ ADDITIONAL INFORMATION

The damage evaluation of concrete has also been done by measuring the penetrated sodium content using Atomic Absorption Spectrometry (AAS). This method involves digestion of the sample using acids and then submitting for sodium determination. In addition, the influence of other major cations, especially Calcium, will interfere with the quantitative determination of sodium. Thus the damage determination using DTA not only involves less time but also highly specific and quantitative.

■ GENERAL EXPLANATION RELATED TO THE DESCRIPTION

Limestone concrete blocks with a square cavity to hold liquid sodium were exposed to sodium fire at 550°C for a period of 30 minutes. Then the remaining unburnt liquid sodium was transferred by suction. Subsequently the surface of the cavity was cleaned with alcohol to remove left over sodium. Samples were collected from the interacted surface for a depth of 50 mm at 10 mm intervals. These samples were subjected to DTA as described above. The content of $Ca(OH)_2$ at various depths as obtained from the peak area at 480 °C from DTA (Fig.3) shows that the concentration is increasing linearly up to about 40 mm depth of interacted concrete. Thus it is clear that DTA is a sensitive means to obtain the $Ca(OH)_2$ content, which in turn is an indicator of the concrete damage.

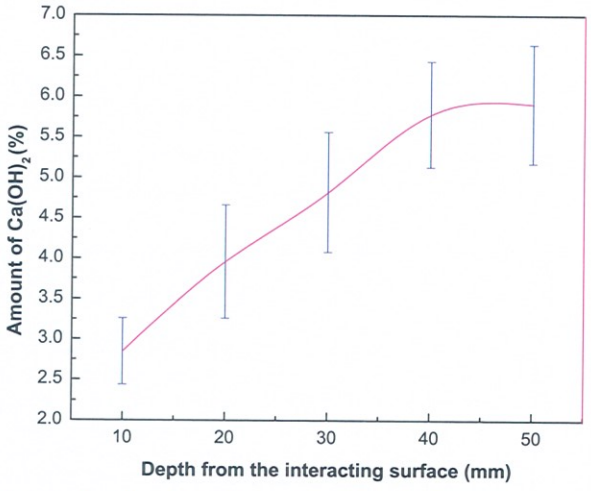

Fig. 3 : Variation of $Ca(OH)_2$ content in one of the interacted blocks

■ BRIEF DESCRIPTION OF THEORETICAL BACKGROUND

In the event of sodium fire on a concrete surface, the temperature at the interface may be about 500 °C. At this temperature the $Ca(OH)_2$ present in the concrete formed during the setting of cements will decompose . This compound provides strength to the concrete through binding the C-S-H (calcium silicate hydrate) gel with the aggregates. Thus an estimation of this compound will provide an insight into the degradation behaviour of the concrete exposed to high temperature sodium fire.

■ ACHIEVEMENT

Thermal analysis of sodium interacted concrete specimens was carried out to determine the $Ca(OH)_2$ content which is responsible for the strength of the concrete. The relative variation of this quantity in the specimens collected from a sodium interacted concrete block as a function of depth revealed that the concrete layer does not show appreciable degradation beyond 30 mm from the sodium-concrete interface. This has been used in deciding to provide a 50 mm sacrificial layer of special concrete in the Steam Generator Building of PFBR.

■ PUBLICATIONS ARISING OUT OF THIS STUDY AND RELATED WORK

K. Sivasubramanian, V.Gopalakrishnan and F.C.Parida, Proc. of International Symposium on Material Chemistry, Dec.2006, Mumbai.

Further inquiries:
Shri K. Sivasubramanian and Shri N. Kasinathan, Safety Engineering Division, Safety Group
IGCAR, e-mail: nkasi@igcar.gov.in

Atmospheric Dispersion of Sodium Aerosol

EXECUTIVE SUMMARY

Large sodium leaks from the Secondary Sodium Systems within the Steam Generator Building (SGB) in a Fast Breeder Reactor based Nuclear Power Plants are within the ambit of Design Basis Events and therefore it is necessary to evaluate the impact of such an event on plant personnel within the plant boundary and on public at site boundary. Atmospheric dispersion and dilution of sodium aerosols is obtained through Gaussian Plume Dispersion Model for large open spaces and through a combination of Eularian Box Model for the velocity field and Monte-Carlo Particle Random Walk Model for space within the plant boundary. This work is utilized to convince the regulatory authorities to realize that a major sodium spillage in such a large facility like PFBR can be adequately managed without subjecting the plant personnel and public at site boundary to any undue risk.

OUTLINE

In the event of sodium leakage in the air filled enclosures of FBRs, the liquid sodium can undergo combustion in the form of column, spray, drop and pools depending of the leakage conditions. Sodium fire is a complex manifestation of exothermically runaway oxidation of sodium metal by oxidizing components of air such as oxygen, moisture and carbon-di-oxide.

The sodium combustion is always accompanied with production of heat, light, smoke and flame. In the event of a sodium fire inside a ventilated building, it is known that about 80 % of the aerosols get deposited within the building and rest escapes out through the ventilation. With these characteristics of sodium leak, it has been estimated that 552 g/s of sodium aerosol can escape out of the SGB in the Prototype Fast Breeder Reactor (PFBR) being constructed in Kalpakkam, in the event of a large sodium leak. Sodium hydroxide (a product of the reaction of sodium with moisture) reacts with the carbon-dioxide present in the air and gets converted to harmless sodium carbonate at a first order rate constant of 0.2 min^{-1}. This is especially so in large open spaces, where there is no dearth of availability of carbon-dioxide.

Toxicology studies of sodium hydroxide on human beings indicates that an airborne concentration of 10 mg/m^3 is acceptable for short durations limited to 30 min and for repeated daily exposures of 8 h, a concentration of 2 mg/m^3 is stated to be acceptable.

Atmospheric dispersion and dilution of sodium aerosols is obtained through Gaussian Plume Dispersion Model for large open spaces and through a combination of Eularian Box Model for the velocity field and Monte-Carlo Particle Random Walk Model for space within the plant boundary, where it is necessary to take into account of intervening buildings. In both these approaches dilution and dispersion is a strong function of the atmospheric wind velocity and the type of weather conditions. A wind velocity of 1 m/s characterizes the coastal area, where PFBR is being constructed, for most of the duration. The Stable F type weather condition gives rise to lowest dispersion.

With these input conditions, the ground level concentration profiles for in the large open space extending to the site boundary is estimated and shown in Figure 1. From the Figure it can be seen that everywhere in the plant site and at the site boundary, airborne aerosol concentration is much less than 2 mg/m^3, if the aerosol release from the SGB is at or above 20 m elevation.

The modified velocity field and the contours of aerosol concentration (for a typical case) are shown in Figure 2. The impact within the plant boundary is estimated for various wind directions and the aerosol release elevations. It was observed that when the aerosols are released at an elevation of 20 m or more, the consequences in any of the important locations in the plant is always less than 2 mg/m^3.

Due to this nature of impact on the areas within the plant boundary, it has also been recommended to let out the ventilation exhaust from the SGB floors below 20 m elevation at an elevation of 20 m or above by suitable ducting.

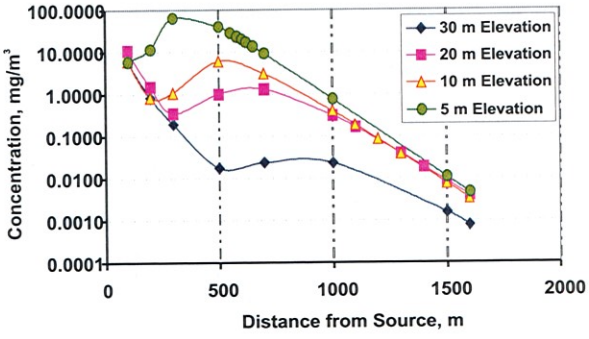

Fig 1: Ground level concentration profiles

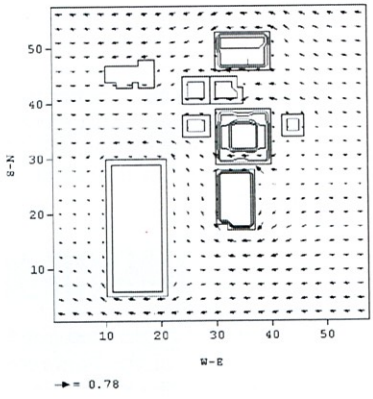

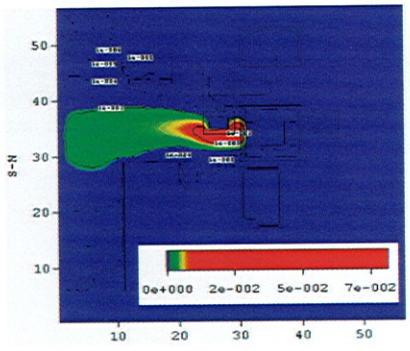

Fig. 2 : Estimation of Aerosol Concentration within Plant Boundary

ATMOSPHERIC AEROSOL DISPERSION - WHAT IS AN ATMOSPHERIC AEROSOL?

Aerosols are tiny particles suspended in the air. Some occur naturally, originating from volcanoes, dust storms, forest and grassland fires, living vegetation, and sea spray. Human activities, such as the burning of fossil fuels and the alteration of natural surface cover, also generate aerosols. Aerosols interact both directly and indirectly with the Earth's radiation budget and climate. As a direct effect, the aerosols scatter sunlight directly back into space. As an indirect effect, aerosols in the lower atmosphere can modify the size of cloud particles, changing how the clouds reflect and absorb sunlight, thereby affecting the earth's energy budget.

GENERAL EXPLANATIONS RELATED TO DESCRIPTION

Sodium Fire and Sodium Aerosols

Hot liquid sodium at temperatures greater than 250°C burns spontaneously when it comes in contact with atmospheric air at rates in the order of 20 kg/h/m^2 to 40 kg/h/m^2, depending on the leaked sodium temperature and availability of oxygen. Sodium monoxide (Na_2O) and sodium peroxide (Na_2O_2) are the combustion products formed with a heat release rate around 110 kW/m^2, which is about 15 times less than that happens in a petrol fire. Though the reaction products are in solid phase, due to the intense nature of the sodium fire, about 30 % of the oxides are thrown out as fine dusty fume into the surrounding atmosphere. These sodium oxides react with moisture available in the air almost instantaneously and forms pure sodium hydroxide particles (of size 1 to 10 m), which is commonly called as "sodium aerosols" and are carried by the air currents around the sodium fire.

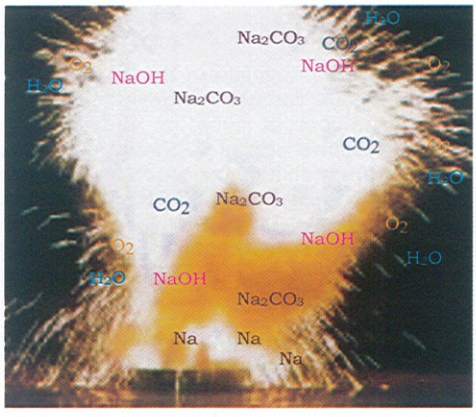

Chemical equations for reaction of sodium with air and water

$$2\,Na \xrightarrow{O_2} Na_2O \xrightarrow{H_2O} 2\,NaOH \xrightarrow{CO_2} Na_2CO_3 + H_2O$$

Health Hazards of Sodium Aerosols

Sodium hydroxide and sodium carbonate constitute the sodium aerosol. Sodium hydroxide is very corrosive and causes severe burns on contact with the skin and also can damage the eyes. The Threshold Limit Value (TLV) is limited to 2 mg/m^3. However, no such limit exists for sodium carbonate.

MODELS APPLIED

The dispersion of sodium aerosols in the atmosphere depends to a large extent on the wind field, weather conditions and on the presence of intervening buildings and structures, especially for distances close to the point of release. For large open spaces, Gaussian Plume Dispersion Model is the most suitable method and it is used to find the consequences at the site boundary. This is a simple, steady state, single point source dispersion model, which gives accurate results for plain, uninterrupted terrains from 100 m to 4000 m from the point of source of release. Within the plant, the intervening buildings and structures alter the velocity field to a large extent. Therefore, a detailed 3-D estimation of the velocity field and concentration was obtained through a computational fluid dynamics (CFD) approach. In this study, a combination of Eularian Box Model for the velocity field and Monte-Carlo Particle Random Walk Model for the aerosols dispersion has been applied.

ACHIEVEMENT

This work is utilized to convince the regulatory authorities to realize that a major sodium spillage in such a large facility like PFBR can be adequately managed without subjecting the plant personnel and public at site boundary to any undue risk. Hence this work can be considered as a technological milestone of high relevance to the Centre.

Further inquiries:
Smt G. Punitha and Shri N. Kasinathan, Safety Engineering Division
Safety Group, e-mail: nkasi@igcar.gov.in

Biomarkers for Radiation Quality and Dose-Rate

EXECUTIVE SUMMARY

In order to measure radiation exposures and estimate radiation risk factors in the event of an accident, it is necessary to identify "fingerprints" of specific radiation. With this in mind, experiments were carried out by exposing human peripheral blood lymphocytes either with low-dose-rate gamma radiation or alpha radiation and the nature of chromosome aberrations studied by both conventional and Fluorescent in-situ Hybridisation (FISH) methods. A 'T' lymphocyte mutation was also established at IGCAR using which a Dose and Dose-Rate Effectiveness Factor DDREF factor of 3.4 was deduced.

OUTLINE

Occupational workers engaged in the nuclear industry receive both external radiation exposure due to high and low dose-rate gamma radiation and also internal exposure due to alpha particles. Radiation Protection requires estimation of risk factors such as the Dose and Dose-Rate Effectiveness Factor (DDREF) which varies with dose-rate and a Relative Biological Effectiveness (RBE) factor which varies with energy. Studies are being carried out at IGCAR to develop assays to estimate an accurate DDREF and RBE for radiation exposures.

RBE: The International Commission on Radiation Protection (ICRP) has recommended an average RBE value of 20 for alpha exposure. However, there are now reports that RBE of alpha particles may vary anywhere between 10 and 100 or more. Since the RBE depends on the choice of the biomarker studied, search for the right "signatures" or "fingerprints" remains a challenge. Alpha radiation is much more likely to produce multiple breaks and cluster damages within a given chromosome than gamma rays, and so yields of intra-chromosomal aberrations are even further increased relative to inter-chromosomal aberrations. Human lymphocytes in blood samples exposed to alpha radiation are being analysed for the ratios of inter-chromosomal to intra-chromosomal aberrations using solid giemsa staining (Fig 1a and 1b) and Fluorescent In-Situ Hybridisation (FISH) techniques (Fig 2a and 2b) that are likely to be effective biomarkers of alpha exposures. A simple and novel method to irradiate human blood lymphocytes in vitro using radon gas emanating from a solid radium source was devised. The difficulties in delivering and estimating exact activity concentrations have been handled in a unique and safe way. Such a method was used to score chromosome aberrations induced by radon and progeny.

DDREF: Since DNA damage and repair at high dose rates are different from those produced at low dose rates, a dose-response curve constructed for high dose rate exposure may not be useful for estimating doses due to low dose-rate exposures. It has been shown that the spectrum of mutations induced at the hypoxanthine guanine phosphoribosyltransferase (HPRT) locus can serve as an indicator of dose-rate and radiation quality. In order to measure mutant frequency at the HPRT locus, a T lymphocyte cloning assay has been established at IGCAR. This study showed that for very low dose rate exposures typically encountered by occupational workers DDREF factors can exceed greater than the recommended value of 2 by ICRP suggesting that DNA damaging effects at these levels of exposure are very low (Fig. 3).

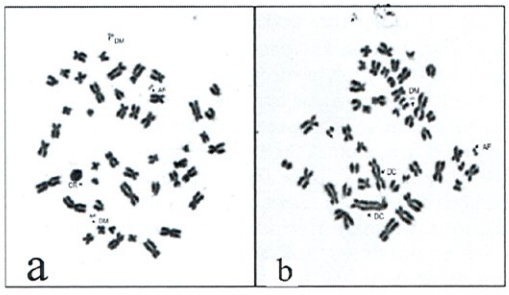

Fig. 1 : (a) Metaphase containing centric ring (CR) and double minutes (DM)- signature of alpha exposure. (b) Metaphase containing multiple aberrations such as dicentrics (DC), acentric fragments (AF) and DM

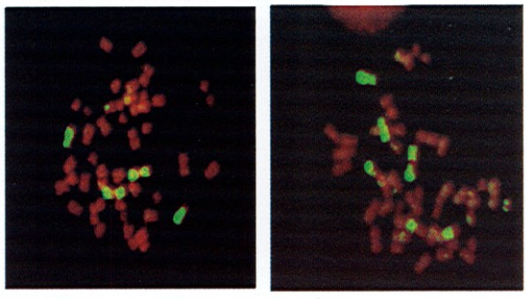

Fig. 2 : (a) Normal Metaphase spread painted with (FISH) probes for chromosome 1 and 4. (b) Metaphase containing portions of chromosome 1 translocated and inserted into other chromosomes

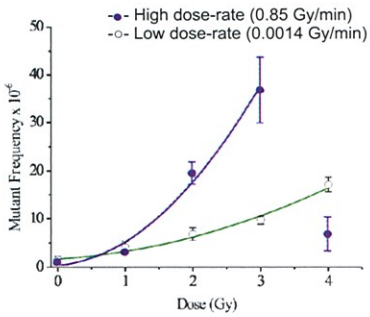

Fig. 3 : Dose response curves for HPRT mutant frequency in blood lymphocytes exposed to high and low dose-rates of gamma radiation giving rise to a Dose Dose-Rate Effectiveness Factor (DDREF) of 3.4

■ BIOLOGICAL DOSIMETRY

Biological dosimetry is a method of measuring the amount of ionizing radiation received by individual using biological materials. This type of dosimeter is useful when an individual is accidentally exposed and no physical dosimetry is available, or if the reading from a physical dosimeter is in dispute. Among the various techniques available, measurement of dicentric chromosome frequency is an authentic method for estimating radiation exposure during an accident (Fig.4).
Chromosome aberrations have proved to be excellent biomarkers of environmental mutagens including radiation. The frequency of dicentric chromosome formed as a result of exposure to ionizing radiation serves as measure of radiation dose and also of radiation risk.

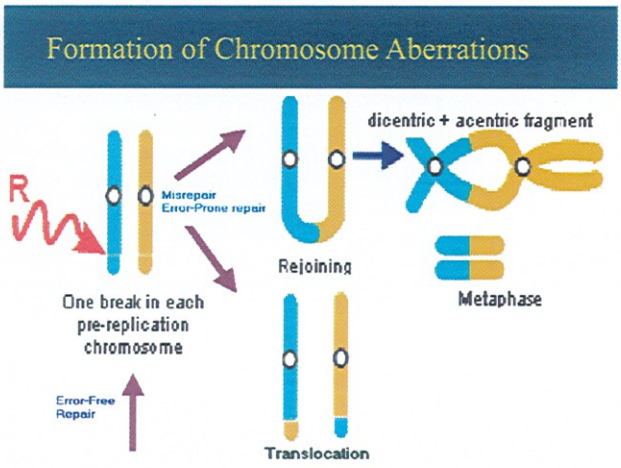

Fig. 4 : Formation of dicentric chromosome and translocation

■ ACHIEVEMENT

The HPRT mutation assay established for the first time in India was used to derive the realistic Dose and Dose-Rate Effectiveness Factor (DDREF) of 3.4 against the recommended value of 2 by the International Commission on Radiation Protection (ICRP)

■ PUBLICATIONS ARISING OUT OF THIS STUDY AND RELATED WORK

1. P.R. Vivek Kumar, Mary N. Mohankumar, V. Zareena Hamza, R.K. Jeevanram, *Radiation Res.*, **165** (2006) 43.
2 P.R. Vivek Kumar, V. Zareena Hamza, Mary N. Mohankumar, R.K. Jeevanram, *Mutation Res.*, **556** (2004) 107.

Further inquiries:
Dr. R.K. Jeevanram and Dr. Mary N. Mohankumar, Radiological Safety Division
Safety Group, IGCAR, e-mail: rkj@igcar.gov.in, marynmk@igcar.gov.in

Characterisation of Aerosols for the Fast Reactor Safety Studies

EXECUTIVE SUMMARY

An Aerosol Test Facility (ATF) has been designed, fabricated and commissioned to carry out aerosol studies pertaining to Fast Reactor Safety. Aerosols from Sodium compound, fuel equivalent and non-radioactive fission products are generated and their characteristics are studied. The studies that are carried-out include (i) The sodium compound aerosol characterization (ii) Characterization of non-radioactive fission products (SrO_2 and CeO_2) (iii) Effect of gamma radiation on the behavior sodium compound aerosols. The studies that are being continued include (i) Chemical characterization of sodium compound aerosols for the known time with known initial mass concentration (ii) Co-agglomeration and co-deposition of sodium and non-radioactive fission products aerosols in a closed environment (iii) Aerosol retention factor in sodium pool (iv) Scavenging of iodine vapour in sodium oxide aerosol and (v) Characterization of sub-micrometer aerosols

OUTLINE

In case Core Disruptive Accident (CDA) conditions in Fast Reactors, excess heat is liberated leading to core melt down. During this period, sodium slug impacts on the vessel head and provides path way for the escape of sodium along with fuel and fission product vapours into the Reactor Containment Building (RCB). Thus RCB is bottled-up with aerosols and there exists a possibility of release of these aerosols through ducts/cracks, resulting in deposition of particulates near the vicinity. Further during normal operation of the reactor, due to the damages/cracks in the coolant pipe, the hot sodium may come in contact with atmosphere resulting in sodium fire. To study the aerosol behaviour, an Aerosol Test Facility (ATF) is designed, fabricated and commissioned (Fig. 1).

The ATF consists of an aerosol chamber of one cubic meter volume, sodium combustion cell for the generation of sodium compound aerosols, a 20 kW non-transferred thermal plasma torch for the generation of fuel equivalent and non-radioactive fission product aerosols, aerosol diagnostic equipments to carry-out measurements in both on-line and off-line and various auxiliary systems such as Data Acquisition System (DAS), chilled water system, pneumatic control system, vacuum system etc.

The initial size particle distribution of sodium compound aerosols after leaving the flame zone is measured using both Optical and Impaction techniques and is found to be about 1 μm for 20 s older particles (Fig.2). The size distribution is essentially attributed to sodium hydroxide aerosol. The initial size distribution of particles does not vary with ignition temperatures over the range of 250-550°C for a confined pool, where as the size increases with increase in Relative Humidity (RH)(50-90 % RH). The suspended aerosol mass concentration is measured experimentally over a period of 5 hrs. With initial mass concentration and initial particle size distribution, the behaviour of suspended mass concentration is predicted using Heterogeneous Aerosol Agglomeration Revised Model (HAARM) code. It is observed that both experimental findings and HAARM code prediction to have good agreement (Fig. 3).

The suspended sodium compound aerosol mass concentration is studied under the field of gamma exposure at the rate of 8.0 mGy/h. The suspended aerosol mass concentration depletes faster in the presence of gamma field than without gamma field. The faster depletion rate is attributed to enhanced Brownian coagulation of bipolarly charged aerosols due to Coulomb force and subsequent gravitational settling. The net Brownian coagulation coefficient (Fig.4) for the aerosol is estimated theoretically and compared with that of experimental value. The average value of coagulation enhancement factor under the gamma field is found to be 4. Chemical characterization of sodium compound aerosol during the first 500 s is being carried out by collecting the sample in gas washing bottle and filter papers. The samples are analysed by conductivity titration method in collaboration with Innovative Instrumentation Section, Electronics and Instrumentation Group. The composition mainly varies between hydroxide to carbonate and carbonate content increases with time.



Fig. 1 : Aerosol Test Facility and Sodium Combustion Cell

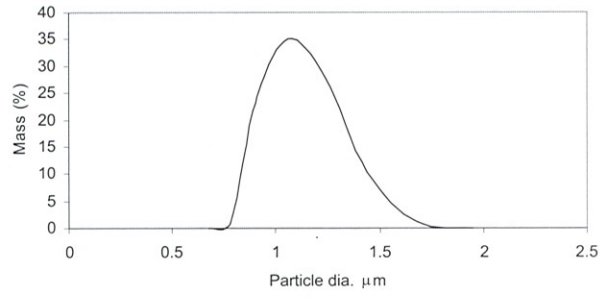

Fig. 2: Initial size distribution of sodium compound aerosol

ADDITIONAL INFORMATION

Aerosols are tiny particles suspended in the air and they are the principle carrier of radioactivity (as an attachment of radioactive substances on it or radioactive aerosol itself) to the environment. The amount and type of aerosols released into the environment depends on (i) The concentration of the aerosols inside the containment at various times following the postulated accidents and (ii) the leakage rates from the containment, stack, and ducts. The released aerosols will be carried away by the wind and fallouts of particulates of the aerosols are expected in the surrounding depending upon the atmospheric conditions. The environmental source term is the amount of activity released into the atmosphere due to the CDA conditions.

AEROSOL STUDIES DURING CORE DISRUPTIVE ACCIDENTS

Aerosol Formation and Characterization

Aerosol generation in the case of Core Disruptive Accidents is by evaporation of material due to high heating and subsequent condensation of vapour resulting homogeneous nucleation of aerosol. The nuclei may be as small as a single molecule for refractory materials, but subsequent collision and coalescence leads to the formation of larger particles. Also they form cluster aggregates when mixed with one or two species (like Na with fission products). Thus characterization of aerosol also includes (i) studies on co-agglomerated aerosols and their co-deposition pattern and (ii) Characterisation of sub-micrometer range of aerosols.

Aerosol Generation in ATF

Sodium Compound aerosols are generated in a sodium combustion cell. It consists of an electrical Bunsen burner to heat sodium upto 550°C under the argon environment and ignited by using compressed air. The fission product aerosols are generated by using a Plasma Torch. The materials are palletized and exposed to plasma flame. It undergo melting, evaporation and blown into the aerosol chamber where it condense to form aerosols.

Aerosol diagnostic equipment

Real time monitoring

(i) The Mastersizer – Volume-size distribution
(ii) The Aerosol spectrometer – Count-size distribution
(iii) The QCM – Mass-size distribution

Off-line Monitoring

(i) The Low Pressure Impactor – Mass-size distribution, sample collection
(ii) Filter paper sampler – Mass concentration

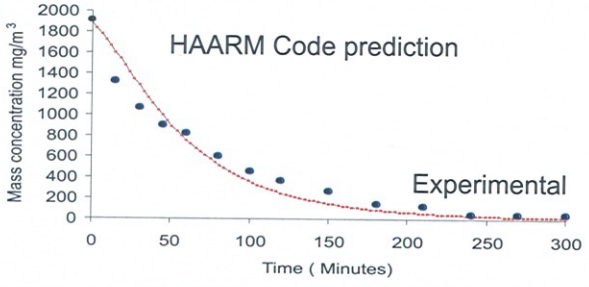

Fig. 3 : Time evolution of suspended sodium compound aerosol in a closed vessel

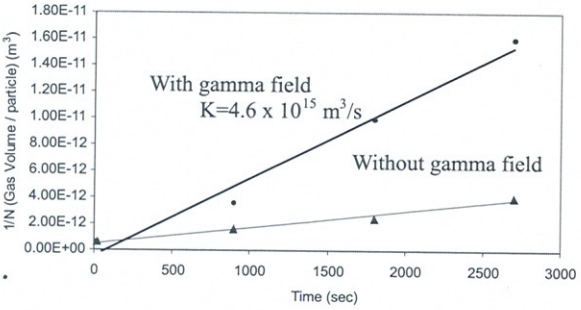

Fig. 4 : Brownian Coagulation coefficient

VARIOUS MODELS AVAILABLE IN THE LITERATURE TO STUDY THE DISTRIBUTION OF AEROSOL

(i) Heterogeneous Aerosol Agglomeration Revised Model – 3 (HAARM) for suspended aerosol mass concentration in a confined environment
(ii) Modified Boltzmann charge distribution on aerosol – for number of charges attached with aerosol under gamma field and coagulation
(iii) Conductivity titration method – the electrical mobility of hydroxyl ion and carbonate ion is different in a water medium and this phenomena is used to quantify the species
(iv) Smoluchowski Coagulation

ACHIEVEMENT

(i) Experimental facility for the rapid and accurate determination of initial sized distribution of sodium compound aerosol over a period of 20 s duration with a resolution of 1 s. All the earlier measurements are off-line and cumulative over a period of minimum 10 minutes.
(ii) Brownian Coagulation Enhancement Factor when the coagulating aerosols are charged under the gamma field has been determined.

PUBLICATIONS ARISING OUT OF THIS STUDY AND RELATED WORK

1. R.Baskaran, T.S. Selvakumaran and V. Subramanian, *Indian journal of pure and applied physics*, **42** (2004)873.
2. R.Baskaran, V. Subramanian and T.S. Selvakumaran, *Indian journal of pure and applied physics*, **44** (2006) 576.
3. V. Subramanian and R. Baskaran, *Nuclear Technology*, **160** (2007) 308.
4. R. Baskaran, C.V. Srinivas, V. Subramaniam, R. Venkatesan and E. Indira, *Ind. J. Environ. Protec.*, **27** (2007) 1.

Further inquiries:
Dr. R. Baskaran and Shri V. Subramanian, Radiological Safety Division
Safety Group, IGCAR, e-mail: rb@igcar.gov.in

Studies on Physics Parameters of Metal (U-Pu-Zr) Fuelled FBR Cores

■ EXECUTIVE SUMMARY

For faster growth of nuclear power in India, it is essential to shift to use of metal fuels in fast breeder reactors (FBR), which gives a higher breeding ratio (BR) and lower doubling time (DT). Steady state neutron diffusion calculations have been done to investigate the various physics parameters of metal (U-Pu-Zr) fuelled FBR cores as a function of reactor parameters like reactor power, smear density and zirconium content in the fuel. A 1000 MWe fast reactor with U-Pu fuel (i.e. metal fuel with no zirconium- which is a theoretical possibility now) can attain a breeding ratio of 1.65 and a reactor fuel doubling time of 6.0 years. For improving the fuel-clad compatibility, it is planned to use a Zr-liner within the clad. This reduces the BR only slightly (1.59). The earlier studies on 500 MWe FBR core with different Zr contents showed that BR improves with reduction in Zr content significantly.

■ OUTLINE

In fast breeder reactors (FBR), the basic thermal and neutronic performance of metal fuels (U-Pu-Zr) is better than oxide ceramic fuels. The metal fuels are generally sodium bonded which increases the total volume fraction of sodium in core. The harder spectrum in the metal-fuelled core results in high breeding ratio. At the same time, the sodium void reactivity effect also becomes more positive. The Doppler reactivity change is lower due to lower operating temperatures.

High breeding ratio results in a low burn-up reactivity swing. In fact with near unity internal BR, it possible to achieve a near zero burn-up reactivity swing per cycle. The low Doppler constant reduces the positive reactivity to be inserted during reactor start-up. Both of these factors help to reduce the required control rod reactivity worths. Longer operating cycle lengths are also easily possible which can increase plant capacity factors.

The fuel pin diameter of 8 mm is chosen for the 1000 MWe FBR. With 271-pins/fuel sub-assembly (SA), and a SA pitch of 168 mm, we require 247 fuel SA for the core (Figure.1 and Table.1). The Pu-inventory per MWe is only slightly larger than 500 MWe core of 6.6 mm pin diameter (Table.2). The Pu composition assumed to be same as that of oxide fuelled Prototype Fast Breeder Reactor (PFBR) under construction at Kalpakkam.

With the U-Pu fuel, the breeding ratio attainable for 1000 MWe fast breeder reactor is 1.65 with a doubling time of 6.0 years. The computed sodium void worth is 7.2 $. It is found that replacing the upper axial blanket with a sodium plenum can reduce the sodium void worth, though it leads to a lower breeding ratio. An approximate estimation using diffusion calculation shows that, this modification can reduce the sodium void to 4.6 $. Also it is found that reducing the fuel smear density can reduce the sodium void worth to a small extent only. Safety analysis done elsewhere indicate that due to higher negative fuel expansion reactivity coefficients, metal fuel core remains safe even with the high positive sodium void reactivity effect.

It is found by earlier study (Table.3), that breeding ratio increases linearly with the reduction of zirconium content in the fuel pellet, even though it leads to a higher sodium void worth. It was clear that the reduction of zirconium in the fuel will decrease the life of fuel pin due to the enhanced pellet-clad interaction. A liner was proposed between the fuel pellet and clad to reduce the fuel-clad interaction. A study has been done in a 1000 MWe U-Pu fuelled FBR and it has been found that zirconium can be used as the liner material as the reduction in BR is small.

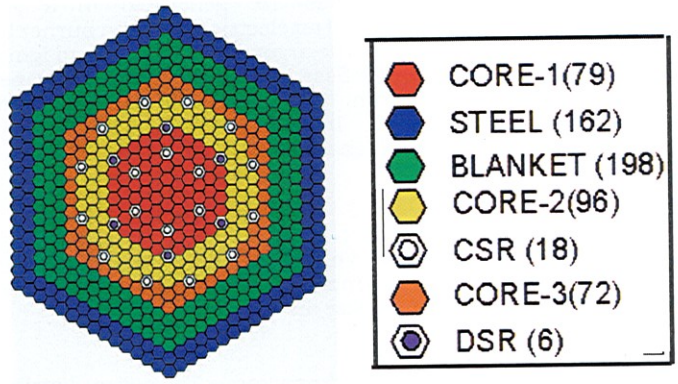

Fig. 1: The Core Configuration of1000 MWe FBR

Table 1
Core Design Parameter of 1000 MWe Metal Fuelled FBR

Efficiency	(+%)	38
Maximum heat Rating	(W/mm)	50
Fuel Pin Diameter	(mm)	8
Clad Thickness - Fuel	(mm)	0.53
Assembly Pitch	(mm)	168
Fuel Pins per Sub-assembly (SA)		271
Blanket Pin Diameter	(mm)	12.75
Clad Thickness – Blanket	(mm)	0.6
Pins per Blanket Sub-assembly		127
Number of SA in core		247
Number of SA in Radial Blanket		198
Number of Control Rods		24
Total Axial Blanket Height	(mm)	600 or 300
Initial Pu39/40/41/42 Ratio	(%)	69/25/5/1

EARLIER STUDIES ON 500 MWe CORE WITH DIFFERENT Zr CONTENT IN THE FUEL

From earlier studies, it was found (Table.3) that a 500 MWe fast breeder reactor having 2 rows of blanket and U-Pu-Zr (10%) fuel can attain a breeding ratio of 1.24 and a doubling time of 15 years. With reduction in Zr content to 6%, the BR and DT become 1.36 and 10.5 years respectively. Compared to oxide core, there is a significant increase in sodium void reactivity effect. The consequence of the higher sodium void effect need to be studied by performing transient analyses. For this purpose, the reactivity perturbation worths and other kinetic parameters have been generated for these cores. The higher breeding ratio, which results in a low burn-up reactivity loss, can be favorably utilized for high fuel burn-up and longer cycle lengths.

GENERAL EXPLANATION RELATED TO THE DESCRIPTION

In Table.2, we compare the parameters of a 1000 MWe core with and without a Zr liner. The Zr liner thickness considered is 0.15 mm. It is found that the effect of Zr-liner is small in BR and sodium void reactivity effect.

Table 2
Physics Parameters of 1000 MWe FBR with U-Pu Fuel

Parameter	Pin Type	
	Reference Pin	Pin with Zr-Liner
Liner Thickness (mm)	-	0.15
Pellet Radius (mm)	3.47	3.32
Core Enrichments in Core1/Core2/ Core3	10.0/ 10.8/ 14.8	10.6/ 11.5/ 15.8
Pu-Inventory (t)	4.23	4.51
Breeding Ratio	1.65	1.59
Reactor Doubling Time (RDT)- years	6.0	7.0
Delayed Neutron Fraction (pcm)	436	427
Sodium Void Worth (pcm)	3159 (7.2 $)	3102 (7.3 $)

Table 3
Physics Parameters of 500 MWe FBR with Oxide and Metal Fuel

Parameter	Fuel Type		
	Oxide	U-Pu-Zr (10%)	U-Pu-Zr (6%)
Enrichments (%)	21/28	15/21	14/18
Pu Inventory (t)	1.99	1.93	1.97
Breeding Ratio	1.05	1.24	1.36
Ratio of Fast to Total Flux	0.58	0.66	0.66
Reactor DT (yrs)	65	15.1	10.5
Doppler Constant (pcm)	-735	-408	-470
Sodium Void Worth ($)	+1.7	+4.6	+5.1

BRIEF DESCRIPTION OF THEORETICAL BACKGROUND

The number densities of various nuclei present in different regions are calculated using the code ATOMIX. The self-shielded cross-sections are calculated using the CONSYST/EFCONSY code system using XSET-98 cross-section data. The k–effective is calculated using the two-dimensional diffusion theory code ALCIALMI. It uses RZ geometry for calculations. The breeding ratio, fast flux, peak linear pin powers and capture to fission ratio are calculated using the two-dimensional code ALEX. The delayed neutron fraction, perturbation worths and other kinetic parameters are calculated using the program NEWPERT.

ACHIEVEMENT

Steady state reactor physics studies have been completed for the metallic fuelled cores, which are planned for the next generation FBR in India. Internal breeding ratio close to unity is achievable with U-Pu fuel. For preventing fuel-clad chemical interaction, a thin zirconium liner within the clad can be used without compromising the breeding potential.

PUBLICATIONS ARISING OUT OF THIS STUDY AND RELATED WORK

1. A.Riyas and P.Mohanakrishnan, *Annals of Nuclear Energy* (Accepted).
2. A.Riyas and P.Mohanakrishnan, Report No. REG/RPD/CPS/72, 2007.
3. A.Riyas and P.Mohanakrishnan, Report No. REG/RPD/CPS/73, 2007.

Further inquiries:
Shri A. Riyas and Dr. P. Mohanakrishnan, Reactor Physics Division
Reactor Engineering Group, IGCAR, e-mail: riyas@igcar.gov.in

KAlpakkam MINI (KAMINI): Beryllium-Oxide-Reflected ^{233}U-Fuelled Reactor

EXECUTIVE SUMMARY

In order to make experimental data like neutron multiplication factor (k_{eff}) useful in the validation of the theoretical model and data used in the calculational model, the configuration of the reactor has to be described very accurately. The uncertainties in the geometry, composition and fabrication tolerances contribute to the accuracy of the experimental measurement of k_{eff}. If the error in k_{eff} prediction due to these uncertainties is less than the targeted accuracy of one percent, then the measurement can be used as a benchmark for the purpose of validating the theoretical prediction of k_{eff}. Benchmarking is the process of describing the reactor very accurately and establishing that the uncertainties in the description will contribute less to less than one percent error in k_{eff} prediction.

OUTLINE

In the calculation of k_{eff} of a reactor lot of nuclear data and complicated computational techniques are used. The present international standard target accuracy in the prediction of k_{eff} is one percent (1000 pcm). In order to achieve this target one has to validate the nuclear data and calculational techniques against the measured k_{eff} values. Since the data used is very large the data and calculational methods have to be validated for a number of measured k_{eff} values. In order to validate the data the reactor where k_{eff} is measured has to be described very carefully as built. Normally k_{eff} is calculated using the nominal composition and nominal geometrical arrangement. Practically there will be some engineering tolerances in the fabrication, uncertainties in the composition, density of the materials, impurities in the materials and errors in the measurement of these parameters. These uncertainties will reduce the accuracy of the calculated k_{eff}. In order to know the accuracy in the k_{eff}, the configuration of the reactor has to be described with all the details. The effect of these uncertainties on k_{eff} has to be estimated and requires lot of sensitivity studies involving the uncertainties in each of the fabricational and compositional error or other uncertainties. Benchmarking is essentially describing the reactor accurately such that error due to the uncertainty in description, lack of data and errors in the measurement will effect k_{eff} prediction by less than one percent. The factors affecting the accuracy of calculated k_{eff} can be classified into three broad categories (viz.) uncertainties in: the geometry, the composition and material densities. The effect of various uncertainties is given in Tables 1, 2 and 3. The overall uncertainty due to these uncertainties is found to be 586 pcm which is less than the target limit of 1000 pcm.

Earlier deterministic calculational methods were used where there were lots of limitations in geometrical modeling of the reactor. Finer details could not be modeled. With the advent of fast computers, Monte Carlo codes have come into the forefront of reactor physics calculations. In these calculations, core could be modeled very accurately. In the present benchmarking, the core was modeled as accurately as possible. In the modeling of the reactor, the fuel content of each subassembly is taken accurately as available from the Quality Assurance(QA) reports. In principle the capability exits to model each plate with its own composition. The fuel subassemblies are having 180 geometrical symmetry and plates are not having this symmetry as each plate has got slightly different composition. During the fuel loading, the orientation of the subassembly at the time of loading was not recorded. Due to non-availability of this information each plate could not be modeled and modeling had to be restricted to average compositions of the plates in each subassembly. Few more minor approximations had to be made due to the lack of data. The uncertainty on the calculated keff due to these approximations is shown to be negligible. The above sensitive studies were used in qualifying this error. For this study, we also used cross-section generated in continuous energy 'A Compact ENDIF Routine' (ACER) format by us. Creation of this benchmark established our capability of generation cross-sections accurate modeling of the reactor and describing the reactor accurately to meet the international standards.

Table 1
Effects of Calculated variations and Standard Uncertainties of Fuel Assembly Dimensions

Parameter	Standard uncertainty	Effect (Δk_{eff}) due to uncertainty
Fuel thickness	0.0001	0.00029
Clad thickness	0.002	0.00025
Spacing between plates	0.0098	0.00126
Thickness of side plates	0.001	0.00050
Length of fuel	0.1	0.00161

Table 2
Calculated Sensitivities of k_{eff} to various densities.

Parameter	Standard uncertainty	Uncertainty in k_{eff} due to uncertainty
Fuel density	0.0118%	0.00004
Fuel mass variation	0.3704%	0.00121
Moderator density	0.027%	0.00008
Aluminum density	0.57735%	0.00021
BeO density	1.7929%	0.00411
Zircaloy density	0.57735%	0.00054
Cadmium density	0.57735%	0.00028
^{233}U	0.1%	0.00083
^{238}U	0.01%	0.00038
Effect of BeO bricks movement in the reflector blocks	0.4667 mm	0.00065

Table 3
Calculated Sensitivities to 100% of Reported Impurities

Parameter	Standard uncertainty of impurities	Standard k_{eff} uncertainty
Impurities in the fuel	40.00%	0.00068
Impurities in clad aluminum	28.57%	0.00030
Impurities in other aluminum	28.57%	0.00139
Impurities in BeO	16.67%	0.00227
Change in Zircaloy composition	57.73%	0.00030
Thorium as impurity	100.00%	0.00033

ADDITIONALBENCHMARKING

The International Handbook of Evaluated Criticality Safety Benchmark Experiments (ICSBEP) handbook, by design, is a compilation of critical, sub-critical, and radiation-transport benchmark experimental data that have been verified, to the extent possible, by reviewing original and subsequently revised documentation, logbooks, internal memos and letters, and by talking with experimenters or individuals who were associated with the experiments or the fabrication of components of the experimental facility. The experimental data have been reduced to a form, called the benchmark specification that facilitates the development of an analytical model of the criticality experiment. Detailed uncertainty analyses are preformed and an overall uncertainty is assigned to the benchmark model k_{eff} value. When used properly, these data allow criticality safety analysts to validate their analytical techniques and nuclear data evaluators to test data performance without repeating the research and data-reduction steps. Currently, the handbook spans over 38,000 pages and contains 442 evaluations representing 3955 critical, near-critical, or sub-critical configurations, 21 criticality alarm placement/shielding configurations with multiple dose points for each, and 20 configurations that have been categorized as fundamental physics measurements that are relevant to criticality safety applications. The handbook is intended for use by criticality safety analysts to perform necessary validations of their calculational techniques and is expected to be a valuable tool for decades to come. The Handbook is currently in use in 60 countries. With respect to ^{233}U critical systems, there are presently 196 systems of experimental benchmarks involving ^{233}U in the Handbook (10 are Metal (Fast spectra); 181 solution (144 Thermal, 29 Intermediate Spectra and 8 Mixed Spectra) and 5 Compound (Thermal spectra) and KAMINI is the 197th configuration

KAMINI REACTOR AND CROSS SECTIONS

KAMINI is a ^{233}U fuelled tank type, beryllium oxide reflected, demineralised light water cooled low power research reactor. This reactor is designed to operate at a nominal power of 30 kWt and uses a low fuel inventory of 590 g of ^{233}U in the form of uranium-aluminum alloy plates. This is the only operating reactor in the world that uses ^{233}U as fuel. Cooling of the reactor is by natural convection and an external heat exchanger cools the tank water to control the inlet temperature. Two absorber type plates (safety control plates) are used for control as well as emergency shutdown of the reactor. This reactor is mainly used for neutron radiography, neutron activation analysis and radiation physics experiments. The horizontal cross sectional view of the core-reflector assembly modeled in the calculation is shown in Fig. 1.

The present trend in Reactor Physics calculations elsewhere is to use Monte Carlo codes which are amenable to model the complicated geometries. Also continuous energy cross-sections have replaced the multi-group cross-sections. We have used the Monte Carlo codes for this study. Also for the analysis of this benchmark continuous energy cross-sections in the ACER format were also generated using in-house capability. The validity of these cross-section generations is verified with the cross-section generated by Korean Atomic Energy Research Institute (KAERI).

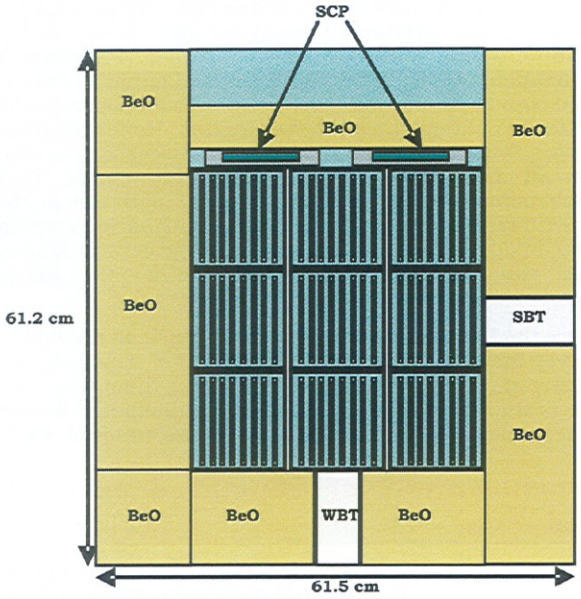

SBT: South Beam Tube; WBT: West Beam Tube

Fig. 1 : Horizontal Cross Section view of core-reflector assembly

ACHIEVEMENT

India has successfully completed the task of benchmarking of KAMINI and is formally listed as a participant and member of the USDOE-NEA lead team in the preparation of the ICSBEP. So far the compilation of these benchmarks was not made available to India. After our contribution to the collection of benchmarks India officially provided access to this vast experimental data which will be useful in validating the nuclear codes and nuclear data.

PUBLICATIONS ARISING OUT OF THIS STUDY AND RELATED WORK

1. E. Radha, C. P. Reddy, S. Ganesan, G. Srinivasan, P.V. Ramalingam and Baldev Raj, International Handbook of Evaluated Criticality Safety Benchmark Experiments, ^{233}U-MET-THERM-001 (2006).
2. E. Radha, C. P. Reddy, S. Ganesan, G. Srinivasan, P.V. Ramalingam and Baldev Raj, The 8th Workshop on Nuclear Data Production and Evaluation, August 25-26, 2005, Pohang Accelerator Laboratory, Pohang, Korea.
3. E. Radha, C. P. Reddy, G.J. Prasad, S. Ganesan, G. Srinivasan, P.V. Ramalingam and Baldev Raj, INSAC-2005: Science Behind Nuclear Technology: November 15-18,2005. BARC, Mumbai.
4. C. P. Reddy, E. Radha, S. Ganesan, G. Srinivasan, P.V. Ramalingam and Baldev Raj, NSRP-16, Radiation Transport: Experiments, Computations & Theory, January 18-20, 2006, Meenakshi College for Women, Chennai.

Further inquiries:
Dr. C.P. Reddy, Technical Services Division
Reactor Operation & Maintenance Group, IGCAR, e-mail: cpreddy@igcar.gov.in

Rapid in-situ Monitoring of Radionuclides in a Postulated Post-accident Scenario

EXECUTIVE SUMMARY

Rapid and in-situ measurement techniques during post-accident scenarios of a nuclear power plant have been developed and standardized. These techniques are sensitive enough to detect the activity levels corresponding to lower limit of intervention levels for speedy implementation of protective measures on the early and intermediate phases of nuclear accidents. Conversion factors have been established for all portable survey instruments that can reliably perform under field conditions and relatively simple to use. The techniques include measurement of ^{131}I activity in milk and ground contamination with ^{131}I, ^{137}Cs and also the fraction of ^{131}I component in a mixture of ^{131}I and ^{137}Cs. A novel portable post-accident radiation survey meter has been developed which include many additional features including energy discrimination.

OUTLINE

Environmental monitoring of ^{131}I in milk

Instruments for measuring ^{131}I must be sensitive enough to detect the activity levels corresponding to lower limit (3,000 Bq/l) of Derived Intervention Level (DIL) for implementation of protective measures in the early and intermediate phases of an accident. In addition, the instrument must be able to perform under field conditions and relatively simple to use. Presently, the survey instruments indicate the radiation field either in dose rate (mR/h) or in counts per second (cps). The DILs for control of foodstuff are available in literature in Bq/l or Bq/kg. Hence reliable conversion factors from mR/h or cps to Bq/l are necessary to be established for all the survey instruments for easier and effective implementation of remedial measures. With this as the objective, experiments have been conducted using various available survey instruments. The experimental arrangement is shown in Fig. 1. Just two litres of milk is adequate for the geometry to be standardized.

Since the DIL for ^{131}I for milk is 3,000 Bq/l, all the battery operated survey instruments with the exception of 'Teletector' can be used during emergency conditions. Amongst them, the most sensitive one is the NaI(Tl) detector based 'Scintillometer' whose Minimum Detectable Activity is 333 Bq/l with an accuracy of ±5%.

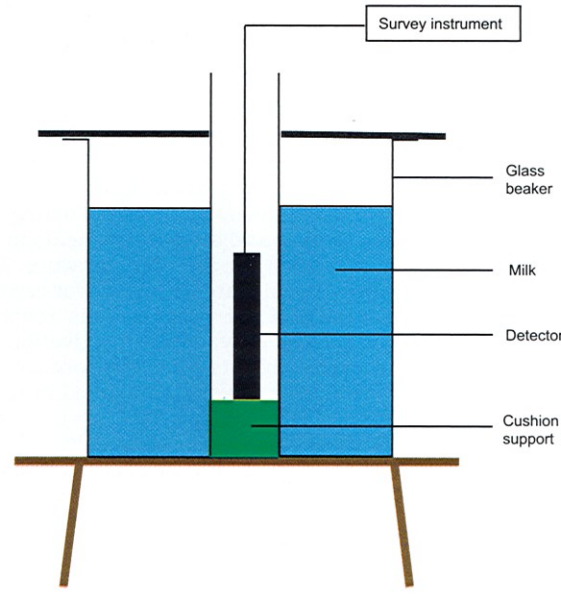

Fig. 1: Experimental arrangement

Measurement of deposited activity of ^{131}I and ^{137}Cs

The conversion factors were estimated for various portable survey instruments for ground contamination with ^{131}I, ^{137}Cs and the mixture of both. In the latter case, estimation of fraction of ^{131}I in a mixture of ^{131}I and ^{137}Cs is successfully accomplished. A 20-m dia pseudo fallout field was created for the studies. Background measurements were made at different locations over the field and an average value was taken. Eighty four point-sources were distributed as recommended in literature for the study. The source distribution is shown in Fig.2. The sources were distributed in such a way that they were concentrated at the center and widely spaced otherwise. The center of the calibration range was organized into a cross-like structure with 20 sources having 10.952 MBq each, about 1.07m apart. The remaining 64 sources, with 43.88 MBq each were placed with 2.14 m grid spacing. The average activity distribution over the whole experimental field was 9.66 MBq/m^2. The activity of ^{131}I in the sources was selected to give a dose rate of one mR/h at the center at one-meter height.

Conversion factors/response factors are obtained for all survey instruments to estimate the ground deposited activity of ^{131}I and ^{137}Cs. It is also possible to find out ^{131}I in the presence of other radionuclides especially ^{137}Cs using these conversion/response factors. The method of rapid monitoring of deposited activity on the ground explained above will help in predicting the possible ingestion dose delivered to thyroid through air-pasture-cow-milk pathway.

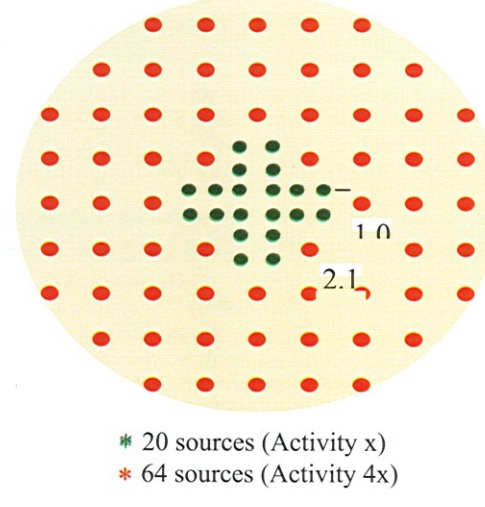

Fig. 2 : Schematic of source distribution

■ ADDITIONAL INFORMATION

The analysis of Design Basis Accident (DBA) for 220 MWe PHWR considers a release of 4.4 TBq of ^{131}I at ground level through containment leaks. While the inhalation dose to thyroid due to this release is estimated to be less than 30 mSv at 1.6 km distance, the ingestion dose would be 500 mSv upto 6 km. One way of assessing indirectly this dose would be to measure the dose rate at one meter above the ground due to the deposited activity. The measurement techniques developed at IGCAR viz., i) monitoring of ^{131}I in milk, and ii) measurement of deposited activity of ^{131}I with and without the interference of ^{137}Cs and ^{137}Cs alone, and the development of a portable post accident radiation survey meter with energy discrimination features would be handy in a post accident scenario.

■ DESIGN AND DEVELOPMENT OF POST ACCIDENT RADIATION MONITOR

Since the conventional radiation survey instruments give only the gross activity/dose rate without any energy discrimination, it would be meaningful while planning the counter-measures, if the contributions due to ^{131}I and ^{137}Cs can separately be measured. With this objective, a novel portable radiation survey instrument has been developed.

The instrument uses conventional Photo Multiplier Tube along with low power hybrid circuits based miniature discriminator. The versatility of the post accident monitor has further been improved by providing five ranges of energy discrimination. With this instrument, it is possible to measure gross activity below and above 500 keV as well as individual discriminator windows for ^{131}I, ^{137}Cs and ^{60}Co. The system has a simple analog meter display. The use of miniature electronics has ensured low power consumption while enhancing the reliability of the system.

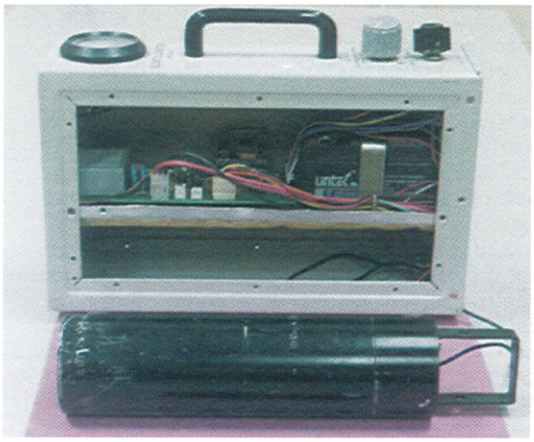

Fig. 3: Post accident radiation monitor

■ GENERAL DESCRIPTION

Based on the existing reactor safety study scenarios, associated source term releases and the three nuclear accidents, ^{131}I and ^{137}Cs have been identified as the radionuclides of major concern with respect to potential dose. The dominant radioiodine intake is through air-pasture-cow-milk pathway. For infants, as milk is the major diet, the contribution due to radioactive iodine to health effects is higher than that from the contribution of other long-lived radionuclides. Due to this, the derived intervention level (DIL) for ^{131}I is much lower (3000 Bq/l) than that for other radionuclides to restrict the thyroid dose.

The standard practice for rapid estimation of the activity deposited on the ground is to measure the radiation dose or flux at a representative point and correlate it to the deposited activity level. This calls for establishment of appropriate conversion factors for various types of survey instruments manufactured in India, which would mainly be used. One can, in principle, theoretically estimate the relationship between the deposited activity of ^{131}I and the dose rate. However, they need to be validated by field measurements.

■ ACHIEVEMENT

Protective measures are to be initiated at the earliest during radiological emergencies i.e., the decision-making should be quick and effective. Towards this objective, the two techniques described above are sensitive, rapid, in-situ and easy for effective implementation of remedial measures. The portable radiation survey meter, designed and developed exclusively for the purpose of post accident monitoring purpose, would lend a helping hand in accomplishing meaningful countermeasures.

■ PUBLICATIONS ARISING OUT OF THIS STUDY AND RELATED WORK

D.N.Krishnakumar, K.M.Somayaji and V.Meenakshisundaram;Proceedings of DAE BRNS National Symp. on "Compact Nuclear Instrumentation and Radiation Detectors", March 3-4. 2005, Defence lab, Jodhpur.

Further inquiries:
Dr. V. Meenakshisundaram, Radiological Safety Division
Safety Group, IGCAR, e-mail: vms@igcar.gov.in

Studies on Radon Exhalation

EXECUTIVE SUMMARY

The gaseous radioactive isotope of Radon, from natural sources has a significant share in the total quantum of natural sources of exposure everyone has been subjected to. Regulatory guides recommend a lower action level of 200 Bq/m^3 for the concentration of Radon in the dwellings. Hence accurate, reliable and easy measurement techniques for the estimation of radon exhalation rate from the building materials are of paramount importance, For the estimation of radon exhalation rate from materials of different matrices, a dedicated experimental facility has been designed and commissioned at IGCAR one of the four nodal centers in India.

OUTLINE

The members of public, in general, are more concerned about the miniscule addition of radiation they receive from nuclear installations but are unaware of the radiation exposure they are constantly subjected to, from different natural sources. The average annual dose received by a member of public due to natural background radiation has been estimated to be 2.4 mSv. Radon-222, the radioactive gaseous daughter product of natural uranium series, which is ubiquitous in nature, is the major source of internal exposure from the natural background. It is reported that indoor exposure due to radon and its progeny is responsible for more than 50% of the dose to humans. It is now well established that exposure to higher levels of radon and its progenies poses a significant health hazard to humans. Presence of uranium, a long-lived natural radionuclide in the building materials such as cement, clay bricks, fly ash, soil, granite stones and gypsum is the main source of indoor radon levels. Lack of adequate ventilation in the houses results in buildup of radon, the gaseous daughter product of natural uranium, thereby increasing the exposure potential further.

ICRP, in its publication 65 has stipulated an action level of 200 Bq/m^3 for radon concentration in dwellings. In order to comply with this, it is necessary to estimate the indoor radon levels through measuring the radon exhalation rates from different types of building materials. A dedicated facility with state of art equipment has been setup at Radiological Safety Division, IGCAR to carry out R&D works related to the measurement of radon/radioactivity content in various materials. As part of development of radon measurement methodologies, a radon exhalation chamber was designed and fabricated.

A small radon exhalation chamber (Fig. 1) of volume 0.7 m^3, with provisions for gas collection was designed and fabricated. This chamber was mainly used for the estimation of radon exhalation rates from small quantities of powder samples. Subsequently, a bigger chamber, of volume 0.125 m^3 made of MS was fabricated in order to evaluate the radon exhalation rate from large size fly ash bricks, granite tiles etc.

The samples to be analyzed are kept in the chamber for a known amount of time and the accumulated radon gas collected in the Lucas cell. The content of the cell is counted in a scintillation cell assembly consisting of photo multiplier tube and a counting system. The radon gas concentration is calculated and the radon exhalation rate (RER) is estimated using the standard methodology (Table 1).



Fig. 1 : Radon exhalation chamber (0.7 m^3) along with scintillation cell assembly

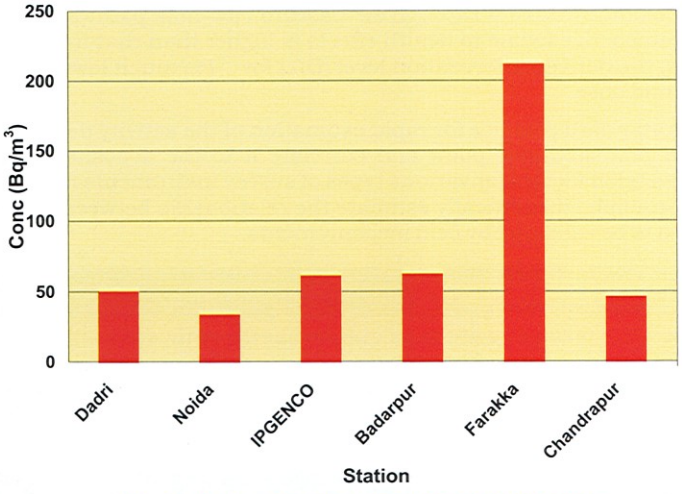

Fig. 2 : Radon concentration in fly ash brick houses

Table 1
Radon Exhalation Rate

Station	Radon Exhalation Rate (Bq/m^2/h)
Orissa	2.5
Neyveli	1.6
Vindhyachal	1.3
Delhi	0.9
Manuguru	1.3

■ ADDITIONAL INFORMATION

India is one of the largest exporters of granite tiles in the world. Several countries importing granite tiles from India have import regulations that insist on certificate for the exhalation rate from the granite tiles. This requires standardization of procedures for the estimation and the subsequent certification. The work carried out at our laboratory enabled rapid assessment and estimation of radon exhalation rates, enabling certification. Fly ash, a waste generated in thermal power power stations, contains trace quantities of natural uranium. One of the ways to utilize the abundantly produced fly ash is to fabricate bricks which can be used in the construction sector. The current production rate of fly ash from Indian thermal power plants is about 100 million tonnes a year whereas the utilisation is about 51 million tonnes. This results in an accumulation of about 50 million tonnes every year requiring huge land area for storage. It is also estimated that the generation would escalate to about 170 million tonnes per year by the end of 11th five year plan. In view of this, Ministry of Environment and Forests, in their rececnt Gazette Notification vide S.O. 513(E) dated 03/04/2007 has made the use of fly ash as a mandatory component in consutrction activities such as building of dwelling units, offices, laying of roads, fly over bridges, land filling and embankments. Considering the hazard potential associated with the fly ash (exhalation of radon) accurate quantification of radioactivity content in the fly ash and also the radon concentration in houses built with bricks made out of fly ash assumes significance. An exhaustive study was carried out to build a nationwide database on natural radioactivity content in Indian fly ash through field and laboratory measurements. This study was carried out by RSD, IGCAR, in collaboration with Fly Ash Utilization Program (FAUP) of Department of Science and Technology (DST), Government of India. Under this study, radon concentration in houses made of fly ash bricks located around six major thermal power stations situated across the country, was estimated for a period of one year covering all seasons (Fig.2). Radon lab is also used for the generation of nationwide radon map of the environment and the estimation of consequent public exposure.

■ RADIATION EXPOSURE

The sources of exposure of general public to radiation are (i) natural (87%) and (ii) man-made (13%). Cosmic radiation, which interacts with the earth's atmosphere and magnetic field to produce a shower of radiation, is one of the components of natural radiation. Traces of primordial radio nuclides, such as natural Uranium, Thorium and Potassium-40, present in earth's crust are the other sources of natural radiation. Radon-222 and Radon-220, the gaseous daughter products of U-238 and thorium respectively, accounts for more than 50% of the exposure (internal) due to natural radiation. In addition, radio nuclides such as Potassium-40 and Carbon-14 that are present in our body gain entry from food chain also form part of exposure due to natural sources. Consumer products such as tobacco, building materials, smoke detectors, combustible fuels etc., form part of man-made sources. The most significant exposure due to man-made source is from medical procedures (12%), such as diagnostic X-rays, nuclear medicine, and radiation therapy. Some of the major isotopes used in medical procedures are Iodine-131, Cobalt-60 and Cesium-137. Of very less magnitude, members of the public are exposed to man-made radiation from nuclear industry. Occupation in a nuclear industry and 'fall out' from nuclear weapon testing are also sources of man-made radiation to general public, though insignificant.

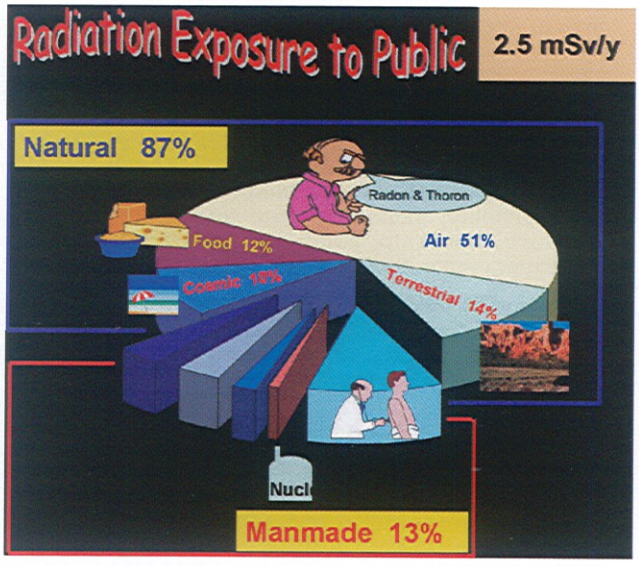

Fig. 3: The defect production rate by different projectiles (Ion beams produce displacement damage at a much faster rate than neutrons

■ SIGNIFICANT ACHIEVEMENT

The mandatory requirement of estimating and certifying the radon exhalation rates from Indian granite tiles, imposed by several countries was complied with. Estimation and certification of radon exhalation rate from granite tiles, exported from India, was done on chargeable basis. The project of creating a comprehensive database on natural radioactivity content in fly ash, after extensive analysis of various samples collected from major thermal power stations situated across the country, was completed and a report has been submitted.

■ PUBLICATIONS ARISING OUT OF THIS STUDY AND RELATED WORK

R.Santhanam, S.Balasundar, V.Gajendiran, B.Dhanalakshmi, V.Meenakshisundaram, R.Indira and Baldev Raj, Fly Ash India-2005 International Conference, Dec. 4-7, 2005, New Delhi, India.

Further inquiries:
Dr. V. Meenakshisundaram, Radiological Safety Division
Safety Group, IGCAR, e-mail : vms@igcar.gov.in

Advances in Thermo Luminescence and Imaging Phosphors

EXECUTIVE SUMMARY

A new high temperature Thermo Luminescence (TL) phosphor, $CaSO_4$:Ag,Tm/Dy, with a glow peak at a relatively high temperature of 375°C has been developed at IGCAR. This is the only TL phosphor known as on to-day which is capable of measuring low radiation doses (~0.1mGy) even at temperatures up to 300°C. For the first time, a simplified co-precipitation technique has been developed by us for the $CaSO_4$:Dy phosphor synthesis which circumvents the cumbersome procedure used so far, evaporation of (highly corrosive) concentrated H_2SO_4. An X-ray imaging plate (IP) has been made using the indigenously synthesized, high PSL sensitive BaFBr:Eu^{2+} storage phosphor.

OUTLINE

$CaSO_4$:Ag,Tm/Dy New Sensitive TL phosphor for high temperature radiation dosimetry

In several practical situations such as in thermal reactor cores in shut down condition, radioactive waste storage areas or primary coolant (sodium) lines in fast reactors there is a need to measure low levels of radiation exposures (<1 mGy) at elevated temperatures. High temperature TL peaks in other phosphors reported so far are not suited for this purpose because of their poor sensitivity. Only high levels of gamma exposures could be measured with these phosphors at elevated irradiation temperatures. Apart from this drawback, there are other problems associated with these high temperature TL peaks such as poor reproducibility, nonlinear dose-response, multiple glow peak structure, batch to batch variation, dependence on certain impurities even in trace quantities etc.

The major TL peak in all rare earth (RE) doped $CaSO_4$ phosphors (with the exception of Ce) occurs at ~200°C which is related to host lattice related defects, namely holes trapped at sulphate radicals near Ca^{2+} vacancies. Co-doping of Ag in $CaSO_4$:Tm/Dy shifts the glow peak from 220°C to 375°C without decreasing the TL sensitivity (Fig.1) The fact that the TSL peak in $CaSO_4$:Ag, Tm/Dy occurs at 375°C indicates that the hole trap in this material is related to Ag rather than to the host lattice related defects. TL process in $CaSO_4$:Ag,Tm/Dy phosphor is explained fully.

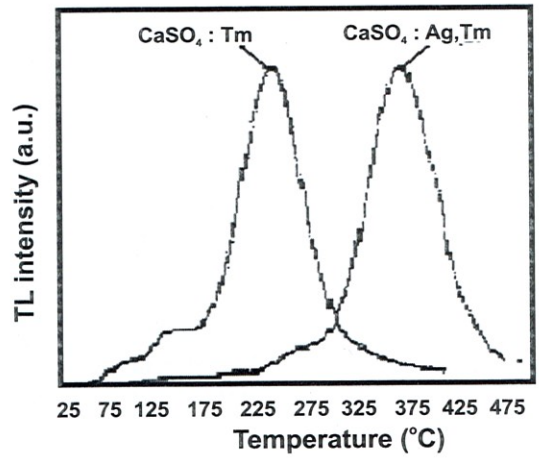

Fig. 1: TL glow curves of $CaSO_4$: Tm and $CaSO_4$:Ag,Tm

TL Process in $CaSO_4$:Ag,Dy

On irradiation

$SO_4^{2-} \rightarrow SO_3^- + O^-$: Due to radiolysis
$Ag^+ \rightarrow Ag^{2+} + e^-$: Ag^+ act as hole trap,
$SO_3^- + e^- \rightarrow SO_3^{2-}$: SO_3^- act as electron trap

On TL readout to 375°C

$Ag^{2+} \rightarrow Ag^{1+}$ + hole :Releases hole to become Ag^+,
SO_3^{2-} + hole $\rightarrow (SO_3^-)^*$: SO_3^{2-} act as recombination centre
$(SO_3^-)^* + Dy^{3+} \rightarrow SO_3^- + (Dy^{3+})^*$
$SO_3^- + O^- \rightarrow SO_4^{2-}$

High Sensitive $CaSO_4$:Dy TLD Phosphor by Co-precipitation

$CaSO_4$: Dy/Tm TL materials are used extensively for the radiation dosimetry purpose due to low cost, high sensitivity , inertness to heat treatment below 700°C and very high storage stability in ambient climatic conditions. In India, more than 75,000 of radiation workers use the TLD badge based on $CaSO_4$:Dy Teflon discs for personnel monitoring. Presently, this phosphor is synthesised by re-crystallization technique requires the evaporation of 1 litre of H_2SO_4 to get 100 g of $CaSO_4$:Dy phosphor. Another recently developed technique here with calcium carbonate as raw material instead of Gypsum also needs evaporation of 150 ml of H_2SO_4 + 450 ml of HCl to dryness to get 100 g of $CaSO_4$:Dy, though this phosphor is 50% more sensitive than those prepared by the conventional methods.

In the new co-precipitation technique, radiation dosimetry grade $CaSO_4$:Dy crystals are precipitated from the solution containing dissolved $CaSO_4$ and Dy_2O_3 using a liquid at room temperature. High TL sensitivity - 20% more, uniform micro-crystalline morphology, lesser glow peak shift and better linearity to gamma dose, better glow curve structure (Fig. 2) and unwanted low and high temperature peaks were absent in the new phosphor while the desired dosimetric peak near 200°C is more intense and simplified recipe make the new phosphor a better alternative.

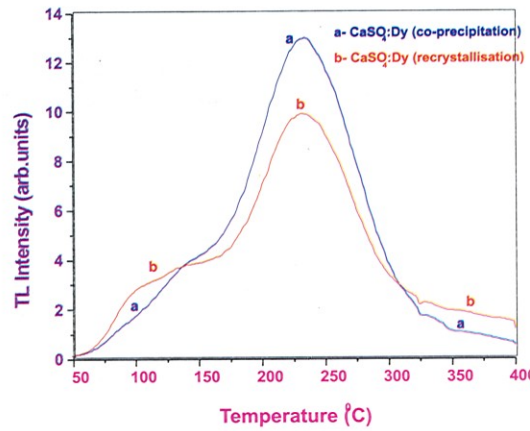

Fig. 2 : TL Glow curves of the phosphor prepared by Co-precipitation and conventional method

THERMO STIMULATED LUMINESCENCE (TL)

When a TL material is exposed to ionising radiation some of the liberated charge carriers (electrons or holes) are trapped at lattice imperfections in the crystalline solid. TL is light emission from materials when heated following the previous absorption of energy from radiation. TL phosphor for dosimetric use should combine the following general properties: (1) high intrinsic efficiency, (2) long storage of trapped charge carriers at room temperature, (3) simple trap distribution, (4) TL spectrum of wave length in the region 300-500 nm and (5) resistance against disturbing environmental factors such as light, humidity etc.

X-RAY IMAGING PLATE BASED ON PSL IN BaFBr:Eu^{2+} STORAGE PHOSPHOR

For over 100 years, X-ray radiography has relied on film as the image detection and display medium. Recently, photographic films are being gradually replaced by imaging plates (IP) based on photostimulated luminescence (PSL) storage phosphor mainly, BaFBr:Eu^{2+}. IP has several advantages over photographic film which include reusability and a wide dynamic range with a linear exposure-response which results in reduced X-ray exposure to patients. A storage phosphor is made in such a way as to store i.e., trap electrons and holes on X-irradiation. On photo stimulation their recombination and subsequent energy transfer results in light emission from activator ion, which form a digital image of the spot, illuminated using He-Ne Laser.

With the aim of indigenously developing an X-ray imaging plate, high sensitive BaFBr:Eu^{2+} storage phosphor has been successfully synthesized recently using high temperature solid state diffusion route in a reducing atmosphere. The photoluminescence (PL) excitation and emission spectra of BaFBr:Eu^{2+} synthesized are compared with that of commercial IP (Fuji) showed very intense characteristic Eu^{2+} peaks. In PSL studies, a broad stimulation spectra in the 480 – 650 nm corresponding to the depopulation of the electrons trapped at $F_{(Br^-)}$ centers is observed in this storage phosphor. Only fluorine excess non-stoichiometric $BaF_{1.015}Br_{0.985}:Eu^{2+}$ compounds were found to give intense PSL. The stimulated luminescence process in this phosphor can be explained on the basis of the presence of interstitial fluorine ions (F_i^-) and bromine ion vacancies prior to X-irradiation (during crystal growth) in non-stoichiometric materials. An IP has been made using this indigenously synthesized storage phosphor.



Fig. 3 : SEM picture of new $CaSO_4$:Dy TL phosphor



Fig. 4 : Skull phantom image recorded in IGCAR- IP

ADVANTAGES OF NEW $CaSO_4$: TL PHOSPHOR BY CO-PRECIPITATION TECHNIQUE

(i) Preparation time is very less. (ii) quantity of concentrated H_2SO_4 evaporated is insignificant (iii) higher TSL sensitivity (iv) uniform crystal morphology (Fig.3) and lower grain size- all grains are mostly cuboidal in shape, quite uniform and small (average size about 25 m), suitable for manufacturing teflon discs in as prepared form whereas the conventional phosphors are mostly (90%) above 75 m and has to be ground for dosimetric applications. The standard practice for rapid estimation of the activity deposited on the ground is to measure the radiation dose or flux at a representative point and correlate it to the deposited activity level. This calls for establishment of appropriate conversion factors for various types of survey instruments manufactured in India, which would mainly be used. One can, in principle, theoretically estimate the relationship between the deposited activity of ^{131}I and the dose rate. However, they need to be validated by field measurements.

ACHIEVEMENT

New recipe of $CaSO_4$:Dy based on co-precipitation technique is not only economical but also compatible for large scale production and a patent has been applied for the technique. An IP has been made with the help of M/s Kiran X-ray screens Ltd, Mumbai using this indigenously synthesized storage phosphor. A comparative study of skull phantom image recorded using a commercial scanner and a commercial Kodak IP as well as our IP at the same X-ray exposure parameters, revealed that all the salient features of the image are seen in the IP made from indigenously synthesized storage phosphor (Fig.4). The sensitivity is comparatively good but the contrast needs improvement.

PUBLICATIONS ARISING OUT OF THIS STUDY AND RELATED WORK

1. Bhushan Dhabekar, Sanjeev Menon, Rajesh Kumar, T.K. Gundu Rao, B.C. Bhatt and A.R. Lakshmanan, *J.Phys. D: Appl. Phys.* **38** (2006)
2. M.T. Jose, R. Sudarkodi@Mohana, A.R. Lakshmanan and S. Nagarajan, NCLA- 2007, Coimbatore, (2007) 257.

Further inquiries:
Dr. M.T. Jose and Dr. U. Madhusoodanan, Radiological Safety Division
Safety Group, IGCAR, e-mail: mtj@igcar.gov.in

Development of a Fast Reactor Core Burnup Code FARCOB

EXECUTIVE SUMMARY

A large fast breeder reactor requires the accurate estimation of power produced in different parts of the reactor core and blanket during any operating condition for a safe and economic operation through out reactor life time. A Fast Reactor COre Burnup simulation code (FARCOB) based on multigroup diffusion theory has been developed in IGCAR for core simulation of PFBR reactor under construction. For burnup simulation, core is divided into radial and axial burnup zones and burnup equations are solved at constant power. For validation, results of FARCOB has been compared with results of other institutes for SNR-300 steady state benchmarks and two burnup benchmarks (ANL 1000 MWe benchmark and BN-600 hybrid core benchmark). It is found that FARCOB results match well with those of the other institutes.

OUTLINE

For examining different design options and in core followup studies, multigroup neutron diffusion theory is still adequate with cost to benefit ratio weighing in favour of diffusion theory relative to neutron transport theory methods. Considering PFBR under construction at Kalpakkam, as an example, it is found that the total neutron flux unknowns is about 2,00,000 per neutron energy group (700 subassemblies upto in-vessel storage location with 50 axial meshes). Use of 10 to 30 neutron energy groups is found to give accurate results as noted in the IAEA-CRP work on BN-600 hybrid core.

For FBR core design, multigroup diffusion theory code FARCOB(Fast Reactor Core Burnup) has been developed which can follow fuel and blanket burnups and compositions in 3-D. Neutron cross-section library used is the ABBN type 26 group library XSET-98. Centre mesh difference scheme is used with triangular meshes in X-Y plane to get the steady state difference equations. Inner iterations are accelerated by finding optimum acceleration parameters of each group using the spectral radius of inner iteration matrix. Chebyshev two parameter acceleration scheme is used for outer iterations using the dominance ratio of the iteration matrix. Double triangle mesh line inversion procedure in X-Y plane further accelerates the iterations to get the converged fluxes and multiplication factor (keff). The excellent comparisons with other established codes in steady state problems are shown in Table 1.

Power distributions are estimated using the neutron fission, capture and slowing down powers in each material. For core power normalization, peak pin power in each fuel and blanket subassembly is computed. Fluxes in 12 adjacent triangle meshes are interpolated to get flux at any point within a subassembly and the pin power at that location. For performing burnup calculations, average power per unit length in each burnup zone and one group, fission, capture and (n,2n) cross-sections of each heavy isotope is computed. The core is divided into different radial and axial burnup zones selected by the user. Heavy isotope number densities are kept track of in each axial hexagonal mesh in core and blankets. Thus the user has freedom to change radial and axial burnup zones for a fresh burnup step or after refueling.

A total 18 heavy isotopes including a lumped fission product is considered in the burnup chain. These coupled set of equations are solved using Runge-Kutta or trapezoidal rule. Generally a step equivalent to 2 months of reactor operation is used as a burnup step during which absorber rod positions are held constant. At the end of the burnup, changed number densities are stored in a file which become the initiating file for next burnup step.

Results of FARCOB for 1000 MWe benchmark are compared in Table-2 with those of ANL. Very good agreements in keff, reactivity loss with burnup and breeding ratio (BR) are found for this high breeding core.

Table 1
Comparison of Multiplication Factors for SNR-300 Static 2-D/3-D Benchmarks

Bench-mark ID No.	Description	Multiplication Factor (keff)	
		FARCOB (IGCAR)	VENTURE - (ORNL) DIF3D* - (ANL)
18-A3	2-D rods in	1.12867	1.12867
18-A3	2-D rods out	1.22833	1.22830
18-A1	3D rods in	1.01668	1.01666*
18-A5	2-D rods in zig-zag boundary	1.12729	1.12728*
18-A5	2-D rods out zig-zag boundary	1.22582	1.22580*
18-A6	3-D zig-zag boundary	1.01507	1.01505*

Table 2
Comparison of keff and BR for 1000 MWe Core Burnup Benchmark

Parameter	FARCOB - (IGCAR)	DIF3D - (ANL)
keff at BOC	0.99747	1.00060
keff at MOC	0.99414	0.99690
Reactivity loss(BOC-MOC)	0.00333	0.00370
keff at EOC	0.99346	0.99540
Reactivity loss(MOC-EOC)	0.00067	0.00150
BR (BOC)	1.531	1.523

BOC- Beginning of cycle,
MOC- Middle of cycle,
EOC- End of cycle

■ RECENT IAEA-CRP AND FARCOB VALIDATION

On the request of Russian federation in 1999, IAEA started in year 2000, a Co-ordinated Research Project(CRP) on BN-600 MOX core design suited for consuming accumulated Pu. The aim of the CRP was to test the adequacy of current tools of all participating institutes in predicting reactivity coefficients and burnup effects in a MOX fuelled BN-600. From, IGCAR, computer code FARCOB was used for burnup effect predictions. The core geometry where MOX fuel region is sandwiched between two enriched U zones is shown in Figure 1. The results of the comparison with the predictions of other institutes employing latest codes generated in 2003 are given in Table 3. It is found that IGCAR predictions match well with those of the other institutes. The high keff predicted by European Union(EU) is due to the use of JEFF 2.2 library which tends to over predict keff with Pu bearing cores.

■ GENERAL EXPLANATION RELATED TO THE DESCRIPTION

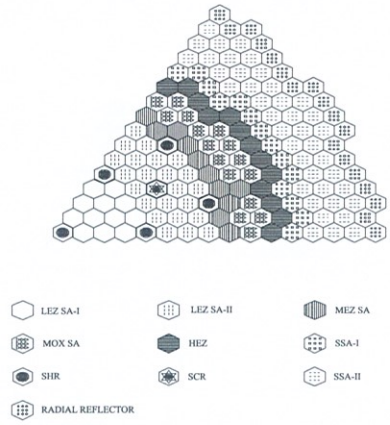

Fig. 1 : Proposed BN-600 Hybrid Core (60° sector)

Table 3
BN-600 Hybrid Core Benchmark - Comparison of Results of Different Institutes for Burnup Effects

Parameter	ANL	EU(CEA)	JNC	IGCAR
keff - BOC	0.99592	1.01546	1.00713	1.00136
keff- EOC	0.97162	0.98914	0.98323	0.97671
Burnup reactivity loss	0.02511	0.02621	0.02414	0.02520
Doppler coeff.				
BOC	-0.00685	-0.00683	-0.00646	-0.00684
EOC	-0.00687	-0.00732	-0.00703	-0.00731

For burning Pu accumulated, FBR is more suitable from the point of view of waste generation, as production of higher actinides is less than in thermal reactors.

■ BRIEF DESCRIPTION OF THEORETICAL BACKGROUND

Finite difference solution of neutron diffusion equation incorporated in FARCOB is similar to those in computer codes VENTURE (ORNL) and DIF3D (ANL). Acceleration procedures of inner and outer iterations including line inversion are incorporated in the solution scheme. Absorber rod heterogeneity treatment, performed extraneous to FARCOB, employs first flight collision probabilities method. Peak pin powers are obtained using a new flux interpolation scheme. Solution of the coupled burnup chains is by the exponential matrix expansion method. The possibility of flexible user defined burnup zones at every burnup step is a novel approach. Fuel/blanket burnups are distributed according to the computed power distribution. Breeding ratios and reaction rates are also computed. Fuel/blanket replacement and shuffling is achieved by a routine extraneous to FARCOB.

■ ACHIEVEMENT

A 3-D core simulation computer code is essential for detailed design of any reactor core. Also, a reactor core simulator is necessary for deciding the day to day operations and for planning the refuelling of any operating power reactor. FARCOB fulfils these requirements for PFBR being constructed at Kalpakkam. Earlier, FARCOB had been used for simulation of FBTR core evolution. Recently it has been used to predict approach to equilibrium of PFBR from BOL. It can be used for design of future metal fuelled FBRs.

■ PUBLICATIONS ARISING OUT OF THIS STUDY AND RELATED WORK

1. P. Mohanakrishnan, *Annals of Nuclear Energy* (Accepted).
2. K.Devan, M. Alagan and P. Mohanakrishnan, Report No. RPD/CPS/61 (2006).

Further inquiries:
Dr. P. Mohanakrishnan, Reactor Physics Division,
Reactor Engineering Group, IGCAR, e-mail: mohana@igcar.gov.in

Development of a Reflectron Time-of-flight Mass Spectrometer for Non-Destructive Analysis of Isotope Ratios in Irradiated B_4C Pellets

EXECUTIVE SUMMARY

A remotely operable laser mass spectrometric facility using a home-built reflectron time-of-flight mass spectrometer (RTOFMS] was developed to determine the ratio of $^{10}B/^{11}B$ in irradiated B_4C pellets from fast reactor control rods. Initial experiments with an unirradiated Fast Breeder Test Reactor (FBTR) pellet and a pellet used as shielding material in PFBR yielded good results. The analysis can be considered practically nondestructive as very small amount of sample (<nanogram) is utilised in the analysis. Direct measurement of $^{10}B/^{11}B$ and the ability to handle larger dimension pellets (40 mm dia X 40 mm length) is the novelty of this method. Such measurement gives information on how much of useful isotope is still available, so that a decision on the reuse of expensive spent control rod pellets can be taken.

OUTLINE

The neutron absorption cross-sections of ^{10}B and ^{11}B for thermal neutrons are 3837 barn (b) and 5 millibarn (mb), respectively, while the values for fast neutrons (corresponding to the neutron energy spectrum seen in a fast reactor), are about 2.7 b for ^{10}B and a much smaller value ($9.7x10^{-5}$ b) for ^{11}B. Hence, boron compounds enriched in ^{10}B are highly suitable to control the number of neutron available in a nuclear reactor, particularly to shut down an operating reactor. The natural abundances of boron isotopes are: 19.89% of ^{10}B and 80.11% of ^{11}B. For various technical reasons, the boron compound, namely boron carbide (B_4C) is widely used as a control rod material in fast nuclear reactors. The extent of enrichment of ^{10}B varies from 65%, for a commercial fast reactor (e.g. Prototype Fast Breeder Reactor [PFBR]), to as high as 90% for small core test reactors (e.g. Fast Breeder Test Reactor [FBTR]). Generally, the B_4C pellets used in the control rods of fast reactors can be 10-40 mm in diameter and up to 50 mm in length. The typical dimensions of control rod pellets used in FBTR are: Diameter: 38 mm, length: 40 mm. Stack of nine such B_4C pellets contained in stainless steel clad is used as control rod in FBTR. ^{10}B present in these B_4C pellets is burned out only to a lesser extent, as the rod is kept out of active core level for considerable part of its life in a reactor (life of control rod is determined not only by the burnt-out fraction of ^{10}B in B_4C, but mostly on the SS clad stability in a radioactive environment) and the maximum burn-up of ^{10}B occurs only in the lower part of the rod. To decide if the pellets from such an irradiated stack can be reused or relocated, one needs to know the $^{10}B/^{11}B$ ratio present in such irradiated pellets. The accuracy needed for such isotope measurements is about ±1%. Though neutron irradiated B_4C is not expected to be radioactive, the common trace impurities such as Eu present in the B_4C pellet can lead to considerable levels of radioactivity. Hence, the method used for the $^{10}B/^{11}B$ ratio measurements on irradiated B_4C pellets needs to be amenable for remote operation. Further more, B_4C is one of the hardest materials known, next to diamond and cubic boron nitride. Any destructive method to analyze isotope ratio of B in B_4C is cumbersome. Hence, a non-destructive method is preferred not only to avoid the difficult dissolution or powdering process, but also because the pellet taken for analysis can be reused, as it is, after the measurement. One such method is laser vaporization mass spectrometry (LMS). In LMS, the laser vaporization removes only a few picograms of the material from the laser-irradiated spot of the surface, without any physical damage to the pellet. For a nanosecond laser pulse, the transiently heated part of surface is typically 0.5 mm in diameter and a few tens or hundreds of Å depth. A laser mass spectrometric facility is developed using a home-built reflectron time-of-flight mass spectrometer (RTOFMS) to analyze the isotopic ratio of $^{10}B/^{11}B$ present in B_4C pellets. The schematic of the facility is shown in Fig.1 and typical mass spectrum obtained for an unirradiated FBTR pellet and a pellet of natural composition used as shielding material in PFBR is shown in Fig. 2. This facility can analyze the isotopic ratio with a spatial resolution of 300 m. The typical values obtained for % of ^{10}B present in FBTR and PFBR pellets are: 90.3 0.4 & 20.7 0.5; the corresponding thermal ionization mass spectrometric values (which is a standard method for isotopic analysis – a destructive method), obtained using the powdered B_4C samples are: 90.65 0.07 & 19.90 0.07, respectively. The facility is ready to handle irradiated pellets inside a glove box.

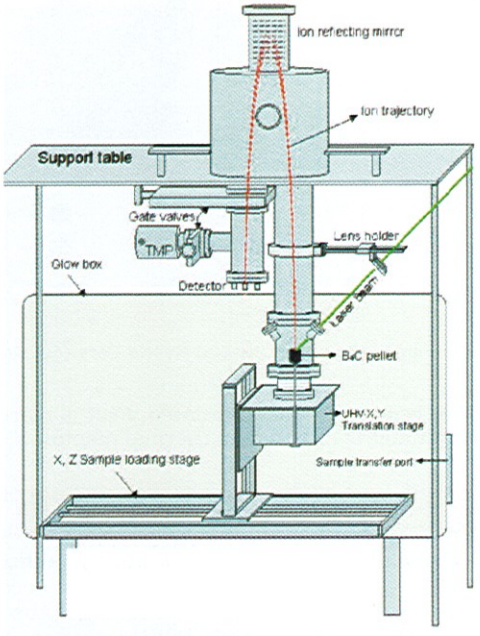

Fig. 1 : Home-built reflection time-of-flight mass spectrometer for the analysis of $^{10}B/^{11}B$ ratio in FBTR control rod B_4C pellet

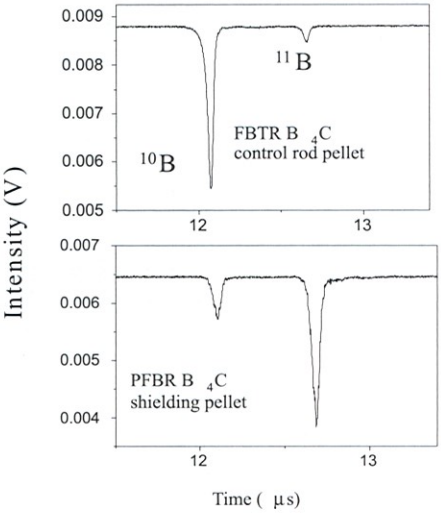

Fig. 2 : Typical mass spectrum of isotopes of B obtained for B_4C pellets.

■ ADDITIONAL INFORMATION

Even though different types of mass spectrometers such as, Magnetic, Quadrupole, Ion-trap etc., are available, we have selected a RTOFMS based technique for this work, because coupling of pulsed laser to TOFMS is more advantageous compared to other mass spectrometers. Also fabrication of a RTOFMS is relatively less complex compared to other types of mass spectrometers.

■ TIME-OF-FLIGHT MASS SPECTROMETER

A time-of-flight mass spectrometer (TOF-MS) is used to quantify various masses of species present in a given sample. For the actual mass analysis, the species are to be produced in the gaseous ion form, as the mass spectrometer can separate and identify only ionic species. In this Laser Mass Spectrometric system, a laser is used to vaporize and ionize the species of boron simultaneously from the boron carbide pellet. In a TOF-MS, the ions so formed are allowed to drift through a filed free vacuum space (drift tube) and at the end of the drift tube, a detector will detect these ions as shown in Fig. 3. Obviously, when all the ions (of different species) are formed with same energy, the ions that are smaller in size (say $^{10}B^+$) will reach the detector first compare to the heavier mass (say $^{11}B^+$). Hence, with suitable calibration, we can quantify the various ions. The Fig. 3 is schematic of linear TOF-MS, where the initial spread in the energy of ions of same mass will lead to considerable spread in the time of arrival, thereby the separation between the peaks get reduced, leading to poor resolution. This limitation of initial energy spread is compensated by allowing the ions to go through a reflecting ion mirror (Fig. 1), thereby the resolution is improved and this configuration of TOF-MS is called a Reflectron TOF-MS.

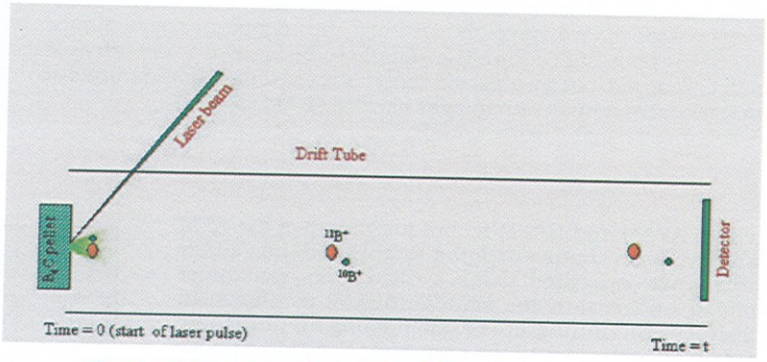

Fig. 3 : Schematic of Linear time-of-flight mass spectrometer.

■ ACHIEVEMENT

It is a unique facility of its kind set up for the first time in the country.

■ PUBLICATIONS ARISING OUT OF THIS STUDY AND RELATED WORK

1. P.Manoravi, M.Joseph, N.Sivakumar and R.Parthasarathy; Report No. IGC-290 (2007).
2. M. Joseph, N. Sivakumar, P.Manoravi and R. Balasubramanian, *Rapid Communications in Mass Spectrometry*, **18** (2005) 231.

Further inquiries:
Dr. T.G. Srinivasan, Fuel Chemistry Division
Chemistry Group, IGCAR, e-mail:tgs@igcar.gov.in

Contact Resonance Imaging using Atomic Force Microscopy

EXECUTIVE SUMMARY

We have shown that one can determine local elastic properties of surfaces using contact resonance imaging ie., Atomic Force Acoustic Microscopy (AFAM) and Ultrasonic Atomic Force Microscopy (UAFM). Both these techniques are combination of atomic force microscopy (AFM) and acoustic waves. We have used commercial piezoelectric PZT, $Pb(Zr,Ti)O_3$ ceramic, to elucidate the capability of the these techniques to image the distribution of local stiffness over the sample surface. We have shown both the techniques give similar results. But, UAFM has an advantage over AFAM because it does not require the sample to be bonded to an ultrasonic transducer. In the UAFM technique the cantilever itself can be excited by a permanently attached ultrasonic transducer. We have shown for the first time that UAFM gives similar contrast inversion images like the AFAM images.

OUTLINE

In both AFAM and UAFM technique the tip of the AFM cantilever is in contact with the sample and then either the sample is excited using a ultrasonic transducer bonded underneath the sample (AFAM) as shown in Fig.1(a) or the cantilever is excited using an ultrasonic transducer attached to the cantilever (UAFM). In both the cases either the amplitude or frequency of cantilever vibration is monitored. Depending on whether the effective elastic constant between the tip and the sample surface is higher (stiff) or lower (soft) the peak of the resonance curve will shift towards a higher or lower frequency, respectively as shown in Fig. 1(b) and Fig. 1(c). The fixed end of the cantilever will have one node of the vibration at a fixed position (substrate end) and the position of the other node will depend on the local rigidity of the sample surface (for the softer region the node will be deeper into the sample, whereas for the harder region the node will be close to the sample surface as shown schematically in Figure 1(b)). Thus when the tip is in contact with the softer region, the wavelength of the cantilever vibration will increase (λ_s), resulting in a decrease of the cantilever's vibrational frequency (f_s). Also, for the softer region the node at the sample end is not very sharply defined as compared with the harder region, resulting in a broadening of the peak (increase in full width at half maximum (FWHM) corresponding to $\Delta\lambda_s$) accompanied by a reduction of the amplitude at the resonance. Thus, as the tip moves towards the softer region, the frequency of vibration decreases or increases if the tip moves towards the harder region. If the excitation frequency of the transducer, which is also used as the reference frequency of the lock-in amplifier, is set slightly above the peak value as shown in Fig. 1(c), and if the tip in contact with the surface moves to a higher elastic constant region then the amplitude of oscillation of the cantilever will increase (marked by arrow 1) and if the tip moves to a lower elastic constant region, then the amplitude of oscillation of the cantilever will decrease (marked by arrow 2). Thus an increase in the amplitude of oscillation of the cantilever corresponds to a higher elastic constant region and a decrease in the amplitude of oscillation corresponds to a lower elastic constant region. If we now choose the transducer excitation frequency and the reference frequency for the lock-in amplifier below the resonance peak then the situation should be reversed. That is, the amplitude of vibration will decrease/increase in regions with higher/lower elastic constant compared with the reference point. This is marked by arrow 3 and arrow 4, respectively, in Fig. 1(c). The images taken at frequency above and below the resonance peak will have contrast inversion of the images. We have seen that this in fact is observed and from this we can know the distribution of local elasticity at nano-scale over the surface of the sample.

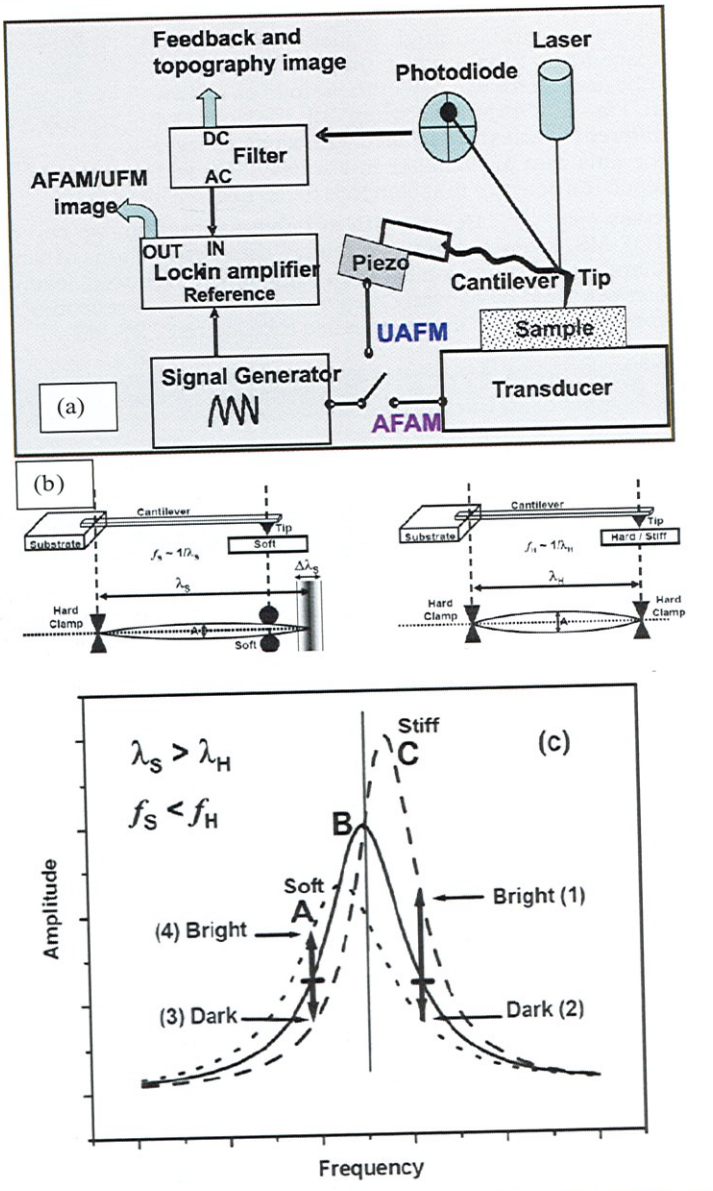

Fig. 1 : (a) Schematic diagram of the experimental setup of AFAM and UAFM. (b) Schematic representation of cantilever vibration when tip is in contact with a hard surface (the nodes are well defined at both the ends of the cantilever) and a soft surface (c) Schematic representation of the resonance curve and the shift of the resonance curve for higher and lower effective elastic constant regions marked as soft and stiff

■ ADDITIONAL INFORMATION ABOUT AFAM

In Fig. 2(a) and 2(b) the images obtained on PZT sample using AFAM with operating frequency above and below the contact resonance peak value respectively are shown. We also show schematically in Figures 2(c) and 2(d) that depending on the orientation of the axis of the unit cell with respect to the probing tip, the soft and the hard axes can be imaged. Since the polarized domains are oriented in different axes and directions, the elastic constant along that axis and direction are also different and hence we see a distribution of ferroelectric domains on the sample surface.

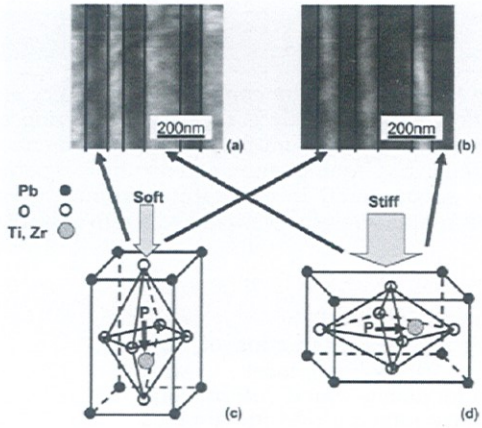

Fig. 2 : AFAM image showing in (a) stiff (bright) and soft (dark) stripe regions and in (b) the stiff (dark) and soft (bright) stripe regions. (c) and (d) shows the schematic representation of the PZT unit cell

■ GENERAL EXPLANATION : COMPARISON OF AFAM AND UFAM

To compare the AFAM and UAFM technique, in Figs. 3(a) and 3(b) we show the AFAM images and in Figs. 3(c) and 3(d) we show the UFM images obtained for the PZT sample. Figs. 3(a) and 3(c) shows the images when the operating frequency was above the contact resonance peak frequency and Figs. 3(b) and 3(d) show the images when the operating frequency was below the contact resonance peak frequency. We observe clearly bright and dark regions on the AFAM and the UAFM images and also contrast inversion when the operating frequency is changed. We have shown that UAFM which does not require a separate ultrasonic transducer for sample excitation also gives the same information and can be used to image the local stiffness of the sample surface.

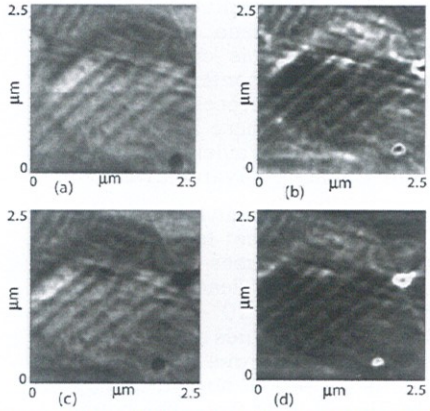

Fig. 3 : AFAM and UFM images of polished bulk sintered polycrystalline PZT sample. (a) and (b) are the AFAM images obtained with operating frequency above (1387 kHz) and below (1370 kHz) the resonance peak respectively and (c) and (d) are the UFM images obtained with operating frequency above (1392 kHz) and below (1362 kHz) the resonance peak, respectively

■ BRIEF DESCRIPTION OF THEORETICAL BACKGROUND

We have explained the contrast inversion of the image using a simple argument based on the resonance curve, where the amplitude of cantilever oscillation changes depending on the local stiffness of the material described schematically in Fig. 1(b) and Fig. 1(c).

■ ACHIEVEMENT

We have shown that using contact resonance technique i.e., both AFAM and UAFM techniques one can image the local elastic properties of the sample at nano scale order. We have also explained the contrast inversion of the image using a simple argument based on the resonance curve, where the amplitude of cantilever oscillation changes depending on the

■ PUBLICATIONS ARISING OUT OF THIS STUDY AND RELATED WORK

1. S. Banerjee, N. Gayathri, S. Dash, A. K. Tyagi, and Baldev Raj; *Appl. Phy. Lett*, **86** (2005) 211913.
2. S. Banerjee, N. Gayathri, S. R. Shannigrahi, S. Dash, A.K. Tyagi and Baldev Raj; *J. Phys. D: Appl. Phys.*, **40** (2007) 2539.

Further inquiries:
Dr. S.Banerjee and Dr. A.K. Tyagi, Materials Science Division
Metallurgy and Materials Group, IGCAR, e-mail:akt@igcar.gov.in

Hydrodynamical Phenomena during Laser Welding

EXECUTIVE SUMMARY

Laser Beam Welding (LBW) technology constitutes a frontier engineering activity. Equipment automation and process parameter optimization are absolutely essential for carrying out the process efficiently and economically. The LBW process involves several turbulent multi phase phenomena involving melt motion in selves and humps. Unless understood comprehensively, such phenomena can have deleterious effect on weld quality. In addition excessive loss of laser power may be encountered in combating various hydrodynamic instabilities. In the present study rigorous computational fluid dynamic analysis was carried out to quantitatively assess various instabilities.

OUTLINE

Laser Beam Welding involves interaction of high intensity ($\phi = 10^4 - 10^7$ W/cm^2) laser with structural metals and alloys. Such interactions generate non-stationary motions and instabilities in the melt pool. A quantitative understanding of such instabilities is essential to optimize process parameters. Other notable non-stationary hydro and gas dynamic phenomena are bulk and near surface turbulent flows of liquid – vapour – gas, large scale (0.1 cm to 1 cm) and small scale instabilities on liquid surface ($\sim 10^{-4}$–10^{-2}cm) involving multiphase flow. Mathematical analysis of such non-stationary phenomena along with experimental model validation is required to address above needs. In this context, various instabilities as well as energy loss processes need to be pinpointed. Notable among these instabilities are thermo-capillary motion, Rayleigh Taylor, Kelvin – Helmholtz and Capillary – Evaporative.

The thermo-capillary instability originates at melt-vapour interface due to surface tension and temperature gradient and causes oscillating disturbance in the melt layer leading to its deformation. At larger intensity $q \sim 10^5 - 10^6$ W/cm^2, the vapour pressure of the melt equals atmospheric pressure. The gas – vapour channel key-hole is formed at these points in which non-stationary movement is found in liquid layer wall. The liquid moves down like goffers and forms bubble which float up and collapse forming porous cavities. Melt motion in key-hole occurs in the form of moving humps and shelves. The phenomenon of melt motion in moving shelves and humps is described in terms of Peclet number P_e, the ratio of forced convection to conduction. The Rayleigh – Taylor instability occurs due to perturbation of the vapour-liquid (melt) interface. A hydrostatic reinstating force normally quels such instability. Capillary motion instability accrues from imbalance between adhesive and cohesive forces in melt-vapour interface. This effect causes concave deformation of the meniscus. The Kelvin – Helmholtz instability accrues from shear velocity existing between two media – i.e. – the melt liquid and the vapour phase. The non-zero curvature in key-hole causes centrifugal forces amplifying ripple vapour recoil force. The hydrodynamic solutions in the melt pool culminate from non-linear disruptive excitation in the melt volume which induces phase shift instability. Various melt layer instabilities in laser welding process leads to generation of moving shelves and humps, vapour jet formation, weld pool forced oscillation, formation of weld seam porosity. These instabilities which severely erode energy efficiency are summarized below. Various Peclet number regimes are assigned to melt pool instabilities. In analogy with laser cutting process, in which instabilities, manifest as Kerf roughness, the wavelengths can be arrived upon.

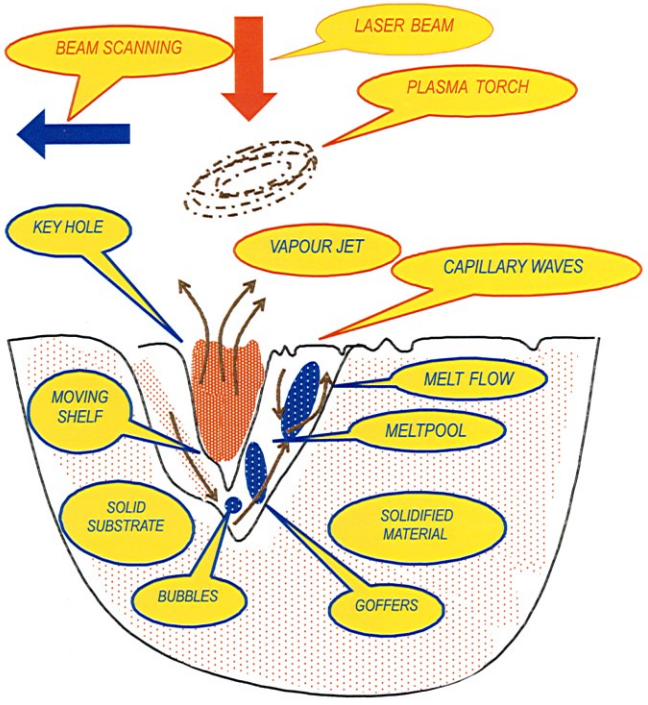

Fig. 1 : Hydrodynamic phenomena in melt pool during laser beam welding

Table 1
Dimensionless regimes for various phenomena in weld pool

Sl. No	Nature of instability	Wavelength of kerf roughness (P_e)	Wavelength
1.	Moving self	$P_e < 2/3$	10^{-2} cm
2.	Oscillation of melt layer	$P_e > 1$	10^{-2} cm
3.	Melt surface flow instability	$P_e < 1$	10^{-3} cm
4.	Melt front deformation	$P_e > 1$	10^{-2} cm
5.	Melt surface deformation	$P_e > 1$	10^{-3} cm

■ ADDITIONAL INFORMATION

Mathematical techniques and methodologies used to unravel LBW phenomena can also be applied to optimize process conditions in laser cutting and electron beam welding. In turn, the hydrodynamic and advanced modeling capability achieved for quantifying turbulent multi phase flow will benefit understanding of other complex phenomena involved in materials processing like combustion synthesis, laser ablation and laser-plasma interaction.

■ GENERAL EXPLANATION RELATED TO THE DESCRIPTION

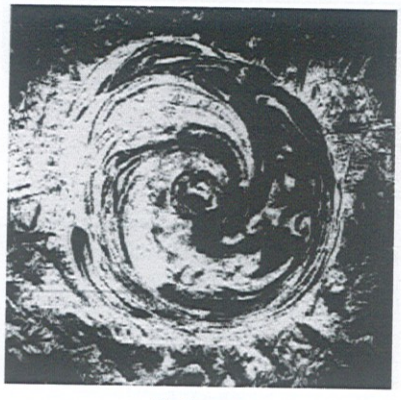

Convective turbulence in melt pool

It is important to understand melt motion in laser welding process. High intensity laser beam causes different instabilities in the melt flow and vapourization of droplets. These effects are responsible for final weld quality. These need to be investigated. The hydrodynamic phenomena involving melt surface and submerged streams, instabilities of the melt front, generation of moving "shelves" and "humps", vapor jets formation and tearing away of the melt droplets causing deterioration of energetic efficiency of the process are quantitatively explained. Additional small-scale instabilities are encountered at enhanced process velocities. Melt surface instability is one such phenomenon. These cause ejection of micro-droplets from the KH wall. Such phenomena have been quantitatively addressed in the present work.

■ BRIEF DESCRIPTION OF THEORETICAL BACKGROUND

Computational modeling of LBW phenomena highlighting interaction of radiative flux with material leading to dynamical thermal transport onto the surface and the subsequent phase transition at solid-liquid gas interface has been dealt with. Also dimensionless analysis of various hydrodynamic instabilities have been carried out.

■ ACHIEVEMENT

Through mathematical modeling of the LBW process fundamental insight into various phenomena in laser induced Key Hole (KH) has been gained. Such insight will definitely add value in designing laser material processing systems like welding and cutting.

■ PUBLICATIONS ARISING OUT OF THIS STUDY AND RELATED WORK

N.Kumar, S. Dash, A.K.Tyagi and Baldev Raj, *Sci. Tech. Weld. Joining,* **12** (2007) 540.

Further inquiries:
Dr. N. Kumar, Dr. A.K. Tyagi and Dr. S. Dash, Materials Science Division
Metallurgy and Materials Group, IGCAR, e-mail: akt@igcar.gov.in

Effect of C/N Ratio on the Microstructure and Hardness of Surface Engineered Over-layers

EXECUTIVE SUMMARY

Growth and characterization of hard, phase pure technologically important over-layers like carbide, nitride and carbonitrides of Ti and Cr by reactive gas phase exposures were explored. The growth conditions like reactant concentrations, exposure time and temperature, to meet the above requirement were optimized by the use of an in-house built TGA-MS system. Over-layers with thickness upto 80 and hardness of about 3000 VHN were achieved. These over-layers were characterized by advanced solid state analytical techniques like SEM, EDAX, XPS, AFM, SIMS, GI&PXRD, tribometry, micro and nano hardness measurements. Preferential texturing, graded microstructure with the associated hardness variation and internal nitridation effects were also investigated.

OUTLINE

Transition metal nitrides, carbides and carbonitrides of Ti and Cr display a wide spectrum of physical, mechanical and chemical properties. These properties make them technologically favourable materials, particularly for surface modification of commercial alloys. In this work, the thermo-chemical modification of Ti and Cr were carried out using a in-house built TGA-MS system by exposures to reactive gases. By varying the ratio of ammonia and methane, the surface properties could be tailored (Fig. 1).

The exposure conditions were optimized by studying the decomposition of the reactive gases by mass spectrometry. Catalytic interaction of substrate and reactive gas on decomposition was also studied. The over-layers were subsequently grown at these optimized conditions (temp: 900 – 1100°C) for durations upto 20 hrs to get a maximum thickness of 80 micron. GI/PXRD investigations (Fig. 2) of these overlayers revealed the presence of TiN, CrN, TiCN at the surface followed by Ti_2N, Cr_2N and TiC_xN_y depending on the chemistry of the gas mixture employed. No unreacted Ti or Cr were found at the surface. Complimentary SEM analysis suggested the presence of a two phase microstructure at the surface with a typical grain size of 2 – 4 micron in a 10 hr nitrided Ti sample. The AFM study of surface topography of these specimens showed an increase in surface roughness from 32 nm to 108 nm with nitridation time from 5 to 10 hrs. The cross-sectional analysis revealed a transition zone due to internal nitridation. However, increase in methane ratio in the gas mixture was found to decrease the kinetics of internal nitridation and hinder the growth of the transition zone. The increase in methane/ammonia ratio from 1 to 4 resulted in increase of the surface hardness from 2000 to 3000 VHN. While the nitrided Cr surfaces showed a peak surface hardness of about 2400 VHN. Cross sectional microhardness measurements confirmed a graded hardness matching with SEM observations (Fig. 3). XPS analysis of carbonitrided specimens indicated the formation of a thin layer of aliphatic carbon at the surface. A detailed nano-indentation study of nitrided Ti samples indicated the formation of a precipitate free zone at the interface of nitride case and transition zone. This transition is found to comprise as thin regions of differently nitrided zones.

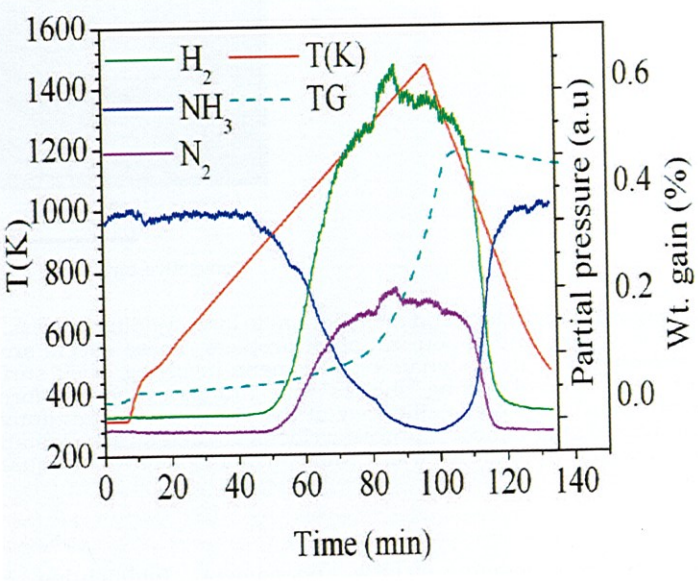

Fig. 1: Typical TGA-MS spectra of Ti nitridation in non-isothermal mode showing the decomposition of reactive gas and formation nitride over-layer

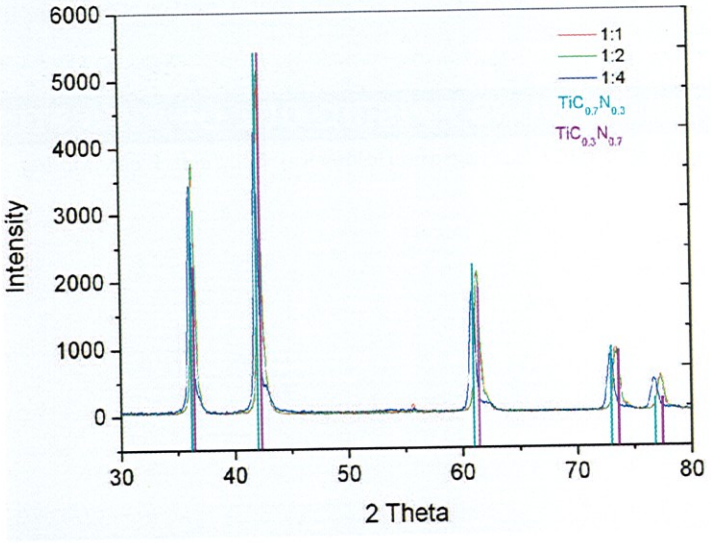

Fig. 2: GI-XRD patterns of carbo-nitrided Ti substrates showing the effect of reactive gas composition (ammonia, methane ratio) on over-layer stoichiometry

■ SURFACE ENGINEERING

Coatings or over-layers are mainly applied to a substrate to protect it from the adverse operating conditions like high temperature, stress, corrosive media and oxidative atmospheres. While the coatings are mainly deposited on the substrate and have a distinct interface, the over-layers are in-situ grown by subjecting the substrate to physical/chemical treatments. Such treatments lead to formation of stable and impervious layers with graded properties ensuring better adhesion between the over-layer and substrate due to metallurgical bonding and little mismatch of properties between the two.

■ GENERAL EXPLANATION RELATED TO THE DESCRIPTION

An engineering component usually fails when its surface cannot adequately withstand the external forces or environment to which it is subjected. The choice of surface material is decided by its thermal, optical, magnetic, electrical, resistance to wear, corrosion and degradation properties. It is uneconomical and unnecessary to prepare the whole component having the above properties while a thin layer at the surface will suffice the requirement. Here arises the necessity for surface engineering where the surface of the component is economically modified to get the desired properties.

Surface engineering includes thermal and mechanical treatments and thermo-chemical diffusion processes. Nitriding, carborizing, carbo-nitriding, boronizing, cyaniding etc, are the common diffusion processes dictated by the exact application. These processes modify both the chemistry and the structure of the surfaces involved. Since the transformation of surface to protective over-layers involves diffusion of species like N, C and B, a graded structure is ensured and sharp interface which is generally a cause for delamination, is avoided.

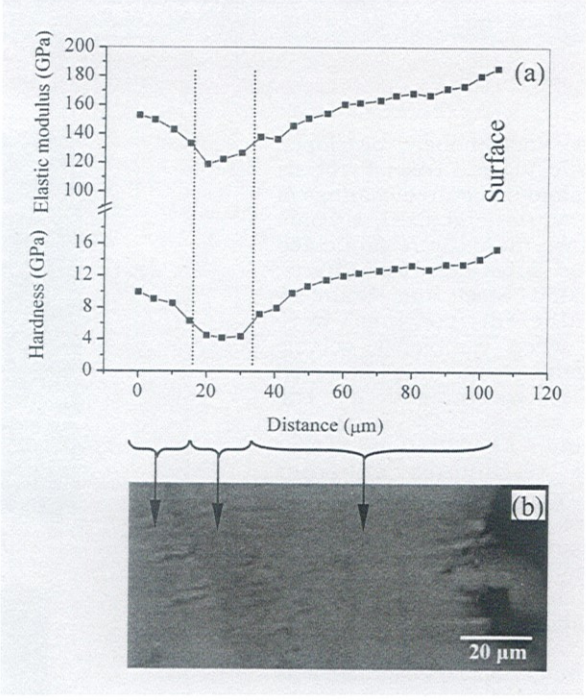

Fig.3 : (a) Nano-hardness and elastic modulus profile of nitrided Ti across different nitrided regions and (b) the corresponding SEM micrograph

■ ACHIEVEMENT

Thick and phase pure over-layers, a requirement for inherent stability, are grown by simple reactive gas phase exposure process. Synthesis conditions were optimized to get layer thicknesses upto 80 micron and hardness values upto 3000 VHN. The resulted over-layers were of graded in nature having excellent adhesion. A simple mechanistic model to explain the above is also formulated.

■ PUBLICATIONS ARISING OUT OF THIS STUDY AND RELATED WORK

1. P.K.Ajikumar, M .Kamruddin, R. Nithya, P. Shankar, S.Dash, A.K.Tyagi and Baldev Raj, *Scripta Materialia* **51** (2004) 361.
2. P.K. Ajikumar, Ananthi Sankaran, M. Kamruddin, R. Nithya, P. Shankar, S. Dash, A.K. Tyagi and Baldev Raj, *Surface and Coating Technology*, **201** (2006) 102 .
3. A. Basu, J. Dutta Majumdar, S. Ghosh Chowdhury, P.K. Ajikumar, P. Shankar, A.K. Tyagi, Baldev Raj and I. Manna, *Surface and Coating Technology*, **201** (2007) 6985.

Further inquiries:
Shri P.K. Ajikumar, Dr. P.Shankar, Dr. M.Kamruddin and Dr. A.K. Tyagi, , Materials Science Division
Metallurgy and Materials Group, IGCAR, e-mail: akt@igcar.gov.in

Novel Techniques for Synthesis of Nanostructured Coatings and Thin Films

■ EXECUTIVE SUMMARY

State of the art facilities for synthesis and characterization of nano-structured coatings have been set up in Surface Science Section, Materials Science Division, IGCAR. The facilities for synthesis include Combustion Chemical Vapour Deposition (CCVD), Laser Assisted Atmospheric CVD (LAACVD), Laser Pyrolysis, Pulsed Laser Deposition (PLD) and Magnetron Sputtering. Among these CCVD, LAACVD, Laser Pyrolysis and PLD are indigenously designed and developed. Various characterization facilities like micro and nano-indenters, scratch tester and atom force microscope (AFM) have also been established.

■ OUTLINE

Using the indigenously developed CCVD, LAACVD and Laser Pyrolysis facilities nano-structured coatings of alumina, yttria stabilized zirconia and anatase titania were fabricated on various substrates viz. Quartz, Silicon, Mild Steel and Stainless Steel. Adherent coatings were obtained when completely volatile metal-organic compounds like acetyl acetonates were used as the precursor in case of CCVD. On the other hand, LAACVD and Laser Pyrolysis techniques adherent coatings were obtained with all precursors from metal nitrates to metal-organic compounds. Surface topography of the films is strongly affected by solution precursor concentration, with smoother films observed at lower concentrations. The advantages of laser over flame as energy source are; it is environmentally friendly and since laser can be focused to very fine spot, patterning is feasible. The microstructures of coatings obtained using the techniques are shown in Figures 1, 2 and 3.

Adopting the two variants of PLD viz reactive PLD (RPLD) and plasma assisted PLD (PAPLD) metal nitrides thin films were fabricated. Metal nitrides like ZrN, NbN and AlN which could not be synthesized by RPLD were made by PAPLD. In PAPLD, for generating plasma a DC coil was incorporated into the system. Since sputtering can occur from the coil, under certain conditions, we have indigenously fabricated a microwave assisted ECR plasma source for coupling with the PLD system to generate plasma inside the deposition chamber. Since a better ion density in the plasma is obtained with ECR, metal nitrides can be synthesized effectively. One significant achievement of the study is that we could synthesize cubic AlN using the technique.

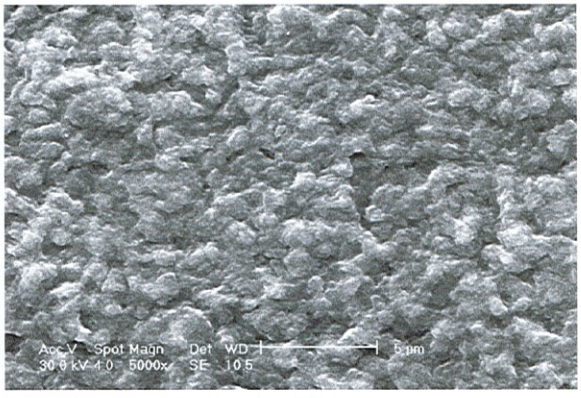

Fig. 1 : SEM image of Al_2O_3 coating by CCVD

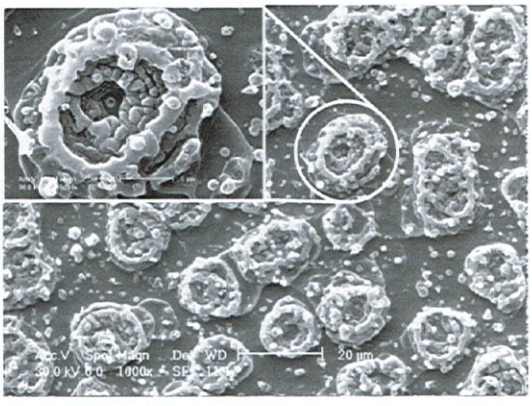

Fig. 2 : SEM image of Al_2O_3 coating by Laser Pyrolysis (insert)magnified image

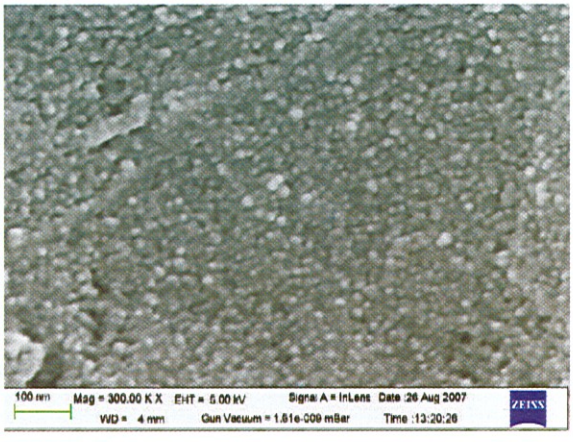

Fig. 3 : SEM image of Al_2O_3 coating by Atmospheric Laser CVD

■ WHAT IS COMBUSTION - CVD?

Combustion-Chemical Vapour Deposition (CCVD) is an open air, flame mediated coating process that employs aerosol to transport coating precursors to the deposition region. The coating precursors are dissolved in a suitable solvent and then atomized and combusted to provide the energy necessary for the chemical reaction to occur. The precursors interact with the flame and form a coating on a substrate held in or near the flame. The aerosol of size 1 to 5 microns were generated using an ultrasonic particle generator and/or an indigenously developed compressed air nebulizer.

■ LASER PYROLYSIS AND LAACVD

In laser pyrolysis technique, the aerosols, generated using an ultrasonic particle generator or compressed air nebulizer, (metal nitrate solution droplets) were passed through a quartz tube (Fig. 4). The laser was coupled in to the quartz tube in a coaxial manner and the laser beam along with the aerosol were directed towards the substrate kept very close to the focal point of the focusing lens. The laser interacted with the aerosol during its transit through the tube as well as at the substrate, leading to reaction with atmospheric oxygen at the substrate forming an oxide coating. By adjusting the process parameters, localized novel nanostructures were obtained. These localized structures are produced because of the Gaussian distribution of laser power coupled with non-equilibrium nature of surface reaction.

In laser assisted atmospheric CVD the coating precursor used is a suitable metal organic compound dissolved in ethanol. The precursor is atomized using an ultrasonic particle generator to produce aerosols of 1 to 5 micron size. Upon laser – precursor aerosol interaction, the metal organic compound underwent vaporization without decomposition and the vapors reacted with the oxygen present in the atmosphere at the laser focused spot on the substrate surface to give oxide coating. Uniform large surface area coatings were obtained by rastering. A computerized raster stage is used for this purpose. Photograph of the Laser Pyrolysis cum LAACVD setup is shown

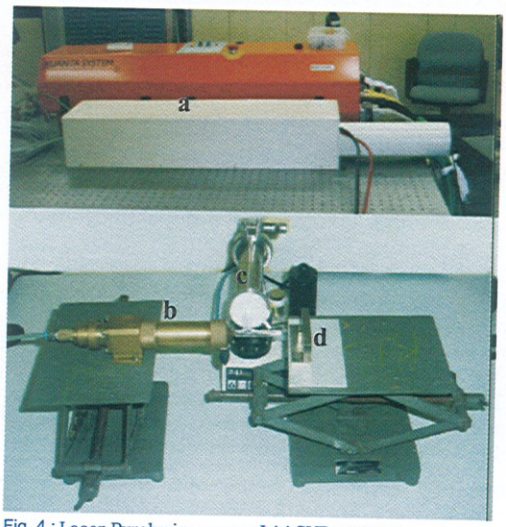

Fig. 4 : Laser Pyrolysis - cum - LAACVD system
a) Fiber optic coupled CW Nd:YAG laser
b) Laser focusing system
c) Ultrasonic particle generator
d) Computerised rastering stage

■ PULSED LASER DEPOSITION (PLD)

PLD is a thin film deposition technique (Fig. 5) where a high power pulsed laser beam is focused inside a vacuum chamber to strike a target of the desired composition. Material is then vaporized from the target and deposited as a thin film on a substrate. This process can occur in ultra high vacuum or in the presence of a background gas, such as nitrogen which is used when depositing nitrides. When the laser pulse is absorbed by the target, energy is first converted to electronic excitation and then into thermal, chemical and mechanical energy resulting in evaporation, ablation, plasma formation and even exfoliation. The ejected species expand into the surrounding vacuum in the form of a plume containing many energetic species including atoms, molecules, electrons, ions, clusters, particulates and molten globules, before depositing on the typically hot substrate.

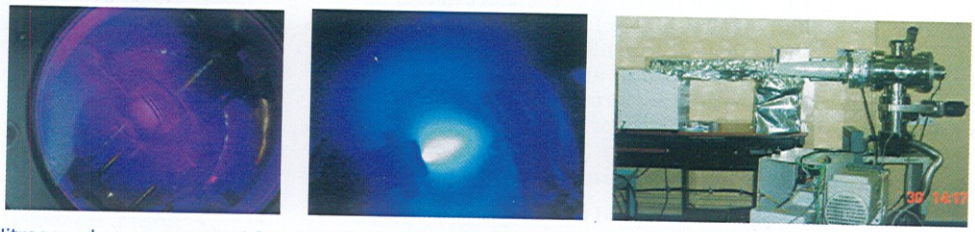

Fig. 5 : Nitrogen plasma generated for nitride film synthesis, PAPLD of TiN and indigenously developed ECR plasma generator

■ PUBLICATIONS ARISING OUT OF THIS STUDY AND RELATED WORK

R.Krishnan, R.Ramaseshan, Tom Mathews, R.Nithya, S.Dash, A.K.Tyagi and Baldev Raj, *Surface Engineering* (In Press)

Further inquiries:
Dr. Tom Mathews, Materials Science Division
Metallurgy and Materials Group, IGCAR, e-mail: tom@igcar.gov.in

Influence of Oxygen on the Reactive Phase Formation of Titanium Disilicide Thin Films

EXECUTIVE SUMMARY

Phase formation in thin films has several unique and interesting features not encountered in the context of bulk material processing and is therefore an active area of basic research. The presence of even low concentration of impurities has a substantial influence on the course of phase formation. Oxygen is by far the most important impurity in Ti-Si diffusion couples since titanium is an efficient oxygen getter. The effect of oxygen as an impurity at the interface in altering reaction kinetics of Ti/Si system is studied with an array of experimental techniques.

OUTLINE

Titanium disilicide with a face-centred orthorhombic structure (C54-$TiSi_2$) is currently used as metal contact in integrated circuits because of its low resistivity (10-20 μΩ cm), good thermal stability and structural compatibility. It is usually prepared through a Ti/Si bilayer reaction or crystallization of co-deposited stoichiometric amorphous alloys. Subjecting Ti/Si bilayers to a two-step rapid thermal annealing leads to the formation of metastable C49-$TiSi_2$ phase in the first stage (~500°C), and annealing at a higher temperature (~750°C) aids its polymorphic transformation to the stable low resistivity C54-$TiSi_2$ phase. However, the reproducibility in thin silicide film may be affected directly by the presence of impurities. One of the major contaminant in the Ti-Si binary system is oxygen owing to its extreme reactivity towards titanium. The main focus of this work is the investigation on the effect of oxygen as an impurity in Ti-Si couples.

Isochronally annealed Ti/Si bilayer samples under conventional vacuum furnace annealing were analyzed with an array of analytical techniques to understand the role of oxygen in the silicidation process.

Specimens annealed at 575 °C reveal the formation of the amorphous silicide compound with the nucleation of Ti_5Si_3 silicide grains. At this temperature the 100% peak of Ti disappears completely, accompanied by the appearance of the 100% peak of Ti_5Si_3 at 40.9° (211). Distinct peaks pertaining to the C54 phase of $TiSi_2$ are also seen at this stage (Fig. 1). The dissolved oxygen from the native oxide aids in the stabilization of the Ti_5Si_3 phase. It is seen that significant diffusion of both Si and oxygen from the native oxide results in the formation of the intermediate Ti_5Si_3 phase. As a result, oxygen from the native oxide is found to significantly influence the phase formation sequence in Ti/Si system under conventional furnace annealing. This oxygen helps stabilize the intermediate Ti_5Si_3 phase. At higher annealing temperature this phase act as a template in the formation of the C54 $TiSi_2$ phase. This is highly desirable in device fabrication.

The oxygen evolving from the interface influences not only reactive phase formation but also has a substantial bearing on the morphology and chemical composition of the surface. Careful analysis of the topographic images reveals that at lower annealing temperatures, isolated columnar structures measuring 400-500 nm in diameter and having an average height of 80 nm are formed. With higher temperatures of anneal, more of the oxygen transported from the native SiO_2 results in formation of more TiO_2 pillars (Fig.2). Further coarsening of these structures contribute to the surface roughness.

XPS investigations indicate the presence of TiO_2 and titanium silicide at the surface. The substantial difference in the conductivity of these two phases are further confirmed with scanning spreading resistance imaging (Fig.3). Interestingly, a comparison of the AFM and SSRM data showed that a nice correlation exist between the topographic and current images.

In summary, the role of oxygen in the phase formation sequence of Ti/Si system is elucidated with an array of techniques. This study is highly desirable in submicron technology to directly obtain the required C54 phase and to circumvent the problem of phase retardation from C49 to C54 with conventional methods.

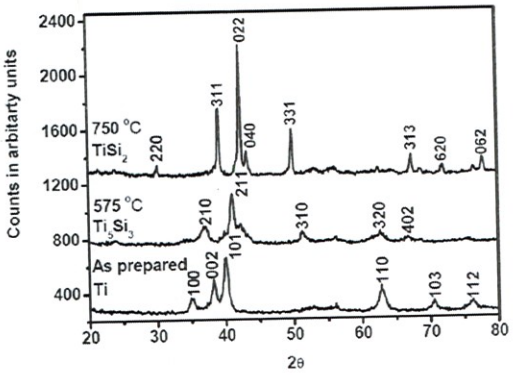

Fig 1:GIXRD spectrum of annealed samples

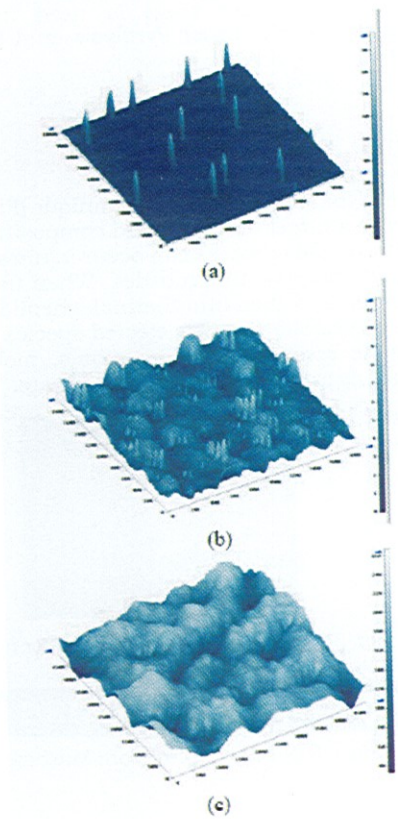

Fig. 2 : Surface morphology of annealed samples at 350 °C (a), 450 °C (b) and 750 °C (c)

ADDITIONAL INFORMATION ABOUT SLILICIDES

Metal silicides are produced by the reaction of a metal and silicon to form electrical contacts to the active regions in silicon devices. Silicides are also used as diffusion barriers, gates metals and local interconnects to reduce the series resistance of the devices, resulting in a higher switching speed. Further, silicides find potential applications as Schottky diodes in bipolar transistors and for IR image sensing. Today, advanced CMOS technology extensively uses the distinct features of silicides in device fabrication due to their novel properties.

GENERAL EXPLANATION RELATED TO THE DESCRIPTION

Scanning spreading resistance microscopy (SSRM) provides two-dimensional information on the electrical conductivity or resistivity of the sample under study. In SSRM, an electrically conductive probe is used to measure the sample's local resistivity. A voltage bias is applied to the tip and the resulting current through the sample is measured as a function of the tip position on the surface. As the resistance can vary over several orders of magnitude, a logarithmic current amplifier is used for SSRM. The amplifier has a current range of seven orders of magnitude spanning from picoampéres to milliampéres. Figure 3 illustrate the correlation in current and topographic features of the Ti/Si sample annealed at 800°C. The gray scale represents black as minimum and white as maximum.

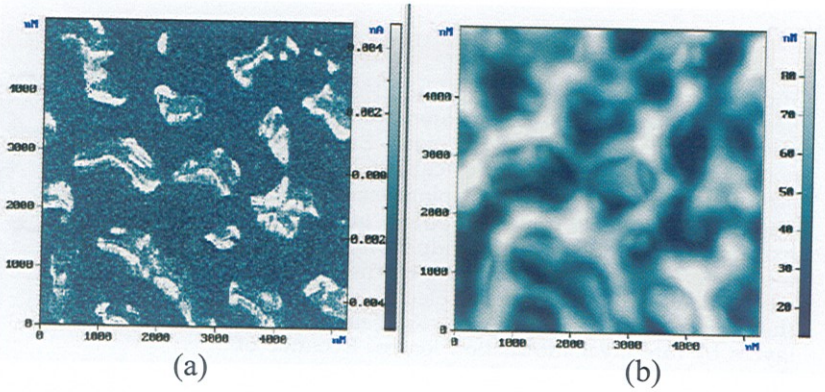

Fig. 3: Current and topographic images acquired simultaneously showing the contrast in current over the surface topography. A correlation between the current (a) and topography (b) can be seen as the current varies between the ridges (TiO_2) and valleys ($TiSi_2$).

BRIEF DESCRIPTION OF THEORETICAL BACKGROUND

In SSRM technique, resistance of the contact can be estimated from the spreading resistance theory as, $R=(\rho/4)$ x Sqrt[(Ti/A)], where is the local resistivity and A is the contact area. The contact area, $A=\{[3N(1-\gamma)/8E]^2 \times (1/r)\}^{1/3}$ x r, where r is the radius in cm, N is the force applied by the tip (in N), and E and γ are the Young modulus and Poisson ratio of the sample, respectively. The typical value of $A \sim 10^{-16} m^2$ and R is in the range of M.

ACHIEVEMENT

The effect of impurity oxygen in phase formation sequence of titanium disilicide is illustrated with an array of analytical techniques. This study provides a possible solution in circumventing the problem of phase retardation from C49 to C54 at submicron device technology. Further, the power of scanning probe microscope is demonstrated in chemical mapping of phases with different electrical conductivity by correlation of their current and topographic images.

PUBLICATIONS ARISING OUT OF THIS STUDY AND RELATED WORK

1. S. Ilango, G. Raghavan, S. Kalavathi, B.K. Panigrahi and A.K. Tyagi; *J. Appl. Phys.* **98** (2005) 073503.
2. S. Ilango, G. Raghavan, M. Kamruddin, Santanu Bera and A. K. Tyagi; *Appl Phys. Lett.*, **87** (2005) 101911.
3. S. Ilango, G. Raghavan, M. Kamruddin and A. K. Tyagi; *Appl Phys. Lett.*, **89** (2006) 192112.

Further inquiries:
Shri S. Ilango, Dr. G. Raghavan, Dr. M. Kamruddin and Dr. A K. Tyagi, Materials Science Division
Metallurgy and Materials Group, IGCAR, e-mail: si@igcar.gov.in

Mapping Conductivity of Graphene Sheets using Conducting Tip of Atomic Force Microscopy

EXECUTIVE SUMMARY

Conductive tip of Atomic Force microscopy (AFM) has been used to map the local conductivity of graphene sheets. It has been observed that the conductivity of graphene sheets is higher when they are loosely bound to the underlying bulk graphite. It has also been observed that zig-zag edges show sharp rise in current than the arm-chair edges indicating enhanced electronic density of states at the Fermi energy of the zig-zag edges than the arm-chair edges.

OUTLINE

Highly oriented pyrolytic graphite (HOPG) is a periodical stack of two-dimensional (2D) graphene sheets (layers) along the c axis. Each sheet comprises hexagonal lattice of carbon bonded by strong σ bonding (sp^2) in the a-b plane (see Fig. 1(a)). The perpendicular π orbital electrons (along the c axis) are responsible for the conductivity along the a-b plane. The conduction occurs by the quantum mechanical hopping of these electrons. Each of these layers is weakly bonded to their neighboring layers by interlayer interaction forces. Because of the weak interlayer interaction forces, the graphene layers can easily slide against each other and peel off easily. It has been pointed out that graphene sheet edges strongly affect the electronic states. The edges of the graphene sheets are of two types: (1) armchair (cis) and (2) zig-zag (trans) edges as shown in Fig. 1(b). It was theoretically shown that graphene sheets having zigzag edges possess edge states localized at the zigzag edges. In contrast, armchair edges have no edge states at their edges, hence making the armchair edge less conducting than the zigzag edge. The atomic force microscope (AFM) with conducting tip can be used to study the local electronic properties of conducting surfaces. We have used the AFM in contact mode with constant applied normal force on the tip. For the present investigation we have used freshly cleaved highly oriented pyrolytic graphite HOPG. By (simply) peeling off the surface layers using scotch tape, we were able to obtain steps and terraces with edges. The peeling off process dislocates the layers laterally and vertically. We have studied only monolayer steps to avoid complexity in the electrical analysis.

In the inset of Fig. 2(a) we show conductance maps showing higher conductance (bright) for the top layer labeled as layer I, the intermediate (II) shows intermediate conductance (gray) and the lowest layer (III) shows the least conductance (dark). We also observe a bright current streak appearing on the top layer edge indicated by an arrow. The intermediate edge does not show this bright current streak on its edge. This observation clearly indicates the presence of two distinct types of edges on these two graphite layers. This is more illustrative in the line profile of the conductance current shown in Fig. 2(a) for the lines marked A and B in the inset. In Fig. 2(b) we show a single ribbon edge containing two types of edges labeled as A and Z. The angle between A and Z is 30° as shown schematically in Fig. 1(b). The edge labeled as Z shows bright current streak and the edge labeled as A does not show this phenomenon.

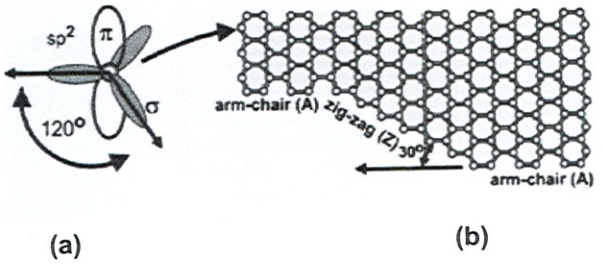

Fig. 1 : (a) Carbon atoms showing sp^2 hybridized σ orbitals in the a-b plane and nonhybridized π orbitals along the c-axis of graphite layer. (b) Graphite sheet/ribbons showing armchair (cis) edge and zigzag (trans) edge obtained.

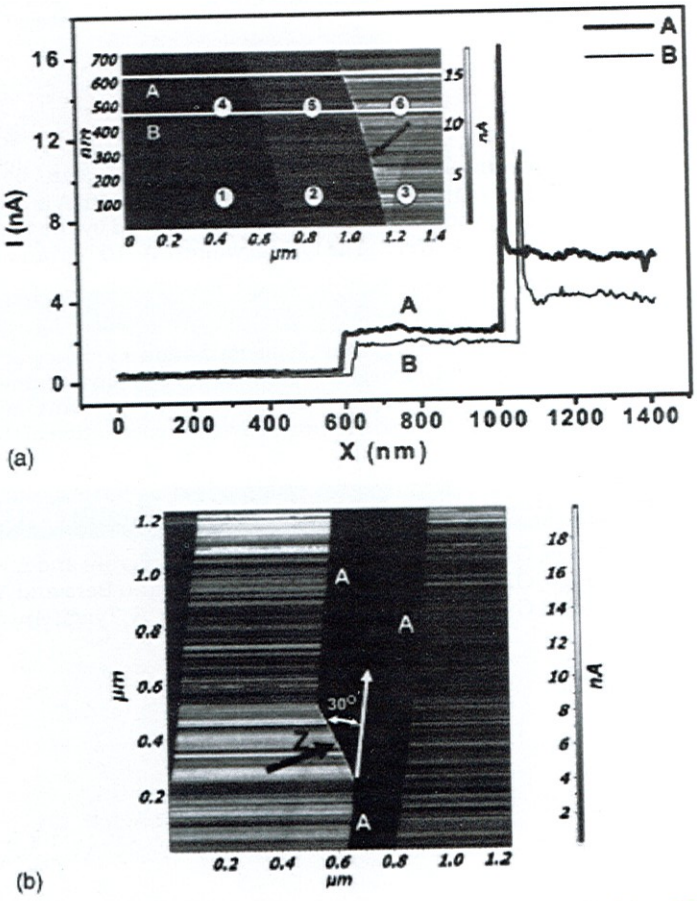

Fig 2: (a) Line profiles of the conductance current of the lines marked A and B, respectively, in the inset. Inset: conductance map showing top layer having high conductance, the intermediate step showing intermediate conductance and the lowest layer showing lowest conductance. Bright current streaks appearing on certain edges are shown by an arrow. (b) Conductance map of a single ribbon edge containing two types of edges labeled A and Z.

ADDITIONAL INFORMATION ABOUT GRAPHENE EDGES

The peeling of the layers was performed manually in an uncontrolled fashion. This can lead to different degrees of applied stress on different layers and cause different amounts of vertical displacement. The one which has a larger step height (c-axis distance) will be less bound causing large orbital overlap along the plane than the ribbon which has a lower step height (c-axis value). We motivate this schematically in Fig. 3. The difference in conductance among the steps can be explained invoking the argument that the loosely bound ribbons are more conducting than the tightly bound layers for the reasons given above.

GENERAL EXPLANATION FOR THE ANOMALOUS CONDUCTIVITY

Now, we will discuss the presence of sharp current peaks observed at the edges shown in the inset of Fig.2(a) and the Z region marked by arrow in Fig. 2(b). As mentioned earlier, there are mainly two types of edges formed on graphene sheets when it is cut. Recently, detailed theoretical calculations have shown that zigzag edges have edge states localized at the edges having a higher electron density. Hence these edges will have higher electrical conductance. Thus, during the mapping of the local conductance these edges will show up as brighter streaks. The layers can be oriented in a different direction with respect to each other and during the tearing process it will tear along any suitable (either zigzag or armchair) direction as we observe in Fig. 2(a). As mentioned earlier, the armchair edges have no electronic edge states and thus show no sharp peak in the current at its edges. Thus, we can say that the edges A are armchair edges and the edge Z is the zigzag edge in Fig. 2(b) (see Fig. 1(b) which shows the angle between the armchair and the zigzag is 30°). The enhancement of the conductance of the graphene sheets depends on the degree of dislodgement of the layers. The larger the dislodgement of the layer the more enhanced is the electrical conductivity. The increase in the conductivity of these sheets can be explained only by assuming that the p electrons on the loosely bound sheets are not much involved in the binding between the layers and hence would have higher mobility leading to higher electrical conductivity of the sheet.

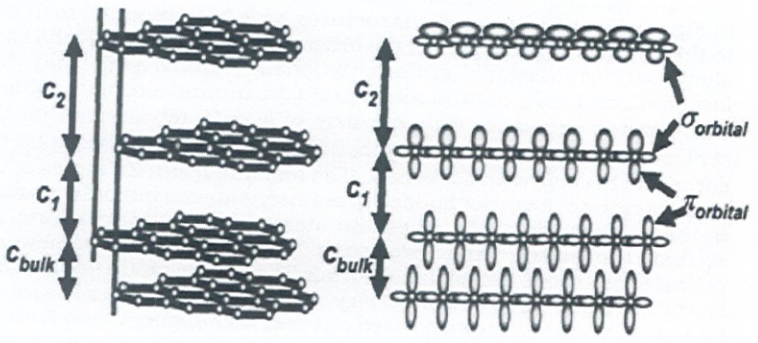

Fig. 3: Schematic representation of graphite layer separations $C_2 > C_1 > C_{bulk}$. The top layer is loosely bound showing the electrons/orbitals are spread out more along the a-b plane causing increase in the overlap of the orbitals leading to higher conductivity.

BRIEF DESCRIPTION OF THEORETICAL BACKGROUND

All the above experimental electronic property we could evaluate using a density functional theory (DFT) with B3LYP/6-31G(d,p) method. This aspect have been presented in an oral presentation in ICMAT 2007, Singapore and the DFT calculation has been submitted for publication (J. Computational Material Science).

ACHIEVEMENT

It has been shown here for the first time using conducting tip AFM that indeed the zig-zag edge has higher density of state at the Fermi energy than the arm-chair edge as predicted by theoretical studies. It has also been shown that isolated graphene sheets are more conducting than when they are in the bulk. This interesting conducting property of graphene sheets can be used for carbon based electronic devices.

PUBLICATIONS ARISING OUT OF THIS STUDY AND RELATED WORK

1. S. Banerjee, M. Sardar, N. Gayathri, A. K. Tyagi and Baldev Raj, *Appl. Phys. Lett.*, **88** (2006) 062111.
2. S. Banerjee, M. Sardar, N. Gayathri, A. K. Tyagi and Baldev Raj, *Phys. Rev. B.*, **72** (2005) 075418.

Further inquiries:
Dr. S.Banerjee and Dr. A.K. Tyagi, Materials Science Division
Metallurgy and Materials Group, IGCAR, e-mail:akt@igcar.gov.in

A Spectroscopic Resolution of the Structure of $Zn(CN)_2$

EXECUTIVE SUMMARY

Two different cubic structures of the negative thermal expansion material zinc cyanide have been reported in the literature: one, an ordered structure (space group $P\bar{4}3m$) where ZnC_4 tetrahedra are linked to neighbouring ZnN_4 tetrahedra with CN bonds and vice versa, and the other, a disordered structure (space group $Pn\bar{3}m$) where N and C sites are indistinguishable. We carried out group theoretical analyses to classify the phonons of different symmetries in the two structures, and also recorded and analyzed the Raman and infrared spectra to resolve the ambiguity about structure. Based on the number of Raman and IR modes expected and observed, we concluded that the compound exists in a disordered structure.

OUTLINE

The structure of $Zn(CN)_2$ was reported to consist of three-dimensional, inter-penetrating, tetrahedral frameworks of Zn-CN-Zn rods as shown in Fig. 1. Two different cubic structures have been reported to fit well to the diffraction patterns. In the ordered structure the CN ions lying along the body diagonal are orientationally ordered such that they form ZnC_4 and ZnN_4 coordination tetrahedra around alternate cations. The 'ordered' structure thus consists of a ZnC_4 tetrahedron (at the centre of the cell) linked to neighbouring four ZnN_4 tetrahedra (at the corners of the cell) with CN bonds. The remaining four Zn atoms at the corners of the cell are not bonded to atoms in this cell but only to atoms in the neighbouring cell. These Zn atoms of each unit cell form the second framework, and two such interpenetrating frameworks pervade the three dimensional lattice.The space group determined from single crystal X-ray diffraction analysis is $P\bar{4}3m(T_2^1, No.215)$. It was pointed out that exchanging C and N atoms did not significantly alter the refinement parameters, i.e., it was possible that C and N populate each other's site with a fractional occupancy of 0.5, giving rise to a disorder in the lattice. Since it is difficult to distinguish between C and N by X-ray diffraction, neutron diffraction was undertaken to unambiguously determine the structure, due to the vastly different neutron scattering lengths of C and N. It was found that a disordered structure with space group $Pn\bar{3}m(O_h^4, No.224)$ fits equally well to the diffraction pattern. In the disordered structure the CN bonds are orientationally disordered or flipped randomly such that both C and N sites are occupied by these atoms with a fractional occupancy of 0.5. Because of the indistinguishability of C and N in this structure the space group also has inversion symmetry. Fig. 2 shows the unit cell for the disordered structure where the origin is shifted by (¼, ¼, ¼) with respect to the unit cell of the ordered structure. The values of the final refinement parameters of the 'ordered' and the 'disordered' structures were essentially the same. A disordered structure was argued to be appropriate because the fitted isotropic thermal parameters for C and N for the ordered structure were found to be quite different. However, this apparent difference was attributed to widely different neutron scattering powers of N and C. We attempted to resolve the ambiguity about the structure, from vibrational spectroscopic considerations. Factor group analyses of the phonon symmetries in both the possible structures of $Zn(CN)_2$ were carried out. Raman and infrared spectra of $Zn(CN)_2$ were recorded and the results are compared with those predicted from factor group analyses. The results point to a disordered structure with space group $Pn\bar{3}m$.

$Zn(CN)_2$ (>99.5%) was obtained from M/s. Alfa Aesar. Raman spectra were recorded in the backscattering geometry using the 488-nm line of an argon ion laser. Measurements at 10 K were carried out using an APD closed-cycle helium refrigerator. Scattered light from the sample was analyzed by a SPEX double monochromator, and detected with a photomultiplier tub. Scanning of the spectra and data acquisition were carried out using a home-built microprocessor-based data acquisition cum-control system. Subsequent to the completion of a scan, data were transferred to a personal computer for further analysis. IR spectra of the sample using (1) CsI pellet, (2) 'Nujol' and (3) high density polyethylene were recorded using a BOMEM DA-8 FTIR spectrometer.

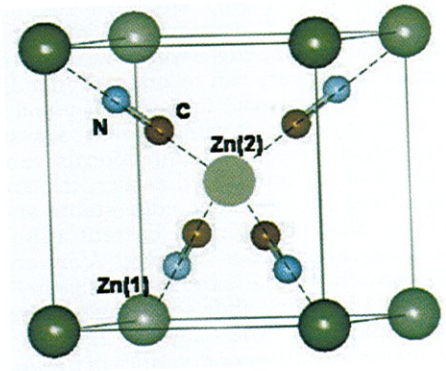

Fig. 1 : Ordered structure of $Zn(CN)_2$, space group $P\bar{4}3m$ Zn atoms are at tetrahedral sites. Vertices of each tetrahedron are populated either by all C or all N atoms

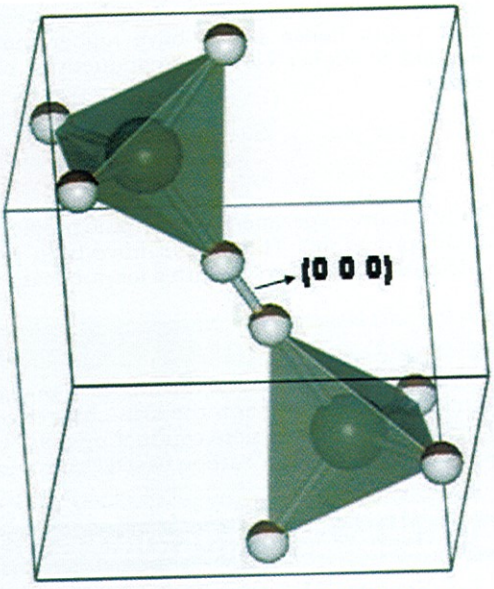

Fig. 2 : Disordered structure of $Zn(CN)_2$, space group $Pn\bar{3}m$ Vertices of each tetrahedron are occupied by carbon or nitrogen with equal probability of 0.5

■ RAMAN AND IR SPECTROSCOPIC TECHNIQUES

Raman spectroscopy and Infrared Absorption spectroscopy are vibrational spectroscopic techniques. They are also known as 'finger printing' techniques for molecules/solids since each molecule/material has its characteristic vibrational spectrum. They arise due to the vibrational motions of chemical bonds in the material, such as C-O, C-C, C-H, O-H, C=C, etc. Since materials can have several different bonds differing in strength, one has in general several vibrational frequencies, corresponding to each of the bonds. IR is commonly employed by chemists for quick recording of spectra whereas Raman spectroscopy finds favor mainly with Physicists for the study of phase transitions in crystals, etc. Raman is a non-destructive technique but the instrumentation could be relatively expensive.

Raman and IR techniques are complementary to each other, and for a good understanding of a material both techniques should in general be employed. For a molecule with a centre of inversion (or a solid with an inversion symmetry), Raman and IR frequencies are mutually exclusive, i.e., they appear at different frequencies. This is the principle that has been useful in the present study to converge upon the disorder structure.

■ FACTOR GROUP ANALYSIS AND EXPERIMENTAL MEASUREMENTS

$Zn(CN)_2$ has two formula units per unit cell. In the ordered structure, as shown in Fig. 1, the Zn(1) atom occupies the tetrahedral 'a' sites at (0, 0, 0) and Zn(2) atom occupies the tetrahedral 'b' sites at (½, ½, ½). C and N atoms occupy distinct 4e sites with C_{3v} site symmetry. Four C atoms around Zn(2) form a coordination tetrahedron. Similarly the four N atoms around Zn(1) (three N atoms from the neighboring cells) form the other coordination tetrahedron. The 30 degrees of freedom arising from the 10 atoms in the cubic unit cell result in 3 acoustic phonons and 27 optical phonons. The 6 degrees of freedom corresponding to the linear molecular ion CN can be divided into 1-internal (stretching vibration), 3 rigid-translations and 2 rigid rotational degrees of freedom. Factor group analysis was carried out using Bhagavantam and Venkatarayudu method. The following irreducible representations of the acoustic and optical phonons were obtained:

$$\Gamma_{optical}(27) = 2A_1(R) + 2E(R) + 2F_1 + 5F_2(R, IR)$$

The correlation method of Fately and Dollish also gave identical results. Out of these, A_1, E and F_2 are Raman active, and F_2 is also IR active. F_1 modes are not optically active. Thus there are 9 optically active modes. All 9 modes are Raman active and 5 of them are IR active as well, for this 'ordered' structure.

Similar analysis of the 'disordered structure' results in 5 Raman active and 2 IR active modes. Comparison of experimental results with those expected from Factor group analysis (Table 1) establishes that the structure should be 'disordered'.

Table 1.
Raman and IR modes observed and expected for the two structures of $Zn(CN)_2$. Note the mutual exclusion of Raman and IR frequencies except for the high frequency mode about 2220 cm^{-1}. This 'anomaly' is attributed to the necessary assumption of indistinguishability of C and N atoms

Number of modes expected from group theory				Observed mode frequencies (cm^{-1})	
"Ordered"		"Disordered"			
Raman	IR	Raman	IR	Raman	IR
9	5	5	2	- 216 334 339 - 2221	178 - - - 461 2218

■ CONVERGING ON THE STRUCTURE OF $Zn(CN)_2$

The striking feature of Table 1 is the mutual exclusion of the observed Raman and IR frequencies, except for the high frequency mode about 2220 cm^{-1}. This mutual exclusion points to a structure with an inversion symmetry, i.e., the disordered structure. The IR frequency at 2218 cm^{-1} is indeed expected here in spite of the arguments from factor group analysis to the contrary, since the CN has a strong dipole moment that should give rise to IR activity. Taking this into account, the structure is still concluded to be disordered, since the 'mutual exclusion' is a strong indication of a centrosymmetric structure, in this case the disordered one. It is noteworthy that several other cyanides such as CuCN, AgCN and AuCN also are known to have this 'head to tail' disorder of the CN ion.

■ ACHIEVEMENT

We have addressed a long standing controversy in the structure of $Zn(CN)_2$, and using spectroscopic techniques, resolved the structure to be disordered. It is noteworthy that this problem could not be satisfactorily solved using X-ray diffraction or neutron diffraction techniques earlier by other research groups.

■ PUBLICATIONS ARISING OUT OF THIS STUDY AND RELATED WORK

T. R. Ravindran, A. K. Arora and T. N. Sairam, *J. Raman Spectroscopy*, **38** (2007) 283.

Further inquiries:
Dr. T.R. Ravindran, Materials Science Division
Metallurgy and Materials Group, IGCAR, e-mail: trr@igcar.gov.in

Observation of Ferromagnetism in Diamagnetic β-Ga_2O_3

EXECUTIVE SUMMARY

We have observed ferromagnetism in bulk β-Ga_2O_3. Thermomagnetization measurements, under field cooled and zero field cooled conditions, imply emergence of a ferromagnetic state just below room temperature. We have established the intrinsic nature of the ferromagnetism through hysteresis measurements. Intensity of red photoluminescence emission changes with heat treatments and upon application of magnetic field. This implies that oxygen vacancies play a vital role in establishing ferromagnetism in β-Ga_2O_3.

OUTLINE

Polycrystalline β-Ga_2O_3 of 99.999% purity was compacted into pellets and fired at 1300°C in a reduced oxygen fugacity for 24 hours. Field cooled and zero field cooled thermomagnetisation curves recorded under an applied magnetic field of 100 and 200 Oe are shown in Fig. 1. The thermograms showed a bifurcation just below room temperature. From the ΔM (M_{FC}-M_{ZFC}) vs T plot (not shown) the FM transition was estimated to be just below room temperature. To confirm the FM ground state, M-H measurements were carried out at 100 K, 55 K and 2 K and are shown in Fig. 2. Notwithstanding small saturation magnetization observed (~10^{-4} emu/g), opening of M-H curves into closed hysteresis loops indicates underlying FM interactions. Superpara-magnetism could not be the cause of observed hysteresis loops as the M vs H/T curves do not collapse into a single curve (top inset of Fig.2) and coercive field and remnant magnetization are temperature independent (bottom inset of Fig. 2).

Paramagnetic impurities, present at a level of 100 ppm could as well give rise to observed very small saturation magnetization However, electron spin resonance under field sweep mode and secondary ion mass spectrometry measurements in depth profile mode were carried out and presence of paramagnetic impurities like Cr, Ni and Fe could be categorically ruled out. Having ruled out the presence of paramagnetic impurities and superparamagnetism, FM observed in β-Ga_2O_3 is concluded to be "intrinsic".

With no obvious source of paramagnetic spins, it is being realized that oxygen vacancies holding electrons with uncompensated spin are involved in establishing the FM state in this class of magnetic material, known as d^0-ferromagnets. To characterize the defect states, photoluminescence (PL) measurements were carried out at room temperature. In addition to a PL emission band due to the lattice, a dominant and rather broad emission in the red region (620 - 900 nm) was observed (Fig. 3). Intensity of this emission dramatically increases upon vacuum annealing and gamma irradiation of the sample, clearly indicating that this emission is related to oxygen vacancies. From the location of the red PL emission, the related defect state is associated with an oxygen vacancy located at the middle of the band gap, 2.8 eV from the top of the valence band. Additionally, upon application of magnetic field ~0.4 T, intensity of the red emission increased dramatically (not shown), indicating a strong coupling between spin states associated with electrons at the vacancies and the magnetism.

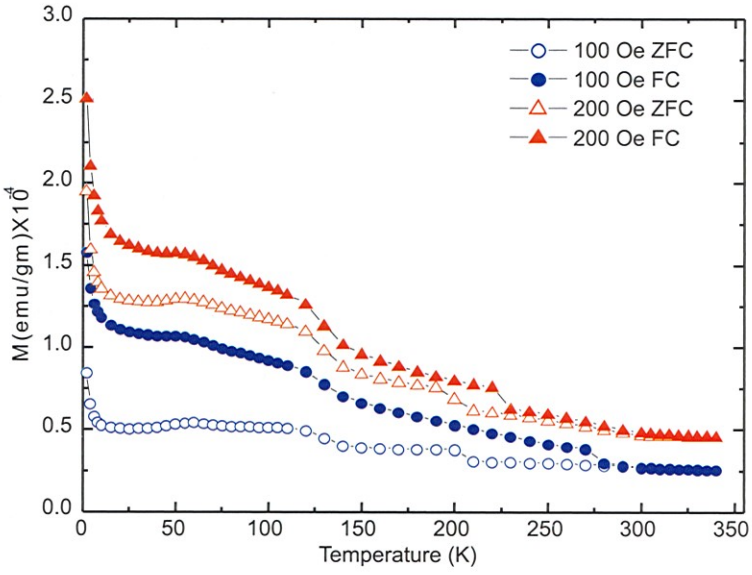

Fig. 1 : Field cooled (FC) and zero filed cooled (ZFC) thermo-magnetization curves of β-Ga_2O_3 in 100 Oe and 200 Oe field

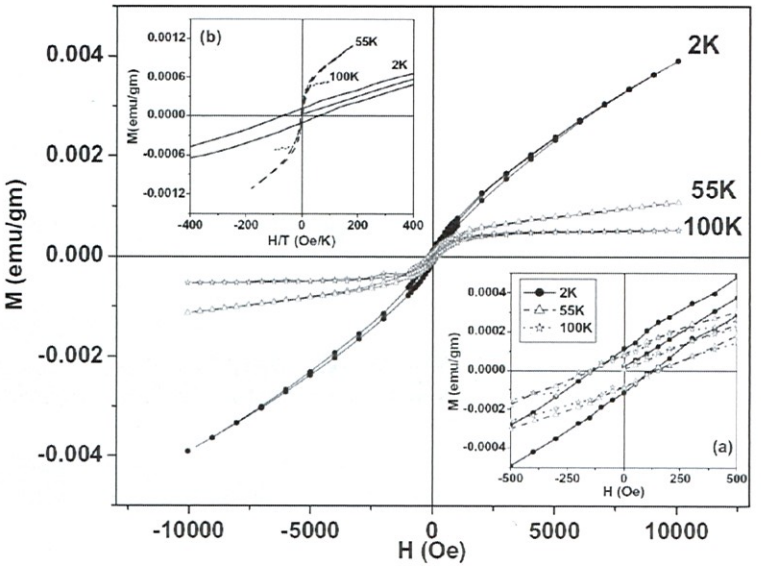

Fig. 2 : M-H curves of β-Ga_2O_3 at 100 K, 55 K and 2 K. Top inset shows the plot of M vs H/T curves. Bottom inset shows the enlarged view of the M-H curve at low fields

OXYGEN VACANCIES IN β-Ga_2O_3

β -Ga_2O_3 crystallizes into monoclinic structure with space group C 2/m. It has two nonequivalent sites for gallium labeled Ga(1) & Ga(2) and three nonequivalent sites for oxygen labeled O(1), O(2) and (3). Among nonequivalent sites for oxygen, the one labeled O(3) is in the plane and at the centre of the triangle formed by the gallium ions. Calculations locate the defect states of O(1)& O(2) just 0.5 eV below conduction band and that of O(3) about 2.8 eV above the valence band.

SPINTRONICS

So far, the micro-electronics community has been exploiting the charge property of the electrons alone. Recently, it has been realized that a huge leap in the computation speed and compaction of memory storage can be achieved, provided that the spin property of the electrons is also simultaneously exploited. Driven by such a fascinating application, a hunt by the materials scientists lead to a class of new materials known as diluted magnetic semiconductors (DMS). DMS are a wide band gap (~3 eV) materials wherein cations are substituted with paramagnetic ions at a few atomic percentage level e.g. GaAs:Mn, TiO_2:Mn. Although very promising, these materials pose a fundamental difficulty, viz., integration of DMS with already existing microelectronic components.

An offshoot of the search is the discovery of exotic class of semiconducting magnetic materials that has been christened d^0-ferromagentic materials. Unlike other class of magnetic materials known to us, d^0-ferromagnetic materials (dFM) carry no obvious source of magnetic moment. It is now being understood that the defects are the vital entities for the observed dFM. To be more precise, anion vacancies hosting electrons, known as colour centers, with uncompensated spins are the hosts for the magnetic moments.

The trick in realizing a dFM lies in the creation of requisite type of defect state that is present sufficient concentration and in the choice of material which can support such configurations.

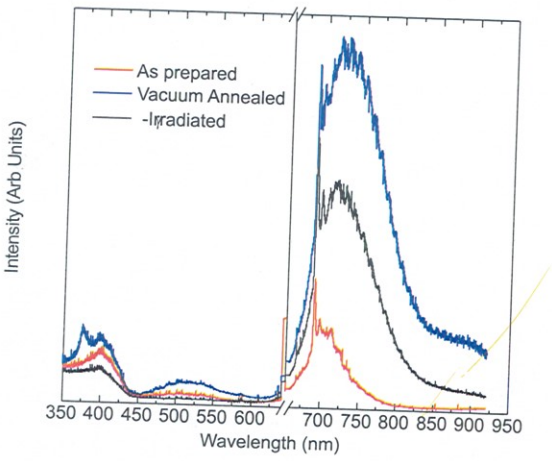

Fig. 3 : Photoluminescence spectrum of pristine, vacuum annealed and γ-irradiated β-Ga_2O_3.

THEORETICAL BACKGROUND

Studies indicate that oxygen vacancies host electron(s) with uncompensated spins. From the photoluminescence measurements, it is conjectured that O(3) oxygen vacancies are the most probable hosts. From the location of the O(3) vacancy in relation to Ga ions, the lowest energy wave function is degenerate of the form $\frac{1}{\sqrt{2}}(p_z \pm s)$ invoking Hund's rule forces parallel alignment of electrons at O(3) vacancy sites resulting in a net spin magnetic moment. Ferromagnetic interaction between these moments may occur most probably through the double exchange interaction, involving Ga-O vacancy pair.

ACHIEVEMENT

Though large numbers of monoxides in thin film form exhibit d^0-ferromagnetism (d^0-FM), TiO_2, HfO_2 and In_2O_3 are the only known d^0-FM material in bulk form. In this fast emerging filed, it is of paramount importance to identify more such materials as they would provide invaluable insight into understanding these fascinating materials and hence to their application. In this context, it is gratifying to observe d^0-FM in β-Ga_2O_3.

PUBLICATIONS ARISING OUT OF THIS STUDY AND RELATED WORK

V. Sridharan, Sangam Banerjee, Manas Sardar, Sandip Dhara, N. Gayathri and V.S. Sastry, Paper No. 232 Condensed matter arxive (2007).

Further inquiries:
Dr. V. Sridharan, Materials Science Division
Metallurgy and Materials Group, IGCAR, e-mail: varadu@igcar.gov.in

Long-range Attraction between Like-charged Colloids

EXECUTIVE SUMMARY

Among the various soft matter systems, charge-stabilized colloidal suspensions (e.g., submicron sized polystyrene latex and silica particles dispersed in water) have gained recognition as tremendously useful model condensed matter systems because of their structural ordering and rich phase behavior. Hence, these systems are of considerable interest to study fundamental questions, which are also relevant for atomic systems. Understanding of this simple model system is far from complete with respect to the effective pair-potential U(r) between the charged colloids arising due to the basic electrostatic interactions among the constituents. Using a confocal laser scanning microscope we probe charged latex suspensions and show that U(r) between like-charged particles exhibits a long-range attractive minimum when effective charge density of the particles is quite high. We also observe stable bound pairs. These observations provide a direct and unequivocal evidence for long-range attraction between like-charged colloidal particles.

OUTLINE

For a very dilute suspension, the pair-correlation function g(r) is directly related to the effective pair-potential U(r) by

$$g(r)=\exp[-U(r)/k_BT] \quad (1)$$

Hence, U(r) can be obtained by measuring g(r). Digital video microscopy and optical tweezer techniques have been used in the past to measure g(r) by imaging the colloidal particles. However, only the particles close to the microscope cover-glass could be imaged in these studies because of the limited depth of focus. The cover-glass has strong influence on U(r). Further, the attraction observed in these experiments is attributed to imaging artifacts and projection errors. Thus, to date, there is no direct experimental evidence for existence of a long-range attractive term in the U(r) of like-charged colloids in a bulk suspension with monovalent counterions.

Observation of long-range attraction in very dilute bulk suspensions requires setting-up right experimental conditions: (a) Particles of high effective charge density, are essential to increase the strength of attraction as well as to increase the counterion concentration in the medium, which mediate the attraction between like-charged particles (b) Elimination of wall effects and (c) Avoiding sedimentation of particles due to gravity. We have selected highly charged polystyrene colloidal particles among our stock of synthesized suspensions to increase the concentration of counterions and redispersed in a density-matched fluid (50:50 H_2O-D_2O mixture) to eliminate sedimentation due to gravity. The effect of charged wall is eliminated by employing a confocal laser scanning microscope for imaging the particles far away (> 200 μm) from charged cover slip. We minimize the impurity ion concentration by completely deionizing the suspension using mixed-bed ion-exchange resins.

We view the colloidal particles deep inside the suspensions with a fast (7.3 frames/sec) scanning CLSM to obtain two dimensional (2D) optical slices We record several thousands of images as time series and several such series from different locations in the sample. We obtain in-plane g(r) (by determining the positions of the particles by image analysis in each frame, and then averaging over several thousands of such frames. The U(r) is obtained from the measured g(r) using Eq. 1. To establish that this methodology is free from imaging artifacts we first reproduce the standard result by preparing a very dilute deionized suspension (volume fraction $\phi = 0.0001$, and diameter d = 780 nm) of latex particles of low surface charge density $\sigma = 0.004\ \mu C/cm^2$. We observe only individual particles (Fig. 1A) undergoing Brownian motion and the U(r) (Fig. 1B) obtained from measured g(r) is found to be screened Coulomb repulsive and fits to the potential form given by Derjaguin-Landau-Verwey-Overbeek (DLVO) theory. In dilute suspension of high charge density ($\sigma = 2.7\ \mu C/cm^2$) latex particles we observe stable bound pairs and higher order particle clusters (Fig. 2). These observations provide direct evidence for existence of long-range attraction between like-charged colloids.

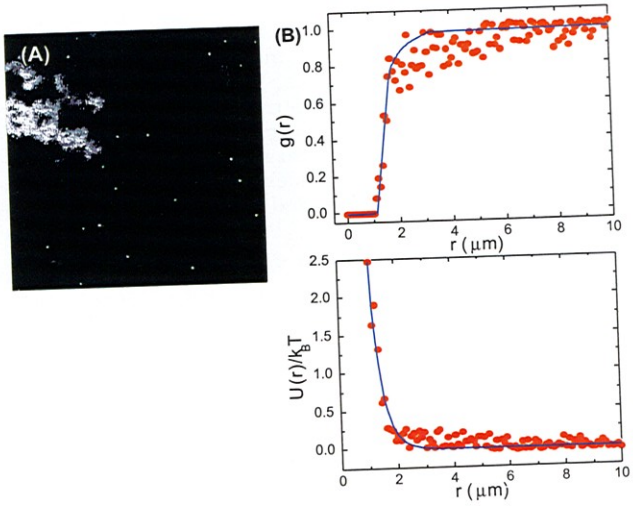

Fig. 1 : A: Confocal image of 780 nm polystyrene particles of low charge density. B: Pair-potential U(r) obtained from measured pair-correlation function g(r) shows screened Coulomb repulsion between like -charged particles

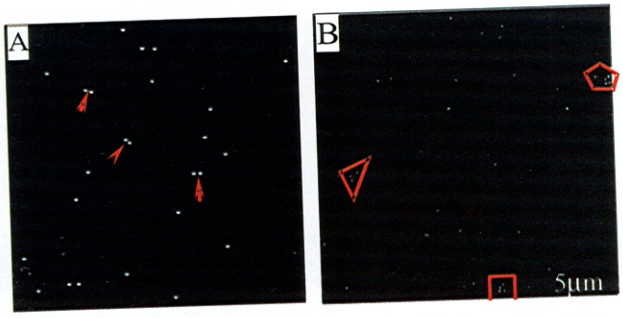

Fig. 2 : Confocal images of 600 nm polystyrene particles of high charge density showing (A) bound pairs and (B) three, four and five particles

CHARGE STABILIZED COLLOIDS

Monodisperse particles having a size in the range of 1 nm to 1μm when dispersed in a polar solvent execute Brownian motion and are known as colloidal suspensions. When two particles approach distance of the order of a nanometer or less, particles experience van der walls attraction. This leads to flocculation and make these suspensions unstable. Stable suspensions are prepared by charging the particles during the synthesis. This is known as charge stabilization. In a charge stabilized suspension, the particles (e.g. polystyrene) are negatively charged with H^+ ions as counterions. Counterions screen the repulsive Coulomb interaction between the particles.

LONG-RANGE ATTRACTION

Existence of stable bound pairs implies an attractive minimum U_m with magnitudes of the order of thermal energy k_BT or more in the pair-interaction U(r) between the like-charged particles. The magnitude of U_m and the interparticle distance R_m at which this attractive minimum occurs, have been measured by obtaining U(r) using Eq. (1). The g(r) and U(r) for two samples with charge densities σ =2.7 and 0.3 μC/cm^2 are shown in Fig. 3. The pair-potential U(r) clearly shows an attractive minimum (Fig. 3) at an interparticle distance of about 1.45 μm which is really long-ranged as it corresponds to about 2.4 times the diameter (d=600 nm) of the particles. Further, the well depth (Fig. 3) is found to be larger (U_m ~ 1.82 k_BT) for particles of σ =2.7μC/cm^2 as compared to that for particles with σ = 0.3 μC/cm^2. Measured experimental U(r) data was found to fit to the following empirical expression $U(r)=A(\exp(-\kappa r)/r) - B\exp(-\kappa r)$, where the constants A, B represent the strength of repulsive and attractive components of the interaction, respectively and κ^{-1} represents the range of interaction.

Our measurements thus confirm the existence of a long-range attractive term in the effective pair-potential between like-charged colloids. The monovalent counterion (H^+ ions) concentration is increased in the system by increasing the charge density on the particles. The attraction is believed to arise from the counter ions mediation between the macro ions.

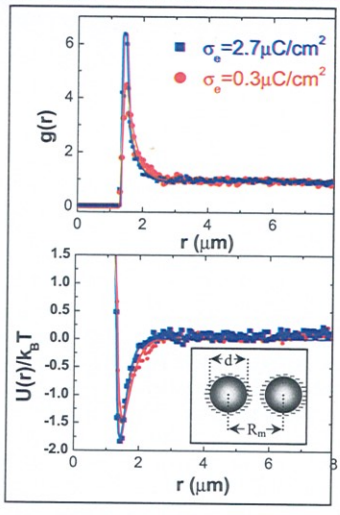

Fig. 3 : Pair correlation function g(r) and the corresponding pair-potential U(r) for particles of high charge density. U(r) shows a long-range attractive minimum R_m ~ 1.45μm

MODELS APPLIED

For suspensions of low charge density particles the counterion concentration is much smaller than salt ion concentration. Under these conditions DLVO theory is expected to provide an accurate description of the pair-interaction between charged colloids, and we indeed obtain the DLVO potential $U(r) = A\exp(-\kappa r)/r$ from our analysis of the experimental data (Fig. 1B). The fitted values of the Coulomb potential strength A, and the inverse Debye screening length are found to be reasonable. For suspensions of charge density particles the counterion concentration is much higher than the salt concentration. Under these conditions the DLVO theory fails. The experimental U(r) (Fig. 3) is found to fit to an empirical expression $U(r)=A(\exp(-\kappa r)/r) - B\exp(-\kappa r)$, where the constants A, B represent the strength of repulsive and attractive components of the interaction. This form resembles Sogami-Ise pair-potential.

ACHIEVEMENT

For the first time, we observed stable bound pairs using a CLSM. By detailed quantitative image analysis of confocal images we find that the measured U(r) has a long-range attractive component with well depths larger than k_BT. These observations provide a direct and unequivocal evidence for the existence of long-range attraction in U(r) of like-charged colloidal particles.

PUBLICATIONS ARISING OUT OF THIS STUDY AND RELATED WORK

B.V.R. Tata, and S. S. Jena, *Solid State Comm.*, **139** (2006) 562.

Further inquiries:
Dr. B.V.R. Tata, Materials Science Division
Materials and Metallurgy Group, IGCAR, e-mail: tata@igcar.gov.in

Atomic Scale Study of Negative Thermal Expansion in Zirconium Tungstate

EXECUTIVE SUMMARY

Perturbed angular correlation study in Zirconium tungstate shows the occurrence of more than one distinct Zr sites. Based on the values of quadrupole parameters it is interpreted that among the four sites observed, one site represents regular ZrO_6 and the other three sites are associated with contracted and distorted ZrO_6. Effective decrease in Zr-O bond length is understood to be due to an increase in the fractions of ZrO_6 octahedra which undergo contraction with temperature, thus explaining negative thermal expansion of the system.

OUTLINE

Zirconium tungstate ZrW_2O_8 is a cubic compound (Cf. Fig.1) consisting of a three dimensional network of corner linked ZrO_6 octahedra and WO_4 tetrahedra, with the latter having one non-bridging W-O bond. This system exhibits negative thermal expansion (NTE) isotropically over the temperature range 4 to 1000 K, whose mechanism is yet to be completely understood. It was earlier understood that a large transverse vibration of the oxygen atom in the middle of the W-O-Zr linkage, which requires corresponding rotations of the polyhedra, is the primary origin of NTE in this material due to unconstrained feature of the structure. Common feature of the existing literature is a dominant role of strong bonds for NTE leading to a volume reduction induced by inward rotation of polyhedra. For understanding NTE it is essential to probe at Zr sites (as WO_4 are more rigid than ZrO_6) using any local technique.

We have carried out ^{181}Hf/ Ta based Perturbed Angular Correlation (PAC) spectroscopy, a hyperfine technique, on this system to probe local structure at ZrO_6. Using this technique Electric Field Gradient (EFG) tensors at the site(s) of occupancy of probe atoms are deduced. Principal component of EFG tensor is proportional to the quadrupole frequency (Q) and is inversely proportional to Zr-O bond length. Asymmetry parameter (ratio of relative change of other two components of EFG and the principal component) is sensitive to orientation distortion if any associated with ZrO_6. PAC measurements were carried out using BaF_2 based three detector, twin fast-slow coincidence spectrometer (Cf. Fig. 2) setup at MSD. Time resolution of the spectrometer is around 660 ps, while the detectors are set for 133 and 482 keV gamma rays. Closed Cycle Refrigerator is used for low temperature measurements while an inbuilt mini furnace is used for high temperature measurements up to 600 K.

A few representative time dependent anisotropy spectra R(t) and their Fourier transform P(w) are shown in Fig. 3. Analysis of the spectra shows that there are four distinct Zr sites experiencing distinct quadrupole parameters such as quadrupole frequency, asymmetry parameters. The fraction which is predominant at 250 K is interpreted to be due to probe atoms occupying regular ZrO_6. This is supported by a point charge model based computation of EFG carried out by us. An increase in the fractions experiencing higher quadrupole frequencies at higher temperature is seen in Fig. 3.

Shown in Fig.4 is the variation of the fractions with the measurement temperature. It is seen that the fraction f_1 representing the regular ZrO_6 octahedra decreases while the other fractions increase with temperature. PAC spectra and the results in terms of variation of quadrupole parameters with temperature are repeatable at room temperature after in-situ measurements till 600 K. This means that the observed quadrupole parameters are due to different equilibrium configurations that ZrO_6 take as a consequence of inward rotations of polyhedra.

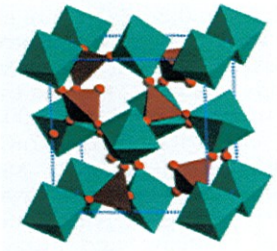

Fig. 1 : Structure of zirconium tungstate.



Fig. 2 : BaF_2 based three detector TDPAC spectrometer that is setup at MSD.

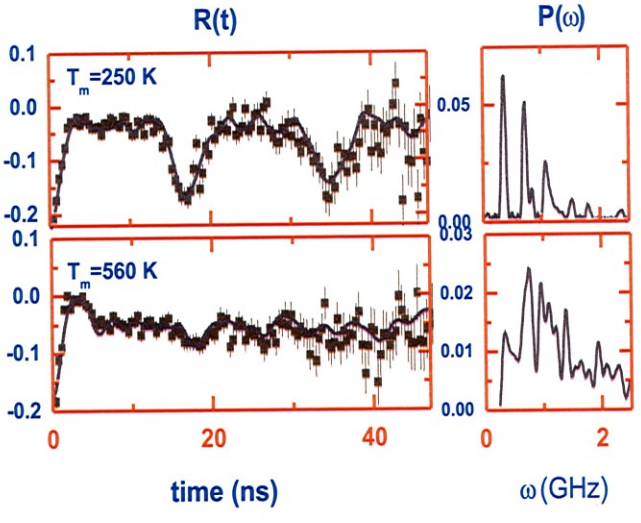

Fig. 3 : Representative TDPAC spectra and Fourier transforms

■ NEGATIVE THERMAL EXPANSION IN ZIRCONIUM TUNGSTATE

Vast majority of materials have a positive coefficient of expansion and their volume increases upon heating. Unusual property of contraction of volume on heating (Negative thermal expansion) is seen in some oxides. In these systems the contraction is small and anisotropic and occurs only over a small temperature range. But Zirconium tungstate exhibits isotropic negative thermal expansion over a large temperature interval 4 to 1000 K. This article is about understanding negative thermal expansion in Zirconium tungstate by studying the variation of quadrupole parameters associated at Zr sites of ZrO_6 using Perturbed Angular Correlation (PAC) Spectroscopy.

■ FURTHER DESCRIPTION

Plotted at the top inset in Fig. 4 is the variation of dl/l with temperature. The mean value of Zr-O bond length is obtained as the average of the negative cubic root of quadrupole frequencies weighted with respect to corresponding values of the fractions. Slope of the plot represents the coefficient of thermal expansion (which is found to be negative having a value of approximately -$6x10^{-5} K^{-1}$.

This implies that the existence of higher frequency components and importantly an increase in the magnitudes of these fractions is essential to obtain a negative slope in the variation of mean Zr-O bond length with temperature. This means that the existence of fractions other than f_1 which represent contracted and distorted ZrO_6 octahedra caused by the inward rotations of polyhedra is essential in explaining negative thermal expansion in zirconium tungstate.

Thus this atomic scale study provides a proof that an effective contraction of distinct ZrO_6 octahedra due to inward rotations of polyhedra accompanied by distortions is a very important factor contributing for the observed NTE in these systems. This study establishes that distortions of polyhedra due to their inward rotations play a very important role and it should be taken in to account for understanding negative thermal expansion in zirconium tungstate.

Detailed electronic structure based computations are required to be done to find out the degree of distortions associated with ZrO_6 octahedra based on the values of quadrupole parameters obtained in the present study. Alternatively the present results could be taken as input parameters (i.e) by invoking the distortions of octahedra while modelling the results of X-ray/neutron diffraction and EXAFS measurements reported in the literature to get the degree of distortions associated with polyhedra.

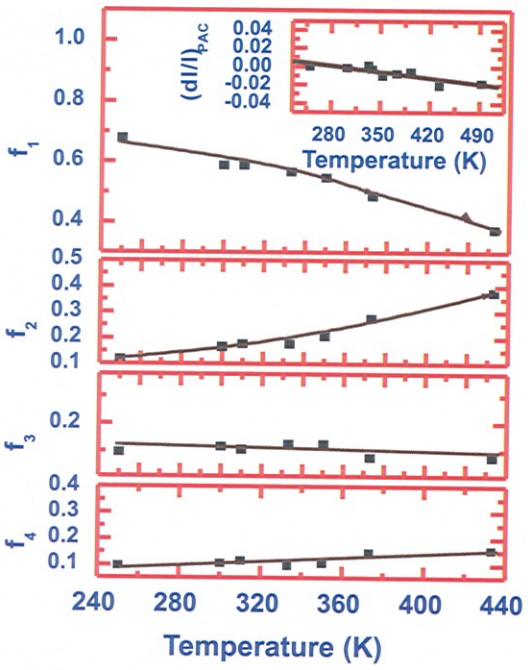

Fig. 4 : Variation of fractions of probe atoms associated with distinct ZrO_6 octahedra. Shown at the inset is the variation of the mean change in Zr-O distance with respect to original length i.e dl/l with temperature

■ ACHIEVEMENT

This work shows that there exists four distinct Zr sites in ZrW_2O_8. Though the mean Zr-O length in each distinct ZrO_6 increases there is an increase in the fraction associated with contracted and distorted ZrO_6 octahedra. This explains the effective contraction of ZrO_6 octahedra and hence the observed negative thermal expansion in this system.

■ PUBLICATIONS ARISING OUT OF THIS STUDY AND RELATED WORK

R. Govindaraj, C. S. Sundar and A. K. Arora, *Phys. Rev. B.*, **76** (2007) 12104.

Further inquiries:
Dr. R. Govindaraj, Materials Science Division
Metallurgy and Materials Group, IGCAR, e-mail: govind@igcar.gov.in

Laser Surface Modification of Thermal Sprayed Aluminium Oxide Coatings

EXECUTIVE SUMMARY

Aluminium oxide coating on metallic substrates has attracted attention for a broad range of applications including wear resistance, oxidation and hot corrosion resistance, heat and thermal shock resistance and electrical insulation. Laser surface modification is an emerging field, wherein lasers are used for imparting superior surface properties on engineering components. In this work, we report the development of high quality dense alumina coatings for providing electrical insulation for DC induction pumps of PFBR. Utility of high power lasers to transform the metastable γ-Al_2O_3 phase present in as-deposited Air Plasma Sprayed (APS) alumina coatings into thermodynamically stable α-Al_2O_3 phase is demonstrated. A host of solid-state analytical techniques including non-destructive laser based optical techniques that have the potential for on-line adaptation have been developed in-house.

OUTLINE

Continuous efforts to enhance the surface properties of the engineering components have resulted in the development of various surface processing techniques. Alumina coatings of 300 m thick over oxygen free high conductivity (OFHC) copper plates were made using Air Plasma Sprayed (APS) technique. These coatings were surface modified using a CW CO_2 laser and a comprehensive investigation of the laser surface modified alumina coatings were carried out using conventional Scanning Electron Microscopy (SEM), X-Ray diffraction and microhardness tests. Laser based non-contact techniques like laser scattering, Laser Raman spectroscopic (LRS) and photoluminescence techniques, hitherto used for characterizing bulk materials, were innovatively used for characterization of laser modified coatings. Evolution of microstructure and associated surface properties like surface roughness, coating density, microhardness and residual stress were quantitatively determined.

XRD patterns of alumina powder used for synthesizing the coating, as-deposited coating and laser treated coatings are shown in Fig 1. While the as deposited coating consisted of predominantly metastable γ-alumina phase, laser treatment restored the thermodynamically stable α-alumina phase. This phase is preferred phase for coatings. While XRD gives average phase information, LRS can be used for phase mapping and detect microlevel inhomogeneties of laser treated surface. The complementary nature of these techniques to probe the modified surface both at macro and micro levels was brought out.

Surface and cross sectional SEM studies have revealed reduction in surface roughness and elimination of inter-lamellar pores, respectively. Laser treatment has reduced the average roughness from ~5 μm to less than 1 μm.

Similarly, the photoluminescence spectra (Fig. 2) were used to evaluate quantitatively the densification of the coating brought about by the laser treatment. As the laser treatment closes the inter-lamellar pores and enhances the volumetric concentration of Cr^{3+} ions, the PL intensity from the laser treated coating is enhanced manifold (thousand times) as compared to the as deposited sample. Also this technique allows one to optimize the process parameters like laser power density.

Also, an in-house developed laser scattering technique enabled us to characterize the reduction of surface roughness as a function of laser power in a non-destructive and non-contact mode. We also found the adhesion strength and hardness of the laser treated coating were nearly doubled as compared to as-deposited coating. Attempts were made to use an ultrasonic technique for evaluation of laser treated depth and interface adhesion in a qualitative manner. A comparative laser surface modification study of two powerful coating techniques used for synthesizing alumina coatings viz., APS and Detonation Gun (D-Gun) were also made.

Thus a host of solid-state techniques were successfully made use of to demonstrate the feasibility of making thicker (~150 μm), denser and harder (~2000 VHN) Al_2O_3 coatings by combining two powerful surface modification techniques with the potential for variety of engineering applications.

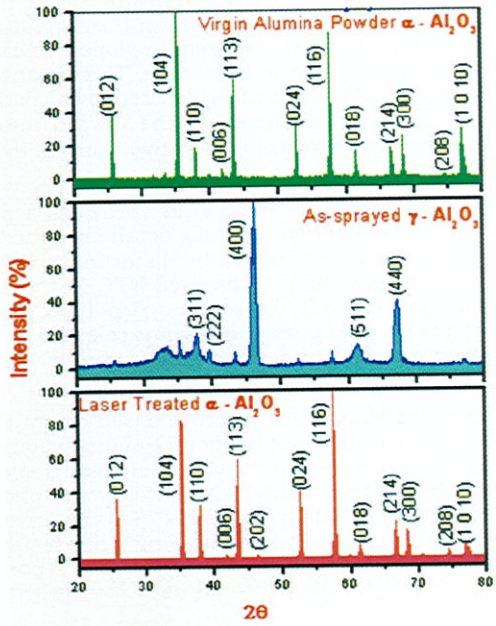

Fig. 1 : X-ray diffractogram of Alumina coatings

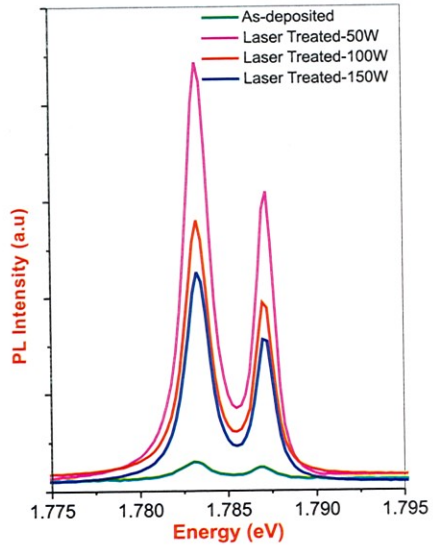

Fig. 2 : Photoluminiscence Spectra of Al_2O_3 coatings.

■ ADDITIONAL INFORMATION ABOUT LASER SURFACE ENGINEERING

Laser is an acronym for Light Amplification by Stimulated Emission of Radiation. It is a clean source of energy. When a laser beam strikes a specimen surface(1) it is either absorbed (2) or transmitted(3) or reflected. The absorbed photons are converted to thermal energy resulting in local temperature surge to a depth of few tens of microns depending on the wavelength, fluence and average power. Lasers are employed over a wide range of applications including basic scientific research, test and measurement, industrial processing, microelectronics, biomedicine, environmental science, avionics, entertainment and telecommunications. Application of lasers in materials processing provide many advantages over conventional methods in terms of increased manufacturing efficiency, decrease in manufacturing costs, ease of automation, superior quality, reliability of the products and enables one to design and develop new products.

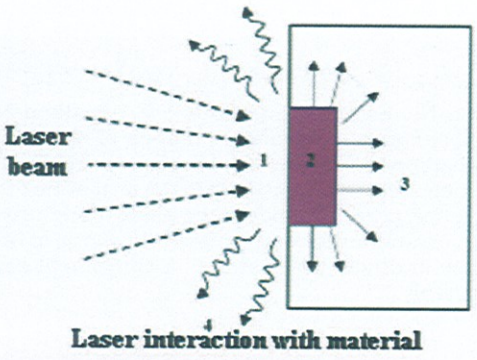

■ CERAMIC COATINGS

Ceramics is the materials science and engineering of inorganic, nonmetallic solids. Ceramic materials are characterized by low density and high temperature strength. They possess superior wear and corrosion resistance. But their low fracture toughness and brittleness makes them unsuitable for many critical applications.

Ceramic coatings over metallic substrates provide a synergetic way of combining the superior properties of ceramics with the desirable properties of metals. They serve diverse and vital functions in the electronics, chemicals, aerospace, energy and manufacturing industries. Alumina, one of the cheapest ceramics, is widely used for variety of applications in both bulk and coatings form.

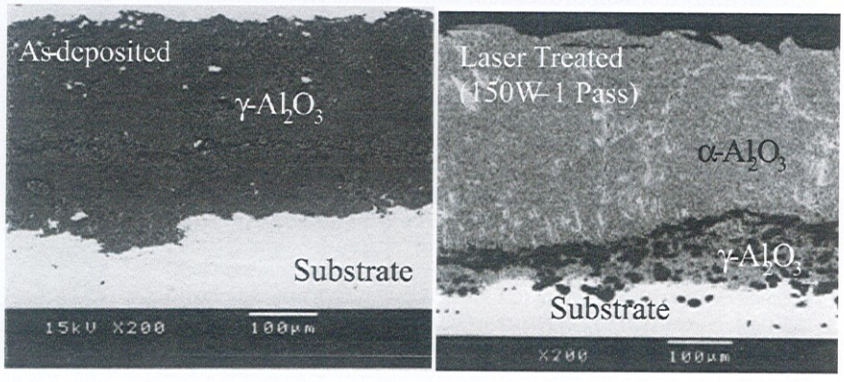

Cross sectional SEM micrographs showing the densification of coatings brought about by laser treatment: As-deposited coating is characterized by typical lamellar structure interspersed with porosities. γ-Al_2O_3 is a metastable phase with a transformation temperature above 1000 C. Only laser heating can transform this metastable phase to a thermodynamically stable α-Al_2O_3 phase without degradation of metallic substrate.

■ ACHIEVEMENT

Based on these studies, air plasma sprayed alumina coatings were developed for sodium DC conduction pumps employed in PFBR. Laser surface modification was used as a value addition technique for imparting superior physico-mechanical properties for application with next generation conduction pumps.

■ PUBLICATIONS ARISING OUT OF THIS STUDY AND RELATED WORK

R. Krishnan, S. Dash, R. Kesavamoorthy, C. Babu Rao, A.K. Tyagi and Baldev Raj, *Surface and Coatings Technology*, **200** (2006) 2791.

Further inquiries:
Shri R. Krishnan and Dr. S. Dash, Materials Science Division
Metallurgy and Materials Group, IGCAR, e-mail: krish@igcar.gov.in

Self Assembly of CdSe Nanorods by Electrophoretic Deposition

EXECUTIVE SUMMARY

CdSe Nanospheres of about 5-7 nm diameter were synthesized by direct chemical reaction process. From these nanospherical particles, nanorods of about 20 nm in thickness were deposited on ITO substrates by electrophoretic deposition technique. Unambiguous HRSEM evidence of electric field driven self assembly of the nanospherical CdSe particles leading eventually to the formation of nanorods was observed. The alignment of the nanoparticles takes place in a direction perpendicular to the plane of the substrate, due to electric field gradient, even without using any templates. The size, crystallinity, composition and shape of the particles were analyzed by XRD, TEM, AFM, HRSEM and EDAX analysis. These findings demonstrate a convenient and simple template-less technique for the formation of nanorods and its assembly.

OUTLINE

CdSe is an important semi conducting material with unique optical and electrical properties, which makes it a promising material in the field of opto-electronic devices, biosensors etc. Growth of nanostructures having different morphologies can result in the modification of its physical properties and improvement in performance characteristics. By tuning the aspect ratio of nanorods one can follow the transition from zero to one dimensional quantum confinement systems. From the application point of view, semiconductor nanorods have already been demonstrated to possess considerable advantages over their quantum dots (QD) counterparts in various fields. These, include improved performance in photo enhanced optical gain as compared to spherical dots while providing polarized lasing. Nanorods and nanowires offer a larger surface area compared to that of films or bulk material in the field of application such as photo electrochemical cells, catalysts and sensors, where the sensitivity or efficiency is proportional to surface area.

Nano particles of CdSe were chemically synthesized by the direct reaction of an alkaline selenium solution with an aqueous solution of CdSe complex. XRD studies confirm the formation of nanocrystalline CdSe particles with cubic structure. TEM micrographs indicated that the as synthesized nanoparticles were spherical in shape and no nanorods were found in the chemically synthesized powders(Fig. 1). The particle size was found to be 5-7 nm matching closely with the estimate from XRD peak broadening calculated using Scherer formula. EDAX studies indicated the formation of compound with nearly equiatomic composition (CdSe type).

The CdSe nano particles were then dispersed in propylene carbonate by ultrasonication and the same was used for electrophoretic deposition (EPD) (Fig.2). HRSEM images are in agreement with GIXRD results confirming the formation of nanorods of CdSe synthesized by electrophoretic deposition on ITO substrates. It could be seen that the nucleation of rods of about 20 nm diameter always occurs at protrusions at the boundaries of an embryo structure. The formation of such embryos with rough corrugated edges is an important prelude before nucleation of nanorods. This nucleus is an island typically with nearly the same composition, but without any orderly arrangement of the nanospherical particles. The protrusions formed on the boundary of the nucleus due to interface instabilities, will be locations of concentrated electric field, leading to self assembly of the charged CdSe nanoparticles. AFM studies clearly identified that each nano rod infact consists of three individual fine strips of ~7nm width, matching well with the diameter of individual nanoparticles of CdSe synthesized by chemical route. Also very clear evidences of particle to particle coagulation leading to rod shaped growth were evident from AFM and HRSEM studies.

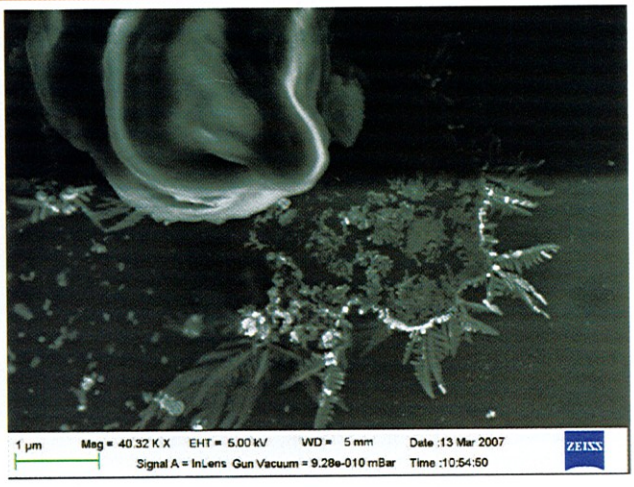

Fig. 1 : Nucleation of rods can be seen to be taking place at asperities, which are expected to be points of high electric field, providing the driving force for alignment of nano particles of CdSe

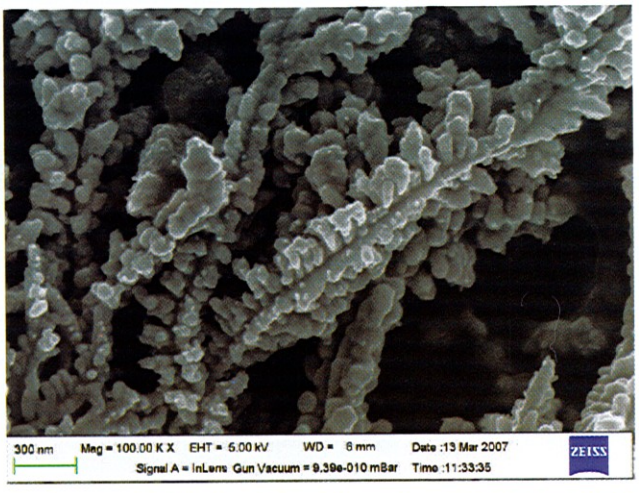

Fig. 2: Electric field driven interaction of the charged nanoparticles during electrophoretic deposition can be seen to result in growth of nanorods. The primary rod growing from the nucleus and plenty of secondary rods nucleating from the primary arm can be seen. The secondary arms are also nearly parallel to each other, suggesting the strong inter-particle interactions during the growth process.

■ ADDITIONAL INFORMATION ABOUT CdE SEMI-CONDUCTING NANOCRYSTALS

Semiconductor nano-crystallites have been the subject of intense studies over the last decade primarily due to their interesting size dependent electronic and optical properties. The fabrication of CdE (E = S, Se, Te) semiconductor nanocrystals has interested researchers, since its optical properties can be tuned by varying its size, resulting in the phenomenon of quantum confinement.

■ CdSe NANOPARTICLES AND NANORODS

CdSe Nanoparticles behave like a tunable fluorophore. It can emit any color across the visible part of the spectrum (Fig. 3). At a size of around 7nm, it emits deep red but is still brown looking. At smaller nanosizes, it can emit photons ranging across the visible part of the spectrum. In cadmium selenide , crystallites of ~ 1.5 nm gives yellow color, 4nm gives red and larger the particle, output color is black.

CdSe nanorods were deposited on ITO substrates by electrophoretic deposition process. A characteristic feature of electrophoretic process is that colloidal particles suspended in a liquid medium migrate under the influence of an electric field (20-1000 V/cm) and are deposited onto an electrode. All colloidal particles that can be used to form stable suspensions and that can carry a charge can be used in electrophoretic deposition. This includes material classes such as polymers, pigments, dyes, ceramics and metals. The process is useful for applying materials to any electrically conductive surface.

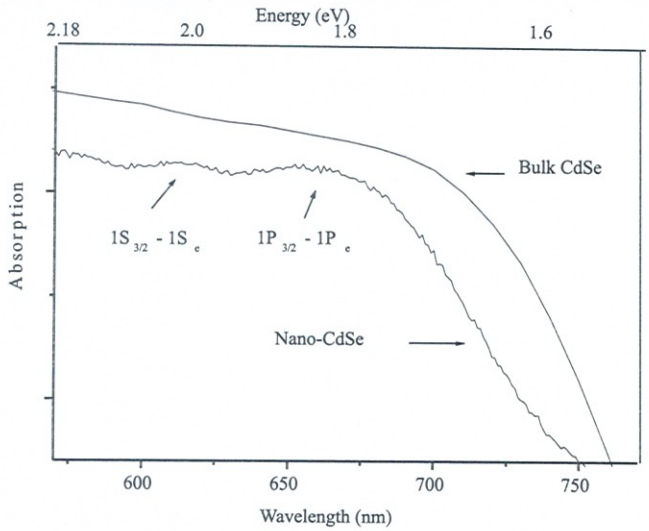

Fig. 3 : Diffuse Reflectance Spectra of nano and bulk CdSe Revealing confinement behaviour.

■ BRIEF DESCRIPTION OF THEORETICAL BACKGROUND

Electrophoretic deposition (EPD) is essentially a two-step process, involving the application of an electric field to the suspension (electrophoresis). In this case the particle motion is motivated by electro-hydrodynamic forces. The self organization mechanism dictates the morphogenesis of fractal architecture. The fractal morphology however depends on the charge and mass of electro-phoretically deposited particle and hence morphology would vary for each system. Such self-organization phenomenon on solid surface is a culmination of non-linear competitive interactions. The surface energy as well as adhesion forces acts against the steric repulsive forces causing manifestation of steady state morphology.

■ ACHIEVEMENT

Growth of CdSe nanorods of well defined shape and size without any template by electrophoretic deposition has been achieved.

■ PUBLICATIONS ARISING OUT OF THIS STUDY AND RELATED WORK

B. Vigneashwari, S. Dash, A. K. Tyagi and S.Austin Suthanthiraraj; *Intl. J. Nanoscience*, (In Press)

Further inquiries:
Dr. A.K.Tyagi, Dr. P.Shankar and Dr. S. Dash, Materials Science Division
Metallurgy and Materials Group, IGCAR, e-mail: akt@igcar.gov.in; pshankar@igcar.gov.in; dash@igcar.gov.in

Substitution of C and Li in MgB_2: It's Effect on T_c and H_{c2}

EXECUTIVE SUMMARY

MgB_2 is a recently discovered superconductor having a moderately high T_c of 39K. Significant increase in the critical magnetic field tolerated by this superconductor has been achieved by ~5 at% C substitution at the B sub-lattice. In our laboratory we have synthesized C substituted MgB_2 for a wide variety of C compositions. We have measured T_c as a function of C content and external magnetic field. Unlike in conventional superconductors $-dH_{c2}/dT_c$ shows an increase with decrease in temperature for a carbon substitution of 5 at%. Raman measurements have been carried out in the C substituted samples. These measurements highlight the importance of the enhanced electron-phonon interaction in determining the T_c variation with C substitution.

OUTLINE

Five years after its discovery the study of superconductivity MgB_2 is still being actively pursued in many laboratories. Unlike the high T_c cuprates MgB_2 does not tolerate chemical substitution. C on the B sub-lattice and Al at the Mg sub-lattice are the only substitutions that have been extensively investigated. Of the two substitutions the former has made more impact, since in spite of depleting critical temperature T_c, C substitution is seen to enhance the critical magnetic field $H_{c2}(0)$ from 15 Tesla to 39 Tesla for C substitution of 5 at%. Fig. 1 shows the structure of MgB_2 that consists of layers of Mg on a hexagonal lattice interleaved with graphitic layers of B.

Following the announcement of 39 K T_c in MgB_2 our lab could quickly reproduce this result on phase pure samples. It was realized that some form of high pressure synthesis was necessary to contain the weight loss due to highly volatile Mg. We employed a sample reaction chamber in which Ar can be pressure locked at 50 Bar and the reaction vessel could be placed in a furnace, where a heat treatment could be performed at 950°C (see schematic in Fig.1) The crystal structure of the reacted MgB_2, the resistivity of the pellet and the diamagnetic signal showing superconductivity are also displayed in Fig.1 Using this apparatus for synthesis we could obtain substitutions of C in $MgB_{2-x}C_x$ with out significant Mg loss. However we soon found that the temperature limitation of 950°C was seriously limiting the extent of C substitution in the sample. We then resorted to sealing the reaction mixtures in Ta tubes, which we could implement with minor modifications in our arc furnace. Having sealed the reactants in Ta tubes, heat treatments could be carried out at 1200°C. We could then obtain a stoichiometric substitution of C by this procedure. In Fig.2 we show the variation of T_c obtained by these C substitutions.

MgB_2 is a text book example of a system in which superconductivity arises mainly due to phonon mediation and conventional BCS theory works well in this system. Extensive band structure calculations with the state of the art description of the electron-phonon interaction have helped in understanding the two-gap behaviour and its consequences on the H_{c2} behaviour in this system. Band structure calculations done on C substitution indicate that electrons doped by C substitution deplete the hole density of states at the Fermi level, which in turn should deplete T_c much faster with C substitution than is observed in Fig.2. It was suggested that the slower variation of the T_c with C substitution could arise as a consequence of an increased electron-phonon coupling strength with C doping. In order to verify if this was indeed true, we performed Raman measurements on the entire set of C substituted samples, synthesized in our laboratory. From a detailed analysis of E_{2g} phonon, B-B vibration, Raman line-width, and γ line position ω, we calculated the electron-phonon coupling strength λ_{2g} using Allens formula

$$\gamma = 2\pi\lambda_{2g} N(0)\omega^2$$

Where N(0) is the calculated variation of the density of states at E_F. λ_{2g} and N(0) were then used in McMillan equation to calculate T_c. A good agreement with the experimentally observed variation in T_c is seen as shown in Fig.2. This implied that the electron-phonon coupling strength has indeed increased due to C substitution.

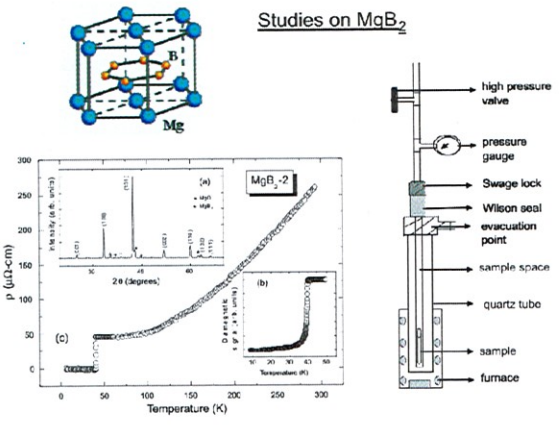

Fig. 1 : Clockwise: Structure of MgB_2, superconducting transition by resistivity, inset diamagnetic signal and XRD patterns, schematic of synthesis assembly

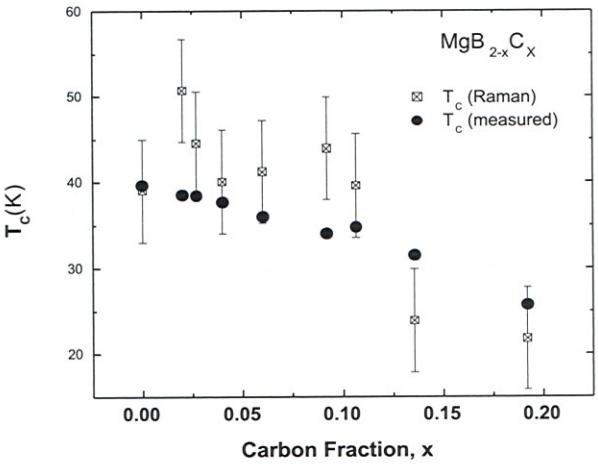

Fig. 2 : Variation of T_c with C substitution, measured and determined from Raman data

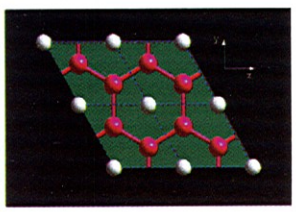

Fig. 3 : E_{2g} B-B vibrational mode

■ WHAT ARE THE CONSEQUENCES OF C DOPING IN MgB_2?

MgB_2 is a binary intermetallic with an intermediate T_c. The raw materials are cheap and the synthesis relatively easy and therefore can be made in large quantities at lower cost. Its intermediate T_c makes 20K operation using closed cycle refrigeration a possibility, cutting down heavily on operational costs of refrigeration for potential applications. Thus MgB_2 could be a viable alternative to the low T_c magnet wire materials viz., Nb_3Sn and Nb-Ti which are routinely employed in the construction of superconducting magnets. The serious drawback of MgB_2 is however is the strong magnetic field dependence of the critical current density, J_c. Research is now on to improve Jc in this material by introducing pinning centers by neutron irradiation, doping nanoparticles etc.

■ H_{c2} MEASUREMENTS IN Li AND C SUBSTITUTED MgB_2

Recently H_{c2} measurements have been carried out in our magneto resistance set up in external magnetic fields of upto 12 Tesla. The resistive transition temperatures were traced for $MgB_{2-x}C_x$ and Li co-doped $MgB_{1.8}C_{0.2}$ as a function of applied magnetic field in the range of 0-12 Tesla. The transitions for the samples with a carbon fraction of x=0.1 is shown in Fig.4. The onset of the transition, defined as T_c is plotted as a function of magnetic field for several of the carbon substituted samples in Fig.5. It can be seen from the figure that with carbon substitution $-dH_{c2}/dT_c$ increases with decrease in temperature. This is in contrast with that seen in pristine MgB_2 and in conventional superconductors, in which it is observed that $-dH_{c2}/dT_c$ decreases with decrease in temperature. The vertical bar line shown in Fig.5 emphasises the fact that even though T_c at zero field has decreased with Carbon substitution of x=0.10, at 20K the sample is superconducting in fields upto 12 Tesla, showing the remarkable improvement in the critical field due to C substitution. The highest $-dH_{c2}/dT_c$ is seen for the x=0.1 and is 1.75 T/K

It is well known that the H_{c2} of a superconducting sample increases with increase in T_c. It will be beneficial to increase the T_c of the C substituted sample in order to enhance the H_{c2} further. To achieve this goal we have co-doped Li in $MgB_{1.8}C_{0.2}$ since Li would provide compensating holes for electron substituted with C. We find a systematic enhancement in T_c with increase in Li content. Further we see that the curvature of dH_{c2}/dT_c of the C substituted sample is remarkably altered due to Li co-doping.

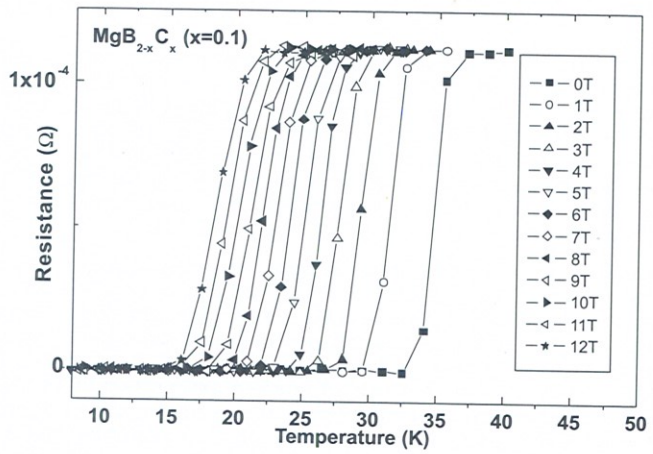

Fig. 4 : Resistance versus temperature in $MgB_{2-x}C_x$, for x=0.1 under different external magnetic fields indicated

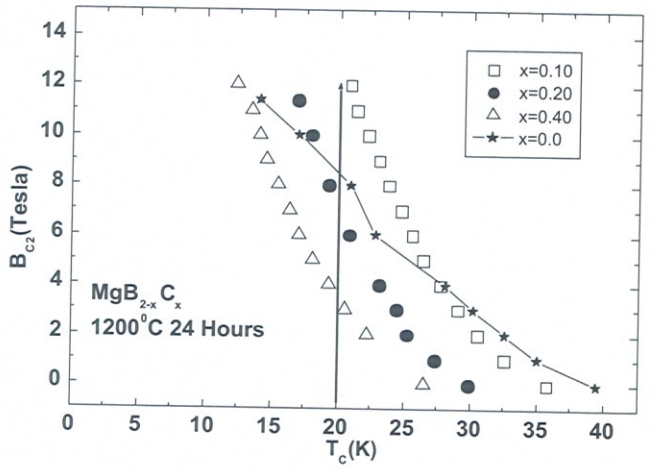

Fig. 5 : The variation of critical field with temperature determined for $MgB_{2-x}C_x$ for carbon fractions, x, indicated

■ PUBLICATIONS ARISING OUT OF THIS STUDY AND RELATED WORK

1. S. Jemima Balaselvi, N. Gayathri, A. Bharathi, V. S. Sastry and Y. Hariharan, *Physica C*, **31** (2004) 4072.
2. S. Jemima Balaselvi, N. Gayathri, A. Bharathi, V. S. Sastry and Y. Hariharan, *Supercond. Sci. Tech.*, **17** (2004) 1401.
3. T.Sakuntala, A. Bharathi, S. K. Deb, N.Gayathri, C.S. Sundar and Y.Hariharan *J. Phys. Cond. Matl.*, **17** (2005) 3285.

Further inquiries:
Dr. A. Bharathi, Materials Science Division
Metallurgy and Materials Group, IGCAR, e-mail:bharathi@igcar.gov.in

Surface Plasmon enhanced Raman Spectroscopy in Metal Nanoparticles

EXECUTIVE SUMMARY

Confinement of surface acoustic vibrational modes in nanoscale metal/semiconductor particles can be experimentally observed through Raman spectroscopy. As an experimental tool it is fast and non-destructive. The technique is also used to measure average sizes of nanoparticles of interest. The symmetrical vibrational modes of nanoscale cobalt particles are detected using this spectroscopy. Intensity of the vibration mode is found to depend strongly on excitation wavelengths. Surface plasmon resonant absorption enhances the mode intensity.

OUTLINE

While bridging the gap between an atomic state and bulk phases of materials, nanoscale materials reveal novel physical and chemical properties which are completely different from those observed in either state of the materials. Size dependent optical responses, confinement of acoustic vibrational Raman modes, exotic structural configurations, reaction catalysis, etc. are some novel properties exhibited by various classes of nanomaterials.

Among various preparation routes, ion implantation is a versatile *bottom-up* technique to synthesize nanoparticles in matrices, and can easily be adapted in industrial lines as a technology of choice for the creation of smart materials. Use of ion implantation has several distinct advantages over other synthesis processes: embedded species are protected by the matrix and hence chemically clean, superior control over depth as well as size distributions, and the process is not limited by the solubility factor of the matrix.

Cobalt-silica nano-composite samples were obtained through implantation of 2.0 MeV Co^{+2} ions into the silica matrix with various doses (from $2x10^{16}$ to $7x10^{16}$ ions cm^{-2}). Tandetron accelerator (1.7 MV) facility of this centre was used to implant the matrix with the cobalt ions. Implanted samples were postannealed in vacuum ($1x10^{-6}$ mbar) at various temperatures. Low-frequency Raman spectra for the cobalt implanted and postannealed samples were recorded in the frequency range 10 to 45 cm^{-1} at 0.5 cm^{-1} step with 15 sec integration time. Grazing-incidence (0.4 degree) X-ray diffraction studies were carried out with Cu-K_α radiation on the cobalt implanted and post annealed silica glass samples in the parallel beam geometry to know about the crystalline nature of the implanted species.

X-ray diffraction peak (Fig.1) at $2\theta = 44.30°$ has confirmed the presence of face-centered cubic cobalt clusters in the postannealed samples. Development of the diffraction peak, after annealing, points to an increase in the volume fraction of that particular phase of cobalt due to the heat treatments. Raman spectra have been recorded in the cobalt-silica samples using different excitation wavelengths (514.5 to 351.1 nm). As shown in Fig.2, intensity of the vibrational modes depends significantly on the wavelength of laser excitations. Strong local field of surface-plasmon resonance in a cobalt nanoparticle with 351.1 nm excitation wavelength might be the reason for the observed enhancement in Raman intensity. As the characteristic surface-plasmon resonance (SPR) wavelength of cobalt nanoparticles in silica is around 345 nm, the increase in the intensity of vibrational modes with the excitation wavelengths in the vicinity of SPR is thought to be due to an enhanced electric field in a nanoparticle of cobalt atoms.

Surface-plasmon resonance enhanced phenomena have different significant influences in the field of optical spectroscopy. The results shown here could be particularly important to tune the excitation wavelength for the Raman scattering spectroscopy experiments. The study, in general, might help to exploit the in-built novelty of nanomaterials, and to tailor the growth of promising materials of this nature.

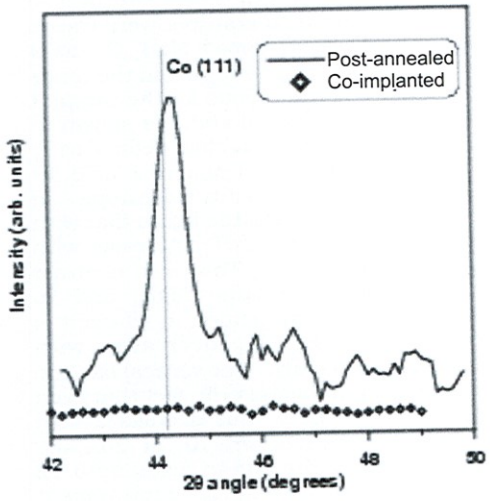

Fig. 1 : Grazing incidence X-ray diffraction patterns of the cobalt implanted ($7x10^{16}$ ions cm^{-2}) silica samples, before and after thermal annealing at 600 °C. Vertical line represents (111) reflection planes of bulk cobalt [JCPDF 15-0806].

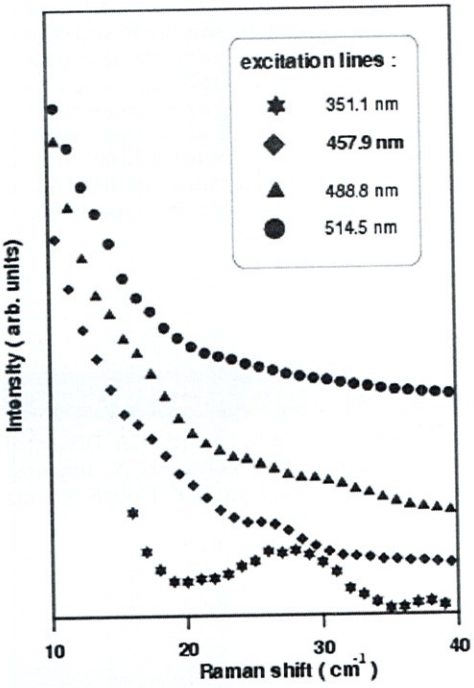

Fig. 2: Intensity enhancement of the surface-acoustic vibrational modes confined to the cobalt nanoparticles is shown as a function of the excitation wavelengths.

■ ADDITIONAL INFORMATION ABOUT SURFACE PLASMON RESONANCE

'Plasmon' is the quantum of collective longitudinal oscillation of valence electron clouds in metals. In typical good (alkali, noble) metals, volume plasmon energy is in the range 5-10 eV. In spherical metallic nanoparticles (~ 10 nm), the corrections for the core polarizability and the effective electron mass shift the plasmon energy into the visible spectral region of 2-3 eV. Why Surface Plasmon? Displacement of the negative charges due to an electric field gives rise to polarization of charges on particle surface (Fig. 3); although all electrons are oscillating with respect to positive ionic background, the main effect producing the restoring force which determines the finite eigen frequency is the surface polarization. Resonance takes place when this frequency matches with the applied field frequency.

■ QUASI-STATIC RESPONSE OF METAL NANOPARTICLES TO LIGHT

In the quasi-static regime, where $\lambda > 2R$, phase shifts or, retardation effects of the electromagnetic field over the particle dimension are negligible. That means dipolar excitations are only predominant. In the general case of multi-polar excitations, phase shifts of the electromagnetic wave in larger particles complicate the optical response. However, in the quasi-static size regime metallic particles feel a field which is spatially homogeneous and constant. Under this condition, application of electrostatics facilitates the understanding of the optical properties of metal nanoparticles. A finite displacement of the conduction electrons with respect to the positive ion-core occurs (illustrated in Fig. 3) in presence of the exciting electric field. Using electrostatic boundary conditions at the particle-dielectric interface, one can calculate the internal field (E_i) as,

$$E_i = E_o \frac{3\varepsilon_m}{\varepsilon + 2\varepsilon_m} \qquad (1)$$

Where ε_m is the dielectric constant of an embedding medium, E_o is the applied field, and ε is the metal dielectric function. In the resonance condition, when denominator in Eq. (1) tends to the minimum, E_i can become orders of magnitude high at the interface. It will depend on the number of surface atoms in the nanoparticle. As for example, number of surface atoms can be as much as the number of atoms in the interior of nanoparticles of sizes 1 to 4 nm.

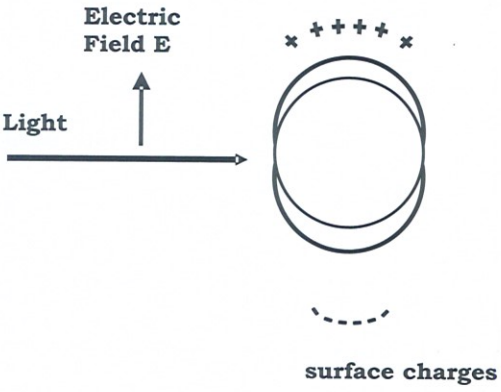

Fig. 3 : Excitation of a dipolar surface plasmon in a metal nanoparticle (size, 2R) by the electric field of an incident visible light (wavelength, λ).

■ PLASMON-PHONON COUPLING IN METAL NANOPARTICLES

Raman scattering due to confined acoustic vibrations (phonons) in metal nanoparticles are studied. There exist various coupling mechanisms between the surface plasmon states and the phonons in metal nanoparticles. In this respect, two mechanisms play important roles in the light scattering studies: (i) modulation of the inter band dielectric susceptibility due to pure radial vibrations (no change in shapes) and (ii) modulation of the surface polarization charges by quadrupolar vibrations (shape changes). The dependence of the low-frequency Raman spectra is studied in connection with the role of the excited surface plasmon states in metallic cobalt nanoparticles. In this particular case, a strong coupling between surface-plasmons and pure radial phonon modes could be observed.

■ ACHIEVEMENT

Importance of studying the vibrational properties of metal nanoparticles with different excitation energies has been experimentally demonstrated. This study elucidates the significance of plasmon-phonon coupling in metallic nanoparticles. Hence, it can be recognized as a benchmark research work in the field of science of nanomaterials.

■ PUBLICATIONS ARISING OUT OF THIS STUDY AND RELATED WORK

P. Gangopadhyay, T.R. Ravindran, K.G.M. Nair, S. Kalavathi, B. Sundaravel and B.K. Panigrahi, *Appl. Phys. Lett.*, **90** (2007) 063108.

Further inquiries:
Shri P. Gangopadhyay and Dr. K.G.M. Nair, Materials Science Division
Metallurgy and Materials Group. IGCAR, e-mail: pganguly@igcar.gov.in; kgmn@igcar.gov.in

Thin Films of Gadolinia Doped Ceria prepared by Pulsed Laser Deposition

EXECUTIVE SUMMARY

Microstructural properties of nano- ionic thin films of gadolinia doped ceria (GDC) prepared by pulsed laser ablation from sintered targets of gadolinia (5-20 mol %) doped ceria are investigated. X-ray diffraction and transmission electron microscopy reveal nanocrystalline grains with textured growth along <111> orientation in these films at low substrate temperature and at lower oxygen partial pressure. TEM study shows a uniform distribution of nanocrystal of 8-10 nm for energies 200mJ/pulse, nanocrystals embedded in a large crystalline matrix of doped ceria for energies in the range 400-600 mJ/pulse and high density of defect . The study also reveals that the substrate temperature and oxygen partial pressure could influence preferred orientation, while the laser energy could significantly influence defect concentration in these films.

OUTLINE

Ceria- based electrolytes have been of interest because of their high ionic conductivity. Replacing Ce^{4+} with divalent or trivalent cations results in the creation of oxygen vacancies and predominantly oxygen ion conductivity over an extended temperature and oxygen partial pressure range. In comparison with ytrria stabilized zirconia (YSZ), Gd-doped ceria (GDC) has significantly higher ionic conductivity and is a candidate for use in solid oxide fuel cells (SOFC) at temperatures less than 873 K, where the electronic contribution in reducing conditions is small. The lower temperature operation can lead to reduced costs and better long term performance by reducing effects of interface reactions. Many studies have been made on the physical properties of GDC and of its applications in SOFCs and sensors. The oxygen gas sensors based on cerium oxide films indicated that the response time of the sensors using films with particle size of 200 nm has been approximately one order of magnitude smaller than that for corresponding sensors using films of particle size of 2μm. Therefore, it is expected that the nanocrystalline films prepared by pulsed laser ablation (PLD) could offer shorter response time. In the present work, the influence of process variables such as substrate temperature, oxygen partial pressure and laser energy on the microstructural properties is investigated.The deposition of films (111) oriented Si from a sintered GDC target was carried out using a KrF excimer laser of 248 nm wavelength (Compex 205 from Lambda Physik) and a turbo pumped deposition system with typical laser repetition rate of 10 Hz using laser energy in the range 200-600 mJ/pulse. In this experiment, the excimer laser was focused onto the GDC target at an angle of incidence of 45°.

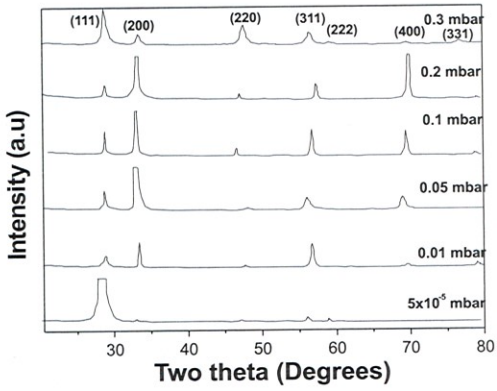

Fig. 1 : XRD patterns of 10 mol% gadolinia doped ceria films at 873 K, at different oxygen partial pressures

It is evident from the XRD patterns that the films are polycrystalline in the temperature range of deposition. The crystallinity of the films is found to increase with increasing substrate temperature. The particle size increases from~15 nm to ~20 nm as the substrate temperature is increased from 473 to 873 K owing to increased mobility of adatoms with increasing substrate temperature. XRD results shown in Fig. 1 indicate a significant influence of the oxygen partial pressure on the growth characteristics of the films. At $5x10^{-5}$ mbar base pressure, the films are weakly crystalline and have (111) orientation. With increasing oxygen partial pressure from 0.01 to 0.2 mbar, the films are (200) oriented. At 0.3 mbar of oxygen partial pressure, there is tendency for the increased growth of polycrystalline films.

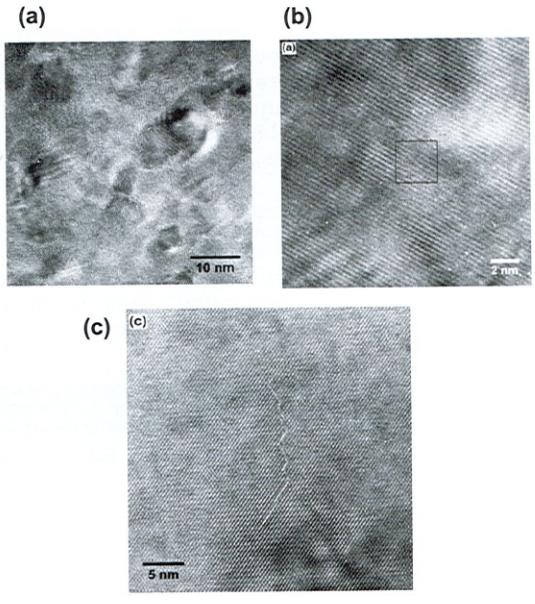

Fig. 2: (a) HREM image of uniformly distributed nanocytallites in the GDC films, (b) dislocations, and (c) growth ledges.

Lattice images were recorded from nanocrystalline as well as from the large crystalline regions for the films deposited in the energy range 400-600 mJ/ pulse. The nanocrystalline regions exhibit crystals of about 7-10 nm size and the interfaces are clean and do not contain any amorphous or secondary phases (Fig. 2 (a)). On the other hand, the large crystalline area contains extended defects (Fig. 2(b)), ledges (Fig.2(c) and lattice bending in the films. The ledges shown are growth related defects which were mostly seen in grains containing (111) planes with the lattice spacing of about 0.35nm. Fig. 3(a) illustrates the Raman spectra of GDC films obtained at 873 K as a function of laser energy. These films were deposited in the base pressure of $3x10^{-5}$ mbar. Like the effect of substrate temperature, laser energy also shows a significant shift in the Raman line and FWHM when it is increased from 200 mJ/pulse to 600 mJ/pulse (Fig. 3 (b)). When Gd replaces Ce at some lattice sites, the Raman line exhibits redshift due to heavier mass of Gd. This redshift depends on the fraction of the substitution. As the laser energy increases, the fraction of Gd incorporated in the film seems to be increasing as suggested by the Raman redshift shown in Fig.3(b). In contrast, FWHM increases with laser energy and saturates beyond 300mJ/pulse indicating that there is a rapid increase in the defect concentration initially and it does not increase significantly at higher laser energies.

■ PULSED LASER DEPOSITION : THE TECHNIQUE AND APPLICATIONS

One of the most important applications of the laser with condensed material is pulsed laser deposition (PLD) because the process is capable of reproducing the composition of the target material to be evaporated. PLD is basically a growth technique in which photonic energy is coupled to the target material to be deposited via electronic processes. Here an intense laser pulse passes through an optical window of a vacuum chamber and is focused onto a solid (the target), where it is partially absorbed. Above a certain power density, significant material removal occurs in the form of an ejected luminous plume. The threshold power density needed to produce such a plume depends on the target material, its morphology, and the laser wavelength. Material from the plume is then allowed to recondense on a substrate, where film growth occurs. The growth process may be supplemented by a passive or reactive gas or ion source, which may affect the ablation plume species in the gas phase or surface reaction, in which case one talks of PLD. The dominant mechanisms in the formation of plume or ablation plasma from the irradiated surface were found to depend sensitively on laser parameters such as energy density (fluence), pulse duration, wavelength, laser repetition rate as well as the material being irradiated. A general feature of ablation plasmas is their high ion and electron temperatures of the order of several thousand Kelvin and their high degree of ionization. The advantages of the PLD process are flexibility, fast response, energetic evaporation and congruent evaporation. With appropriate choice of ablation wavelength and absorbing target material, high energy densities are absorbed by a small volume of material, resulting in vaporization that is not dependent on the vapor pressures of the constituent cations or sub-oxides. This leads to an excellent composition control in the ablated films. The development of PLD process has got considerable impetus because of its application in the synthesis of high quality single crystalline and multi-layer materials of technological significance. One can also visualize PLD as a technique capable of forming new materials, not obtainable by other conventional vapor deposition techniques, simply by varying the energy of the atoms on the surface by controlling the kinetic energy of the vapor, substrate temperature and the time between the laser pulses. The pulsed laser ablation can also be used in a controlled way to obtain three dimensional islands of uniform size in a self-assembling process. In the present work, the application of PLD to synthesize nano-ionic thin films of gadolinia doped ceria as a function of process parameters is illustrated.

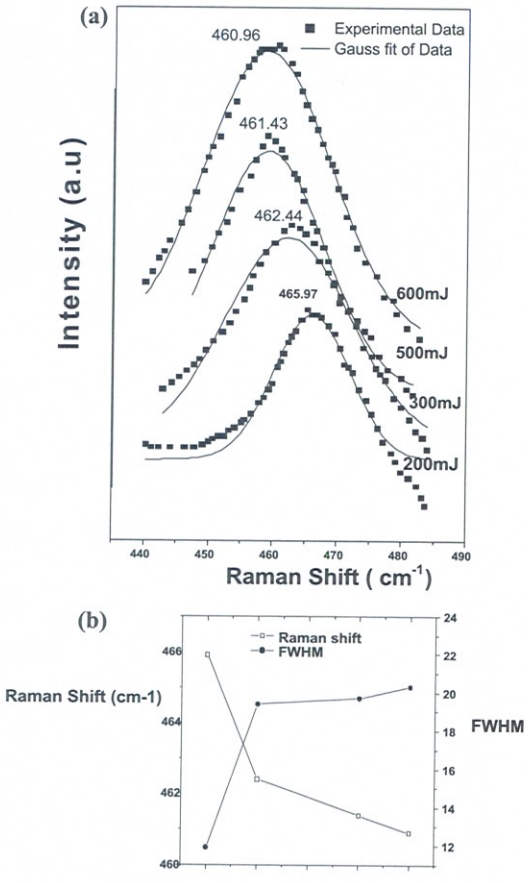

Fig. 3 : (a) Raman spectra of the films prepared at different laser energy at a substrate temperature of 873 K, and (b) Raman shift and FWHM versus laser energy

■ ACHIEVEMENT

(i)The studies on influence of the substrate temperature, oxygen partial pressures and laser energy on the growth characteristics of thin films of GDC indicate that the films are mostly nanocrystalline and grain size increases with increasing substrate temperature. Oxygen addition during the growth of the film is found to alter the film orientation from (111) to (200) in the partial pressure range 0.1-0.2 mbar. (ii) TEM shows that the films have a uniform distribution of grains of about 8-10 nm size for laser energy 200mJ/ pulse. In contrast, the films ablated with energies in the range 400-600 mJ/pulse resulted in nanocrystals embedded in a larger crystalline matrix. Higher laser energy increases not only the deposition rate but also growth induced defects like dislocations and growth ledges in the large grained region. Raman spectra also provide evidence for the defect concentration as a function of laser energy in the GDC films grown by pulsed laser ablation.

■ PUBLICATIONS ARISING OUT OF THIS STUDY AND RELATED WORK

1. P. Kuppusami, S.N. Padhi, K. Muthukkumaran, E. Mohandas and V.S. Raghunathan, *Surf. Eng.*, **21** (2005) 172.
2. S. Selladurai, K.Muthukumaran, P.Kuppusami, R.Divakar, E.Mohandas and V.S. Raghunathan, *Ionics*, **12** (2006) 365.
3. K. Muthukkumran, P. Kuppusami, R. Srinivasan, K. Ramachandran, E. Mohandas and S. Selladurai, *Ionics*, **13** (2007) 47.
4. P. Kuppusami, K. Muthukumaran, R. Divakar, R. Kesavamoorthy, E. Mohandas, V.S. Raghunathan and S. Selladurai, *Ionics* **13** (2007) 343.

Further inquiries:
Dr. P. Kuppusami and Shri E. Mohandas, Physical Metallurgy Division
Metallurgy and Materials Group, IGCAR, e-mail: pk@igcar.gov.in ; mohandas@igcar.gov.in

A Plasma assisted MOCVD Process for Synthesis of CrN/Ni Composite Coatings

EXECUTIVE SUMMARY

Plasma assisted MOCVD process employs low power (~ 70 mW/cm^2) DC plasma which cracks metal organic vapors and other gaseous precursors followed by subsequent deposition on heated (~ 550° C) substrates. Right choice of the metal organic compounds is crucial as volatility and thermal stability are the most important criteria in their selection. Chromium acetyl-acetonate and nickel acetylacetonate-ethylenediamine were used as MO precursors for Cr and Ni, respectively. These coatings were nanocrystalline and possessed a clustered microstructure. A hardness between CrN (2300HV) and Ni (450HV) coatings could be tailored by forming Ni-CrN composite coating of varying composition, thus providing a high flexibility in the design of the coating.

OUTLINE

Coatings have revolutionalised the properties of engineering components in terms of their life extension and aesthetics. Plasma assisted metal organic chemical vapor deposition (PAMOCVD) of chromium based coatings is relatively new. Using this technique, coatings with different chemical composition and mechanical properties can be produced. The method of controlling the deposition process is pictorially represented in Figure 1. It shows how the temperature of the precursor (T_c) is changed during the deposition process from start to stop, represented by temperatures T_{start} and T_{stop}, respectively. The idea is derived from the thermogravimetric (TG) analysis of the precursor shown in the inset. It has been carried out by controlled heating of the solid Cr precursor in He ambience while continuously measuring weight loss due to volatilization. This viewgraph reveals that vaporization begins as early as 100° C and continues until about 260° C. This temperature range has been used for deposition of the film (for CrN). Assuming that no chemical reactions take place during sublimation, the partial pressure of the precursor in the gas phase is expected to increase with increase in temperature, given that the chamber volume is constant. Thus, temperature was used as a tool for controlling the amount of vapor and hence the deposition process.

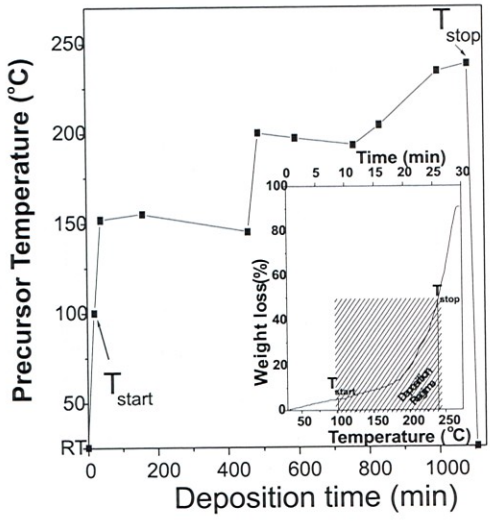

Fig. 1 : Plot showing how the precursor temperature is varied as a function of deposition time in order to control the precursor flow rate into the deposition chamber. The idea is derived from the thermo-gravimetric analysis of the precursor shown in the inset.

Choice of right precursor is possibly the most important step towards the success of a PAMOCVD process. Two essential criteria in this selection are (a) complete volatility at reasonable temperatures, and (b) non reactivity in the vapor phase. Figure 2 shows the (TG) graph of the mixtures of $Cr(acac)_3$ and $Ni[(acac)_2en]$ in different proportions (by weight of Ni with respect to Cr precursor). The results reveal that in all proportions, the mixtures undergo a single step weight loss with no decomposition. Pure Cr and Ni vapor sources sublimate in a narrow temperature range of 220-260°C. But, mixed precursors sublimate in a wider temperature range. For instance, precursor mixture of 50 wt% Cr and 50 wt% Ni has a sublimation temperature range of 150-285°C. The early onset of sublimation in this precursor is one of its characteristic advantages. It can be utilized to control with ease the partial pressure of the precursors. It should be mentioned here that the precursors that sublime over a small range of temperature are difficult to control and may require expensive temperature flow controllers. The volatile nature of the mixtures of the two precursors can be effectively utilized to engineer composite coatings of desired composition. It is also observed from this figure that the loss at the end of the process is 100% for the Cr and Ni precursors, while there are about 5-9% residues left for the mixtures of these two precursors. The residues are a reaction product of the Cr and Ni precursors.Coatings with different compositions such as CrN, Ni and CrN/Ni composites were developed using the PAMOCVD technique. Inset in Fig. 2 shows how the Vickers micro-hardness (with 50g load) of these coatings varies with addition of Ni-precursor to Cr-precursor. Ni films are softer (440 HV) than either CrN (2300 HV) or CrN/Ni films. Hardness of the composite films reduce to 1700 HV on adding 50 wt.% of nickel precursor to chromium precursor. Thus, addition of nickel makes the CrN film less hard, and provides a convenient method to tailor the hardness of the composite coatings.

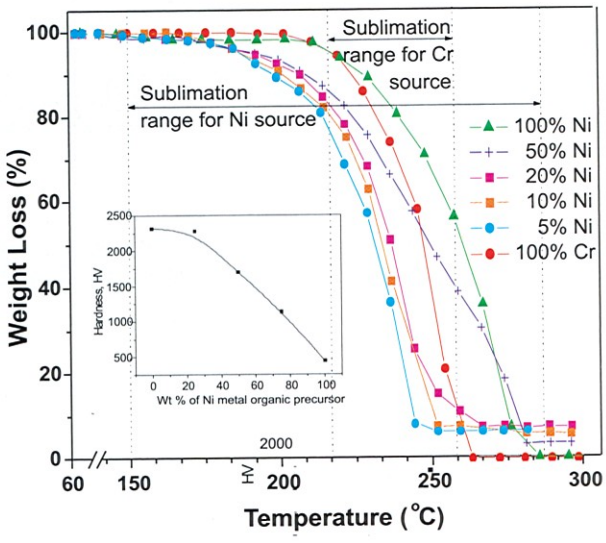

Fig. 2: Thermogravimetric analysis of various proportions of $Cr(acac)_3$ and $Ni[(acac)_2en]$ mixtures in helium atmosphere. Inset shows how hardness of the coating can be tailored by addition of Ni.

This work is a part of the R&D programme of PFBR on development of wear resistant coatings on type SS316 L.

■ ADDITIONAL INFORMATION ABOUT THE PAMOCVD PROCESS

In PAMOCVD technique, vapors of a metal-organic compound are cracked in sub-atmospheric conditions using a low power DC discharge which generates plasma. Neutral and charged species in the plasma undergo chemical reaction at the substrate site to deposit the desired material. As compared to the conventional thermal MOCVD technique, this is far superior in that the substrate temperature can be low as it is not employed for cracking of precursors, and also that the coating thickness is uniform over wider area.

■ COMPOSITE COATINGS

A composite, is a mixture of two or more different materials, each of which have, in most cases, widely differing properties. Its overall property is a weighted average of the individual constituents' properties. There are many such materials available in nature, viz., bones, bamboo and crab shell, to name a few. But it is important to design synthetic composite materials. One such example is the CrN/Ni composite demonstrated here. Figure 3 shows the bright field Transmission Electron Microscope (BF-TEM) image of a Ni-CrN composite thin film synthesized using a mixture of 25% Ni and 75% of Cr precursors. Some globular particulates (~50-100nm) and some particles with planar edges (~50-80nm) can be seen in the micrograph. Convergent beam micro-diffraction from the particles with planar edges reveals single crystal Ni (inset-left). Similar study from the globular particles reveal CrN, but with a number of overlapping zone axes. This indicates that the rounded particles are clusters of CrN crystallites. Selected area diffraction (SAD) pattern (inset-right) taken from the matrix excluding the particles exhibits polycrystalline CrN rings. Thus, the morphology of the composite film may be summarized as a mixture of Ni single crystals and CrN nano clusters embedded in a polycrystalline CrN matrix. It has been shown earlier in Fig. 2, that such a morphology does result in a decrease in the hardness (2250HV) of CrN coating. It has also been shown there that the hardness can be lowered further by increasing the fraction of Ni. This development also paves the way to synthesize functionally graded coatings, in which the hardness can be graded across the coating thickness such that there is a soft Ni rich material at the interface with substrate and an ultra hard CrN at the top.

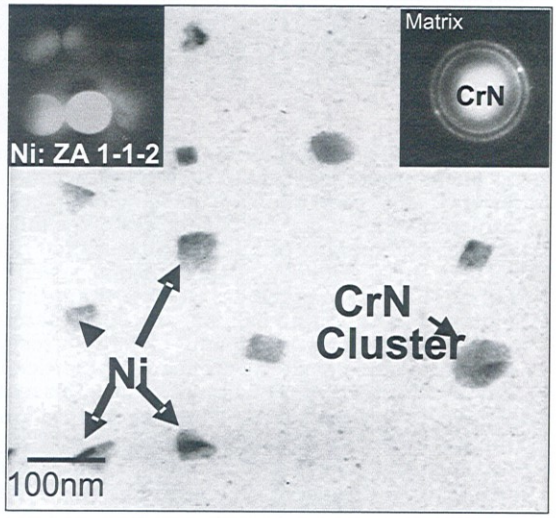

Fig. 3 : BF-TEM image showing CrN clusters and Ni crystals embedded in a nanocrystalline CrN matrix. The insets show the diffraction patterns from a Ni crystal and the CrN matrix

■ WHY COMPOSITE COATINGS ARE IMPORTANT

Micro-hardness is an index for the mechanical properties of coatings. Often ultra hard coatings such as CrN (~2300HV) are brittle. Besides, difference in their thermal expansion coefficient with respect to the substrate (viz. SS) lead to the development of large shear stress at the substrate-coating interface during thermal cycling. They eventually spall off during operation. Herein lies the importance of the development of composite coatings in which the hardness can be controlled at will by the amount of the second phase.

■ ACHIEVEMENT

The process for nanocomposite coatings of CrN /Ni on SS and ceramic substrates has been developed on a laboratory scale and demonstrated that hardness of the composite coatings can be tailored by controlled addition of Ni to the CrN matrix. The problems of adhesion and spalling of the hard CrN coatings have also been successfully circumvented by forming these composites.

■ PUBLICATIONS ARISING OUT OF THIS STUDY AND RELATED WORK

1. P. Antony Premkumar, P. Kuppusami, Arup Dasgupta, C. Mallika, K.S. Nagaraja, V.S. Raghunathan, *Mater. Lett.* **61** (2007) 50.
2. Arup Dasgupta, P. Antony Premkumar, P. Kuppusami, V.S. Raghunathan and K.S. Nagaraja, Proc. International Symposium on Advances in Stainless Steels, Apr. 9-11, 2007.
3. Arup Dasgupta, P. Antony Premkumar, Falix Lawrence, L. Houben, P. Kuppusami, M. Luysberg, K.S. Nagaraja, V.S. Raghunathan, *Surf. Coat. Technol.* **201** (2006) 1401
4. P. Antony Premkumar, Arup Dasgupta, P. Kuppusami, P. Parameshwaran, C. Mallika, K.S. Nagaraja and V.S. Raghunathan, *Chem. Vap. Dep.* **12** (2006) 39.
5. P. Kuppusami, Arup Dasgupta, O.M. Sreedharan, Falix Lawrence, V.S. Raghunathan, Baldev Raj, K.S. Nagaraja and P Antony Premkumar, Patent No: 198325 Dt. 17.1.2006.
6. P Antony Premkumar, K.S. Nagaraja, P. Kuppusami, Arup Dasgupta, V.S. Raghunathan, C. Mallika and Baldev Raj, Indian Patent Application Number: 272/CHE/2005.
7. Arup Dasgupta, P. Kuppusami, Falix Lawrence and V.S. Raghunathan, P. Antony Premkumar and K.S. Nagaraja, *Mat. Sci. & Engg. A* **374** (2004) 362.

Further inquiries:
Dr. Arup Dasgupta and Dr. P. Kuppusami, Physical Metallurgy Division
Metallurgy & Materials Group, IGCAR, e-mail: arup@igcar.gov.in; pk@igcar.gov.in

Nanostructured Thin Films Of TiAlN And TiN prepared by Magnetron Sputtering

EXECUTIVE SUMMARY

Nanocrystalline thin films of titanium nitride and titanium aluminium nitride were deposited on (111) Si substrates by reactive d.c. magnetron sputtering under various nitrogen flow rates and at constant substrate temperature. The effect of nitrogen flow rate on the structural and electrical properties of TiN_x and $Ti_{1-x}Al_xN$ thin films deposited at substrate temperatures of 973 K and 773 K, respectively is investigated. While the resistivity of TiN_x films showed a minimum at a nitrogen flow rate of 5 sccm, the resistivity of $Ti_{1-x}Al_xN$ films increased with increasing nitrogen flow rate.

OUTLINE

Titanium nitride (TiN) thin films exhibit remarkable physical and chemical properties. Due to their high thermal stability, low electrical resistivity and good diffusion barrier characteristics, TiN thin films find numerous applications in microelectronics industry. But TiN coatings oxidize at temperatures ≥873 K and lose their hardness and hence are not very suitable for dry cutting and high speed cutting tools. Instead of adding further metalloids to the titanium-nitrogen composition, addition of aluminium as a substitute of titanium has produced good results concerning wear and oxidation resistance. Al atoms can substitute some of the Ti atoms in TiN lattice in various proportions and thus form $Ti_{1-x}Al_xN$ structure. The latter material not only greatly enhances the wear, thermal, and mechanical properties of the coating, but also improves its oxidation resistance. TiN_x and $Ti_{1-x}Al_xN$ thin films were deposited on (111)-oriented silicon wafers at different N_2 flow rates by reactive d.c. magnetron sputtering. The TiN_x films were prepared by sputtering a 99.99% pure Ti disc of 3 inch diameter and 2 mm thickness in a mixture of high purity argon (99.99%) and nitrogen (99.99%) plasma. The $Ti_{1-x}Al_xN$ thin films were prepared by sputtering a composite target comprised of discs of 99.99% pure Ti and Al having surface area in the ratio 2:1 in a mixture of high purity argon (99.99%) and nitrogen (99.99%) gas. In both the cases, the sputtering was carried out in a stainless steel chamber of 45 cm diameter and 20 cm height using a Mighty MAK, US sputtering gun of 3 inch diameter.

The deposition rates and the grain size of both types of films decreases with increasing nitrogen flow rates. The decrease in the deposition rate is attributed to differential target poisoning. The TiN_x films are polycrystalline at all N_2 flow rates and exhibit only δ-TiN phase. The $Ti_{1-x}Al_xN$ films are polycrystalline only at lower nitrogen flow rates (≤ 5 sccm). At nitrogen flow rate of 2 sccm, the $Ti_{1-x}Al_xN$ films are composed of Ti(Al)N (B1 NaCl) phase as well as Al(Ti)N (Hexagonal close packed) phase (Fig.1). At higher flow rates of nitrogen (≥10 sccm), only Ti(Al)N phase is observed because of the decreased sputtering rates of the poisoned composite target. The lattice parameter of TiN_x films initially increases with increasing nitrogen flow rates due to possible transformation from substoichiometric to stoichiometric and slightly hyperstoichiometric TiN and remains almost constant beyond 5 sccm. But the lattice parameter of $Ti_{1-x}Al_xN$ films initially remains almost constant with increasing nitrogen flow rates and starts decreasing at flow rates >10 sccm. The latter could be related to the incorporation of more nitrogen atoms through the generation of metal vacancies.

The grain size of both types of films decreases with increasing N_2 flow rates (Fig. 2). The grain size of TiN_x films decreases from 36 nm to 10 nm and the grain size of $Ti_{1-x}Al_xN$ films decreases from ~14 nm to 5 nm as the N_2 flow rate is increased from 2 sccm to 30 sccm. HREM images of TiAlN and TiN showed mostly nanocrystalline containing a high concentration of defects in the films. For instance the TiN films prepared at 673 K show dislocations and bending of lattices because of the fact that these films are formed by a non-equilibrium process (Fig. 3). Nanoindentation technique showed a hardness exceeding 20 GPa for TiN (Fig. 4) and TiAlN films prepared under optimized processing conditions. Photoacoustic measurement of the thermal properties of the films revealed that the thermal diffusivity and thermal conductivity of the TiAlN and TiN thin films is very much less than the bulk values. Results demonstrated that the thermal conductivity is drastically reduced due to increased phonon scattering for fine grained materials, particularly when the grain size is of nanometer dimensions.

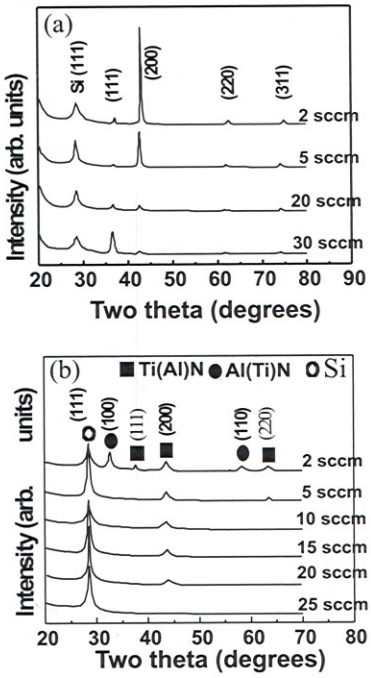

Fig. 1 : XRD patterns of (a) TiN thin films and (b) TiAlN thin films deposited under different N_2 flow rates

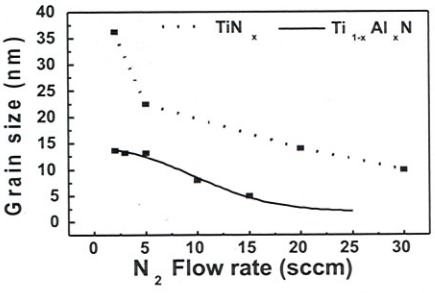

Fig. 2: Variation of grain size of TiN_x and $Ti_{1-x}Al_xN$ films with N_2 flow rate.

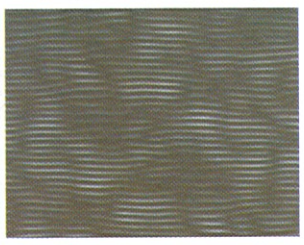

Fig. 3 : HREM of TiN film formed at 673 K showing a high concentration of dislocations

MAGNETRON SPUTTERING PROCESS

The sputtering deposition process is performed in a vacuum chamber where argon atoms are ionized and accelerated to strike a target material, for example, aluminium. Coating material enters the vapor phase through a physical process (momentum exchange) rather than by a chemical or thermal process. The argon atom dislodges aluminum atoms when it strikes the target, then these ejected aluminum atoms strike the steel part to be coated, and this continuous process eventually applies a dense aluminum coating to the steel part. Figure 5 depicts the basic sputter technology. By simply adding a magnetic field to the target material, the sputter rate can be greatly increased. The magnetic field causes more of the ionized argon atoms to strike the target and this increases the amount of aluminum atoms being ejected. This process is called magnetron sputtering.

Thin films prepared by sputtering exhibit different structure and properties depending on the growth conditions and process parameters. Due to their several potential applications, an understanding of the structure and properties of the TiN and $Ti_{1-x}Al_xN$ thin films as a function of deposition parameters is very important. Hence a comparative study on the influence of nitrogen flow rate on the structural and mechanical properties of TiN_x and $Ti_{1-x}Al_xN$ thin films prepared by DC magnetron sputtering has been carried out.

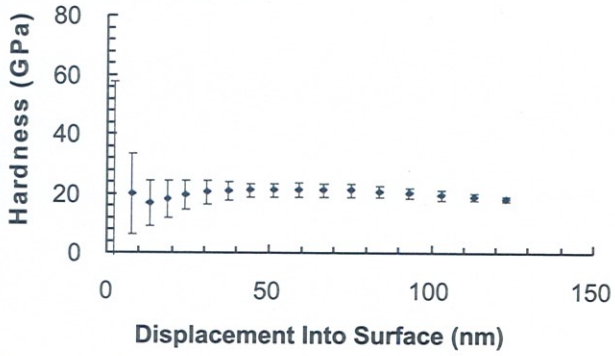

Fig. 4 : Nanohardness as a function of penetration depth for TiN films

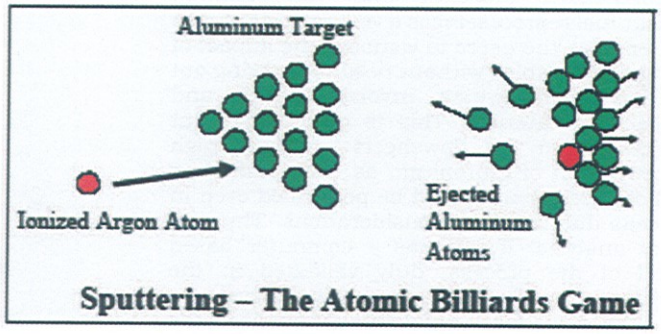

Fig. 5 : Schematic of sputtering process

ACHIEVEMENT

It has been demonstrated that hard coatings of TiAlN and TiN could be prepared under optimum processing conditions using magnetron sputtering. The preferred orientation of these films could be altered by the appropriate flow rates of nitrogen. The study also suggested that these films contain nanocrystals and a high density of defects especially when they re formed at low deposition temperatures. The thermal conductivity of these films decreased considerably compared to those of bulk materials due to a reduction in grain size. The lower thermal conductivity of these films are technologically important and are best suited for heat resistance coating and thus these films might enhance tool life, and optimum machine performance.

PUBLICATIONS ARISING OUT OF THIS STUDY AND RELATED WORK

1 A. Albert Irudayaraj, P. Kuppusami, R. Thirumurugesan, E. Mohandas, S. Kalainathan, and V.S. Raghunathan, *Surface Engineering*, **23** (2006) 7.

2. A. Albert Irudayaraj, R. Srinivasan, P. Kuppusami, E. Mohandas, S.Kalainathan, and K. Ramachandran, *Intnl J Mod. Phys B.* **21** (2007) 3889.

3. A. Albert Irudayaraj, P. Kuppusami, R. Thirumurugesan, R. Srinivasan, E. Mohandas, K. Ramachandran, and S. Kalainathan, Intl. Symposium of Research Students on Materials Science and Engineering, Dec 18-20, (2006) IITM, Chennai.

Further inquiries:
Dr. P. Kuppusami and Shri E. Mohandas, Physical Metallurgy Division
Metallurgy and Materials Group, IGCAR, e-mail: pk@igcar.gov.in ; mohandas@igcar.gov.in

Modeling of Nuclear Solvent extraction: Issues and Indigenous Development

EXECUTIVE SUMMARY

An indigenous computer code SIMPSEX (SIMulation Program for Solvent EXtraction) for 30% TBP system for simulation of high plutonium PUREX flowsheets has been developed. SIMPSEX uses the activity coefficients as opposed to empirical models of SEPHIS code and performance of the published SEPHIS code was found to be inadequate for high plutonium flowsheets (Pu/(U+Pu)= 0.25 to 0.75) SIMPSEX code was exclusively used for analysis of solvent extraction part of high plutonium CORAL flowsheet. This code was used to analyze the stage profiles of Pu, U and HNO_3 in extraction and strip contactors for all the cycles of operation except for the electrolytic partitioning cycle and nevertheless it can handle partitioning step with externally generated U(IV), Hydroxylamine nitrate(HAN) and acetohydroxamic acid (AHA). Few hundred simulations were done for finalizing the feed concentrations, variations in flow rates, feed point locations etc. for safe operation.

OUTLINE

Comprehensive modeling and simulation in nuclear fuel reprocessing is a very important step as it enables the users to visualize the impact of change in variables without need of carrying out an experiment which involves fissile and radioactive materials. This is quite important particularly in the flowsheets involving high concentration of plutonium, as each and every kind of experiment cannot be performed even in hot-cells due to safety considerations. Thus for safety analysis, if one has a computer based model of the process, duly validated in the operating range for various published flowsheets with the required degree of confidence, the computer simulation experiments can be performed with out any risk or consequences thereof.

The different types of reactor fuels require different type of reprocessing flowsheets. The extractant for nuclear solvent extraction process (also called PUREX process) is universally accepted as tri-n-butyl phosphate (TBP), diluted with an aliphatic diluent for favorable physical properties, the actual process option used for reprocessing spent PHWR fuels is quite different than the option used for reprocessing FBR fuels. The increased content of plutonium in FBR fuels poses problems like criticality and related size limitations, Pu(IV) polymerization and third phase formations. High burnup attained and relatively short cooling of the FBR fuel poses additional problems of intense activity and fast degradation of solvent and diluent. Thus for FBR fuel reprocessing, the chosen contactor must have a very short time of phase contact as well as high contactor efficiency. Since feed plutonium concentrations are quite high, there should be excellent recovery and even during process upsets, plutonium losses in the raffinate must be under control limit. Due to possible variation in stream flow rates, the plutonium accumulation and problems like third phase formation and possible criticality should be avoided in all the conditions. With this constraint computer code development and validation should be carried out.

Fig.1 shows a typical analysis of CORAL flow sheet cycle. Fig.2 shows reduction in the Pu(IV) distribution coefficient due to presence of acetohydroxamic acid in the PUREX system. Fig.3 shows a conceptual; step for macro-level U-Pu separation based on complexant based U-Pu separation.

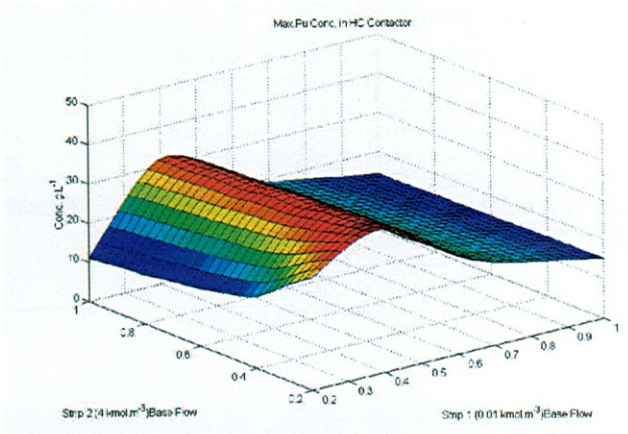

Fig. 1: Variation of maximum Pu concentration in side the HC contactor: SIMPSEX results for 70%U+30%Pu flowsheet

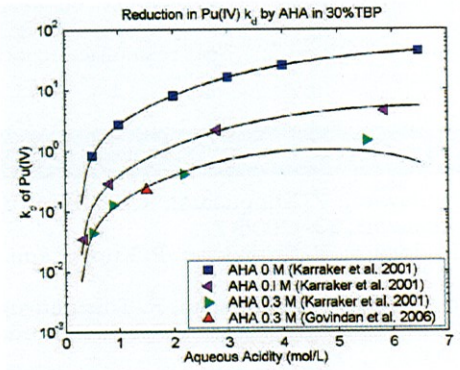

Fig. 2: Comparison for Pu(IV) distribution coefficients , in presence as well absence of Acetohydroxamic acid (AHA). Points are reported experimental values. Lines are simulated values from model developed at IGCAR

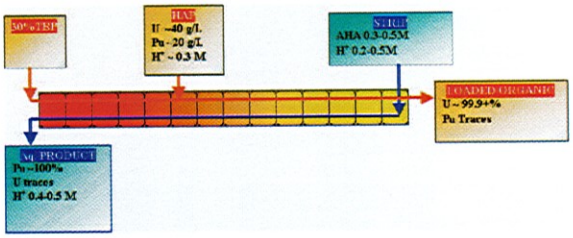

Fig. 3 : Proposed schematic flowsheet for U-Pu Separation for FBR feed compositions

■ EVOLUTION OF MODELS FOR PUREX DISTRIBUTION EQUILIBRIA

PUREX process distribution equilibria models are classified into two distinct classes-models based on black-box approach and models based on the reaction schematics and stoichiometry. The first class consists of the models based on purely empirical approach. In these type of models, a complex numerical correlation (with out any basis to stoichiometry) is fitted to the experimental data either generated in-house or from the PUREX data bank with help of non-linear regression and estimation techniques. The distribution coefficient correlations are rudimentary in nature and results have potential inaccuracy for nitric acid distribution as well as high plutonium regions of operation. The models pertaining to the second class are based on the reaction schematics and stoichiometry and are written in terms of molal or molar concentrations as thermodynamic activities of all the species involved are not directly measurable quantities.

Depending upon the treatment of aqueous phase and organic phase activity coefficients stoichiometry based models can be defined in four-ways-

(i) Classical approach I (ideal behaviour): In this approach, activity coefficients are assumed to be constant and unity but it suffers from two major shortcomings- applicability only to dilute solutions and assumption of ideal conditions (unity activity coefficients) for shaping this form of equation is theoretically incorrect as it is non-ideality, which generates separation between the components.

(ii) Classical approach-II (Non-ideal behaviour): In this approach, it is acknowledged that Liquid Liquid Extraction (LLE) system is highly non-ideal and effect of activity coefficients is embedded in the reaction parameter It was persuaded at Karlshruhe and almost simultaneously at ORNL, (also termed as SEPHIS Model 1). However it did not fit to vast extraction data and Department of Energy (DOE) researchers replaced this model with models based on non-linear analysis (SEPHIS Ver.2, (1973), Ver.3 (1975) and Ver.4 (1980). The published models (SEPHIS Ver.2 and Ver.3) could not account for the presence of macro plutonium concentrations. In the SEPHIS model Ver.4, it is stated that a empirical correction factor is applied on the predicted results from SEPHIS model Ver.3. However, there is no information in the literature on the form of "correction equation". No new information has been published in open literature on fate/status of the SEPHIS models.

(iii) Neo-Classical approach (Non-ideal behaviour) In this approach, organic phase activity coefficients are assumed constant (citing the non-availability in the literature) where as aqueous phase activity coefficients are considered. The constant k is evaluated by regression between k_D and the system compositional parameters. The work by ANL researchers (1988) and Japanese researchers (1997) are example of this approach. These models suffer from the empirical treatment of organic phase conditions.

(iv) Quasi-Thermodynamical Approach (Non-ideal behaviour) In this approach, organic phase activity coefficients are assumed not to be constant. Aqueous phase activity coefficients are considered for the key solutes. From the limited available data, a ratio of organic phase activity coefficients is calculated and correlated as a function of system compositional variables.

■ ACHIEVEMENT

Indigenously developed SIMPSEX Code was extensively used for analysis of CORAL and Demonstration Fuel Reprocessing Plant (DFRP) flowsheets for stage-profile analysis with SIMPSEX and these results were used in the calculations of aqueous weir dimension of CORAL & DFRP CORAL flowsheets were simulated with SIMPSEX and were analyzed for several combinations of operating variables. SIMPSEX was used in simulation of crucial U-Pu partitioning by several methods like partial, externally generated U(IV) based reductive as well as pre-reduction, HAN based and based on the simulation studies, a AHA based alternate partitioning flowsheet has been proposed.

■ PUBLICATIONS ARISING OUT OF THIS STUDY AND RELATED WORK

S. Kumar and S.B. Koganti, Report No. IGC-284 (2006).

Further inquiries:
Shri Shekhar Kumar, Reprocessing Research and Development Division
Reprocessing Group, IGCAR, e-mail: shekhar@igcar.gov.in

Thermodynamic Modelling of Molten Salt Electrorefining Process

EXECUTIVE SUMMARY

Molten salt electrorefining is the pyrochemical process for reprocessing metallic fuels. Modelling plays an important role in the development of the electrorefining process. A computer code, PRAGAMAN, has been developed for the simulation of the electrotranport behaviour of the various metal constituents during the electrorefining process. The code is based on the thermodynamic equilibria among the metals and chlorides of actinides, minor actinides and fission products in the anode/cathode and electrolyte salt respectively. The code enables incorporation of various combinations of anodes and cathodes such as liquid cadmium anode/cathode and solid anode/solid cathode and the possible conditions with respect to saturation of a given element in liquid cadmium.

OUTLINE

Modelling the molten salt electrorefining process is an integral part of the development programme for the process. Various types of models for the electrorefining have been developed around the world using equilibrium thermodynamics, finite element method and fluid mechanics based methods. The approach using equilibrium thermodynamics takes into consideration mass balance requirements and at the Gibbs energy of formation of various species in the molten salt and the anode/cathode. A typical equilibrium reaction taking place in the electrorefining cell among a pair of elements, say, U and Pu and their chlorides is as shown below

$$Pu + UCl_3 \rightarrow U + PuCl_3$$

Similar reactions could be envisaged among the pairs of elements encountered in the spent fuel and their chlorides. Under the special restricted equilibrium conditions prevailing in the cell, the ratios of the activities of two elements in two phases in equilibrium are equal rather than the activities themselves being equal as in classical equilibrium. The equilibrium constant relationship is evaluated which involves activity coefficients of UCl_3 and $PuCl_3$ in the molten salt and in liquid cadmium. The total amount of solute metal at any step of electrotransport will remain constant even though the composition at the anode and cathode will change as equilibrium is established. Mass balance equations are established for various solute elements present in the electrorefiner. The equations are solved for the unknown compositions of U, Pu and other elements at anode, cathode and in the salt phase. In case of only U and Pu electrotransport, PRAGAMAN code has 16 different subroutines to solve the different sets of nonlinear equations depending on the conditions that could be encountered during the electrorefining cell. At each step of electrotransport, the condition at the anode and cathode can be any of the 16 different possibilities. The subroutines are called into an electrotransport loop which subsequently solves the nonlinear equations depending on the composition of the solute elements and salt phase at anode and cathode.

The computations have also shown that when both the liquid cadmium anode and cathode are unsaturated with respect to both U and Pu, then both get electrotransported at equal rates. That is, Pu/U ratios at the anode and cathode remain constant and equal under these conditions. However, when saturation with respect to one element in any one of the phases occurs, predominant transport of that element prevails.

As an example, a typical Pu profile is shown in Figure 2 where the feed conditions are such that U is initially saturated at the Cd anode. Therefore the rate of electrotransport of U or depletion rate from the Cd anode is faster than that for Pu. At around 16% electrotransport, U gets saturated at the cathode and this condition of saturation with respect to U at both anode and cathode prevails until 71% electrotransport. Until 71% electrotransport, there is no Pu electrotransport and therefore the amount of Pu at anode and cathode remains constant. After 71% electrotransport when U gets unsaturated at the anode, Pu again gets electrotransported to the Cd cathode.

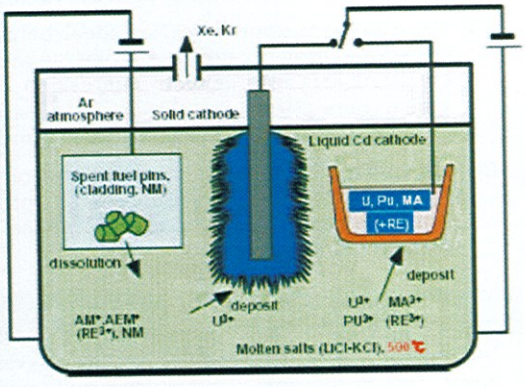

Fig. 1 : Schematic diagram of molten salt electrorefining process

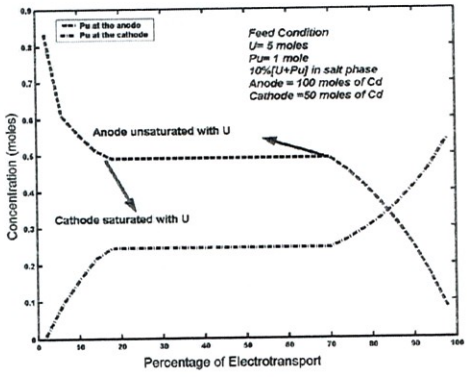

Fig. 2 : Simulated profile of Pu electrotransport from liquid Cd anode to liquid Cd cathode

ADDITIONAL INFORMATIONA ABOUT THE NUMERICAL METHODS USED IN THE MODEL

In the case of U and Pu only, there are 16 possible conditions with respect to the different possible combinations of liquid cadmium as anode/cathode and solid mandrel anode/cathode. All the different possibilities lead to different sets of nonlinear equations the degree of nonlinearity of which varies depending on the number of unknowns. The saturation conditions of U and Pu at both liquid cadmium anode/ cathode lead to sets of linear equations involving solution of sparse matrices. Conjugate Gradient method and Nelder Mead optimization method are some of the numerical methods used in the solution of nonlinear equations.

TYPICAL ELECTROTRANSPORT BEHAVIOUR TO A SOLID CATHODE

In the electrorefining process, when a solid cathode is used, deposition of U alone takes place due to the higher thermodynamic stability of $PuCl_3$ compared to UCl_3. However, when the ratio of $PuCl_3$ to UCl_3 in the salt increases above 2, then Pu deposition will also occur.

The code enables computations for these cases also. The simulated electrotransport behaviour of U and Pu to a solid cathode is shown in Figure 3. It is seen from the figure that U alone gets transported until 65% of electrotransport. As U alone gets deposited, the ratio of $PuCl_3$ to Ucl_3 increases. When the ratio reaches a value of 2, which is at 65 % electrotransport in this case, Pu also starts getting deposited at the cathode.

This deposition behaviour at solid cathode enables one to process the irradiated U-Zr blanket from a metal fuelled FBR. The blanket contains about 2% of Pu produced by breeding. Processing using a solid cathode removes U selectively, thus enriching the anode with respect to Pu. When the concentration of Pu in the anode reaches a value of 20-25%, roughly that of the core fuel, the processing is stopped and the anode constituents are mixed with spent core fuel from the reactor, for pyroprocessing using a liquid cadmium cathode.

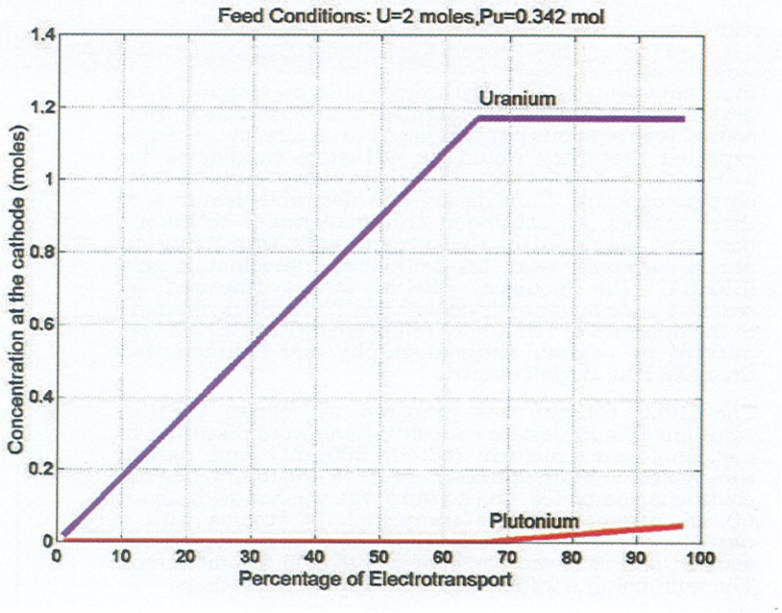

Fig. 3: Simulated electrotranport behaviour of U and Pu to a solid cathode

THERMODYNAMIC BASIS FOR THE SEPARATION OF ELEMENTS DURING ELECTRO PROCESS

The separation is achieved by exploiting the difference in the thermodynamic stabilities of the chlorides of U, Pu and the fission products. The highly electropositive alkali, alkaline earth and rare earth elements, whose chlorides are very stable, are easily oxidized but are difficult to reduce. The noble metals whose chlorides are the least stable, do not get oxidized and stay as metals in the anode itself. U and Pu whose chlorides are of intermediate stability are converted to their chlorides, get electro transported to the cathode where they are reduced and deposited as metals.

ACHIEVEMENT

Our own simulation code has been developed which can predict the transport behaviour for the various conditions that could be envisaged to prevail during the electro-refining process.

PUBLICATIONS ARISING OUT OF THIS STUDY AND RELATED WORK

1. Suddhasattwa Ghosh, B.Prabhakara Reddy and K.Nagarajan, Report No. IGC-278.
2. Suddhasattwa Ghosh, B.Prabhakara Reddy and K.Nagarajan, THERMANS 2006, University of Rajasthan, Jaipur.
3. K.Nagarajan, T.Subramanian,B.Prabhakara Reddy, P.R.Vasudeva Rao and Baldev Raj, *Nucl. Technol.* (In Press).

Further inquiries:
Dr. K. Nagarajan, Fuel Chemistry Division
Chemistry Group, IGCAR, e-mail: knag@igcar.gov.in

Determination of Lanthanides in Uranium Matrix of Pyroprocessing Samples using Reversed Phase HPLC

EXECUTIVE SUMMARY

A novel HPLC based separation technique was developed using Bis-2-ethylhexyl succinamic acid (BEHSA) modified reversed phase support for the isolation and quantitative determination of lanthanides as a group in uranium matrix. Hundreds of samples obtained from pyrochemical reprocessing of molten salts containing lanthanides in uranium matrix (e.g. 1: 20,000) were separated and determined within 7 minutes using the coated support. The advantage of the present HPLC technique lies in the simultaneous separation and assay of total lanthanides and uranium whereas other analytical methods necessitate the separation of uranium matrix prior to lanthanide assay.

OUTLINE

In recent years, N, N-dialkyl amides have been shown to be promising candidates for actinide recovery. Since their solubility in aqueous phase is found to be very low, it can be expected that they would be attractive candidates for actinide separations employing extraction chromatography. Considering the desirable features of these amides, an extraction chromatographic technique has been developed in the present work with using an amido carboxylic acid, bis-2-ethylhexyl succinamic acid (BEHSA). The modifier, BEHSA was synthesized by reacting succinic anhydride with bis-(2-ethylhexyl) amine in the presence of THF under reflux condition. BEHSA was purified by column chromatography and characterized using FT-IR and NMR spectra.

The HPLC column was prepared as follows: BEHSA solutions of appropriate concentrations were dissolved in methanol-water mixture (60:40, 500 mL) and passed through the column at a flow rate of 0.5 mL/min. When the coating is completed, the column was washed with about 60 mL water. After the completion of studies with a particular modifier concentration, the coated support was washed and removed completely with 100 mL methanol. The same column was reused for subsequent coatings.

The retention for uranium increases with increase in BEHSA content and uranium could be well resolved from lanthanides for a BEHSA concentration kept at 1 mM and above. The influence of mobile phase pH and its concentration on the retention behavior of U(VI) and lanthanides was investigated. Separation of U from lanthanides as well as from Th is shown in Fig.1.

A 5 mM BEHSA modified support was chosen for the quantitative analysis. This is for accommodating lanthanides during analysis in the presence of large quantities of uranium. A solution of α-HIBA, 0.1 M, pH: 2.5 was used for the elution. Uranium (5-200 μg/mL), and lanthanide (2-50 μg/mL) samples were separately injected for preparing the calibration plots (r^2=0.999).

The efficiency of the pyrochemical process is evaluated by analysing cathode deposit and this requires analysis of lanthanides in low levels in uranium matrix. Based on the investigations with BEHSA modified C_{18} support, an advanced characterization method has been developed for the rapid and accurate analysis of lanthanide elements in uranium matrix (typical ratio, 1: 20,000). About 200 pyrochemical samples were analysed for their lanthanide contents in uranium matrix. Uranium contents of these samples were also determined directly or with suitable dilution. For e.g. a separation of Nd (1 ppm) from U matrix (19.8 mg/mL) is shown in Fig.2. The results of these investigations were compared with standard analytical methods. For e.g. in one study, the lanthanide contents were measured using ICP-OES after removing uranium matrix with solvent extraction and the results were compared with HPLC. The concentration of uranium was also measured by standard analytical method, Davies and Gray and compared with HPLC. The lanthanide as well as uranium values were found to be in good agreement (within ±2%). These studies established that the HPLC method is fast, reliable and can provide accuracy required for a typical regular analysis. It is to be noted that the HPLC technique does not require pre-separation of uranium for the assay of lanthanides whereas it is a pre-requisite with other analytical techniques.

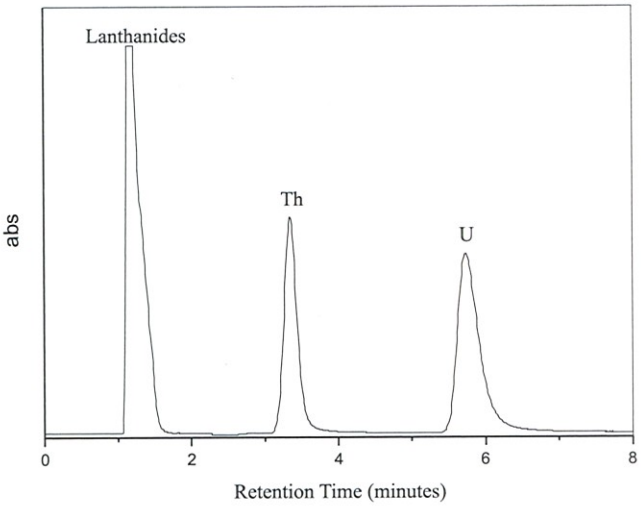

Fig. 1 : Rapid separation of Lanthanides, Th and U from BEHSA coated column

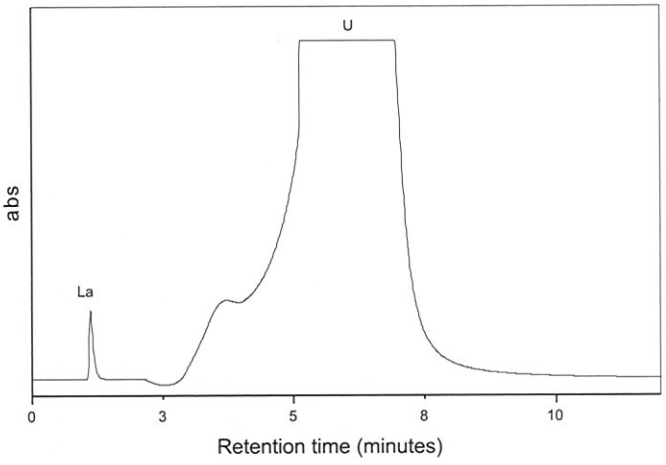

Fig. 2 : Separation of La from U matrix of pyro chemical sample using BEHSA coated column

ADDITIONAL INFORMATION ABOUT HIGH PERFORMANCE SEPARATION USING HPLC

High Performance Liquid Chromatography (HPLC) has revolutionized as a powerful separation and analytical tool in the field of chemistry, biology, medicine, pharmacy, chemical technology, food science and many more. Major advantages of HPLC are its ability to provide rapid and high performance separations. Reversed phase HPLC became powerful technique for separation of lanthanides and actinides. In this technique, a suitable extractant is generally coated onto the reversed phase support for separation of individual metal ions from mixture. The major advantages of this technique include reproducibility, high efficiency separation and easy regeneration of support.

PREFERENTIAL RETENTION OF URANIUM OVER LANTHANIDES FROM THE MODIFIED SUPPORT

Fig.3 shows various species of hydroxyisobutyrate complexes of uranium as a function of pH of α-HIBA (0.1 M). In the case of uranium, the dominant species at various pH's are (i) anionic species, $[UO_2 (IBA)_3]^-$ at pH 3.5 and above, (ii) the neutral species, $[UO_2 (IBA)_2]$ at pH 3 and (iii) the positively charged species at pH 2.5. Hence the lower retention for uranium at pH 2.5 is attributed to the sorption of dominant positively charged species because of its lower hydrophobicity with a single HIBA moiety. The increase in retention at pH 3 is attributed to the sorption of mainly neutral $[UO_2(IBA)_2]$ whereas its further increase beyond pH 3 is attributed to the sorption of the predominant anionic complex. Higher retention for anionic species is attributed to the fact that the resultant charge distribution is sufficiently diffused that the complex exhibits a degree of hydrophobicity that permits sorption onto the support. However, the lanthanide-hydroxyisobutyrate complexes are weakly held on to the support, suggesting that these complexes are interacting mainly through hydrophobic interaction only.

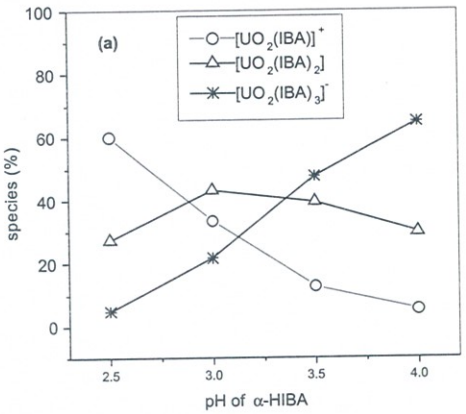

Fig. 3 : Speciation of uranium-HIBA complex as a function of pH

BRIEF DESCRIPTION OF THEORETICAL BACKGROUND

The pK_a of amido carboxylic acid, BEHSA was measured and found to be 4.9. The calculation indicated that BEHSA ionises to an extent of only 0.4, 1.2, 3.8 and 11.2 % at pH 2.5, 3, 3.5 and 4 respectively. Thus BEHSA does not dissociate significantly at a mobile phase pH less than 4 where most of the experiments were carried out in the present work. BEHSA modified support retain uranium and lanthanide hydroxyl isobutyrate complexes through the carbonyl group coordination also in addition to its hydrophobic interaction. However, it is understood that at pH 4 and above, BEHSA also influences on the retention of both uranium and lanthanides through its COO^- moiety. It is observed that the dissociation of α-HIBA (pK_a: 3.77) at pH 4 is about 63% which is much higher than that of BEHSA.

ACHIEVEMENT

The BEHSA modified support offered an excellent base-line separation of uranium from lanthanides. The BEHSA coated support was exploited for the rapid separation of lanthanides from uranium, which offered high-resolution separation. Lanthanides could be accurately estimated in the presence of about 20,000 times of uranium. The advantage of the present HPLC technique lies in the simultaneous separation and assay of total lanthanides and uranium whereas other analytical methods necessitate the separation of uranium matrix prior to lanthanide assay.

PUBLICATIONS ARISING OUT OF THIS STUDY AND RELATED WORK

1. Ch. Siva Kesava Raju, M.S. Subramanian, N. Sivaraman, T.G. Srinivasan and P.R. Vasudeva Rao; *J. Chromatography A*, **1156** (2007) 34.
2. S. Vandarkuzhali, P. Venkatesh, S. Ghosh, G. Seenivasan, B. Prabhakara Reddy, N. Sivaraman, T. Subramanian and K. Nagarajan; *J. Electroanal. Chem.* **611** (2007)181
3. Ch. Siva Kesava Raju, N. Sivaraman, M. S. Subramanian, T.G. Srinivasan and P.R. Vasudeva Rao; "HPLC-2006" - 30th International Symposium on High Performance Liquid Phase Separations and related techniques, June 17-23, 2006 San Francisco, USA.
4. S. Vandarkuzhali, P. Venkatesh, S. Ghosh, G. Seenivsan, B. Prabhakara Reddy, N. Sivaraman, T. Subramanian and K. Nagarajan, International Pyroprocessing Research Conference, August 2006, Idaho National Lab, USA.

Further inquiries:
Dr. T.G. Srinivasan, Fuel Chemistry Division
Chemistry Group, IGCAR, e-mail:tgs@igcar.gov.in

Synthesis of Red-Oil and Related Studies

EXECUTIVE SUMMARY

Runaway reaction between TBP and Nitric Acid at elevated temperatures and resultant red oil formation were studied in a High Pressure High Temperature Chemical Reactor. The work aims at development of a mathematical model describing the red oil event and enabling its computer simulation. Several single–phase and two-phase experiments (closed vent) at different concentrations of HNO_3 were conducted. A commercial red oil incident (closed vent) was simulated and it resulted in the rapid pressurization of the order of >1000 psi/min.

OUTLINE

Liquid-liquid extraction (LLE), also known as solvent extraction (SX), is a cost effective industrial process to recover, purify, or separate metals. Although several solvents can effectively extract uranium, plutonium, or thorium from acid solutions, the commercially chosen solvent is only Tri-butyl phosphate (TBP). Most solvent extraction operations in the PUREX process, used to recover valuable material from spent nuclear fuel with TBP have been performed safely for decades. Similarly there is apprehension that runaway reactions of nitric acid with industrial solvent extraction solvents mixtures are potentially damaging in nature as evident from the explosion occurred in BNFL in early seventies which caused closure of the plant as well as the sealing the fate of BUTEX (diBUTyl carbitol EXtraction) process for nuclear fuel reprocessing. However during evaporation of wastes for reduction of waste volumes, there is a distinct possibility that complexes of TBP and nitric acid can undergo runaway reaction leading to excessive nitration resulting in forming of red-coloured liquids, commonly known as "red oil". Red-oil, having nitration product of hydrocarbons as a major constituent, is prone to rapid oxidation, leading to rapid pressurization resulting in containment failure. The gaseous products includes N_2, CO, CO_2, NO, N_2O. Liquid products include di-butyl phosphoric acid, butyl nitrate and water. Gaseous products are the reason for the violent explosion.



Fig. 1 : Synthesized Red oil at IGCAR

In fact, there have been several instances of explosive-type reaction with TBP/nitric acid systems in industrial processes. The latest occurrence was at TOMSK-7 facility in Russia at which faulty operations is believed to have resulted in the runaway of a solution of considerable volume of TBP inadvertently saturated with strong nitric acid and heated resulting in explosive failure of the storage vessel and subsequently blowing out a wall of the reprocessing building. The damage to the building is believed to have been a result of the deflagration of flammable gases, most likely butene and CO, released from the initiation explosion.

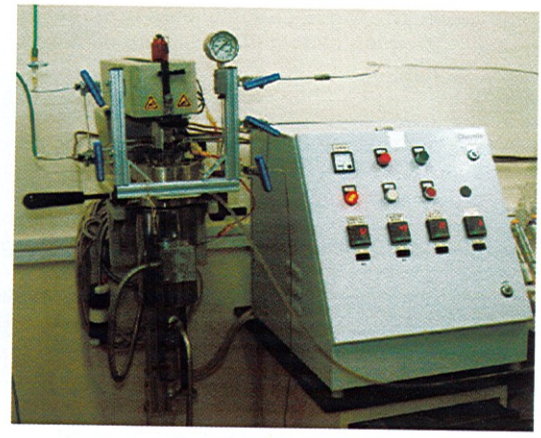

Fig. 2 : A view of High-Pressure Autoclave Setup

Controls for prevention or mitigation of a red oil explosion are generally categorized as controls for temperature, pressure, mass and concentration. Maintaining a temperature of less than 130°C is generally accepted as a means to prevent red oil explosions. Sufficient venting serves to keep pressure from destroying the process vessel, while also providing the means for evaporative cooling to keep red oil from reaching the runaway temperature. Mass controls utilize wash with diluent or kerosene followed by enhanced settling in decanters or hydroclones to remove organics from feed streams entering process equipment capable of producing red oil. Limiting the total available TBP is another mass control that mitigates the consequence of a red oil explosion by limiting its maximum available explosive energy. Finally concentration control can be utilized to keep the nitric acid below 10M. None of the controls should be used alone; rather they should be used together to provide effective defense in depth for prevention of a red oil explosion.

Fig.1 shows a sample of synthesized red-oil. Fig.2 shows a view of high-pressure autoclave (Max. allowable working pressure (MAWP) of 227 bars and max. allowable working temperature (MAWT) of 445 °C) installed at IGCAR for study of runaway reactions.

■ WHAT IS RED-OIL?

In Reprocessing of fast reactor fuels, 30% TBP solvent is used. This solvent has a small solubility in the aqueous phase. During concentration of the process solutions by evaporation route, if these trace level organics are present, above 130 oC, a runaway reaction between TBP and nitric acid is initiated leading to rapid pressurization and finally in containment failure if proper venting is not provided. Intermediate product of this runaway reaction is nitrated organic solvent which is red in color. Hence this event is termed as red-oil formation.

■ RED-OIL SYNTHESIS EXPERIMENTS

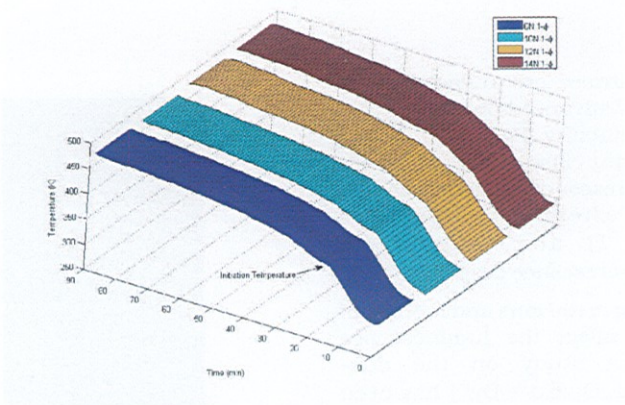

Fig. 3: Comparison of single-phase experiments for temporal temperature profiles

Fig.3 shows temporal variation of pressure and temperature inside reactor under different operating conditions.

The main results from the Red-oil related work done at Reprocessing Research and Development Division are as follows-

- TBP-Nitric acid runaway reaction starts only at the temperatures at or greater than 130 °C (403.15 K). This was found valid for all the runs either single or two phase system.
- Once the runaway reaction starts, the heating rate increases due to auto catalytic reactions involved and pressure starts to shoot up. This feature can be used to detect on-set of runaway reactions and for setting of process interlocks to prevent energetic reaction to happen.
- The pressure generated per g or per mL of the Feed TBP is a function of several variables like acidity of the equilibration, amount of acid present in the system during reaction and the temperatures prevailing during reactions.
- The most important finding is that for prevention of red-oil formation, 10 M limit as earlier proposed in the literature is strictly not valid as found from the recent experiments carried at RR&DD. Red-oil event was observed in the experiments with nitric acid as low as 2 M concentrations. Thus safety guidelines based on the classical literature are obsolete. New guidelines for the red-oil –safety are required.

■ ACHIEVEMENT

Red oil was synthesized for the first time in India and its physical properties were determined. It was established that presence of metallic nitrates was not essential for red-oil formation as thought earlier. The limit on acid concentration was also found to be considerably less than the conventional values. In fact in these experiments, red-oil could be formed even at 2M aqueous acidity. Various single-phase as well as two-phase experiments have been completed and further studies are in progress.

Further inquiries:
Shri Shekhar Kumar, Reprocessing Research and Development Division
Reprocessing Group, IGCAR, e-mail: shekhar@igcar.gov.in

Long Afterglow Phosphors

EXECUTIVE SUMMARY

Phosphorescence (afterglow) refers to the light emission at room temperature from a material that persists after removal of the excitation source. A long glow green phosphorescent material based on strontium aluminates has been developed. This indigenous phosphor once irradiated with visible light exhibits intense emission for hours in absence of any exciting light. This material can act as a path finder in industrial environment during black out conditions. It can also be used to find out different components in dark if these are painted with this material. The enhanced light output of this phosphor is at par with the available international commercial phosphors.

OUTLINE

Phosphors based on oxide matrices are attractive host materials for the development of advanced phosphors due to their ease of synthesis and stability. Rare earth doped aluminates serve as an important class of phosphors for fluorescent lamp and phosphorescence applications. We have developed a long afterglow phosphors $Sr_4Al_{14}O_{25}:Eu^{2+},Dy^{3+}$ (Fig. 1) and studied its photoluminescence and phosphorescence properties.

The stoichiometry of the reacting metal ions and method of preparation can significantly affect the luminescence properties of a phosphor. A study on the non-stoichiometry behavior of ($Sr_4Al_{14}O_{25}:Eu^{2+}$, Dy^{3+}) has been carried out to understand the mechanism of phosphorescence phenomenon in aluminates and develop a Long After Glow Phosphor. The stoichiometry was varied by taking different Sr/Al molar ratio. Photoluminescence intensity of both the strontium deficit and rich phosphors was enhanced whereas no definite correlation was observed between the afterglow intensity and non-stoichiometry. Notably the photoluminescence emission maxima were either blue or green shifted in case of non-stoichiometric phosphors whereas the afterglow emission maxima were not affected by the non-stoichiometry. Substitutional effect of divalent cations (Ca^{2+},Ba^{2+}) were also studied. A white afterglow material was formed during the synthesis in the presence of higher calcium concentration. (Fig. 2) This phosphor emits two photons at 440 nm and 530 nm and the blend of these light produced a white afterglow emission. Presence of silver ions in this host interestingly, enhanced the afterglow intensity nearly 10 times but no significant change in the Phosphoryl or After Glow Luminiscence emission intensity was observed in the presence of sodium. Addition of silver enhanced significantly the afterglow intensity by decreasing the trap depth and increasing the trap density by more than an order of magnitude.

The strontium aluminate phosphor was synthesized via ceramic route and combustion synthesis route. The photoluminescence and afterglow emission were compared. (Fig. 3) The afterglow intensity of phosphor synthesized through ceramic route and combustion route were comparable. However, the particle size of combustion synthesis route was in the order of nanometers.

We have also studied barium aluminate doped with cerium/manganese prepared through solid state reaction method. It exhibited strong photoluminescence. Substitution of barium by calcium or strontium has remarkably enhanced the cerium luminescence. Energy transfer from cerium to manganese was observed and the luminescence was enhanced by more than two orders of magnitude. Substitution by other divalent ions such as Ca^{2+}/Sr^{2+} in place of Ba^{2+} enhanced the photoluminescence intensity by three times.

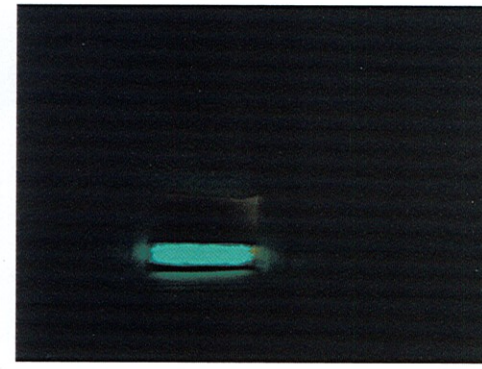

Fig. 1 : Afterglow emission from $Sr_4Al_{14}O_{25}:Eu^{2+},Dy^{3+}$ at 490 nm



Fig. 2 : As synthesized phosphor through combustion synthesis

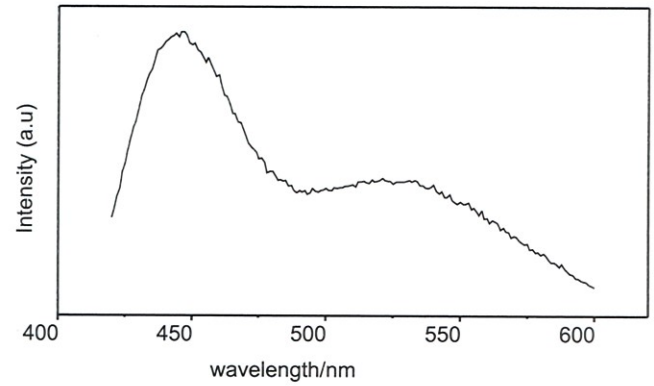

Fig. 3 : Afterglow emission of white afterglow phosphor ($Sr_4(Ca)Al_{14}O_{25}:Eu^{2+},Dy^{3+}$)

■ ADDITIONAL INFORMATION ON PHOSPHORS AND PHOSPHORESCENCE

This material can be painted on switch panels in hospitals, homes and industrial work places so that in case of power trip the switch concerned can be switched off to avoid damages to the appliances due to possible surge current when the power returns.

■ COMBUSTION SYNTHESIS

The solid-state reaction route has several shortcomings such as prolonged reaction time, larger grain growth, poor homogeneity and it could be mitigated by alternate routes offered by wet-chemistry. The salient features of these methods are that the starting materials can be mixed at molecular-level and temperatures for forming the products are reasonably low as compared to conventional solid-state reactions. For any combustion reaction to take place, a fuel and an oxidizer are necessary. When the mixture of fuel and oxidizer is heated the mixture grows in to a foamy frothy occupying the entire reaction vessel and then gets self ignited followed by combustion. It is an exothermic reaction that occurs with evolution of heat. Once ignited the energy necessary for combustion reaction is being supplied from the reaction itself, and hence it is called as Self-propagating High temperature synthesis. Phosphors prepared by the combustion method have low density and appear fluffy. Ultra fine particles are produced through this process due to the evolution of gases. As more gases are released the agglomerates are either not formed or disintegrated in to fine particles.

■ BRIEF DESCRIPTION OF THEORETICAL BACKGROUND

The afterglow luminescence occurs due to the thermally stimulated recombination of trapped charged carriers. Upon UV or visible light irradiation, the charge carriers (electron and holes) are formed. These carriers are trapped in the meta-stable traps. Due to the thermal energy available at room temperature these charge carriers are slowly released from the traps. Subsequently, they undergo recombination near a luminescence center releasing energy. The energy released is then transferred to a dopant ion ((e.g.) Eu^{2+}) which in turn gets excited. This excited Eu^{2+} emits green light during its de-excitation. The observed delay in emission (i.e) the afterglow is due to time the trapped electrons spend in meta-stable states before returning to the luminescence centers.

■ ACHIEVEMENT

Commercially available afterglow strontium aluminate phosphors are proprietary materials and hence the exact composition and phase responsible for its long glow is not known. The indigenous phosphor developed by us gives an equivalent intense emission and its afterglow persistence time is comparable to that of the commercial ones. This phosphor irradiated by room light/sunlight glows for hours together in the dark in absence of any excitation.

■ PUBLICATIONS ARISING OUT OF THIS STUDY AND RELATED WORK

N. Suriyamurthy and B.S. Panigrahi, *Journal of Luminescence*, (In Press).

Further inquiries:
Dr. B.S. Panigrahi, Technical Services Division
Reactor Operations and Maintenance Group, IGCAR, e-mail:bsp@igcar.gov.in

Shri N Suriyamurthy, Radiological Safety Division
Safety Group, IGCAR, e-mail: suriya@igcar.gov.in

Nitric Acid Loop for Long Term Corrosion Evaluation

EXECUTIVE SUMMARY

A 400 liter capacity dynamic nitric acid loop has been designed and constructed for evaluating the corrosion performance of AISI type 304L SS over long operating periods under plant simulated conditions. Corrosion resistance of the materials in different metallurgical conditions, namely, cold worked, solution annealed, sensitized, alloy composition, etc. will be evaluated in this loop in flowing nitric acid at different flow velocities (upto 1.55 m/s) and temperatures (313, 333, 353, 380 K and vapour phase). The data generated over a long period of exposure (up to 10,000 h) would be used to arrive at an acceptable corrosion rate of AISI type 304L SS used for applications in nitric acid service. The availability of such a reliable and useful data will be helpful in predicting the remnant life of the components used in the reprocessing plants by developing suitable analytical and modeling tools of the corrosion processes

OUTLINE

The corrosion evaluation of conventional AISI type 304L SS used for the reprocessing plants is presently evaluated as per ASTM A262 practice C (HUEY test) (ASTM, A262-91, 1991). The test is also recommended by the United States Nuclear Regulatory Commission (USNRC) for evaluating the materials intended for nitric acid service in reprocessing plants (USNRC Regulatory Guide 3.37, 1975). It is an accelerated test involving boiling nitric acid of 65% Nitric acid and the experiments are conducted by immersing the test coupon for five times of 48 h periods in the solution. A small volume of the acid is used in a 1-L flask (350 ml) and every 48 h fresh solution is used. The major drawbacks of this test procedure are that the specimens are tested in highly concentrated medium in static condition, the total test period is shorter, and it is specific to evaluate intergranular corrosion only. The testing procedure assesses resistance to intergranular corrosion, and does not simulate the plant conditions. It is well known that AISI type 304L SS used in nitric acid medium undergoes several types of corrosion other than intergranular corrosion, namely, end-grain attack, transpassive dissolution, vapour phase attack etc. So, it is evident that comprehensive corrosion assessment of AISI type 304L SS by ASTM A262 practice C test is impossible, taking into consideration the ranges of concentration of nitric acid used, temperature of operation, impurities and redox chemicals present, and the metallurgical state of the materials used in the plant. The limitations of the current approach motivated us to design a dynamic nitric acid loop made of AISI type 304L SS, with flowing nitric acid at different temperatures to evaluate the corrosion performance of materials used in reprocessing plants (Fig. 1).

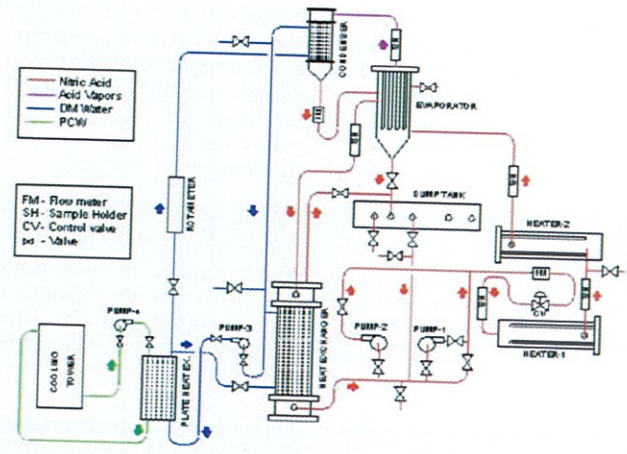

Fig. 1 : The flow diagram of Nitric Acid Loop.

A loop has been designed with 400 L capacity for evaluating the corrosion performance over long operating periods under plant simulated conditions. Corrosion resistance in different metallurgical conditions, namely, cold worked, solution annealed, sensitized, alloy composition etc. will be evaluated in flowing nitric acid at different flow velocities (up to 1.55 m/s) and temperatures (313, 333, 353, 380 K and vapour phase). The data generated over a long period of exposure (up to 10,000 h) would be used to arrive at an acceptable corrosion rate of type 304L SS. The availability of such a data will be helpful in predicting the remnant life of the components used in the plants by developing suitable analytical and modeling tools of the corrosion processes. Currently, the loop is operating with 304L SS samples of solution annealed, sensitized (923 K/L h) and welded conditions, used in demonstration fast reactor reprocessing plant. Results obtained after seven campaigns of cumulative 4850 h of operation indicated insignificant corrosion rates (<1 mpy) upto 353 K, beyond which it increased with time as shown in Figure 2. Non-destructive testing using eddy current and ultrasonic methods and surface examination by SEM, in addition to in service inspection of the loop components, are also being carried out. Presently, the loop is operating for more 1000 h operations. The long-term operation of the loop, and the resultant corrosion data of the materials, will provide valuable information on the life and performance of the actual components in the operating plants, and in qualifying materials under realistic conditions for reprocessing plant applications.

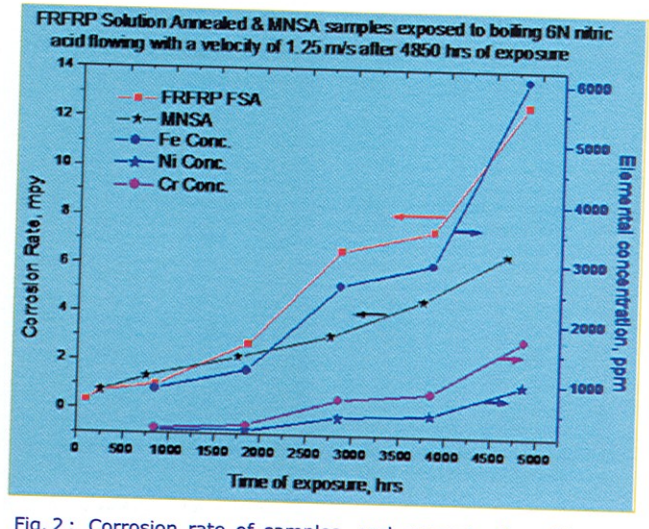

Fig. 2 : Corrosion rate of samples, and concentration of ions in HNO_3 after seven campaigns of cumulative 4850 h operation.

■ ADDITIONAL INFORMATION

AISI type 304L stainless steel used for the reprocessing plants is presently evaluated as per ASTM A262 practice C (HUEY test) which is recommended by the United States Nuclear Regulatory Commission (USNRC) for evaluating the materials intended for nitric acid service in reprocessing plants. It is an accelerated test involving boiling nitric acid of 65% concentration, and the experiments are conducted by immersing the test coupon for five times of 48 h periods in the solution. The major drawbacks of this test procedure are that the specimens are tested in highly concentrated medium in static condition, the total test period is shorter, and it is specific to evaluate inter granular corrosion. Comprehensive corrosion assessment of 304L SS by ASTM A262 practice C test is difficult, taking into consideration the ranges of concentration of nitric acid used, temperature of operation, impurities and redox chemicals present, and the metallurgical state of the materials used in the reprocessing plants. This motivated to design a dynamic nitric acid loop made of type 304L SS, with flowing nitric acid at different temperatures to evaluate the corrosion behaviour of materials used in reprocessing plants.

■ GENERAL EXPLANATION RELATED TO THE DESCRIPTION

Austenitic stainless steels used in the reprocessing plants are qualified as per ASTM A262 practices which are basically accelerated corrosion testing methods. Long term evaluation of the corrosion behaviour under plant operating simulated conditions are necessary to qualify the materials for plant applications as well as to predict the corrosion behaviour of components used in the plant. A dynamic nitric acid loop of 400 litres capacity of 6N HNO_3 was thus designed, constructed and operated with samples of AISI type 304L SS used in the reprocessing plant. The tested samples would also be examined by nondestructive testing methods like eddy current and ultrasonics, as well as the loop components undergo inservice inspection. SEM examination of the samples, and the chemical analysis of loop acid also provide valuable information. Currently, the loop has operated seven campaigns with 4850 h of cumulative operation, and has produced valuable information on the corrosion behaviour of type 304L SS used in the plant. Further campaigns up to 10,000 h are planned to generate additional data on the performance of the type 304L SS used in the plant.

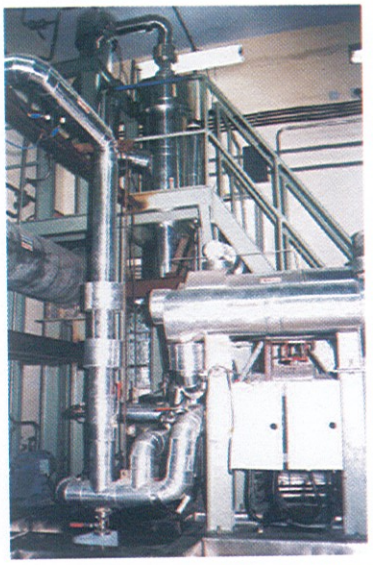

Fig. 3 : Photograph of Nitric Acid Loop

■ BRIEF DESCRIPTION OF THEORETICAL BACKGROUND

Selection of materials for reprocessing and waste management applications is a challenging task as no failure of any nature is acceptable for these applications. Extensive laboratory scale R&D has been carried out to evaluate materials for specific applications. The materials qualification for reprocessing plant components was carried out so far as per ASTM A 262 Practice C which is a short term accelerated test in concentrated nitric acid. Though these data give a broad based guidance in the selection of materials for different applications, the confidence level in choosing a particular material for a specific application can only be increased by carrying out long term/accelerated tests under static/dynamic conditions as the case may be. In this direction, a dynamic nitric acid loop to study the corrosion behaviour of austenitic stainless steels in simulated reprocessing plant conditions has been designed, built and operated.

■ ACHIEVEMENT

Design, construction and operation of a dynamic nitric acid loop of 400 litres capacity for conducting long term corrosion evaluation of stainless steels used for reprocessing applications. For the first time such a loop has been used to generate long term corrosion rate data to study the corrosion behaviour of stainless steels used in reprocessing applications. The loop simulates the plant operating conditions, and provides a test bed for qualifying the stainless steels for critical applications in reprocessing plants.

■ PUBLICATIONS ARISING OUT OF THIS STUDY AND RELATED WORK

Baldev Raj and U. Kamachi Mudali, *Progress in Nuclear Energy*, **48** (2006) 283.

Further inquiries:
Dr. U. Kamachi Mudali, Corrosion Science and Technology Division, Metallurgy and Materials Group, IGCAR, e-mail: kamachi@igcar.gov.in

BREAKTHROUGHS





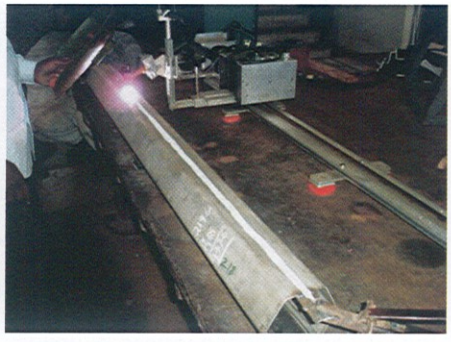



ENGINEERING

Post Irradiation Examination of FBTR Fuel Subassembly after 100 GWd/t Burn-up

EXECUTIVE SUMMARY

Fast Breeder Test Reactor at Kalpakkam uses a unique, indigenously developed mixed plutonium-uranium carbide as fuel. Post irradiation examination (PIE) of the FBTR fuel subassemblies carried out in the Radiometallurgy Laboratory hot cells at IGCAR at different burn-ups has facilitated the prediction and extension of life of the fuel beyond the design estimates. The analysis of the PIE data obtained from a fuel subassembly (FSA) after 100 GWd/t burnup with respect to dimensional changes, fission gas release, the residual ductility of the clad, cladding strains, porosities available in the fuel to accommodate further swelling gave enough confidence to increase the burn up of FBTR fuel to the present level of 154 GWd/t without any failure

OUTLINE

Post-Irradiation examination (PIE) plays a significant role in determining the performance and residual life of fuel and structural materials used in the reactor and it gives valuable feedback to the designers, fabricators, and reactor operating personnel. A series of alpha tight hot cells with inert nitrogen atmosphere ventilation have been established in the Radio Metallurgy Laboratory (RML) to carry out PIE of pyrophoric mixed carbide fuel of FBTR. The hot cells of RML have state-of-art techniques covering a wide spectrum of non-destructive as well as destructive metallurgical examinations of irradiated materials. The non-destructive techniques include visual examination, dimensional measurements, X-ray and neutron radiographic examinations, eddy current testing and leak testing. The destructive techniques include metallography, fission gas extraction and analysis, high temperature tensile tests, micro-hardness, small specimen test techniques and Transmission Electron Microscopy (TEM) studies.

For the mixed carbide fuel composition used in FBTR, a design limit of burn-up was fixed at 50 GWd/t based on out of pile experiments and theoretical studies. The PIE on 25 GWd/t & 50 GWd/t however revealed that the fuel has a lower swelling rate than the expected and sufficient fuel-clad gap was available to increase the burn-up further without initiation of Fuel Clad Mechanical Interaction (FCMI).

The fuel subassembly and the fuel pins (Fig. 1) after 100 GWd/t burnup were in healthy condition without any gross abnormalities. Dimensional Measurements indicated significant increase in the dimensions of hexagonal wrapper and fuel pins. Fuel pins showed a maximum diameter increase at the center of the fuel column corresponding to a total strain of 1.6 %. This strain includes both the dilation of the clad diameter due to void swelling as well as creep deformation resulting from FCMI. However, these were within the limits imposed by fuel handling and coolant flow considerations. Eddy current testing and X-Radiography of the fuel pins did not indicate any abnormalities.

The metallographic examination of the fuel cross section revealed the complete closure of the fuel-clad gap at the center of fuel column indicating the onset of Fuel Clad Mechanical Interaction (FCMI) and restrained swelling of fuel. Typical photomicrographs of the fuel-clad cross section at different burn-ups are shown in Fig. 2. The presence of cracks and porosities available in the fuel indicated that further swelling can be accommodated before FCMI exert stress on the clad. The fission gas release of 4 to 14 % was found to be less than expected resulting in negligible pressure in the plenum of the fuel pin. High temperature tensile tests on the irradiated clad revealed that the uniform elongation of the clad has reduced from the pre-irradiation value of 6.83 % to around 3 % at reactor operating conditions. The tensile test results on clad tube indicated the presence of sufficient strength and residual ductility. Void swelling of the clad, which is one of the important radiation damage in structural materials, was estimated to be 4.4% by immersion density measurements. The analysis of the above PIE data enabled the increase of the FBTR fuel burn up to the present level of 154 GWd/t.

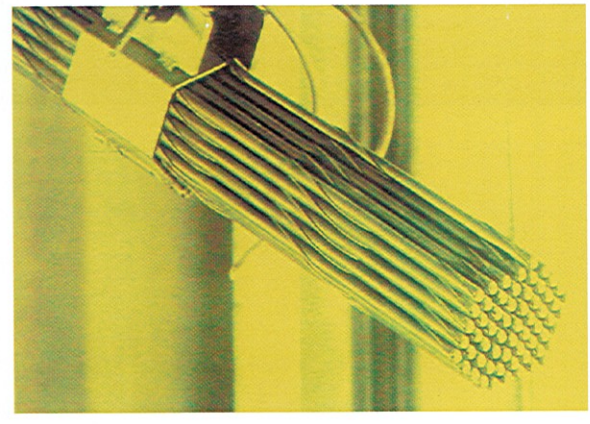

Fig. 1 : The cluster of FBTR fuel pins after 100 GWd/t burn-up viewed through the hot cell

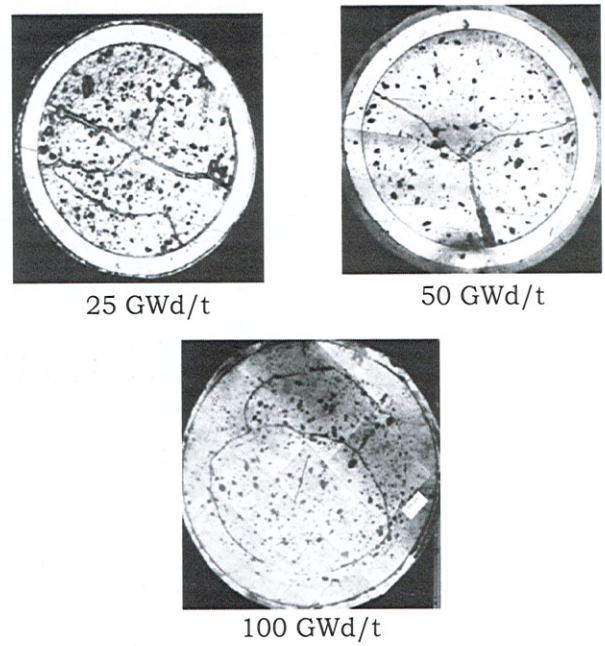

Fig. 2 : Comparison of micrographs of fuel pin cross section at the centre of fuel column after (a) 25, (b) 50 and (c) 100 GWd/t burn-up

■ ADDITIONAL INFORMATION ABOUT PYROCHEMICAL REPROCESSING

Post irradiation examination (PIE) aims at generating and evaluating data that can provide valuable insight into the in-reactor behavior of fuels and structural materials. PIE is a vital link in the nuclear fuel cycle. Various physical, metallurgical and chemical methods are employed for complete characterization of irradiation behaviour of fuels and structural materials. The examinations are carried out either in-pile, or out-of-pile such as pool side inspection facilities or shielded facilities like hot cells etc. PIE draws inputs from reactor operation data, reactor physics data and fuel fabrication data like initial chemical and physical conditions essential for arriving at a meaningful conclusion during PIE. Results of out-of-pile experimental data like fuel-coolant interaction at the temperature of operation, corrosion behavior of structural materials etc. are also useful in evaluating the PIE data.

■ GENERAL EXPLANATION RELATED TO THE DESCRIPTION

Hot cells are shielded enclosures with dynamic containment and leak tight design features for handling highly radioactive material in isolation from the operator's environment. PIE in hot cells employs both non-destructive and destructive examinations to obtain information on the irradiation performance of fuel and structural materials.Non-destructive examinations on the fuel sub-assemblies/fuel pins such as visual examination, dimensional profile, eddy current test, leak testing etc provides information on the structural material integrity. X-radiography enables to quantify the fuel swelling, pellet-pellet gap and pellet-clad gap. Neutron radiography provides complementary information regarding fissile material redistribution and fission product redistribution.

Destructive examinations such as fission gas extraction and analysis provides information on the release of fission gases from the fuel matrix to the plenum and the consequent build up of pressure in the fuel pin. Metallographic examination of the fuel cross section gives valuable information on the fuel restructuring behaviour, fuel-clad gap, cracking pattern etc. Clad microstructure provides information on the fuel-clad chemical interactions such as corrosion, carburization etc. Mechanical testing is used to evaluate the deterioration of mechanical properties due to neutron irradiation. Immersion density and gas pycnometry methods are employed for estimation of volumetric swelling of fuel and clad. Electron microscopy of specimens throws light on the irradiation induced microstructural evolution in structural materials.

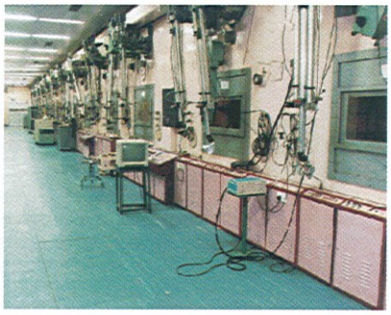

A view of the hot cell facility established for carrying out post-irradiation examination of FBTR fuel ands structural materials

■ BRIEF DESCRIPTION OF THE BACKGROUND

The FBR core materials are subjected to a high neutron flux (10^{15} n/cm^2/sec) coupled with high temperatures (523-973K). A host of irradiation effects occur in the fuel and structural materials due to the aggressive environment. These include swelling of fuel due to accumulation of fission products, redistribution of fission products and actinides, changes in the chemical state of the fuel, fuel restructuring, generation of internal pressure in the fuel pin due to release of fission gases etc.

In structural materials, significant microstructural alterations occur due to high level of atomic displacements induced by neutron irradiation. Major phenomena affecting structural materials are void swelling, irradiation creep, phase stability and changes in mechanical properties. The variations in the dimensions of the fuel subassemblies occur due to void swelling, creep, differential swelling due to gradients in neutron flux and temperature, etc. Engineering consequences of these irradiation-induced changes determine the residence time of core components and hence limit the achievable burn up. PIE plays a vital role in characterization of these irradiation effects in fuel and structural materials of FBRs.

■ ACHIEVEMENT

The stage-wise assessment of performance and estimation of residual life of FBTR fuel has helped in progressively enhancing the Linear Heat Rating and burn-up of the unique fuel. Compared to the initial design limit of 50 GWd/t, the burn-up has now reached 154 GWd/t without any fuel pin failure. The setting up and operation of hot cell facilities for PIE of highly irradiated, plutonium rich fuels has enabled to master the complex technology and is paying rich dividends in the design of such facilities for reprocessing and fuel fabrication.

■ PUBLICATIONS ARISING OUT OF THIS STUDY AND RELATED WORK

1. N.G.Muralidharan, C.N. Venkiteswaran, V. Karthik, P.A. Manojkumar, S. Sosamma, C. Babu Rao, V. Venugopal and K.V. Kasiviswanathan; *Int. J. Nuclear Energy Science and Technology*, **1** (2005)191.
2. Baldev Raj, S.L.Mannan, K.V.Kasiviswanathan, M.D.Mathew, V.Karthik, C.N.Venkiteswaran, M. Sai Baba and P.Puthiyavinayagam, *Materials and Processes*, **18** (2006)1.
3. C.N.Venkiteswaran, N.G.Muralidharan, A. Vijayaraghavan, Jojo Joseph, V. Venugopal and K.V.Kasiviswanthan, Int. *J. Nuclear Energy Science and Technology*, **2** (2006)352.
4. K.V. Kasiviswanathan, C.N. Venkiteswaran, V. Karthik, V. Venugopal, N.G. Muralidharan & Jojo Joseph, Proceedings of the International Conference on Advances in Nuclear Materials, *J. Nucl. Mater.*, (In Press).

Further inquiries:
Shri K.V. Kasiviswanathan, Group for Remote Handling, Robotics, Irradiation Experiments and PIE
Metallurgy and Materials Group, IGCAR, e-mail: kasi@igcar.gov.in

Development of Ti-5Ta-1.8Nb Alloy for Fast Reactor Fuel Reprocessing Applications

EXECUTIVE SUMMARY

An α + β Ti-5%Ta- 1.8%Nb alloy has been developed as structural material for reprocessing applications due to its excellent corrosion resistance. Based on an extensive experimental investigation the transformation temperatures (β transus and Ms) were evaluated for the first time. Study of phase transformations, structure – property correlations and weldability resulted in the identification of process parameters and optimum microstructure with good corrosion and mechanical properties. A comprehensive understanding of corrosion and deformation mechanisms and texture has been achieved. The performance of this alloy as a filler in commercial grade Ti welds has been evaluated. Scaling up of production and fabrication into industrial components is in progress to evaluate its performance as an alternative structural material for future reprocessing plants.

OUTLINE

A Ti-5Ta-1.8Nb alloy has been developed as a candidate material for structural applications, in view of its excellent resistance to three phase corrosion in highly oxidizing media. The experimental program consisted of five main components with an objective to generate a complete data base for this alloy with respect to its fabrication and process flowchart, design of optimum microstructure, weldability, property evaluation and basic studies on the mechanisms of corrosion, deformation, phase transformation and texture in the alloy.

The Ti-5Ta-1.8Nb alloy consisted of a microstructure of alternate lamellae of α and β phases (Figure 1), with the solutes Ta and Nb repartitioned into the β phase. Based on chemistry and microstructure the alloy was classified as α+β alloy. The high temperature β transformed to a variety of phases, each characterized by morphological and microchemical features, resulting in a myriad of microstructures and properties. The structures ranged from serrated α, Widmanstatten α and martensitic α depending on the temperature, time and cooling rate. Using a combination of electron microscopy, calorimetry and computational methods the β transus and Ms temperature have been evaluated for the first time as 1140 and 1103K respectively. The Ti-Ta-Nb alloy exhibits interesting deformation and transformation textures, which have been studied by X-ray diffraction and Electron Back Scattered Diffraction techniques. A method to determine the orientation of the parent β from the orientation of the product α phase has been developed based on Burgers Orientation Relationship.

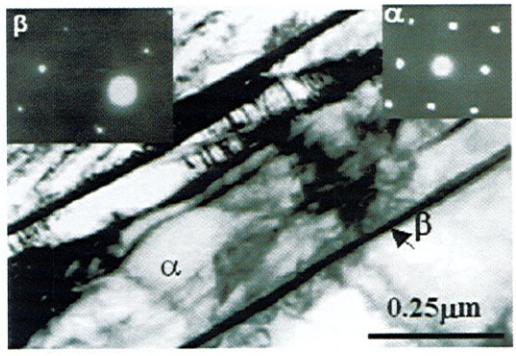

Fig. 1 : Widmanstatten microstructure showing alternate lamellae of α and β phases.

An acicular microstructure is known to be detrimental to corrosion resistance since it forms micro galvanic cells leading to selective dissolution of Ti in α phase. It was necessary to design a microstructure which possessed large fractions of equiaxed α grains with β particles distributed at random. A thermo-mechanical processing (TMP) schedule of hot working in the α+β phase field followed by room temperature processing with an intermediate β quenching and strain relieving treatments resulted in an equiaxed structure, which also showed a low corrosion rate. Further improvement of properties was achieved by special treatments resembling that of commercial α+β alloys. Figure 2 shows the detrimental and beneficial microstructures.

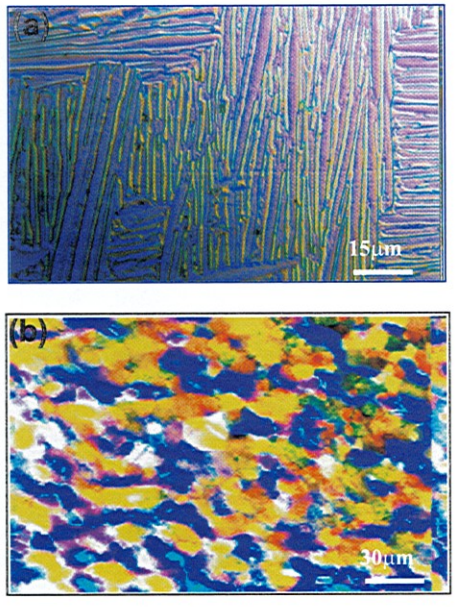

Fig. 2: (a) Detrimental lamellar microstructure and (b) Desirable equiaxed microstructure

The Yield Strength, UTS and elongation for the alloy are above 300, 400 MPa and 28% respectively which are far above the design criteria. The deformation mechanisms were established as twin and slip for α and slip for β phase. A systematic property evaluation showed that the alloy with a microstructure of very fine (nm sized) β precipitates in a predominantly equiaxed matrix showed the lowest corrosion rate of < 1mpy and adequate mechanical property. This alloy was obtained by solution treatment and aging. Based on the above the thermo-mechanical and heat treatment conditions for the alloy were optimized.

The Ti-Ta-Nb alloy showed good weldability and the weld possessed good mechanical properties. The Procedure Qualification Record (PQR) and Welding Procedure Specification (WPS) for this alloy have been established for the first time. The thermal cycle of different regions in the weld was also computed. The corrosion rates of the weld was low (<1mpy) and comparable to the base metal. The performance of Ti-Ta-Nb as filler in a weldment of commercial grade Ti showed excellent corrosion resistance. The excellent properties and performance exhibited by the alloy on a laboratory scale has led to the scaling up of production and fabrication of industrial components.

■ FAST REACTOR FUEL REPROCESSING

Reprocessing of fast reactor fuel is challenging due to the high radioactivity and fission products because of high Pu content. This also necessitates the use of nitric acid of higher concentrations (11.5M) than thermal reactors (8M). Hence the structural material for critical in components like dissolver, evaporator should be resistant to corrosion in these highly oxidising media. The dissolution of carbide fuel also requires an electrolytic oxidation to avoid the interference of organic compounds with the solvent extraction process. Stainless steel which is conventionally used for thermal reactor fuel reprocessing, is replaced by materials like Ti or Zr and their alloys.

■ MATERIAL SELECTION FOR REPROCESSING APPLICATIONS

The selection of a material for any chemical process plant is a complicated decision involving many parameters such as corrosion resistance, mechanical properties, weldability, availability, cost etc. A nuclear plant is more demanding since the materials not only need to perform their function for extended periods of time in non-maintainable areas, but also this performance has to be demonstrated and safety ensured. The structural engineering materials utilised for nuclear fuel reprocessing are steel, both carbon and stainless, alloys of titanium and zirconium. Commercial grades of Ti have shown good performance. However, to improve corrosion behavior of the welds and for increasing the life time of the plant, materials with superior corrosion resistance are being developed. The comparison of corrosion rates of different alloys of titanium is shown in Figure 3. It can be seen that the Ti-5Ta-1.8Nb alloy possesses the lowest corrosion rate and is a candidate material for structural applications.

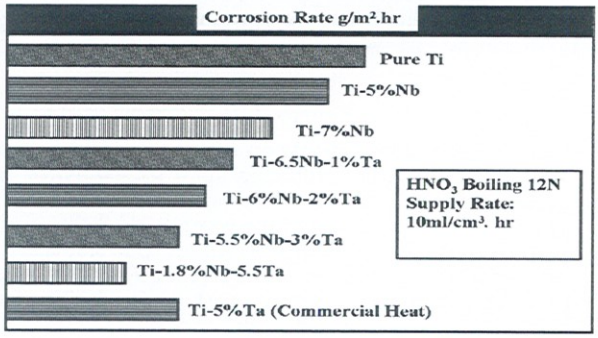

Fig. 3: Schematic of corrosion rate of different titanium alloys in boiling nitric acid

■ CRITERIA FOR ALLOY DESIGN

Ti and its alloys derive corrosion resistance from a thin, adherent, passive oxide film on the surface, whose characteristics depend on the environmental conditions. Titanium has excellent corrosion resistance in hot concentrated nitric acid, which can be further enhanced by alloying additions and microstructural design, which is the basis of the design of an $\alpha+\beta$ ternary alloy of Ti.

■ ACHIEVEMENT

A new alloy of Ti-5Ta-1.8Nb has been developed as an alternative material for structural applications in highly corrosive media. This study established a comprehensive understanding of phase transformations, structure- property relationships, texture and weldability in this developmental alloy. The study also provided valuable inputs for the processing and fabrication flow chart of this alloy. Microstructure control through design of heat treatments was achieved, which is being incorporated into the specification of DFRP. Scaling up of the fabrication from laboratory to industrial scale has been accomplished.

■ PUBLICATIONS ARISING OUT OF THIS STUDY AND RELATED WORK

1. T. Karthikeyan, Arup Dasgupta, S.Saroja, M.Vijayalakshmi and V.S.Raghunathan, *J. Nucl. Mater.*, **335** (2004) 299.
2. T. Karthikeyan, Arup Dasgupta, S.Saroja and M.Vijayalakshmi, *J.Mater. Engg. Perf.*, **14** (2005) 241.
3. R. Mythili, V. Thomas Paul, S.Saroja, M. Vijayalakshmi and V.S. Raghunathan, *Mater. Sci. and Engg. A*, **390** (2005) 299.
4. T. Karthikeyan, Arup Dasgupta, A.J. Khan, S. Saroja, M. Vijayalakshmi, D. Bhattacharjee and V.S. Raghunathan, *Mater. Sci. & Engg. A*, **393** (2005) 294.
5. R. Mythili, S.Saroja, M. Vijayalakshmi and V.S. Raghunathan , *J. Nucl. Mater.*, **345** (2005) 167.
6. T. Karthikeyan, R. Mythili, S. Saroja and M. Vijayalakshmi, *Metals Materials and Processes*, **18** (2006) 282.
7. R. Mythili, S. Saroja, M. Vijayalakshmi and V.S. Raghunathan, *Mater. Sci. & Engg. A*, **43** (2007) 454.
8. R. Mythili, A. Ravi Shankar, S. Saroja, V.R. Raju, M. Vijayalakshmi, R.K. Dayal, V.S. Raghunathan and R. Balasubramaniam, *J. Mater. Sci.*, **42** (2007) 5924.
9. Arup Dasgupta, T. Karthikeyan, S. Saroja, V.R. Raju, R.K. Dayal, M. Vijayalakshmi and V.S. Raghunathan, *J.Mater. Engg. Perf.*, **16** (2007) 800.
10. A. Ravi Shankar, R.K. Dayal, R. Balasubramaniam, V.R. Raju, R. Mythili, S. Saroja, M. Vijayalakshmi and V.S. Raghunathan, *J. Nucl. Mater.*, **372** (2006) 277.

Further inquiries:
Dr. Saroja Saibaba, Physical Metallurgy Division
Metallurgy and Materials Group, IGCAR, e-mail: saroja@igcar.gov.in

A Remotely Operable Welding Facility for Fabrication of Fuel Pins for Test irradiation

EXECUTIVE SUMMARY

Fuel pins for irradiation in nuclear reactors are fabricated in alpha tight glove boxes using fuel pellets obtained by compaction of powder. Remote fabrication of fuel pins will be necessitated for fabrication with materials emitting gamma radiation such as minor actinides. Sol-gel based fuel fabrication methods such as vibro-comapction of fuel in the form of microspheres to produce Sphere-Pac pins are more amenable for remotisation than the powder-pellet route. A remotely operable welding facility has been developed and incorporated in a glove box which forms a part of demonstration facility for remote fabrication of test fuel pins based on sol-gel methods. The remote welding was demonstrated by fabricating a vibrocompacted fuel pin containing uranium oxide microspheres.

OUTLINE

Sol-gel based fuel fabrication methods eliminate powder handling and the associated problems such as exposure of personnel to radiation etc. In these methods, fuel is produced in the form of microspheres which are vibro-compacted to form a sphere-pac fuel pin. A facility for fabrication of sphere–pac test fuel pins is being set up at IGCAR in collaboration with BARC. The remotely operable pin welding facility forms a part of the facility for test fuel pin fabrication (Fig.1 & 2). The process of sphere-pac fuel pin fabrication involves the filling up of microspheres into fuel tube having the bottom end plug already welded, vibro compaction, loading of insulation pellet and a plenum spring and then welding the top end cap. In order to demonstrate remote fabrication, the equipments have been designed for operations inside a glove box by using master slave manipulators. The pin is held in vertical position on a vibrator chuck assembly and filled with sintered microspheres by means of a feeder. The vibro-compacted pin is moved to the welding station after loading with insulation pellets and a spring. The welding station contains an 'XY' positioning system and a special remote welding facility. The fuel clad tube is made out of D-9 material and the end plugs are made out of stainless steel AISI 316M. In order to fill and contain helium bonding gas inside the fuel pin, top end closure welding is carried out under helium atmosphere in a welding chamber. The severity of the service conditions inside a nuclear reactor demands reliable and repeatable weld integrity and hence the end closure welds are subjected to Helium leak tests, X-radiography and metallography with stringent acceptance criteria. The tube has to be handled in vertical position before encapsulation due to process requirements and hence the welding is to be performed in vertical position. The remotely operable vertical welding facility has been designed to weld the top end plug in 2G positions welding keeping the tube in vertical position. The facility consists of a special leak tight welding chamber equipped with a 'XY' positioning system for loading the fuel tube, a stepper motor driven system for rotating the tube, a end plug feeder and electrode holder with remotely operable features. In the above facility, two fractions of natural uranium oxide microspheres, produced through sol-gel route, were filled and end closure welded in 2G position, inside the welding chamber. Pulse Gas Tungsten Arc (GTA) welding process was selected with a power source equipped with weld monitoring software for data storage on PC. Fuel tube gripping & handling was carried out with pneumatic grippers aided with master slave manipulators. The center line alignment of the clad tube and plug, electrode position, orientation, arc gap adjustment and joint fit-up are carried out remotely and monitored by a CCTV camera attachment with a Video grabber & image analysis software for measuring and ensuring consistency during every weld. Parametric studies were conducted on number of representative dummy tubes and end plug welds to optimize the welding parameters. Dummy fuel pins have been successfully welded using this facility and the weld joints have been qualified by radiography & metallographic examinations. Fuel tube filled with natural uranium microspheres and internals were qualified by radiography. The remote operational & maintenance procedures were demonstrated and standardized with this facility.

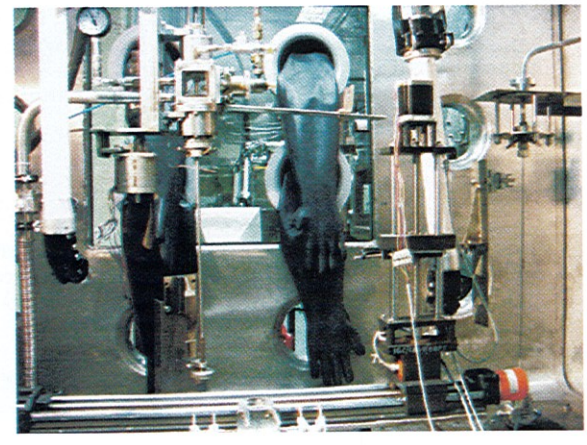

Fig. 1 : Remote welding facility

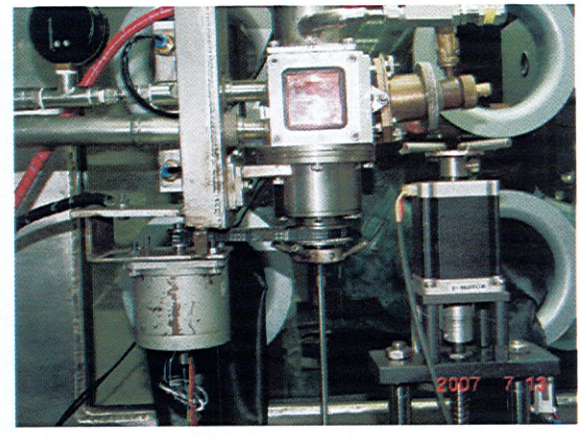

Fig. 2: Welding in process

SOL-GEL BASED FUEL FABRICATION METHODS

A glove box, is an alpha tight enclosure that is designed to allow a operator to manipulate radioactive materials while being in a different atmosphere from the object. Master slave manipulator is a device used to move or manipulate hazardous materials for reasons of safety inside a containment box. Fuel fabrication process by sphere pac route, is readily amenable to remotization and automation as it involves handling solutions and fluid like microspheres. As the number of mechanical operations is less, sphere-pac pin fabrication is simpler. Further, the nitrate solutions from the reprocessing plants can be used as feed for sol-gel process eliminating the reconversion step involving powder handling.

GENERAL EXPLANATION RELATED TO THE DESCRIPTION

Welding of end plug to tube in vertical position involved development work on the welding chamber as it involved remote operation & maintenance and parametric studies on welding parameters for evaluation by destructive & non destructive techniques. The over all dimensional deviations and bowing of the pin due to weld induced distortion are to be controlled to meet the stringent requirements of the final assembly tolerances. Hence it is necessary to maintain precise part tolerance and weld parameter control. The welding parameters & conditions have to be standardized, for qualification of the welding chamber, procedure and operator. The requirement of filling of helium gas at 1 Kg/cm^2 (gauge) pressure inside the fuel pin necessitates the welding to be carried out in a helium environment filled chamber. It is harder to start an arc because of the high ionization potential of helium. The power source used for welding is a microprocessor based inverter DC power source. The Pulse GTA welding process is selected since the process is suitable for joining thin walled tubes and the process has an accurate means of selecting the welding parameters which is desirable for automation of welding process. Welding in 2G position is difficult since the molten metal will tend to drip downward due to gravity and to minimize this, welding parameters are to be selected carefully. The end plug has been designed with an edge preparation machined to close tolerances to suit the clad tube dimensions and thin wall thickness of clad which is 0.45 mm. Checks on quality of end plug welds were carried out as per the PFBR specifications (Fig. 3). Around 50 weld samples were carried out to establish the procedure and welding parameters in 2G position.

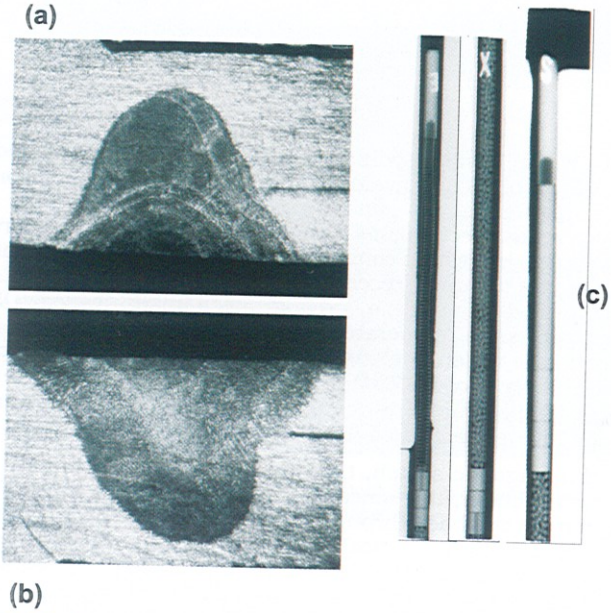

Fig. 3 : Typical Digitized radiography image of (a) & (b) End plug c/s side 1 & 2 at 50X magnification © Spring region, Fuel column Plenum portion of a dummy fuel pin.

BRIEF DESCRIPTION OF THEORETICAL BACKGROUND

Pulsed DC TIG-welding, makes it possible to weld uniform welds with deeper penetration at the same heat input. A PC with a frame grabber card, video camera and analysis software, facilitated distant and online visual inspection of the welds. The weld should be free from any defects and the minimum weld penetration should be 110% of the wall thickness. In few cases slightly excess penetration is tolerated within acceptable limits. Advanced vision systems can reduce operator strain and permit inspection at a faster rate. Image analysis software is being upgraded for automatic identification of defects like lack of side wall fusion etc., and facilitates storage of data during production. Welding qualification and inspection plan during production will also be as per the PFBR end plug weld specifications.

ACHIEVEMENT

The remote welding facility is the first of its kind in our country and the commissioning of this facility forms a significant milestone in the development of remote fuel fabrication process.

PUBLICATIONS ARISING OUT OF THIS STUDY AND RELATED WORK

T.V.Prabhu , G.Ravisankar and K.N.Mahule, National Welding Seminar 2006, Indian Institute of Welding, Chennai.

Further inquiries:
Shri G. Ravisankar, Chemical Facilities Division
Chemistry Group, IGCAR, e-mail:grs@igcar.gov.in

An Active Laboratory Scale Facility for Molten Salt Electrorefining Studies

EXECUTIVE SUMMARY

Molten salt electro-refining is pyrochemical method ideally suited for reprocessing metallic fuels-The development of which is very important for metal fuel cycle. A laboratory scale facility having high purity argon atmosphere with <20 vpm of moisture and oxygen has been used for the last twelve years for studies on uranium based alloys. The facility has been made suitable for handling radioactive samples and electro-refining studies on plutonium bearing material have been initiated

OUTLINE

Molten salt electro-refining offers several advantages such as less number of steps, reduction in cooling time etc. over the aqueous methods for reprocessing metallic fuels. It is a high temperature electrochemical process operated at 773 K and uses molten salts such as LiCl-KCl which are sensitive to moisture. The actinide metals handled by the process are highly pyrophoric. Hence a high purity argon atmosphere has to be maintained in the facility in which molten salt electro-refining has to be carried out.

The electro-refining process exploits the differences in the thermodynamic stabilities of the chlorides of actinide fuel materials, U and Pu and those of the fission products to achieve the separation. It uses LiCl-KCl eutectic as electrolyte, spent fuel as the anode and molten cadmium or a solid rod as the cathode. There is no experience with this process in our country and has to be developed for the first time.

A high purity argon atmosphere laboratory scale facility for carrying out studies on molten salt electro-refining process was set up and is being operated for the last twelve years (Fig. 1). It comprises five interconnected glove boxes. It is has integrated systems for argon gas feed, exhaust, purification and recirculation. The system is maintained at a negative pressure of 25-40 mm with respect to the ambient, as it has to handle radioactivity. The argon gas inside the facility is monitored periodically for the oxygen and moisture contents. which are maintained below 20 vpm each.

The facility incorporates equipment for salt preparation, electro-refining at 773 K , distillation of salt/cadmium and an induction heated facility for reaching temperatures upto 1400 K for melting the actinide metal residues obtained after distillation of cadmium and salt. The facility has been extensively used for the studies on uranium based alloys such as U-Zr, U-Ce-Pd etc. for determination of the separation factors for Zr, Ce and Pd. Injection casting of U and the U alloy rods have also been carried out in this facility

The necessary leak tight conditions for handling radioactitvity were ensured and electro-refining experiments have been initiated. Considering the fact that even worldwide very few studies on electro-refining have been carried out especially on plutonium bearing alloys, the development assumes significance. About 20 g Pu metal was taken and equilibrated at 773 K with LiCl-KCl eutectic salt containing stoichiometric quantities of $CdCl_2$. About 7 g of $PuCl_3$ was loaded in the electrolyte salt.

Electro-refining experiments were carried out using Pu metal immersed in cadmium metal as the anode, the above salt as the electrolyte and a solid rod as the cathode. Dendritic deposit of Pu metal (Fig.2) was obtained on the cathode which was covered with the electrolyte salt. The metal deposit was melted by dipping the cathode rod in a crucible containing excess of LiCl-KCl. Globules of metals obtained are being characterized. Characterisation of the salt, deposit and anode samples are in progress for working out the material balance.



Fig. 1 : Electro-refining cell inside glove box



Fig. 2 : Pu metal deposited on solid cathode

ADDITIONAL INFORMATION ABOUT PYROCHEMICAL REPROCESSING

Pyrochemical Reprocessing techniques use molten salts and molten metals at high temperatures to achieve the separation of fuel materials and other constituents of the spent fuel for enabling refabrication of fuel pins using the fuel materials thus recovered. Molten salt electro-refining is a pyrochemical method that is considered ideally suited for reprocessing metallic fuels.

GENERAL EXPLANATION RELATED TO THE DESCRIPTION

U-Pu-Zr alloys are, in general, used as the metallic fuels in sodium cooled fast reactors. In India, it is proposed to introduce metal fuels in FBRs in the next decade. Molten salt electro-refining offers several advantages over the currently developed and practised aqueous reprocessing methods for reprocessing the metallic fuels. Hence there is an urgent need to develop the molten salt electro-refining process. and other associated process steps.

In this process, as shown in the schematic diagram (Fig. 3), spent fuel cut into pieces and immersed in the electrolyte salt of LiCl-KCl is the used as the anode and a solid rod or molten cadmium cathode is used as the anode. It is possible to separate U from the spent fuel and deposit it on the solid cathode whereas co-deposition of U and Pu is possible on cadmium cathode. The salt covering the metal deposit on a solid cathode or the cadmium in case of cadmium cathode is distilled off and the residue of U/Pu metals are melted to recover them as buttons.

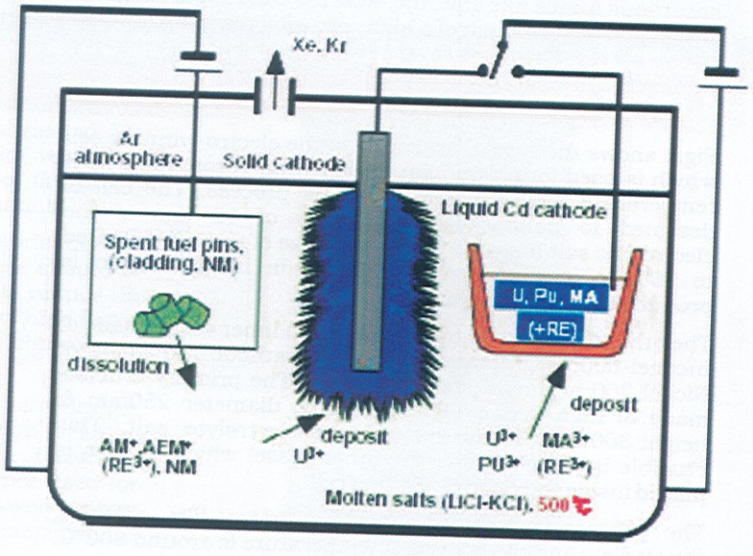

Fig. 3 : Schematic diagram of the molten salt electro-refining process

THERMODYNAMIC BASIS FOR SEPARATION

The chlorides of the alkali, alkaline earth and the rare earth fission products are more stable than those of U and Pu whereas those of noble metal fission products are less stable. Thus in the process, U and Pu are transported to cathode and deposited, the alkali, alkaline earth and rare earth fission products go to the salt and stay there. Noble metals remain in the anode itself.

ACHIEVEMENT

There is little experience in this technology in this country. The technology is complex in view of the high temperature and high purity requirements. Experience with the process operation especially on active samples will give inputs for designing a future reprocessing plant based on this process. Thus commissioning of an active facility for forms an important milestone for metal fuel cycle.

Further inquiries:
Dr. K.Nagarajan, Fuel Chemistry Division
Chemistry Group, IGCAR, e-mail:knag@igcar.gov.in

Modifications to Improve Plant Availability in Fast Breeder Test Reactor

EXECUTIVE SUMMARY

Most of the unscheduled outages in FBTR were from the steam-water circuit. The contact type reheaters which were used in the steam water system were prone to level fluctuations, resulting in cascade tripping of the feed water pumps and ultimately in reactor LOR. The reheaters were replaced by non-contact, shell and tube type design. The Steam Generator Leak Detection system in each secondary loop was having one detector, and any malfunctioning of the complex detection system would result in spurious trip of the reactor. The system was triplicated in each loop and wired to trip the reactor in 2/3 mode. These major modifications resulted in minimizing unscheduled outages and improving the plant availability.

OUTLINE

Steam and water system forms the tertiary loop of the heat transport system of FBTR. It consists of three sub systems viz; condensate system, feed water system and steam system. In the old condensate system there were three direct contact type heaters viz; Low Pressure heater #1 (LPH #1), Low Pressure heater #2 (LPH #2) and deaerator with its integral hot well (Fig.1). Since free water level is maintained in LP heaters, pumps were provided at the outlet of these capacities to transfer water from one capacity to another. Level in the LP heaters was maintained by controlling the outflow of water from the heaters with the level control valve of each capacity. All the pumps viz; condensate extraction pump (CEP), condensate booster pump (CBP) and deaerator lift pump (DLP) had trips on low level in its suction capacity and high level in its discharge capacity. The free hot well levels of the capacities were very sensitive to mild process / power supply disturbances. These level fluctuations led to tripping of CEP, CBP & DLP and consequent reactor trip (on an average 3-4 reactor trips per year). Hence it was decided to replace the direct contact type heaters LPH # 1&2 with surface type heaters. Fig.2 depicts the modified condensate system. In this system, CEP takes suction from main condenser / dump condenser (MC / DC) and discharges condensate to DLP suction. DLP discharges water into deaerator through LPH#1 and LPH#2. The CBP has been dispensed with. The new LP heaters are shell and tube type heat exchangers and hence the level control circuits of LPH #1 & 2 were also dispensed with, thus simplifying the system. By the use of surface type heaters and necessary modifications in the logic circuitry of the pumps, the system was made more rugged and immune to process disturbances. Retrofitting of the new heaters in place of old ones had many technical challenges, which were faced successfully.

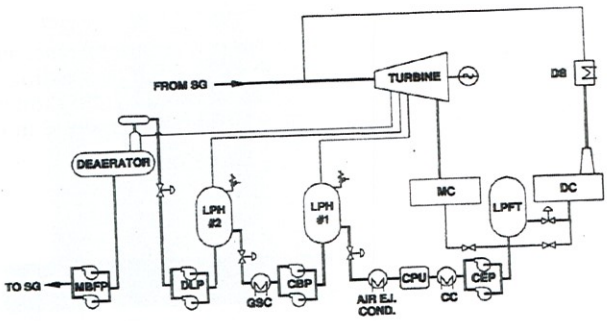

Fig. 1 : Schematic of the old condensate system

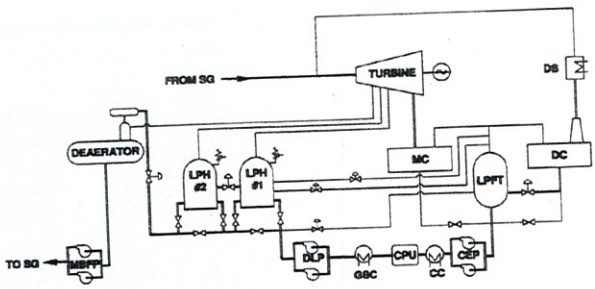

Fig. 2 : Schematic of the modified condensate system

Steam Generator (SG) in FBTR is a once through flow heat exchanger in which sodium flow through the shell side and water /steam through the tube side. In case of breach in tube integrity, the high pressure water /steam leaks into sodium resulting in sodium water reaction ($2Na + 2H_2O = 2\ NaOH + H_2$). Any leak of water/steam from the tube side to the sodium in the shell side of the SG is detected at the incipient stage by a sensitive and complex Steam Generator Leak Detection System (SGLDS). The hydrogen produced during Na/H_2O reaction gets dissolved in sodium and is taken to the Nickel (Ni) diffuser kept at 450°C. The hydrogen diffuses through the tubes of Ni diffuser to the shell side, which is maintained at a very high vacuum of 10^{-8} torr by Sputter Ion Pump (SIP). An increase in the current of SIP indicates leak in SG tubes. The SIP current is wired to order LOR based on absolute value of the current as well as the rate of rise of the current. Each secondary loop in FBTR was provided with one SGLDS. There was no provision to confirm the genuineness of a leak signal and the availability of the system was very much dependent on the single channel. To have redundancy in SGLDS, to improve availability of the plant and to avoid spurious actuation of leak signal, the system was duplicated in the first phase by adding one more Ni diffuser-vacuum system in series with the existing SGLDS. A 3rd system with its own reheater-economizer, Ni diffuser and SIP was then added. The retrofitting and commissioning was completed in February, 2006. The safety logic on SG leak was modified to incorporate 2/3 coincidence on SGLDS leak signals to initiate safety actions on the reactor. The system was calibrated and put into regular operation (Fig. 3).

■ ADDITIONAL INFORMATION

The steam generators in fast reactors have high temperature and high pressure water–steam on the tube side and high temperature, low pressure sodium on the shell side. Any small leak of water-steam into the sodium can lead to what is called `self wastage' and `adjacent wastage', i.e. the tube / shell material can be eaten away by the rise in local temperature at the leak point due to the generation of hydrogen, escalating into larger leaks from the leaky tube and adjacent tubes. It is hence essential to detect any water-steam leak at the incipient stage itself (typically at mg/s levels). Sensitive systems are hence provided for steam generator leak detection.

■ GENERAL EXPLANATION RELATED TO THE DESCRIPTION

Sodium samples from the steam generators are passed through a nickel diffuser. The nickel diffuser has thin walled tubes housed in a shell. Sodium flows through the tubes, and the shell is maintained at ultra-high vacuum by a sputter ion pump. The sodium in the diffuser is maintained at high temperature (450±1°C). Hydrogen from sodium diffuses through the thin walls of the nickel tubes. The Sputter Ion Pump (SIP) maintains the high vacuum (<10^{-8} torr) continuously, and any fall in the vacuum due to increased diffusion of hydrogen from sodium gives rise to an increase in the SIP current. The SIP current is thus an indicator of hydrogen concentration in sodium. Since the SIP has to maintain the ultra high vacuum on a continuous basis, it is essential to have a reliable and rugged SIP. Earlier, Mass Spectrometer (MSM) based hydrogen detector was used, but due to its high cost and maintainability, the SIP current itself is now used for the SGLDS.

Due to its continuous duty, SIP can malfunction. Also, if there is a drift in the temperature of the nickel diffuser, the system can give spurious signals. Hence it is essential to have redundancy. In addition to improving the plant availability, it also enables differentiation of any genuine leak signal from spurious signal. The triplication also improves system maintainability.

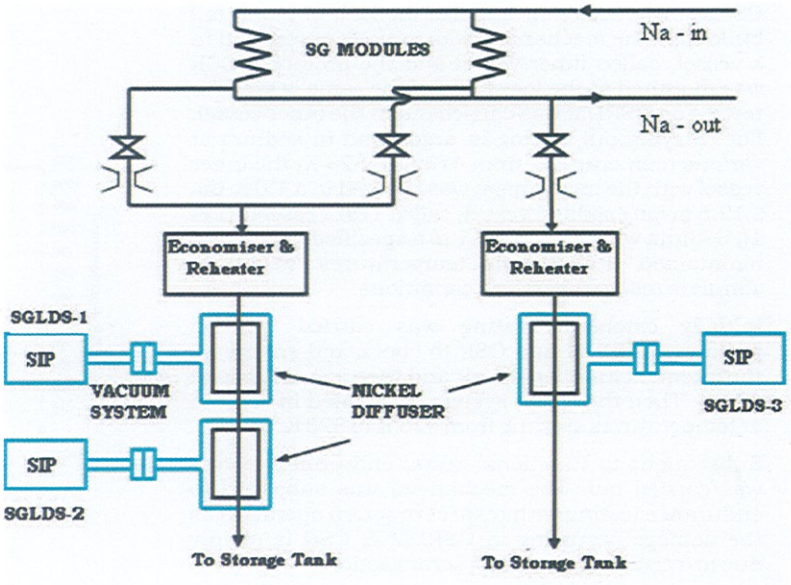

Fig. 3 : Schematic of SGLDS system

■ ACHIEVEMENT

The modifications in condensate system and SGLDS have improved the plant availability by minimising unscheduled outages. For example, in the 13th irradiation campaign for 39 days from 1st October 2005 to 19th November 2005, the availability was 94.8%. Though there was one LOR from the steam-water system during the period, it was due to procedural error and not due to system malfunctioning. With both these modifications, plant availability is expected to be high in the coming campaigns.

■ PUBLICATIONS ARISING OUT OF THIS STUDY AND RELATED WORK

1. Feasibility study report on replacing contact type LP heaters with Surface type. No. 98A09-RPT-M-001
2. Minutes of 306th Station Operation Review Committee (SORC) meeting
3. Minutes of 140th Safety Review Committee-Operation (SARCOP) meeting
4. M. Subramaniyam and G. Srinivasan, Proposal on triplication on SGLDS No. ROD/FBTR/S-RS-12/63342/TN-598
5. Engineering Change Notification ECN 7/2005
6. G. Bhaskar, K. Dinesh and K.V. Suresh Kumar, Commissioning Report No. ROD/FBTR/S-RS-12/33420/CR-102

Further inquiries:
Shri K.V.Sureshkumar, Shri.G.Srinivasan and Shri.P.V.Ramalingam
Reactor Operations and Maintenance Group, IGCAR, e-mail: kvsuresh@igcar.gov.in

Qualification of Control & Safety Rod Drive Mechanism and Control & Safety Rod for Prototype Fast Breeder Reactor

EXECUTIVE SUMMARY

Control & Safety Rod Drive Mechanism (CSRDM) & Control & Safety Rod (CSR) form a part of first shutdown system in Prototype Fast Breeder Reactor (PFBR). Since, the safety of the reactor as a whole depends upon the reliable performance of CSR & CSRDM, they are qualified by comprehensive testing carried out in simulated reactor operating conditions. The root cause analysis was carried out on the problems encountered during assembly & testing and necessary modifications were incorporated. The test results are satisfactory and CSRDM & CSR are qualified for use in the reactor.

OUTLINE

CSRDM was tested in Engineering Hall III (43 m tall building). The mechanism was initially assembled in a vessel, called inner vessel and the prototype CSR was mounted at the lower end of the same vessel. Air testing on CSRDM was carried out in the inner vessel. For carrying out testing in argon and in sodium at various temperatures from 473 K to 823 K, the inner vessel with the mechanism was lowered in a 1.0 m dia x 12.6 m long sodium vessel, called Test Vessel-1 (TV-1). Sodium was filled in TV-1 to a specified height and maintained at different temperatures so as to simulate reactor operating conditions.

Initially extensive testing was carried out on prototype CSRDM and CSR to check and ensure all the intended functions in air and then in hot argon at 473 K. Then the whole system was tested in sodium at temperatures starting from 473 K to 823 K.

Subsequent to functional tests, endurance testing was carried out. The mechanism was subjected to endurance testing with respect to scram operation as the damage occurring in CSRDM & CSR is mainly due to fatigue cycles during scram action.

At first, the endurance testing was carried out in sodium for 500 cycles of scram operations maintaining the temperature at 803 K, and 60 cycles of gripper operations at 473 K, keeping CSRDM & CSR (Mark–I) in aligned condition. Based on the test results, the design of CSR was improved. Then endurance testing was carried out in sodium for another 1093 cycles of scram operations, maintaining the temperature of sodium at 823 K, and 120 cycles of gripper operations at 473 K with a misalignment of 30 mm between CSRDM and CSR (Mark–II). In addition to this, tests carried out in air, argon and sodium at different temperatures amount to 450 cycles.

As per ASME guidelines, CSRDM has been so far qualified for 14 years of life in reactor and CSR is qualified for its total life.

CSRDM and CSR were taken out of the sodium vessel and cleaned thoroughly using water vapour-CO_2 process, DM rinsing and drying at sodium removal facility.

Later, the upper part of the mechanism was dismantled fully for inspection. Inspection reveals that no part in CSRDM upper part related to translation and scram action has undergone any deterioration that may affect the satisfactory operation of the mechanism.

Fig. 1 shows the displacement characteristics of CSR and Fig. 2 shows the dynamic oil pressure developed in dashpot during scram action.

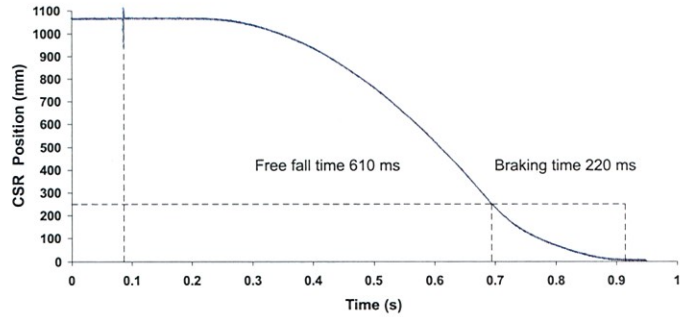

Fig. 1: Displacement of CSR during Scram

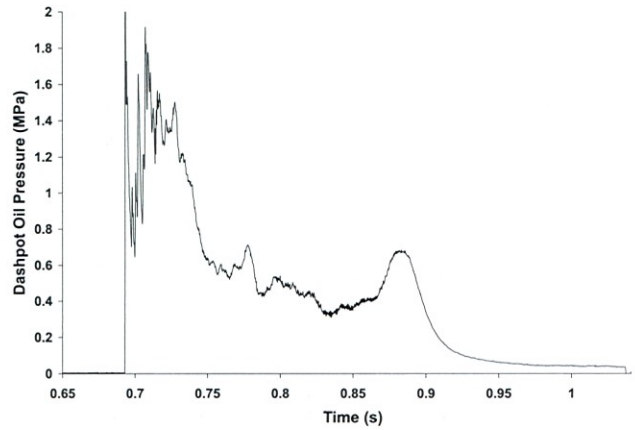

Fig. 2: Dashpot Characteristics during Scram

PFBR SHUT DOWN SYSTEMS

In Prototype Fast Breeder Reactor, there are two independent, fast acting, diverse shutdown systems, each comprising of sensors, logic circuits, drive mechanisms and neutron absorber rods having boron carbide pellets. The absorber rod of the first system is called Control & Safety Rod (CSR) and that of the second system is called Diverse Safety Rod (DSR). The respective drive mechanisms are Control & Safety Rod Drive mechanism (CSRDM) and Diverse Safety Rod Drive mechanism (DSRDM).

DESCRIPTION OF CSRDM

The photograph of CSRDM is provided in Fig.3. Overall length of CSRDM is about 12.3 m. The mobile assembly of CSRDM consists of guide tube, translation tube and gripper subassembly. Gripper subassembly having three fingers is attached at the bottom end of the translation tube. Gripper operating rod and sheath are housed in the translation tube, which moves inside tube sheath. The gripper fingers are operated manually from the top of CSRDM at a height of about 12 m during shutdown condition of the reactor.

The mobile assembly of CSRDM is held by an electromagnet (EM). A roller screw-nut mechanism is used for raising and lowering the EM, which is fixed to the nut. Motor drive assembly rotates the translation screw to raise or lower the EM and hence the mobile assembly. When CSR is coupled to the gripper of the mobile assembly, it also translates up or down based on the direction of rotation of the motor. Both the EM and mobile assembly slide over two guide columns fixed to support tube. Teflon bushes are provided at the contact surfaces. The mobile assembly is also guided by two colmonoy bushes, one at the level of V-ring seal block and the other in sodium at the lower end of the tube sheath. The corresponding surfaces of the translation tubes are hard chromium plated. Hence there are guides at four levels for the mobile assembly, when it is coupled with the EM and guides at three levels, when it is released from the EM.

On receiving the scram signal, the EM is de-energised and the mobile assembly of CSRDM along with CSR is released to fall under gravity. It falls down freely from its operating position. At the end of free fall travel, the mobile assembly is decelerated by an oil dashpot for the remaining 250 mm travel.

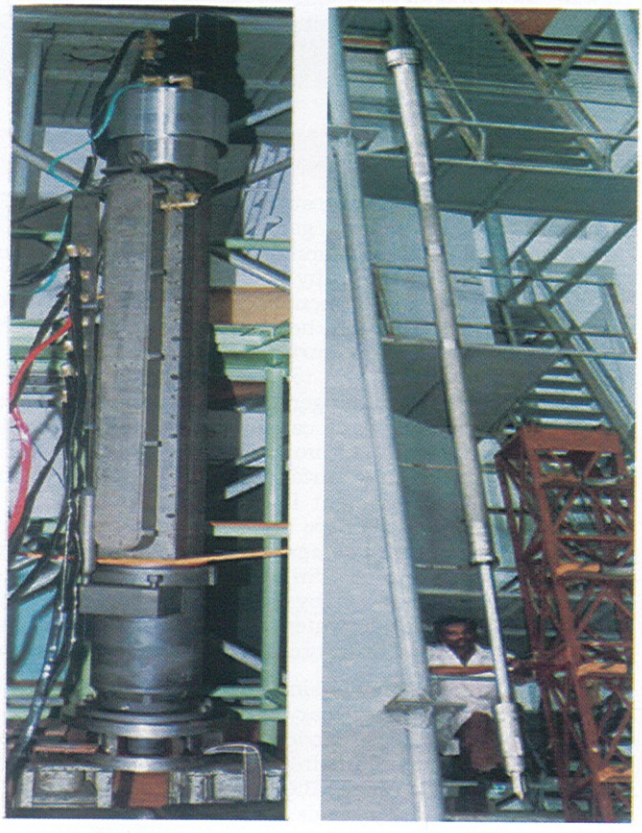

Upper Part Lower Part

Fig. 3: Photographs of CSRDM

BRIEF DESCRIPTION OF THEORETICAL BACKGROUND

Structural analysis was carried out to find out the frictional forces acting on the mobile assembly with CSR during scram operation. The performance of CSRDM & CSR in sodium was theoretically simulated to find the translational characteristics during free fall and braking travel of scram action. The theoretical results match well with the experimental results.

ACHIEVEMENT

The testing has enhanced the confidence level for safe and reliable operation of CSRDM and CSR in PFBR. The testing carried out has qualified the system for use in reactor and provided basis for licensing the erection of CSRDM and CSR on reactor pile.

PUBLICATIONS ARISING OUT OF THIS STUDY AND RELATED WORK

V. Rajan Babu, R. Veerasamy, D. Rangaswamy, K. Narayanan, S.C.S. Pavankumar, S.K. Dash, C. Meikandamurthy, K.K.Rajan, M. Rajan, P. Puthiya Vinayagam, P. Chellapandi and S.C. Chetal, 14th International Conference on Nuclear engineering (ICONE-14), July 2006, Florida (USA).

Further inquiries:
Shri V. Rajan Babu, Reactor Components Division, Reactor Engineering Group, IGCAR, e-mail: vrb@igcar.gov.in
Shri R. Veerasamy, Components & Instrumentation Development Division, Fast Reactor Technology Group, IGCAR
e-mail: rvs@igcar.gov.in

Mitigation of Gas Entrainment for Prototype Fast Breeder Reactor

EXECUTIVE SUMMARY

Thermal-hydraulics of the reactor plays a significant role in the safe, economic and compact design of the reactor. One of the issues to be resolved is the entrainment of argon cover gas into liquid sodium in the primary side of PFBR. This entrained gas bubbles when circulated in primary circuit can lead to reactor operational problems. Hence it is important to mitigate gas entrainment at the free surface of hot pool. High free surface velocity along with the presence of various immersed components in the hot pool is the cause of gas entrainment from free surface. The present study aims to choose an appropriate device to mitigate gas entrainment by reducing the free surface velocities. The study was conducted in a large size, 1:4 scale model of the primary side of PFBR in water. The experimental findings revealed that the introduction of baffle plate in the pool reduces the free surface velocities and thereby gas entrainment.

OUTLINE

There is large sodium free surface in the hot pool of PFBR. Argon, which is an inert gas, is provided above the free surface of hot pool to accommodate volumetric expansion of sodium and to prevent any contact between sodium and atmosphere. The entrainment of cover gas from the sodium – argon interface, into the hot pool is possible by various mechanisms (such as surface vortices etc.]. Then this entrained gas can flow to the cold pool through the Intermediate Heat Exchanger (IHX) and enter the active core. This phenomenon can cause unfavorable operational problems. Hence it is important to mitigate the gas entrainment at the free surface of the hot pool. The primary cause of gas entrainment into the hot pool is high free surface velocity. Therefore the gas entrainment can be reduced by achieving a comparatively quiescent free surface. This study aims to choose an appropriate device to minimize the cover gas entrainment by reducing free surface velocities. A large scale (1/4 scale) water model of PFBR primary circuit (SAMRAT) was used to carry out these parametric studies.

This experimental model simulates the geometry of all the components in PFBR primary circuit in one fourth scale. The experimental studies carried out earlier in this model predicted the maximum free surface velocity in hot pool around 1.12 m/s in PFBR. The preliminary visual gas entrainment studies revealed that a large amount of gas is entrained from the free surface at nominal operating condition of reactor. Therefore it was thought of as a necessity to reduce the free surface velocity. Ring type devices (baffle plates) attached to the inner vessel was chosen to reduce the free surface velocities in the hot pool.

Initially parametric studies were carried out numerically to achieve the optimum dimension of baffle plate and it's location inside the hot pool. It was found from the numerical study that the choice of a baffle plate with radial size of 125mm and located above the intermediate heat exchanger inlet window is most suitable for reducing the free surface velocity to 0.25 m/s in model, which is equivalent to 0.5 m/s in PFBR.

Based on the above numerical study, the selected configuration of baffle plate was fabricated and installed in SAMRAT model. The baffle plate as fixed with the inner vessel is shown in Fig. 1. Parametric studies were carried out by varying the vertical location of the baffle plate. For each experimental run, velocity was measured at the free surface to find out the maximum magnitude. Visual observation of the free surface was carried out to find out occurrence of free surface vortices. The effectiveness of baffle plate for converting the turbulent free surface to a comparatively quiescent free surface is shown in Fig. 2. It is evident from this figure that the baffle plate is very effective to reduce the free surface activities that are responsible for gas entrainment phenomena. A fair agreement was found between the numerical prediction and the experimental measurement.

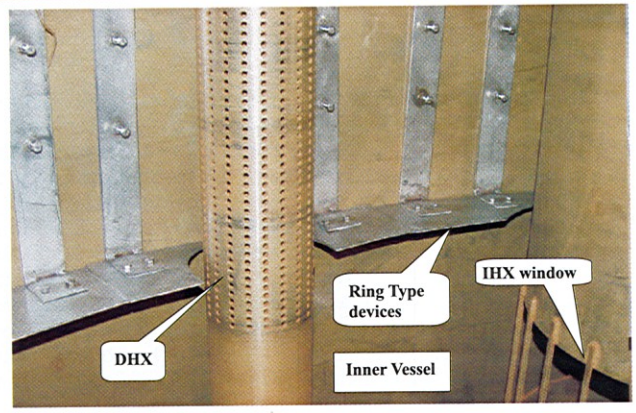

Fig. 1: Baffle Plate fixed in the model



Without Baffle plate



With baffle plate

Fig. 2: Free surface flow pattern at various experimental conditions

■ PROBLEMS DUE TO GAS ENTRAINMENT IN LMFBR PRIMARY CIRCUIT

The entrained gas bubbles in the primary circuit can lead to the following problems:
1) A large variation in the gas content of the core possibly causes a reactivity fluctuation.
2) Bubbles are nucleation sites for boiling or cavitation.
3) If large bubbles can get trapped in a sub assembly, burn out of fuel pins may occur.

■ VARIOUS GAS ENTRAINMENT MECHANISMS

The entrainment of cover gas into the hot pool is possible by four major mechanisms. These mechanisms are as follows:

1) Liquid fall – if the vertical velocity is very large near the free surface the flow rises above the mean free surface forming a local hump. The flow, which rises above the free surface, falls back to the sodium surface as a liquid fall. The interaction between the falling liquid and the pool causes entrainment of cover gas.

2) Vortex activated entrainment – the horizontal sodium flow at the free surface past to the immersed structures (IHX, PUMP, etc.) can form Von-Karman vortices. The rotating vortices have dimples of gas at the centre. If these vortices encounter strong vertical downward currents, it can lead to entrapment of gas in sodium. This is shown in Fig. 3.

3) Drain type vortex: This is also known as 'bathtub' vortex. This type of vortex can be formed if the submergence level of IHX widow is low.

4) Shearing of Gas-Liquid interface: if the free surface velocity is very large (>2 m/s) the surface waves generated can lead to gas entrainment.

By careful investigation of above mechanism it was found that the vortex activated entrainment is the only probable mechanism of gas entrainment in PFBR.

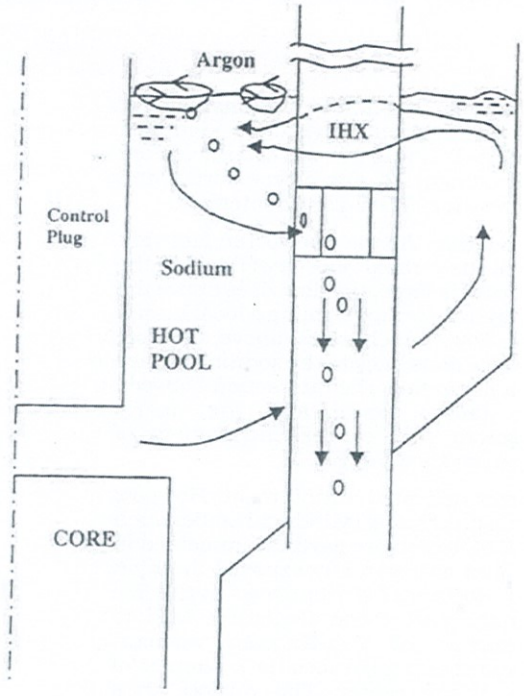

Fig. 3 : Vortex activated gas entrainment

■ BRIEF DESCRIPTION OF SIMILARITY CRITERIA FOLLOWED

In general, the gas entrainment phenomenon is governed by three non dimensional parameters i.e., Reynolds (Re, ratio of inertia force and viscous force), Froude (Fr, ratio of inertia force and gravity force) and Weber number (We, ratio of inertia force and surface tension force). It is not possible to simulate all these three numbers in a scaled model test. However the effect of Re is insignificant if the flow is in turbulent region. Thus both Fr and We number have importance for gas entrainment study. For simulating both Fr and We number simultaneously using water as simulant, a 5/8 scale model is required. However from the published reports it was found that the importance of We number becomes less significant for large scale models (scale ≥ 1/8) as distortion in We number decreases. Hence experiments carried out with Fr similitude in this ¼ scale model.

■ ACHIEVEMENT

The present baffle arrangement for avoiding gas entrainment is the result of tests with different devices and is critical for PFBR design. Hence this work can be considered as a technological milestone of high relevance to the Centre.

■ PUBLICATIONS ARISING OUT OF THIS STUDY AND RELATED WORK

1. I. Banerjee, L. Chandra, D. Laxman, A. Kumar, C.A. Gopal, N. S. Shivakumar, G. Padmakumar, C. Anand Babu, G. Vaidyanathan; International Congress on Advances in Nuclear Power Plants (ICAPP-2007); France, May 13-18, 2007, Nice, Acropolis.
2. D. Ramdasu, N. S. Shivakumar, G. Padmakumar, C. Anand Babu, G. Vaidyanathan, International Congress on Advances in Nuclear Power Plants (ICAPP-2007), May 13-18, 2007, Nice, Acropolis, France.

Further inquiries:
Shri Indranil Banerjee and Shri G. Padmakumar
Separation Technology and Hydraulics Division, Fast Reactor Technology Group, IGCAR, e-mail: gpk@igcar.gov.in

Understanding the Mechanisms of Gas Entrainment in PFBR Hot Pool and Design Solutions

EXECUTIVE SUMMARY

The mechanisms of gas entrainment in the sodium free surfaces of pool type fast breeder reactor, its transportation through heat exchangers (IHX) and pump to grid plate, agglomeration of the gas inside the grid plate and its passage through the core need to be understood well. This is an important safety problem as passage of argon gas through core leads to positive reactivity. This problem has been studied in detail through multi-dimensional computational flow dynamics analysis and experiments. Design solutions to mitigate gas entrainment have been proposed.

OUTLINE

Potentially four different mechanisms of gas entrainment have been identified namely 1) Liquid fall, 2) Vortex activated entrainment, 3) Drain-type vortex and 4) Shearing of Gas-Liquid Interface.

Liquid fall: This is due to the fact that when the vertical velocity of liquid in the hot pool is large, the flow rises above the mean free surface forming a local hump. The flow, which rises above the free surface, falls back to the sodium surface as a liquid fall. The interaction between the falling liquid and the nearly stagnant pool causes entrainment of argon as shown in Fig.1.

Vortex activated entrainment: Hot pool consists of many cylindrical bodies such as IHX, which are partially immersed in sodium and partially exposed to argon gas. Horizontal sodium flows at the free surface past these structures lead to formation of Von-Karman vortices. These rotating vortices have dimples of gas at the center. The vortices thus generated travel along the liquid. If these vortices encounter strong vertical downward currents before their dissipation, it can lead to entrapment of gas in sodium.

Drain-type vortex: The drain-type vortex, occurs when the submergence level of IHX window, for the IHX-inlet velocity is inadequate. In this type of entrainment, a long gas core is formed around the drain location starting from the free surface. Presence of such a vortex can lead to transportation of large quantity of argon gas.

Shearing of Gas-Liquid Interface: When the free surface velocity is large, the shearing interface between sodium and argon gas becomes unstable leading to generation of surface waves. The waves can lead to gas entrainment near the free surface.

Mitigation of Gas entrainment in hot pool: The core flow enters the hot pool as a horizontal jet (also called core jet) in between the skirt and the subassembly-top. It induces a large anti clockwise circulation zone, which occupies almost the entire hot pool. The maximum horizontal velocity with which the jet enters the hot pool is ~3 m/s and as a result of this the maximum horizontal velocity on the free surface is ~1.0 m/s.

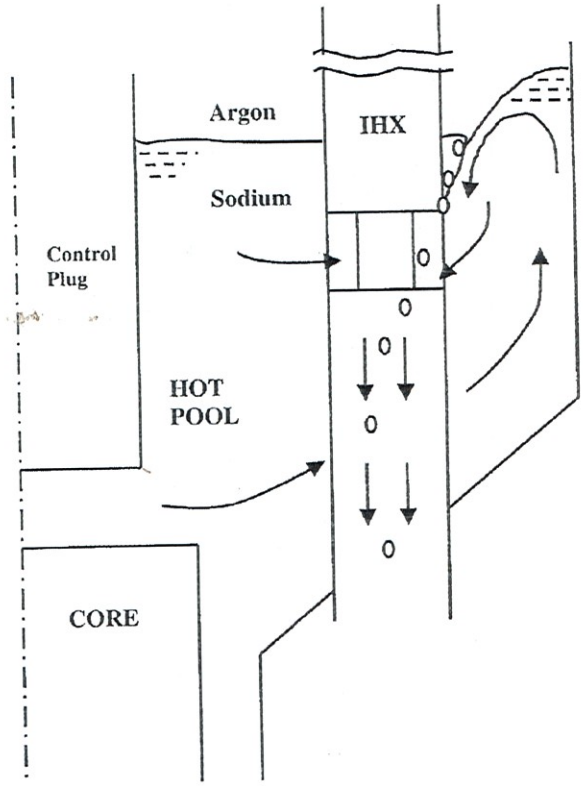

Fig. 1 : Liquid fall induced Gas Entrainment

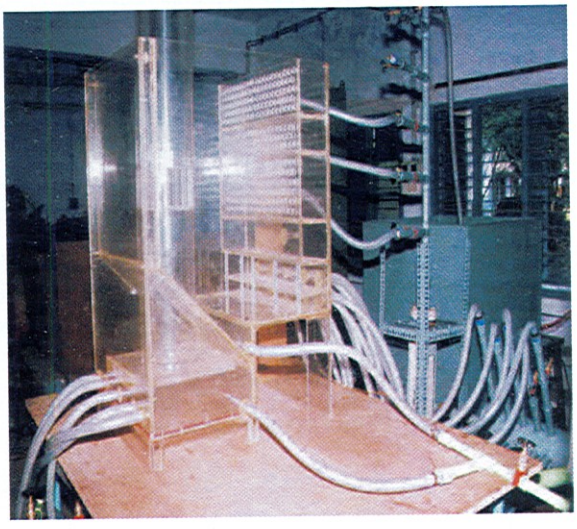

Fig. 2: 1:9 Scale model for gas entrainment studies

The reason for this high value is the presence of skirt. By keeping the free surface velocity low, sodium free level can be made quiescent and possibility of gas entrainment can be reduced. Reduction of free surface velocity is possible by altering the hot pool flow pattern in such a way that the influence of core jet is minimized near the free surface. Experiments on 1:9, 1:18 and 1:27 scaled models have been carried out at IIT Madras to find out the minimum hot pool level above IHX inlet window to mitigate gas entrainment (Fig.2). These experiments have provided more understanding of the gas entrainment phenomena.

Detailed 3D thermal hydraulic studies were carried out to see the efficacy of using baffles fitted to inner vessel upper shell, redan and / or control plug in reducing free level velocity. The effect of a minor modification in the skirt, in the form of providing circumferential slots either in the top or middle of the skirt was also studied.

Based on the above studies, design provisions have been recommended. As per this, it is required to lower the large rotatable plug inner shell in addition to introduction of a baffle plate above IHX inlet. With this, the free level velocity of ~ 1 m/s as seen in Fig.3 without any baffle, has been reduced to 0.31 m /s (Fig.4) with introduction of design provisions. This implies that there is no risk of gas entrainment in PFBR.

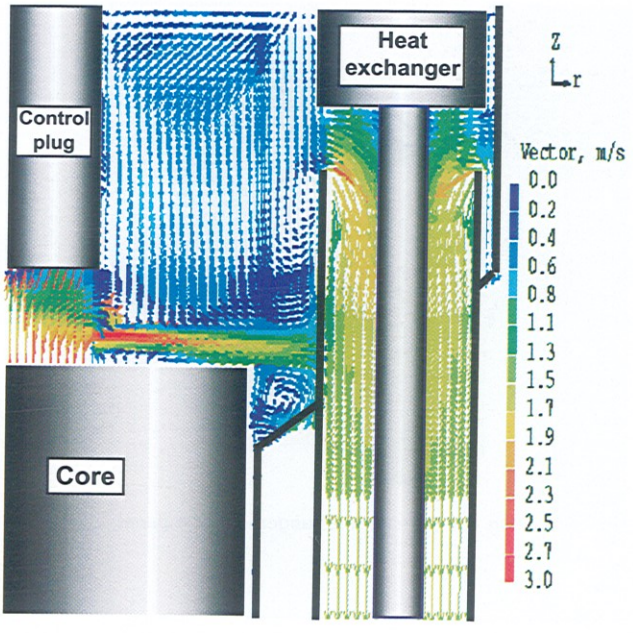

Fig. 3: Flow distribution without baffle plate

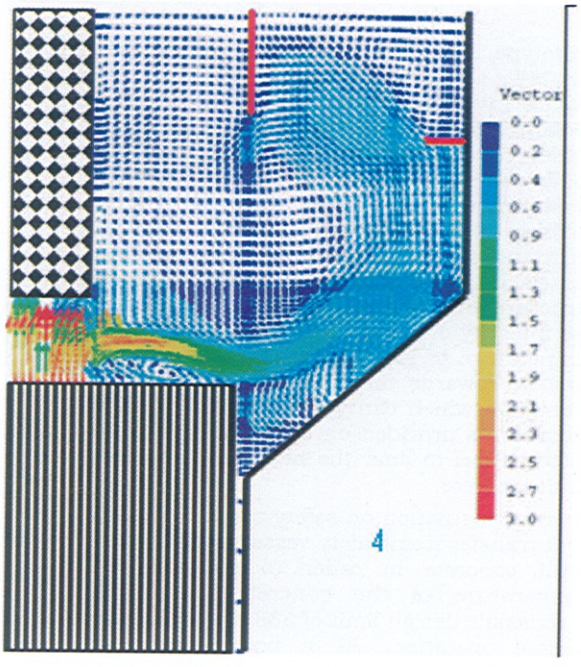

Fig. 4 : Flow distribution with design provisions baffle plate

■ ACHIEVEMENT

Understanding the gas entrainment mechanism and complex Computational Fluid Dynamics (CFD) analysis with experimental validation have been carried out in the most comprehensive manner.

The problem of gas entrainment in the hot sodium pool in PFBR , the critical issue to hold the safety clearance has been resolved successfully.

Further inquiries:
Shri P. Selvaraj, Mechanics and Hydraulics Division
Reactor Engineering Group, IGCAR, e-mail: pselva@igcar.gov.in

Design and Development of Thermal Insulation for PFBR Safety Vessel

EXECUTIVE SUMMARY

In a pool type fast reactor, to reduce heat transferred to reactor vault, stainless steel plate type insulations are provided in the form of panels around safety vessel. As these type of insulations are not commercially available, the same has been designed and fabricated indigenously using 0.1mm thick sheets stacked to form panels. Dimples are provided to ensure spacing between the sheets. Experiments were carried out with polished sheets as well as panels to confirm compliance of design. The manufacture of the panels were completed overcoming several challenges and have been assembled over safety vessel signaling the successful completion of design and development of thermal insulation panels for safety vessel.

OUTLINE

Prototype Fast Breeder Reactor (PFBR) is a 500 MWe sodium cooled pool type reactor. All reactor internals including core and primary coolant (sodium) are contained in a single vessel called main vessel. To contain the sodium in the unlikely event of leak in main vessel and to ensure minimum sodium level to facilitate core cooling, safety vessel is provided surrounding main vessel. The load from these vessels is transferred to cylindrical concrete structure known as reactor vault. Considering the integrity of concrete structure, maximum temperature to which it can be subjected is limited. Towards this, SS plate type thermal insulation which can withstand high gamma radiation is provided on outer surface of the safety vessel to limit the heat flux to reactor vault concrete.

Thermal insulation on safety vessel limits the heat transfer from safety vessel to the reactor vault concrete in order to maintain the temperature of the concrete within the permissible design limit of 338 K (65°C) under normal operation, 20 % power operation, isothermal operation and 363K(90°C) under Safety Grade Decay Heat Removal (SGDHR) condition.

The SS plate type insulation is designed in the form of panels, each measuring ~1m x 1m (Fig.1). These types of insulations work on the principle of thermal radiation shielding. The introduction of one plate between two radiating surfaces reduces the heat exchange between the two through radiation mode by half. Each panel consists of two slabs interconnected through studs. In each slab, 17 plates of 0.1mm thick mirror polished sheets are encased in a box of 1mm thick whose surfaces are also mirror polished. Multiple panels are secured all over the outer surface of safety vessel through studs welded on outer surface of safety vessel. The thickness of 0.1mm is specified for sheets so that the load on safety vessel due to insulation is kept to minimum.

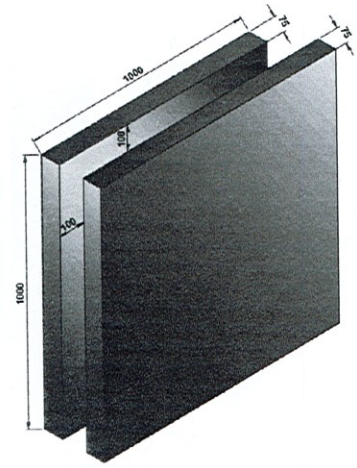

Fig. 1 : Schematic arrangement of a panel

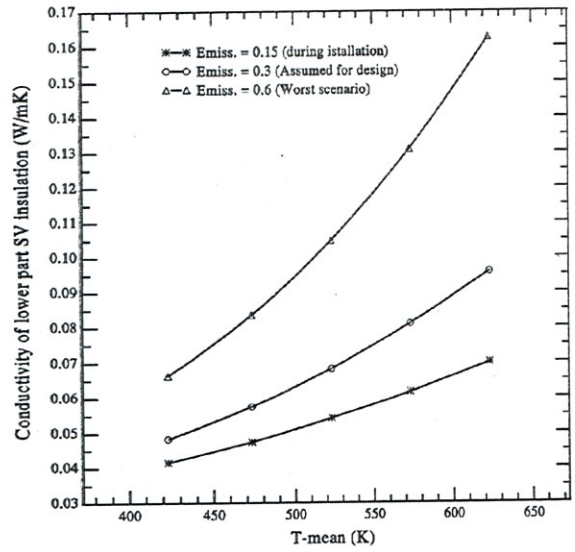

Fig. 3 : Emissivity Vs Thermal conductivity

THERMAL INSULATION

The thickness of insulation panels and the number of insulation sheets in each panel are based on optimisation study carried out towards restricting the heat flux to reactor vault concrete. The maximum size of insulation is fixed as 150mm considering the influence it has on the overall dimension of reactor vault. With this, optimisation studies carried out indicates number of sheets in each panel to be 34 Nos. to restrict the heat flux to reactor vault concrete within acceptable limits. The heat transferred through radiation mode depends on the surface emissivity and hence mirror polish has been specified for these sheets which give a surface emissivity as low as 0.05. The effect of surface emissivity of the insulation sheets over heat flux has been studied (Fig.2). To avoid streaming between two panels, the two slabs are assembled with an offset of 100mm so that on assembly, the gap created between slabs of adjacent panels are closed with the other set of slabs from the same panels.

As the sheets are very thin, maintaining the spacing between them is really a challenging task. A gap of 4.26mm was specified in the design and dimples were provided to achieve the required spacing. Initially, trials with 100mm dimple spacing did not yield desired results. Subsequently, the spacing was reduced to 50mm and with this required spacing between sheets could be achieved.

The major challenge was faced in the forming of dimples. During the initial trials, the dimple was found to be tearing. This problem was solved by specifying a material of low hardness but within the permissible range and by increasing the fillet radius between the dimple and the sheet. Subsequent trials proved the effectiveness of the steps taken to improve dimple forming and the problem of dimple tearing was resolved.

The other challenge was with respect to stacking of the sheets one over the other. Due to self weight as well weight of sheets supported over it, total height of the stack was not achieved. Towards, this, novel spacing arrangement with multiple spacers was designed and incorporated. Fig.3 gives view of one typical insulation panel.

As no direct correlation is available between surface roughness and the emissivity, experiments were carried out to evaluate the emissivity of the plates polished and the same has indicated that the mean emissivity to be 0.047 which matches with the design intent value.

Further, experiments were carried out in an experimental set-up, at IGCAR, to assess the heat transferred through the insulation panels and the results have reinforced the theoretically calculated values enhancing the confidence in design.

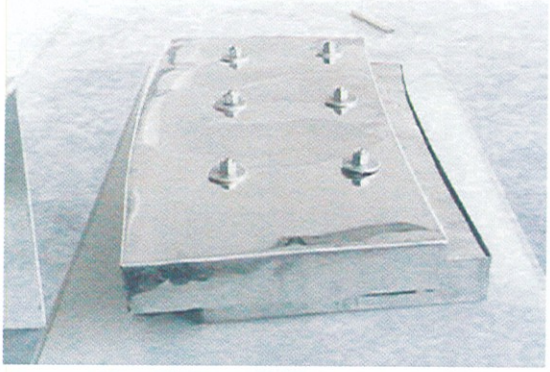

Fig. 3 : Typical Thermal Insulation Panel



Fig. 4 : Assembly of Thermal Insulation Panels over Safety Vessel

ACHIEVEMENT

The safety vessel thermal insulation panels have been fabricated as per the technical specification meeting all the design intents. Experiments conducted to measure emissivity and heat transfer have reinforced the design calculations. Fixing of panels over safety vessel has been successfully carried out (Fig.4) concluding the successful design, development and manufacture of thermal insulation panels for the first time within the country.

The design and development and successful assembly of thermal insulation panels over safety vessel has ensured meeting design limits for the concrete of reactor vault which is essential for safe operation of the reactor.

Further inquiries:
Shri V. Balasubramaniyan, Reactor Components Division
Reactor Engineering Group, IGCAR, e-mail: bala@igcar.gov.in

Investigation of Lifting off Core Subassemblies under Seismic Excitations

EXECUTIVE SUMMARY

The stability of the fuel subassemblies, supported on the grid plate and held in position by self weight is demonstrated under seismic loading by shake table testing. The concern is the lifting of the subassemblies under combined effects of upward coolant flow under pressure of 0.7 MPa and upward accelerations generated by vertical seismic excitation. It is also demonstrated that with the applications of multiaxial excitations, the lifting off problem is completely ruled out even up to 1 g (g-acceleration due to gravity) peak ground accelerations in the vertical direction.

OUTLINE

In order to ensure the required core flow, the pressure of sodium in the grid plate (GP) is maintained at about 0.7 MPa, which develops an upward lift on each of the fuel subassembly (FSA), equivalent to 0.28 g, in case of pump running at 110 % design flow rate. Being less than 1 g, the net gravitational force acting on each subassembly is always downward and hence there is no fear of any uplift. The seismic analysis of reactor assembly indicates that the peak vertical acceleration of grid plate can be as high as 0.88 g under Safe Shutdown Earthquake (SSE). Hence, there is a concern of lifting off subassembly during seismic events, in particular under vertical excitation.

In this investigation, upward displacement of subassemblies is quantified under combined effect of upward fluid force and vertical seismic excitations. SSE is assumed to occur during the worst situation, viz. beginning of life where each core subassembly is freely standing on the grid plate without any resistance from the adjacent ones and the pump is running with 110 % of the design flow. The vertical displacements of subassembly are determined through shake table experiment.

The test subassembly considered here is the prototype one being manufactured for PFBR. The bundle for test assembly is fabricated using steel rods made of carbon steel with the simulated length and weight (adjusted by adding steel plates appropriately. The corresponding sleeve is also a typical prototype sleeve being manufactured for the PFBR. The sleeve is supported on a rigid structure which is bolted to the grid plate. The upward fluid pressure and seismic vertical excitations are applied simultaneously. The fluid pressure is applied at the bottom of foot by a specially designed setup as shown in Fig.1.

Vertical seismic excitations as shown in Fig.2 are applied by using triaxial shake table of 10 t capacity. A dedicated data acquisition system with 64 channels is used for capturing the structural response under seismic excitation. It is connected with the linear variable differential transformers (LVDT) and triaxial accelerometer provided at the specimen through cables. Three LVDTs are used for measuring the relative displacement of the SA with respect to GP top. The test setup is shown in Fig.3

A constant pressure of 0.7 MPa is maintained at the bottom during seismic tests. FSA is subjected to vertical excitation as per the time history depicted in Fig.2 by varying the peak acceleration values in 3 steps, viz. 0.5 g, 1.0 g and 1.5 g respectively.

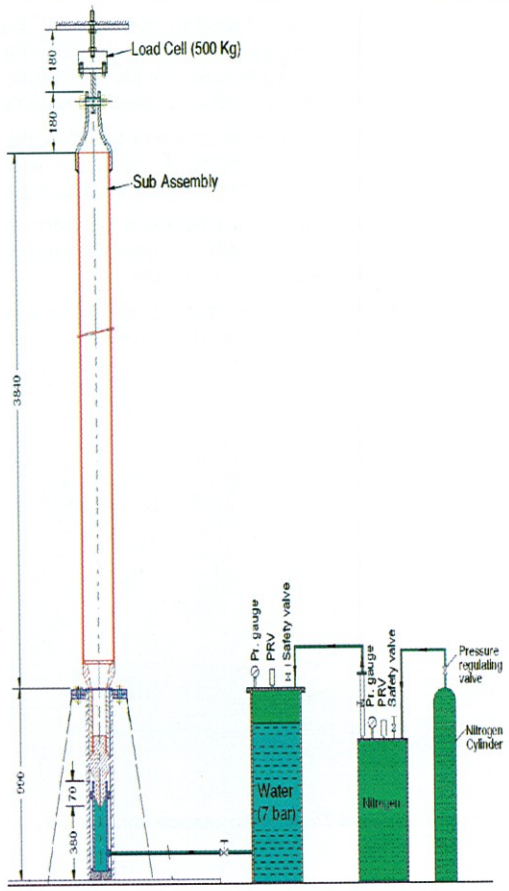

Fig. 1 : Test setup for SA lift-off study

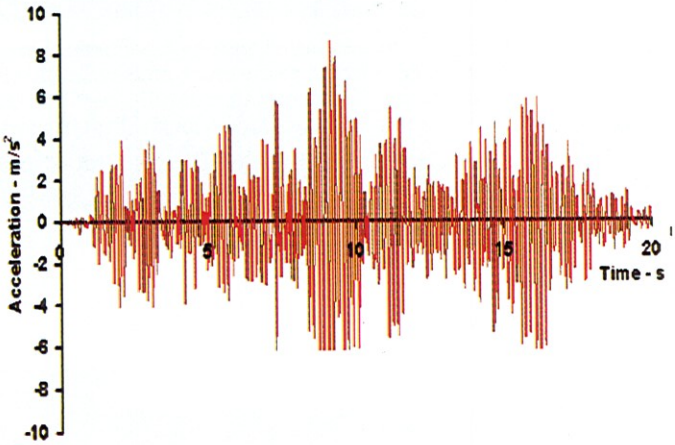

Fig. 2 : Vertical acceleration at GP support

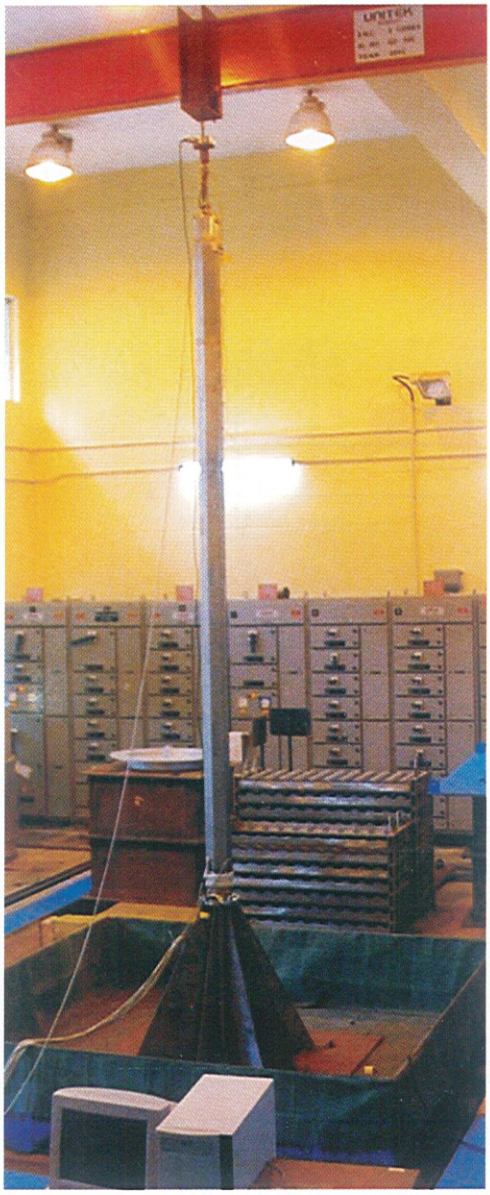

Fig. 3 : Test setup mounted on the shake table

Average values of all the three LVDT are given in Fig.4 for the maximum peak vertical acceleration of 0.5 g and 1.0 g respectively, which are insignificant. Since we have tested a single FSA, the presence of neighboring FSA will also increase further resistance towards detachment. This experiment has demonstrated the incapability of FSA detachment from the GP even under severe earthquake.

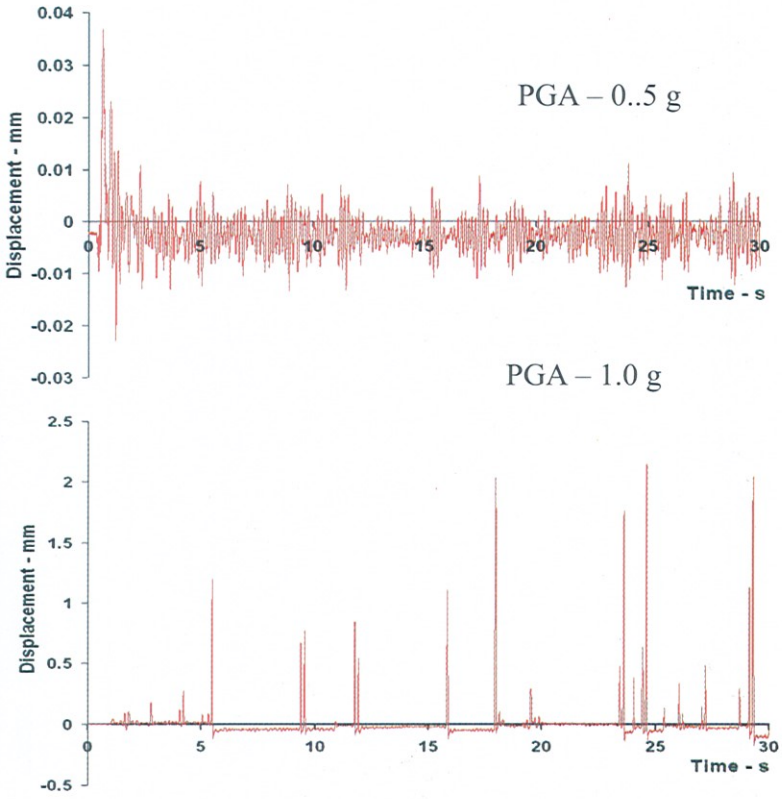

Fig. 4 : Vertical displacement of FSA

■ ACHIEVEMENT

Design and development of a novel test setup to apply simultaneously upward fluid pressure along with the seismic excitations is an innovative idea.

An important study to demonstrate to safety committee that there is no fear of lift off the core subassemblies under seismic events

■ PUBLICATIONS ARISING OUT OF THIS STUDY AND RELATED WORK

P. Chellapandi, V. Rajan Babu, P. Puthiyavinayagam, S.C. Chetal and Baldev Raj, Report No. ICONE15-10859, Proceedings of 15th International Conference on Nuclear Engineering, April 22-26, 2007, Nagoya, Japan.

Further inquiries:
Shri P. Puthiya Vinayagam, Reactor Components Division
Reactor Engineering Group, IGCAR, e-mail: vinayaga@igcar.gov.in

Investigation on Buckling of PFBR Vessels under Seismic Loadings with Fluid Structure Interactions

EXECUTIVE SUMMARY

An integrated analysis for determining realistic dynamic forces and critical buckling loads at any instant during the seismic event has been carried out for the reactor assembly vessels of Prototype Fast Breeder Reactor (PFBR). The inner vessel is found to be the most critical component which buckles under seismic forces induced by a safe shutdown earthquake with a load multiplier of 1.52, which is higher than the minimum factor of safety of 1.3 required as per the design code RCC-MR (2002)

OUTLINE

The critical failure mechanism that decides the structural design of thin vessels of Prototype Fast Breeder Reactor (PFBR) is buckling under seismic event. The main vessel which houses the entire primary sodium circuit, inner vessel which separates the hot and cold sodium pools and thermal baffles which protects the main vessel from the heat flux emanating from the hot pool are the important structures to be analysed. The investigation of buckling risks of these vessels calls for determination of dynamic forces, in particular the dynamic pressure distributions developed on the vessel surfaces and evaluation of buckling strength. The seismic events generate complicated unsymmetrical pressure distributions which have both temporal and spatial variations. In a classical way, the analysis is carried out in an uncoupled way, in the sense that determination of seismic forces in the first phase, estimation of integrated forces and moments in the second phase and evaluation of critical buckling load factor in the third phase for each vessels. In this analysis, the realistic stress distribution is naturally lost. Another approach would be evaluating the critical buckling load factor at each time step employed for the seismic analysis. This approach consumes considerable computer time making the solution not practicable. In view of these difficulties, an integrated analysis is established through which the realistic critical buckling loads and associated mode shapes are evaluated based on buckling analysis under the dynamic forces generated at a few critical time steps only. The critical time steps are those at which the strain energy developed is maximum in the vessels due to compressive and shear stresses generated during the seismic event.

Seismic analysis is carried out by applying the seismic excitations at the reactor assembly support simultaneously in the two mutually perpendicular horizontal directions (X and Y directions) under safe shutdown earthquake (SSE). The possible randomness on the generated support time histories are accounted properly by compressing the time scale by 10 % as well as by expanding the time scale by 10 %. Axisymmetric analysis is carried out with fourier option assigning the harmonic wave number, equal to 1 for the horizontal excitations. In order to obtain the lowest critical buckling load factor in a single analysis including 3D geometrical features, buckling analysis is performed on 3D geometries. Towards this, the pressure/force distributions extracted from axisymmetric analysis at the given critical time step, are translated to corresponding 3D geometries. The finite element mesh is shown in Fig.1. The pressure distributions on the vessels extracted at the critical time steps are depicted in Fig.2.

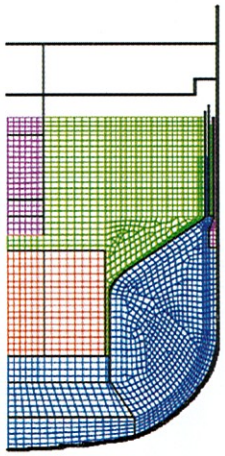

Fig. 1 : FE model of PFBR reactor assembly

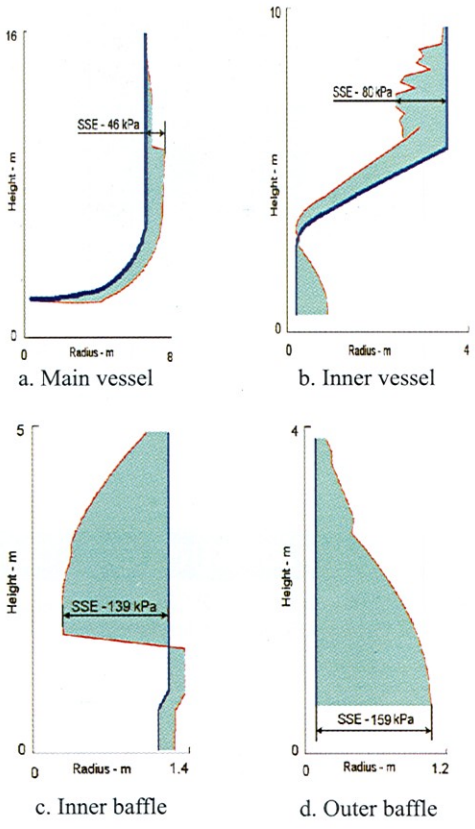

Fig. 2 : Pressure distributions at a critical time step

■ GENERAL EXPLANATION RELATED TO THE DESCRIPTION

For the buckling analysis, half symmetric geometries are generated for the main vessel, inner vessel and integrated geometry of inner and outer thermal baffles. Since the main vessel and thermal baffles are symmetric structures, 3D geometries are generated by 180° rotation of the respective axisymmetric elements. The buckled mode shapes of main vessel, thermal baffle and inner vessel obtained at a critical time step are shown in Fig.3. The critical buckling load factors are shown in Table-1.

Table-1
Critical buckling load factors

Sl.No	Component	X-direction	Y-Direction
1	Main vessel	2.72	3.0
2	Inner vessel	1.52	1.6
3	Outer baffle	3.0	2.56
4	Inner baffle	3.0	2.4

The design adequacy is checked as per the design code RCC-MR (2002) which specifies a requirement of minimum 1.3 factor of safety on the computed critical buckling load for the SSE. This means that the minimum critical buckling load should be more than 1.3 times the loads developed under SSE. With the minimum load factors of 2.72, 1.52, 2.56 and 2.4 computed for the main vessel, inner vessel, outer and inner thermal baffles respectively, it is demonstrated that the critical vessels in the reactor assembly respect the buckling design criteria of RCC-MR.

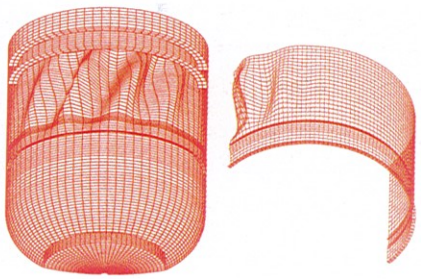

a. Main vessel b. Thermal baffle vessel

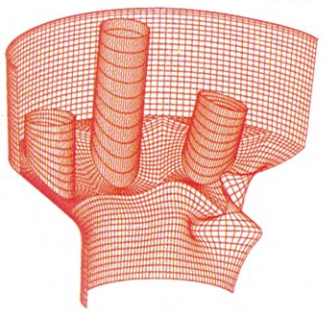

c. Inner vessel

Fig. 3 : Buckled mode shapes of vessels

■ ACHIEVEMENT

The complex analysis is done to demonstrate the structural integrity of reactor assembly components under seismic loadings with an innovative analysis methodology by addressing all the associated complexities. This is an important analysis to get the safety clearance for PFBR.

With the realistic analysis, possibly minimum thicknesses have been selected for reactor assembly components with higher confidence.

■ PUBLICATIONS ARISING OUT OF THIS STUDY AND RELATED WORK

P.Chellapandi, S.C.Chetal and Baldev Raj, *ASME Trans. Pressure Vessel and Piping* (In Press).

Further inquiries:
Dr. P. Chellapandi, Nuclear Engineering Group
Reactor Engineering Group, IGCAR, e-mail: pcp@igcar.gov.in

Laser Heated Diamond Anvil Cell facility for Synthesis of Novel Materials

EXECUTIVE SUMMARY

In the recent decade the Laser Heated Diamond Anvil Cell (LHDAC) technique has become the preferred tool to study materials at extremely high pressures and temperatures on account of (a) accessibility to Pressure (P) and Temperature (T) ranges not possible by conventional methods; (b) ultrapure sample environment; (c) highly localized heating of the sample. Applications of the LHDAC include exploration of P-T phase diagrams of materials, search for novel phases like superhard and harder-than-diamond materials, simulation of planetary interiors etc. Keeping some of these in mind, a state of-the-art LHDAC facility has been set-up successfully to study materials under very high pressures (~ 1 Mbar) and temperatures (~ 5000 K). There are some unique features in this facility, like a fully automated scan routine to achieve uniform areal heating of the sample using nanomotion systems and an indigenous imaging arrangement.

OUTLINE

The Diamond Anvil Cell (DAC) is a tool par excellence to compress matter to very high static pressures. High strength of the diamonds coupled with their excellent transmittance to almost the entire electromagnetic spectrum has led to extensive in situ studies on a myriad of pressure induced phenomena in materials using X-ray diffraction and various spectroscopic techniques. This wide-range transmittance of diamonds can be exploited to focus high power IR laser beams on to the sample squeezed in the DAC, thereby subjecting it simultaneously to very high temperatures of over 5000 K and pressures of over many megabars. This technique, called the Laser Heated Diamond Anvil Cell (LHDAC) is emerging as an unique route for investigating materials and synthesizing novel phases in the hitherto unexplored P-T region. The LHDAC technique can be utilized for simulating, in the laboratory, the extreme environments such as those existing in Earth and other planetary interiors. At such extreme conditions, nature of the chemical bonding in elements changes and the chemical reactivities generally increase such that direct elemental reaction between even inert species becomes possible. This can lead to the formation of novel and exotic phases. Synthesis of nitrides of C, B, Si and Ge that are expected to rival diamond in terms of hardness is one of the frontline problems addressed by LHDAC researchers. Other applications of the LHDAC include study of melting phenomena and structural transitions in a variety of materials.

At Materials Science Division, IGCAR, a state-of-the-art LHDAC facility has been set-up recently for investigating materials behaviour up to ~1 mbar and ~5000 K simultaneously (Figs. 1 and 2). This facility essentially consists of an indigenously developed DAC, a 120 W CO_2 laser (λ=10.6μm; continuous wave; single mode), a X-Y Nanomotion system, and IR compatible optical components. In this technique, the challenge lay in heating the ultra tiny sample (~75 μm diameter) that is "squeezed" between the two diamond anvils to very high-temperatures using an invisible high power IR laser without causing damage to the diamonds and other supporting materials. This has been achieved using simple and cost effective ideas like a webcamera–microscope combination for real-time imaging (now, upgraded with a CCD imaging system), indigenously designed vibration free tables and optical mounts. The use of the nanomotion system, for which the control software was developed inhouse, played a critical role in achieving the above successfully. A CCD based spectrometer has been included in the set-up to (a) record the grey body spectrum emitted by the sample for temperature estimation using Planck distribution; and (b) to record luminescence from a ruby chip, located inside the DAC, excited by 514.5 nm line from an argon ion laser for pressure determination.

Valuable experience in sample synthesis at high-pressures and high-temperatures have been gained using this IGCAR LHDAC facility. In particular, two experiments that demonstrated the capability of this facility and mastery over the difficult technique are conversion of graphite to a diamond-like translucent phase at ~14 GPa and ~2000 K and successful synthesis of the semiconducting material InSb by direct heating of In and Sb at ~2000K and ~0.5 GPa.

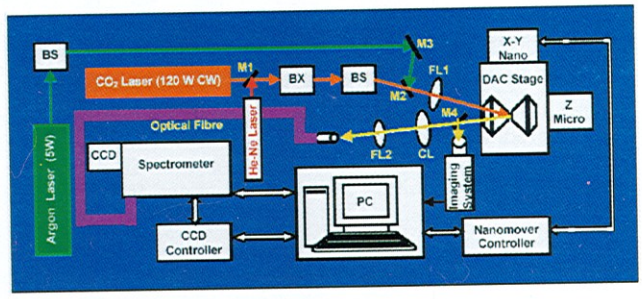

Fig. 1 : Schematic of the LHDAC set-up; M1, M2, M3 and M4: Mirrors; BS: Beam Steerer; BX: Beam Expander; FL1 and FL2: Focussing Lenses; CL: Collecting Lens;

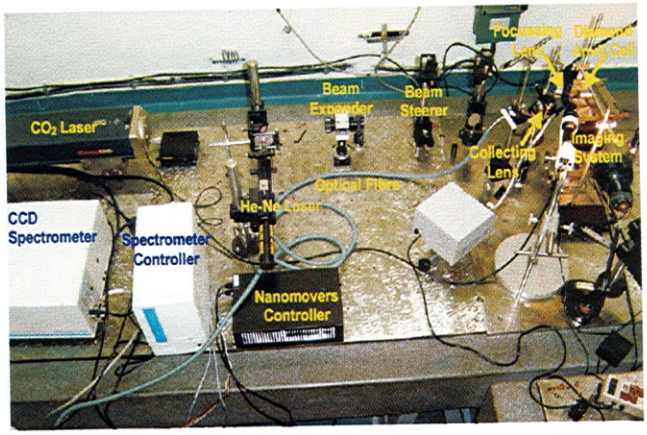

Fig. 2 : Photograph of the LHDAC set-up; All components, including the lasers are mounted on a granite table located on a special foundation, structurally isolated from the rest of the building to minimize vibrations.

EFFECTS OF PRESSURE AND TEMPERATURE ON MATERIALS BEHAVIOR

Apart from expected changes in the unit cell volume, dictated by the Equation of State of the material under study, high-pressure affects the material in principally two ways, namely induction of structural and electronic changes. Structural changes include increased densification and phase transitions from one structure to another, generally involving change in crystallographic symmetry. Electronic changes result from increasing overlap of the electronic orbitals, leading to transitions like metal-insulator, normal-superconducting, magnetic-nonmagnetic, etc. Expectedly, structural and electronic effects are often interrelated and influence each other. Simultaneous application of high temperature enhances the kinetics and brings about interesting interplays with the pressure induced perturbation of the electronic and crystal structures, resulting in novel ground states of the material.

PHASE TRANSITION OF GRAPHITE TO DIAMOND-LIKE MATERIAL

It is well known that diamond is a metastable phase of carbon and can be synthesized, even without the aid of any catalyst, in the laboratory by subjecting carbon in one of its myriad forms like graphite or fullerene to very high pressures and temperatures. This experiment was taken up as the first problem in order to test the IGCAR LHDAC facility and gain experience in handling the difficult LHDAC technique.

A high purity graphite chip (linear dimension ~75 μm), sandwiched between two KBr layers was loaded in the DAC (Fig.3). The KBr layers were used to thermally insulate the sample from the diamond anvils as also provide optical windows. At a pressure of ~14 GPa and at a CO_2 laser power of ~15 Watts, exothermic reaction characterised by flashes of very bright light got initiated. The temperature was estimated to be ~2000 K. Using the nanomovers, the sample was rastered by the CO_2 laser beam. After the heating event lasting for nearly 45 minutes, it was seen that the entire graphite chip had become translucent to light, indicating formation of a new diamond-like translucent phase (Fig. 3). Photographs at the bottom depict views of the graphite sample through the table of one of the diamond anvils. The three photos correspond to the state of the sample before heating, during laser heating and after laser heating. It can be seen that after laser heating, the sample has become translucent to light.

In Fig.3, the red beam represents the heating CO_2 laser (10.2 m) while the green beam represents the argon ion laser (514.5 nm) used to excite ruby luminescence for pressure measurement.

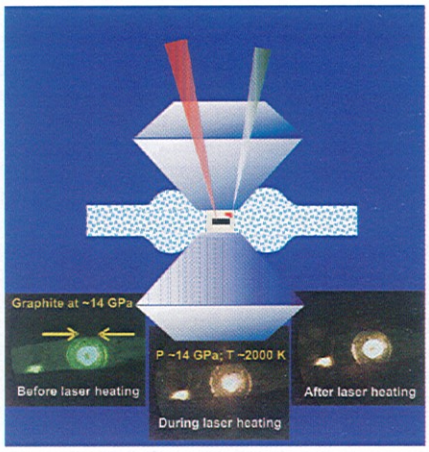

Fig. 3 : Illustration of a typical sample assembly for LHDAC experiments and webcamera pictures showing heating of graphite at high pressure and temperature using IGCAR LHDAC

WHAT IS A DIAMOND ANVIL CELL (DAC)?

DAC is a device used to generate very high pressures on materials. It essentially consists of two identical gem quality diamonds shaped in the form of anvils and aligned perfectly (Fig.3). One of them is mounted on to a piston and the other on to a cylinder. A pre-indented metal gasket, with a 200 μm (dia) X 75 μm (depth) hole to act as sample chamber, is spaced between the two culets (the flat polished tip of the diamond is called the "culet"). Very high pressure is generated on the sample when the piston is moved against the cylinder using an appropriate arrangement. IGCAR DACs have been designed to do high-pressure experiments up to a maximum of 1 million atmospheres. To get a feel for the pressure, it may be noted that the pressure at the Earth's core is about 3.5 million atmospheres.

ACHIEVEMENT

Very few laboratories across the world have mastered the LHDAC technique, owing to the intricacies involved and risks of frequent, irreversible damage to the diamond anvil cells (DAC). In IGCAR, several LHDAC heating experiments, each lasting for few hours have now been done. Careful inspection of the DAC has not revealed any damage to the cell or its constituents, demonstrating the high-level of perfection in the optics that has been designed and set-up. With this success, IGCAR is looking forward to establishing a similar facility centered around the XRD beamline at INDUS-II synchrotron (Indore). The published report on IGCAR LHDAC has attracted widespread attention and has received compliments from eminent scientists from within the country and abroad.

PUBLICATIONS ARISING OUT OF THIS STUDY AND RELATED WORK

N. Subramanian, N. V. Chandra Shekar, N. R. Sanjay Kumar and P. Ch. Sahu , *Current Science*, **91** (2006) 175.

Further inquiries:
Dr. N. Subramanian, Materials Science Division
Metallurgy & Materials Group, IGCAR, e-mail: subbi@igcar.gov.in

Pulse Power Systems

EXECUTIVE SUMMARY

The potential application of Pulse Power System is wide ranging. It varies from intense neutron production to laser excitation, transient chemistry to radiography, fusion research to weapons research and radiation effect studies to collective acceleration. Various methods have been developed in the past for the generation of high voltage, high current fast impulses like Marx generators or swinging type LC generators. The present work is about an alternative and more compact method developed at IGCAR based on excitation of toroidal magnetic fields and resonance excitation techniques.

OUTLINE

Studies on pulsed magnetic fields for the generation of high voltage, high current, fast impulses for accelerating charged particle beams have been carried out at the Safety Group at IGCAR. The generation of these accelerating potentials is based on the familiar induction principle. The studies include the investigations of toroidal magnetic fields, resonance excitation, magnetic flux concentration, choice of pulse shaping and switching techniques, and study of different induction modules. Two different approaches of generating the high power impulses have been investigated, namely 1) the excitation of toroidal cavities by creating sheet currents of kilo ampere magnitude using fast switching techniques and 2) The resonance excitation method, where the energy exchange from the primary to the secondary is maximized by controlling the coupling parameters. Both methods have excellent energy transfer efficiency.

The use of toroidal excitation, high frequency resetting of cores, and multichannel triggering to achieve higher repetition rate, offers many advantages and open up several possibilities. The multiturn toroidal excitation not only provides excellent power transfer capability but also drastically cuts down the number of switching modules needed. As a result, the system offers great flexibility in the choice of the beam energy and current for a given power of induction module. These systems are compact and inexpensive to build compared to other types of pulsed accelerators. There is scope for further exploitation of the technique to build extremely stable high voltage systems.

The next phase of work pertains to increasing the power available from such modules. This has been achieved by increasing the pulse repetition rate by different means. In the first approach the retentive field of the magnetic core material is offset by sending a reserve current of suitable magnitude, thus enabling the core to be ready sooner for the next pulse. Duty cycle increase upto 10 times are possible by this method. The second approach uses multi channel triggering, where by a train of pulses are generated at desired intervals, each pulse generated by sensing the decay of the previous pulse. At present it is possible to generate a train of 10 pulses in 5 millisecond interval.

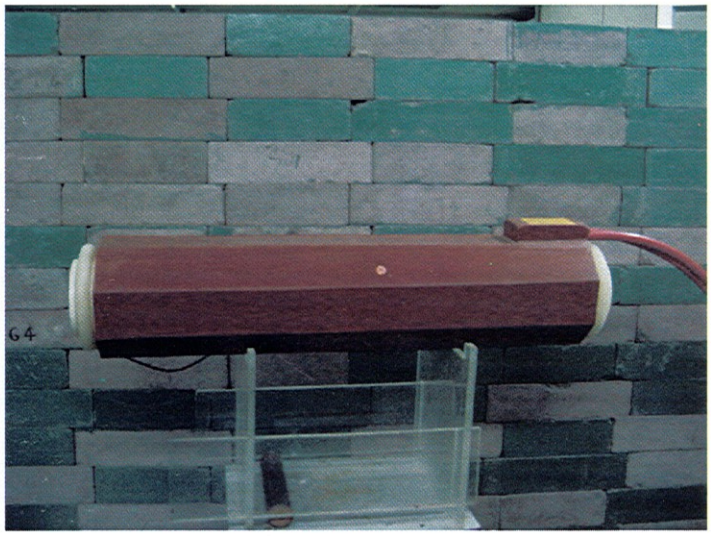

Fig. 1 :150 kV Pulse Power System

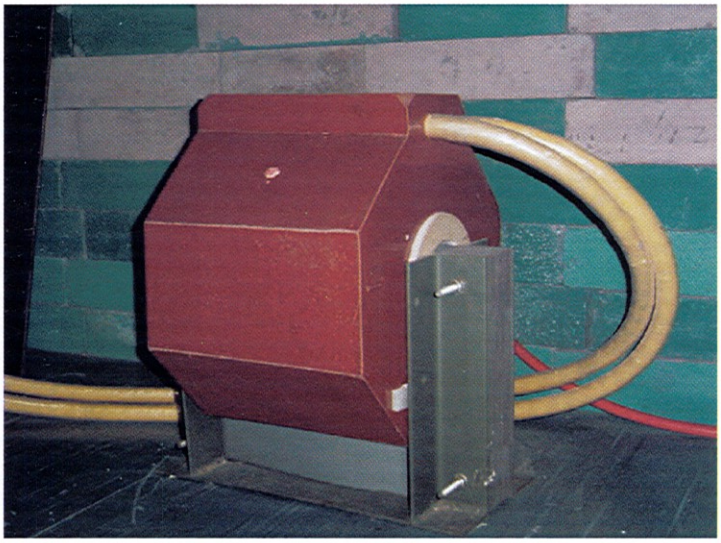

Fig. 2 : 150 kV Power Isolation System

■ PULSE POWER SYSTEMS

Generally we have high voltage and low current accelerators. But when it comes to high current and high voltage systems, this pulse power technology is best suited. The current capability of the induction modules developed at IGCAR opens up new possibilities of self-reliance.

■ ACHIEVEMENT

The first phase of study has led to the development of the following test modules

I) A Module rated for 100kV, 200mA negative polarity

ii) A variable high module with a maximum supply of 60 kV. The current rating is 200 mA. The polarity is switch selectable

iii) A linear induction module capable of bipolar pulses with a rating of 120 kV and 100mA.

iv) A Toroidal module of 150kV positive pulses and 150 mA current. Core size: 30 cm I.D, 40 cm O.D. This module is specifically designed to provide easy access to the switching system for servicing.

On the application side of the test module, the positive pulses from the induction module have been used with an X-ray tube (Model:DRA-2-125/30/50,BEL make) for producing pulsed X-rays. A dose of 1R at 30 cm was obtained.

As a demonstration model, on the application side of the high power induction modules, currently the concentration is on building an Intense Pulsed Neutron Source, first of its kind in India. The main reaction is a D-T reaction. The pulsed potentials needed for the acceleration of the deuterium beam are generated by the techniques described above. Every thing about this pulsed neutron source is novel and the effort is totally indigenous. A rotating target of tritium on a titanium matrix deposited on a copper plate is employed. The ion source is a single cusped magnetic field ion source. The pulsing of the ion source also uses the technology described above.

■ PUBLICATIONS ARISING OUT OF THIS STUDY AND RELATED WORK

1. V. Venkatesam, A Modular Device for Generating High Voltage Impulse (Resonance Excitation) - Patent No. 191316.
2. V. Venkatesam, A Modular Device for Generating High Voltage Impulse (Toroidal Excitation) - Patent No. 191318.

Further inquiries:
Shri V. Venkatesam, Radiological Safety Division
Safety Group, IGCAR, e-mail: vv@igcar.gov.in

Fire Suppression Performance Evaluation of Sodium Leak Collection Tray

EXECUTIVE SUMMARY

Sodium Leak Collection Trays (LCT) are deployed as a passive sodium fire protection device under the secondary sodium pipelines in the Steam Generator Buildings of Fast Breeder Reactors (FBR). The design of Leak Collection Trays (LCT) is based on immediate channeling of burning liquid sodium on to the funnel shaped Slopping Cover Tray (SCT) to the Sodium Hold-up Vessel (SHV) below it, in which sodium fire extinguishes due to oxygen starvation. Performance of LCT is measured by the proportion of un-burnt sodium left over and it is a strong function of sodium leak rate, amount of sodium leaked and initial sodium temperature. Processes involved in the operation of the LCT are thermal hydraulics of the flow of hot sodium over the cold surface of the SCT, gravity draining into the SHV and combustion kinetics of sodium, with almost all the processes occurring simultaneously. Several performance evaluation tests have been carried out on a prototype LCT and valuable data have been obtained, which can serve as an excellent benchmark. Simplified and more detailed CFD simulation for predicting the behavior of the device have also been carried out

OUTLINE

Liquid sodium is used as a coolant in Fast Breeder Reactor (FBR) systems. In the rare case of failure of a sodium bearing component, sodium can leak out and react with oxygen in the air and catches fire, when oxygen concentration in the air is more than 5% and the sodium temperature is more than 200°C. Design provisions to defend against such sodium leaks and the resultant fires play an important role in the safe operation of a fast reactor. In order to collect the leaked sodium and mitigate the consequences of sodium fire in the Steam Generator Buildings (SGB) of FBR, Leak Collection Trays (LCT) is provided.

Experimental studies on the evaluation of a PFBR leak collection tray have been carried out in the Safety Engineering Division. Twenty eight thermocouples were mounted at different locations of the tray for continuous monitoring of the temperatures. The maximum tray surface temperature is in the range of 900 to 950°C in all the tests. Temperatures at different depths in the sodium collected in the hold-up vessel monotonically decreased with time, with the maximum at 350°C. The chemical analysis of the samples indicated burning of sodium was only in the range of 4 to 25%, depending on the test conditions, as against about 70 % that normally occurs in a large open pool exposed to air, which is considered as satisfactory.

Processes involved in the operation of the LCT are thermal hydraulics of the flow of hot sodium over the cold surface of the SCT, gravity draining into the SHV and combustion kinetics of sodium, with almost all the processes occurring simultaneously. This gives a challenging opportunity for modeling and predicting the behavior of the device. Hence, the data available from the test results, as given in the Table 1, can form a good benchmark.

Table 1
Data available from the test results

Test Variables	Test Numbers		
	MS-2	MS-3	MS-4
Mass of Sodium (kg)	40	38	35
Sodium Temperature (°C)	530	538	550
Dumping Period (s)	120	180	210
No. of Drain Pipes open in SCT	3	1	1
Relative Humidity %	73	76	65
Ambient Temperature (°C)	31	28	28
Mass of Sodium burnt (kg)	10	1.5	3.5
Un-burnt Sodium left over SCT (kg)	4	0.5	0.5
Un-burnt Sodium collected in SHV (kg)	26	36	31
Overall un-burnt sodium (% loaded)	75	96	90



Fig. 1 : Performance testing of sodium leak collection tray

■ ADDITIONAL INFORMATION ON THE SODIUM LEAK COLLECTION TRAYS

The leak collection tray mainly consists of two sloping plates (angle 200) forming a funnel like structure supported on the sodium hold-up vessel. These sloping plates with V-shape orientation rapidly guide the leaked sodium to a central drain-pipe, which ends at 20 mm above the bottom surface of the hold-up vessel. The drained sodium is accumulated in the hold-up vessel with limited exposure to air. A vent pipe of smaller diameter is provided on the slopping plates to facilitate the easy draining of the leaked sodium.

The size of the bottom hold-up vessel of the tray chosen is 1200 mm x 500 mm x 500 mm and that of the top funnel like structure is 1200 mm x 1000 mm. The capacity of the hold-up vessel is 300 liters. Drain-pipe of 50 NB size and a vent pipe of size 25 NB are used. Three experimental runs were carried out by pouring sodium at 530 - 550 0C into the tray in open-air conditions. Fig. 1 shows the sodium just being let into the tray in one of the tests and a sketch of the LCT is available in Fig.2.

■ GENERAL EXPLANATION RELATED TO THE DESCRIPTION

CFD analysis of sodium fire in LCT is being carried out at IIT Madras, by using general purpose CFD code FLUENT. Fig. 3 shows the temperatures on SCT and in SHV while sodium combustion. Sodium burning rates observed in this analysis are in good agreement with the experimental results. Further optimization of LCT is being carried out.

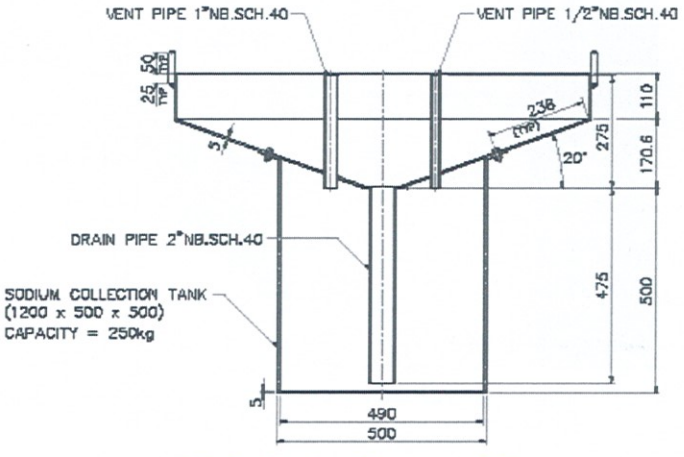

Fig. 2 : Details of Prototype of LCT

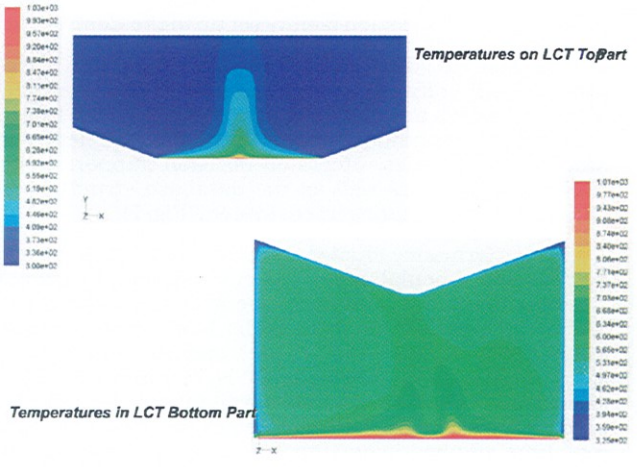

Fig. 3 : Simulation of Sodium Combustion in LCT

■ ACHIEVEMENT

The data collected in the evaluation tests of the Leak Collection Trays can be considered as a good international benchmark for validating the mathematical models being developed to describe the transient thermal hydraulic and combustion phenomena involved. The design of LCT for secondary sodium systems of PFBR will be optimized using the numerical model developed and validated with the test results.

■ PUBLICATIONS ARISING OUT OF THIS STUDY AND RELATED WORK

1. F.C. Parida, P.M. Rao, S.S. Ramesh, B. Malarvizhi, V. Gopalakrishnan, E.V.H.M. Rao, N. Kasinathan and S.E.Kannan, 14th International Conference on Nuclear Engineering (ICONE - 14) July, 17 - 20, 2006, Florida, USA.
2. S.V. Diwakar, T. Sundararajan, S.K. Das, P. Mangarajuna Rao and N. Kasinathan, ICONE15-10403, Proceedings 15th International Conference on Nuclear Engineering, April 22-26, 2007, Nagoya, Japan.

Further inquiries:
Shri P. Mangarjuna Rao and Shri. N. Kasinathan, Safety Engineering Division
Safety Group, IGCAR, e-mail: nkasi@igcar.gov.in

Real Time Decision Support System for Radiological Emergency

EXECUTIVE SUMMARY

A Geographic Information System based Decision Support System (GIS-DSS) is developed for carrying out the geo-spatial analysis of radioactivity spread in the event of an inadvertent air borne release at Kalpakkam. The system consists of two parts, the first one is the customized site specific weather data assimilation and meteorological forecast model for Kalpakkam region and the other one is the web based decision support system. The beta version was commissioned in a PC based cluster computing system. Interactive spatial querying and display for designated clients in the intranet was demonstrated. The system is operational in live mode.

OUTLINE

Radiological safety of the environment is given utmost importance in fast breeder reactor technology development. Advanced state of art techniques are adopted in the radiological environmental impact assessment. The on-line Decision Support System for Emergency Response Management is one such facility set up in the Centre (Fig. 1).

In contrast to the readily available Decision Support System(DSS) software for nuclear emergency like RODOS, ARAC etc. which are very detailed and tuned to the European and American conditions respectively, the DSS developed at Kalpakkam provides integrated decision support based on AERB guidelines as well as the database structure of the national disaster management system (Fig. 2).

A high performance cluster computing system is developed for real-time calculations of the environmental parameters. Weather being the vital component of the environment, a numerical weather forecast model MM5 is customised for Kalpakkam region and made operational in parallel computing system. The system is operational and daily forecast for Kalpakkam is made available on-line in LAN. The predicted meteorological parameters are given as input in real time plume dispersion model used in the Decision Support System for radiological emergency.

Monte Carlo simulation of dispersion of air borne pollutants is another component in the DSS. For the local real time dispersion, a Lagrangian particle model with input data from sparsely distributed meteorological stations is developed. The model accounts for the complexities of coastal atmospheric boundary layer and complex topography. The combination of pollution model and the weather forecast model can be applied to many different situation and conditions of terrain, pollutant and weather. Tracer dispersion experiments are being planned for estimating diffusion parameters for Indian coastal condition.

Finally, the radiological impact in the form of dose to the population and deposited activity is simulated and, based on the limits set for evacuation, sheltering and food control, spatial decisions are displayed through a web portal in the intranet. Spatial data base like the land cover, soil texture, water bodies, village boundary, population details and transport network are dynamically linked with the computed dose values and interactive query is enabled using a Geographic Information system.

Major part of the development was carried out in collaboration with several Institutions in the country. The indigenous Web-GIS query modules are developed by an expert group in Regional Remote Sensing Service Centre (RRSSC), Indian Space Research Organisation, Nagpur. Further, the terrain, land-use and soil texture data used as input to the weather forecast model MM5 and the query module of the DSS are the realistic data base prepared by resource organizations like RRSSC, National Bureau of Soil Survey NBSS-LUC, IARI, Nagpur and Survey of India.

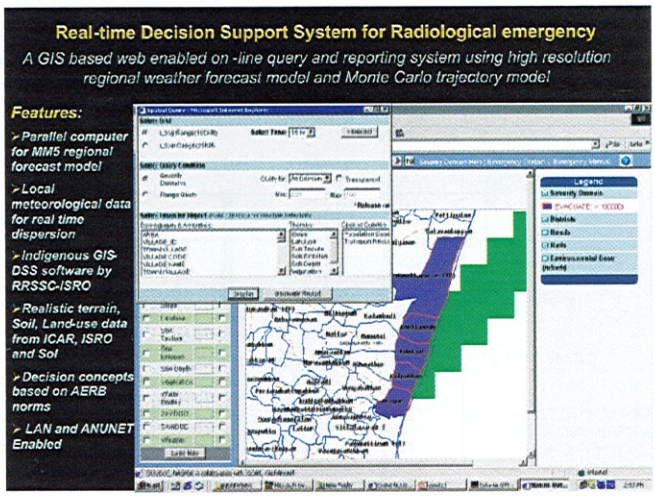

Fig. 1 : Web enabled spatial query and response system showing area affected under a hypothetical accidental condition



Fig. 2 : Cluster Computing system for regional weather forecast

■ DECISION SUPPORT SYSTEM

The Prototype Fast Breeder Reactor has been designed considering all safety aspects especially those that can lead to a Core Disruptive Accident (Design Basis DCA). However, as a part of emergency preparedness plan, a decision support system is imperative in providing necessary input to take counter measures in the event of an inadvertent atmospheric release. The most important input is the radioactive plume transport and its spatial pattern prediction for the next few hours. Hence the need arises for a high resolution localized forecast system for the meteorological field which is estimated in the present DSS by operational mesoscale meteorological model MM5 in parallel computing cluster.

■ COMPLEXITIES IN MODELING EFFLUENT DISPERSION IN AIR

Though theoretical and numerical codes are widely used for estimating the climatological pattern of radiological impact due to a nuclear installation at the design stage itself, they do not often account for the non-homogenous non-stationary conditions leading to a complex wind field over the local region. For example, at Kalpakkam coast, the land-sea breeze and the associated atmospheric internal boundary layer (IBL) greatly influence the dispersion. A phenomenon called coastal fumigation leads to sudden increase in concentration near the ground during the sea breeze in daytime. A study on the data from environmental radiation monitors and Ar^{41} activity released routinely from existing power plant as tracer, the fumigation phenomena was confirmed. Hence a numerical sea breeze model is developed and is used for predicting local dispersion pattern.

Experimental Facility for Meteorological Study

Validation of the models need field experiments and meteorological campaigns. A network of 50 m towers and a sodar system provides the required input data for the model. Intensive field campaigns called Coastal Atmospheric Boundary Layer Experiments (CABLE series) are also conducted jointly with Indian Institute of Tropical Meteorology, Universities and other research institutes.

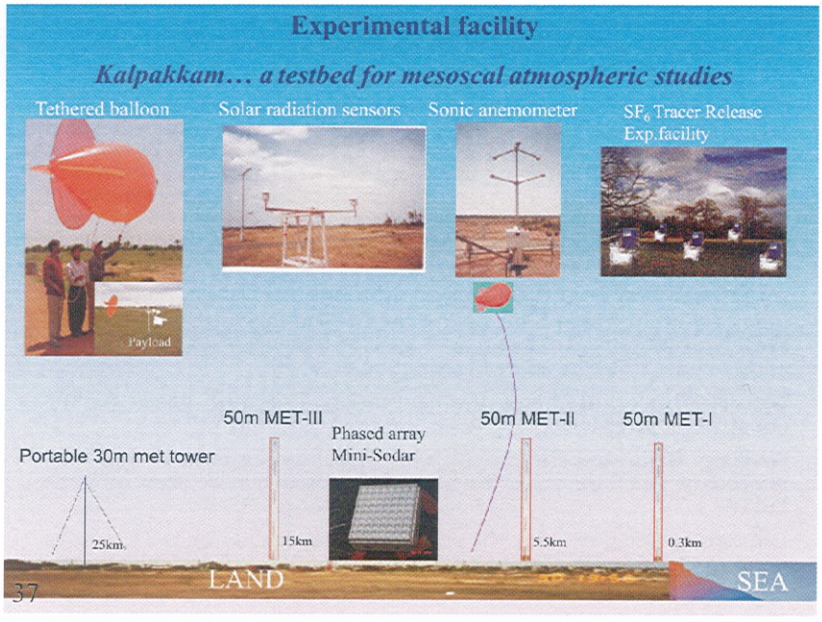

Meteorological measurements systems including SODAR, Tethered Balloon and Sonic anemometers used for Coastal Atmospheric Boundary Layer Experiment (CABLE) series for validating site specific models.

■ ACHIEVEMENT

The real time web enabled Decision Support System is functional in live mode with on-line automatic access to the local and global data for initialising the numerical model. All the data of surface boundary condition are extracted from analysis of remote sensing satellite imagery. The system provides a prototype model for designing a disaster management system even for natural disasters.

■ PUBLICATIONS ARISING OUT OF THIS STUDY AND RELATED WORK

1. C.V. Srinivas and R. Venkatesan, *Atmospheric Environment*, **39** (2005)1497.
2. Srinivas C.V, Venkatesan R., Muralidharan N.V., Someshwar Das, Hari Dass and P. Eshwar Kumar, *J.Earth System Science*, **115** (2006) 1.
3. R. Venkatesan, R. Mathiyarasu and K. M. Somayaji, *Atmospheric Environment*, **36** (2002) 2933.

Further inquiries:
Dr. R.Venkatesan and Shri K.M. Somayaji, Radiological Safety Division
Safety Group, IGCAR, e-mail: rv@igcar.gov.in

Digital Design Verification

EXECUTIVE SUMMARY

For safety systems of nuclear reactors, electronic hardware systems are preferred to software systems wherever feasible. This is because, for software, terms like reliability and quality are difficult to quantify. Electronics and Instrumentation Division (EID), IGCAR has designed and developed a number of complex digital circuits using Very Large Scale Integration (VLSI) techniques for the Safety Systems of PFBR. These designs have been implemented using Very High Speed Integrated Circuit (VHSIC) Hardware Description Language (VHDL). These circuits have been tested extensively and found to function well. But here, since the hardware design was also done using a HDL, it was thought necessary to perform extensive verification of the HDL code used in the design. Therefore, a collaboration project was undertaken with Indian Institute of Technology, Madras (IIT-M) for the development of generic tools for the verification of VLSI designs made at IGCAR.

OUTLINE

As part of the digital verification project, IIT-M was to develop a methodology that can be used for testing large-scale designs in a highly automated fashion. VHDL designs of IGCAR would be handed over to IIT-M in phases. IIT-M would provide third-party evaluation of these designs by verifying their functional correctness and provide detailed test plans for verifying the hardware. They would also detail the methodology that would be developed as part of this research and recommend a set of tools and strategies that can be used to verify other future designs of IGCAR.

IIT-M has performed verification of the designs using *e* verification language in Specman Elite environment. The various components of the environment are shown in Fig. 1. *e* can be used to construct components to do the following functions.

Generation: *e* automates the generation of stimuli based on the constraints provided.

Driving Stimulus: *e* provides a simulator interface and the necessary mechanism to drive the generated test vectors into the DUT.

Collecting Output: After the stimulus is applied to the DUT, output is produced from the DUT. *e* provides a simulator interface and the necessary mechanism to receive data from the DUT

Data Checking: Data value checks compare the output data values against the expected data. Temporal assertions monitor the functional protocol at important interfaces. Temporal checking constructs are used to build protocol monitors.

Coverage: Functional coverage tells the verification engineer if the test plan goats have been met.

As part of the project, IGCAR engineers and scientists handed over six VHDL designs to IIT-M for verification, which are as follows.

- Error Detection and Correction (EDAC) Controller
- Sequencer for Analog Input Card
- Controller for Analog Output Card
- Stand-Alone Fine Impulse Test (SAFIT) System for FBTR
- Safety Logic with Fine Impulse Test (SLFIT) System for PFBR
- VME Interface Controller (Master)

This phase included preparation of detailed design specifications and frequent visits to IIT-M for handing over the designs, finalizing the test plans and providing other required inputs to the IIT-M team.

Following this, IIT-M started verification of the designs. For each design, the first step was the preparation of a test plan. The test plan was then submitted to IGCAR for approval. After a few iterations to ensure that the test plan would really cover all the areas that need to be tested, it was approved by the IGCAR team.

In parallel to this, IIT-M handed over a document detailing the Generic Test bed for verification of digital designs. It includes a Generalized Interface (that would vary from design to design), Random Data Generator, Event Queue, Dispatcher, DUT (Device Under Test), Result Collector, Result Queue, Checker and Coverage Unit. The block diagram for the generic test bed is shown in Fig. 2.

IIT-M has completed verification of all the six designs handed over by IGCAR. Reports including detailed specifications, test plan, outputs from the verification tool and coverage metrics for all the projects have been submitted by IIT-M and reviewed and approved by IGCAR.

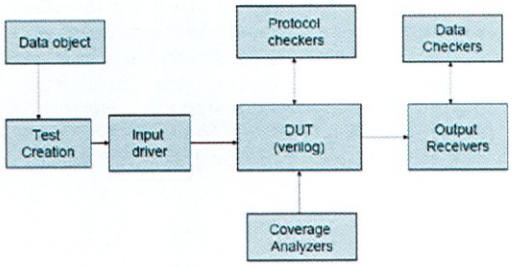

Fig. 1 : Components of the Verification Environment

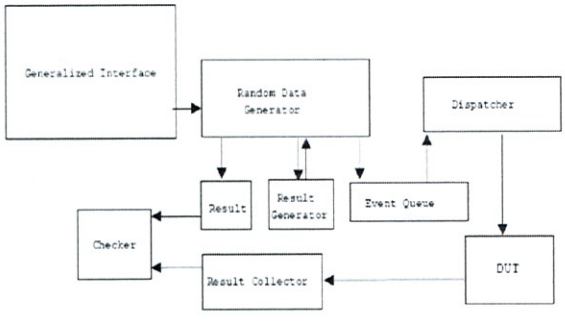

Fig. 2 : Generic Test bed for Verification of Digital Designs

ADDITIONAL INFORMATION ABOUT VERIFICATION

What is verification?
Verification is a process that ensures conformance of a design to some predefined set of expectations. In case of digital design verification, the expectations are defined by the specifications. Verification can be described as the reverse process of design, in that it starts from the implementation and confirms that the specifications are met. The goal of verification is to demonstrate functional correctness of a design, attempt to find design errors and to attempt to show that the design implements the specification.

TYPES OF VERIFICATION

The two types of verification techniques generally used for verifying digital designs are

- Simulation-based Verification
- Formal Verification

In Simulation-based verification, a variety of test cases are fed to the DUT, simulated and tested against expected behaviour. But here, the verification is confined to those areas that are encountered during simulation. On completion of application of test cases, a coverage metric is provided based on the constraints provided. A typical coverage output provided by Specman Elite is shown in Fig. 3. Simulation, by its very nature, only exercises a tiny percentage of all possible design behavior. Each individual test resets the design to a known state and then applies a series of changes to the inputs. Even across an extensive test suite, many legal input sequences are never exercised.

Formal property verification is a formal technique used to verify formal properties. The specifications themselves are specified mathematically in the form of a formal property specification. The technique mathematically verifies the implementation against the formal property specifications. It thus verifies that all properties of the design satisfy the properties.

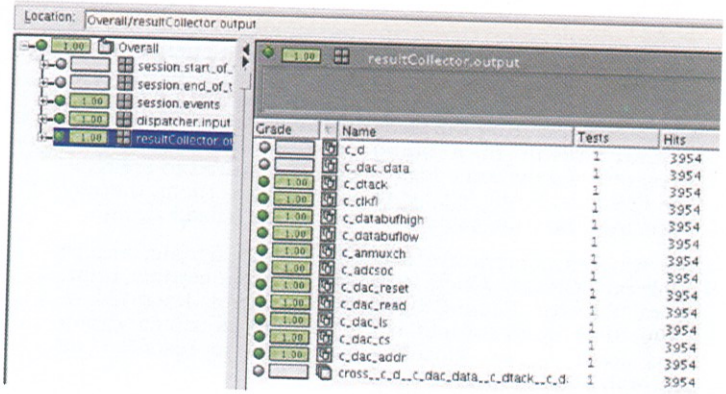

Fig. 3 : Screenshot of a sample Coverage Output from Specman Elite

COVERAGE

A key requirement in verification is having a reliable metric that shows the progress towards hitting all the verification goals. Functional coverage, a metric that tracks which functionality of the device was verified, is being recognized as a highly reliable measure. The *e* verification language has built-in functional coverage constructs, supporting basic item coverage, transition item coverage and cross coverage. Basic item coverage tells the engineer if all the legal values of an interesting variable have been covered. Transition item coverage tells the engineer if all legal transitions of a state machine have been covered. Cross coverage allows the engineer to examine the cross product of two or more basic or transition items to check if all interesting combinations have been covered.

ACHIEVEMENT

The *e* verification language significantly reduces the time needed to create a verification environment and test suite, as well as enables the most modern and powerful verification methodologies. Using a high-level verification language that is combined with the built-in engines of a test bench automation tool, a project team can be more productive much sooner in the project schedule, thus reduce the time and resources needed for the verification environment and significantly increase the quality of the final product.

PUBLICATIONS ARISING OUT OF THIS STUDY AND RELATED WORK

1. M.K. Misra and S. Ilango Sambasivan, Verification Report for Error Detection and Correction (EDAC) Controller
2. L. Srivani and S. Ilango Sambasivan, Verification Report for Sequencer
3. Saritha P. Menon and S. Ilango Sambasivan, Verification Report for Analog Output Controller
4. M.K. Misra and Saritha P. Menon and S. Illango Sambasivan, Verification Report for SAFIT System for Reactor Protection System of FBTR.

Further inquiries:
Shri S. Ilango Sambasivan, Electronics and Instrumentation Division
Electronics & Instrumentation Group, IGCAR, e-mail: sis@igcar.gov.in

Pulse Coded Safety Logic System for PFBR

EXECUTIVE SUMMARY

Reactor safety logic is designed to initiate safety action against Design Basis Events. The reactor is shutdown by de-energizing electromagnets and dropping the absorber rods under gravity. In Prototype Fast Breeder Reactor (PFBR), shutdown is effected by two independent shutdown systems, viz., Control and Safety Rod Drive Mechanism (CSRDM) and Diverse Safety Rod Drive Mechanism (DSRDM). Two separate safety logics are developed for CSRDM and DSRDM, i.e., Safety Logic with Fine Impulse Test (SLFIT) for CSRDM, and Pulse Coded Safety Logic (PCSL) for DSRDM. The PCSL primarily utilizes the fact that the vast majority of faults in the logic circuitry result in static conditions at the output. It is arranged such that the presence of a dynamic logic signal is required to hold the shutdown actuators and any DC logic state will release them. It is a dynamic, self-testing logic and fail safe design.

OUTLINE

PCSL processes the trip parameters and drives Electromagnet (EM) Coils of DSRDM. It de-energises the EM coils when there is a demand for shut down. The dynamic self-testing principle used in PCSL, primarily utilizes the fact that the vast majority of faults in the logic circuitry result in a static condition at the output. Presence of a dynamic logic signal is required to energise the EM coils. Static logic state de-energises them, thereby shutting down the reactor. This results in failsafe design.

All trip parameters are triplicated logic signals, except Manual SCRAM, which is a potential free contact input from Control Room(CR)/Backup Control Room(BCR). Logic '0' or 'open contact' is represented as trip condition and logic '1' or 'closed contact' is represented as normal/healthy condition.

In PCSL, each redundant channel of trip parameters is combined with unique coded pulse train (Fig.1). This pulse train labels the individual inputs in such a way that the status of each input can always be identified. All stages of the logic are continuously exercised by these coded pulse trains which check every logical combination, thus providing continuous on-line testing.

Three trains of pulses, Code-A, Code-B, Code-C are generated (as per timing diagram shown in "Fig. 1"). These pulse codes repeat after every 10 clock cycles (T1 to T10). Code-A pulse is super-imposed along with the channel A trip parameter (CH-A). Then the trip circuit output A1 will be same as code-A pulse when the channel A is normal and at logic '0' when CH-A is tripped.

Similarly, Code-B pulse & Code-C pulse are super-imposed along with the channel B of trip parameter (CH-B) & channel C of trip parameter (CH-C) respectively. Then, the trip circuit output B_1 and C_1 will be the same as Code-B and Code-C when the channels CH-B and CH-C are healthy.

The trip circuit output A_1, B_1 & C_1 are processed by the voting logic and output is defined as:

$$V_{2/3} = A_1B_1+B_1C_1+C_1A_1$$

For single parameter, output waveforms are shown in Fig.1. For multiple parameters, guard line logic concept (Fig.2) has been used to process all the 14 parameters. For multiple parameter system, Set & Reset pulse generated to propagate the pulses from first to the last parameter. Since EM Coil is energized by DC voltage, a pulse to DC converter has been used. To energise the EM Coil, high current (1 to 1.5 amp.) is required, so Power MOSFET has been used to drive the high current. For checking the healthiness of MOSFETs, two pulses have been used.

PCSL system is a safety critical system, so diagnosis of PCSL system is very much essential. PCSL system is inherently fail-safe, but the likely faults are to be diagnosed. For that, a diagnostic logic has been designed which annunciate the stuck faults of the logic, pulse pattern faults, clock oscillator failure, cross link failure and MOSFET failure.

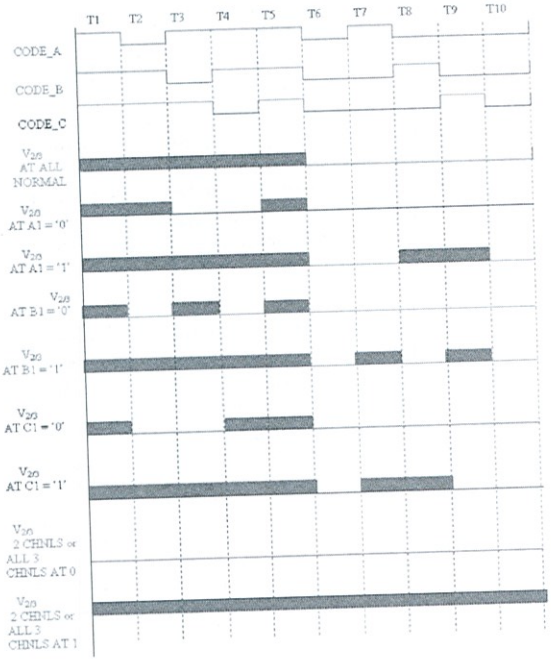

Fig. 1 : PCSL Timing Diagram

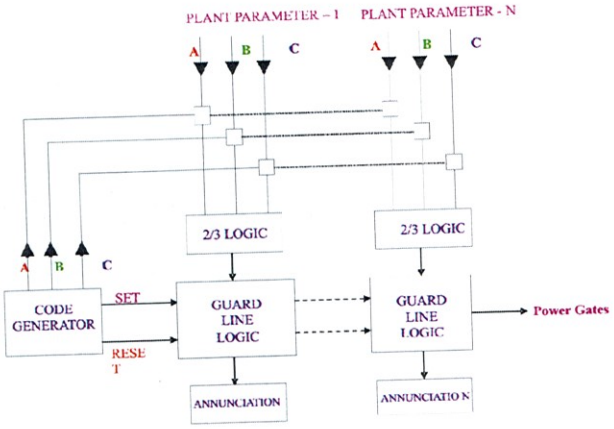

Fig. 2 : Concept of Guard Line Logic

■ ADDITIONAL INFORMATION ABOUT PULSE CODED SAFETY LOGIC SYSTEM

Being a safety critical system, functionality of the PCSL is to be tested exhaustively. To check the functionality, a manual 'hard wired' Simulator is developed. This Simulator consists of a Signal Simulator, a CR Simulator and a BCR Simulator. The Signal Simulator feeds all the inputs to PCSL system as a reactor and the CR Simulator feeds Manual SCRAM and Manual Inhibition inputs as well as it displayed all the alarm to be displayed at CR. The BCR Simulator feeds the input and displaying the alarms at BCR.

■ PCSL SYSTEM DEVELOPED USING VLSI TECHNOLOGY

Safety logic can be developed using relays, computer, magnetic core (laddic devices) or solid state logic. On the basis of response time, reliability, power consumption and flexibility, solid state logic is preferred to develop the PCSL. Among the solid state logic, an option was available to develop it by discrete components. In discrete components, there is less flexibility, more power consumption and more components hence more interconnection. More components and interconnection will reduce the reliability but a high reliability system for PFBR is required. To overcome these constraints, Very Large Scale Integration (VLSI) technology has been used for development of PCSL system and hence ALTERA make was chosen for Complex Programmable Logic Devices (CPLDs) as it has a feature of In-system Programmability and low power consumption. Digital design has developed using ALTERA MAX+PLUS tool in Schematic form. The design is verified thoroughly through simulation and then programmed in the ALTERA CPLDs.

Redundant Clock Oscillator

Since PCSL System is based on dynamic logic. It is very much dependent on the clock. If clock fails, PCSL system leads to SCRAM of reactor as a spurious trip. To avoid this spurious trip, redundant clock oscillator is provided. The circuits check the healthiness of clocks and display it through local LEDs. If one clock fails other clock is in operation within no time and failure indication is provided at CR.

Latch and Latch fault Detection

To avoid spurious trip and partial control rod drop, 50 ms latch is provided in the logic. Latch design in such a way that it is will not delay trip signal. It has memory reset provision. To check the healthiness of Latch, offline test facility is provided. The latch fault indication is provided locally.

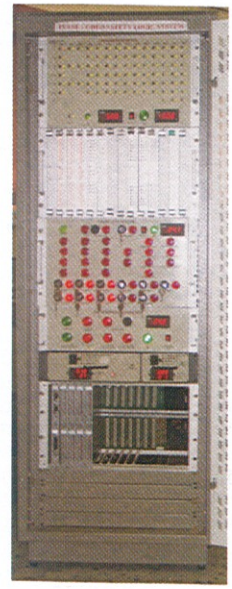

Functional Prototype PCSL System

■ PRINCIPLE OF PULSE CODED LOGIC

The PCSL is based on the principle of presence of pulses at the input stage and propagation of the pulses up to the output stage of safety logic, for the purpose of normal reactor operation. The logic level stuck at '0' or '1' at output stage results in de-energization of EM coil and reactor trip. Each of the redundant channels is combined with a unique pulse train. When these coded signals are processed by the voting logic, a pulse train is generated under normal reactor operating condition. In case of failure of one channel, pulses are present. However, in case of two channels or all the three channels are faulty or tripped, pulse train is no longer produced. The PCSL is designed in such a way that, non-availability of pulse trains at the output stage results in reactor trip. Thus, when a single channel is tripped, the reactor will be still in normal operation. When any two channels or all the three channels are tripped, the reactor will be tripped.

■ ACHIEVEMENT

Pulse Coded Safety logic is developed for the first time in India. Hence, its functionality has to be checked thoroughly before it is installed in the reactor. To prove the functionality, first a three parameter based system has been developed and demonstrated successfully. A full fledged Functional Prototype PCSL System has been developed and its functionality is also tested successfully. Industrial grade PCSL system is under fabrication at ECIL, Hyderabad.

■ PUBLICATIONS ARISING OUT OF THIS STUDY AND RELATED WORK

1. Md. Najam Anwer, N. Satheesh, B. Krishnakumar and S. Ilango Sambasivan, 1st National Conference on Nuclear Reactor Safety, November 25-27, 2002, Mumbai.
2. Md. Najam Anwer, N. Satheesh, B. Krishnakumar and S. Ilango Sambasivan, Report No. PFBR/66300/1014/Rev.0, May 2005.
3. Md. Najam Anwer, N. Satheesh, B. Krishnakumar and S. Ilango Sambasivan, Report No. PFBR/66300/SP/1011/Rev.0, June 2005.
4. Md. Najam Anwer, N. Satheesh, B. Krishnakumar and S. Ilango Sambasivan, Report No. PFBR/66300/DN/1015/Rev.0, December 2005.
5. N. Satheesh, Md. Najam Anwer, B. Krishnakumar and S. Ilango Sambasivan, Report No. PFBR/66300/DN/1017/Rev.0, December 2006.

Further inquiries:
Shri S. Ilango Sambasivan, Electronics & Instrumentation Division
Electronics & Instrumentation Group, IGCAR, e-mail: sis@igcar.gov.in

Reliability Analysis of Safety Critical I&C Systems of PFBR

EXECUTIVE SUMMARY

Defense in Depth, Diversity, Redundancy, Safety etc are the various design criterion for designing I&C systems of a Nuclear Reactor. Safety Critical Systems form the second layer of defense in a Nuclear Reactor. They are provided to assure safe shutdown of the reactor, removal of heat from the reactor core during any deviation from normal operation and containment of radioactivity during accident conditions. The Safety Critical systems require a very high reliability. Failure of a Safety Critical System to perform its function results in the loss of life, damage to the equipment and Severe environmental effects. Various reliability analysis methods are applied on the Instrumentation and Control System (I & C Systems) like Safety Logic systems, and Real Time Computer Based Core Temperature Monitoring System to evaluate the risk involved in the event of failure.

OUTLINE

Safety in nuclear reactors is of paramount importance. Safety could be defined as "freedom from unacceptable risk of physical injury or of damage to the health of people, either directly or indirectly as a result of damage to the property or to the environment". A system could fail but it should fail in safe mode.

The I & C systems for safety can be broadly classified into two categories, viz. i) Safety-Critical systems and ii) Safety-Related systems. The Safety Critical systems form the second layer of defense and are provided to assure safe shutdown of the reactor, removal of heat from the reactor core during any deviation from normal operation and containment of radioactivity during accident conditions. The Safety Critical systems, for example Core Temperature Monitoring system, require a very high reliability.

Prototype Fast Breeder Reactor contains many Safety Critical Systems like, Safety Logic Systems (Safety Logic with Fine Impulse Test for Shutdown system 1, Pulse Coded Safety Logic System for Shutdown system 2), Core Temperature Monitoring System, etc. Atomic Energy Regulatory Board specifies target for the Safety Critical System. The probability of failure on demand of the system should be less than the target. During the design of a Safety critical system, reliability target of the system will be considered among other requirements.

Various reliability analysis techniques like Failure Modes and Effects Analysis (FMEA), Fault Tree Analysis (FTA), Event Tree Analysis are performed as a part of Probabilistic Risk Assessment. Relex Software, shown in Figure 1, is popularly used to perform these analyses. FMEA is a bottom up approach where the failures of each component of the system are identified along with their modes of failures. Effects of those failure modes on the system are analyzed. Fault Tree Analysis is a Top down approach, where the failure of system in a particular mode is taken as top event and the causes of that failure along with the inter relation between the causes are analyzed until we reach basic causes. Apart from these qualitative methods there are many quantitative reliability analysis methods used to compare different topologies, and evaluate the probability of failure on demand.

Calculation of failure rate forms the basis for Quantitative reliability analysis. For electronic components, US MIL 217-F Notice-2 standard provides empirical formulas to find out the failure rate. Reliability prediction of electronic components is done by Parts Stress method or Parts Count Method. In case, for any component, if the failure rate is not available, failure rate data given by the manufacturer is used in the calculations. While arriving at the failure rate, the derating of the component, quality level, temperature, intended environment are taken into consideration.

IEC 61508 provides guidelines for the determination of probability of unsafe state of the system. Using these guidelines, the probability of unsafe state can be calculated at different conditions. Verification and Validation of the Software and Hardware should be done to verify whether the system is matching the requirements or not.

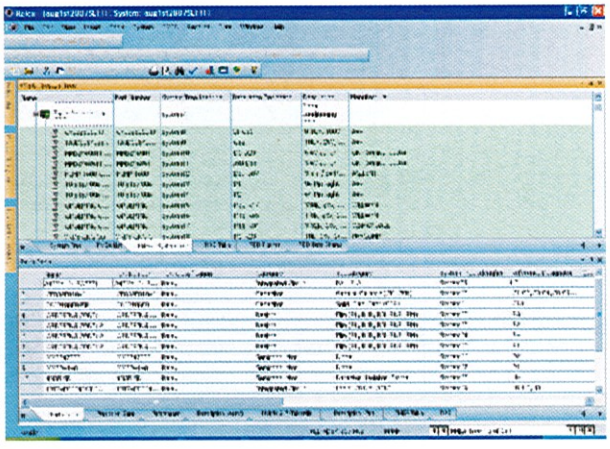

Fig. 1 : Relex Software

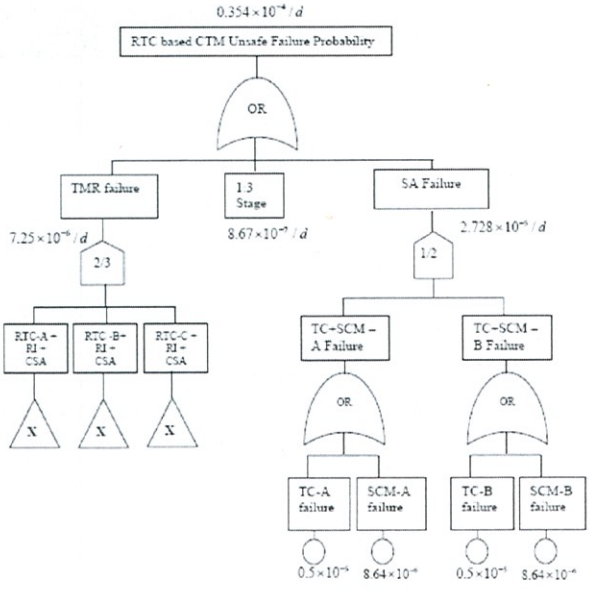

Fig. 2 : Example Fault Tree Model

RELIABILITY ANALYSIS

Reliability is the probability of a system/device performing its purpose adequately for the period of time intended under the operating conditions encountered. There are many quantitative analysis techniques like Reliability block Diagram, Fault Tree Analysis, Event Tree, Markov Model. Failure modes and effects analysis, Fault tree analysis etc qualitative techniques are used to compare different systems. Reliability of a system is only as good as the least reliable sub-system. Reliability can be improved by using redundancy. Quality, diversity, number of spare parts, Mean Time to failure are the other parameters that affect the system/device reliability.

RELIABILITY PREDICTION

The term Reliability Prediction denotes the process of applying mathematical modeling and data for the purpose of estimating field Reliability of system before the empirical data about the system is available. Reliability Prediction provides the quantitative baseline needed to assess progress in reliability design. In 1962 first version of US military Handbooks, "US MIL-217", was published by US Navy which became the standard for Reliability Prediction.

FMEA

"*Failure modes and effects analysis*" is an inductive analysis technique used to study the effects of component failure modes on a system. It is usually the first activity performed during reliability analysis of any system. It identifies the effects of various components on the functionality of the system. It starts from the knowledge of component failure modes and considers the effects of each failure on subsystems and the system. It involves the study of all components in a system and is often applied also to higher level assemblies and systems. It checks whether proposed components, with their known failure modes, fulfill system-level system safety requirements. This method proceeds from known cases of failure to unknown effects.

MIL-217F HANDBOOK

In 1962 first version of US military Handbooks, "US MIL-217", was published by US Navy this became the standard for Reliability Prediction. US MIL-217F-notice 2 titled "Reliability Prediction of Electronic Equipment", is the latest version of the handbook. US MIL-217 includes a series of empirical failure rate models developed using historical piece part failure data for a wide array of component types. All models predict reliability in terms of failures per million operating hours and assume an exponential distribution (constant failure rate), which allows the addition of failure rates to determine higher assembly reliability. Failure rate of each component is obtained by multiplying the base failure rate with the Pi factors. This method is still used by many agencies to compare different designs. Many people also feel that it is an outdated standard.

ACHIEVEMENT

The Reliability analysis of Safety Logic Systems and Core Temperature Monitoring system proved the safety of the system theoretically. The results are used as inputs in the Level 1 Probabilistic Safety Assessment of PFBR.

PUBLICATIONS ARISING OUT OF THIS STUDY AND RELATED WORK

1. Bh. Ravikumar, L. Srivani, Manoj Kumar Misra, N. Sridhar and S. Ilango Sambasivan, Report No. PFBR/66300/DN/1019.
2. N. Satheesh, J. Selva Solomon, D. Thirugnanamurthy, B. Krishnakumar and S. Ilango Sambasivan, Report No. PFBR/63110/DN/1010.
3. L. Srivani, Bh. Ravikumar, N. Sridhar and S. Ilango Sambasivan, Report No. PFBR/63110/DN/1010.
4. L. Srivani, Bh. Ravikumar and S. Ilango Sambasivan, International Conference ICRESH-05, Dec. 2005, MUMBAI.

Further inquiries:
Shri S. Ilango Sambasivan, Electronics & Instrumentation Division
Electronics & Instrumentation Group, IGCAR, e-mail: sis@igcar.gov.in

Real Time Computers for Instrumentation and Control of PFBR

EXECUTIVE SUMMARY

The advent of powerful Microprocessors has enabled the extensive use of computers in Instrumentation and Control Systems in Nuclear Power Plants. They are presently deployed in all categories of Reactor Control including Safety Critical Systems such as Core Temperature Monitoring and Reactor protection. It is proposed to deploy Real Time Computers with Triple Modular Redundant architecture for Safety Critical and Dual, Hot standby redundant configuration for Safety Related Systems for PFBR.

OUTLINE

The use of Real Time Computers in Safety Critical applications is pioneered by the fast reactor program. Fast reactors have a higher power density in the order of 500 kW/litre in the reactor core and the liquid metal coolant flows through the fuel subassemblies to remove the heat efficiently. Plugging in any one of the fuel subassembly can lead to clad hotspot and fuel meltdown and hence has to be detected immediately in order to initiate safety action. This necessitates the monitoring the output temperature of all the fuel subassemblies and further derivation of mean output temperature, mean temperature gradient across the core and the comparison of the actual temperature rise with the expected temperature rise for every subassembly for early warning on plugging. Since many derived parameters from all the fuel subassemblies and extensive computational requirements, the use of computers in Safety Critical Systems becomes inevitable in Fast Reactors. Computer based control systems for safety applications in nuclear power plants have to meet not only functional performance and interface requirements, but in addition they have to meet the regulatory requirements like enhanced reliability, safety and security. To achieve high reliability and availability, redundancy and fault tolerance features are to be provided and the overall system design should have high mean time between failures and low mean time to repair.

To cater the requirement of Real Time Computers for fast reactors, Electronics & Instrumentation Division, IGCAR has standardized on Versa Modular Euro card or VME backplane bus for entire range of computer based systems. Motorola MC68020 processor board (Fig. 1) and host of Input and Output cards have been developed and tested. The salient features of the cards include advanced diagnostics feature like single bit memory correction and double bit error detection for static memories, smart Analog input card (Fig.2) with built in calibration facility, Analog Output Card, Optically Isolated Digital Input/Output card with online testability and status display feature, Mono-shot configurable Relay output card incorporating fail safe design, ensuring the safety of the plant in case of either failure of the host central processing unit or software crash. In addition Switch over Logic card has been developed which will be used in hot stand-by configuration. The function of this card is to detect healthiness of the redundant computers. The healthiness is primarily determined by presence or absence of watchdog pulses. Pulse failure is considered as non-availability of the system and the Switch over Logic card route the relevant outputs of the healthy computer to the plant.

All the boards have been designed as per AERB safety guide. VLSI device have been used to reduce the number of components and interconnects on board. State of the art, Industrial standard, analysis software packages such as Signal Integrity, Thermal-hot spot and EMI/EMC were used to identify earlier design errors on board prior to fabrication. All the boards were also subjected to stringent environmental tests such as Temperature cycling, Damp/Dry heat tests and are qualified to work in harsh Industrial environments. The verification and validation on digital design as sequencer logic of analog input card and interface logic of analog output card has been successfully carried out on digital designs such at IIT Madras.

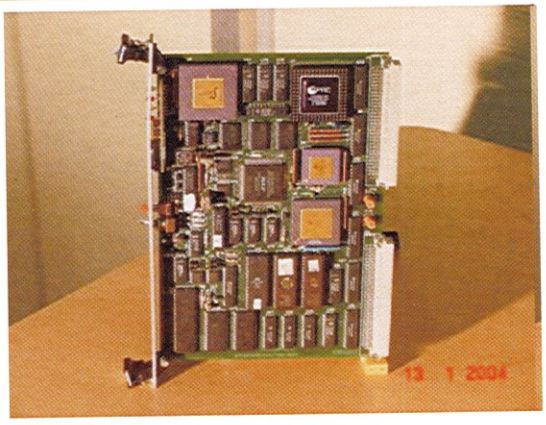

Fig. 1 : VME bus based MC68020 CPU card features:

- CPU: MC68020 @ 25 MHz
- FPP: MC6882 @ 25 MHz
- VME controller: VIC068A
- EPROM: 1MB, 16 WIDTH
- Serial Ports: 2 Numbers
- Local Area network: Two hardware TCP/IP modules

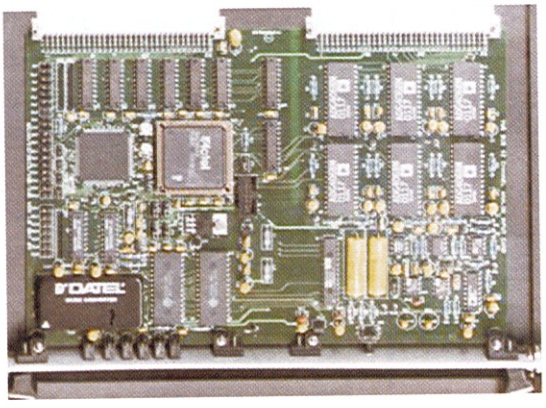

Fig. 2 : VME bus based Analog Input card features:

- Number of channels: 30
- Input Voltage range: ± 5V, ± 10V,
- ADC resolution: 16 bits
- On board sequencer for scanning operation.

VME BUS

VME bus is IEEE 1014, 1987 standard, which specifies a high performance backplane bus for use in microcomputer systems that employ single or multiple processors. The bus includes four sub-buses and supports 8, 16 or 32 bit data transfers over non-multiplexed 32-bit address and data highway. The transfer protocols are asynchronous and fully hand-shaken. The interrupt bus provides the Real Time Interrupt services to the system, whereas the Arbitration buses provide the services of allocation of bus mastership in case of multiple processor system. The mechanical specifications of boards, backplane, sub-racks and enclosures are based on IEC 297 specification, also known as Euro Board form factor.

INCORPORATION OF FAIL SAFE FEATURE IN THE DESIGN

Safety is very important especially when Real Time Computers are executing Safety Critical Functions. Provision for fails safe feature calls for improved strategy right from design to final deployment.

The high Mean Time between failures for such systems is achieved by providing adequate design margins, noise immunity, proper cooling, adhering to stringent quality policy for hardware component selection and quality control during manufacture. In addition the design must provide built in features for online fault detection and fault indication.

All the cards designed on VME bus incorporate extensive online diagnostics features for fault detection and health monitoring through the watchdog timer. The watchdog timer forms the heartbeat of the entire computer system. Since plant outputs are controlled through actuation of relays, watchdog features were also integrated into the Mono-shot Relay output board. This ensures that, in case of either system power failures or the failure of the CPU software, the plant outputs terminates to fail safe mode, thus preventing the catastrophe on the operating plant.



Fig. 3 : Refurbishment of Real Time Computers at CDPS,FBTR

APPLICATIONS OF VLSI TECHNOLOGY

The state of the art VLSI packages were used to integrate several thousands of discrete digital logics in to the reprogrammable, reconfigurable VLSI chips. This implementation has enhanced the reliability of the individual system due to reduction of components and also catering to the obsolescence of certain digital integrated circuit chips.

ACHIEVEMENT

The Integrated, Dual, Hot standby, Real Time Computer system consisting of CPU, Analog Input, Digital input and Mono-shot Relay cards has been used to successfully replace Unipower-30 , which is the part of Central Data Processing System of FBTR (Fig. 3). The present arrangement consists of three independent Real Time Computer Systems to carry out safety Critical, Safety Related and Non-Safety functions.

PUBLICATIONS ARISING OUT OF THIS STUDY AND RELATED WORK

1. N. Sridhar, J. Selva Solomon, V. Mythili, D. Thirugnanamurthy, B. Krishnakumar and S. Ilango Sambasivan, Report No. PFBR/66120/DN/1004
2. G. Venkat Kishore, N. Sridhar, B. Krishnakumar, S. Chandrasekaran and S. Ilango Sambasivan, Report No. PFBR/66120/DN/1000
3. B. Ramaswamy Pillai, G. Venkat Kishore, M.A. Sanjith, S. Chandrasekaran and S. Ilango Sambasivan, Report No. PFBR/66120/DN/1002

Further inquiries:
Shri S. Ilango Sambasivan, Electronics & Instrumentation Division
Electronics & Instrumentation Group, IGCAR, e-mail: sis@igcar.gov.in

Safety Logic with Fine Impulse Test (SLFIT) System for Prototype Fast Breeder Reactor

EXECUTIVE SUMMARY

While Control and Safety Rods (CSR) are used for startup, control of reactor power, controlled shutdown and SCRAM, the Diverse Safety Rods (DSR) are used only for SCRAM. The respective drive mechanisms are called as CSRDM & DSRDM. For SDS-1, Safety Logic with Fine Impulse Test (SLFIT) System is provided. For SDS-2, Pulse Coded Safety Logic (PCSL) System is provided.

OUTLINE

Prototype Fast Breeder Reactor (PFBR) is provided with two independent, fast acting and diverse shutdown systems namely SDS-1 & SDS-2 to detect any abnormalities in reactor core and to initiate safety action. Each system consists of sensors, signal-processing systems, logic systems, drive mechanisms and absorber rods. The absorber rods of the first system are CSR and that of the second are called as DSR. There are nine CSR and three DSR. SLFIT system receives trip parameters from neutron flux monitoring, failed fuel detection, sodium flow monitoring, reactor inlet temperature monitoring systems and performs logical operations to drive Electro-Magnet (EM) coils of Control & Safety Rods (CSRs). SLFIT system de-energizes the EM-Coils whenever a trip parameter crosses its threshold limits or there is a demand for reactor shut down. The trip parameters are triplicated in nature i.e. Triple Modular Redundancy (TMR) concept is employed to achieve high reliability and availability. Being a safety critical system, features like Design Diversity, Independence, Isolation, High Reliability and Testability have been incorporated in to the design and implementation of SLFIT System [Fig. 1].

The main building blocks [Figure: 2] for SLFIT System are Signal Conditioning Circuits, 2/3-Logic Circuits, Grouping Logic Circuits, Timer & Latching Circuit, FIT Logic Circuit, FIT Logic (Diagnostics) Circuit and EM-Coil Drive Circuit.

Due to the tremendous growth in Very Large Scale Integration (VLSI) technology, Integrated Circuits (ICs) have made digital systems more reliable by reducing the number of external interconnections from one device to another. In ICs the connections are internal to the ICs, where they are protected from poor soldering, breaks or shorts in connecting paths on a circuit board, and other physical problems. ICs have also drastically reduced the amount of electrical power needed to perform a given function.

SLFIT system is built using VLSI technique. The digital logic circuits for the SLFIT System have been implemented using Very High Speed Integrated Circuits (VHSIC) Hardware Description Language (VHDL) and the designs are fused in to One-Time-Programmable (OTP) Field Programmable Gate Array (FPGA) Devices, which are based on anti-fuse technology.

The EM-Coil drive circuit is built using Insulated Gate Bipolar Transistors (IGBTs).

The probable faults in Digital ICs is stuck-at fault, which implies the fault effect to be a line segment stuck at logic 0 or 1 (i.e. stuck-at 0 or stuck-at 1). For SLFIT System, stuck-at 1 is a unsafe fault, which need to be detected on-line in a minimum possible time. To prevent Safety Logic System failing in unsafe mode, an on-line test facility i.e. Fine Impulse Test (FIT) logic is provided. FIT Logic monitors the healthiness of Safety Logic System on-line and detects safe and unsafe failures. FIT logic injects short duration (1 ms) trip pulses periodically at the input of Safety Logic in required combinations and verifies the propagation of these pulses at the output of Safety Logic System. Each parameter is tested with a periodicity of 3 minutes. Whenever a fault is detected, the operator is informed for further action.

SLFIT system shall remain functional even under stringent environmental conditions. Hence, industrial version of the system will be subjected to Electro Magnetic Interference (EMI)/Electro Magnetic Compatibility (EMC), Environmental and Seismic qualifications.

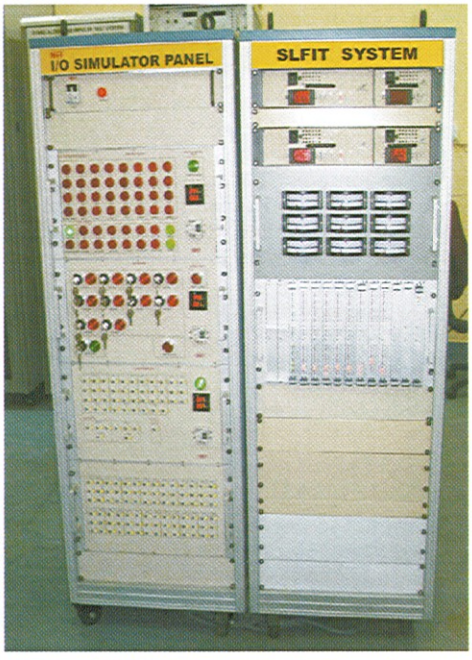

Fig. 1 : SLFIT System

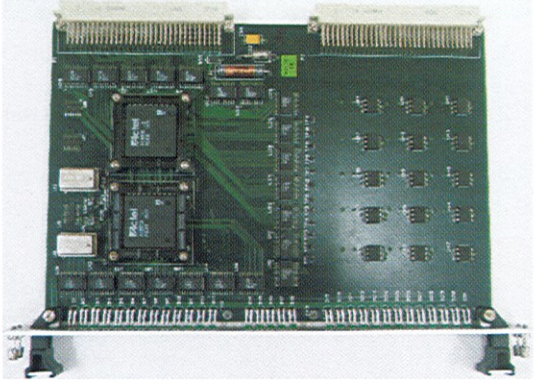

Fig. 2: One of the Hardware Modules of SLFIT System

SAFETY LOGIC WITH FINE IMPULSE TEST (SLFIT) SYSTEM

What is a Safety Critical System ?
Safety-Critical System is a system whose failure or malfunction may result in:

- death or serious injury to the people or
- loss or severe damage to the equipment or
- environmental harm.

FPGA DESIGNS FOR SLFIT SYSTEM

The digital logic circuits of SLFIT System like 2/3-voting logic, Grouping Logic, Timer & Latching Circuit, FIT Logic and FIT Logic (Diagnostics) is implemented using FPGA devices. The following important steps are involved in designing FPGA based designs [Figure: 3].

Design Entry: Resistor-Transfer-Level (RTL) coding of the design specifications using VHDL.

Design Verification: Once the specifications are captured in VHDL, the VHDL code needs to be verified at different stages of the design cycle for it's correctness. For this Functional Simulation, Timing Simulation is carried out. To check the code for it's functionality, test vectors are generated and fed to the design, according to the input test vectors, output of the design is checked. Further, as part of third party Verification, Indian Institute of Technology, Madras (IIT-M) has completed the verification of all the VHDL designs of SLFIT System.

Design Synthesis: Once the VHDL code is verified, the next step is to synthesize the code for implementation in a specified type of device. Synthesizer translates the VHDL code in to a gate-level net-list and optimizes the design for a target technology.

Design Implementation: Synthesizer output is fed to the design implementation tool for place & route to a target device and for generating the timing information.

Device Programming & Testing: Finally, the device is programmed using FPGA programmer and tested for it's functionality with the real world inputs.

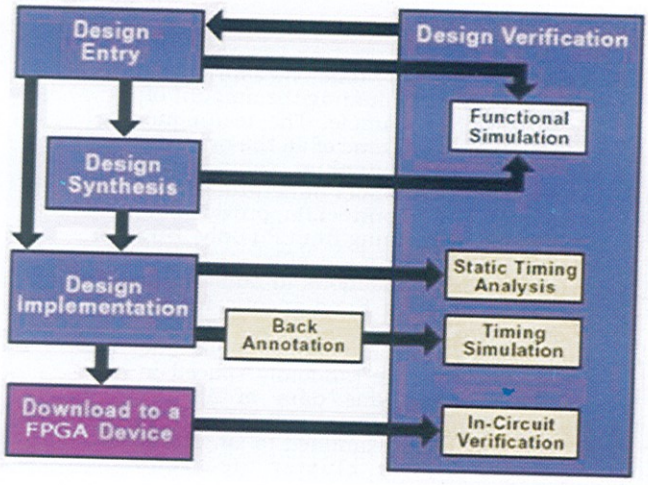

Fig. 3 : FPGA Design Flow

REACTOR SHUTDOWN SYSTEM FOR PFBR

As per the safety criteria for Nuclear Reactors, there shall be at least two reliable, independent, automatic, fast acting shutdown systems provided for the reactor, operating as far as possible on diverse principles. The purpose of reactor shutdown system is to quench the fission chain reaction in order to reduce the heat generation and bring and maintain the reactor in a desired sub-critical state when required. SLFIT System, which is part of SDS-1 is used to trigger the shutdown process. The principles of redundancy, diversity, independence, isolation, fail-safe design and testability are incorporated in to the design and implementation of SLFIT System.

ACHIEVEMENT

The functional requirements of SLFIT system for PFBR have been demonstrated. Testing of SLFIT Prototype System is completed and the fabrication of industrial version of the SLFIT System is in progress at M/s. ECIL, Hyderabad.

PUBLICATIONS ARISING OUT OF THIS STUDY AND RELATED WORK

1. M. K. Misra *et.al.* Report No. PFBR/66300/DN/1010 Rev.A
2. M. K. Misra and N. Sridhar, Report No. PFBR/66300/SP/1003 Rev.1
3. M. K. Misra and N. Sridhar, Report No. PFBR/66300/DN/1016 Rev.1

Further inquiries:
Shri S. Ilango Sambasivan, Electronics & Instrumentation Division
Electronics & Instrumentation Group, IGCAR, e-mail: sis@igcar.gov.in

Particle Arrival Time Recording Technique for Comprehensive Plutonium Assay

EXECUTIVE SUMMARY

The system assays plutonium by examining the arrival time of neutrons associated with the spontaneous fissions of ^{240}Pu isotopes in the presence of background reaction neutrons. The fission neutrons are time correlated while the background neutrons are random in time. In order to distinguish the time correlated fission neutrons from the random neutrons, the time stamp of all the incoming neutron pulses are recorded. After recording the arrival time of neutrons in a fast memory of sufficient size, the data is analysed off line to identify the time clusters which are indicative of the number of fissions and hence the amount of Plutonium in the sample. The correlation analysis based on this time arrival information is done in the PC off-line. The overall supervisory software is developed in VB 6. With suitable modification in the analysis software, the technique can be adapted for assay of ^{239}Pu by active neutron interrogation.

OUTLINE

The particle arrival time measurement method is used in evaluating the amount of ^{240}Pu in the given sample. The technique measures the arrival time of all the neutron pulses from the Plutonium sample. By knowing the total number of neutrons, one can calculate the amount of Pu, provided all the neutrons are coming from Pu only. But in real situation, there are other neutrons coming from some reactions in addition to those neutrons from Spontaneous fission (SF) of Pu. The SF neutrons from ^{240}Pu are always released in a cluster, while the reaction neutrons are randomly spaced in time. The arrival time data of all the incoming neutron pulses (obtained using this technique), are examined to single out the characteristic cluster neutrons (coincident neutrons) of Pu from the random reaction neutrons. By further careful analysis of the coincident neutrons data, the amount of Pu can be calculated. The arrival time method can be extended to evaluate the ^{239}Pu also by induced fission method.

Refer to the block diagram in the Fig.1. The neutron pulses are generated form neutron detector system. A 16-bit counter counts the periodic pulse stream of a 4MHz clock. The outputs of the 16-bit counter at any instant are indicative of elapsed time. Every incoming neutron pulse is directed to latch the current output of the 16-bit counter, in a fast dual port 16 bit memory (FIFO). Thus the memory content in sequence provides the time of arrival of all incoming neutron pulses in order. In this way all the incoming pulses are made to record their time addresses without any loss. The 8031 based microcontroller card transfers the data from the memory to a PC. The time correlation analysis is done in the PC. The arrival time is measured with an accuracy of 250 ns.

Preliminary testing of the system has been carried out using the neutron collar with an Am-Be source (non time correlated neutrons) as well as FBTR fuel pins (time correlated neutrons). A software analysis of the time of arrival data was carried out with the above data to obtain the true coincidence count rate. In addition, optimization of the various parameters like pre-delay, gate width, etc was also carried out for the system. Fig 2 presents a calibration curve obtained using four FBTR fuel pins. As can be seen from the figure, the correlation between ^{240}Pu and coincidence counts is fairly good.

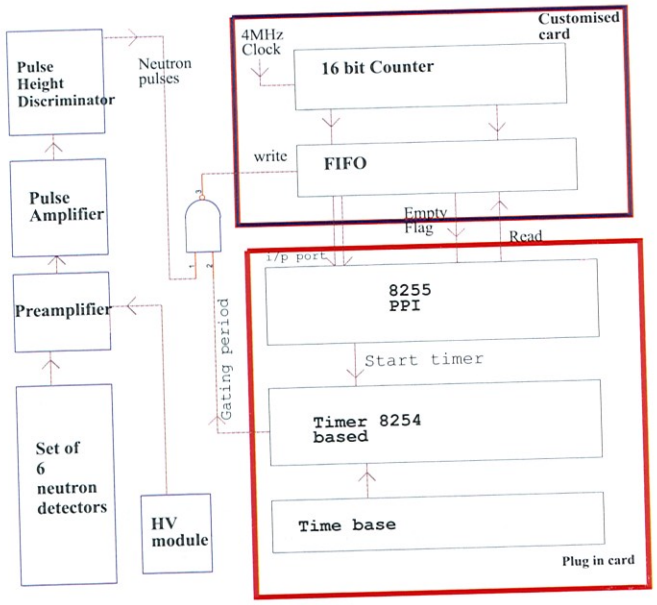

Fig. 1 : Block diagram of the system

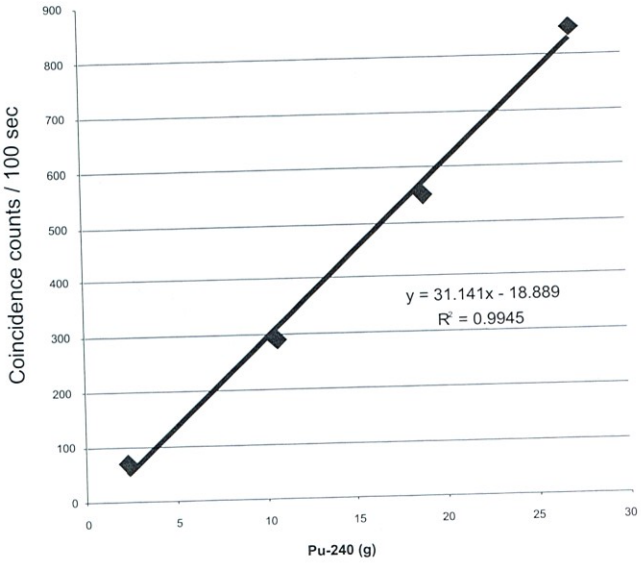

Fig. 2 : Calibration curve obtained using FBTR fuel pins

■ BRIEF DESCRIPTION OF THE BACKGROUND

When a plutonium isotope undergoes spontaneous fission, two or more neutrons are emitted almost simultaneously. The probability for detecting another neutron from the same fission decreases approximately exponentially with time, whereas the probability for detecting a random neutron is constant with time. To distinguish the time correlated neutron events from the random events (including the neutrons from different fissions), all the pulses are examined for two equal gate periods*, by the coincidence analysis routine. In this routine, the arrival time of adjacent neutron pulses are examined to count the number of pulses within the gate period from the selected pulse. The first time gate is opened to count the neutrons that can be due to either time correlated SF counts or random neutron counts. As a result, the counts accumulated during this gate are called the R+A counts (real fission counts + accidental counts). Following a long delay to ensure that any time correlation is removed, a second time gate is opened for the same duration as the first. The long delay is several times as long as the detector die away time (neutron life time in the detection system). This second gate counts only random events and the counts accumulated are called the accidental counts (A). The net difference in counts received during the two gates is the net real (R) coincident count and is related to the spontaneous fission counts in the sample.

*The gate period is approximately chosen to be the life-time of the neutrons or the detector die away time in the detection setup. The detector die away time of the neutrons is calculated from the exponential time profile plot generated in another analysis routine using the arrival time data, in software. The exponential profile obtained for coincident neutrons emitted by the fuel pins is shown in Fig 3. The number of counts accumulated in every 10 μs period for the all the pulses is plotted over a period of 250 μs. The die away time of the counting system is calculated to be around 100 μs.

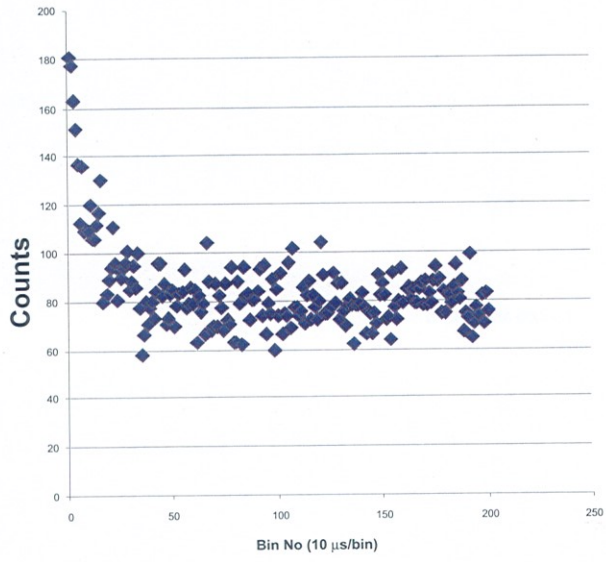

Fig. 3 : The exponential profile obtained using a FBTR Mark II fuel pin

■ ACHIEVEMENT

Retaining the basic concept, an eight channel pulse arrival time measurement unit is developed to meet the counting requirement for induced prompt fission neutrons from ^{239}Pu. Meanwhile two channels of the eight channels are adapted for the liquid scintillation coincidence counting system for the tritium assay.

■ PUBLICATIONS ARISING OUT OF THIS STUDY AND RELATED WORK

1. R.Parthasarathy, D.Saisubalakshmi, and C.R.Venkatasubramani, National Symposium On Nuclear Instrumentation – NSNI-2004, Feb. 2004, IGCAR, Kalpakkam.
2. R.Parthasarathy, D.Saisubalakshmi and C.R.Venkatasubramani, Nuclear & Radiochemistry Symposium (NUCAR-2007) NI-5, February 14-17, 2007, The Maharaja Sayajirao University of Baroda, Vadodara.

Further inquiries:
Shri R. Parthasarathy, Chemical Facilities Division
Chemistry Group, IGCAR, e-mail:partha@igcar.gov.in

Fabrication of Dummy Fuel Sub Assemblies (DFSA) for Core Mechanics Experiments

EXECUTIVE SUMMARY

Dummy fuel sub assemblies (DFSA) will be instrumented to measure the displacement and interaction loads between the sub assemblies by simulating reactor condition. Hexagonal is the slenderest component in the DFSA and it is cold formed from the circular tubes. Alternatively, it was fabricated from sheet by forming in two halves and welded. Activated flux assisted Tungsten Inert Gas welding (A-TIG) is employed to join the long seam of hexagonal sheaths. 110 DFSA were manufactured meeting specifications. The A-TIG welding totally eliminates the need for edge preparation, filler wire addition and enhances the penetrating power in the weld pool. Hence, single pass weld with higher welding speed was achieved.

OUTLINE

Introduction

DFSA will be instrumented to measure displacement and interaction loads between sub assemblies to validate core restraint system design and to check the mechanical interlock along with grid plate sleeve. The actual fuel sub-assemblies for PFBR are manufactured from 20% cold worked D9 material by extrusion / pilgering process, which resists void swelling and irradiation creep. Due to non availability of cold formed hexagonal sheaths for the experiments, an alternative manufacturing method has to be evolved. Central workshop IGCAR does not have the pilgering facility; hence it was decided to fabricate the hexagonal sheaths by forming and welding. A novel A-TIG welding technology was developed and used in welding of hexagonal sheath.

Fabrication of Hexagonal Sheath

The required sheet was sheared in Hydraulic Guillotine Shear with a dimensional accuracy of ± 0.5 mm. The hexagonal shape was bent in press brake machine in three stages using conventional die and modified punch. The edge preparation was done by manual grinding due to less thickness and geometry of hexagonal. A special welding fixture was made to control mismatch and distortion during welding. The GTAW process was used. Distortion is inevitable in austenitic stainless steel welding due to high thermal expansion (17×10^{-6} m /m °K) and low thermal conductivity (16.3 W/m°K). The distortion will affect the geometrical tolerance of the component. The combination of controlled heat input (≤ 1000 J / mm), sequential welding and use of appropriate welding fixture, the distortion was controlled to minimum. The inter pass temperature was maintained less than 393°K. In GTAW process, the production rate is less due to limitation in the welding speed.

Development of A-TIG

Material Joining Section (MJS) of IGCAR has developed activated flux for GTAW process and it will enhance the penetration in the weld pool. The development has been proven in laboratory level. The laboratory level proven technology was applied successfully on production scale. The activated flux which is in paste form was applied on the seam joint as shown in Figure 1. During welding activated flux changes the convection movement in the weld pool form centrifugal to centripetal as shown in the Figure 2 and there by deep penetration is achieved. The non destructive test DPI, RT / UT was carried on A-TIG welded sheaths. The destructive testing like, tensile test and bent tests were also carried. The micro hardness test was carried out on the welded samples from GTAW and A-TIG. The micro structure analysis revealed that the weld metal has columnar dendritic microstructures. The micro hardness measurements have shown good ductility in the A-TIG weld metal. A-TIG welded specimens have also passed inter-granular corrosion tests (ASTM A262 practice A & C). The delta ferrite examination was also carried out on the A-TIG welded sheaths. The DT & NDT test results were meeting all the design requirements and also a considerable welding time was saved by 70 % as compare to conventional method. So, the hexagonal sheaths were welded using A-TIG welding process.

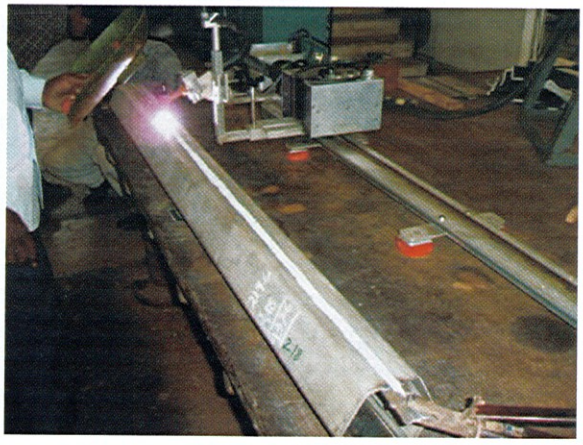

Fig. 1 : Photograph of A-TIG welding under progress in hexagonal sheath

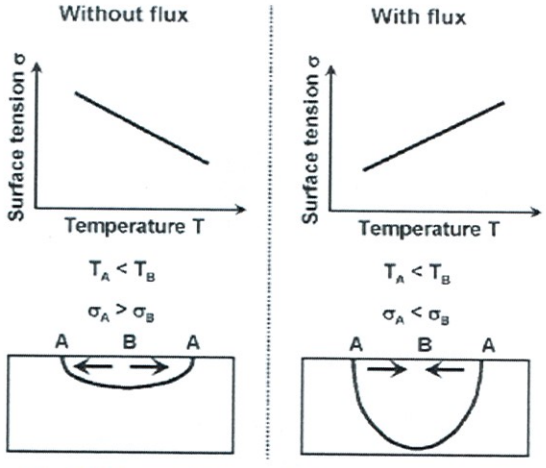

Fig. 2: Schematic diagram of Marangoni Convection

WHAT IS ATIG WELDING

An effective improvement in the GTAW process termed Active Tungsten Inert Gas (A-TIG) welding. Before welding, a fine layer of an inorganic powder, known as activating flux is deposited on the surface to be welded. The resulting depth of penetration is increased by a factor of 1.5 to 4 in comparison with the penetration depth

GENERAL DESCRIPTION

Dummy fuel sub assemblies (DFSA) will be used for experiments. Hexagonal is the slenderest component in the DFSA and it is cold formed from the circular tubes. Alternatively, it was fabricated from stainless steel sheet by forming in two halves and welding. GTAW process was used for welding of hexagonal sheath and production rate is less due to limitation in the welding speed. Material Joining Section (MJS) of IGCAR has developed activated flux for GTAW process and it will enhance the penetration in the weld pool as shown in Figure 3. The laboratory level proven technology of Activated flux assisted Tungsten Inert Gas welding (A-TIG) was applied successfully on production scale to join the long seam of hexagonal sheaths. 110 DFSA were manufactured meeting specifications. The A-TIG welding totally eliminates the need for edge preparation, filler wire addition and enhances the penetrating power in the weld pool with controlled distortion. Hence, single pass weld with higher welding speed was achieved. It increases the production rate by three times as compared to conventional GTAW process.

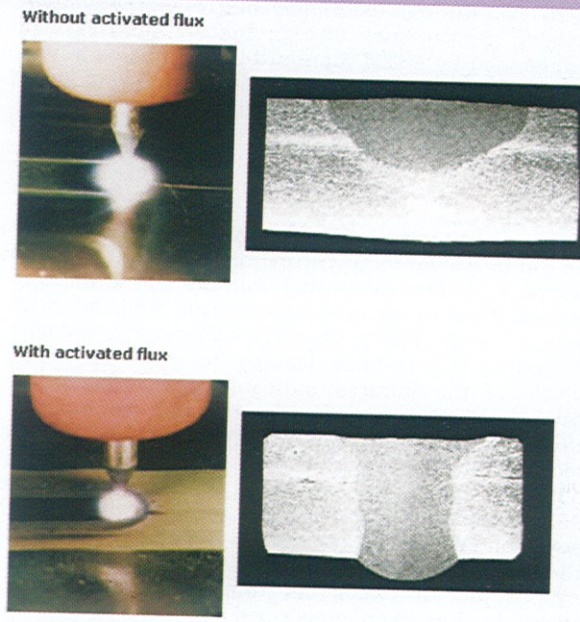

Fig. 3 : Photograph of Weld without / with activated flux

MECHANISM OF ATIG

There are two mechanisms that play important role in activating the effect of flux.

1) Marangoni effect: It refers to the convection movements due to the surface tension gradient on the weld pool surface. During TIG welding the surface tension gradient is negative and the convection movements are centrifugal and it leads to shallow penetration. The addition of activated flux induce an inversion of the convection currents changing the sign of the surface tension gradient, resulting convection movements changed to centripetal. Hence, the penetration depth increases.

2) The arc constriction effect: a) The flux acts as an insulating layer reducing the current density at the outer radii of the arc column and thus increases the current density at the center, increased magnetic force which leads to strong convective flow downwards in the weld pool and thus to significantly increased weld depth. b) The flux powder (Titanium dioxide) also causes the formation of an anode spot on the surface of the joint which attracts the electrons from the cathode (Tungsten electrode) causing deeper penetration. c) Negative ion formation at the edge of the arc could increase current density at the centre of the anode and thus increase the weld depth. It increases the production rate by three times as compared to manual GTAW process and it gives consistent quality and excellent bead appearance.

ACHIEVEMENT

The developed and laboratory proven activated flux technology was applied successfully on production scale. The flux assisted welding totally eliminates the need for edge preparation, filler wire addition and enhances the penetrating power in the weld pool with controlled distortion. Hence, single pass weld with higher welding speed was achieved. It increases the production rate by three times as compared to manual GTAW process and it gives consistent quality and excellent bead appearance.

PUBLICATIONS ARISING OUT OF THIS STUDY AND RELATED WORK

1. P. Sivaraman, M. Krishnamoorthy, N. Easwaran, R. Veluswamy and A. S. L. Kameswara Rao, International Symposium on Advances in Stainless Steels – 2007.

Further inquiries:
Shri A.S.L. Kameswara Rao, Central Workshop Division
Engineering Services Group, IGCAR, e-mail: aslkr@igcar.gov.in

Image Processing for Quality Assurance of Sheathed Thermocouples

EXECUTIVE SUMMARY

Performance of the thermocouple is related to a variety of parameters such as fusion of junction weld, wall thinning, spacing etc. While general continuity checks help in assessing the thermocouple, a deeper insight into the physical construction through techniques like radiography help in evaluating the condition of the thermocouple and thus prevent unreliable performance and premature failures. The experimental results clearly reveal that while radiography recommended by ASTM Standard-.E 235, helps in visualizing the inner details, application of digital image processing aids in a quantitative characterization resulting in more reliable quality assurance especially in the case of small diameter thermocouples and also digital archiving.

OUTLINE

Sheathed thermocouples are widely used in the nuclear and other industries for temperature measurement. It had been observed in a few cases that initially the stainless steel sheathed thermocouples function quite well, but within a short span (especially in the high temperature areas), their performance deteriorates leading to premature failures. Analysis of the failures indicated open junction welds (mostly due to improper fusion) and wall thinning. It was thus felt that additional quality checks are essential especially for thermocouples to be used in the critical application areas. In fact ASTM E-235-88 (re-approved 1996) "Standard specification for thermocouples, sheathed, Type-K for nuclear or other high reliability applications" outlines the various inspections to be carried on the thermocouple to check its integrity. Conventional radiography has been prescribed for the detection of the cracks, voids, inclusions and discontinuities in the sheath wall. However, in the case of thermocouples with diameters less than 4 mm, detectability of features in the radiograph becomes very difficult. This calls for the application of Digital Image Processing (DIP) techniques for better image sensitivity and quality and quantitative feature characterization.

Sheathed thermocouples with diameters less than 4 mm were subjected to high sensitivity radiography. An optimum voltage and a large source to film distance of 1000 mm was used to reduce the overall unsharpness in the radiographs.

The radiographs were then digitized and the region of interest identified. The image was then subjected to appropriate filtering for noise reduction and for enhancing the edges of the images. The image contrast was then enhanced using histogram equalization (Figure 1). The diameter of the weld ball, individual elements and sheath thickness were measured. Line profiling and number of pixels were used for the measurements. The pixels were calibrated based on the actual dimensions of the thermocouple. For better accuracy and to minimize errors, pixel calibration was carried out separately for horizontal and vertical measurements.

Evaluation of the radiographs after image processing revealed that the weld ball in both the thermocouples radiographed was observed to be elliptical. Error estimation was also done through reverse calculation of the thermocouple diameter. The variation in actual value and estimated value was observed to be a maximum of 25 microns. The error on the positive side can be explained as being due to the small geometrical unsharpness, inherent magnification (again small) in radiography and of-course the uncertainty in location of the edge (minimal because of the edge enhancement). However this error is quite reasonable.

Based on this successful application, a flow chart has been formulated for image processing of radiographs of small diameter thermocouples.



Fig. 1 : The edge-enhanced radiographic image of hot junction of 2.0 mm thermocouple after 10X magnification

Table 1 (a) & (b)
Summaries of the measured and expected values

Thermocouple (Dia)	Element Diameter		Average Sheath Thickness	
	Measured (mm)	Expected (mm)	Measured (mm)	Expected (mm)
2 mm	0.387	0.41 ± 0.03	0.291	0.28 ± 0.02
4 mm	0.912	0.96 ± 0.03	0.368	0.38 ± 0.02

Thermocouple (Dia)	Average spacing between		
	Sheath and Weld Ball (mm)	Sheath and Elements (mm)	Elements (mm)
2 mm	0.248	0.337	0.213
4 mm	1.024	0.601	0.393

■ ADDITIONAL INFORMATION

Experimental investigations clearly reveal that digital image processing aids in reliable quantitative feature characterisation. The purpose of a standard is to ensure reliability and product quality. Standards are revised and updated periodically to keep in pace with the stringency specifications and technological developments. The present standard E 235 has already recommended the use of non-film techniques for imaging. In view of this experimental investigation, it is recommended that the ASTM standard E-235 can also incorporate or suggest the use of appropriate image processing especially for thermocouples with diameter less than 4 mm for enhanced and reliable quality assurance.

■ GENERAL DESCRIPTION

Temperature and its distribution is one of the basic and key parameters employed as an indicator of functioning of an industrial component or plant. For the measurement of temperature, thermocouples are most widely used. Stainless Steel sheathed thermocouples are the preferred ones for temperature measurement especially in the nuclear reactor; due to its better mechanical properties and chemical compatibility.

Quality checks are essential especially for thermocouples to be used in the critical application areas. One of the best quality checks is the application of radiography. In the case of thermocouples with diameters less than 4 mm (Figure 2), detectability of features in the radiograph becomes very difficult. This calls for the application of digital image processing techniques for better image sensitivity and quality and quantitative feature characterization.

At the authors lab, thermocouples with diameters less than 4 mm were subjected to high sensitivity radiography. The radiographs were digitized and then subjected to a variety of image processing techniques. The fine details within the thermocouple could be clearly visualized and dimensional measurements made with great accuracy.

The experimental results clearly bring to fore the advantages of digital image processing especially in the case of radiographs of smaller diameter (< 4mm) thermocouples thus making inspection more reliable and robust.

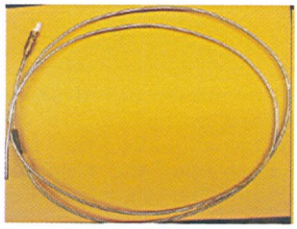

(a) 4 mm diameter

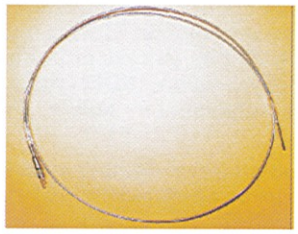

(b) 2 mm diameter

Fig. 2 : Typical Photographs of Thermocouples

■ ACHIEVEMENT

Digital image processing has been successfully applied for enhancement and quantitative characterization of sheathed thermocouples with diameters less than 4 mm. Based on this approach, a procedure has been formulated for image processing of radiographs of small diameter thermocouples. It is recommended that the ASTM standard E-235 can also incorporate or suggest the use of appropriate image processing especially for thermocouples with diameter less than 4 mm for enhanced reliability and sensitivity of inspection.

■ PUBLICATIONS ARISING OUT OF THIS STUDY AND RELATED WORK

B.Venkatraman, Baldev Raj, M.Menaka and R.Subbaratnam, *Materials Evaluation*, **65** (2007) 499.

Further inquiries:
Dr. B. Venkatraman, Quality Assurance Division
Engineering Services Group, IGCAR, e-mail: bvenkat@igcar.gov.in

Development of Morphological and Wavelet based Methods for Feature Extraction from Thermal Images

EXECUTIVE SUMMARY

In automated adaptive welding system, IR images are to be captured in real time, analysed for thermal features that can be attributed to defects and quantitatively characterized for acceptance/rejection. Quantitative characterization requires application of advanced image processing tools. Edge detection is an important image processing operation. Traditional approaches using classical edge detectors fail when the images are noisy. Wavelet Transforms help to overcome this difficulty. This is demonstrated on thermal images of welds with lack of penetration using wavelet based Sobel and Prewitt edge detectors.

OUTLINE

In spite of the numerous advances in the science and technology of welding, defects do occur sometimes leading to failures. Conventionally, the quality of the weld is ascertained only after the welding has been completed through the use of Non Destructive Testing (NDT) techniques such as ultrasonic or radiography. Since each of these techniques is applied only after the welding is completed, a lot of time, material and manpower are wasted before one comes to know about the soundness of the weld. With greater emphasis on automation during manufacturing process, automated NDT has gained prominence. One of the Non-Destructive Evaluation (NDE) techniques that are being increasingly applied for online monitoring is thermal imaging.

In automated adaptive welding system using IR sensors, IR images are to be captured in real time and based on the isothermal pattern the quality of welding is to be judged. Once thermal features are detected and attributed to defects, it is necessary to quantitatively characterize them for acceptance / rejection.

Quantitative characterization requires the application of advanced image processing tools for feature extraction and dimensional measurements. Edge detection is an important image processing operation which helps in detecting the Region of Interest. Traditional approaches that use classical edge detectors work fine with high quality pictures, but often are not good enough for noisy pictures because they cannot distinguish edges of different significance as they primarily focus on the coupling between image pixels on a single scale. Recent developments in Multi Scale Analysis such as Wavelet Transform help to overcome this difficulty.

Thermal images were acquired during online welding using an IR camera positioned appropriately. During the root welding stage, defects such as lack of penetration were introduced intentionally. These defects were confirmed through radiography subsequently. About 6 pads were welded with LP and thermal images acquired. Thermal image of the root weld with the LP was used for further analysis.

The first step was to convert the color image into a gray scale image to reduce computational complexity. Analysis of the images obtained after application of the classical Prewitt and Sobel filter indicates that along with the actual edges, the edges of the noise also got enhanced. This is because Multiscale Edge detection is not possible with the conventional Prewitt & Sobel Masks. Wavelet based edge detectors provide a facility for varying the scaling factor, which helps in differentiating the weak edges from strong edges.

This is a collaborative work between IGCAR, Kalpakkam and Satyabama University, Chennai. Analysis of the thermal image depicting lack of penetration reveals that compared to the edge detection performance of Classified Sobel & Prewitt filters wavelet based edge detectors provide better results by removing the noise.

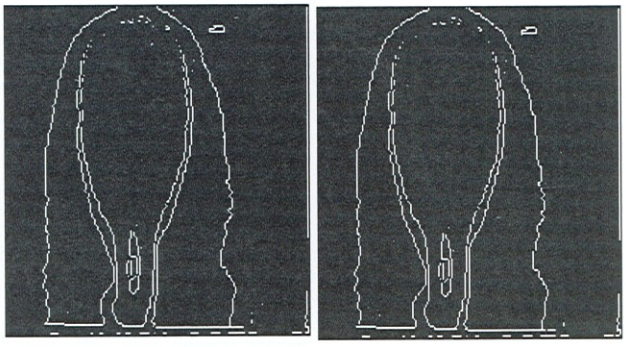

Fig. 1: Edge detection using (a) Sobel Filter, (b) Prewitt Filter

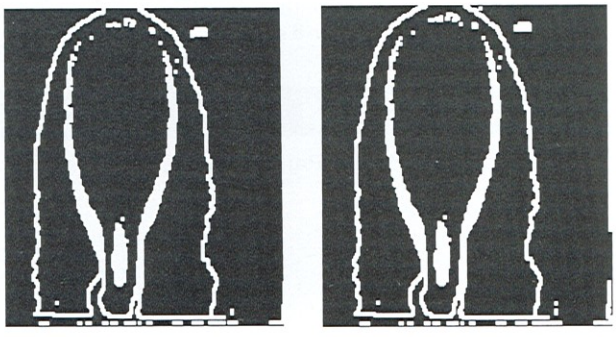

Fig. 2: Filling Operation after dilation on (a) Sobel filtering image (b) Prewitt filtering image

■ ADDITIONAL INFORMATION

The procedures thus evolved can be used for detection and characterization of other defects such as porosities and tungsten/slag inclusion which are commonly formed during the welding process. The technique can also be adapted for other NDE methods such as radiography.

■ GENERAL EXPLANATION RELATED TO THE DESCRIPTION

Welding is one of the widely used methods for joining metals. Conventionally, the quality of the weld is ascertained only after the welding has been completed using Non Destructive Testing (NDT) techniques. Recently online weld monitoring using IR sensors has also been established. Infrared (IR) Imaging is an advanced NDE technique based on the detection of infrared radiation. IR imaging during welding is based on the fact that a good weld would produce isothermal patterns which are symmetrical, while a weld with defects or arc misalignment etc. would produce isothermal patterns which are not symmetrical.

In this work, thermal images were acquired during online welding using an IR camera. Defects such as lack of penetration were introduced intentionally. The thermal images were then subjected to image processing. In this work, the performance of classical edge detectors and wavelet based edge detectors were compared using the weld defect-lack of penetration defect-formed during the welding process.

Wavelet based edge detectors provide a facility for varying the scaling factor, which helps in differentiating the weak edges from strong edges. The edge detected images using classical and wavelet based Prewitt filter is shown in Fig. 4 respectively. Comparing figure 3 and figure 4, it can be observed that using appropriate scaling factor, that apart from noise removal, the wavelet based Prewitt detector is more truthful in reproducing the edges compared to the classical Prewitt mask.

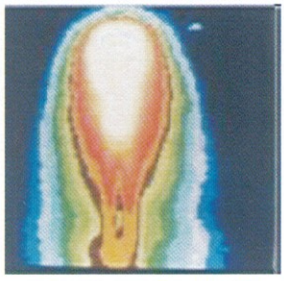

Fig. 3 : Thermal Image of root pass of weld with lack of penetration.

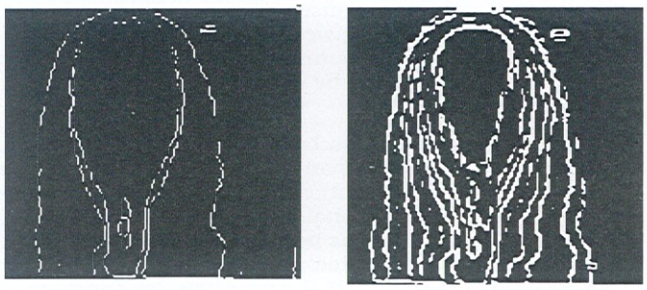

a b

Fig. 4 : Edge detection using (a) Classical Prewitt mask (b) Wavelet based Prewitt edge detector with a scaling factor

■ BRIEF DESCRIPTION OF THEORETICAL BACKGROUND

In edge detection using classical derivative approach, derivatives which yield high values, at places where gray level changes rapidly are used to find edges of an image. In the present study, two dimensional derivatives for lack of penetration in thermographs are computed with the help of edge masks namely Prewitt and Sobel. In Prewitt operator, while approximating the first derivative, similar weights are assigned to all the neighbors of candidate pixel whose edge strength is being calculated while in the case of Sobel operator, higher weights are assigned to the pixels close to the candidate pixels. In the case of Wavelet based Edge detectors, the edge detectors can be viewed as discretized wavelet functions. The convolution with edge detectors gives the wavelet transform of the image at a certain scale. Once a continuous model is obtained, scales can be changed and objects can be detected at different scale levels.

■ ACHIEVEMENT

This work highlights the successful application of wavelet based methods for analysis of thermal images. The edge detection performance of Classical Sobel and Prewitt filter are compared with the developed wavelet based Sobel and Prewitt Edge detectors. It is found that wavelet based edge detectors provide better results by removing the noise and the results are analyzed subjectively. It is the multi scale edge detection property of wavelet that has helped in removing the noise.

■ PUBLICATIONS ARISING OUT OF THIS STUDY AND RELATED WORK

N.M.Nandhitha, N.Manoharan, B.Sheela Rani, B.Venkataraman and Baldev Raj, Proceedings of 12th Asian Pacific Conference on NDT, November, 2006, New Zealand.

Further inquiries:
Dr. Baldev Raj, Director, IGCAR
e-mail: dirsec@igcar.gov.in

Development of Novel Combination of Immersion Technique and Time of Flight Diffraction for Examination of Weldments with Thicknesses less than 6mm and its Applications to Evaluation of Hexcan Welds of Thickness 3 mm

EXECUTIVE SUMMARY

Time of flight diffraction (TOFD) is now a well-developed non-destructive testing (NDT) technique and has been applied successfully for accurate sizing of defects in thick sections. Codes of practice such as ASME now permit TOFD for routine examination of welds greater than 12.5 mm in thickness. Examination of thinner sections by TOFD has its own problems. As the thickness of the specimen reduces, the lateral wave, diffracted signals from the tips of the discontinuity and the back wall echo merge together making it difficult or impossible to identify and size discontinuities. By a novel combination of immersion and TOFD, examination of specimens of thickness down to 3mm has been carried out successfully.

OUTLINE

Time of flight diffraction (TOFD) technique is an advanced ultrasonic non-destructive testing method which can be used for accurate sizing of the discontinuities. This method is based on the time difference between the diffracted signals obtained from the tips of the discontinuity. Time difference between the diffracted signals is directly related to the spatial extent of the discontinuity.

Internationally TOFD has been recommended for weldments with thickness greater than 12.5mm. Very few studies have been undertaken internationally for specimen thickness less than 12.5mm. International reports tell that TOFD combined with signal processing has been applied to specimen thickness down to 6mm. As the thickness of the specimen decreases, lateral wave, diffracted echoes from the discontinuity and the back wall echo merge together and hence defect detection and characterization is not possible. This problem has been successfully overcome at the Quality Assurance Division, IGCAR using a novel combination of TOFD and immersion.

For initial studies, three stainless steel plates with artificial reference defects were chosen. Plate 1 was 10 mm thick and had five side drilled holes of 2 mm diameter at different locations. Plate 2 was 5 mm thick with 5% and 10% notches and two side drilled holes (2 mm diameter) and Plate 3 was 3 mm thick with 5% and 10% notches. Since the plates were quite large and the region of interest was small, a dam was constructed to maintain the required water path, (Fig. 1(a)).

The parameters to be considered was thickness of the water column over the material and probe tilt. Based on the time of flight equations, the time difference between lateral wave and back wall echo was computed as a function of probe tilt for specimens of different thickness. It was observed that as the probe separation and the propagation angle inside the material decreases, this time difference increases which leads to better spatial resolution (Table 1). The required lower probe separations were not possible in conventional TOFD because of the size of the probes.

Based on the experiments on the reference specimens, further examinations were carried out on welded specimens of thickness 3.15mm. These specimens pertain to the hexagonal sheath (Hexcan) of the fuel sub-assembly. The weld specimens had defects such as lack of penetration and porosity which were earlier confirmed through radiography. The combination of TOFD and immersion could pick up these defects which was not possible with conventional TOFD method. Typical image of experimental set up and the TOFD images are shown in Fig. 1.

The welded specimens were subjected to radiography and the radiographic images were processed with appropriate methodologies and dimensions of the defects estimated. Dimensional measurements from radiographs were compared with the dimensions from TOFD measurement. A very good correlation was obtained with errors being less than 5%.

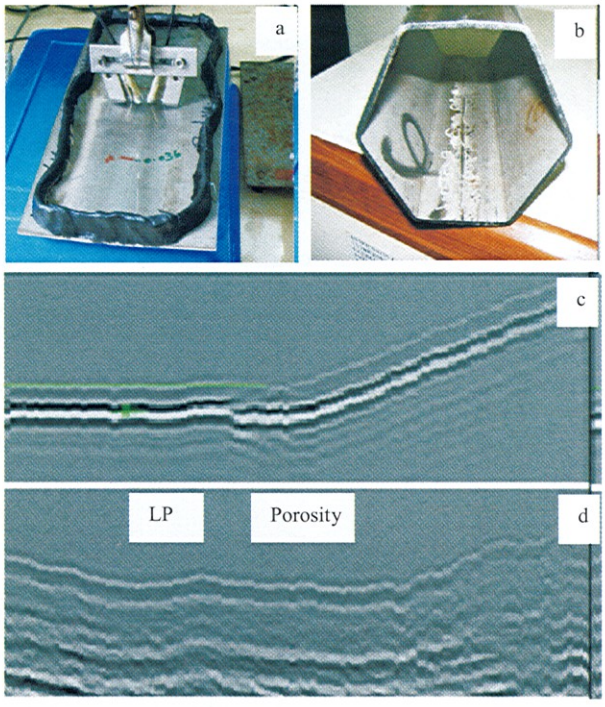

Fig. 1 : (a) Experimental setup (b) 3.15 mm thick welded Hexagonal sheath (c) TOFD image of a welded plate having no defect (slop is due to curvature of the plate) and (d) TOFD images indicating lack of penetration and porosity.

Table 1
Different parameters to be considered for immersion TOFD

Probe tilt in water (φ)	Wave propagation angle inside the material (θ)	Probe Separation (2S) (mm) for plates of		Time difference between lateral wave and back wall echo (μSec)	
		5mm	3mm	5mm	3mm
2.5	10	1.2	0.7	1.483	0.889
3.7	15	1.8	1.1	1.396	0.837
4.9	20	2.4	1.5	1.312	0.787
6.1	25	3.1	1.9	1.228	0.737
7.2	30	3.8	2.3	1.147	0.687
10.2	45	6.6	4.0	0.894	0.536
12.5	60	11.5	6.9	0.623	0.374
13.6	70	18.2	10.9	0.427	0.255

APPLICATION OF SHEAR WAVES

The above mentioned experiments were repeated with shear waves also. The first critical angle for steel in immersion setup is 14.5° and the second critical angle is 27.5°. Within this range of angles only shear wave mode exists in the specimen. Since the angle of tilt for producing shear waves is larger than that for longitudinal waves, there is considerable probe separation and the time difference between the lateral wave and back wall echo is also more. This results in better spatial resolution. All the discontinuities could be detected by shear wave mode with accuracies better than ±5%.

GENERAL EXPLANATION RELATED TO THE DESCRIPTION

The principles of conventional pulse echo ultrasonics for materials characterization is well established. When these waves incident on a discontinuity inside the material, diffraction of waves occur at the tips of the discontinuity together with reflection, scattering and mode conversion. Since reflection depends on the orientation of the defect and angle of examination, it is not applicable at all conditions. The advantages which allow the time of flight diffraction (TOFD) technique for exact sizing is that it is independent of the defect orientation and amplitude of the diffracted echoes. Geometrical arrangement of the set up is shown in Fig. 2. Two transducers, one act as a transmitter (T) and the other act as a receiver (R), are placed in a pitch-catch mode. Four signals arrived at the receiver is lateral wave, which traveling just below the surface, diffracted echo from the top (1) and bottom (2) of the discontinuity and the reflected back wall echo.

Since diffraction takes place at the extremities of the discontinuity, time difference between diffracted echoes gives the spatial extent of the discontinuity. The sizing technique based on the measurement of time difference between the diffracted signals is called time-of-flight diffraction technique. Depth and size of the discontinuity can be obtained by solving simple trigonometric relations by knowing the transit time between the diffracted echoes from the top and bottom of the defect and also the lateral wave and back wall echoes. Lateral wave and the back wall echo will act as the reference signals.

In TOFD technique the probe separation is directly related to the thickness of the material and angle of the probes. Probe separation is so adjusted in such a manner that the most energetic axial beams of the probes should meet at a point at $2/3^{rd}$ of the thickness of the specimen. Probe separation can not be reduced beyond a minimum because of the physical size of the available probes. This difficulty could be overcome in immersion TOFD by taking sufficient water path length. Fig. 3 shows the schematic of the experimental set for immersion TOFD indicating the beam propagating angle and the beam path.

Experiments were conducted by the Quality Assurance Division of IGCAR using reference defects (notches) and the parameters such as probe tilt and probe angle for good defect indication optimized. Based on this, the experimental study was extended for the practical case of examining thin walled weldments in hexscan. All defects in the welds could be detected successfully and dimensions measured with errors less than 5 % (compared to radiography).

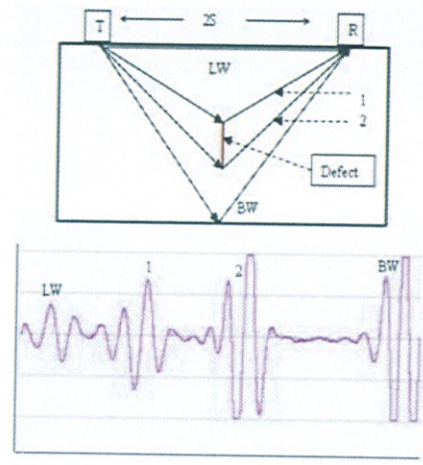

Fig. 2 : TOP: Geometrical arrangement of TOFD method
BOTTOM: Different signals reached at the receiver

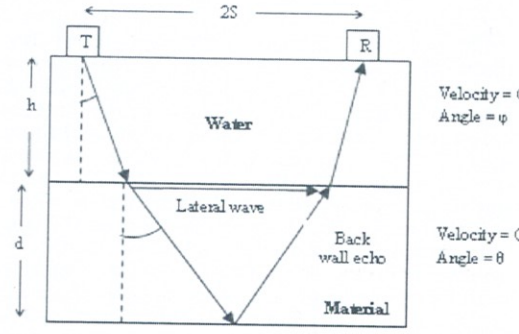

Fig. 3 : Beam path and angle of propagation through water and material in the immersion

BRIEF DESCRIPTION OF THEORETICAL BACKGROUND OF IMMERSION TOFD

Distances having equal transit time are directly proportional to the sound velocities. Ultrasonic wave velocity in water is approximately one-fourth the velocity in steel. Since the sound velocity ratio for steel to water is 4, distance having equal transit time in water is 4 times greater than that for steel. Hence the signals which are very close together in steel will be well separated after traveling through water of sufficient path length. Also the required wave propagation angle inside the material can be achieved using the phenomenon of refraction. The beam spread in water is considerably low compared to that in steel. Hence the added water path length will not affect reception part in terms of reduction in received energy.

ACHIEVEMENT

Overall the experiments successfully established that TOFD with immersion could be a reliable tool for defect detection in thin weldments overcoming the inherent limitations of TOFD.

Further inquiries:
Dr. B Venkatraman and Shri R Subbaratnam, Quality Assurance Division
Engineering Services Group, IGCAR, e-mail: bvenkat@igcar.gov.in; rsu@igcar.gov.in

Double Oxide Coating on Titanium for Reconditioning (DOCTOR)

EXECUTIVE SUMMARY

Titanium shows excessive corrosion rates (> 20 mpy) in boiling 11.5 M nitric acid being used for the dissolution of spent nuclear fuel from fast breeder reactors. This is mainly due to the concentration range of nitric acid and the high iron content in the material. In order to overcome this problem, a double oxide coating for reconditioning of titanium (DOCTOR) has been developed which reduces the corrosion rates to ~ 5 mpy. The improvement in corrosion resistance is due to the formation of smooth and nanograined TiO_2 on the surface. Electrochemical and surface investigations correlated the corrosion resistance to the above consideration. Qualification of the above process with scaled up titanium vessels supported the application of the above technology to fabricated titanium dissolver vessels of fast reactor fuel reprocessing plants.

OUTLINE

Titanium undergoes severe corrosion in the HNO_3 concentration range of 40-55%, and when the material contains high iron content. The presence of iron greater than 0.05 wt% in titanium leads to segregation of iron and formation of iron-rich intermetallics. Detailed electrochemical investigations indicated that the presence of iron in excess of 0.05% in solid solution, iron–titanium intermetallics at the surface, and iron embedment on titanium, significantly decreased the passivation characteristics of titanium and enhanced active and transpassive dissolution. The high corrosion rate of titanium in concentrated nitric acid motivated to develop a suitable passivation technology for improving the corrosion resistance.

Considering that the passivation technology needs to be implemented for fabricated components, treatments like thermal oxidation, metal spraying, PVD etc. are not considered for this purpose. Chemical/electrochemical anodisation is a unique way of forming a surface oxide layer that can protect and distinctly enhance the corrosion resistance of several metals and alloys. However, it has been reported in the literature that upon anodisation in several chemical media, the corrosion resistance of titanium is not improved significantly in nitric acid medium. The salient features of the passivation technology development related to: (i) a method to dissolve the iron particles segregated/enriched at the surface using chemical solutions by simple immersion method; (ii) application of nitric acid based solution containing redox ions that can enhance anodic oxidation for forming a stable oxide layer; (iii) further stabilisation and growth of oxide layer in an alternate chemical solution; and finally, (iv) conditioning of the surface layer. Several electrochemical treatments have been attempted for improving the corrosion resistance (Table 1). After such treatments, the specimens were tested as per ASTM A262 practice C in boiling 11.5 N HNO_3 solution and the average corrosion rates obtained indicated, that anodising for 24 h in a solution of nitric acid containing Ru, Cr and HF, and then subsequent anodic treatment in a solution of 10% ammonium persulfate gave the best results. The corrosion rate reduced to about 4 and 6 mpy (0.1–0.15 mm/year) in the Huey test.

This passivation technology for developing a corrosion resistant layer on titanium has been named as double oxide coating on titanium for reconditioning (DOCTOR), and can be used for surface modification of dissolver made of titanium. After the DOCTOR coating, the surface developed a smooth appearance (Fig. 1), and also exhibits higher polarization resistance and lower capacitance confirming superior corrosion resistance. Atomic force microscopic investigation of the coated surface revealed the presence of smoothly distributed fine oxide particles of TiO_2 (200 - 500 nm) over the surface (Fig. 2). Titanium forms various types of oxide films on the surface depending on the conditions of preparation. The formation of films in a fluorinated condition in nitric acid leads to dissolution controlled film formation mechanism. The passivation layer developed on the surface establishes equilibrium with the highly corrosive environment in the dissolver and ensures corrosion resistance for long life. This is similar to the pickling and passivation of stainless steels, or hot conditioning of carbon steels in high temperature water systems.

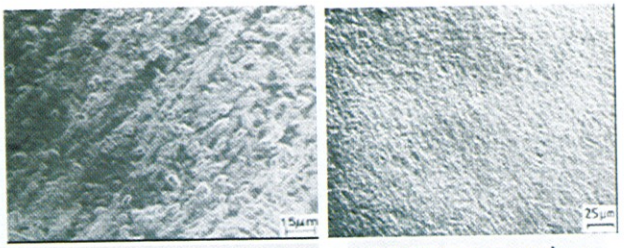

Fig. 1 : SEM micrographs showing nonadherent and loose TiO_2 formed on titanium in the condensate region, and a smooth TiO_2 coating developed by DOCTOR coating process

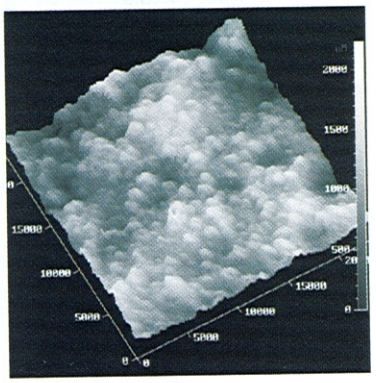

Fig. 2 : AFM image showing the formation of nanograined (200-500 nm) oxide particles and a smooth coating of titanium dioxide on the surface after DOCTOR coating

Table 1
Conditions of various surface modification processes, and the corrosion rate data obtained

No.	Test Condition	Electrolysis Parameters		Average Corrosion Rate in Huey Test
		Potential (V)	Duration (h)	
1.	Conc. Nitric Acid	10	0.5	19 mpy
2.	10% Sulfuric Acid	12	100	18 mpy
3.	10% Ammonium Persulfate	5	50	18 mpy
4.	10% Ammonium Persulfate	12	50	16 mpy
5.	10% Ammonium Sulfate	12	100	24 mpy
6.	(i) Nitric Acid +1 ml HF +30 mg Ru + 30 mg Cr^{6+}, followed by (ii) 10% Ammonium Persulfate	5 12	24 20	8, 6 mpy
7.	(i) Nitric Acid +1 ml HF+ 30 mg Ru + 30 mg Cr^{6+}, followed by (ii) 10% Ammonium Persulfate	5 12	24 50	4 mpy

■ ADDITIONAL INFORMATION

High iron content in commercially pure titanium grade-2 material is of great concern for the fabrication of electrolytic dissolver as corrosion of iron-rich segregation and precipitates yield high corrosion rates (~ 20 mpy) in boiling nitric acid. To over come this difficulty, a novel "Double Oxide Coating on Titanium for Reconditioning (DOCTOR)" coating process has been developed for the surface modification of titanium to eliminate the iron, which is contaminated or embedded or segregated on the surface. According to this process, a stabilized TiO_2 coating with high corrosion resistance is developed through double anodic oxidation process that can show acceptable corrosion rates (< 5 mpy) for boiling nitric acid service. Currently, the process has been standardized with scaled up sizes of actual dissolver and will be considered for application to future dissolvers of fast reactor fuel reprocessing plants.

■ GENERAL EXPLANATION RELATED TO THE DESCRIPTION

Currently, the process has been standardized with scaled up sizes of actual dissolver and is being considered for application to future dissolvers of fast reactor fuel reprocessing plants. It is to be mentioned here that no other chemical or electrochemical processes are hitherto available for corrosion protection of components made of titanium with high iron content for application in highly corrosive nitric acid environments.

■ BRIEF DESCRIPTION OF THE BACKGROUND

Titanium dissolves as Ti^{4+} ions during corrosion and the formation of protective TiO_2 film over the surface depends on the availability of threshold Ti^{4+} ions in the solution. Inadequate availability of the ions results in the formation of loose and non-adherent scale formation which corrodes the surface. Such a situation arises for titanium when it is used in HNO_3 concentration of 40-55% and with high iron contaminated surface (> 0.05% Fe). The current development deals with this unique problem in two ways, (i) by dissolving the excess iron in the surface, and (ii) by developing a smooth and nano-grained TiO_2 by anodic passivation process. This has been achieved by (i) initially dissolving the surface with suitable composition of HNO_3 and HF in the solution, and (ii) stabilizing the TiO_2 formation with the help of ions like Ru^{4+}, Cr^{6+}, Ag^{2+} etc. present in the medium under electrolytic conditions.

■ ACHIEVEMENT

DOCTOR coating process is a unique technology by which highly corroding titanium vessels could be protected insitu by forming nano-grained TiO_2 coating over the surface of fabricated components. Thus fabricated titanium vessels showing high corrosion rates in nitric acid could be made useful by applying DOCTOR coating process.

Further inquiries:
Dr. U. Kamachi Mudali, Corrosion Science and Technology Division
Metallurgy and Materials Group, IGCAR, e-mail: kamachi@igcar.gov.in

BREAKTHROUGHS

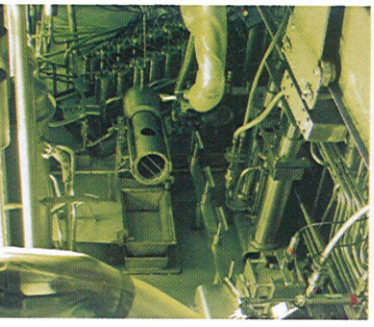
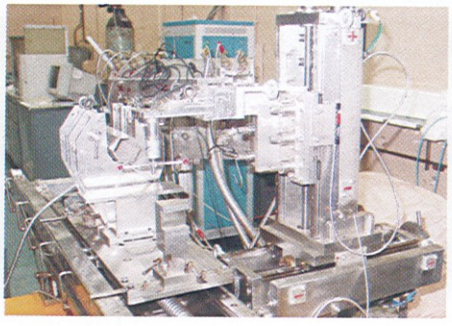



TECHNOLOGY

Technology Development for Hardfacing of Large Components using Ni base Hardfacing Alloys

EXECUTIVE SUMMARY

Systematic study on the effect of dilution from base metal on hardness and wear properties of Ni base hard facing alloys have shown that dilution adversely affect the properties of this alloy. Further, a comparison of plasma transferred arc (PTA) and Gas Tungsten Arc Welding (GTAW) process for hardfacing using these alloys showed that, dilution is consistently high in the latter while it can be controlled easily in the former by suitable selection of the process variables. In addition, PTA process is highly amenable for automation. Accordingly, PTA process is chosen for hardfacing of various components of prototype fast breeder reactor (PFBR). Many intricate and large components of PFBR like grid plate sleeve and large, bottom plate of grid plate assembly, have been successfully hardfaced using this process. Indian industries actively collaborated with IGCAR and participated in the successful execution of these jobs.

OUTLINE

Due to induced radioactivity consideration arising from Co^{60} isotope, it was necessary to switch over from more widely used Co-based hardfacing alloys to cobalt free alloys for hardfacing application in various PFBR components. Ni base hardfacing alloys, which have already been used in various fast breeder reactors worldwide was the alternate material though weldability of these alloys are poor compared to Co based alloys. A systematic study on hardfacing of these alloys using GTAW process, which was initially considered for hardfacing based on wide experience that existed with deposition of Co based alloys using this process, revealed that dilution from base metal is considerably high if this process is used for deposition of Ni base alloys. Studies also revealed that dilution has considerable effect on hardness (Fig. 1) and wear resistance (Fig. 2) of the deposits. Further, significant variation in microstructure of the deposit with increase in dilution from the base metal was also observed. The adverse effect of dilution on the deposit existed even up to 2 mm from the fusion boundary, the desirable maximum thickness recommended for the hardfacing coating on various PFBR components. Further, GTAW process is not easily amenable for automation. Hence, PTA process, which is highly amenable for automation was considered for depositon. Studies on deposits made by this process showed that it is possible to considerably reduce dilution in thse deposit by careful choice of deposition parameters (Fig.1).

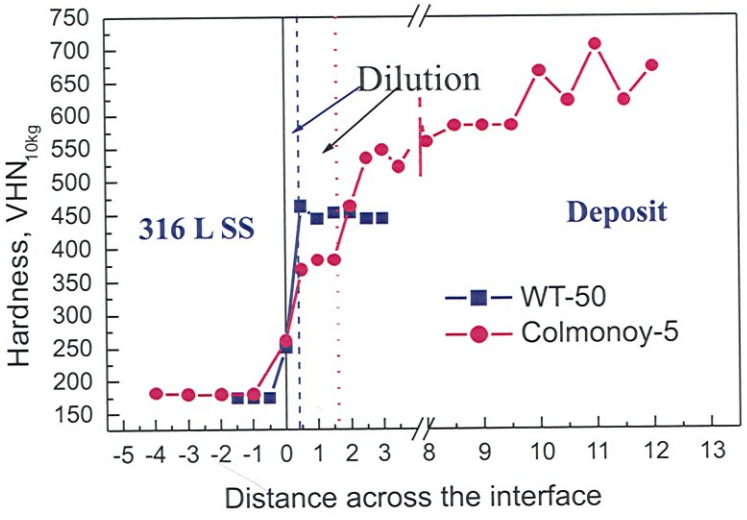

Fig. 1: Variation on hardness with thickness of deposit

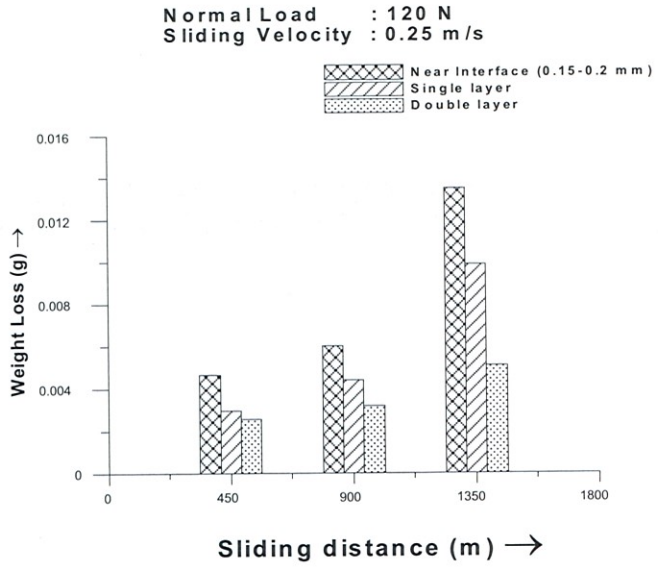

Fig. 2: Variation of wear loss versus sliding distance for a) Interface (maximum dilution) b) Surface of the first layer deposit and c) Surface of the two layer deposit (dilution minimum)

■ ADDITIONAL INFORMATION ABOUT THE PROCESS

Using information generated on systematic study of dilution during GTAW deposit, a procedure for fabrication bushes made from the Ni base hardfacing alloy was developed which involved weld build up and precision machining. The bushes made by this procedure met all the requirement and this procedure is now being adopted for fabrication of the bushes made of this material to meet the requirement of PFBR. Figure 3 shows various stages involved in the design.

■ GENERAL EXPLANATION RELATED TO THE DESCRIPTION

Using PTA process, various components of PFBR have been hardfaced successfully. They include diameter grid plate sleeves (where hardfacing has to be carried out in the inner surface of 80 mm ID tube at depth of more than 500 mm from one end of the sleeve) and large component like bottom plate of grid plate (diameter of 6.2 m) assembly. In the case of former a small PTA torch which can pass through the sleeve was indigenously developed and in the case of latter, automation of the deposition process considerably reduced the number of overlaps in the deposit which were the potential locations for cracking. It was also necessary to demonstrate that distortion of the components during hardfacing is kept well within the machining allowance available. By continuous improvement in process parameters, design and quality controls, all these requirements were successfully met. Figure 4 shows the hardfaced bottom plate of the grid plate assembly fabricated during technology development. This was made possible by the constant interaction between design and welding engineers at IGCAR and industries that actually fabricated the components and carried out the hardfacing operation.

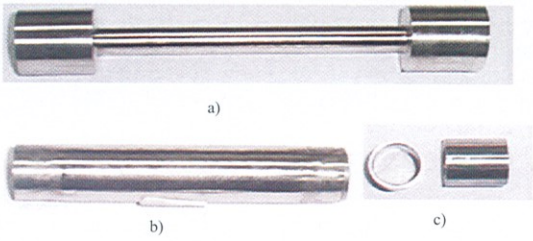

Fig. 3 : Various stages involved in the fabrication of bushes using weld deposition by GTAW process a) Stainless steel rod chosen for weld deposition, b) rod after deposition, c) bushes after machining



Fig. 4 : Bottom plate of grid plate assembly after hardfacing during technology development

■ ACHIEVEMENT

1. Choosing the optimum deposit thickness considering dilution from base metal, deposition process, distortion of the components and machining allowance available
2. Development of procedure for hardfacing of various PFBR components
3. Technology development for fabrication of bushes made of hardfacing alloys using weld deposition technique

■ PUBLICATIONS ARISING OUT OF THIS STUDY AND RELATED WORK

1. C.R. Das, S.K. Albert, A.K. Bhaduri and G. Kempulraj, *J. Mater. Process. Tech.*, **141** (2003) 60.
2. C.R. Das, S.K. Albert, A.K. Bhaduri, C. Sudha, and A.L.E. Terrance, *Surface Engineering*, **21** (2005) 290.
3. C.R. Das, S.K. Albert, A.K. Bhaduri and Nithya Ravindran, *Materials Science and Technology* (In Press).

Further inquiries:
Dr. A.K. Bhaduri, Materials Technology Division
Metallurgy and Materials Group, IGCAR, e-mail: bhaduri@igcar.gov.in

Comprehensive In-Service Inspection System for PFBR Vessels

EXECUTIVE SUMMARY

In-service inspection (ISI) plays a major role in monitoring the condition of nuclear power plant structures and components. Based on the information gathered during inspection and the studies carried out, it is possible to assess the extent of damage if any and take corrective measures to keep effects of ageing under control. The use of remote devices and robotic systems is essential for ISI of nuclear plants due to the presence of high radiation levels and limited access. Automation of ISI procedures and related non-destructive testing techniques results in significant performance enhancement in terms of efficiency, cost and time. A comprehensive ISI programme has been conceived for the inspection of PFBR main vessel (MV) and safety vessel (SV) at IGCAR.

OUTLINE

A comprehensive ISI system has been conceived for the ISI of MV and SV of PFBR based on free roving four-wheeled concept. The vehicle (VENTURE) is a four-wheeled remote controlled robotic device to carry NDE equipment into the interspace for enabling volumetric examination of welds and visual examination of external surface and internal surface of the MV and SV respectively. The MV-SV interspace will be at 150 °C at the time of inspection. Designing a remotely operated robotic vehicle system capable of working at this temperature is the challenge involved in this development.

The vehicle will be maneuvered by means of four independently driven wheels with steering capability, two resting on each vessel. The vehicle consists of a central structure about which two orthogonal arms are articulated. The wheels that are pressing on each vessel are placed at the ends of each arm. Each wheel will have traction and steering actuators with encoders for position feedback. The vehicle has a collapsible design to facilitate insertion through the openings provided from the operating floor, into the vessel inter-space. The device will be lowered into the interspace by a winch through one of the six inspection openings provided on top of the reactor vault and the anti-convection barrier. Figure 1 shows the photograph of the prototype vehicle "VENTURE" developed in collaboration with BARC. Once inserted in to the interspace the vehicle can be expanded to provide reaction needed to maintain the device in position against gravity and the frictional force required for traction. Inherently this gives the vehicle the capability of adapting to the variations in the interspace.

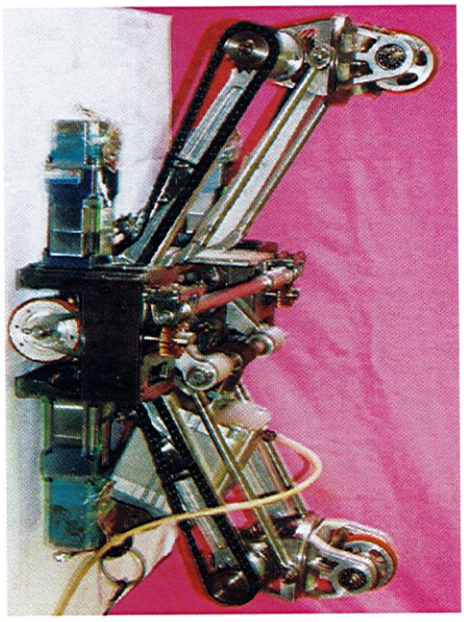

Fig. 1: VENTURE

A separate wheeled-vehicle (DISHA) with a scissor-jack mechanism is being developed to rest on the anti-convection barrier (ACB) and move around the interspace to inspect the dissimilar weld and in-situ weld because of the difficulty in using VENTURE due to the limitations in available headroom and increased interspace near the dissimilar weld zone. The ACB will be used as track for DISHA.

Handling devices and chambers for the ISI system have been conceptualized and few accessories like cable take-up/release and mono-articulated chain has been conceptualized.

NDE modules viz, Ultrasonic Test module (UT) and Visual Examination (VE) modules are the payloads to be carried by the VENTURE and DISHA for inspection of the MV and SV. Figures 2 (a) & (b) show the prototype UT module and VE module developed at IGCAR.

The objectives of the control of the ISI devices are manifold right from controlling the devices, actuation of NDE modules with acquisition and archiving the inspection data and controlling the auxiliary handling systems. Distributed control architecture with a master controller with human-in-control loop and a PC-based supervisory control is envisaged for the safe and effective operation and control of the inspection device. Soft and hard interlocks in the control algorithm will ensure safe functioning of the device while carrying out the inspection. The position and orientation for tracking of the devices in the interspace will be provided by Giant Magneto-Resistive (GMR)-based encoders and Micro Electro Mechanical Systems (MEMS)-based inclinometers capable of withstanding the temperature. This device-tracking is further supplemented by the visual data of the permanent landmarks engraved on the safety vessel surface provided by the on-board camera system.

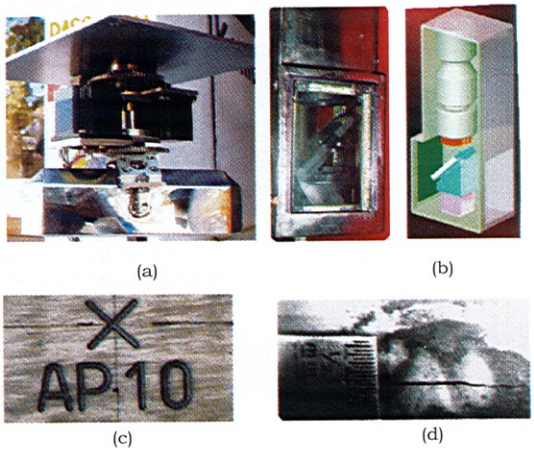

(a) (b) (c) (d)

Fig. 2: Various Prototype NDE Modules developed (a) UT Module (b) VE module and (c),(d) The test images captured by VE Module

■ PFBR IN-SERVICE INSPECTION

Objective of the ISI campaign is to inspect the critical welds on MV and dissimilar weld between roof slab shell and MV of PFBR. The inspection programme is to be implemented according to ASME B and PV Code, Section XI, Div 3.

The ultrasonic examination of dissimilar metal weld between MV and roof slab is to be done according to Table IMB 2500-1.Ultrasonic examination of C seam weld of support structure of shell of CSS to CSS and weld between support shell and MV also follows the same standards. VTM – 2 method is will be used for the visual examination of the entire MV outer surface.

■ GENERAL EXPLANATION RELATED TO THE DESCRIPTION

Continuous or periodic surveillance is essential to ensure that the nuclear power plant structures and components remain healthy and functional throughout the plant life. The ISI of nuclear plants are far more complex than that of conventional plants due to the presence of high radiation levels making access to the components to be inspected difficult. In addition to this other environmental conditions like temperature, humidity, aggressive chemical vapours etc. also have to be dealt with while planning and executing the examination. Limited access and high radiation level necessitate the use of remote inspection techniques using robotic devices during ISI. Robotics and automation facilitates faster inspection with better accuracy, repeatability and increased reliability of test data. Automation also facilitates accurate revisits of specific inspection sites for ISI of critical components during subsequent inspection, thus making periodic surveillance for monitoring of defects detected earlier. In light of above reasons, it is planned to carry out periodic inspection of PFBR main vessel and safety vessel during the service period. Figure 3 shows the half section of the PFBR assembly pictorially depicting the VENTURE and it handling systems in place. The main vessel of PFBR is 12.9 m in diameter and the safety vessel surrounds the main vessel with a nominal annular gap of 300 mm which varies by 50 mm during the service. This annular gap is utilised for the inspection of both vessels.

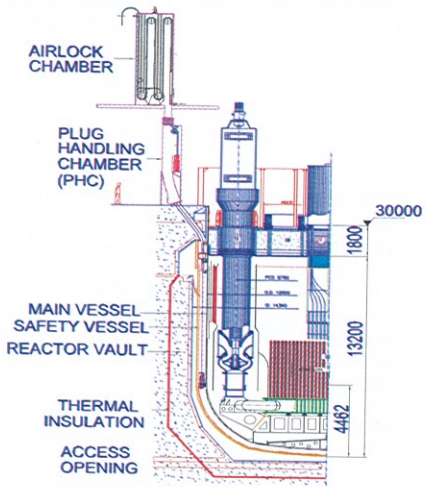

Fig.3: Half vertical section of PFBR Reactor assembly

■ BRIEF DESCRIPTION OF THEORETICAL BACKGROUND

It is mandatory to identify critical areas of plants and structures for carrying out ISI, using remote/automated devices and the access for such an inspection, along with the strategies for inspection has to be incorporated in the design stage itself and demonstrated before the actual commissioning of the plant. Therefore, in this context, the knowledge garnered from these developmental activities is vital. These developments are vital in ensuring low plant down time and conforming to the quality guidelines set in place by the safety regulatory board.

■ ACHIEVEMENT

Prototype ISI device "VENTURE" has been developed in collaboration with BARC, Mumbai. Prototype UT and VE modules have been developed at IGCAR. Testing and validation of the prototype ISI device integrated with all payloads in a mock-up test facility are being carried out at IGCAR. Prototype VE module has been tested and validated at room temperature and the images of marking and a simulated weld crack captured by the vision system are shown in Figs 2 (c) & (d). Additionally the concept of the proposed cable take-up and release mechanism has also been tested by a prototype model developed. Feedback on the orientation of the device is provided by cooled MEMS-based tilt sensors. A prototype tilt sensor using commercially available sensing elements with necessary electronic circuit has been developed and tested. A 3D Virtual Planning environment for the ISI of PFBR MV and SV has been carried out in collaboration with Indian Institute of Science, Bangalore. This modeling and simulation is aimed at implementing a 3D environment using which planning and visualization of the motion of the inspection device in the interspace can be accomplished.

■ PUBLICATIONS ARISING OUT OF THIS STUDY AND RELATED WORK

1. K.V.Kasiviswanathan, C.Rajagopalan, Goutam Kumar Guin and Baldev Raj, *J. Non Dest. Eval.*, **4** (2005) 39.
2. Design Report No: PFBR/30000/DN/1042/Rev-C.
3. Report No: PFBR/30000/SP/1044.

Further inquiries:
Shri K.V. Kasiviswanathan, Group for Remote Handling, Robotics, Irradiation Experiments and PIE
Metallurgy and Materials Group, IGCAR, e-mail: kasi@igcar.gov.in

Remote Visual Inspection of a Dissolver Vessel in Fast Reactor Fuel Reprocessing Plant

EXECUTIVE SUMMARY

Reprocessing of spent fuel is a crucial stage in Indian Nuclear Energy Programme since it facilitates recovery of fissile fuel. Reprocessing of spent fuel involves operations in highly disordered and radioactive environment. Reliable performance and safe operation of fuel reprocessing plants is essential for sustained throughputs. Consequent to successful commissioning of a reprocessing plant, periodic in-service inspection (ISI) and monitoring of critical plant components is necessary in order to ensure that service-induced defects & abnormalities are detected and remedied beforehand. During ISI and in many instances, limited access, radiation and acidic environment prevailing in a reprocessing plant obviate direct human intervention necessitating remote tools and gadgets. Remote visual inspection was carried out successfully in **CO**mpact facility for **R**eprocessing of **A**dvanced fuels in **L**ead cells (CORAL) at Kalpakkam.

OUTLINE

Visual examination is one of the ISI techniques for the inspection of the internal surface of the dissolver vessel in the reprocessing plants. As part of ISI of dissolver vessel in CORAL, a remote inspection device using a camera was developed and successfully demonstrated in CORAL. The dissolver vessel is located inside a lead-cell containment box and the device has to be deployed inside the dissolver vessel through a double door port, of size ϕ 273 mm x 250 (L) mm. The device including the camera had to be light weight and compact in view of the limitation of the in-cell handling equipment.

The device has two degrees-of-freedom namely, a vertical telescopic movement and an azimuth motion facilitating visual scan of the entire inner surface. The position of the camera with respect to the vessel during viewing can be identified by physical marking laid out externally on the vessel. Collapsible feature is incorporated in the device to facilitate its posting into the containment box through the double door port. The device has modular construction to facilitate easy assembly and maintenance. The telescopic stage consists of 5 stages having a total travel range of 430 mm and the azimuth motion has 360° travel. Overall size of the device in the collapsed state is ϕ 195 X 305 mm. A ¼"CCD-based camera with a resolution of 320 TV lines with ring lighting using LEDs was used for the visual inspection. Fig.1(a) & (b) shows the photographs of the inspection device in collapsed and extended condition. Fig.1(c) shows the camera with ring lighting. Since the observations have to be recorded for future reference as baseline data, a VHS recorder was used for storing the video images while a video monitor was used for on-line viewing.

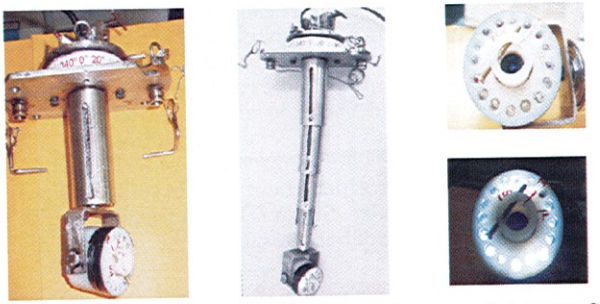

a) In collapsed condition **b) In extended condition** **c) Array of LEDs for lighting**

Fig. 1: Photographs of the remote inspection device with camera and LED lighting used for the visual inspection

The scanner had to be posted into the containment box in two sub-assemblies through the double door port and then through the blister box behind the cell. The device can be made to cover the full depth of the vessel by lowering it along guideposts in 5 stages and there is provision for locking at any of these predefined locations along the guide post. Both the vertical and azimuth motions are manually controlled. The telescopic members are constructed using different diameter pipes sliding into each other causing linear motion. A steel wire rope attached to the bottom-most pipe is carried through the telescopic pipes to a capstan located at the top of the azimuth stage. The telescopic motion is achieved by rotating the capstan via a knob that releases or takes up the wire rope. Azimuth motion is achieved by rotating the azimuth stage using three equi-spaced protruding pins. Both telescopic and azimuth stages have markings by which the position and orientation of the camera inside the vessel can be determined with an accuracy of 1mm for telescopic and 10 degrees for azimuth motions.

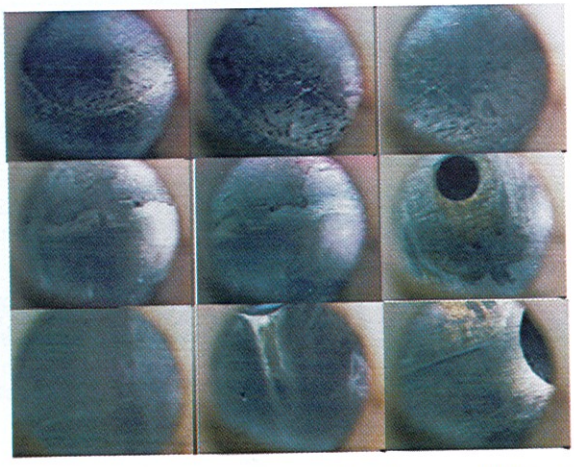

Fig. 2 : Images of critical areas of dissolver vessel obtained during the inspection campaign

Visual inspection of the dissolver vessel limb in CORAL was successfully carried out. Since the observations have to be recorded for future reference as baseline data, a VHS recorder was used for storing the video images while a video monitor was used for on-line viewing. It was seen that the vessel remains free of remnants after dissolution of the fuel and there is no clogging of chute. All accessible welds and surface of the vessel limb were examined closely. All ports especially the one leading to the chopper was seen clearly. In general, no degradation or corrosion has been observed. The significance and consequences of the visual inspection data obtained in this campaign can be analysed during the subsequent inspection campaigns.

■ ISI OF DISSOLVER VESSEL

In addition to visual examination of the inner surface of the dissolver vessel, it is planned to examine the wall thinning of the dissolver vessel due to corrosion by Ultrasonic testing and surface pitting by Laser-based inspection technique. A 2-axis telescopic scanner has been developed for this purpose. The scanner has a telescopic axial motion and an azimuth motion facilitating cylindrical surface scan. The scanner with UT probe has been tested and validated in a mock-up dissolver vessel. A laser triangulation system with mechanical scanner has been developed and tested in collaboration with RRCAT, Indore.

■ GENERAL EXPLANATION RELATED TO THE DESCRIPTION

Dissolver is the important equipment in a nuclear fuel reprocessing plant. After chopping of the irradiated / spent fuel pins in a chopper, the bulk material will be fed to the dissolver vessel where electrolytic dissolution is carried out in boiling concentrated nitric acid by passage of current through the electrodes. The final dissolver solution contains several fission products and ions. Failure of the dissolver will cause leakage of radioactive material-contained liquid to the operating area, which is not acceptable. Hence, periodic inspection of the dissolver vessel is essential to assess the effects of corrosion-induced damage. Fig.3 shows the sectional elevation of the dissolver vessel. The inner diameter of the vessel is 100 mm and depth is 560 mm upto sparger level located inside the vessel. The vessel has number of ports which require to be inspected for clogging to the extent possible.

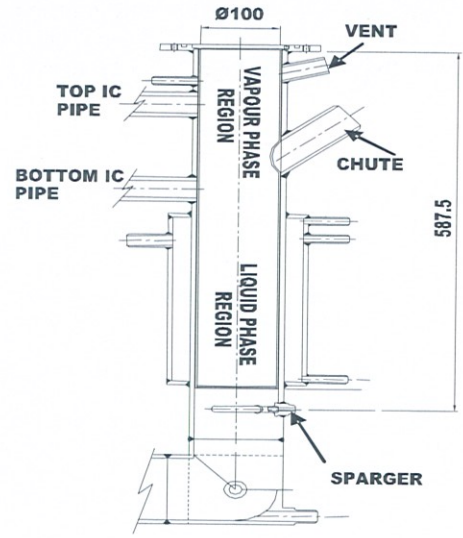

Fig. 3 : View of the dissolver vessel

■ BRIEF DESCRIPTION OF THEORETICAL BACKGROUND

As part of the program for comprehensive in-service inspection of critical components of the reprocessing plants, the dissolver vessel of the CORAL is required to be inspected periodically using NDE techniques to assess its healthiness and integrity. One of the NDE techniques envisaged is visual examination using a camera and remote device.

■ ACHIEVEMENT

A challenging task of remote visual inspection of a dissolver vessel as part of ISI has been successfully completed. Such comprehensive ISI campaigns in reprocessing plants especially for dissolver are not reported worldwide and it is a significant step forward in our ISI programme. The development of various gadgets for the ISI and its validation using a mock-up facility and successful implementation in the field has given immense confidence for undertaking such tasks in other areas of reprocessing plant. The ISI is also being extended using NDE techniques such as UT and Laser triangulation for fine detection of corrosion damages like wall thinning and surface pitting. The feedback gained from the experience of this campaign will be put to use while designing such systems for the demonstration as well as plant-level reprocessing facilities. Such feedbacks are also useful in providing various plant features and equipment layouts at the design stage itself for future reprocessing plants.

■ PUBLICATIONS ARISING OUT OF THIS STUDY AND RELATED WORK

Internal report No: IGC/ITG/PIRD/LMC-ISI/DIS/VI/01/06 released on April 05, 2006

Further inquiries:
Shri K.V. Kasiviswanathan, Group for Remote Handling, Robotics, Irradiation Experiments and PIE
Metallurgy and Materials Group, IGCAR, e-mail: kasi@igcar.gov.in

Ultrasonic Procedure for In-service Inspection of Shell Weld of Core Support Structure in the Main Vessel of PFBR

EXECUTIVE SUMMARY

A new ultrasonic test methodology has been developed for in-service inspection of shell weld of core support structure of main vessel. This involves testing of the shell weld from outside surface of the main vessel sector using normal beam ultrasonic transducer. This methodology can be used to detect defect of any orientation at any location in the support shell plate and shell weld, except at the locations masked by the inlet pipes. This methodology has been successfully demonstrated on the main vessel sector mock up. The ultrasonic testing, using this methodology, indicated that a defect down to 20 % wall thickness (~ 6 mm) on both sides of the support shell plate and the shell weld can be detected reliably.

OUTLINE

An innovative ultrasonic test methodology has been developed for in-service inspection of the shell weld of the core support structure (CSS) in the main vessel of PFBR. The inspection of this weld immersed in sodium required development of a special methodology because of the restricted access to the weld, curvature of the main vessel and ultrasonic beam skewing that occurs at the K type weld used for joining the main vessel to the support shell plate. The developed methodology involves inspection from the outside surface of the main vessel, using normal beam ultrasonic transducer. Figure 1(a) shows the experimental setup, ultrasonic transducer position, and scanning region (A to B). The simulated shell weld of the CSS is shown in Fig. 1(b).

The developed methodology involves inspection of support weld through the core support plate from the knuckle portion of the main vessel, which is about 450 mm away from the weld to be inspected. Because of the presence of curvature in the main vessel, ultrasonic beam enters the weld overlay at an angle to the support shell structure (Fig. 1). Further, because of the presence of columnar grains in the austenitic stainless steel weld overlay and the K weld, ultrasonic waves get skewed and enter the support shell structure at an another angle. Beyond this point, ultrasonic wave propagates in the support shell structure at this angle and gets reflected every time it encounters the plate surface. When the wave encounters any defect/interface in the shell plate, ultrasonic wave is reflected from the defect/interface and picked up by the same transducer. By changing the location of the transducer, these angles can be changed and hence defect at any location including in the shell weld of the core support structure can be detected.

The developed methodology has the advantage that inspection at multiple angles of ultrasonic wave propagation can be achieved just by moving a single normal beam ultrasonic transducer along the curved surface of the main vessel (A to B in Fig. 1). Multiple angle beam inspection would ensure the detectability of defects of any orientation. The methodology has been tested on the main vessel sector using standard artificial defects. In order to simulate the defects in the shell weld of actual main vessel, a 30 mm thick stainless steel plate was welded at the top of the shell plate of the main vessel sector mock up using a K-type weld. Notches of dimensions 10 % and 30 % of wall thickness, made in this weld have been successfully detected. Figure 2 shows a typical signal from a 9 mm deep notch in the simulated shell weld of CSS located at a distance of 450 mm from the outer surface of the main vessel. This is the first time worldwide that such a methodology has been developed for inspection of a critical weld, which was originally designed to be non-inspectable, thus enhancing the reliability and safety of the reactor system.

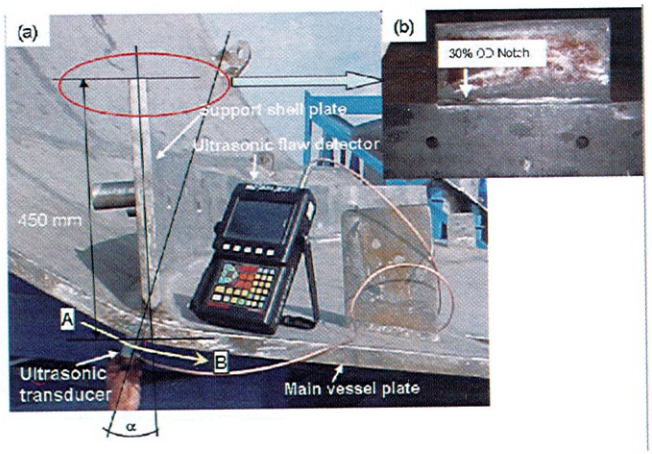

Fig. 1 : (a) Experimental setup for the inspection methodology showing the transducer location in the close-up view of support shell and (b) Stainless steel plate welded at the top

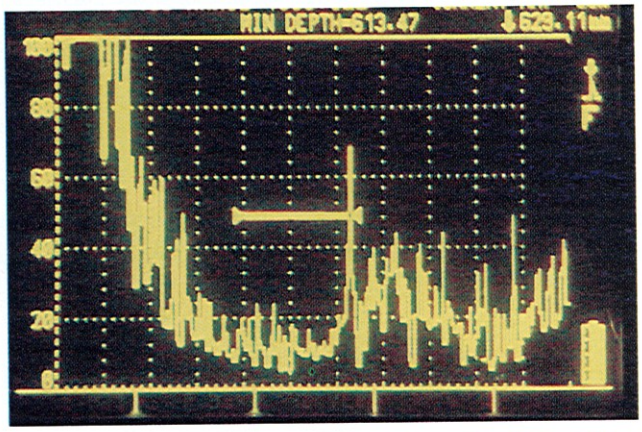

Fig. 2 : Ultrasonic signal from 9 mm OD notch, as shown in Fig. 1(b)

■ ADDITIONAL INFORMATION

For enhanced reliability and safety requirements, detection of through and through crack in the CSS shell weld is required. Using the developed ultrasonic methodology, a defect of 20% wall thickness or more could be detected.

■ GENERAL EXPLANATION RELATED TO THE DESCRIPTION

In order to enhance the reliability and safety of the reactor system, it became utmost essential to develop inspection methodology for the inspection of the critical weld (shell weld of the core support structure in the main vessel of PFBR) which was originally designed to be non-inspectable. The inspection of these welds poses challenge for ultrasonic inspection, due to limited access to weld, immersion of weld in sodium, curvature in the main vessel and the presence of another K-weld. The presence of curvature and dendritic structure pose serious difficulty in the ultrasonic inspection of stainless steel components. In this particular study these have been used as an advantage for inspection. The developed methodology involves inspection from the outside surface of the main vessel, using normal beam ultrasonic transducer.

The inspection of the shell weld is carried out from the outside surface of the main vessel as indicated by arrow shown in Fig. 3, using normal beam ultrasonic transducer. The presence of curvature in the main vessel, results in ultrasonic beam entering the weld overlay at an angle to the support shell structure (Fig. 3). Further, because of the presence of columnar grains in the austenitic stainless steel weld overlay and the K weld, ultrasonic wave gets skewed and enters at an angle to the support shell plate (Fig. 3). Beyond this point, ultrasonic wave propagates in the support shell structure at an angle and gets reflected every time it encounters the plate surface. When the wave encounters any defect/interface in the shell plate, ultrasonic wave is reflected from the defect/interface and is picked up by the same transducer. By changing the location of the transducer, angles can be changed and hence a defect at any location and orientation in the core support structure can be detected/ evaluated, except at the locations hidden by the inlet pipes.

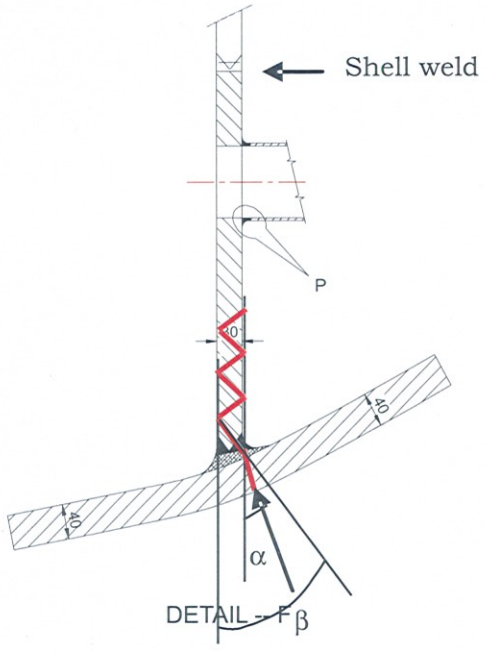

Fig. 3: Cross sectional view of the core support structure showing the support shell weld

■ BRIEF DESCRIPTION OF THEORETICAL BACKGROUND

With the help of the curvature of plate ultrasonic beam enters at different angles into the overlay and K-weld during scanning over the plate surface. Due to presence of dendritic grains at weld region ultrasonic beam skews and enters in the support shell structure and makes it inspectable for any defect.

■ ACHIEVEMENT

An innovative methodology has been developed for in-service inspection of the shell weld of the core support structure (CSS) in the main vessel of PFBR. The developed methodology provides multiple angle beam ultrasonic inspection just by moving a single normal beam ultrasonic transducer along the main vessel plate. This is the first time worldwide that such a methodology has been developed for inspection of a critical weld, which was originally designed to be non-inspectable, thus enhancing the reliability and safety of the reactor system.

■ PUBLICATIONS ARISING OUT OF THIS STUDY AND RELATED WORK

1. Anish Kumar, K.V. Rajkumar, G.K. Sharma, T. Jayakumar and Baldev Raj; Proceedings of International Conference on Advances in Stainless Steels, ISAS-2007, April 9-11, 2007 Chennai.
2. PFBR report No. 31250/DN/1069/A dated 06/02/07.

Further inquiries:
Dr. T. Jayakumar, Non Destructive Evaluation Division
Metallurgy and Materials Group, IGCAR, e-mail: tjk@igcar.gov.in

Centrifugal Extractors in the Back End of Fuel Cycle and other Applications

EXECUTIVE SUMMARY

Centrifugal Extractors (CE) are efficient liquid – liquid contacting devices wherein valuable solutes can be extracted selectively by solvents based on their distribution coefficients. There are varieties of solvent extraction equipment operating in the chemical, petrochemical, pharmaceutical and metallurgical industries based on un-agitated columns like spray, packed and perforated plate columns, mechanically agitated columns like, pulsed columns, reciprocating columns, rotary devices like, rotating disk column (RDC) and mixer settlers. Centrifugal extractors score over others due to intense energy input and phase separation by centrifugal force of 100-500g leading to very compact size. For fast kinetics systems, the residence time is few seconds (5-10) as opposed to 3-5 minutes in liquid pulsed column and 5-10 minutes in mixer-settler.

OUTLINE

Centrifugal extractor is a liquid-liquid mass transfer device wherein solute transfer can occur between two immiscible liquid phases. Centrifugal extractors are more attractive in fuel reprocessing step of Fast Breeder Reactor (FBR) fuels with the burn-up values of 10^{15} times more compared to CANDU fuel. Due to higher activity of the aqueous solutions the solvent Tri-Butyl Phosphate (TBP) undergo degradation leading to loss of U and Pu. Since the stage residence time in centrifugal extractors are typically 5-10 seconds as against 3-5 minutes in column type of extractors and 5-10 minutes in mixer settler, these units are favored. Fig.1 shows the typical working of the annular centrifugal extractor. The annular centrifugal extractor devised by Agonne National Laboratory (ANL) simplifies the design for remote maintenance compared to Oak Ridge National Laboratory (ORNL) design. Both heavy and light phases are fed into the annular gap between the inner rotating bowl and outer stationary bowl leading to one of the phase being dispersed in the other continuous phase. Thus annular gap serves as a mixer and the mixed phase (dispersion) flow down the annular gap and enters below the rotary bowl and the stationary baffles at the bottom of the stationary bowl and enters the rotating bowl.

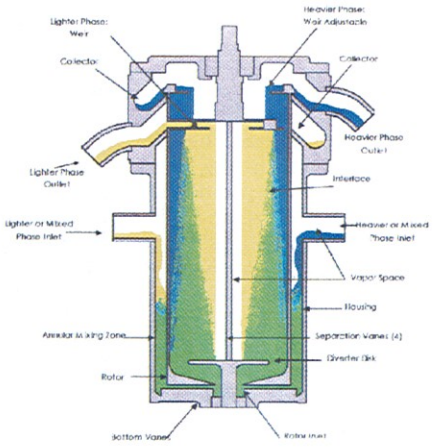

Fig. 1 : Separation of Phases in Centrifugal Extractor

Within the rotating bowl the dispersion experiences the centrifugal force many times that of gravity and the heavy phase separates near to the inner wall of the bowl and the light phase separates towards the centre of the bowl. The light phase over flows over the light phase weir ring and thrown out in to the light phase collection chamber exiting the unit through a pipe. The heavy phase flows through the under flow passage at the I.D. of the bowl and subsequently flows over heavy phase weir and collects in the heavy phase collection chamber exiting through a pipe. At IGCAR, two types of units (fixed inter-phase and variable inter-phase units) were employed in CORAL facility for the processing of mixed carbide fuel irradiated to 100 GWd/t and the experience of these units were obtained. Fig.2 is the schematic of the fixed weir type wherein the interface position is adjusted to be in the centre of the separating zone for the given liquid densities. Interface position will be dictated by the pressure balance between heavy and light phase thickness under the respective weirs. Fig.3 shows two heavy phase weirs and one light phase weir for adjusting the interface position. In general the light phase weir dimension will be fixed based on the rotor size selected for a desired throughput. Fixed weir configuration will be adopted if the densities of each phase are known whereas variable interface design can work for any densities of liquid pair without physically changing the heavy phase weir by applying the calculated air pressure on the primary heavy weir.

The interface position r_i can be calculated from pressure balance of the light phase and heavy phase under light phase weir and the heavy phase under the heavy phase weir taking account of the head between the two weir plates and

$$r_i = \sqrt{\frac{r_a^2 - \left(\frac{\rho_o}{\rho_a}\right) r_o^2}{1 - \left(\frac{\rho_o}{\rho_a}\right)}}$$

where, r_i is the interface position, r_a, and r_o, are the actual liquid radii at heavy phase weir and the light phase weir and ρ_a and ρ_o are the densities of heavy and light phases. The actual position of the liquid under the weirs depends on the flow rate of the respective phases and angular velocity of the rotating bowl.

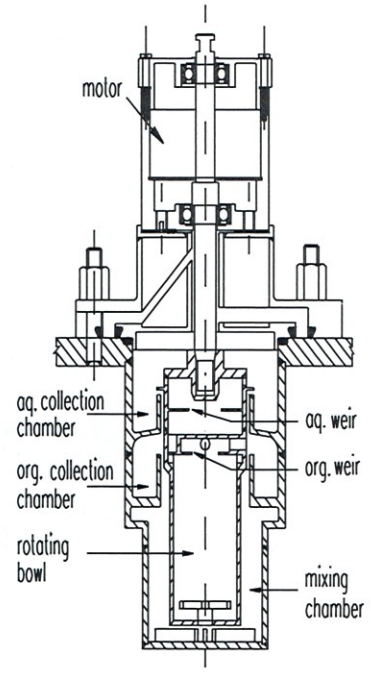

Fig. 2 : Single Stage CE with Fixed Weir

■ ADDITIONAL INFORMATION

Reprocessing Group, IGCAR initiated the development of Centrifugal Extractors and the first unit with 50 mm bowl was fabricated in 1977 and an annular 8 stage CE bank successfully processed the irradiated thorium fuel for the recovery of U-233 in two campaigns with a gap of 12 years. Prior to 1992, IGCAR has demonstrated the working of up to 100 mm CE bowls. The first CE used in large reprocessing application was at Savannah River plant. ANL has introduced annular mixing concept and simplified the design and made amenable for remote maintenance. CINC a US company, based on the annular ANL technology, scaled up the units and commercialized for chemical, pharmaceutical and hydrometallurgy industry and even applied to cleaning of oil spills in ocean. Apart from CINC, a French company, Robatel is also the major commercial supplier. Recently Heavy Water Board (HWB) is interested in building large size centrifugal extractors for recovery of uranium from phosphoric acid and large throughput unit work was initiated in collaboration with IGCAR and BARC.

■ DESIGN OF CENTRIFUGAL EXTRACTOR

The dimensionless dispersion number N_{Di} proposed by ANL workers can be used for the design of the centrifugal extractors and N_{Di} is defined as given below;

$$N_{Di} = \left(\frac{Q}{V}\sqrt{\frac{\Delta Z}{\bar{a}}}\right) \quad where \quad \bar{a} = \bar{r}\omega^2 \quad and \quad \bar{r} = \frac{2}{3}\left(\frac{r_b^3 - r_o^3}{r_b^2 - r_o^2}\right)$$

where, Q is the volumetric flow rate of the combined phases, V is the effective separation zone volume, ΔZ is the width of the separation zone which is equivalent (r_b - r_o) and $\bar{a}$ is the average acceleration in the separation zone defined by the above equation. For a given solvent extraction system N_{Di} values can be experimentally obtained by conducting experiments in the small centrifugal extractor or even from batch gravity settling data and the same N_{Di} values can be used for scale up.

Φ is the mixing intensity W/kg, can be calculated as given below. ANL workers arbitrarily classified 435 W/kg as high, 114 W/kg as medium and 27 W/kg as low and they have given a correlation for power consumption in the annular gap, wherein 'm' is the mass of the fluid in the annular gap, 'H_C' is the liquid height in the annulus, '$R_{r,o}$' is the outside radius of the rotating bowl, 'Δr_C' is annular gap width, 'N' is the rpm, 'μ' is the viscosity of the continuous phase, 'ρ' is the fluid dispersion density and 'ω' is the angular velocity.

$$\phi = \left(\frac{P}{m}\right) \quad P = 0.0261\, H_C\, R_{r,o}^{3.75}\, (j\omega)^{2.75}\, \rho^{0.75} \left(\frac{\mu}{\Delta r_C}\right)^{0.25}$$

$$j = 0.0554 \log(N_{Re}) + 1.368 \quad valid\ for\ 3\times10^3 < N < 1\times10^6$$

$$N_{Re} = \left(\frac{2j\rho\omega R_{r,o}\Delta r_C}{\mu}\right)$$

The amount of the liquid build-up H_C in the annular gap depends on the annular gap, the gap clearance between the bottom of the rotary bowl and the radial baffles, baffle height and the diameter of opening at the bottom of the rotary bowl. HC can be either experimentally evaluated or through CFD analysis.

Compact Reprocessing of Advanced Fuel in Lead Cells (CORAL) facility for irradiated U, Pu carbide fuel has three CE banks of 16 stage each fixed weir type (H_A, H_C, 1A) and two interface controlled banks of 16 stage each (1C and 2A). Interface controlled banks have a novel passive rotary water seal incorporated in each stage. Though there is no maintenance requirement of the seal, often the water has to be filled in each rotating water seal. Based on the cumulative operating experience over the last three years it is decided that fixed weir type of centrifugal extractors are simple to operate and are preferred for Demonstration Fuel Reprocessing Plant (DFRP).

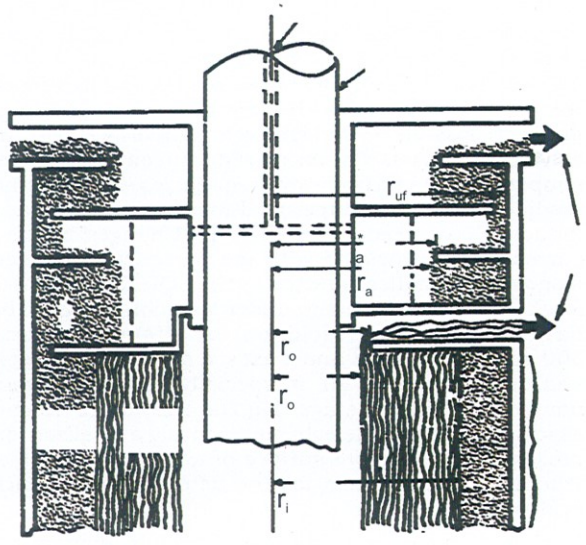

Fig. 3 Weir arrangement for Interface Adjustment

■ ACHIEVEMENT

CORAL is a unique facility with all SX cycles operated with centrifugal extractors for processing irradiated mixed carbide fuel with burn up of 100 GWd/t. Valuable experience is obtained in terms of the extraction efficiency and remote maintainability. Large sized centrifugal extractors (250 mm, 500 mm) are being developed for other than the reprocessing applications. IGCAR collaborates with academic institutes in realizing the goals.

■ PUBLICATIONS ARISING OUT OF THIS STUDY AND RELATED WORK

1. B.D. Kadam, J. B. Joshi, S.B. Koganti and R. N. Patil, *Chemical Engineering Research & Design*, (In Press)
2. Sandesh S. Deshmukh, Vedantam Sripriya, Jyeshtharaj B. Joshi and Sudhir B. Koganti, *Ind. Eng. Chem. Res.*, **46** (2007) 8343.
3. Sreepriya Vedantam, Jyeshtharaj B. Joshi and Sudhir B. Koganti, *The Canadian J. Chem. Engg.*, **84** (2006) 279.
4. Sreepriya Vedantam, Jyeshtharaj B. Joshi and Sudhir B. Koganti, *Ind. Eng. Chem. Res.*, **45** (2006) 6360.

Further inquiries:
Dr. S.B. Koganti,Reprocessing Research and Development Division
Reprocessing Group, IGCAR, e-mail:koganti@igcar.gov.in

Development of SQUID Based System for Non-Destructive Evaluation

EXECUTIVE SUMMARY

Superconducting Quantum Interference Devices (SQUID), which are the most sensitive detectors of magnetic flux signals, have been developed at IGCAR using advanced micro-fabrication techniques. A novel SQUID based set-up for non-destructive evaluation based on a precision X-Y-θ scanner has been designed and developed. The set-up has been used for the characterization of subsurface defects using low frequency eddy current technique and for monitoring the progressive transformation of magnetic δ ferrite into nonmagnetic phases in a SS316 L(N) weldment specimen subjected to low cycle fatigue loading at 600°C. The results highlight the potential of SQUID based non-destructive evaluation as an emerging new technique.

OUTLINE

SQUID sensors, which are the most sensitive detectors of magnetic flux available today with a sensitivity of ~10fT/√Hz, have been developed at IGCAR through a sustained research and development program which is unique in the national context. To harness the high sensitivity of the SQUID sensors for nondestructive evaluation (NDE), a SQUID based set-up for NDE has been designed and developed with a capability to perform characterization of samples in both the low frequency eddy current testing mode and the remnant magnetization measurement mode. Fig.1 shows a photograph of the SQUID based set-up for NDE, which is currently operational at IGCAR. The set-up incorporates an in-house developed thin film Nb SQUID, Flux Locked Loop electronics, a liquid helium cryostat with a low stand-off distance and a precision X-Y-θ scanner.

In the conventional eddy current testing, the depth of defect detection is limited by the skin depth of the material under investigation. In a SQUID based set-up, low frequency sensitivity of the SQUID sensor and the use of superconducting pick-up loop make it possible to detect even subsurface defects. A double-D excitation coil is used to excite eddy currents in the specimen at room temperature at relatively low frequencies ~200Hz, while a first order gradiometer made of superconducting wire is used as a pick-up loop inductively coupled to the SQUID. Changes in the induced eddy current flow associated with the presence of a defect manifest as magnetic anomalies detected by the SQUID. The X-Y-θ scanner used for scanning the specimen under a stationary liquid helium cryostat has a positional resolution of 25μm, a stroke length of 300 mm along both X and Y axes, a scanning speed of 1-50 mm/sec and is equipped with a specially designed nonmagnetic and nonmetallic sample stage. Fig.2(a) shows the magnetic anomalies associated with the defects representing a localized loss of thickness present on the bottom surface of a 10 mm thick aluminum plate. Potential of the system for the detection of subsurface defects is evident from the data.

Fatigue damage limits the life of a high temperature component, especially in the welded region. Presence of an optimum amount of magnetic δ-ferrite in the austenitic weld-metal is desirable to prevent hot cracking in the weldment. However, the magnetic δ ferrite structure is highly unstable during high temperature service and transforms to nonmagnetic carbides and brittle inter-metallic phases (ex. σ-phase). To investigate the potential of the SQUID based NDE set-up in tracking such transformations in a stainless steel 316L(N) weldment, low cycle fatigue tests were conducted at a strain amplitude of ±0.6% using an Instron servo hydraulic fatigue testing machine under total axial strain control mode at 600°C. As the sample was scanned under the cryostat, SQUID output revealed a characteristic magnetic anomaly when the center of the gauge length of the sample passed under the pick-up loop indicating the presence of a magnetic phase at the location of the weld. As shown in Fig.2(b), the amplitude of the magnetic anomaly was only $0.05\Phi_0$ for the fatigue fractured sample as compared to 1.78 Φ_0 for the virgin sample. Fig.2(c) and 2(d) show the results of a more detailed study indicating the decrease of δ-ferrite content as a function of number of fatigue cycles. Capability of the system in capturing such phase transformation augurs well for further development of the technique.

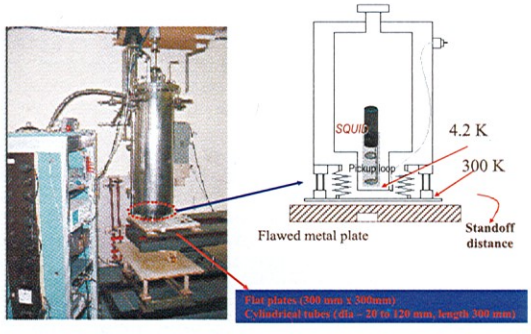

Fig. 1: Set-up for SQUID based non-destructive evaluation

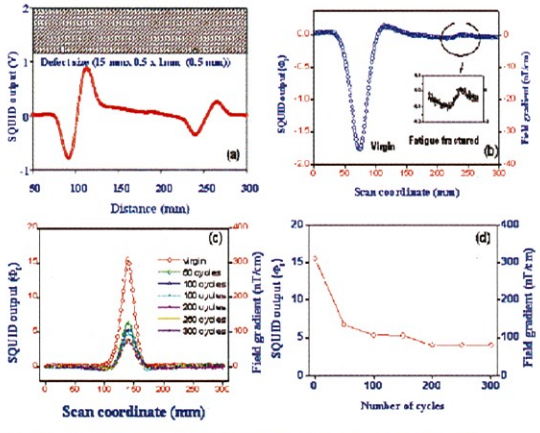

Fig 2: SQUID based non-destructive evaluation of
(a) sub-surface defects in a thick aluminum plate;
(b) SS316L(N) weldment (virgin and fatigue fractured)
(c) flux profile for the weldment at different fatigue cycles (d) change of SQUID output for the weldment at different fatigue cycles

■ WHAT IS A SQUID ?

SQUID is a magnetic flux sensor based on Josephson effect and flux quantization in closed superconducting rings. It consists of a closed loop of superconductor which is interrupted by two Josephson junctions. Critical current of the SQUID depends sensitively on very small changes in magnetic flux coupled to it. SQUID devices developed at IGCAR are based $Nb/AlO_x/Nb$ as Josephson junctions and operate when cooled to 4.2 K. Their sensitivity is so high that it is possible to detect even the tiny magnetic fields associated with the human physiological activities, which are not detectable by any other sensor technology.

■ SQUID BASED NDE

Nondestructive evaluation refers to techniques that allow characterization of functionality of a material or component without compromising its continued usability. Common techniques for nondestructive evaluation are ultrasonics, eddy currents, magnetic flux leakage, acoustic emission etc. SQUID based NDE is a new emerging technique, which harnesses the high sensitivity of the SQUID for detection of magnetic signals in the context of non-destructive evaluation.

Eddy currents are induced in conducting specimens when subjected to alternating magnetic fields. The amplitude of the induced eddy currents decays exponentially from the top surface and the decay is characterized by a skin depth. At high frequencies, induced eddy currents are confined to the surface regions and do not sample the deep subsurface defects. If the frequency is lowered to increase the depth of penetration, the signal-to-noise ratio suffers since the voltage induced in the pick-up loop is proportional to the rate of change of magnetic flux. SQUID based NDE overcomes these limitations imposed by the skin depth (1) by use of superconducting pick-up loops, which sense the magnetic field B directly rather than its time derivative dB/dt and (2) by use of SQUID sensors whose sensitivity is independent of frequency down to ~1Hz.

Ferromagnetic phases exhibit a remnant magnetization even after the magnetizing field is removed. High sensitivity of the SQUID allows one to detect the presence of even a small volume fraction of a ferromagnetic phase dispersed in a matrix and study the transformation of such magnetic phases to nonmagnetic ones.

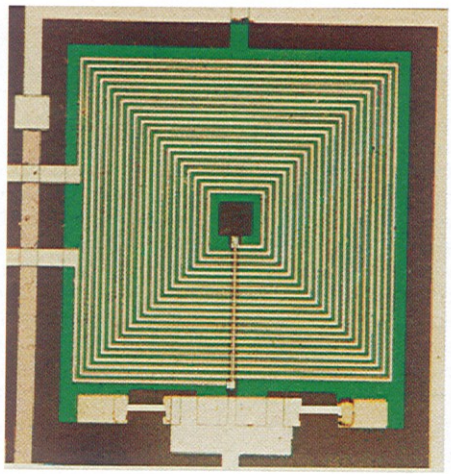

Fig. 3: Photograph of the DC SQUID sensor developed at IGCAR

■ BRIEF DESCRIPTION OF THEORETICAL BACKGROUND

Numerical computations were performed to investigate the eddy current distribution excited by the double-D coil in the 10mm thick Al plate carrying a defect on its bottom surface representing a localized loss of thickness. Computations were performed for a set of 20 different locations of the defect relative to the common axis of the pick-up loop and the excitation coil. For each location, flux density B was calculated at a grid of points in two parallel planes coincident with the planes in which the lower and upper loops of the gradiometer were located. Flux density was numerically integrated over the area of each of the two loops to obtain flux Φ_L and Φ_U threading through the two loops of the gradiometer; output voltage of the SQUID is proportional to Φ_L-Φ_U. Variation of this quantity with the scan coordinate was found to be in qualitative agreement with experimental results obtained using the SQUID based NDE set-up.

■ ACHIEVEMENT

The work represents culmination of an activity comprising of fabrication of SQUID sensors, development of control electronics and the design and development of SQUID based measuring systems. In addition to the SQUID based NDE set-up described here, several other SQUID based measuring systems such as SQUID magnetometer has also been developed. A SQUID based Magnetoencephalography (MEG) system for non-invasive studies of human brain is currently being developed under a DST sponsored project at IGCAR to measure the extremely small magnetic fields associated with neural currents.

■ PUBLICATIONS ARISING OUT OF THIS STUDY AND RELATED WORK

1. R. Nagendran, M.P.Janawadkar, M.Pattabiraman, D.K. Baisnab, R. Baskaran, L.S. Vaidhyanathan, Y. Hariharan, Baldev Raj, A.Nagesha, M.Valsan and K. Bhanusankara Rao, *NDT&E international*, **40** (2007) 215.
2. R. Nagendran, M.P.Janawadkar, M. Pattabiraman, Dipak Kumar Baisnab, J.Jayapandian, R.Baskaran, L.S.Vaidhyanathan, Y. Hariharan, A. Nagesha, M. Valsan, K. Bhanusankara Rao and Baldev Raj, *Trans. Appl. Supercond.*, **17** (2007) 3824.
3. M. Pattabiraman, R. Nagendran and M.P. Janawadkar, *NDT&E International*, **40** (2007) 289.

Further inquiries:
Shri R. Nagendran, Materials Science Division
Metallurgy and Materials Group, IGCAR, e-mail:nags@igcar.gov.in

Penetration Enhancing Activated Flux for TIG Welding of Stainless Steels

EXECUTIVE SUMMARY

Specific activated flux has been developed for enhancing the penetration performance of the TIG welding process for welding of type 304 LN and type 316LN stainless steels. A significant increase in penetration of over 300% has been observed in single pass TIG welding. The significant improvement in penetration was attributed to constriction of the arc and the reversal of Marangoni flow. The use of flux has been found to overcome the variable weld penetration observed during autogenous TIG welding of austenitic stainless steel with less than 50 ppm silver. There was no degradation in the microstructure and mechanical properties of welds produced by A-TIG welding compared to that of conventional TIG welding process.

OUTLINE

The major limitations of TIG welding of austenitic stainless steels are due to the limited thickness of material which can be welded in a single pass, poor tolerance to cast to cast variations and the low productivity. The thickness of austenitic stainless steel that can be welded in single pass is normally restricted to 3 mm with argon as shielding gas. Therefore, improvements in weld penetration have long been sought in austenitic stainless steel welds produced by TIG welding process because TIG welding result in high quality welds besides providing for precise control of heat input and low cost of the equipment. A novel variant of the TIG welding process called A-TIG is known to overcome the limitations. This process involves applying a thin coating of the activated flux on the joint prior to welding. The flux is patent protected and is not reported in literature.

The specific activated flux has been developed in the present work for enhancing the penetration during autogenous TIG welding of type 304LN and type 316LN stainless steels. The use of activated flux produced a significant increase in penetration of 10 – 12 mm in single pass TIG welding of 304LN and 316LN stainless steels. The significant improvement in penetration achieved using the activated flux developed in the present work was attributed to the constriction of the arc as well as reversal of Marangoni flow in the molten weld pool. The constriction of the arc during A-TIG welding could be seen clearly from the IR thermal images of the arc column and was also evident from the decrease in weld bead width by half compared to that of conventional TIG welding. So, combined operation of the above two mechanisms only lead to increased penetration by as much as 300% in 304LN and 316LN stainless steels produced by A-TIG welding. Figures 1 and 2 show the effect of flux on depth of penetration and weld bead width for type 304LN and type 316LN stainless steels. The use of activated flux has been found to overcome the variable weld penetration observed in 316LN stainless steel with less than 50 ppm of sulphur as shown in Fig. 2. Fig. 3 shows the weld cross sections of the A-TIG and multipass welds on 316LN stainless steel. The A-TIG weld was made in single pass while the multipass weld was made with 11 passes. The A-TIG welds produced in the present work were sound and passed radiographic examination and bend tests without any indications. There was residual fused flux layer produced on the face of the A-TIG welds that had to remove using wire brush. The use of activated flux was found not to cause any significant change in the chemical composition of the weld metals compared to that of the base metals. The transverse strength properties of the 304LN and 316LN stainless steel welds produced by A-TIG welding exceeded the minimum specified strength values of the base metals. Improvement in toughness values were observed in 316LN stainless steel produced by A-TIG welding due to some refinement in the weld microstructure in the region close to the weld centre. There was no degradation in the microstructure and mechanical properties of the A-TIG welds compared to that of the welds produced by conventional TIG welding. So activated flux developed in the present work has greater potential for use during the welding of structural components made of 304LN and 316LN stainless steels.

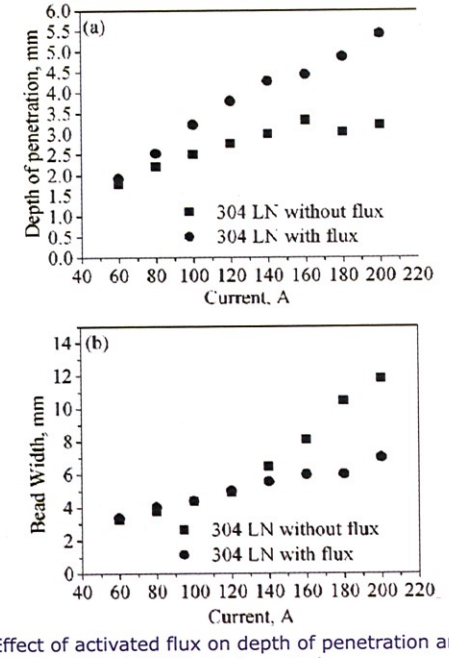

Fig. 1: Effect of activated flux on depth of penetration and weld bead width for 304LN stainless steels

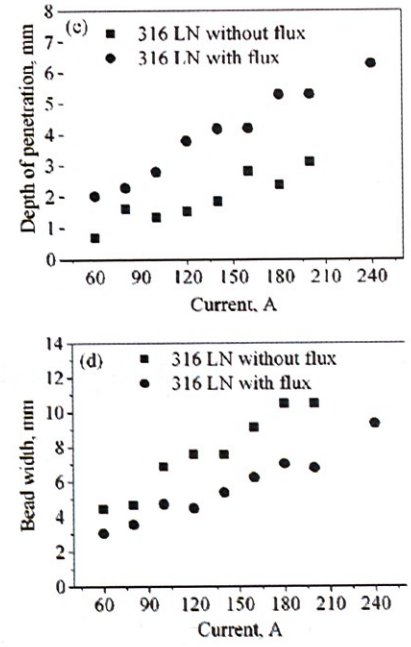

Fig. 2: Effect of activated flux on depth of penetration and weld bead width for 316LN stainless steels

■ SIGNIFICANCE OF A-TIG WELDING PROCESS

The implementation of the A-TIG welding process would result in a significant increase in weld penetration in austenitic stainless steels and overcomes penetration variability as a result of chemical composition differences between heats of material. It would also result in reduced heat input reduction in distortion, reduction in cost, improved productivity and overall improved quality. Use of activated flux has also been found to improve the mechanical properties of the welds compared to conventional TIG welds.

■ GENERAL EXPLANATION RELATED TO THE DESCRIPTION

The flux in the form of powders is made into a paste by mixing with acetone and the paste is applied on the surface to be welded by means of a brush. The acetone evaporates within seconds leaving a layer of flux on the surface.

The A-TIG process is suitable for any position welding. By employing A-TIG process, overall welding costs can be reduced upto 50%. These economics in fabrication costs can be achieved through:

a. Reduction in bevel preparation requirements
b. Decrease in number of weld passes
c. Shortening of welding times
d. Reduced consumption of welding filler wire
e. Elimination of back gouging and grindin
f. Reduced distortion

Typical applications include pipes and tubes in nuclear industry, Fabrication of pressure vessels and tube to tube sheets in heat exchangers in the power and chemical industries, hydraulic cylinders and undercarriage legs in aerospace industry.

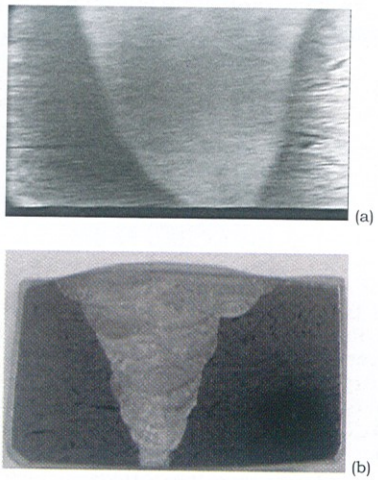

Fig. 3: Cross section of the 316 LN Stainless steel weld (12 mm thick) produced by (a) ATIG welding (b)Multi-pass TIG welding (11 passes)

■ BRIEF DESCRIPTION OF THEORETICAL BACKGROUND

The activated flux which gets vaporized during welding will constrict the arc by capturing electrons in the outer regions of the arc. Electron attachment can take place in the cooler peripheral regions where the electrons have low energy in a weak electric field. Towards the centre of the arc where there is a strong electric field, high temperatures and very high energy electrons and ionization will dominate. Thus restricting current flow to the central region of the arc will increase the current density in the plasma and at the anode resulting in a narrower arc and a deeper weld pool. A reversal in the Marangoni flow caused by the change in the coefficient of surface tension from negative to a positive value due to an increase in the dissolved oxygen content creates a narrow and deep weld pool. Combined operation of the above two mechanisms only lead to increased penetration by 300% in A-TIG welding.

■ ACHIEVEMENT

The use of activated flux has produced a significant increase in penetration of 10 – 12 mm in single pass TIG welding of type 304 LN and 316 LN stainless steels. The use of flux also has been found to overcome the variable weld penetration observed in austenitic stainless steels with less than 50 ppm of sulphur. The use of flux has caused no degradation in the microstructure and mechanical properties of welds compared to that produced conventional TIG welding. The use of flux therefore would result in significant cost reduction as there is no requirement for edge preparation and filler metal addition. This in-house developed Activated flux has been successfully field-tested and demonstrated for all its claimed advantages for welding of dummy core subassemblies made of 304L SS.

■ PUBLICATIONS ARISING OUT OF THIS STUDY AND RELATED WORK

1. An international patent "Tungsten Inert Gas Welding Flux for enhancing Penetration in Single Pass for austenitic stainless steels" has been filed for the development of activated flux for TIG welding of austenitic stainless steels (patent no. PCT/IN06/00442/dt. 8/11/06)
2. M. Vasudevan, A.K. Bhaduri, and Baldev Raj, Microstructure and Mechanical Properties of Austenitic Stainless Steels, International Welding Congress, February 16 – 19, 2005 Mumbai.

Further inquiries:
Dr. M. Vasudevan, Materials Technology Division
Metallurgy and Materials Group, IGCAR, e-mail: dev@igcar.gov.in

Demonstration of Reprocessing of High Burn up Carbide Fuels

■ EXECUTIVE SUMMARY

Fast reactor fuel reprocessing is an important component of the three stage Indian nuclear power programme which is aimed to enhance the utilisation of indigenous resources. In the CORAL (COmpact Reprocessing of Advanced fuels in Lead cell) facility for demonstrating the Fast reactor fuel reprocessing, which was commissioned in Dec 2003, reprocessing of FBTR mixed carbide spent fuel pins with various burn ups such as 25, 50 and 100 GWd/t, was successfully carried out. Several equipment and systems which have been designed and developed at the Reprocessing Laboratory, were validated at CORAL. This provides a launching pad for the optimization of design and operation of vital equipment and systems of future plants.

■ OUTLINE

The spent fuel subassembly from Fast Breeder Test Reactor (FBTR) is dismantled at the Post Irradiation Examination Facility and the pins are loaded in magazine. This magazine, kept in special alpha tight container in a shielded cask, is transported to the CORAL facility, where it is charged to the containment box. Several transfers have been carried out without alpha contamination which proved the design features of fuel transfer system. The fuel pins are then chopped in a Single Pin Chopper for dissolution of the fuel in a titanium dissolver by electro oxidative technique. Chopping was carried out in argon atmosphere to avoid flashes as the fuel pins of FBTR are pyrophoric in nature. The examination of the hulls after dissolution of the fuel indicated that the present design of chopper is ideally suited for the slender pins of FBTR. The Inspection of the chopped pin pieces also revealed that there was no significant crimping and hence the fuel loss in the hull is very less.

As the dissolution of the Plutonium-rich mixed carbide fuel of FBTR, is found to be very sluggish, boiling under refluxing conditions with high nitric acid is chosen for dissolution. The fuel solution after dissolution was clarified using an air turbine driven centrifuge for removal of clad fines. During the campaign, the centrifuge bowl was visually inspected which did not show any measurable quantity of undissolved solids. Solvent extraction using Tri-butyl phosphate solvent with an alkane diluent is used to separate Uranium and Plutonium from the fission products. This solvent preferentially extracts Uranium and Plutonium, leaving behind the fission products in the aqueous phase itself. The solvent loaded with Uranium and Plutonium is stripped with nitric acid for further processing of the fissile material. The solvent is recycled back for reuse. This solvent extraction is carried out in Centrifugal Extractors designed and developed specifically for fast reactor fuel reprocessing to reduce the radiation damage to the solvent. These Centrifugal Extractors performed very satisfactorily and the campaigns provided a lot of information for fine tuning the design, operation and maintenance philosophy. The product containing Uranium and Plutonium are separated by oxalate precipitation and calcined to their respective oxides.

The process performance of these campaigns was very good as the raffinate losses were very low. The purity requirements could be achieved in a single cycle of solvent extraction itself, though three cycles are provided in the facility. The campaigns provided an opportunity to optimize the flow sheet conditions to reduce the waste volumes. For cleaning the solvent before reuse, an ammonium carbonate process was developed and implemented after extensive experiments in the laboratory.

The operational experience proved that it is possible to have control over α-contamination by adopting the policy of remote operation and maintenance. It is supplemented by contact maintenance in glove boxes, wherever required. The experience with CORAL operations indicates that for small scale operations, it is possible to address criticality issues with a combination of ever safe geometry design with administrative controls.

Several campaigns with spent fuel of various burn up such as 25, 50 and 100 GWd/t have been carried out successfully without any radiological event.

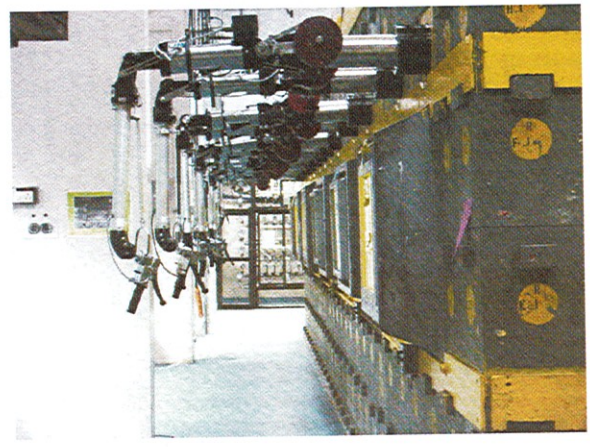

Fig. 1: Hot cell with articulated manipulators

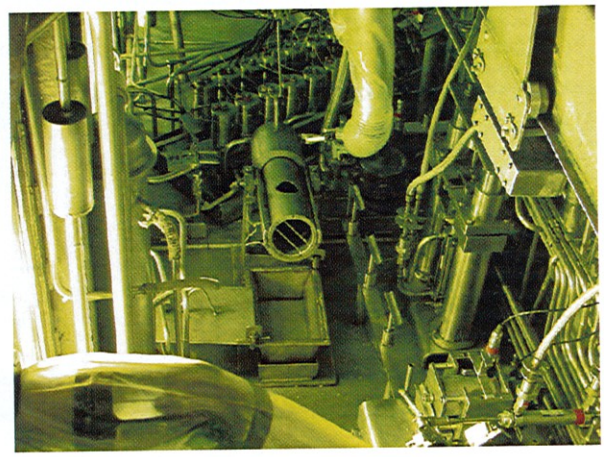

Fig. 2: Equipments inside the CORAL

■ CARBIDE FUEL REPROCESSING

Plutonium and Uranium Carbide fuel with 70 % plutonium is the driver fuel for FBTR. This fuel has good thermal conductivity and neutron characteristics. But reprocessing of this fuel poses unique problems as the fuel is pyphoric in nature and the dissolution of the fuel yields soluble organics which interfere in solvent extraction. This requires special care in the design and operation. High Plutonium in the fuel adds another dimension to the complexity as criticality accident issues have to be addressed in the plant and process design.

■ CORAL

CORAL comprises of lead shielded hot cell with 250 mm or 200 mm thick lead shielding (depending upon the β, γ radioactivity in different zones). The cell is a compact one and constructed on an area of 11m * 2 m. The overall height is 3 m. A α-tight stainless steel containment box of 10 m long, 1.2 m wide and 1.5 m high is housed inside the lead shielding. The cell is provided with six radiation-shielding windows and six pairs of articulated arm type master slave manipulators to facilitate remote operation and maintenance of different equipments and systems. In addition, a α-tight blister box provides access for direct maintenance of small gadgets, which can be brought out of the cell. Specially designed tanks (annular or slab type) have been installed to store solutions containing Plutonium to meet the safety requirements of criticality. About two Km of intricate stainless steel piping involving 3000 bends and 2000 X-Radiography joints has been successfully completed within the limited area of the facility. The dense of piping is a challenging task for the manipulation by welders. Around 35 process vessels and 30 equipments are installed in the hot cell. Since large concentrations of plutonium are handled, the hot cell facility is designed α-tight in addition to providing criticality control measures and like thermal reactor fuel reprocessing where cells with β,γ, shielding is sufficient.



Titanium Dissolver

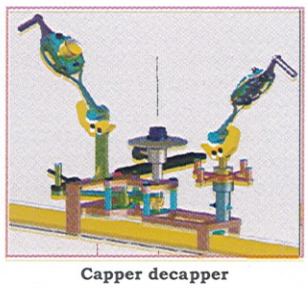

Capper decapper

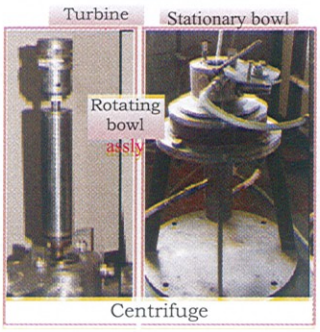

Centrifuge

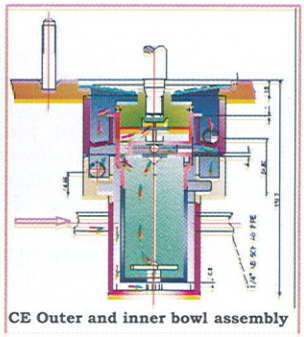

CE Outer and inner bowl assembly

Fig. 3: Some of the Reprocessing equipment at CORAL

■ ACHIEVEMENT

Uranium and plutonium from the highly active spent reactor fuel were separated to the required purity and recovery. Several gadgets designed & developed for this activity has performed very satisfactorily and has provided vital inputs for future plants. Reprocessing of this type of fuel has been carried out successfully for the first time in the world.

■ PUBLICATIONS ARISING OUT OF THIS STUDY AND RELATED WORK

R. Natarajan and Baldev Raj, *J. Nucl. Sci. Tech.*, **44** (2007) 393.

Further inquiries:
Shri R.Natarajan, Reprocessing Group
IGCAR, e-mail: rnr@igcar.gov.in

Diffusion Alloyed Platinum Electroplated Titanium Electrodes for Electrochemical Processes

EXECUTIVE SUMMARY

In the acid killing by electro-reduction process, concentration of nitric acid in the high level waste (HLW) from the spent nuclear fuel reprocessing plant has to be brought down from about 4 to 0.5 M in order to reduce the amount of HLW by subsequent evaporation and to minimise the corrosion in waste tanks during storage of the concentrated waste solution. For this purpose, electrodes with high performance and corrosion resistance are demanded. Platinum electroplated titanium (PET) has been selected as electrodes for this purpose, however, plated surfaces have numerous defects affecting the integrity of the electrodes during service. Pt electroplated Ti (PET) and diffusion alloyed PET (DAPET) of plating thickness 3, 5, 7 and 10 μm was evaluated for their performance. The electrochemical reduction of 4 and 8M nitric acid to near neutral conditions was carried out with the above-said anodes and Ti cathode at various cathodic current densities. The PET and DAPET electrodes could withstand and function well at much higher cathodic current densities (up to 80mAcm−2). It is recommended that for plant applications at high current density and acidity, Pt electroplated to a thickness of above 7 μm over Ti substrate followed by diffusion alloying may be employed to make a compromise between the energy efficiency of the process and the life extension of the anode.

OUTLINE

Platinum finds extensive application as electrode materials in chemical and electrochemical industries due to its high conductivity, good electrocatalytic activity, and excellent resistance to oxidation and corrosion. However, owing to its high cost in bulk form, platinum is put to practical use by electroplating a thin layer over high corrosion resistant substrates such as titanium, niobium and tantalum. Platinum electroplated Titanium (PET) electrodes have become an inevitable component in electrochemical industries, and in particular to electrochemical processes wherein high corrosive and radiation fields are envisaged. One such application is the use of PET electrodes in the spent nuclear fuel reprocessing plants.

One of the mechanisms involved in the failure of the electroplated anodes during continuous use is by delamination of Pt from the surface. When delamination occurs in PET electrodes, the plated Pt gets detached from the surface and titanium metal would be exposed to the electrolyte resulting in the failure of the electrode. In addition, the plated surface, depending on the thickness, would develop a number of defects (Fig. 1) like micropits, microcracks, etc. The micro cracks were formed during the stress relieving process (to remove the residual stresses produced in the material during the plating process). Ti substrate attracts Pt from the bath solution in all directions and there would be some discontinuity in the Pt layer on the Ti surface, which were observed as pits or islands. The pit is not bare Ti but a layer of Pt with lower thickness. With increased thickness of plating, the micro cracks formed were more pronounced and when the thickness exceeded the limiting value, peeling off of Pt would occur. As the thickness of plating increases, the formation and propagation of cracks also increase owing to stress relieving process. At locations where the micro cracks meet each other, they form junctions such as triple points in which the most wide and deep opening would be present on the surface as is evident

Platinum electroplated titanium is subjected to a heat treatment in vacuum well above the hcp (α) to bcc (β) structure transition temperature of Ti for sufficiently longer durations, inter diffusion of Pt (deposited over the surface of Ti) occurs in the bcc lattice of Ti, as this high temperature phase is a open structure with more void space. This treatment produces intermetallic Pt–Ti compounds on the surface and delays the process of delamination of elemental Pt and thus extends the life of the electrode. During diffusion annealing of PET anodes, an inter-diffused layer is formed between Ti surface and plated Pt (Fig. 2).

Therefore, industries using plated electrodes for continuous operation at high current density conditions in corrosive environment should exploit this diffusion annealing procedure to extend the life of the electrodes.

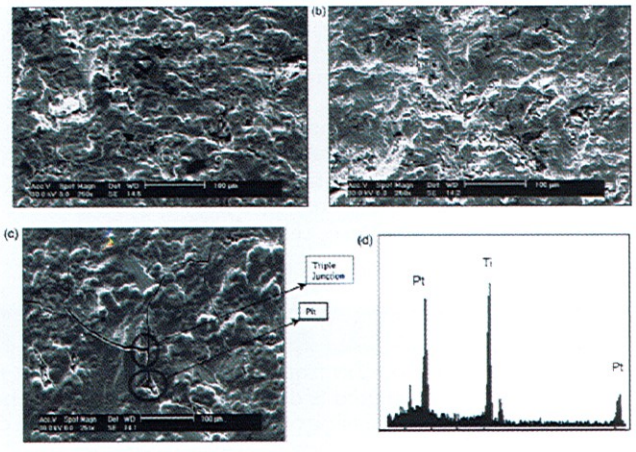

Fig. 1 : SEM micrographs showing platinum electroplated surface of titanium showing various defects

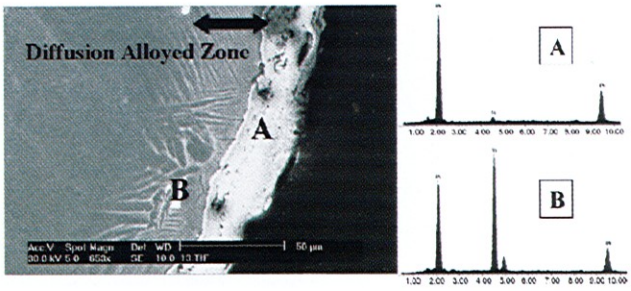

Fig. 2 : SEM micrograph of diffusion annealed PET sample showing the presence of Pt in the inter diffused zone 'B' within the Ti substrate

■ ADDITIONAL INFORMATION

Platinum electroplated titanium electrodes are candidate materials for applications in electrochemical processes employed in reprocessing plants. One of the draw back of the electrode is the defects present on the plated surface which allows an easy path for the penetration of electrolyte leading to corrosion of titanium and failure of the electrode. To overcome this difficulty, a novel diffusion alloying process has been evolved by which an inter-diffused layer enriched with PtTi intermetallics is developed. Thus the penetration of corrosive electrolyte would meet the diffusion alloyed intermetallic zone, and hence the corrosion attack and failure of electrode would be avoided.

■ GENERAL EXPLANATION RELATED TO THE DESCRIPTION

One of the mechanisms involved in the failure of the platinum electroplated titanium electrodes during continuous use is by delamination from the surface. When delamination occurs in PET electrodes, the plated Pt gets detached from the surface and titanium metal is exposed to the electrolyte resulting in the failure of the electrode. During diffusion alloying of PET anodes, an interdiffused layer is formed between Ti surface and plated Pt. The interdiffused layer comprises the intermetallic compounds $PtTi_3$ and PtTi. When delamination occurs, the DAPET electrode is not susceptible to sudden failure due to the adherent Pt-Ti interdiffused layer which protects the surface of Ti substrate. The electrodes were employed in the electrolytic destruction of nitric acid from 4 or 8 M to near neutral conditions. The rate of destruction of the acid and the rate constant were computed from the experimental results using kinetic equations. A comparison was made on the current efficiency of the process with respect to plating thickness and current densities to facilitate the performance evaluation of the electrodes, and the electrodes are seen to be performing at comparatively lower efficiency levels (Table 1). Therefore, industries using Pt plated Ti electrodes for continuous operation at high current density conditions in corrosive environments are recommended to use diffusion alloyed electrodes.

Table 1
Comparison of the performance of the anodes, PET and DAPET in terms of energy efficiency of the electrolytic process

S. No.	Anode	Rate of reduction ($mol.A^{-1}.h^{-1}$)	Rate constant ($mol.L^{-1}.h^{-1}$)	Current efficiency (%)
1	3-PET	0.0167	1.781	67.2
2	5-PET	0.0179	1.911	73.9
3	7-PET	0.0197	2.103	79.4
4	10-PET	0.0196	2.089	78.8
5	3-DAPET	0.0183	1.964	73.6
6	5-DAPET	0.0189	2.016	76.0
7	7-DAPET	0.0194	2.080	77.9
8	10-DAPET	0.0197	2.096	79.0

■ BRIEF DESCRIPTION OF THEORETICAL BACKGROUND

The Ti base metal undergoes a solid state phase transformation from hcp (α) to bcc (β) structure at about 1163 K. When platinum electroplated titanium is subjected to a heat treatment in vacuum well above the transition temperature of Ti for sufficiently longer durations, inter diffusion of Pt (deposited over the surface of Ti) occurs in the bcc lattice of Ti, as this high temperature phase is an open structure with more void space. This treatment produces intermetallic Pt-Ti compounds on the surface and delays the process of delamination of elemental Pt and thus extends the life of the electrode.

■ ACHIEVEMENT

Platinum plated titanium electrodes consists of inherent defects generated during electroplating process which hinder the performance and service life. Diffusion alloying process has been established to develop an inter-diffusion zone consisting of inter-metallic phases of Pt-Ti, which improved the corrosion resistance and performance during electrolytic acid killing experiments.

■ PUBLICATIONS ARISING OUT OF THIS STUDY AND RELATED WORK

C. Mallika, B. Keerthika and U. Kamachi Mudali, *Electrochimica Acta*, **52** (2007) 6656.

Further inquiries:
Dr. U. Kamachi Mudali, Corrosion Science and Technology Division
Metallurgy and Materials Group, IGCAR, e-mail: kamachi@igcar.gov.in

Corrosion Resistant Dissimilar Joints between AISI Type 304L SS and Titanium

EXECUTIVE SUMMARY

To link titanium and zirconium metal based (Ti, Zr-2, Ti–5%Ta, Ti–5%Ta–1.8Nb) dissolver vessels containing highly radioactive and concentrated corrosive nitric acid solution to other nuclear fuel reprocessing plant components made of AISI type 304L stainless steel (SS), high integrity and corrosion resistant dissimilar joints between them are necessary. Fusion welding processes produce secondary precipitates which dissolve in nitric acid, and hence solid-state processes are proposed. Among various dissimilar joining processes available for producing titanium-304L SS joints with adequate strength, ductility and corrosion resistance, explosive joining has been found to produce corrosion resistant joints with acceptable corrosion rates and bend ductility. Based on the results, dissimilar joint produced by the explosive joining process was adopted for CORAL plant application.

OUTLINE

The fabrication and qualification of DMW joint between titanium and AISI type 304L SS is crucial in the reprocessing plant especially because of zero failure requirements due to corrosion. Fusion welding processes produce secondary precipitates which dissolve in nitric acid and hence, solid-state processes are proposed for joining titanium and AISI type 304L. In Japanese reprocessing plants, both explosive bonded and diffusion bonded sections are used. A direct bonding between titanium and type 304L could be achieved by vacuum diffusion bonding with the pre-cleaning of the surfaces using ion sputtering. High corrosion resistance in severely corrosive nitric acid with adequate mechanical strength and bend ductility are the minimum requirements for this purpose. Solid-state welding processes, viz. explosive bonding, diffusion bonding and friction welding were considered for fabricating this DMW joint to achieve adequate mechanical properties and corrosion resistance. The friction-welded and explosive-bonded pipe joints were subjected to detailed investigations including non-destructive examinations such as liquid penetrant, radiography and ultrasonic testing. The joints passed all the NDT tests as per the acceptance standards (Table 1).

The explosive bonding process produces a bonding by high velocity impact of the work pieces caused by a controlled explosion/detonation. The bonding is produced within a fraction of a second. The important interrelated variables in explosive bonding are (1) collision velocity (2000–5000 m/s), (2) collision angle (3) flyer plate velocity and (4) nature of explosive. Smooth surface finish of titanium and type 304L SS are obtained in order to create a better interface after explosive joining operation. The cladded plate was subjected to a stress-relieving heat treatment at 540°C for 1.5 h.

Three-phase corrosion tests were conducted in 11.5 N boiling nitric acid for both friction welded and explosive-bonded pipe joints. It was observed that for both the joints, the corrosion rate in the condensate phase is markedly higher than in the liquid and vapour phases. Detailed optical and scanning electron microscopy examinations of the specimens exposed to the condensate phase indicated severe corrosion attack of the friction-welded joints with wide opening at the interface (Fig. 1(a) and (b)). In the case of the explosively welded joint, the interface was free from corrosion, but corrosion attack at the 'vortex' region of the AISI type 304 L SS was noticed. In general, the average corrosion rate of the friction-welded joint in vapour and condensate phases was marginally lower than the explosively welded joint. The corrosion rate of the friction-welded joint could be attributed to the selective loss of material at the 'trench' formed at the joint interface, an unacceptable situation for structural integrity considerations. Thus, explosively welded joints showed better performance as compared to friction-welded joints from corrosion point of view.

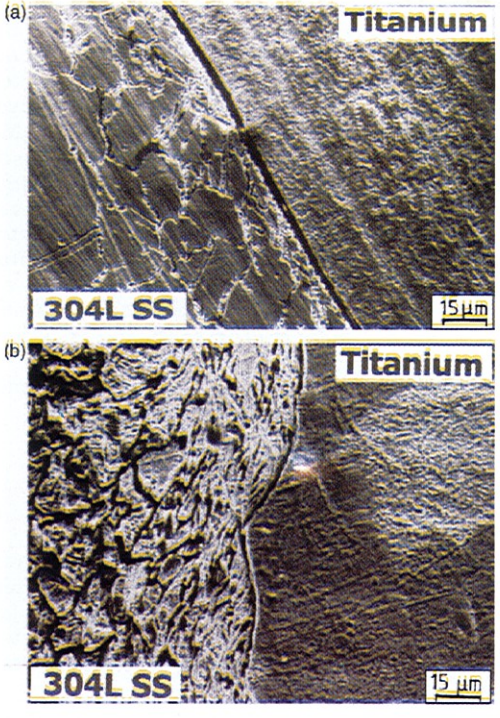

Fig. 1: SEM micrographs showing severe corrosion attack of the friction-welded joint (a) with wide opening at the interface compared to (b) smooth interface of explosive joint

Table 1
Results of Non-destructive, mechanical and Corrosion Tests

Tests	Friction welded joint		Explosive bonded joint	
Non-destructive tests				
Liquid penetrant test	Passed		Passed	
Radiography	Passed		Passed	
Ultrasonic test	Passed		Passed	
Mechanical tests	*Test 1*	*Test 2*	*Test 1*	*Test 2*
Tensile tests				
Ultimate tensile streangth (MPa)	462	495	397	457
% Elongation	Negligible	Negligible	21.4	19.7
Bend tests				
Root bend (bend angle at failure)	<5°	<5°	60°	76°
Face bend (bend angle at failure)	<5°	<5°	80°	106°
Three-phase corrosion tests				
Liquid phase (avg. corrosion rate) (mpy)	0.48		0.44	
Vapour phase (avg. corrosion rate) (mpy)	0.72		1.5	
Condensate phase (avg. corrosion rate) (mpy)	10.07		12.03	

ADDITIONAL INFORMATION

A methodology was evolved for the erection of titanium dissolver equipment in containment box of the cell made of AISI type 304L SS as titanium cannot be welded directly to AISI type 304L SS. The welding of titanium equipment to stainless steel by appropriate design was a preferred one instead of mechanical fastening. A 6 mm Ti Grade 1 plate was clad with 12 mm 304L SS plate, and then it was machined and welded to the top flanges of the dissolver. It was essential that while welding the clad-ring to the dissolver flange at the bottom, it must be welded segment by segment (Fig. 2). In addition, cooling the welded segment to room temperature was practiced, in order to avoid over heating of the clad portion which other wise may lead to opening up of the bonded area.

GENERAL EXPLANATION RELATED TO THE DESCRIPTION

For fast reactor reprocessing plant facilities, titanium has been used for fabricating dissolver vessel in CORAL plant. The dissolver needs to be connected to the rest of the process vessels and piping made of AISI type 304L stainless steel. The fabrication and qualification of this dissimilar metal weld joint is crucial in the reprocessing plant. High integrity dissimilar joints with adequate corrosion resistance, mechanical strength and bend ductility are essential for uninterrupted operation of reprocessing plants. Several dissimilar joints were made by advanced fusion welding methods as they produce joints with poor corrosion resistance. Dissimilar joints of titanium to 304L SS prepared by solid state joining processes were considered as the best option. Commonly employed dissimilar joining processes are roll bonding, pressure welding, explosive welding, and diffusion bonding. Since no melting occurs at the interface, secondary precipitates are not formed by these processes and hence the corrosion resistance is not affected significantly during service. Development of dissimilar joints between titanium and stainless steel thus has been achieved by explosive joining processes with acceptable corrosion resistance.

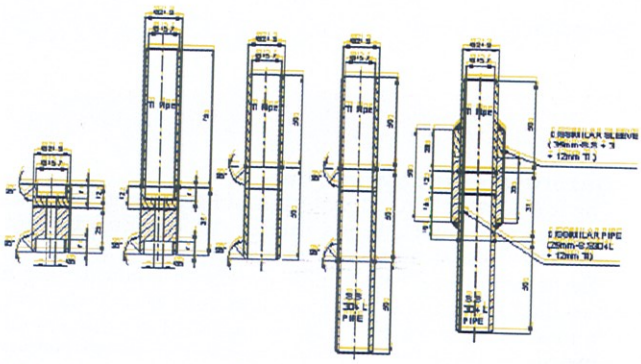

Fig. 2 : Design sequence of the dissimilar joining of titanium and type 304L SS

BRIEF DESCRIPTION OF THEORETICAL BACKGROUND

Dissimilar joints of titanium to 304L SS prepared by solid state joining processes are considered as the best option to provide good corrosion resistance. Commonly employed dissimilar joining processes are roll bonding, pressure welding, explosive welding, and diffusion bonding. Since no melting occurs at the interface, secondary precipitates are not formed by these processes and hence the corrosion resistance is not affected significantly during service. Thus explosive joining was considered as the best option based on mechanical, NDT and corrosion testing parameters to link between titanium and AISI Type 304L stainless steel.

ACHIEVEMENT

Corrosion resistant dissimilar joints of titanium and AISI type 304L stainless steel has been achieved for application in CORAL reprocessing plant through systematic R&D studies on corrosion and mechanical properties. The explosive joining parameters were initially established for optimising the micro-structural and corrosion aspects of the joints. A design sequence was achieved for plant applications.

Further inquiries:
Dr. U. Kamachi Mudali, Corrosion Science and Technology Division
Metallurgy and Materials Group, IGCAR, e-mail: kamachi@igcar.gov.in

Development of a Computer Controlled Machine for Remote Profilometry and Laser Based Dismantling of Irradiated FBTR Fuel Sub-Assemblies

■ EXECUTIVE SUMMARY

A remotely operated computer controlled machine has been developed, installed and successfully operated inside the hot cells of Radio metallurgy Laboratory at IGCAR to meet the dual objectives of precise dimensional measurements and remote laser based dismantling of high burn-up FBTR fuel subassemblies (FSAs), as part of Post Irradiation Examination (PIE). The four-axis machine makes use of a touch trigger sensor assembly with radiation resistant linear scales on all axes for dimensional measurements. The acquired data is used for the reconstruction of 3-D profile of the subassembly for the analysis of dimensional deformations due to irradiation. The machine can also carry out longitudinal and transverse cutting of stainless steel inner and outer hexagonal sheaths using a laser torch assembly or a motorized diamond wheel assembly.

■ OUTLINE

Quantifying the deformation

The fuel and structural materials of Fast Reactors undergo dimensional deformations due to the combined effect of thermal stresses and neutron induced swelling and creep. The deformations can lead to excessive loads during fuel handling operations in the reactor and it can also cause changes in reactivity. It is essential to measure the changes in dimensions very precisely to evaluate whether they pose any constraints in fuel handling operations and in increasing the burn-up of the fuel. Figure1 shows the dimensions of a normal FSA, and a typical deformed FSA. Table 1 shows the major dimensional parameters that need to be measured and evaluated on the irradiated FSA. High level of gamma radiation, irregular/distorted nature of the object and the requirement of high level of measurement accuracy provide immense challenges in developing a machine suitable for remote operation and maintenance.

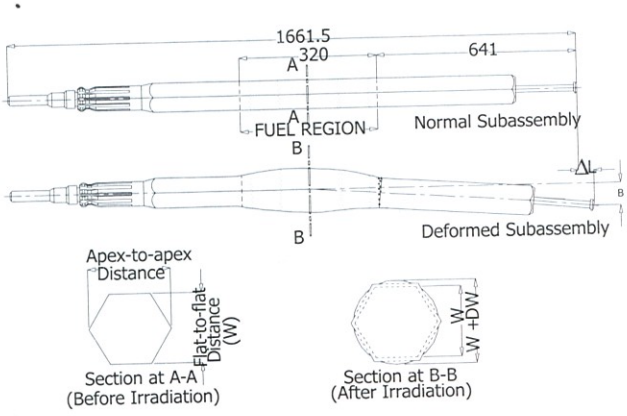

Fig. 1: Sketch showing normal and deformed FSA

Dismantling of FSA for extracting fuel pin bundle

The fuel pin bundle has to be extracted from the FSA for carrying out Post-Irradiation Examination (PIE) on the fuel pins. Transverse cutting or dismantling of the outer and inner hexagonal sheaths of the FSA is required to disengage the fuel pin bundle from it. Longitudinal cutting also may become necessary if the bundle remains stuck within the hexagonal sheath due to the diametrical increase and distortions of the fuel pins. Laser-based dismantling has been chosen for development due to its various advantages such as non-contact nature of cutting, fast cutting, ease of remote operation, minimum remote repair/replacement of parts, absence of coolant and minimum generation of waste such as dust & chips over other techniques. Challenges in this work involve precise delivery of required laser power at the cutting location with optimized parameters and avoiding welding between the outer and inner hexagonal sheaths of FSA during cutting.

A machine has been developed to fulfill the following objectives.

- Quantify the deformation of high burn-up FBTR FSA
- Develop expertise in dismantling of FSA using laser

Table 1
Dimensional parameters to be measured on FSA

Dimensional parameter to be measured on FSA	*Nominal value*	*Max. expected increase*	*Cause of change*	*Accuracy of measure-ment needed*
Length	1661.5	5mm	swelling	± 0.5mm
Head-to-foot-misalign-ment	1.0	7mm	Differen-tial swelling + creep	± 0.5mm
Flat-to-flat distance	$49.8^{+0.2}$	1.5mm	swelling + creep	± 0.05mm
Apex-to-apex-distance	57	1mm	swelling	± 0.05mm

■ ADDITIONAL INFORMATION ABOUT THE SYSTEM DEVELOPED

The machine developed to meet the above requirements consists of a mechanical system located within the hot cell, its motion control system and a laser system located outside the hot cell. An induction type touch trigger sensor and a custom made software facilitate dimensional measurements and profilometry of FSA. The laser system connected to the cutting nozzle inside the hot cell through a fibre optic cable enables dismantling of FSA. Cutting is also possible using a wafer-thin diamond cutting wheel.

■ GENERAL EXPLANATION RELATED TO THE DESCRIPTION

Figure 2 shows a photograph of the 4-axis system developed indigenously. It has a 2 m long horizontal machine bed on which an X-carriage moves holding the FSA. A vertical column located in the middle carries a YZ-stage that can alternately hold different tool assemblies for the touch-trigger-sensor, laser cutting nozzle and the diamond cutting wheel. The X,Y, and Z stages are mounted on precision LM guides. Stepper motors, ball screws, linear displacement scales, limit switches, touch-trigger-sensor, laser cutting nozzle etc. used in the system can withstand > 10^8 rads of gamma radiation.

The motion control system consists of components like the stepper motor drives, PC, motion control card, motion control software etc. located outside the cell and components like stepper motors, radiation resistant linear scales, limit switches, touch trigger sensor, etc., integral with mechanical system kept inside the hot cell. They are linked through power, signal and control cables that pass through leak-tight penetrations on the hot cell wall.

The laser system (Fig. 3) has been developed by RRCAT, Indore. It consists of a pulsed Nd-YAG laser, power supply, control panel, chiller and a fiber-optic cable fitted with cutting nozzle. A miniature cutting-nozzle was specially developed for facilitating its introduction into the hot cell through the existing service penetrations and a new mini-glove-box in a leak-tight manner.

Calibration of the measurement system is carried out on a 55 m diameter cylindrical mandrel before and after carrying out the dimensional measurements and profilometry on the FSA. From about ninety data points on the cross section of the mandrel, thirty circles are generated by selecting three equally spaced points and the mean deviation in diameter is calculated to establish the accuracy. It has been established within ± 0.02 mm.

Figure 4a shows an image of a fuel subassembly reconstructed using the data obtained from the profilometry, and 4b shows its top view. All the required dimensional parameters are embedded in the reconstructed image with the originally envisaged accuracies and can be easily extracted. Figure 5a shows a photograph of the FSA being cut using the laser nozzle outside the hot cell. The kerf-width was found to be less than 0.5 mm. Figure 5b shows cut segments of the dummy wrapper. Figure 5c shows a photograph of the FSA being cut using the laser nozzle inside the hot cell.



Fig 2 : Four axis mechanical system



Fig . 3 Laser system with power and control units



(a) 3-D image of 154 GWd/t FSA fuel subassembly in ACAD

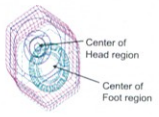

(b) 3-D Top view

Figure 4 Reconstructed image of a fuel subassembly

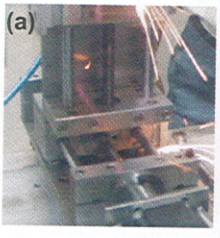

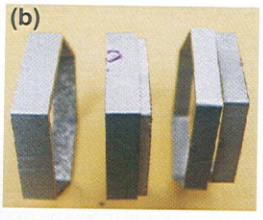

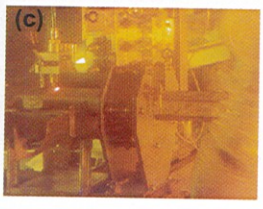

Fig. 5: Laser cutting in progress outside and inside the hot cell; cut segments of dummy wrapper FSA

■ BRIEF DESCRIPTION OF THEORETICAL BACKGROUND

Due to the combined effect of service conditions such as stresses, temperature and neutron flux, the structural materials inside the reactor undergo deformation. Irradiation induced swelling and creep cause increase in dimensions. Swelling takes place under the influence of temperature and neutron flux and creep takes place under the influence of stress, temperature and neutron flux. The maximum temperature and flux seen by the FSA are 425°C and 2.2 X 10^{15} n/cm^2/s. The deformations of FSA can lead to changes in reactivity as well as excessive loads during fuel-handling-operations within the reactor. Hence dimensional measurement and profilometry are essential components of PIE at Radiometallurgy Laboratory (RML).

■ ACHIEVEMENT

A remotely operated computer controlled machine has been developed, installed and operated inside the hot cells of RML at IGCAR. It has been successfully used to carry out precise dimensional measurements of the stainless steel hexagonal sheath of the FBTR FSA that has seen 154 GWd/t burn-up, to evaluate the deformations undergone by it in the reactor and to reconstruct its 3-D image. Along with other PIE data, this will help in evaluating whether the burn-up of FBTR FSA can be increased. The machine has also been used to dismantle the FBTR FSA remotely using laser. The experience gained will be utilized to develop a production-scale system for the inspection and dismantling of FBTR and PFBR FSAs prior to reprocessing.

■ PUBLICATIONS ARISING OUT OF THIS STUDY AND RELATED WORK

A. Vijayaragavan , Shaji Kurien, V Anandaraj , V.L Balakrishnan, Jojo Joseph and K.V. Kasiviswanathan; International Symposium on Advances in Stainless Steel, April 9-11, 2007, Chennai.

Further inquiries:
Shri Jojo Joseph, Post-Irradiation Examination Division
Metallurgy and Materials Group, IGCAR, e-mail:jojo@igcar.gov.in

Development & Fabrication of D9 Pressurised Capsule and Material Irradiation Capsule

EXECUTIVE SUMMARY

Pressurised capsules made of D9 alloy have been developed to determine the in-reactor creep performance of indigenously developed D9 alloy. Two numbers of non-instrumented irradiation capsules for irradiation of specimens of alloy D9 and type 316 stainless steel (FBTR quality) in FBTR have been fabricated to generate baseline irradiation performance data on these materials at low temperature and low fluence irradiation conditions. D9 is the alloy selected for PFBR fuel cladding and wrapper tube and Type 316 SS (FBTR quality) has been used in the fabrication of reactor vessel and other block pile components in FBTR.

OUTLINE

D9 alloy

D9 alloy is modified type 316 stainless steel with controlled additions of titanium and silicon. It has also reduced chromium content and increased nickel content. Its swelling resistance to neuron irradiation, and irradiation creep behavior are better than those of type 316 stainless steel.

Development of D9 pressurised capsule

D9 tube of 6.6 mm outer diameter and 0.45 mm wall thickness is closed by welding at one end and fitted with special end plug at the other end, which enables filling of gas at the desired pressure into the tube using a pressurising system. After pressurising, the gas entry path is sealed with a soft gasket and welding is carried out to close the special end plug with a cap. The diameter of the special end plug has been designed to accommodate all features within the diameter of 6.6 mm. The length of the pressurised capsule is about 74 mm. Capsule with an internal pressure of 6.5 MPa has been successfully developed (Fig. 1).

Design and Fabrication of Material Irradiation Capsule

Two numbers of non-instrumented irradiation capsules for irradiation of specimens of alloy D9 (Fig. 2) (pressurised capsules, tensile and swelling specimens) and type 316 stainless steel - FBTR quality (tensile and swelling specimens) in FBTR have been fabricated. The aim of the experiment is to generate baseline irradiation performance data on the indigenously developed D9 alloy, and type 316 SS (FBTR quality) at low temperature and low fluence irradiation conditions. D9 is the alloy selected for PFBR fuel cladding and wrapper tube and Type 316 SS (FBTR quality) is with more stringent composition specifications than the corresponding ASTM grade and has been used in the fabrication of reactor vessel and other block pile components in FBTR.

D9 pressurised capsules have been fabricated and arranged in five partitions in an irradiation capsule along with D9 disk specimens. These pressurised capsules were fabricated from indigenously developed D9 alloy clad tube of outer diameter 6.6 mm and 0.45 mm wall thickness. A gas mixture of 97% argon and 3% helium was used for the pressurisation. The hoop stresses that will be developed in the pressurised capsules at the irradiation temperature are 30, 60 and 90 MPa respectively. The second irradiation capsule contains small size flat tensile specimens and disk specimens of both D9 alloy and type 316 SS (FBTR Quality), and D9 tubular tensile specimens. Holes have been drilled on the wall of irradiation capsules to allow the reactor sodium to enter and surround the specimens during irradiation. The irradiation temperature of specimens will be the same as temperature of sodium (346 to 350 deg. C). The irradiation capsules are assembled in two special steel subassemblies and will be loaded in the 4th ring of FBTR for irradiation. After irradiation, the irradiation capsules will be taken to Radio metallurgy Laboratory and post irradiation examination will be conducted.

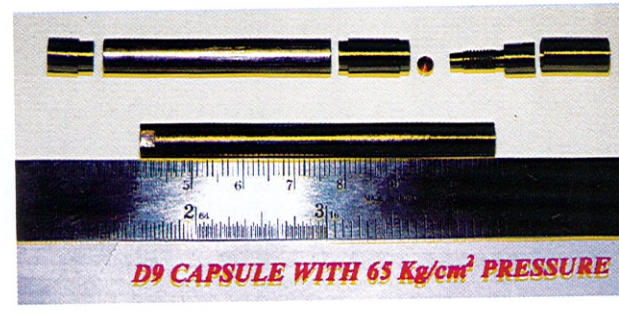

Fig. 1 : D9 pressurised capsule with 6.5 MPa internal pressure

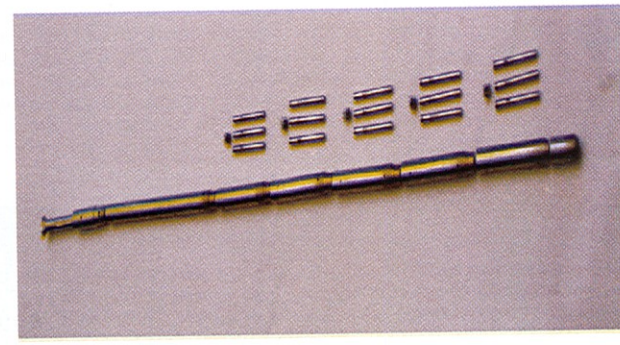

Fig. 2 : View of irradiation capsule with D9 pressurised capsules and D9 disk specimens (Before assembly and welding)

■ EFFECT OF RADIATION ON MATERIALS

Due to intense neutron flux and high temperature that prevails in a nuclear reactor, there will be degradation in the mechanical properties of materials such as ductility, impact strength and in-reactor creep strength. The impingement of neutrons on the structural material in the reactor causes extensive displacement of lattice atoms from their normal position and a variety of defect structures get produced. Subsequently, there is gradual degradation in performance of materials. For instance, the material hardens, its ductility reduces, its creep rate increases, and its volume increases due to appearance of voids. These changes can be determined by carrying out irradiation experiments in a reactor under controlled experimental conditions and testing the irradiated samples in hot cells.

■ GENERAL EXPLANATION RELATED TO THE DESCRIPTION

Creep is time dependent deformation of materials under stress and temperature. Normally, this strain occurs at elevated temperatures and is known as thermal creep. Irradiation creep is the additional deformation due to presence of neutron flux. Thermal creep occurs above about one third of absolute melting temperature whereas irradiation creep is found in materials even at low temperatures. Irradiation induced swelling and creep are important phenomena that affect the design, operation and performance of core structural materials of Fast Breeder Reactors (Fig. 3).

There are many methods by which irradiation creep experiments are carried out. Use of pressurised capsules is one such important method to determine irradiation creep particularly in non-instrumented irradiation experiments.

The pressurised capsule is made of the same material for which the irradiation creep data is required. It is in the form of a gas filled tube with both ends sealed. A pressurising gas such as argon is filled in the pressurised capsule at high pressure. The filling pressure of pressurised capsule at room temperature is chosen in such a way that the target stresses are attained at the desired temperature of irradiation in the reactor.

The material specimens including pressurised capsules are kept in irradiation capsules, which are in turn locked in special steel subassemblies. These special sub assemblies are loaded in Fast Breeder Test Reactor for irradiation.

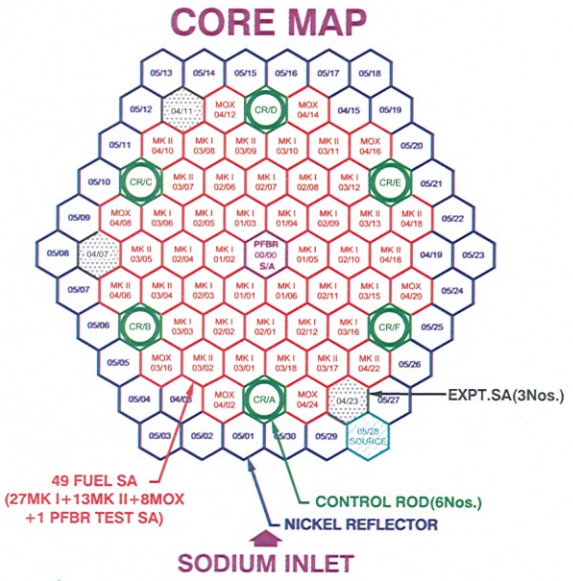

Fig. 3 : Typical core plan of FBTR in which the special subassemblies with irradiation capsules containing pressurised capsules & other specimens are loaded in the 4th ring during 14th irradiation campaign

■ BRIEF DESCRIPTION OF THEORETICAL BACKGROUND

Pressurised capsule is designed as a thin wall cylinder subjected to high pressure. The pressure of gas filled at room temperature is determined from the mass of the gas and using gas laws. Pressure developed at high temperature is also determined using gas laws. It is aimed to obtain the steady state creep rate of the material, which can be used in design calculations. Maximum temperature of pressurised capsules in the irradiation capsule in case of sodium flow blockage in the special subassembly has been calculated to verify the stress that will be developed in the pressurised capsule in that condition and the stress is found to be within safe limit.

■ ACHIEVEMENT

Development of pressurised capsule of 6.6 mm diameter with high pressure is a challenging task and it has been successfully carried out. The proposal for irradiation in FBTR has been approved by statutory safety committees.

■ PUBLICATIONS ARISING OUT OF THIS STUDY AND RELATED WORK

S.Murugan, K.A.Gopal, P.K.Chaurasia, V. Venugopal, P.V.Kumar, K.V. Kasiviswanathan, P. R. Vasudeva Rao and S.C. Chetal; Report No. IGC/ MMG/ IDEAS /D9 /VENTED CAP/ 01/ 2006/ Rev. 0, Oct. 2006.

Further inquiries:
Dr. S. Murugan, Remote Handling, Irradiation Experiments and Robotics Division
Metallurgy and Materials Group, IGCAR, e-mail: murugan@igcar.gov.in

Development of Miniature Specimen Test Techniques

EXECUTIVE SUMMARY

Miniature specimen test techniques enable the characterization of mechanical properties using extremely small volume of the material. Though they have their origin in materials development programmes for the nuclear industry, the miniature specimen test techniques find very promising applications in the field of remaining life assessment, failure analysis, properties of weldments, coatings etc. At IGCAR, research and development work on miniature specimen test techniques includes development of high precision loading equipment, test fixtures, experimental design and implementation, standardization of experimental procedures, data acquisition and analysis techniques. The applications of these techniques for evaluating the properties of weldments, irradiated materials, aged materials and coatings have been successfully demonstrated at IGCAR.

OUTLINE

The miniature specimen test techniques developed at IGCAR are mainly Shear Punch (ShP) and Ball-Indentation (BI) tests.

In shear punch testing, a cylindrical punch with a flat end is forced to punch a hole in a clamped small disc specimen. The load-displacement plot obtained during the punch test is similar to that of a conventional tensile test and properties obtained by analyzing the test curve are correlated with the corresponding conventional tensile properties. Figure 1 shows the shear punch test fixture designed and developed at IGCAR.

The Ball-Indentation (BI) test technique is another miniature specimen technique that requires a very small volume of test material and can be adopted for in-situ testing on real structures. In ball-indentation test, the indenter is driven at a constant speed into the test material and progressive multiple loadings/partial unloading is performed at the same test location. The applied indentation loads and associated penetration depths acquired during the BI test are used to calculate stress-strain values based on well established mathematical relationships. Figure 2 shows the indigenously developed test system for carrying out ball-indentation tests.

These miniature specimen test techniques have been put to use for various applications. In one of the applications, the shear punch technique has been used for evaluating the changes in mechanical properties of irradiated SS316. By using small specimens for testing irradiated materials, it makes it possible to take them out of the hot cells and conduct mechanical testing in comparatively simple and controlled enclosures with reduced radiological hazards (Fig. 3). A tensile-shear punch property correlation obtained using various cold rolled SS316 serves as the base-line data. Small specimens of 8 mm diameter extracted from the irradiated SS316 at different locations corresponding to different neutron fluence (dpa) were shear punch tested and conventional tensile property changes were estimated using the derived correlations.

In another application, both shear-punch and ball-indentation tests have been used to determine the degradation in mechanical properties of modified 9Cr-1Mo steel on aging at 650°C. For this, shear punch and ball-indentation test methodologies were first benchmarked with the conventional tensile testing and validated using various heat treated microstructures of modified 9Cr-1Mo steel. The changes in tensile properties of the modified 9Cr-1Mo after various times of ageing at 650°C have been obtained using Shear punch and Ball-Indentation tests (Fig. 4). This study demonstrates the ability of both shear punch and ball-indentation tests to effectively map the progressive degradation of modified 9Cr-1Mo on ageing at elevated temperatures. The present study can be extended to assess the service-induced degradation of the actual component through these small specimen test techniques.

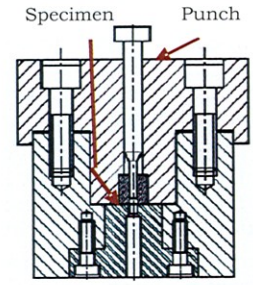

Fig. 1 : Shear Punch Test Fixture

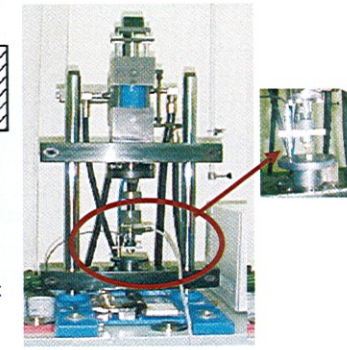

Fig. 2 : Indigenously developed table top ball-indentation test system



(a)

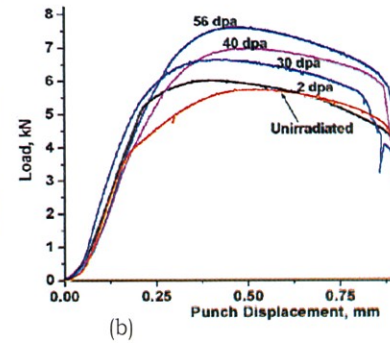

(b)

Fig. 3 : Shear punch testing of irradiated SS316 specimens (a) test setup (b) test plots at various fluence

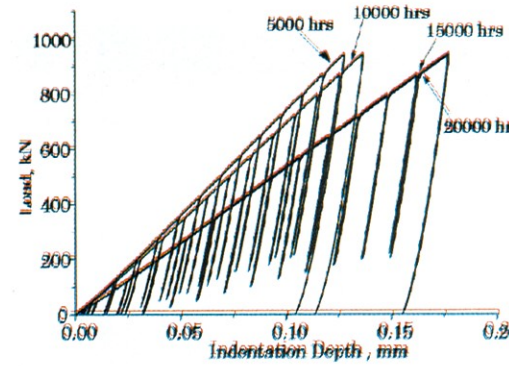

Fig. 4 : The ball-indentation test curves of mod 9Cr-1Mo steel on aging at 650°C for different

■ ADDITIONAL INFORMATION

The concept of specimen miniaturization has its origin in the nuclear industry, where because of expensive and limited irradiation space, specimen sizes were miniaturized for experimental irradiation programmes in reactors. The miniature specimen test techniques can be broadly classified into the following categories: (a) Tests, which are based on miniaturization or scaling down of conventional specimen size (like miniature tensile, fatigue, impact and fracture toughness tests) (b) Tests that are based on novel techniques using disk sized specimens of approximately 0.3 mm thickness (like disk bend tests, shear punch / small punch tests). (c) Techniques based on ball-indentation (BI) testing.

■ GENERAL EXPLANATION RELATED TO THE DESCRIPTION

The small specimen test techniques like disk specimen tests (shear punch, small punch) and ball-indentation tests do not have equivalent conventional counterparts. These novel test techniques need to be first validated and benchmarked before being effectively put to use. The methodology adopted at IGCAR is to first carry out experiments which involve performing both conventional and small specimen tests on various simulated heats of widely ranging microstructures and mechanical properties prepared from the alloy of interest. The data from the small specimen test technique is analyzed, compared and correlated with the corresponding conventional test properties. For an unknown condition of the alloy, using the small specimen test and the correlations derived, the conventional properties of the bulk material are obtained.

Using this methodology, an excellent linear correlation (Fig. 5) between conventional tensile and shear punch tests has been demonstrated for a wide variety of materials such as AISI type 304 stainless steel, AISI type 316 stainless steel, 2.25Cr-1Mo & 9Cr-1Mo ferritic steels etc. Similarly the ball-indentation (BI) tests have been standardized for accurately evaluating the tensile properties for various materials like AISI 1025 carbon steel, 2.25Cr-1Mo steel, modified 9Cr-1Mo steel and AISI 316 steels. A methodology has been developed for including the usually ignored pile-up effects in calculating the stress- strain data from ball-indentation tests for the ferritic steels. Figure 6 reflects the excellent agreement between the stress- strain curve estimated from ball-indentation tests and the conventional tensile stress-strain curves for modified 9Cr-1Mo steel.

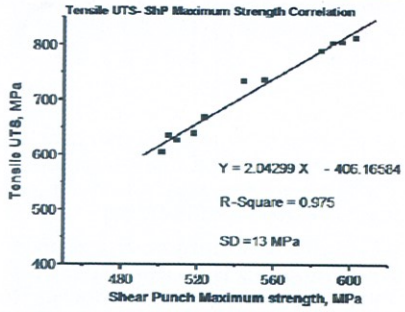

Fig. 5 : The shear punch–tensile correlation for Mod 9Cr-1Mo steel

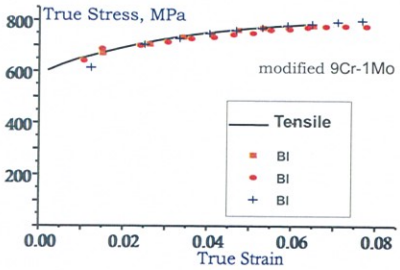

Fig. 6 : Excellent agreement between BI and tensile stress strain curves

■ BRIEF DESCRIPTION OF THEORETICAL BACKGROUND

Shear Punch testing is basically a blanking operation and the principal mode of deformation is shear occurring in the narrow clearance zone between the specimen and lower die surface. The relations between the shear and the uniaxial tensile is linear in nature. However, the shear punch-tensile correlations equations for strength and ductility parameters are mostly empirical in nature due to the complex stress states in the clearance zone. Indentation tests using spherical indenters are unique because the geometry of indentation changes with increasing penetration, corresponding to unique stress-strain value for a particular depth. As a result, spherical indentation test technique is a unique method for determining the complete stress-strain curve of metals using a greatly reduced volume of test material. Compared with the conventional hardness tests, this technique offers both strength and ductility parameters from analysis of the measured indentation load-depth curve.

■ ACHIEVEMENT

Miniature specimen test techniques developed in-house have been validated and benchmarked with conventional mechanical tests for various alloy classes. Their applications in number of areas like properties of irradiated materials, weldments, aged conditions and coating etc have been successfully demonstrated. These techniques will be used for assessing service-induced degradation of the actual structure through in-situ ball-indentation tests and shear punch tests with very small volume of scooped out material.

■ PUBLICATIONS ARISING OUT OF THIS STUDY AND RELATED WORK

1. V.Karthik, K.Laha, P.Parameswaran, K.V.Kasiviswanathan and Baldev Raj, *J. Testing and Eval.*, **35** (2007).
2. V.Karthik, K.V.Kasiviswanathan, A.Vijayaraghavan, K.Laha and Baldev Raj, *Trans. IIM* (In Press).

Further inquiries:
Shri V.Karthik, Post-Irradiation ExaminationDivision
Metallurgy and Materials Group, IGCAR, e-mail: karthik@igcar.gov.in

Single Pin Chopper

EXECUTIVE SUMMARY

Single pin chopper (SPC), compared to bundle chopper, is the ideal choice for fast reactor fuels to avoid crimping. This is because of the slender nature of the fuel, SPC for FBTR spent fuel is designed, manufactured, tested and commissioned at COmpact Reprocessing of Advanced fuel in Lead Cell (CORAL). This is compact and amenable for remote maintenance. SPC consists of fuel pin feeding, magazine rotation, gripping and cutting mechanisms. Since this rich Pu bearing carbide fuel is used first time in the world, many experiments and simulations were done to validate the design. The machine is operating successfully for past five years achieving a bench mark of chopping spent fuel irradiated up to 100 GWd/t.

OUTLINE

CORAL (COmpact Reprocessing of Advanced fuel in Lead Cell) is a versatile radioactive research facility for the development of special purpose machines with remote operation and maintenance features apart from serving as the pilot plant for establishing the process flow sheet for FBR fuels.

In fast reactor fuel reprocessing chop leach process is adopted. Chopping is done to expose the surface of the fuel to the dissolvent. In this process the fuel alone is dissolved leaving the clad as hull.

While, in thermal reactor reprocessing plant, bundle shearing machine is used, but in fast reactor reprocessing plant single pin shearing is preferred, in order to reduce the crimping of fuel pin due to slender nature of the pin with the thin clad. Also generation of fines will be less.

The chopper machine as shown in Fig.1 consists of fuel pin feeding, magazine holder indexing, gripping and cutting mechanisms. Feeding mechanism consists of rack and pinion driven by stepper motor. The push rod moves the pin to the required length for shearing. Magazine holder indexing is by an advanced pawl & ratchet mechanism actuated by pneumatic cylinder that rotates the magazine for feeding the next pin. Gripper consists of stationary and movable grippers actuated by a pneumatic cylinder and cutter consists of cutting tool and spring-loaded shunter actuated by a pneumatic cylinder for chopping the pin.

The magazine containing 10 pins in an array on its circumference is aligned to the equipment, locked and its doors are opened. The chopper operation consists of fuel pin feeding, gripping and cutting. After cutting the pin cutting tool moves along with the shunter and in return stroke pin falls in to the dissolver chute and cutting tool returns to its original position, which prevents flying of cut bits. The sequence of operation follows till one fuel pin is completely chopped, then the push rod retracts to its original position, indexing of magazine takes place to align the next pin. A microprocessor based control unit carries out the sequence of operation automatically as per the logic diagram given in Fig. 2. In order to view the cutting operation carried out in side the chopper box there is provision for fixing camera remotely inside the chopper box. Argon gas is purged in to the chopper unit during chopping to avoid fire hazard, as carbide fuel is pyrophoric in nature and it is exhausted through the dissolver off gas system.

Based on the experimental data on rate of dissolution and powder generation the cut pin length is optimized to 25-30 mm. Several campaigns of chopping have been conducted in this machine with spent fuel from FBTR. Fuel pins with burn ups varying from 25, 50, 100 GWd/t have been chopped without any problems. With this machine 10 pins are chopped in less than 2 hours.

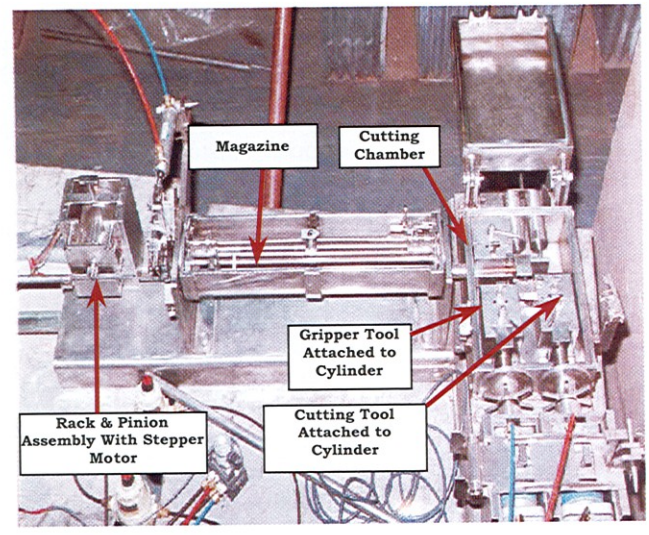

Fig. 1 : Single Pin Chopper

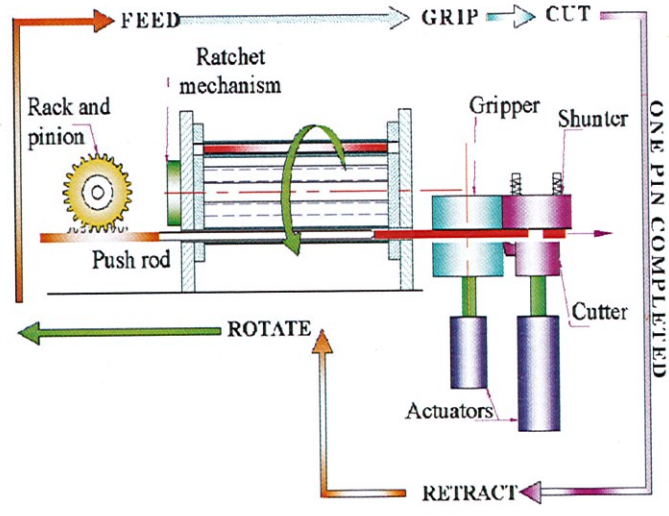

Fig. 2 : Working logic – a schematic Diagram

■ SINGLE PIN CHOPPER

In Reprocessing of fast reactor fuels, Chop-Leach process is usually adopted. This involves cutting of the spent fuel pins into small pieces inside shielded cells, remotely. Various types of choppers are employed based on the fuel pin characteristics and the throughput requirements. Single pin chopper is one such design, employed for chopping of the slender pins of fast reactor fuels. In this design, a single pin is fed and cut at a time, which enables to avoid crimping of these pins. Crimping of pins reduces the reaction rate as the dissolvent will not be contact with the fuel surface.

■ GENERAL EXPLANATION RELATED TO THE DESCRIPTION

The SPC as shown in Fig.3 is made modular in design such that any package like feed, rotate, grip and cut with respective drives can be remotely replaced or maintained. Even the magazine containing of fuel pins is also aligned and replaced from the equipment remotely. All the parts are manufactured and aligned in such a way, remote maintenance can be carried out by general-purpose manipulator with the special gadgets. All the operations are viewed through CCTV.

Mostly pneumatic actuators are chosen for radiation and toxic environment. The material of construction of the parts is either Stainless steel(SS)304 or SS410 depending on strength, corrosion and wear resistance requirements.

A spacer wire is helically wound over the fast reactor fuel pins for flow of coolant, in the sub assembly. During first campaign of spent fuel chopping this spacer wire having very high tension got entangled and posed difficulties in fuel pin feeding and cutting mechanism. These issues were analysed, addressed successfully by suitable modifications in gripping and cutting tool. The feed back and experiences gained with the SPC at CORAL was very much useful in development of various types of choppers required to meet the capacities of future fast reactor reprocessing plants.

The material specimens including pressurised capsules are kept in irradiation capsules, which are in turn locked in special steel subassemblies. These special sub assemblies are loaded in Fast Breeder Test Reactor for irradiation.

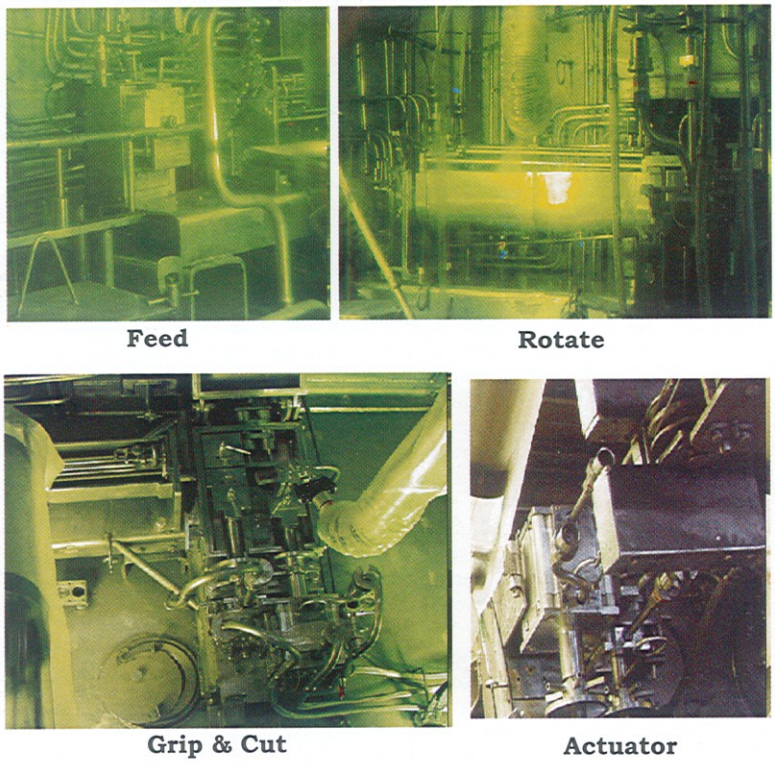

Fig. 3: SPC Mechanism

■ BRIEF DESCRIPTION OF THEORETICAL BACKGROUND

a) **Cutting Tool:** T-42 (10% Cobalt) of hardness 65RC is used to cut irradiated 20% CW SS316 fuel pin having hardness in range of 18-20 RC. The shear force required to cut is estimated to be 1200 kgf. The optimum velocity of the cutting tool was arrived based on spent fuel characteristics, fuel dislodgment, and wear resistance of tool. The clearance between the cutting tool and stationary blade is kept low to reduce the crimping.

b) **Gripper:** The gripper profile is designed such that pinching will not occur. Gripping system is designed to balance the excessive force while gripping.

c) **Magazine Holder:** Magazine holder indexing is by advanced pawl and ratchet mechanism, which provides accurate positioning, self-locking and maintenance free operation.

■ ACHIEVEMENT

The equipment is manufactured to strict interchangeable tolerances by special machining techniques. Rigorous simulation was carried out using different types of simulated fuel rods and performance found satisfactory. The equipment was commissioned at CORAL and is operating successfully for past 5 years. This machine is first of its kind in the world, which has handled rich Pu bearing carbide fuel irradiated up to 100 GWd/t. This experience with this machine enables scaling up the capacities for future plants.

Further inquiries:
Shri A.Ravisankar, Reprocessing Plant Design Division
Reprocessing Group, IGCAR, e-mail: aravish@igcar.gov.in

Duel Frequency Saturation Eddy Current Examination of Ferromagnetic Tubes

EXECUTIVE SUMMARY

For quality assurance of modified 9Cr-1Mo ferromagnetic steam generator (SG) tubes during manufacturing, eddy current and ultrasonic non-destructive evaluation (NDE) methods are employed. Eddy current examination of these tubes is difficult due to variations in magnetic permeability and hence, D.C. saturation method is followed. During manufacturing of these tubes, extended wall thickness variations within acceptable limits of ultrasonic testing have produced disturbing signals during eddy current examination. In order to detect defects in these regions, a two-frequency approach has been developed based on the wall thickness measurements made by ultrasonic testing. The approach has shown identical detection performance in wall thickness variation regions as well as other regions for detection of standard reference 1.2 mm diameter hole. After establishing suitable thresholds for implementing the accept/reject criteria, this approach has been successfully implemented in production-line to test 600 SG tubes of PFBR. Apart from enhanced quality assurance of SG tubes, significant cost saving has been resulted in.

OUTLINE

Stringent quality control of modified 9Cr-1Mo steel tubes of SGs is ensured using eddy current (EC) and ultrasonic testing (UT) techniques during manufacture of tubes at Nuclear Fuel Complex (NFC), Hyderabad (Figure 1). Immersion ultrasonic testing is performed for detection of longitudinal and transverse defects and for measurement of wall thickness. Two 190 focussed angle beam transducers (5 MHz) and two 190 angle beam ultrasonic transducers are used in bidirectional scanning mode for detection of longitudinal and transverse defects, respectively. For eddy current testing, localized variations in magnetic permeability of the tube have predominant influence on the impedance of EC coil and do not allow full wall examination due to skin-effect. The permeability variations drastically reduce signal-to-noise ratio (SNR). To overcome this, DC saturation based EC testing procedure has been developed after systematic optimisation of saturation current, EC signal parameters, pulling speed, tube centering, and demagnetization enabling reliable detection of calibration defects. This optimised procedure is being routinely used at NFC for examination of SG tubes.

During ultrasonic examination of one lot of SG tubes, gross wall thickness variations extending 100 mm and in the depth range of 0.05 to 0.1 mm have been detected on the inner side surface thickness. These variations, attributed to improper pilgering of tubes, are within the acceptable limits. However, they produce large amplitude signals during saturation EC testing as typically shown in Figure 2. In order to detect defects, if any, present in those regions of the tubes, first of its kind, two-frequency EC technique has been developed. This approach involves

- Identification of defect-free tubes with known wall thickness variations based on ultrasonic data
- Introducing standard localised defects in wall thickness variation regions
- Optimisation of two-frequency mixing procedure for suppression of wall thickness variations
- Validation of mixing procedure to detect localised defects in wall variation region
- Determination of appropriate threshold for accept/reject criterion

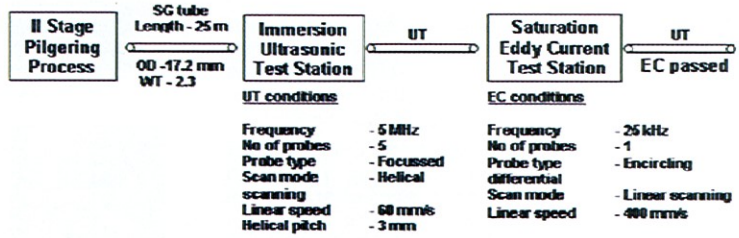

Fig. 1 : Non-destructive examination of steam generator

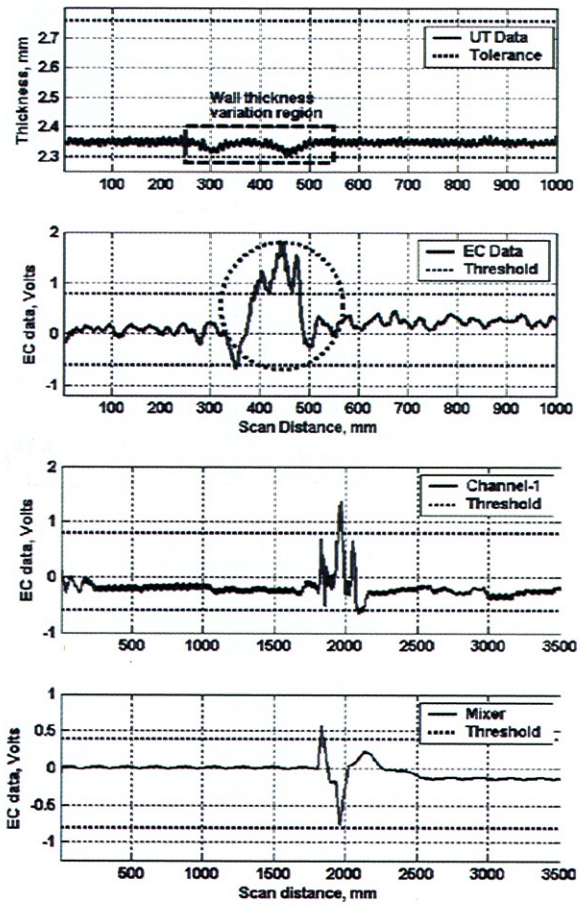

Fig. 2 : Ultrasonic wall thickness data using a 5 MHz normal beam probe and EC response for the thickness variation region (Top). Channel-1 and mixer channel EC data for a 1.2 mm diameter reference hole in wall thickness variation region (bottom)

■ ADDITIONAL INFORMATION

For validating this approach, the ultrasonic testing results of tubes are innovatively used to introduce reference defects. Six tubes which are ultrasonically defect-free and found to be having variations in wall thickness in the range of 0.012 to 0.130 mm are chosen for optimising the two-frequency mixing procedure. For recording and evaluation purpose, signals from channel-1 and mixer channel are oriented along the Y-axis of the strip chart recorder and the amplitude is measured. Using this procedure all recorded and rejected indications of channel-1 data from wall thickness variation regions are verified in the mixer channel.

■ GENERAL EXPLANATION RELATED TO THE DESCRIPTION

The channel-1 and mixer channel data for 1.2 mm diameter hole in the wall thickness variation region is shown in Figure 2. Through the use of a separate threshold, it is possible to reliably detect localised defects in the wall thickness variation regions.

The following criterion has been arrived at for acceptance and rejection of a tube based on the K_c value: ($K_c = A_d / A_r$, where A_d is the signal amplitude of a defect indication and A_r is signal amplitude of the 1.2 mm diameter reference hole)

$K_c < 0.5$ for accept

$0.5 > K_c < 1$ for Record and accept

$K_c > 1$ for Reject

■ BRIEF DESCRIPTION OF THEORETICAL BACKGROUND

As the tubes are ferromagnetic, D.C saturation based EC technique is employed. In this technique, the tube material is magnetised to near saturation region such that the variations due to magnetic permeability are minimized and the disturbing signals that reduce the signal-to-noise ratio (SNR) are not produced. In that situation, encircling differential EC probe embedded in the magnetising solenoid coil can detect localised defects. The observed disturbing signals during EC testing due to extended wall thickness variations are similar to that of the support plate signals from heat exchanger tubes using a bobbin type coil. In case of heat exchanger tubes, two-frequency mixing technique is adopted for eliminating the disturbing signal from support plate for detection of localised defects, if any, under it. In an analogous manner, a two-frequency approach is proposed to suppress the high-amplitude signals from the wall thickness variations which mask feeble indications of localised defects, if any. The challenge in implementing two-frequency mixing technique, in the present case, is the lack of proper reference standard replicating such extended wall thickness variations to tune the mixer settings for suppressing the disturbing signals. Further, fabrication of a reference standard replicating the wall thickness variations is difficult, essentially because, the variations are on the ID side. In view of this, this approach innovatively uses the ultrasonic thickness measurement data.

■ ACHIEVEMENT

This approach has been successfully implemented at NFC, Hyderabad to test more than 600 tubes having wall thickness variations. A total of 15 tubes have been rejected based on the conventional EC testing i.e. channel-1 threshold, due to localised defects in regions other than wall thickness variations. Four tubes have been rejected based on the mixer channel threshold, due to localised defects in wall thickness variation region. This effective procedure is routinely used at NFC for imparting stringent quality control of SG tubes. This approach can be applied to other similar situations in metallic tubes.

■ PUBLICATIONS ARISING OUT OF THIS STUDY AND RELATED WORK

1. B.P.C. Rao, S. Thirunavukkarasu, T. Jayakumar and Baldev Raj; INSIGHT-Non-Destructive Testing and Condition Monitoring (Journal of the British Institute of Non-Destructive Testing) **49** (2007) 698.
2. Internal Report No: IGCAR/NDED/EMSI/1/2005, July 2005.

Further inquiries:
Dr. B. P. C. Rao, Non Destructive Evaluation Division
Metallurgy and Materials Group, IGCAR, e-mail: bpcrao@igcar.gov.in

Establishing Acceptance Criteria for Minor Defects in Fast Breeder Reactor Fuel Pin End Plug Welds

■ EXECUTIVE SUMMARY

End plug welds on the fuel pins are the critical parts in the reactor core subassemblies. Perfect weld joints are practically impossible and a few minor weld defects are inevitable. In order to minimize the rejection of fuel pins during fabrication, the acceptance criteria has been established based on simulated creep tests and numerical simulations.

■ OUTLINE

The fuel pin clad is one of the critical elements in the core sub assembly, the weld configuration needs to be qualified thoroughly to ensure reliable operation without any failure so that this will not restrict the maximum achievable burnup in the reactor. Welding of end plugs on the fuel pins after filling the fuel pellets is the most challenging task in the fuel subassembly fabrication. This is because the end plugs are solid metal that is to be welded with thin clad tube (~ 0.3 mm). The defects are observed in the form of gas pockets (Fig 1). The effects of presence of gas pockets in the weld zones are investigated based on experimental and numerical simulations.

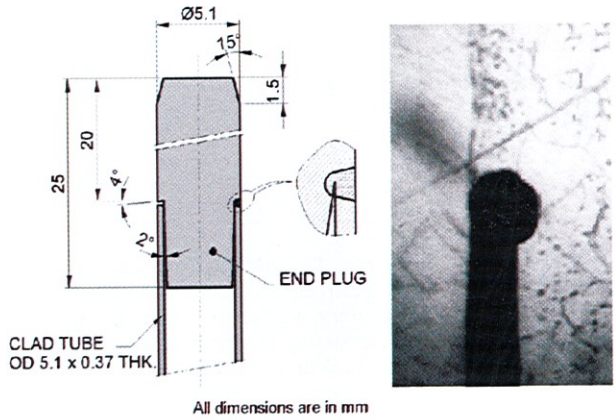

Fig 1: Details of end plug weld and a typical defect

Creep damage is the governing failure mode for this weld and hence, it is simulated experimentally on a few practically achieved end plug welds. The temperature in the region of the end plug is 823 K under steady state operation. The fission gas pressure accumulated at the end of 200 GWd/t burnup can be 12 MPa (maximum). The clad material is 20 % cold worked SS 316 M. Fuel pins with an end plug weld were tested at 973 K under an internal pressure of 20 MPa to account for possible uncertainties in the fission gas release phenomenon. The test setup is shown in Fig 2. A leak in the pin is the indication of failure which is detected by a fall in the steady state pressure in the chamber. Totally six pins were tested and leaks occurred after 1104 h (min) and 1188 h (max). The observed cracks were investigated thoroughly by image analysis. Fig 3 shows that the crack is longitudinal in nature caused by hoop stress effects and is observed just below the weld joint.

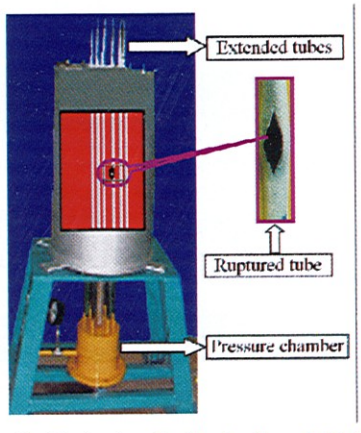

Fig. 2 : Test setup for the testing of 6 tubes

The permissible creep life of the end plug at 823 K has been extrapolated from the experimental data (lowest creep life is 1104 h at 973 K) using the Larson Miller Parameter. This yields the rupture life at the design temperature of 823 K, equal to 1.75×10^7 h. Even though, there can be inherent uncertainties in such large extrapolations, this gives a feel of permissible core life. Further, when compared to the permissible design lives (about 3 years) arrived at, the extrapolation is well within the normally acceptable range in such design exercise.

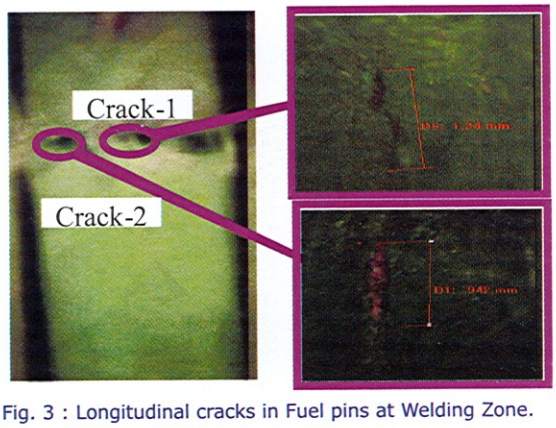

Fig. 3 : Longitudinal cracks in Fuel pins at Welding Zone.

A factor of safety on life is derived as 11, in consistent with RCC-MR With this, the design life is worked out as $1.75 \times 10^7/11$ h which is equal to 1.6×10^6 h (182 y). This is longer than the target life for the sub-assembly, even after accounting for possible life reductions under irradiation and fission gas environment at this location. However, the fuel pin life will be limited by the accumulated neutron dose with burnup and the end plug weld will not impose any restriction on

In order to predict the creep life using the design code RCC-MR, the required stresses are determined by inelastic analysis using the finite element method. Analysis is carried out including creep deformation / relaxation effects. Towards this, the fuel pin along with end cap (dimensional details are shown in Fig.1) is modeled using axisymmetric elements for the elastic-creep analysis by CAST3M computer code issued by CEA, France. Analysis is performed for sufficiently long time (1500 h) to get the saturated state of stress. The distributions of saturated σ_θ and σ_l are depicted in Fig.4. The peak σ_l occurs at the inner surface at the weld junction. The maximum occurs on the outer surface, at a location ~ 1.5 mm below the weld junction.

The creep crack initiation life is estimated using the experimentally generated average stress rupture curves as shown in Fig.5. The governing stress σ_{eq} is expressed as a function of both the Von-Mises stress (σ_{VM}) and the hydrostatic stress component (σ_H), as recommended in RCC-MR as:

$$\sigma_{eq} = 0.867.\sigma_{VM} + 0.4.\sigma_H.$$

Corresponding to the governing stress (σ_{eq}) of 133 MPa, the predicted life is 1050 h, which compares well with the test results (1104 h-minimum and 1188 h-maximum). It is to be noted that the σ_{eq} is nearly equal to (135 MPa) which initiates the crack in the longitudinal direction. The predicted location of crack initiation (~1.5 mm below the weld junction as extracted from Fig.4 is close to the observed crack location (Fig.3). The local bulging observed in the experiment (Fig.3) has been developed during the tertiary creep stage.

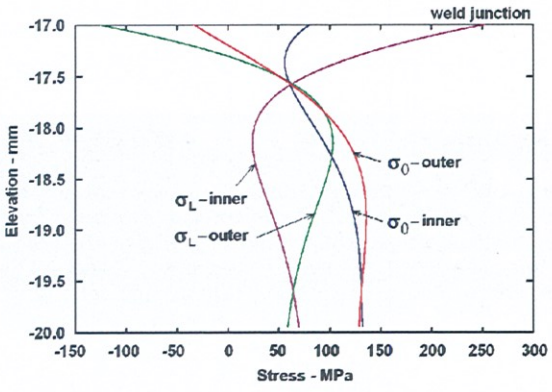

Fig. 4 : σ_θ and σ_l distributions

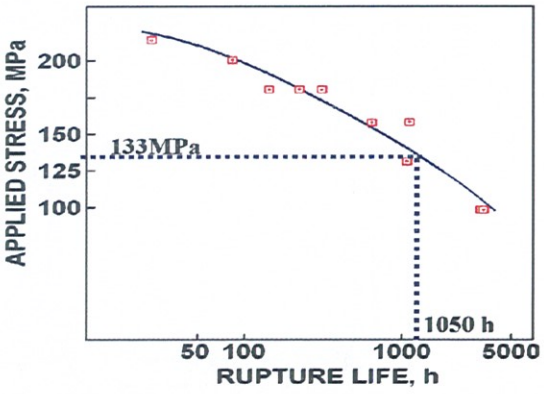

Fig. 5 : Creep rupture property of 20 % CW SS 316 M

■ ACHIEVEMENT

The challenging aspect is that the analysis method developed in conjunction with the design code RCC-MR could be able to predict life of the end plug weld accurately.

The investigation helps to ensure that the targeted fuel burnup will not be limited by accumulated creep damage in the end plug weld in general.

■ PUBLICATIONS ARISING OUT OF THIS STUDY AND RELATED WORK

P. Chellapandi, R.Srinivasan, S.C. Chetal and Baldev Raj, *International Journal of Pressure Vessel and Piping*, **83** (2006) 556.

Further inquiries:
Dr. P.Chellapandi, Nuclear Engineering Group
Reactor Engineering Group, IGCAR, e-mail: pcp@igcar.gov.in

Establishing design basis loads for Reactor Vault of Prototype Fast Breeder Reactor

EXECUTIVE SUMMARY

In the double wall concept adopted for the reactor vault of Prototype Fast Breeder reactor (PFBR), the inner wall which supports the safety vessel is subjected to its own self weight and weight of the safety vessel (250 t) which are insignificant. However, the same is subjected to very high loads (~6300 t), in case , a safe shutdown earthquake (SSE) occurs when the inter-space between main vessel and safety vessel is filled with liquid sodium consequent to a postulated leak in the main vessel. This article gives the basis of defining such high load on the inner wall along with experimental validations.

OUTLINE

Under normal operating condition with the absence of sodium in the inter-vessel space between main vessel and safety vessel, the loads transmitted to the inner wall is insignificant (the dead load of ~ 250 t only acts in the vertical direction). The major load acts on it during a seismic event under main vessel leaked condition. The sodium levels are indicated in Fig.1 during normal as well as main vessel leaked conditions.

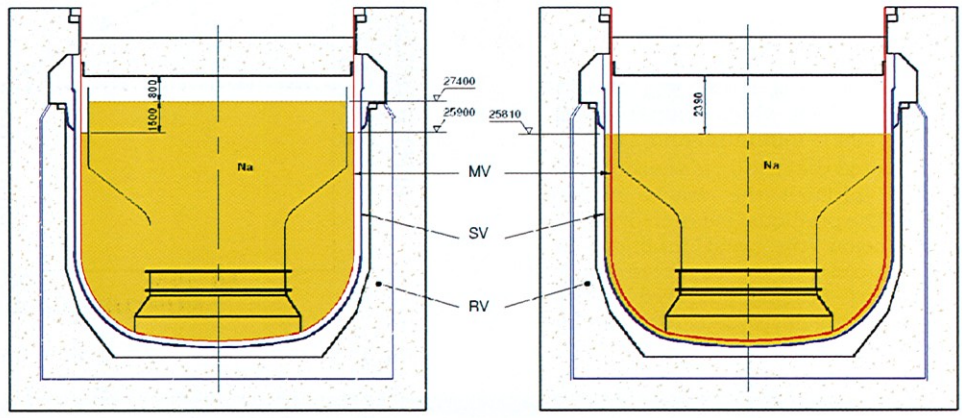

Normal condition

Main vessel leaked condition

Fig. 1 : Sodium levels in the reactor assembly

Towards demonstrating the structural integrity of reactor vault under such extreme loading condition, detailed finite element analysis has been carried out using CAST3M issued by CEA France.

The first step in the analysis is finite element discretisation of various geometries such as reactor assembly including reactor internals and sodium, sodium free levels and fluid-structure interactions, safety vessel and reactor vault. The finite element mesh thus developed is shown in Fig.2.

Generally seismic excitations have got maximum energies in the frequency range of 1-50 Hz. Accordingly, frequencies and associated modeshapes have been determined in the second step. The analysis indicates two important additional modes of natural vibration viz.in-plane and out-of-plane vibration of main vessel and safety vessel coupled by liquid sodium confined in the intervessel space. These modes are responsible for generating high inertia forces on the inner wall during SSE. The natural frequecies (4.4 Hz in-plane and 7.7 Hz out-of-plane) and associated mode shapes are shown in Fig.3. The in-plane mode contributes signicantly for the vault loadings, rather than out-of-plane mode.

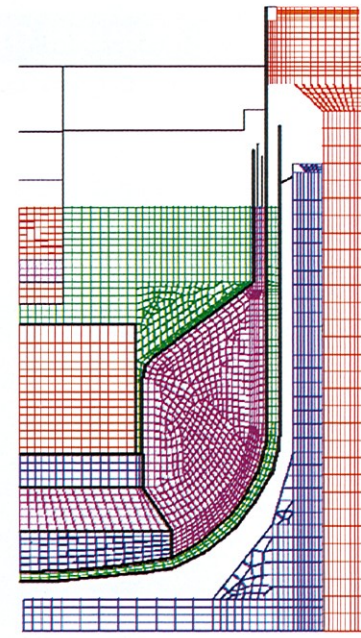

Fig. 2 : Finite element mesh

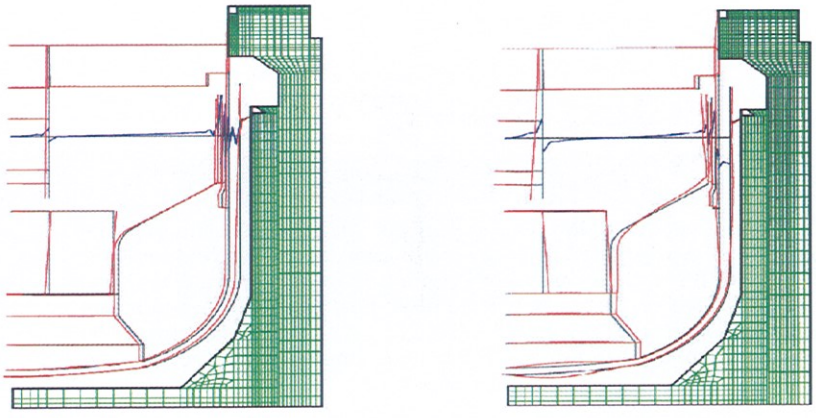

In-plane 4.4 Hz Out-of-plane 7.7 Hz

Fig. 3 : Important natural vibration mode shapes and frequencies

■ GENERAL EXPLANATION RELATED TO THE DESCRIPTION

The third step is the seismic response analysis by which seismic forces on the vaults are quantified. The vertical force on the inner wall experiences peak dynamic force of 270 t in the vertical direction which has to be added with about 250 t dead load acting at the support location. Further, additional shear forces and bending moments are also generated during seismic events. The peak shear force and bending moment values acting on the inner wall are insignificant when there is no leak in the main vessel (20 t and 500 t-m), which however increase significantly (250 t and 6300 t-m respectively) under SSE with main vessel leaked condition. For these forces, the structural integrity of inner wall is ensured as per AERB safety guide.

In order to validate the results, $1/10^{th}$ scaled down model was fabricated and experiments have been conducted in the 10 t capacity shake table available at IGCAR. The model has both main vessel and safety vessel made of aluminum and the reactor walls are simulated with aluminum shells filled with iron shots to simulate natural frequencies (Fig.4).

The forces transmitted to reactor vault are computed from the dynamic strain measurements made on the vessels. The model has also been analysed using CAST3M and results are validated (Fig.5).



Fig. 4 : Test model on shake table

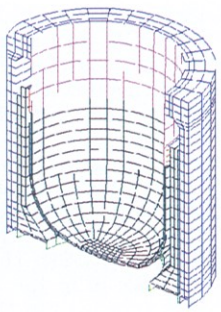

Fig. 5 : FE model for the test mockup

■ ACHIEVEMENT

Challenging and complex analysis with validation has been carried out to quantify the design basis loads for which reactor vault has been designed. This is very important to ensure the structural integrity of the reactor vault under extreme loading conditions.

This investigation provided an important input data for the reactor vault design and also raises the confidence of the reactor vault design.

Further inquiries:
Dr. P.Chellapandi, Nuclear Engineering Group
Reactor Engineering Group, IGCAR, e-mail : pcp@igcar.gov.in

Eddy Current Position Sensor for Diverse Safety Rod Drive Mechanism of Prototype Fast Breeder Reactor

EXECUTIVE SUMMARY

Diverse Safety Rod Drive Mechanism (DSRDM) is an important safety mechanism of PFBR. During reactor operation the Diverse Safety Rod (DSR) is held in position above the reactor core, by an electromagnet. On receiving the SCRAM signal, the electromagnet de-energizes, thus releasing the DSR, which drops under gravity. It is decelerated by the sodium dash pot after traveling free-fall distance and rests at bottom most position. It is mandatory to check whether the DSR has reached the bottom most deposited position and also to measure the free fall time. An Eddy Current based Position Sensor (ECPS) is designed. The sensor is tested in sodium environment using a model.

OUTLINE

In PFBR, there are three Diverse Safety Rod Drive Mechanisms (DSRDM) in the control plug, which hold the diverse safety rods (DSR). During normal operation, DSRs are held outside the active core region by an electromagnet. On receiving SCRAM signal, the electromagnet de-energizes and drops the DSR, which falls under gravity in sodium. DSR gets decelerated due to damping action of sodium in the dash-pot after traveling a certain free-fall distance. It is mandatory to check whether the DSR has reached the bottom most deposited position and also to measure the free fall time. An eddy current based position sensor (ECPS) compatible with the liquid sodium environment has been designed for incorporation in DSRDM to meet this requirement.

A critical constraint in this important requirement is that it is not possible for the sensor to have any electrical connectivity with the in-core components. To circumvent this problem an indirect excitation through inductive coupling is incorporated in the design of the sensor Also an innovative pick-up coil has been incorporated to isolate the extremely weak signals of the sensor and detect them with efficiency.

Schematic diagram of the sensor coil arrangement is shown in Figure 1. The primary and pick-up coils are located in the mobile assembly of DSRDM and secondary, signal transfer and sensor coil, which are connected serially are located on the stationary DSR sheath side. The secondary coil is placed concentric to the primary and similarly signal transfer coil is placed concentric to the pick-up coil. The induced voltage in secondary would drive a circulating current in all the three coils on secondary side. The magnitude and phase of this current depends on the total impedance of coils on secondary side. When the DSR is dropped, the sodium in the DSR subassembly is displaced by DSR. The impedance of sensor coil changes with the DSR is in the deposited condition as compared to non-deposited condition. Accordingly, flux linkage with pick-up coil varies, thereby changing the voltage induced in it. This indicates presence of DSR near sensor coil.

Space constraint is a challenge for accommodating ECPS in DSRDM. A mechanically compliant design has been adopted. The design (Fig.2) was arrived after going through a number of rigorous design iterations. A detailed parametric study was done with respect to coil design, DSR material, and operating frequency using computer simulation to arrive at the balanced requirement of both the space constraints and high sensitivity.

The ECPS model (Fig.3) was fabricated for testing. All coils were made with MI cables for suitability to high temperature and sodium service. It was first tested successfully in air. Later the ECPS model was introduced in Test Vessel-2 of SILVERINA (Commissioned during SILVER Jubilee of IGCAR for sodium(Na) testing). The tests were conducted at various temperatures in sodium. Sensitivity of the order of 10% to 13% was achieved at 550 °C. This sensitivity is sufficient for detection of DSR.

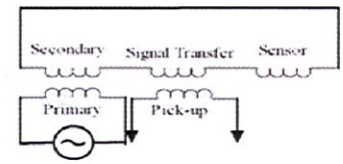

Fig 1: Schematic diagram of ECPS

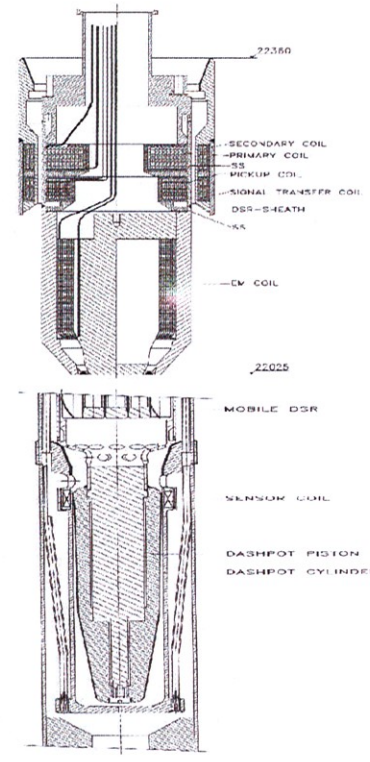

Fig. 2 : Optimised design of ECPS



Fig. 3 : ECPS testing in sodium environment

■ ADDITIONAL INFORMATION

Eddy current based sensors are widely used as position sensors in many engineering applications and as proximity detectors in security applications. These operate on the principle of magnetic induction. However, these sensors as such cannot be adopted for our application due to the critical restriction that it is not possible for the sensor to have any electrical connectivity with the in-core components. The innovative indirect excitation adopted in this design overcomes this restriction. The eddy current position sensor operates by detecting the change in the sensor coil impedance, as a result of a target approaching the vicinity of the sensor. But due to the restriction in accessing the output from the sensor coil, an innovative pick-up coil is designed to measure the change in impedance.

■ GENERAL EXPLANATION RELATED TO THE DESCRIPTION

There are three Diverse Safety rod (DSR) in the core of the PFBR. During normal operation of the reactor, DSR is held outside the active core region by electromagnet, which is at the bottom end of Diverse Safety Rod Drive Mechanism (DSRDM). DSR moves inside a stationary hexagonal sheath. Both together are called as Diverse Safety Rod- Sub Assembly (DSR-SA). DSRDM is partially immersed and DSR-SA is fully immersed in hot sodium. Whenever there is a SCRAM signal, the electromagnet holding the DSR gets de-energised and the DSR falls under gravity. At the end of the free fall, it is decelerated by a sodium dash pot and is brought to rest. The specified free fall time of DSR plus the response time of the electromagnet should be within prescribed limits to ensure fast shutdown of the reactor. We need a position indication system to record the free fall time/total travel time of DSR whenever it is dropped into active core during SCRAM action. The free fall time is defined as the time elapsed between the instant at which the DSR is detached from the Electromagnet of DSRDM and the instant at which the dashpot action is initiated. The test set-up for sodium testing of ECPS is shown in Figure.4. The primary coil is excited, which generates induced voltage in the secondary side. The current in the sensor coil, which is located in the dashpot region, generates an oscillating magnetic field, which induces eddy current as the target (DSR with ferromagnetic piston) traverses near the sensor coil thus reducing the impedance of the coil. The restriction in accessing the output from sensor coil is overcome by the novel design of pair of signal transfer and pick-up coils. Hence the movement of the DSR, near the sensor coil is reflected as change in impedance in sensor coil, which is sensed via the pick-up coil.

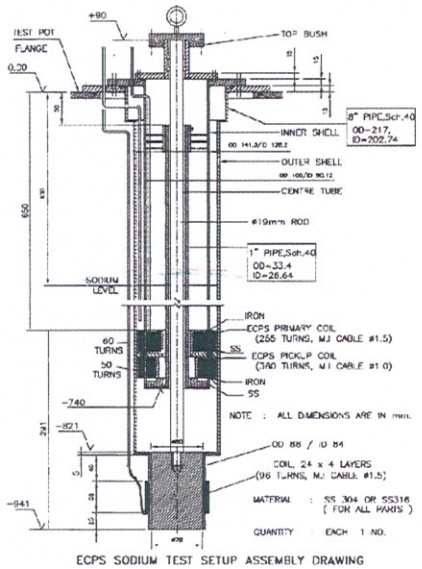

Fig. 4 : Test set-up for sodium testing of ECPS

■ BRIEF DESCRIPTION OF THEORETICAL BACKGROUND

According to the Faraday's law of Induction, the induced eddy current flows in an electrical metal conductor (target), if the conductor is located in a time changeable magnet field. The magnet field is generated here by an alternating current flowing in a coil. The eddy current generates an opposite magnet field, which superimposes with the exciting magnet field. As a consequence, the impedance of the sensor coil changes. Similarly the ECPS works on the principle of mutual inductance. As the ferromagnetic piston of the DSR approaches the sensor coil, the impedance of the coil changes, which in turn varies the impedance of all the three coils in the secondary side. The change in impedance in the sensor coil is sensed using mutual inductance through a pick-up coil. The change in impedance indicates the presence of DSR near the sensor coil.

■ ACHIEVEMENT

An indirect excitation has been incorporated in eddy current based position sensor for the first time. An innovative pick coil has been introduced, again for the first time, to isolate the extremely weak signals and detect them with efficiency. The design is optimised using computer simulations to meet the dual requirement of both the space constraints and high sensitivity.

■ PUBLICATIONS ARISING OUT OF THIS STUDY AND RELATED WORK

1. S. Sosamma, R. Vijayashree and C. Babu Rao, Report No. PFBR/31130/EX/1004/R-A, July, 2004.
2. S.K. Dash, S. Sosamma and G. Vijayakumar, Report No. IGC/FRTG/STG/ED&SS/99118/EX/3010/REV-A, Dec 2005.
3. Prashant Sharma, S.K. Dash, G. Vijayakumar and S. Sosamma, Report No. PFBR/31130/EX/1009/REV A, Feb 2007.

Further inquiries:
Dr. C. Babu Rao, Non Destructive Evaluation Division
Metallurgy and Materials Group, IGCAR, e-mail: cbr@igcar.gov.in

Optical Fibre based Distributed Sensor for Temperature Measurement

■ EXECUTIVE SUMMARY

At present, the temperature measurement in the sodium loops is done at a few locations using conventional sensors. It is desirable to make measurement at as many locations as possible. A Rama.. scattering based optical fiber sensor is developed for distributed temperature measurement. This sensor has been tested on a test loop erected for this purpose.

■ OUTLINE

At present, the temperature measurement in the sodium loops of breeder reactors is done at a few locations through thermo-wells and Resistance-Temperature Detectors (RTD)s. It is likely that temperature variations can occur at intermediate points also. Some of these local temperature excursions may cross the safety limits, which will not be detected. It is desirable that such events be detected such that the monitoring is comprehensive and the damage, if any, can be minimized. This requires distributed temperature measurement. A programme is undertaken to study the feasibility of using optical Fibre sensor for such distributed temperature measurement.

A distributed temperature measuring system based on Raman scattering in optical fibres is developed in association with Raja Ramanna Centre for Advanced Technology (RRCAT), Indore.

In order to study the feasibility of using the fibre sensor in sodium circuits, a test loop has been designed and erected in Hall 3 (Fig. 1). The test loop is provided with automated differential heating system and equipped with conventional temperature sensors. The optical fibre sensor is carefully laid on the loop along with the conventional sensors. Measurements were made using both conventional thermocouples and Raman scattering based fibre sensor system. Optical fibre based measurements were within 5 per cent error limits of the measurements made using thermocouples. In addition, temperature could be recorded all along the pipe length (Fig.2).

The system will further be tested in the sodium test loop and later will be deployed for to the sodium circuits in reactors.



Fig. 1: Test loop for testing optical fibre based distributed temperature sensor

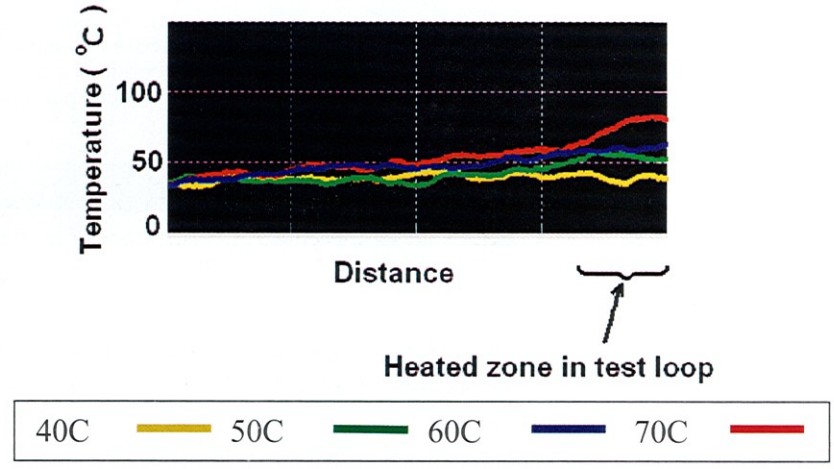

Fig. 2 : Typical temperature profiles on the test loop obtained using optical fiber based Raman sensor

■ ADDITIONAL INFORMATION ABOUT FIBER OPTIC SENSORS

Optical fibre based distributed sensors have been widely used to monitor temperature. The main advantage of the system is that the fibre itself is the sensing element. Distributed temperature sensing technology shows real advantages over conventional temperature sensing technology when a temperature profile of the installation is required or when a large number of sensing points is crucial. Therefore this technology lends itself to long length applications (pipelines, tunnels, power cables, conveyor belts), applications where only small sensors can access (oil wells) and safety critical applications where it is important to have all points monitored (refineries, LNG plants, electrochemical processes).

■ GENERAL EXPLANATION RELATED TO THE DESCRIPTION

Raman scattering based distributed temperature sensor comprises the following. A pulsed laser is injected into the optical fibre which is the sensing element. In the fibre the photons interact with the molecules of the fibre material. The spectrum of the backscattered light includes the Rayleigh, the Brillouin and the Raman backscattered light. The Raman backscattered light is caused by thermally influenced molecular vibrations. Consequently, the Raman backscattered light carries the information on the temperature of the fibre and can be used to obtain information about the temperature distribution along the fibre. The Raman backscattering light has two components: the Stokes (I_s) and the Anti-Stokes (I_a) component (Fig. 3). They can be separated from the primary and the Rayleigh backscattered light due to their differences in wavelength. The Stokes component is only weakly dependent on temperature, while the Anti-Stokes component shows a strong relation to temperature. The ratio of the intensities of Stokes and Anti-Stokes components is a measure of temperature. Since the injected light is a pulse of a few nano seconds, the time of arrival of instantaneous back scattered intensity can be correlated with the distance along the fibre length from where it is scattered.

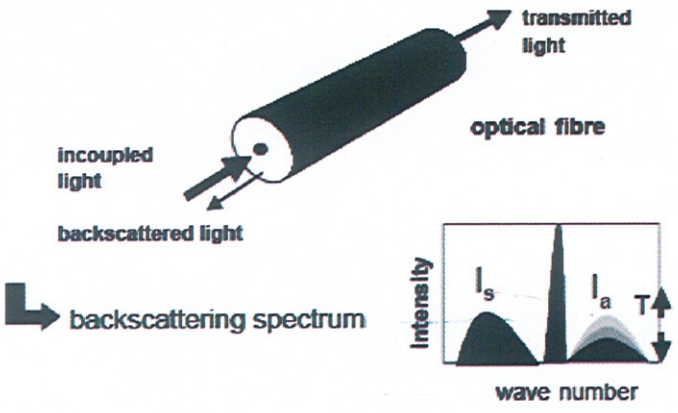

Fig. 3 : Measuring Principle

■ BRIEF DESCRIPTION OF THEORETICAL BACKGROUND

The ratio of the intensities of the Anti-Stokes to the Stokes line shows temperature dependence and is given by

$$\frac{I_a}{I_s} = \frac{(n_o + n_k)^4}{(n_o - n_k)^4} \exp\left(\frac{-hcn_k}{kT}\right)$$

I_a - intensity of Anti-Stokes-component, I_s - intensity of Stokes-component
n_o - light wave number, n_k - shift of light wave number
h - Planck action quantum c - velocity of the light within the optical fiber
k - Boltzmann-constant T - temperature

■ ACHIEVEMENT

Optical fibre is laid on a test loop, and distributed temperature measurement is achieved using a novel method based on scattering.

■ PUBLICATIONS ARISING OUT OF THIS STUDY AND RELATED WORK

1. C. Pandian, S. Sosamma, C.Babu Rao, T.Jayakumar, Baldev Raj, Kasinathan, N.Murali, Vishal Paunikar, Suresh Kumar, KK.Rajan, S.D.V.S.J. Raju, Manoj Kumar Saxena, Sanjay Kher, Indore National Symposium on Science and technology of Glass and Glass –Ceramics(NSGC-06) Sept 15-16 2006 at BARC, Mumbai
2. C. Pandian, A.K.Jena, C.Babu Rao, T.Jayakumar, Baldev Raj, PHOTONICS-2006, Dec 13-16, Hyderabad.
3. Manoj Kumar Saxena, S.D.V.S.J. Raju , Sharma, Sanjay Kher, Pandian.C, Sosamma.S, C.Babu Rao, M.Kasinathan, N.Murali, T.Jayakumar, Baldev Raj, National Laser Symposium-06, Dec 5-8 at RRCAT, Indore.
4. SPIE Optics East, September 9-12, 2007, Boston, U.S.A.

Further inquiries:
Dr. T. Jayakumar, Non Destructive Evaluation Division
Metallurgy and Materials Group, IGCAR, e-mail: tjk@igcar.gov.in

Remote Field Eddy Current Technique for In-Service Inspection of Ferromagnetic Tubes

EXECUTIVE SUMMARY

Eddy current non-destructive evaluation of installed ferromagnetic tubes is difficult due to variations in magnetic permeability. D.C. Saturation method can not be applied for small diameter tubes such as modified 9Cr-1Mo tubes of steam generators of PFBR due to lack of space for placing magnetizing coils. In this regard, comprehensive remote field eddy current (RFEC) technology comprising of high-performance instrument, finite element model optimized flexible tungsten-carbide/depleted-Uranium probes capable of negotiating the expansion bend regions by gravity and a wavelet transform based signal processing method for detection of defects in tubes (even in the presence of electrically-conducting sodium deposits on the tube outer surface and also in the defects was developed). This technology has demonstrated reliable detection of 10% wall thinning in the tubes and has been successfully employed for in-service inspection (ISI) of full-scale SG test facility built at IGCAR.

OUTLINE

Periodic in-service inspection of steam generators (SG) is important. For inspection of ferromagnetic SG tubes, remote field eddy current technique is a natural choice, essentially because conventional eddy current testing is inadequate. As shown in Figure 1, RFEC technique uses separate exciter and receiver coils and low-excitation frequencies for non-destructive examination of metallic tubes from tube-side. In this technique, induced voltage in a receiver coil placed at 2 to 3 tube diameters away from the exciter coil is measured using a lock-in amplifier. Reliable detection and sizing of defects in steam generator tubes requires that the excitation frequency is optimized and the receiver coil is positioned in remote-field zone. In this regard, detailed finite element analysis has been carried out to examine the electromagnetic field-defect interactions in the RFEC technique using an axi-symmetric finite element model and a 3-D code developed in-house. Triangular and hexahedral meshes have been employed in axi-symmetric and 3-D models, respectively and RFEC signals due to various types of defects have been predicted at different frequencies and inter-coil spacing. The test frequency, excitation current and receiver coil location and its size have been optimised using the models. Figure 2 shows predicted induced voltage in receiver coil at different frequencies for different coil positions for frequency optimisation based on RFEC intensity and measured induced voltage at 1100 Hz for model validation.

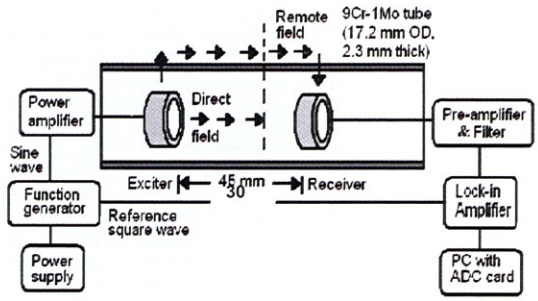

Fig. 1 : Schematic of remote field eddy current testing

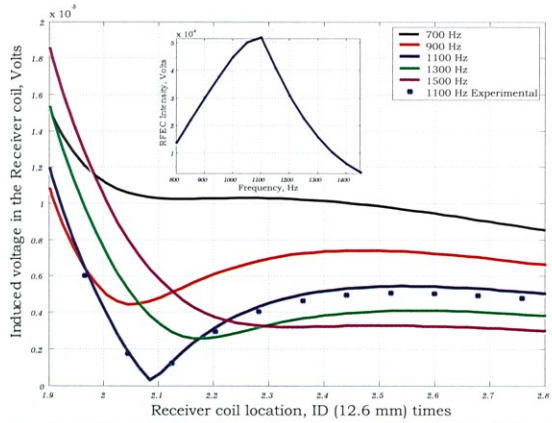

Fig. 2 : Predicted induced voltage in receiver coil at 700, 900, 1100, 1300 and 1500 Hz as a function of receiver coil location and measured induced voltage at 1100 Hz. The inset shows the intensity of back entered remote field with excitation frequency

ADDITIONAL INFORMATION

The SGs have only one side access (top) and the tubes have expansion bends at approximately one-thirds height. In this regard, flexible RFEC probes have been developed for easy negotiation of probe through the bend regions. High density tungsten carbide and depleted uranium rings have been used for easy sliding of the probe by gravity during probe lowering and controlled pulling by winch mechanism (Figure 3). High sensitivity instrument with lock-in amplifier, filters and low-distortion power amplifiers has been developed for enhanced detection of wall loss defects in tubes. Wavelet transform based signal processing method and duel-frequency method have been developed to suppress signals due to bend regions and support plates enabling detection of defects in these regions. As sodium is used as coolant on the shell side, presence of sodium deposits in defective regions, if any, is expected to influence the RFEC signals, essentially because sodium is electrically conducting. In this regard, experimental studies are carried out in this regard, by exposing a few SG tubes having uniform wall loss grooves to sodium environment in a specially designed test vessel (Figure 3). Definite change in the shape of RFEC signals is observed and it is possible to approximate the volume of sodium deposited in defects. Further, using an invariant signal parameter quantitative characterization of defects has been possible despite the presence of sodium in the defects.

■ GENERAL EXPLANATION RELATED TO THE DESCRIPTION

RFEC technique uses separate exciter and receiver coils that are kept inside tube. The separation distance is usually 2 to 3 times the inner diameter of the tube. Low frequency sinusoidal excitation usually in the range of 50 Hz to 2 kHz, is applied to the exciter coil to generate time varying magnetic fields. The eddy currents induced in the tube wall, as a result, generate secondary magnetic fields. The primary and secondary fields travel axially and radially. In such a situation, there exist two regions of importance: i) the region inside the tube wall where the field due to the exciter coil decays exponentially along the axial direction, called the direct field region and ii) the region inside the tube wall where the concentrated flux in the tube wall enters back into the tube at a distance where the direct field component is less, called the remote field region. The magnetic flux in the remote field region is attenuated and lagged in phase. When receiver coil is placed in the remote field region, the back entered magnetic flux induces a voltage which carries the information of condition of tube wall. The amplitude and phase lag of this induced voltage are measured and correlated with the wall loss or the presence of defects. The exciter and receiver coils are moved in tandem and the trajectory thus formed by the amplitude and phase lag of the induced voltage during the coils transit over a defect is called RFEC signal.

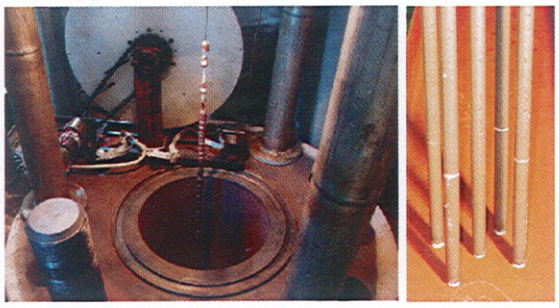

Fig. 3 Flexible RFEC probe with Tungsten carbide and depleted uranium rings used for ISI of SG tubes (left) and photograph showing residual sodium in grooves (left) after draining sodium in sodium studies

■ BRIEF DESCRIPTION OF THEORETICAL BACKGROUND

As the tubes are ferromagnetic, D.C saturation based EC technique is employed. In this technique, the tube material is magnetised to near saturation region such that the variations due to magnetic permeability are minimized and the disturbing signals that reduce the signal-to-noise ratio (SNR) are not produced. In that situation, encircling differential EC probe embedded in the magnetising solenoid coil can detect localised defects. The observed disturbing signals during EC testing due to extended wall thickness variations are similar to that of the support plate signals from heat exchanger tubes using a bobbin type coil. In case of heat exchanger tubes, two-frequency mixing technique is adopted for eliminating the disturbing signal from support plate for detection of localised defects, if any, under it. In an analogous manner, a two-frequency approach is proposed to suppress the high-amplitude signals from the wall thickness variations which mask feeble indications of localised defects, if any. The challenge in implementing two-frequency mixing technique, in the present case, is the lack of proper reference standard replicating such extended wall thickness variations to tune the mixer settings for suppressing the disturbing signals. Further, fabrication of a reference standard replicating the wall thickness variations is difficult, essentially because, the variations are on the ID side. In view of this, this approach innovatively uses the ultrasonic thickness measurement data.

■ ACHIEVEMENT

The in-house technology has demonstrated performance superior to the international state-of-the art. Using this technology along with a winch mechanism for probe handling it is possible to reliably detect and size 10% wall thinning in the tubes. This technology has been successfully used for in-service inspection of full-scale SG test facility built at IGCAR. This technology development is a major step and an essential regulatory requirement for safe and reliable operation of SGs of FBRs. This is being implemented in the PFBR being constructed at Kalpakkam. This technique can be readily applied to other ferromagnetic tubes in heat exchangers, boilers and condensers for detection of defects and corrosion wall loss.

■ PUBLICATIONS ARISING OUT OF THIS STUDY AND RELATED WORK

1. S. Thirunavukkarasu, B.P.C. Rao, S. Vaidyanathan, T. Jayakumar, P. Kalyanasundaram, Internal Report No: PFBR-01950-DN-1007-Rev-A.
2. S. Thirunavukkarasu, R. Chellapandian, B. Sasi, B.P.C. Rao, T. Jayakumar, K.V. Kasiviswanathan, P. Kalyanasundaram, Internal Report No: IGCAR/NDED/EMSI/SGTF-RFEC/2006/1.

Further inquiries:
Dr. B. P. C. Rao, Non Destructive Evaluation Division
Metallurgy and Materials Group, IGCAR, e-mail: bpcrao@igcar.gov.in

Impact Echo and Ultrasonic Examination Methods for Evaluation of Sodium Fire Exposed Concrete

EXECUTIVE SUMMARY

Impact echo and through transmission low frequency ultrasonic (500 kHz) studies have been carried out on concrete blocks and extracted core specimens, before and after exposure to sodium fire, in order to establish nondestructive methodologies for assessment of damage consequent to exposure to sodium fire. The decrease in ultrasonic velocity and increase in ultrasonic attenuation are observed upon exposure to sodium fire. Further, the graded damage from the exposed surfaces due to sodium fire is characterized by carrying out studies on the core specimens extracted from different depths. Ultrasonic velocity and attenuation measurements were correlated with the compressive strength determined on the cylindrical core specimens extracted from the sodium fire exposed blocks. Further, the damage is found to be confined to within about 70 mm deep from the surface exposed to the sodium fire. The study also indicated that impact echo testing can be used in-situ to detect damage to the concrete structures having one side access only.

OUTLINE

Sodium resistant lime stone aggregate concrete is used as sacrificial layer over the structural concrete in the steam generator building floors of PFBR, where hot sodium is likely to spill during any leakage. It is required to optimize the thickness of the sacrificial layer and develop a non-destructive methodology for assessment of damage to concrete structures due to sodium fire in case of any sodium leakage. With these objectives in view, systematic studies have been undertaken to develop impact echo and low frequency ultrasonic based nondestructive methodologies for assessment of damage to concrete structures due to sodium fire and also to determine the depth of damage consequent to sodium fire.

A set of lime stone aggregate concrete blocks of dimensions 600 x 600 x 300 mm having a cavity of dimension 300 x 300 x 150 mm at the center of the larger area side (Fig. 1) was cast. After 28 days of curing of the concrete blocks, 25 kg of sodium at about 723 K was poured in the cavity. Sodium was burnt in the cavity for about 30 minutes. Impact echo studies were carried out on these concrete blocks before and after the sodium fire exposure. Ultrasonic velocity measurements were also carried out on back surface of the blocks using double transducer impact echo technique. Impact echo testing was carried out at centers of 75 mm square grids, marked on all the surfaces of the blocks. Low frequency ultrasonic velocity and attenuation measurements were carried out on the cylindrical core specimens of 50 mm diameter extracted from the as-cast and sodium fire exposed blocks. Figure 2 shows the variation in velocity with average distance from sodium exposed surface. Compressive strength measurements have been carried out on 80 mm long core specimens and these were correlated with the ultrasonic velocity and attenuation.

All the cubes exhibited similar acoustic properties in the as-cast condition. Both impact echo testing and low frequency (500 kHz) ultrasonic measurements indicated decrease in ultrasonic velocity and increase in attenuation due to exposure to sodium fire. This is attributed to damage to the concrete blocks, in terms of generation of micro-cracks and decrease in water content. Compressive strength was also found to decrease due to exposure to sodium fire. The ultrasonic velocity could be correlated linearly with the compressive strength in the core specimens.

These studies clearly demonstrated the usefulness of impact echo and ultrasonic techniques for evaluating the damage in sodium fire exposed concrete. The results also indicated that thickness of the sacrificial layer of sodium resistant concrete required for preventing damage to the main structure and thus ensuring its integrity is about 70 mm.

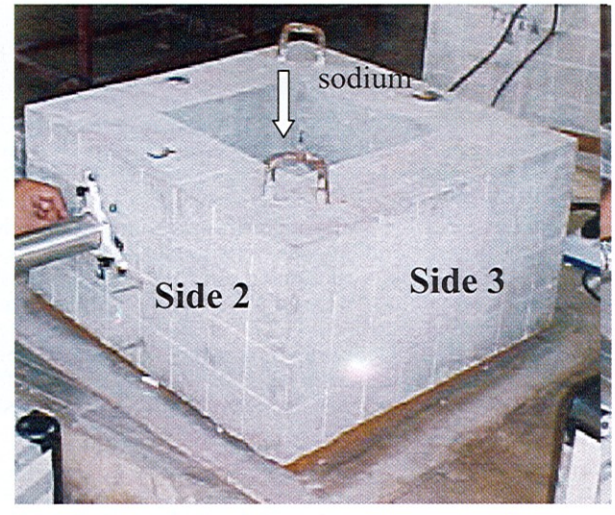

Fig. 1 : Photograph of a typical concrete block

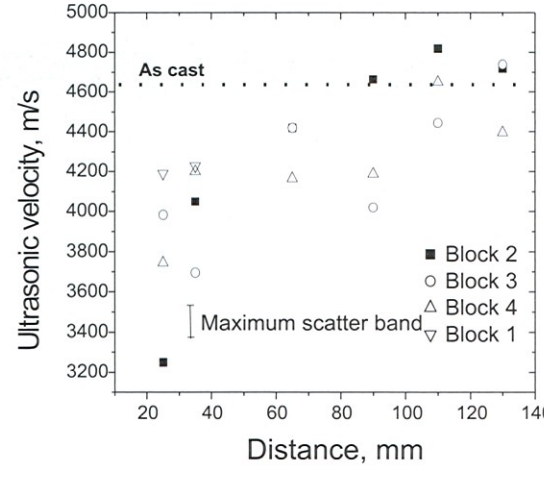

Fig. 2 Variation in ultrasonic velocity with average distance from sodium exposed surface

■ IMPACT ECHO TESTING

The impact echo testing is developed mainly for the inspection of highly attenuating structures such as concretes. Impact of a spring loaded steel ball against the structures generates stress waves/low frequency sound waves that propagate in the material. The stress waves get reflected at the interfaces/defects. Reception of these waves and analysis of them hence provides information about the defect and thickness (structure) information. The analysis of the received signals is done in frequency domain to extract the required information. Use of impact echo method has several advantages such as easy application on rough surfaces, very well near surface resolution and adequacy of only one side access. The additional benefit of deployment of using this technique is that they are portable and hence in-situ assessment of thick civil structures can be made reliably.

■ GENERAL EXPLANATION RELATED TO THE DESCRIPTION

Impact echo testing is a method based on the use of stress waves for non destructive evaluation of concrete structures. Impact of spring loaded steel balls are used to generate low frequency stress waves in the structure and produce transient resonances whose frequencies are related to location of flaws. The piezoelectric transducer detects displacements perpendicular to surface caused by reflected stress waves and the signals are analyzed in frequency domain. The inverse of the frequency obtained, provides the information about the flaw location. The experimental set up for impact echo testing is given in Fig. 3.

The mathematical relation to find out thickness/flaw location from the frequency is given below:

$$T = \beta \frac{C_p}{2f}$$

T=Thickness; Cp= Wave velocity; f=Frequency; β=Shape factor

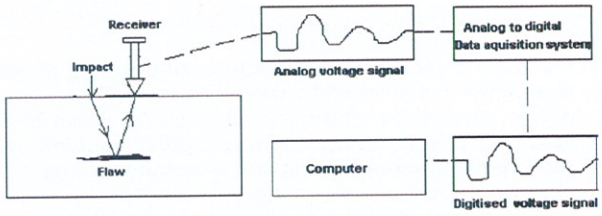

Fig. 3 Experimental set up for impact echo testing

■ BRIEF DESCRIPTION OF THEORETICAL BACKGROUND

The damage caused to the concrete structure upon exposure to sodium, in terms of generation of micro-cracks and evaporation of moisture, leads to increase in ultrasonic attenuation and decrease in ultrasonic velocity. Increase in ultrasonic attenuation is essentially caused by the increased scattering of ultrasonic waves due to presence of micro cracks, whereas, decrease in ultrasonic velocity is caused by the reduced modulus.

■ ACHIEVEMENT

The present study revealed that the damage due to sodium fire is essentially confined to within about 70 mm deep from the surface exposed to the sodium fire. This indicated that thickness of the sacrificial layer of sodium resistant concrete required for preventing damage to the main structure and thus ensuring its integrity is about 70 mm. The study also indicated that impact echo testing can be used in-situ to detect damage to the concrete structures having one side access only.

■ PUBLICATIONS ARISING OUT OF THIS STUDY AND RELATED WORK

1. Anish Kumar, K.V. Rajkumar, Govind K. Sharma, K.B. Dhayalan, V. Venkatachalapathy, T. Jayakumar, C.S. Pillai, S.E. Kannan and Baldev Raj, NDE 2005, Dec. 2005, Kolkata
2. T. Jayakumar, Anish Kumar, K.V. Rajkumar and Govind Kumar Sharma, Report No. IGC/IE/NAC/2005 dated

Further inquiries:
Dr. T. Jayakumar, Non-Destructive Evaluation Division
Metallurgy and Materials Group, IGCAR, e-mail: tjk@igcar.gov.in

Continuous Type Oil Level Sensors for the Dashpots of Control and Safety Rod Drive Mechanisms in Prototype Fast Breeder Reactor

EXECUTIVE SUMMARY

Pulsating type high precision oil level sensors have been developed from concept to industrial grade products entirely through in-house efforts in IGCAR. The development includes associated pulse handling, data processing and presentation devices for real time monitoring of oil levels in the dashpots of Control and Safety Rod Drive Mechanisms (CSRDMs) in PFBR. The sensors provide continuous indication of oil levels in the range 0 – 60 mm within the active sensing region. These will capture rapidly the sudden change in oil level in the event of scram action of the control rods, satisfying the major purpose for which the level sensors have been developed. Real time measurement with high precision may also enable monitoring of onset of oil leak, if any, during normal operation of the reactor.

OUTLINE

Oil level is sensed by sensitive monitoring of small shift in capacitance of a vertically mounted specially designed capacitive device, caused by change in oil level. An assembly of uniformly spaced multiple number of rectangular stainless steel plates is the capacitor assembly whose capacitance changes on account of change in fractions of two dielectric media, namely oil and air (or any inert gas), within the electrode gaps. The capacitor is in the timing circuit of a compact logic gate oscillator and, hence, shift in digital pulse frequency at the output of the oscillator is directly related to change in oil level. Photograph of a set of nine sensors is shown in Figure 1.

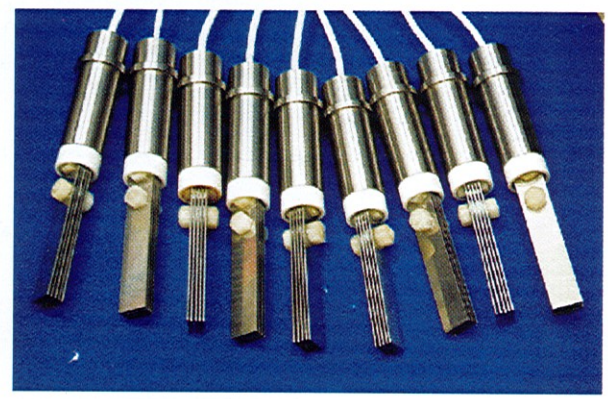

Fig. 1 : Oil level sensors for the dashpots of CRDMs in PFBR

The oil level sensor and the dielectric type thermal sensor are capacitive components in specially designed low power consuming logic gate oscillator circuits which are embedded in the probe head and require only 5V DC supply from an external source. The trains of rectangular pulses at the outputs of the level and thermal sensors from a given probe are processed by two independent signal processing and data presentation systems (System-A and System-B) (Fig. 2).

Each in-house designed and made stand-alone embedded processor in System-A performs the following functions: (i) simultaneous pulse counting in six channels for determination of pulse frequencies at the outputs of level and thermal sensors from three probes, (ii) evaluates quadratic equations for conversion of pulse frequencies to heights of oil level from the tips of the level sensing electrodes after neutralisation of thermal effect, and (iii) displays and stores oil level data at two seconds interval.

The other laboratory made system, System-B, on the other hand, is a computer based data acquisition, processing and presentation unit with built-in user friendly features in addition to those available with System-A. Serial communication with a computer is established through an in-house developed 18-channel embedded pulse handling unit that receives pulses from nine probes simultaneously and count them for the preset duration. It transmits pulse count data to the computer for further processing, display and storage. The dedicated application software enables real time level visualisation, graphic presentation of level data as a function of time, on-line availability of stored data for last 24 hours in 96 time segments for quick review and analysis, easy navigation between probes and time segments, zooming for ascertaining minor level shifts etc.

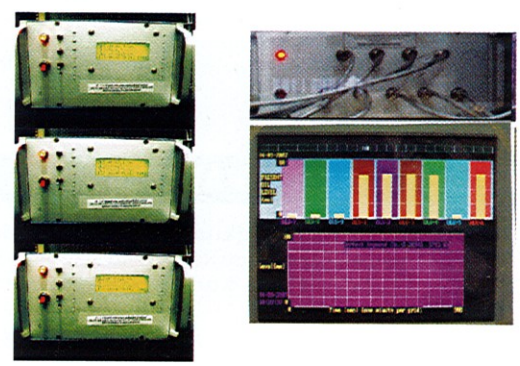

Fig. 2 : In-house developed two independent systems for pulse handling, data processing and presentation for real time applications of the sensors: SYSTEM-A (left) and SYSTEM-B (right)

The pulse frequencies are measured at 5 mm interval over the full range of 0 – 60 mm along the entire oil level sensing span. Level height from the tip of the sensing electrodes (h) in millimeter Vs. frequency (f) in kHz are numerically fitted to yield a quadratic equation, [$h = a.f^2 + b.f + c$], which is used later in the system software to convert on-line the output frequencies to oil level heights during operation of the level sensor. Such calibration equations are sensor specific and, hence, are obtained separately for every probe. An example of numerically fitted calibration data is shown in the Figure 3.

■ NEUTRALISATION OF MINOR TEMPERATURE EFFECT

Sensors are designed to operate with hot oil. The embedded thermal sensor at the probe head permits neutralisation of the overall thermal effect through incorporation of our own pulsating type thermal sensor in each level probe. Minor thermal effect on a typical sensor output for a given oil level can be seen in the time dependent measurement with the imposed thermal profile as recorded by the built-in thermal sensor. Slightly negative slopes (df_t / df_l), derived from the straight line fitted thermal sensor output (f_t) vs. the level sensor output (f_l) are established first and then used later during real time measurements for on-line conversion of the level sensor output frequency at temperature t (f_l') to that at the calibration temperature (f_l^c) before application of the calibration relationship for determination of the height of oil level in millimeter. These slopes are determined for every probe.

■ PERFORMANCE AND RUGGEDNESS

High performance of the sensors stems mainly from direct generation of primary signal in the digital domain. The oil level influences the oscillation frequency of the specially designed very low power consuming oscillator embedded right on top of the probe head. The oscillator oscillates between logic states '0' and '1', resulting in rectangular pulses of 5 V amplitude at its output, which can easily be driven over long distances. At room temperature the standard deviation of level data, measured after transmission of the primary signals by about 100 meters, is less than 0.1 mm. Stability of signal output has also been satisfactory for continuous operation over eight hours each time on several days by placing the level sensor in contact with hot oil within a top loading furnace controlled at 100°C.

Long term structural integrity is ensured by partial embedment of the electrode structure within a resin, use of multiple fasteners and spacers of insulating materials within a double cylindrical probe covers of teflon and stainless steel. For mounting on the dashpots, the teflon gasket sealed carbon steel locknut arrangement will provide leak tight and stable housing. All components selected for mechanical construction are suitable for continuous operation at elevated temperatures. The rigidity of the electrode structure is adequate for withstanding the turbulence of oil pool within the dashpot during fall of the control rod on scram.

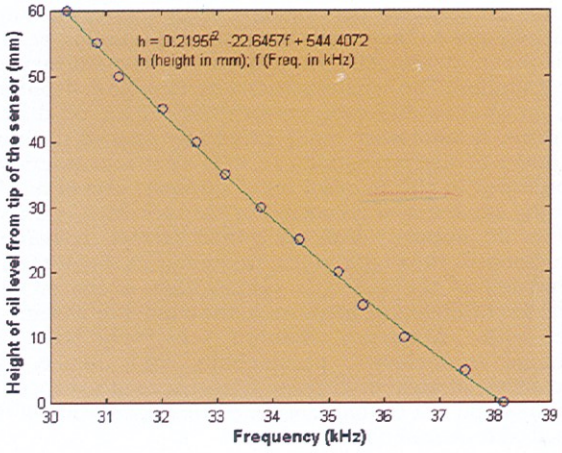

Fig. 3 : Pulse frequency to oil level relationship for a typical dashpot oil level sensor.

■ BRIEF DESCRIPTION OF THEORETICAL BACKGROUND

A set of equally spaced and vertically mounted rectangular electrodes of the specially constructed parallel plate capacitor assembly acts as the level sensor. At any level of oil within the sensing region, the gaps between the electrodes are filled partially by the oil and the rest by the gaseous medium (air or argon) above the oil level. Because of significant difference in dielectric permeability between the gaseous medium and the oil, the effective permeability, and hence the capacitance of the level sensing capacitor assembly, is a function of oil level. This assembly being the capacitive component (C) in the timing circuit of the R-C-oscillator, the time constant (R.C) varies with change in oil level and, hence, the output pulse frequency (which is proportional to 1 / RC) is thus a function of oil level.

■ ACHIEVEMENT

Besides development of the oil level sensors for a reactor as mentioned, the simplified generic approach is very effective for high precision level sensing of any non-conducting liquid. Such level sensors have also been developed to monitor CCl_4 and silicon oil levels in the process tanks of a sol-gel facility for preparation of fuel micro-spheres. This development has also paved the way for realisation of sensitive and reliable differential pressure sensors for atmosphere control applications.

■ PUBLICATIONS ARISING OUT OF THIS STUDY AND RELATED WORK

Development notes and technical brochures were prepared for restricted circulation among those concerned with instrumentation in reactors.

Further inquiries:
Shri B. Saha, Innovative Instrumentation Section
Electronics and Instrumentation Group, IGCAR, e-mail: saha@igcar.gov.in

Transformer Oil Monitoring

EXECUTIVE SUMMARY

A pulsating sensor has been developed for monitoring transformer oil degradation. The in-house developed device of new kind has been tested at CPRI, Bangaluru with a large number of service oil samples from different transformers, and compared with the conventional techniques for oil characterisation. The device qualified for its use as the rapid screening instrument by the maintenance personnel.

OUTLINE

Slow build up of oxidation products as a result of chemical reactions with oxygen and moisture from environment under the prevailing service conditions and physical ingress of polar molecules such as water cause the dielectric permeability of the service oil in any transformer to increase with time. A pulsating sensor has been developed for monitoring transformer oil degradation. The sensor is basically capable of detecting minor shift in dielectric permeability of the oil during service. A laboratory made uniformly spaced multiple number of disc type stainless steel electrode assembly, immersed in the mineral oil of interest, serves as the timing capacitor of an oscillator circuit which is driven by a dc supply. With all other factors remaining unchanged, the digital pulse frequency at the output is governed by the dielectric permeability of the oil that acts as the dielectric medium in the capacitor assembly. The pulse frequency changes sensitively with the change in dielectric permeability and, hence, the reduction in measured pulse frequency with respect to the fresh oil is a measure of dielectric degradation of the used oil during service.

The measurement set up is shown schematically in Figure 1. Frequency can be measured by any of the commercially available hand-held frequency meter. However, for a detailed study, the frequency data as a function of time can also be recorded through a PC using a laboratory developed interface hardware and software.

The digital pulse frequency data as a function of time for fresh oil as well as for a slightly degraded oil using a typical device is shown in Figure 2. Decrease in pulse frequency for the used oil corresponds to increase in the dielectric permeability by about 1.6 %. Thus, precise frequency data permits monitoring of very minute shifts in dielectric permeability, hence enabling early detection of onset and progress of degradation in the quality of service oil.

Under an MoU between IGCAR and Central Power Research Institute (CPRI), the devices made in IGCAR were tested at CPRI along with the conventional standard techniques for degradation assessment. Two hundred oil samples from power transformers of different ratings were collected and evaluated by the Dielectric Laboratory of CPRI for the standard characteristics viz., interfacial tension, neutralization value, dielectric dissipation factor, resistivity, breakdown voltage and water content following the prescribed procedures. The digital pulse frequencies were also recorded by CPRI on each sample using the pulsating sensor based oil monitoring devices. Thus, seven parameters were determined experimentally on every oil sample.

It was observed that the pulse frequency, as measured by the IGCAR devices, reduced by about seven percent for service oils nearing rejection compared to that for the fresh oil. As the devices permit precise measurement of frequency shifts less than 0.2%, onset of degradation is detectable at an early stage.

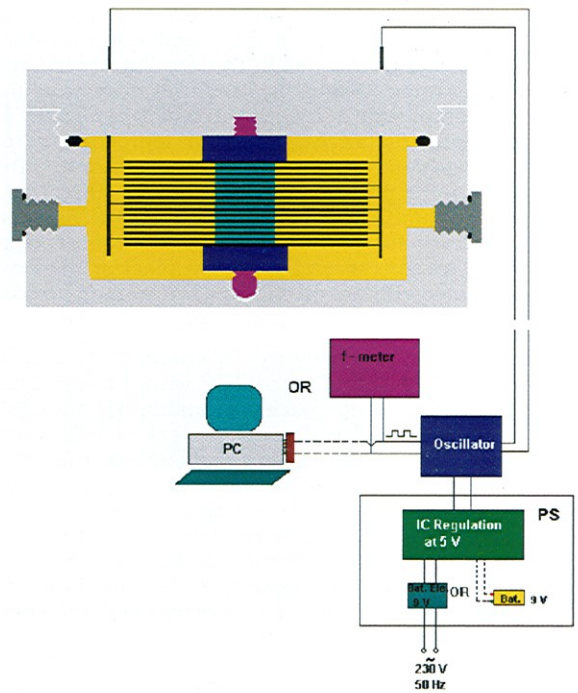

Fig 1 : Schematic representation of the oil monitoring device

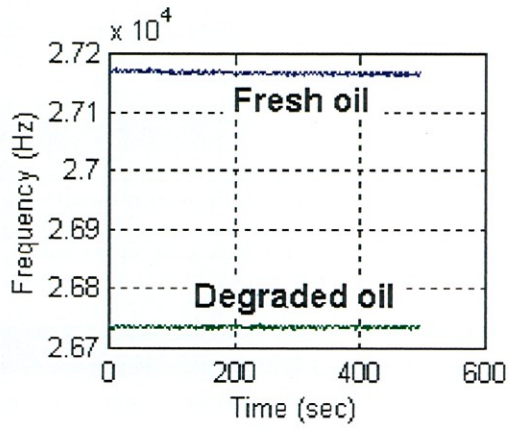

Fig. 2 : Pulse frequencies recorded as a function of time for fresh oil and a sample of service oil

■ AS A NON-DESTRUCTIVE AND RAPID OIL SCREENING DEVICE

The correlations among the conventionally determined standard parameters, ie among interfacial tension, neutralization value, dielectric dissipation factor, resistivity, breakdown voltage and water content, were comparable with those between the digital pulse frequency measured by IGCAR devices and the standard parameters. The conclusion of the joint evaluation by IGCAR and CPRI was that, as the pulsating sensor based new technique of IGCAR is simple, the transformer maintenance personnel may use it as a screening test for deciding whether the oil sample should be sent to a central laboratory for full evaluation towards further actions with respect to treatments for reuse or disposal.

■ ADAPTATION FOR ON-LINE MONITORING

Features such as (i) compact and rugged probe design, (ii) ease of pulsed digital signal generation at the probe head, (iii) noise free signal transmission, and (iv) reliable means of pulse frequency measurement with high precision, led to design and development of on-line probes.

A flange mounted prototype on-line device (Fig. 3) is in operation for over two years with an 11-kV transformer in IGCAR. Trouble free and stable field operation of the probe demonstrated usefulness of this unique product for continuous vigil on the quality of transformer oil in service.

The sensing element is a capacitor assembly which is constructed out of circular polished stainless steel discs profiled by wire cut EDM. The discs are closely spaced with uniform gaps and are electrically separated from the adjacent ones by flat teflon rings over the supporting rod.

The miniature pulse generation electronics is enclosed within a small cylindrical enclosure placed close to the sensing element and fixed on the same side of the mounting flange. A dielectric type pulsating temperature sensor is also provided close to the sensor. Thus the sensors and the associated signal generation electronics remain immersed within oil for the on-line device.

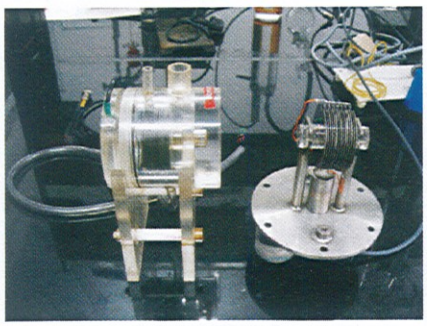

Fig. 3 : Photograph of off-line and on-line transformer oil degradation monitoring probes

■ BRIEF DESCRIPTION OF THEORETICAL BACKGROUND

Hydrocarbon molecules constituting the transformer oil experience strong electric field in presence of occluded species like oxygen and moisture. Progressive damage to the oil is on account of build-up of polar/polarisable oxygenated hydrocarbon molecules generated by electric field assisted oxidative chemical reactions. Dielectric permeability of the oil, thus, increases at a very slow rate. The capacitance of a device, with such oil as the dielectric medium, is a function of the extent of contamination. Hence, the pulse frequency at the output of an oscillator, configured with this capacitor in the timing circuit, decreases as the oil quality deteriorates.

■ ACHIEVEMENT

1) New kind of inexpensive devices for off-line and on-line monitoring of transformer oil.
2) Realisation of a field monitoring kit for rapid and non-destructive assay of ethanol in petrol (as a spin-off)

Further inquiries:
Shri B. Saha, Innovative Instrumentation Section
Electronics and Instrumentation Group, IGCAR, E-mail: saha@igcar.gov.in

An Indigenous Device for Water Film Thickness Monitoring

EXECUTIVE SUMMARY

In-house developed unique pulsating type position and conductance sensors were integrated for development of a device for determination of water film thickness. The device was deployed for rapid measurement of variation in film thickness across falling water layer sliding along a weir crest at different flow rates towards optimisation of conditions for avoidance of flow separation. Measurements were needed in a water simulated facility to test the weir crest design of the thermal baffle located inside the main reactor vessel of PFBR. Construction and operational details of the horizontally mountable device for this application are described.

OUTLINE

Film thicknesses were determined by configuring a laboratory made pulsating position sensor that enabled measurement of linear displacement of a horizontally mounted thin moving rod perpendicular to the vertically falling water surface. A pair of tiny electrodes as conductance sensor, mounted aboard the moving rod at its tip, projecting in the direction of the rod, sensed air-water interface in front as well as the water-solid surface interface behind the film. The displacement during movement of the rod from one interface to the other is the measure of water film thickness. The device is shown schematically in Figure 1.

The other end of the rod was fixed to a cylindrical ferrite core which is partially placed within an inductor coil, and the linear movement was effected manually by turning slowly a teflon screw head, the non-threaded end of which pushed the ferrite core and remained always in contact with it by action of a spring. The inductor was part of an oscillator circuit, the output of which was a train of pulses with frequency at any instant was determined by the position of the ferrite core and hence that of the tip of the rod. Shift in pulse frequency was calibrated appropriately against independently measured displacements prior to deployment of the device.

The pair of closely placed electrodes for conductance sensing at the tip of the bar was again a part of another oscillator of different kind, the output pulse frequency of which was governed by the conductance offered by the medium that was in contact with the electrodes at a given moment. Initially, during measurement, as the tip approaches the water film from air space, the pulse frequency is nearly zero. Frequency jumps as soon as the tip touches the air-water interface. The design of the sensor was such that, thereafter, it increased with progressive movement towards a value determined by the conductivity of water. The device had a 0.1 mm thick stainless steel sheet fixed to the ends of its three legs, which is pressed firmly against the solid surface, resulting in the film flowing over the sheet in a small region. Conductance, and hence the pulse frequency, increased sharply when, on further advance of the tip, the electrodes touched the stainless steel surface at the other end of the film. With no further movement in the forward direction being possible, the pulse frequencies in both conductance and position channels attained upper limiting values. Likewise, during retraction, the air-water interface was trapped again by sudden fall of pulse frequency to near zero in the conductance monitoring channel.

The device made use of laboratory made conductance and position sensors. Oscillators were designed to provide rectangular pulses of 5V amplitude. The pulses were fed directly to a personal computer through its parallel port and were recognised and counted simultaneously for a given duration under software control for determination of pulse frequencies. The pulse frequencies as a function of time were displayed graphically in real time for both conductance and position monitoring channels in two separate windows. Response in both these channels for three cycles of forward and reverse movements, as acquired and viewed on-line, is shown in Figure 2.

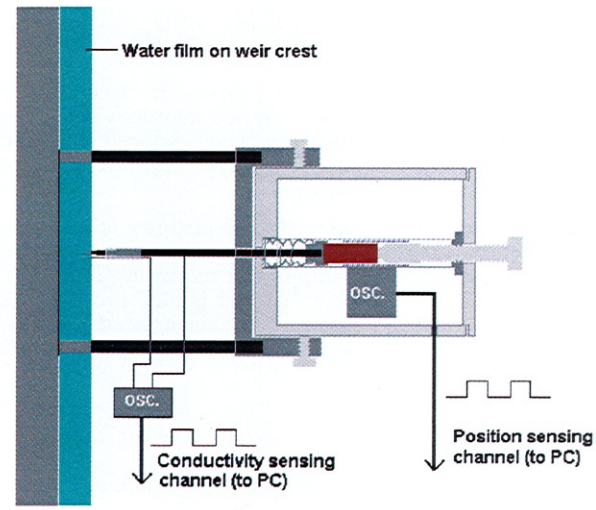

Fig 1 : Schematic representation of the laboratory made water film thickness measurement device

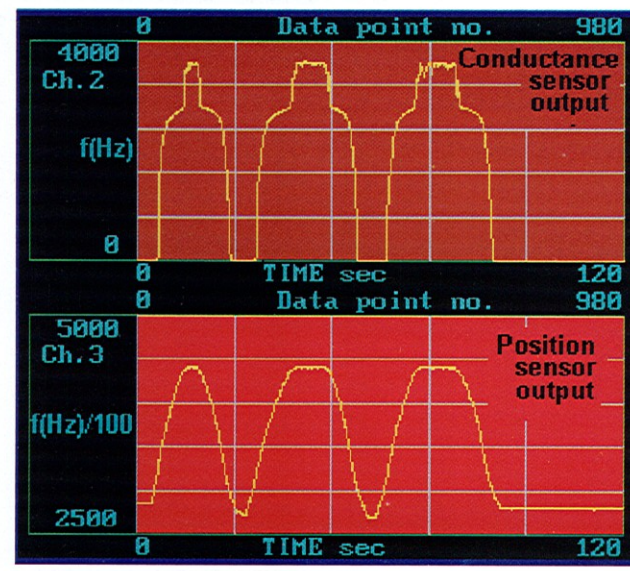

Fig. 2 : Pulse frequency data as functions of time from conductance and position sensing channels in separate graphic windows, as viewed in real time during measurement

■ PERFORMANCE OF THE DEVICE

The device was designed for measurement of thickness of the film in the range 0 – 10 mm. Inherent standard deviation of 0.3 mm for was largely due to small ripples introduced by the hand-held dynamic device in addition to unavoidable factors such as surface tension that manifests when the conductance sensing electrode tips touch or leave the air-water interface.

■ EXTRACTION OF WATER FILM THICKNESS DATA

The difference in measured pulse frequencies in position monitoring channel, between the upper limiting value, corresponding to the steel-water interface, and that at the instant of sharp change in conductance as the rod enters or leaves the air-water interface, provided data on displacement from one interface to the other and, hence, the film thickness. Thickness data in duplicate was obtained in one cycle of forward and reverse movement. Three such cycles were repeated in succession at a given location and flow rate. The film thickness values are thus average of six data in each case. The manner by which the change in frequency in the position sensing channel corresponding to film thickness was derived is further depicted in the Figure 3 by presenting the data from both the channels together. Movement of the rod between two interfaces across the film thickness is derived from the frequency shift to displacement relationship established prior to measurement.

The vertical lines correspond to onset or disappearance of conductance signal. The points of intersections with the position sensor output plot give the pulse frequencies corresponding to the position of the tip at air-water interface, with the mean value depicted by the lower horizontal line. The frequency shift from the upper horizontal line, the water-solid surface interface, provides data on displacement of the tip between the interfaces and, thereby, the film thickness.

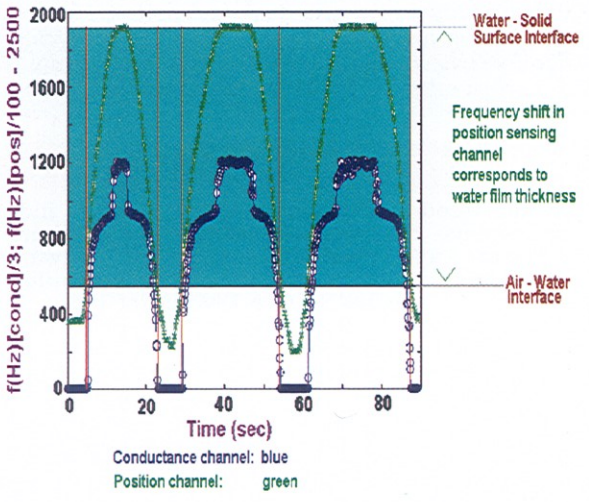

Fig. 3 : Time dependent pulse frequency data from position and conductance monitoring channels during forward and reverse movements of the rod in three cycles

■ BASIC APPROACH TO SENSING

Position sensing is realised through partial positioning of a ferrite rod within an inductor coil. The inductor is placed in the timing circuit of a specially designed miniature R-C-L oscillator with fixed R and C. The digital pulse frequency at the output changes as the inductance (L) offered by the coil varies sensitively with the movement of ferrite rod. Likewise, an electrode pair is placed in the timing circuit of an appropriately designed R-C oscillator with fixed C to measure conductance. The output digital pulse frequency changes as the conductance (1/R) varies. Similarity in approach to the directly measurable primary signal and absence of any signal conditioning hardware led to development of the compact device for water film thickness monitoring.

■ ACHIEVEMENT

The device has been used successfully for an important application as mentioned above. Designers of the weir crest could experimentally determine the drag coefficient. The device design is of generic nature and can be adopted for thickness monitoring of any conducting liquid film or solid layer, with much better precision for the latter. There is also a definite scope for total automation, if needed.

■ PUBLICATIONS ARISING OUT OF THIS STUDY AND RELATED WORK

K. Veluswamy, G.R. Ravi Prasan, M.P. Pradeep, P. Sahoo, P. Selvaraj, P. Chellapandi and B. Saha,Design note Report No. PFBR/31260/DN/1007/Rev.A (2004).

Further inquiries:
Shri B. Saha, Innovative Instrumentation Section
Electronics and Instrumentation Group, IGCAR, e-mail: saha@igcar.gov.in

Embedded Design Simplifies Experimental Automation

EXECUTIVE SUMMARY

The advancement in solid state technology to function in all possible environmental conditions provides a clear pathway for innovation in research and development. The programmable embedded design plays a major role in modern technological development. Visualization and implementation of required interface design with the intelligent programmable embedded components like FPGA, ASIC, DSP, PSoC, microcontrollers, etc. provides an easy means of user-friendly design automation. Generally, for any laboratory as well as industrial automation, the tasks required for automation are sensing and controlling physical variables like position, temperature, pressure, flow, etc. This page describes how the embedded design and virtual instrument software simplifies experimental automation using PCs through its standard interfacing technique.

OUTLINE

Recent trend in laboratory as well as in industrial equipments designs are coming up with minimal hardware and maximal support of software. An inexpensive embedded Raman spectrometer automation system at Materials Science Division of Indira Gandhi Centre for Atomic Research, Kalpakkam, built with a single Programmable System On-Chip (PSoC), a Cypress Micro system's mixed array microcontroller, is described, which allows the on-line acquisition of Raman spectroscopic data and the control of the spectrometer operation, uses PC as a window based graphical user interface (GUI). The menu driven user-friendly software in virtual instrument (VI) control program written in LabVIEW ver.7.1, a graphical language, interacts with the embedded single chip design for the total automation of the experiment. The system design in a single chip can be programmed for any automation requirements of other spectroscopic techniques by appropriately programming the PSoC chip and providing the user required virtual instrument menu driven control software.

The user friendly menu driven virtual instrument program interacts with the embedded PSoC design through its serial interface. Fig.3. shows the menu driven user-friendly virtual instrument program front panel diagram of PSoC-Raman spectrometer automation. The on-line graph of the sample zinc cyanide, $Zr(CN)_2$, acquired for the preset time of 5 seconds with stating wave number 2200 cm^{-1} and final wave number 2240 cm^{-1} in step of 0.5 cm^{-1} has been seen in the Fig.3. The menu driven GUI program has the facilities like (i) storing the data in the user specified file path, (ii) loading the previous spectrum form the user file path, (iii) automatically configure the initial, final and step wave number on the graph immediately after the user entry, (iv) print spectrum, (v) clear spectrum and (vi) functioning as a rate meter for initial setting up of the laser intensity, slit widths, etc, in the spectrometer. The panel diagram includes user variable parameters like sample name, laser power, wave length, slits information as a user file for proper documentation of the experiment. A novel and cost effective embedded design automation of Raman spectrometer setup using a single Programmable System on Chip (PSoC), interfaced with PC and controlled by the virtual instrument program provides wider range of counting and preset time and works under window environment of PC.

In PSoC, the main advantage is, one can program the choice of user required function module, say enhancing the counting facility more by using the "interrupt on terminal count" and reloading the counter and start counting again. By invoking the interrupt whenever the counter reaches terminal count and register it as carry bit, enhances the counting ability to more than its capacity say 64k counts. This design approach finds potential application in laboratories and industries for event counting applications. This way the designer tools are playing vital role in programming the user module and interaction with built-in M8C microcontroller. For UART communication, any baud rate clock can be generated with PSoC as per the designer requirement.

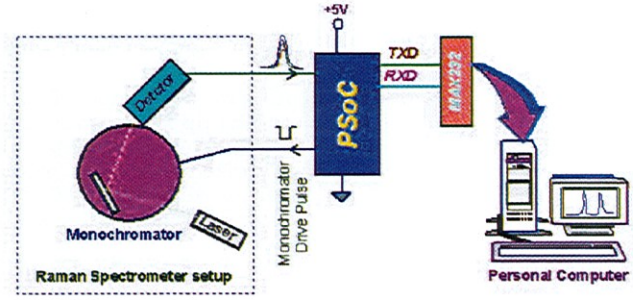

Fig 1 : Block diagram of Raman spectrometer experimental setup

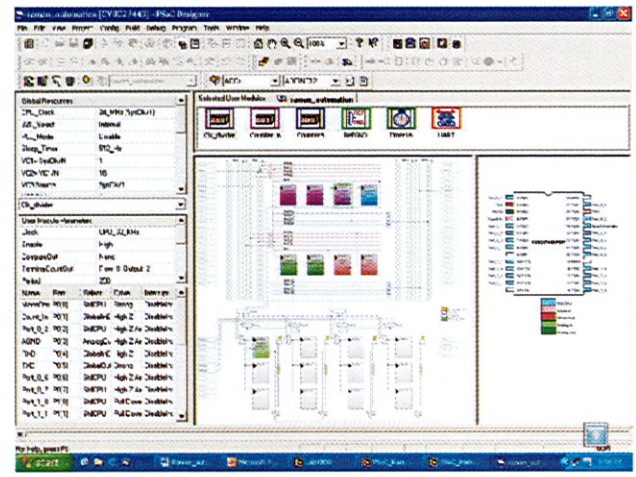

Fig. 2 : Virtual instrument program panel diagram for PSoC - Raman spectrometer automation design

■ SINGLE CHIP PSoC EMBEDDED DESIGN

A single PSoC device can integrate as many as 100 peripheral functions with a microcontroller, saving customers design time, board space, power consumption. Easy-to-use development tools enable designers to select the precise peripheral functionality they desire, including: Analog functions (amplifiers, ADCs, DACs, filters and comparators) and Digital functions (timers, counters, PWMs, SPI and UARTs). PSoC family's analog features include: rail-to-rail inputs, programmable gain amplifiers and up to 14-bit ADCs with exceptionally low noise, input leakage, voltage offset. PSoC devices include: up to 32 KB of flash memory, 2 KB of SRAM, an 8x8 multiplier with 32-bit accumulator, power and sleep monitoring circuits, hardware 12C communications.

■ EXPERIMENTAL AUTOMATION DESIGN DESCRIPTION

From the PSoC designer screen, the placed user modules like 16 bit counter, timer, clock circuit for serial communication baud rate generation, UART for serial communication, reference ground in the analog block for ground isolation, for Raman spectrometer automation can be easily identified. After that the editor screen in the PSoC designer helps the designer to configure their automation sequence i.e, functionality of the user modules as well as the functional interaction between the user modules, through the compiler (assembler or 'C') in the editor screen of the designer tool. The in-circuit emulator permits the design to interact with the actual experimental setup and test the functionality of the embedded design in an actual environment. After confirming the program sequence, the blank PSoC chip can be programmed and used for the actual requirement.

Using PSoC designer tool, a blank PSoC chip has been programmed to count the detector pulses for the user preset time and controls the monochromator motor drive to move to the next user required wave number position. The count pulses have been transferred to PC memory through serial port. A 16-bit counter and a timer has been designed within the PSoC chip for counting the detector pulses from Raman setup for the user defined preset time. Interrupt handler routine in PSoC editor program, enables wider range of counting above 64K and preset time from milli-seconds to several hours, but uses only 16-bit counter/ timer functions, by using interrupts through PSoC editor program written in 'C' compiler.

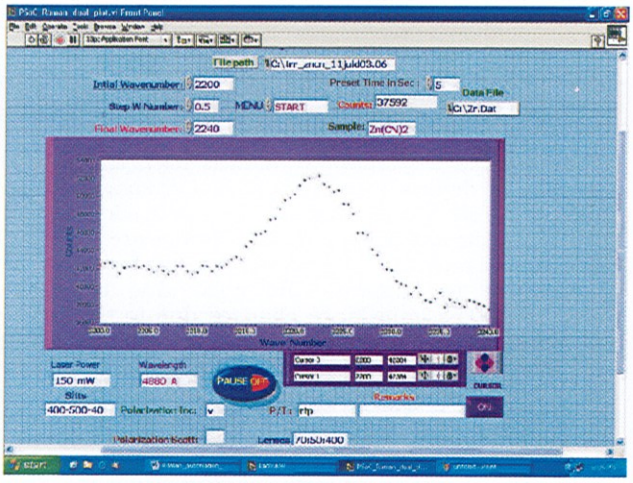

Fig. 3 : Virtual instrument program panel diagram for PSoC -Raman spectrometer automation design

■ BRIEF DESCRIPTION OF THEORETICAL BACKGROUND

Raman spectroscopy is a light scattering technique, in which a photon of light interacts with a sample to produce scattered radiation of different energies. It can be used for applications as wide ranging as chemical identification, characterization of molecular structures, effects of bonding, environment and stress on a sample. Raman spectrometers measure the energy and intensity of inelastically scattered light from the vibrations of the molecules in the substance through which light passes. This vibration scatters the light and changes its energy from that of the incident light. The difference in energy between the incident photon and the Raman scattered photon is equal to the energy of a vibration of the scattering molecule. A plot of intensity of scattered light as a function of energy difference is a Raman spectrum.

■ ACHIEVEMENT

This single chip embedded design automation provides unlimited wider range of counting and preset time and works under window environment of PC. This indigenous design automation consumes less power and permits any future enhancement of design possible in the same PSoC chip, since it is a flash memory programmable embedded silicon technology. USB port interfacing standard of this design permits easy to connect any brand new PCs.

■ PUBLICATIONS ARISING OUT OF THIS STUDY AND RELATED WORK

1. J.Jayapandian, Application Note AN2374. Cypress Micro system. WA. 18th July 2006.
2. J.Jayapandian, R.Kesavamoorthy and A.K.Arora, NSI-31, Oct. 2006, Gwalior.

Further inquiries:
Shri J.Jayapandian, Materials Science Division
Metallurgy and Materials Group, IGCAR, e-mail: jjp@igcar.gov.in

Eigen Vector based Approach for Enhancement of Non-destructive Evaluation Images of Defects

■ EXECUTIVE SUMMARY

Eigen vector based approach is developed for enhancement of non-destructive evaluation (NDE) images of defects in carbon steel plates. Eddy current and magnetic flux leakage (MLF) images obtained by raster scanning of eddy current (EC) coil and giant magneto-resistive (GMR) sensor, respectively are influenced by variations in magnetic permeability, surface roughness and lift-off. These variations produce incoherent noise as compared to systematic impedance change or leakage flux variations produced by defects. Eigen pairs of image covariance matrix are determined and the significant Eigen pairs that have the maximum information of defects are utilized to suppress noise due to disturbing variables and to reconstruct images. This approach has resulted in a significant improvement in signal to noise ratio (SNR) and looks attractive for reliable detection of shallow fatigue cracks as well as deep-surface defects in carbon steels.

■ OUTLINE

Non-destructive evaluation (NDE) is used for detection and imaging of defects in materials. In ferromagnetic materials such as carbon steel, impedance change in eddy current probe due to defects and permeability variations are usually of same phase angle and this makes even the multi-frequency methods inadequate to suppress the noise due to permeability variations. The impedance changes due to the permeability variations are incoherent whereas the impedance changes due to defects extend spatially depending on the foot-print of the eddy current probe used. Similarly, the magnetic leakage flux from deep-surface defects is feeble and contains undesirable and incoherent noise from variations in magnetic permeability, surface roughness and stress. Utilising the incoherent nature of noise, an innovative approach based on Eigen value and Eigen vector (Eigen pair) has been developed. In this approach, the energy packing property of the Eigen values is effectively utilized to suppress incoherent noise and to reconstruct images. This approach involves determination of Eigen pairs of image covariance matrix and reconstruction of images after considering the significant Eigen pairs having the maximum information of the defects. The insignificant Eigen pairs mostly represent the incoherent noise due to permeability variations are ignored in the reconstruction during the inverse transform. The performance of the approach is assessed on eddy current images of surface defects in 25 mm thick carbon steel plate and on MFL images of deep-surface defects in 12 mm thick carbon steel plates.

A carbon steel plate (thickness 25 mm) consisting of a 2.5 mm diameter hole is used in the studies. Using a 3.5 mm diameter surface absolute eddy current probe, images of 2.5 mm diameter hole (depth 0.25 mm) and a notch (length 10 mm, width 0.5 mm, and depth 0.5 mm) are obtained at an excitation frequency of 50 kHz. Using a C-core electromagnet (4A current) and high-sensitive GMR sensor, MFL images of notches (length 15 mm, width 0.5 mm) located at 3.1 mm, 6.3 mm and 8.6 mm below the surface of 12 mm thick carbon steel plates are obtained. The EC and MFL images are used for validation of the approach.

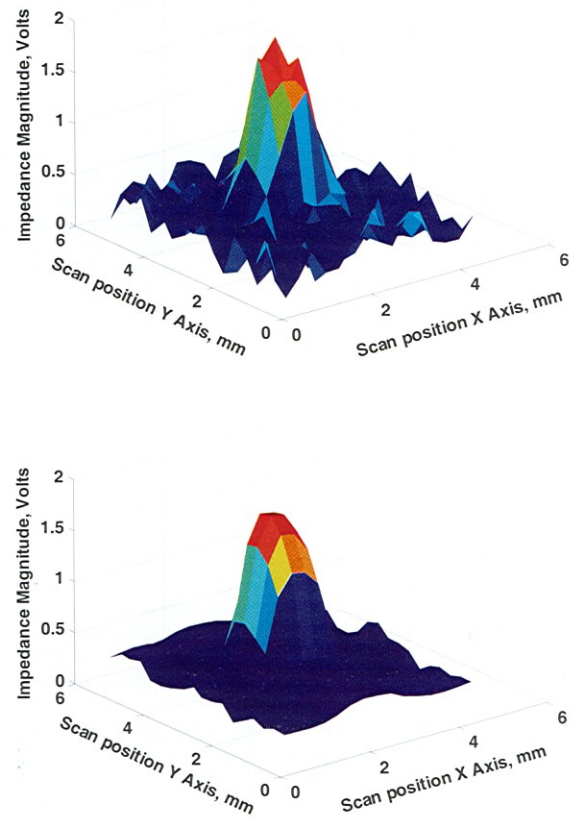

Fig. 1: Raw eddy current image of a 0.25 mm deep hole in carbon steel plate (up) and the image after reconstruction after taking the most significant Eigen value (down)

■ ADDITIONAL INFORMATION ON THE VALIDATION OF THE APPROACH

Typical EC raw image of 0.25 mm deep hole and the reconstructed image are shown in Fig. 1. The MFL images of deep-surface notch located at 8.6 mm below surface and that of 1.1 mm deep surface-breaking notch are shown in Fig. 2 along with the reconstructed images by the Eigen vector approach. As can be observed, there is a significant enhancement in the quality of EC and MFL images after processing. The quality of reconstruction has been assessed by determining an empirical parameter called, noise reduction factor (NRF) which is ratio of average noise amplitude in a defect-free region in a raw image to that of the same region in reconstructed image. The NRF is found to be high when the most significant Eigen pair is used for reconstruction. However, when more Eigen pairs are included in the reconstruction, NRF is found to decrease. This is due to the fact that the smaller Eigen pairs which contain the incoherent noise information of magnetic permeability variations contribute to the reconstruction process resulting in image degradation.

GENERAL EXPLANATION RELATED TO THE DESCRIPTION

A significant improvement in signal-to-noise ratio (SNR) is observed after processing, as given in Table 1. This approach is very attractive for processing NDE images affected by incoherent noise due to local variations in material properties, coupling etc. and particularly useful for processing images from regions in operating components for detection of very shallow and incipient fatigue cracks that disturb structural integrity.

Notches	SNR		
	Raw	Processed	Enhancement factor
Near-side notch (1.1 mm deep)	2.04	6.25	3.06
Far-side notch located below 3.1 mm surface	9.45	15.92	1.68
Far-side notch located below 6.3 mm surface	6.85	11.13	1.64
Far-side notch located below 8.6 mm surface	3.52	5.64	1.60

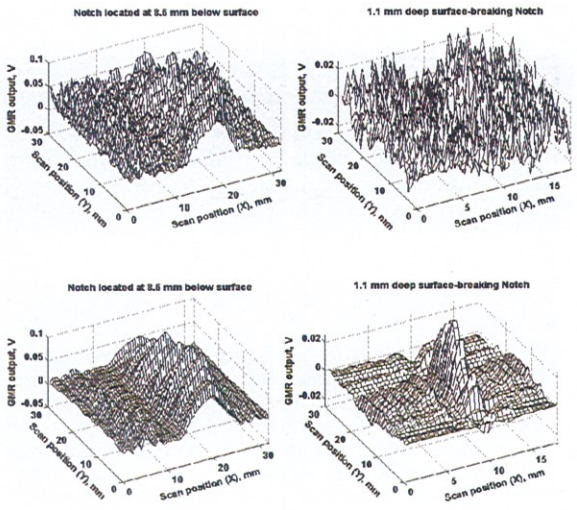

Fig. 2 : Raw (top) and processed (bottom) MFL images of a notch located 8.6 mm below surface and a 1.1 mm deep surface-breaking notch in carbon steel plates

BRIEF DESCRIPTION OF THEORETICAL BACKGROUND

Eigen values are a special set of scalars associated with a linear system of equations (i.e., a matrix) that are sometimes also known as characteristic roots or characteristic values. Eigen values and Eigen vectors are determined by Eigen decomposition of a square matrix and represent the energy content of a system. The Eigen vectors of image covariance matrix form an orthonormal set of vectors which are used as kernels to transform the original image matrix to variance domain where the significant Eigen values and the associated Eigen vectors point in the direction of maximum variance of the image data set. This transformation is popularly known as Karhunen Loeve Transform (KLT). It is a linear transform used to represent a dataset with a new set of basis functions such that the greatest variance by any projection of the data set lies on the principal axis and is also invertible. The basis vectors unlike other linear transforms (cosine or sine transforms) are derived from the original data set itself. Forward and inverse KLT necessary for this approach is implemented using MATLAB software. In the proposed approach, the energy packing property of the Eigen values is effectively utilized to reconstruct images free from noise due to permeability variations. In NDE, so far this kind of approach has been predominantly used to arrive at an optimal set of features from a set of signals for quantification using artificial intelligent schemes. However, the proposed approach is developed and applied to suppress noise due to magnetic permeability variations in eddy current and flux leakage images of defects.

ACHIEVEMENT

Eigen value based approach has been able to suppress incoherent noise due to magnetic permeability variations in eddy current and MFL images of defects. This approach has enabled reliable detection of deep-surface notch located at 8.6 mm below surface. This approach can also be applied to other ferromagnetic materials and also to other types of NDE images. This approach looks very attractive for detection of feeble signal producing defects such as shallow fatigue cracks as well as deep-surface defects in ferromagnetic steels. Further, the reconstructed images can be used as input images for artificial intelligent schemes for quantitative characterization of defects.

PUBLICATIONS ARISING OUT OF THIS STUDY AND RELATED WORK

1. P. Kalyanasundaram, S. Thirunavakkarasu, B.P.C. Rao, T. Jayakumar and Baldev Raj, *J. of Research in NDE*, **18** (2007) 13.
2. B.P.C. Rao, S. Thirunavukkarasu, K. Krishna Nand, T. Jayakumar, P. Kalyanasundaram and Baldev Raj, *Non Destructive Testing and Evaluation*, **23** (2007) 35.

Further inquiries:
Dr. B.P.C. Rao, Non Destructive Evaluation Division
Metallurgy and Materials Group, IGCAR, e-mail: bpcrao@igcar.gov.in

Fabrication of Electrochemical Oxygen Sensor for use in Sodium

EXECUTIVE SUMMARY

Development of yttria doped thoria (YDT) solid electrolyte material for its use as electrochemical oxygen sensor for liquid sodium has been carried out in collaboration with CGCRI, Kolkata. Ceramic thimbles of dimensions 25 mm long, 7 mm outer diameter and 1.5 mm wall thickness with 99% of the theoretical density were prepared. Oxygen sensors have been fabricated wherein these YDT thimbles were soldered to low expansion FeNi48 alloy using a suitable glass sealant.

OUTLINE

Yttria doped thoria (YDT), an oxide ion conducting solid electrolyte, which, has been identified as the most suitable materials for monitoring oxygen concentration in liquid sodium coolant of fast breeder reactors. This material is used as a tube or a thimble form for oxygen sensing applications. The powders of this electrolyte are shaped into a suitable form followed by sintering at elevated temperatures to yield an impervious product with helium leak rate < 10^{-9} std. l/s to enable its use in molten sodium. There are no local manufacturers of this item; neither it is available to us due to embargo restrictions.

When the ceramic forms are produced from YDT powders prepared by conventional solid state method, sintering at high temperatures (ca. 2273 K) is needed to meet the required specification. An associated problem with sintering at these high temperatures is grain growth, which, results in poor mechanical strength of the sintered product. In addition to these problems, the technology of making impervious YDT bodies is not available in open literature.

To overcome the problems encountered in the high temperature process, it is important to synthesize YDT in nanocrystalline form enabling the compacts to be sintered at lower temperatures. To achieve this goal, a novel combustion synthesis method has been developed, whose flow sheet is shown in Fig. 1, using ethylene glycol and citric acid as the gelling agents. Using this method, it has been possible to synthesise nanocrystalline YDT powders with average crystallite size of 15 nm.

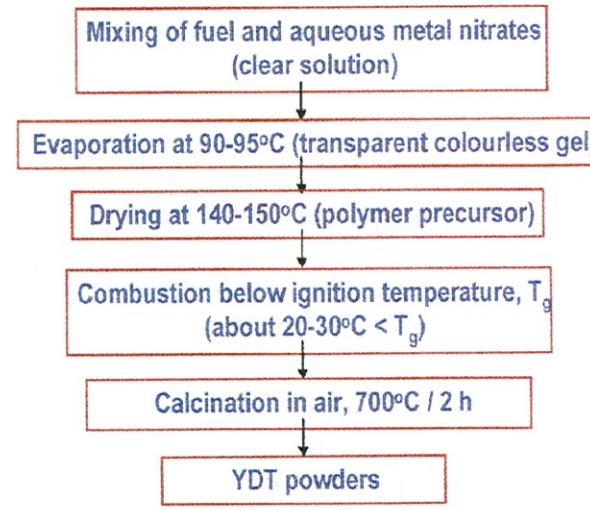

Fig. 1 : Flow chart depicting the synthesis of YDT powder by novel combustion method

The same flow sheet was used to scale-up the synthesis of this powder in batches of 50 grams. For the synthesis of electrolytic grade YDT powders, the transition metal impurities that would present in the commercially available thorium nitrate need to be eliminated. For this purpose, thorium was precipitated as oxalate first. Thorium oxalate was then washed thoroughly using hot water, dried and converted to oxide by heating it in air at 973 K for 2 h. The oxide product was analyzed for its iron, chromium and zinc content and were found to be below 20 ppm. Thoria powder thus prepared and yttrium nitrate with very low transition metal impurities were used in the synthesis of YDT by the combustion method. At each processing step, the purity of the product was checked.

Either polyvinyl alcohol as binder or ZnO as the sintering aid were added to the YDT powders prepared by the combustion technique to obtain high-density sintered product. Results of the experiments showed that high density YDT products (> 99% of theoretical density) that meet the required low helium leak rate of the order of ~ 10^{-9} std. l/s were obtained when ZnO was the additive and the sintering temperature was 1923 K. The sintered products, whose scanning electron micrograph is shown in Fig.2, have an average grain size of 0.5 μ.

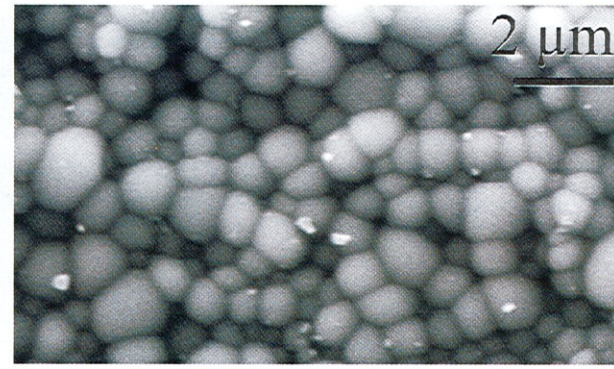

Fig. 2 : Scanning electron micrograph of YDT pellet sample sintered at 1923 K using ZnO sintering aid

YDT thimbles of dimensions 25 mm long, 7 mm outer diameter and 1.5 mm wall thickness were fabricated using this optimized procedure in collaboration with CGCRI, Kolkata. For this purpose, the powders were pressed in the form of rods by cold isostatic press, machined and sintered.

■ ADDITIONAL INFORMATION ABOUT YTTRIA DOPED THORIA

Thoria crystallizes in cubic form and shows electronic conductivity at very high temperatures. By substituting certain lower valent cations in thoria, oxide ion vacancies can be created, thereby the oxide ion conductivity can be enhanced. When thoria is doped with 7.5 % of yttria, maximum oxide ion conductivity has been identified. This composition is the candidate material for use in liquid metal system as its lower electrolytic domain boundary is 10^{-40} atm of oxygen at ~ 723 K. But, this solid electrolyte has poor thermal shock resistance and mechanical strength. Thus, posing a technological challenge to use this material in liquid sodium systems wherein large numbers of thermal cycling are anticipated.

■ ASSEMBLING OF SENSORS USING YDT BODIES

The general problem in using a long tube (~ 150 mm normally) of YDT as sensor in liquid sodium is that it will experience a large temperature gradient along its length during its in-sodium service, which could lead to its failure. However, by using a thimble of 25 mm long and completely immersing it into sodium, the life-time of the oxygen sensor can be enhanced.

To make a sensor using the YDT thimble, it needs to be attached to a metallic component using a sealing agent, which has adequate thermal expansion properties compared to that of YDT and the metallic part. The sealing agent should also be compatible with liquid sodium at the sensor operating temperature.

Fermi alloy (Ni – 50%, Fe – 48 % & Cr – 2%) was found to have matching thermal expansion coefficient with YDT. This alloy was prepared, forged in the form of rods and machined to the dimensions needed for sensor assembly. From detailed literature studies, the suitable glass composition was identified and prepared. Its compatibility with liquid sodium was also studied. In collaboration with CGCRI, Kolkata, the glass sealing conditions were optimized so that the seal exhibits helium leak rate below 10^{-9} std. l/s.

Figure 3 shows the schematics of the sealing of YDT thimble with Ferni alloy using the glass.

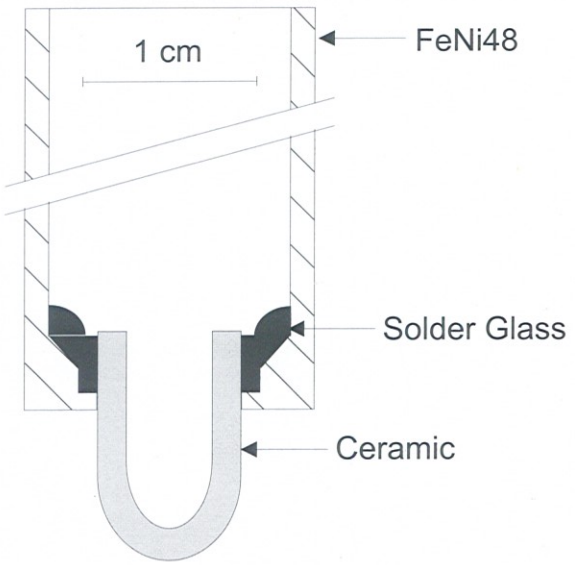

Fig. 3 : Schematics of YDT sealing with Ferni alloy component

■ BASIC APPROACH TO SENSING

Solid electrolyte for use in thermochemical / kinetic studies should exhibit a transport number of 0.99 for the ion of interest and should show negligibly low contribution from electronic carriers. Nernstian behaviour of the device will be observed only under these conditions which can be met when the oxygen pressures are within the electrolytic domain boundaries. Since equilibrium oxygen pressures encountered in liquid sodium circuits are very low and zirconia based electrolytes are not chemically compatible with liquid sodium at the sensor operating temperatures of ca.723 K, only YDT can be utilized for oxygen sensing in sodium coolant circuits.

■ ACHIEVEMENT

Solid electrolyte grade yttria doped thoria, with fine grain microstructure has been fabricated in the form of thimbles. By using a suitable glass, these thimbles could be sealed to the low expansion FeNi48 alloy with the seals exhibiting very low leak rates (helium leak rate < 10^{-9} std. l/s).

■ PUBLICATIONS ARISING OUT OF THIS STUDY AND RELATED WORK

1. Rajesh Ganesan, S. Vivekanandhan, T. Gnanasekaran, G. Periaswami, Raman S. Srinivasa, *J. Nucl. Mater.* **325** (2004) 134.
2. V. Jayaraman, D. Krishnamurthy, Rajesh Ganesan, A. Thiruvengadasami, R. Sudha, M.V.R. Prasad and T. Gnanasekaran, *Ionics* (In Press).

Further inquiries:
Dr. T. Gnanasekaran, Liquid Metals and Structural Chemistry Division
Chemistry Group, IGCAR, e-mail: gnani@igcar.gov.in